

# UC San Diego

## UC San Diego Electronic Theses and Dissertations

### Title

NONLINEAR FINITE ELEMENT MODEL UPDATING FOR NONLINEAR SYSTEM AND DAMAGE IDENTIFICATION OF CIVIL STRUCTURES

### Permalink

<https://escholarship.org/uc/item/62r7p58r>

### Author

Ebrahimian, Hamed

### Publication Date

2015

Peer reviewed|Thesis/dissertation

UNIVERSITY OF CALIFORNIA, SAN DIEGO

**NONLINEAR FINITE ELEMENT MODEL UPDATING FOR  
NONLINEAR SYSTEM AND DAMAGE IDENTIFICATION OF  
CIVIL STRUCTURES**

A dissertation submitted in partial satisfaction of the requirements for the degree

Doctor of Philosophy

in

Structural Engineering

by

Hamed Ebrahimian

Committee in charge:

Professor Joel P. Conte, Chair  
Professor Robert R. Bitmead  
Professor Raymond A. de Callafon  
Professor Gilberto Mosqueda  
Professor Benson P. Shing

2015

Copyright

Hamed Ebrahimián, 2015

All rights reserved.

The dissertation of Hamed Ebrahimiyan is approved, and it is acceptable in quality and form for publication on microfilm and electronically:

---

---

---

---

---

Chair

University of California, San Diego

2015

# **DEDICATION**

To my Family.

## EPIGRAPH

**Oogway:** My friend, the panda will never fulfill his destiny, nor you yours, until you *let go of the illusion of control.*

**Shifu:** Illusion?

**Oogway:** Yes. Look at this tree, Shifu. I cannot make it blossom when it suits me, nor make it bear fruit before it's time.

**Shifu:** But there are things we can control. [Kicks the tree causing several peaches to fall] I can control when the fruit will fall. [One peach hits him on the head. Oogway chuckles] And I can control... [Tosses the peach in the air and chops it in half] ...where to plant the seed. [Punches a hole in the ground and catches the seed] That is no illusion, Master. [Throws the seed into the hole]

**Oogway:** Ah, yes. But no matter what you do, that seed will grow to be a peach tree. You may wish for an apple or an orange, but you will get a peach.

**Shifu:** But a peach cannot defeat Tai Lung!

**Oogway:** Maybe it can. [Covers the seed in dirt] *If you are willing to guide it. To nurture it. To believe in it.*

**Shifu:** But how? How? I need your help, master.

**Oogway:** No. *You just need to believe.* Promise me, Shifu. Promise me you will believe.

This conversation is a part of Kung Fu Panda\* movie.

(\*) *Kung Fu Panda*, Directed by John Stevenson and Mark Osborne, Written by Jonathan Aibel and Glenn Berger, DreamWorks Animation, 2008.

# TABLE OF CONTENTS

<b>SIGNATURE PAGE .....</b>	<b>iii</b>
<b>DEDICATION .....</b>	<b>iv</b>
<b>EPIGRAPH .....</b>	<b>v</b>
<b>TABLE OF CONTENTS.....</b>	<b>vi</b>
<b>LIST OF FIGURES.....</b>	<b>x</b>
<b>LIST OF TABLES.....</b>	<b>xviii</b>
<b>ACKNOWLEDGMENTS.....</b>	<b>xx</b>
<b>VITA .....</b>	<b>xxiv</b>
<b>ABSTRACT OF THE DISSERTATION .....</b>	<b>xxv</b>
<b>CHAPTER 1: INTRODUCTION .....</b>	<b>1</b>
1.1.    STRUCTURAL HEALTH MONITORING.....	1
1.2.    STRUCTURAL HEALTH MONITORING BASED ON NONLINEAR SYSTEM AND DAMAGE IDENTIFICATION.....	4
1.3.    NONLINEAR SYSTEM AND DAMAGE IDENTIFICATION BASED ON NONLINEAR FINITE ELEMENT MODEL UPDATING .....	6
1.4.    RESEARCH OBJECTIVES AND SCOPES.....	7
1.5.    DISSERTATION OUTLINE.....	9
REFERENCES.....	16
<b>CHAPTER 2: EXPERIMENTAL-ANALYTICAL CORRELATION STUDY OF THE BEHAVIOR OF REINFORCED CONCRETE COMPONENTS AND SUB- ASSEMBLIES USING STRUCTURAL FINITE ELEMENTS AND SMEARED CRACK APPROACH .....</b>	<b>17</b>
2.1.    INTRODUCTION .....	17
2.2.    CONCRETE MATERIAL CONSTITUTIVE MODEL.....	22
2.2.1. Background.....	22
2.2.2. Employed constitutive model .....	26
2.2.3. Uni-axial tensile behavior.....	26
2.2.4. Uni-axial compressive behavior .....	28
2.2.5. Total strain-based rotating crack formulation.....	31

2.3.	STEEL MATERIAL CONSTITUTIVE MODEL .....	34
2.3.1.	Giuffré-Menegotto-Pinto model .....	34
2.3.2.	Experimental validation of the proposed steel model .....	37
2.4.	INCREMENTAL-ITERATIVE NONLINEAR ANALYSIS .....	38
2.5.	EXPERIMENTAL-NUMERICAL CORRELATION STUDIES .....	39
2.5.1.	Cantilever RC beam component tested by Popov et al.....	39
2.5.2.	Beam-column joint tested by Ruitong et al. ....	45
2.5.3.	Beam-column joint with floor slab tested by Cheung et al. ....	50
2.6.	CONCLUSIONS.....	61
	ACKNOWLEDGMENTS .....	64
	REFERENCES.....	65

**CHAPTER 3: NONLINEAR FINITE ELEMENT RESPONSE SIMULATION OF THE BNCS BUILDING ..... 70**

3.1.	INTRODUCTION .....	70
3.2.	OVERVIEW OF THE SHAKE TABLE TEST PROGRAM .....	74
3.2.1.	Structural system of the building specimen.....	74
3.2.2.	Instrumentation layout .....	78
3.2.3.	Seismic tests .....	79
3.3.	NONLINEAR FINITE ELEMENT (FE) MODELING AND ANALYSIS .....	81
3.3.1.	FE Simulation Platform.....	81
3.3.2.	Material constitutive models .....	82
3.3.3.	Finite elements.....	85
3.3.4.	Modeling of inertia and damping properties .....	89
3.3.5.	Incremental-iterative nonlinear time history analyses .....	91
3.4.	NONLINEAR TIME HISTORY ANALYSES RESULTS.....	92
3.4.1.	Structural level response.....	93
3.4.2.	Story level response.....	102
3.4.3.	Component level response.....	105
3.4.4.	Strain gauge and crack level response .....	112
3.5.	SEQUENTIAL VERSUS INDIVIDUAL NONLINEAR TIME HISTORY ANALYSIS.....	115
3.6.	CONCLUSIONS.....	117
	ACKNOWLEDGMENTS .....	120
	APPENDIX 3.I: DATA PROCESSING .....	121
3.I.1.	DATA CLEANSING PROCEDURE.....	121
3.I.2.	EVALUATING THE AVERAGE FLOOR ABSOLUTE ACCELERATIONS.....	121
	APPENDIX 3.II: MATERIAL PARAMETERS.....	124
3.II.1.	CONCRETE MATERIAL PARAMETERS .....	124
3.II.2.	STEEL MATERIAL PARAMETERS .....	127
	REFERENCES.....	128

**CHAPTER 4: PARAMETRIC IDENTIFICATION OF HYSTERETIC MATERIAL CONSTITUTIVE LAWS IN NONLINEAR STRUCTURAL FINITE ELEMENT MODELS USING EXTENDED KALMAN FILTER..... 132**



4.1.	INTRODUCTION .....	132
4.2.	KALMAN FILTER (KF) .....	137
4.2.1.	KF for linear systems.....	137
4.2.2.	KF for nonlinear systems.....	140
4.2.3.	Parameter estimation using EKF .....	143
4.3.	NONLINEAR FE MODEL UPDATING USING EKF .....	145
4.3.1.	Problem statement .....	145
4.3.2.	Nonlinear FE modeling and analysis method.....	146
4.3.3.	Parameter estimation – Nonlinear FE model updating framework .....	147
4.3.4.	FE response sensitivities using DDM.....	151
4.3.5.	Proposed algorithm for nonlinear FE model updating using EKF .....	155
4.4.	VERIFICATION CASE STUDIES .....	156
4.4.1.	Example #1: steel cantilever pier.....	157
4.4.2.	Example #2: three-story three-bay 2D steel moment frame .....	176
4.5.	CONCLUSIONS.....	187
	ACKNOWLEDGMENTS .....	190
	REFERENCES.....	191
<b>CHAPTER 5: NONLINEAR STRUCTURAL PARAMETER ESTIMATION AND UNCERTAINTY QUANTIFICATION USING BAYESIAN INFERENCE METHOD.....</b>		<b>195</b>
5.1.	INTRODUCTION .....	195
5.2.	NONLINEAR FINITE ELEMENT MODEL UPDATING .....	198
5.3.	PARAMETER ESTIMATION .....	199
5.4.	PARAMETER ESTIMATION UNCERTAINTY QUANTIFICATION.....	212
5.5.	VALIDATION STUDIES USING SIMULATED DATA .....	218
5.5.1.	Validation Study 1: Cantilever Steel Column .....	220
5.5.2.	Validation Study 2: 2D Moment Resisting Steel Frame .....	251
5.6.	CONCLUSIONS.....	273
	ACKNOWLEDGMENTS .....	275
	APPENDIX 5.I: DERIVATION OF THE EXACT FISHER INFORMATION MATRIX .....	276
	REFERENCES.....	281
<b>CHAPTER 6: OUTPUT-ONLY STRUCTURAL SYSTEM AND DAMAGE IDENTIFICATION USING STOCHASTIC NONLINEAR FINITE ELEMENT MODEL UPDATING.....</b>		<b>286</b>
6.1.	INTRODUCTION .....	286
6.2.	OUTPUT-ONLY NONLINEAR SYSTEM AND INPUT IDENTIFICATION .....	289
6.3.	RECURSIVE ML ESTIMATION METHOD .....	293
6.4.	STOCHASTIC FILTERING METHOD .....	304
6.5.	DIRECT DIFFERENTIATION METHOD (DDM) FOR FINITE ELEMENT RESPONSE SENSITIVITY ANALYSIS WITH RESPECT TO UNIFORM BASE EXCITATION.....	311
6.6.	VALIDATION STUDY .....	313
6.6.1.	3D RC frame building structure .....	314

6.6.2. Recursive ML estimation method.....	318
6.6.3. Stochastic filtering method.....	327
6.7. CONCLUSIONS.....	339
ACKNOWLEDGMENTS .....	340
APPENDIX 6.I: DERIVATION OF THE EXACT FISHER INFORMATION MATRIX FOR THE JOINT INPUT-MODEL PARAMETER ESTIMATION PROBLEM .....	342
APPENDIX 6.II: DERIVATION OF THE TRADITIONAL KALMAN GAIN MATRIX .....	350
REFERENCES.....	351
<b>CHAPTER 7: IDENTIFIABILITY ASSESSMENT FOR NONLINEAR STRUCTURAL SYSTEM IDENTIFICATION PROBLEMS .....</b>	<b>355</b>
7.1. INTRODUCTION .....	355
7.2. STRUCTURAL SYSTEM IDENTIFICATION THROUGH NONLINEAR FE MODEL UPDATING – PROBLEM STATEMENT .....	359
7.3. IDENTIFIABILITY ASSESSMENT BASED ON THE CRAMÉR–RAO LOWER BOUND 363	
7.4. IDENTIFIABILITY ASSESSMENT BASED ON INFORMATION-ENTROPY APPROACH 366	
7.5. NUMERICAL CASE STUDY.....	372
7.5.1. Description of the RC building structure and developed FE model...	373
7.5.2. Identifiability assessment of the FE model parameters .....	377
7.5.3. Miscellaneous discussions.....	386
7.6. CONCLUSIONS.....	393
ACKNOWLEDGMENTS .....	395
APPENDIX 7.I: APPROXIMATING THE A POSTERIORI EXPECTATION.....	397
APPENDIX 7.II: FINDING THE EVIDENCE .....	399
APPENDIX 7.III: DERIVATION OF THE FISHER INFORMATION MATRIX .....	402
REFERENCES.....	403
<b>CHAPTER 8: CONCLUSIONS.....</b>	<b>408</b>
8.1. SUMMARY OF RESEARCH WORK PERFORMED AND NOVEL CONTRIBUTIONS ..	408
8.2. SUMMARY OF MAJOR FINDINGS AND LIMITATIONS OF THE RESEARCH WORK	414
8.3. RECOMMENDATIONS FOR FUTURE RESEARCH WORK .....	419

## LIST OF FIGURES

FIGURE 1.1: I-35W ST. ANTHONY BRIDGE COLLAPSE IN MINNESOTA IN 2007 .....	3
FIGURE 2.1: UNI-AXIAL STRESS-STRAIN CONSTITUTIVE LAW OF CONCRETE USED IN THIS STUDY.....	31
FIGURE 2.2: GIUFFRÉ-MENEGOTTO-PINTO UNI-AXIAL CONSTITUTIVE MODEL FOR STEEL. ....	36
FIGURE 2.3: ESTIMATION OF KINEMATIC HARDENING PARAMETER, $b$ , FOR THE STEEL MODEL BASED ON MONOTONIC TENSILE TEST RESULTS.....	37
FIGURE 2.4: EXPERIMENTAL VALIDATION OF THE PROPOSED STEEL MODEL FOR #4 REBAR (38MM IN LENGTH), WITH TWO DIFFERENT STRAIN LOADING HISTORIES (A, B). ....	38
FIGURE 2.5: BEAM 43 AS TESTED BY POPOV ET AL. [47] .....	41
FIGURE 2.6: DETAILS OF FINITE ELEMENT MODEL FOR BEAM 43 (DIMENSIONS ARE IN MM). ....	43
FIGURE 2.7: COMPARISON OF THE FE SIMULATED FORCE-DEFORMATION RESPONSES OF BEAM 43 WITH THE EXPERIMENTAL RESULTS. ....	43
FIGURE 2.8: UNIT 1 AS TESTED BY RUITONG ET AL. [49];.....	46
FIGURE 2.9: DETAILS OF FINITE ELEMENT MODELS FOR UNIT 1 (DIMENSIONS ARE IN MM). ....	48
FIGURE 2.10: COMPARISON OF THE FE SIMULATED FORCE-DEFORMATION RESPONSES OF UNIT 1 WITH THE EXPERIMENTAL RESULTS; (A) MODELS 1 AND 2; (B) MODELS 3 AND 4. ....	50
FIGURE 2.11: UNIT 2D-I AS TESTED BY CHEUNG ET AL. [51] .....	52
FIGURE 2.12: TYPICAL SHELL ELEMENT WITH TYPICAL INTEGRATION POINTS. ....	53
FIGURE 2.13: DETAILS OF FINITE ELEMENT MODELS FOR UNIT 2D-I (DIMENSIONS ARE IN MM). ....	55
FIGURE 2.14: COMPARISON OF THE FE SIMULATED FORCE-DEFORMATION RESPONSES OF UNIT 1 WITH THE EXPERIMENTAL RESULTS; (A) EAST-WEST DIRECTION; (B) NORTH-SOUTH DIRECTION. ....	57
FIGURE 2.15: COMPARISON OF THE MEASURED AND FE-ESTIMATED CURVATURE PROFILE OF THE NORTH AND SOUTH BEAMS AT DIFFERENT DUCTILITY LEVELS.....	58
FIGURE 2.16: COMPARISON OF THE EXPERIMENTALLY MEASURED EQUIVALENT STRESS AND THE FE-ESTIMATED STRESS IN LONGITUDINAL BEAM REBARS; (A) STRAIN IN TOP D20 BAR OF NORTH AND SOUTH BEAMS; (B) STRAIN IN BOTTOM D24 BAR OF EAST AND WEST BEAMS.....	60
FIGURE 3.1: VIEWS OF THE BUILDING SPECIMEN; (A) BARE STRUCTURE; (B) COMPLETED BUILDING. ....	75
FIGURE 3.2: STRUCTURAL DETAILS OF THE BUILDING SPECIMEN (UNITS ARE IN METERS). ....	77

FIGURE 3.3: CONTRIBUTION OF DIFFERENT COMPONENTS AND SUB-SYSTEMS TO THE TOTAL WEIGHT OF THE COMPLETED BUILDING (EXCLUDING FOUNDATION).....	78
FIGURE 3.4: ACCELERATION TIME HISTORIES OF THE SEISMIC TEST MOTIONS ACHIEVED AT THE FOUNDATION LEVEL (EAST-WEST DIRECTION) AND THEIR 5% DAMPED RELATIVE DISPLACEMENT RESPONSE SPECTRA. ....	80
FIGURE 3.5: UNIAXIAL STRESS-STRAIN BEHAVIOR OF CONCRETE MODEL.....	84
FIGURE 3.6: (A) COMPLETE FE MODEL OF THE TEST SPECIMEN STRUCTURE; ..... FE MESH DETAILS AT (B) FLOOR 2, (C) FLOOR 4, AND (D) ROOF; JOINT DETAILS AT (E) SOUTH-WEST CORNER OF FLOOR 2, (F) SOUTH-MIDDLE OF FLOOR 2, (G) SOUTH-EAST CORNER OF FLOOR 2, AND (H) SOUTH-MIDDLE OF FLOOR 4 .....	88
FIGURE 3.7: CORRELATION OF THE FE PREDICTED VERSUS MEASURED (A) PEAK FLOOR ABSOLUTE ACCELERATION, (B) PEAK INTERSTORY DRIFT RATIO, AND (C) PEAK TOTAL STORY SHEAR NORMALIZED BY THE TOTAL WEIGHT OF THE BUILDING. ....	96
FIGURE 3.8: COMPARISON OF FE PREDICTED AND MEASURED (A) PEAK FLOOR ABSOLUTE ACCELERATION ENVELOPES, (B) PEAK INTERSTORY DRIFT RATIO ENVELOPES, AND (C) PEAK TOTAL STORY SHEAR ENVELOPES NORMALIZED BY THE TOTAL WEIGHT OF THE BUILDING. ....	97
FIGURE 3.9: RELATIVE PREDICTION ERROR FOR (A) PEAK FLOOR ABSOLUTE ACCELERATION, (B) PEAK INTERSTORY DRIFT RATIO, AND (C) PEAK TOTAL STORY SHEAR.....	98
FIGURE 3.10: COMPARISON OF FE PREDICTED AND MEASURED TIME HISTORIES OF SELECTED RESPONSE PARAMETER FOR (A) FB-1: <i>CNP100</i> AND (B) FB-5: <i>DEN67</i> . ....	101
FIGURE 3.11: COMPARISON OF FE PREDICTED AND MEASURED TSS VS. IDR HYSTERETIC RESPONSE FOR (A) FB-1: <i>CNP100</i> , (B) FB-4: <i>ICA100</i> , AND (C) FB-5: <i>DEN67</i> . ..	104
FIGURE 3.12: NORMALIZED PREDICTION ERROR OF THE TOTAL ABSORBED ENERGY TIME HISTORY AT THE STORY LEVEL FOR (A) FB-1: <i>CNP100</i> , (B) FB-4: <i>ICA100</i> , AND (C) FB-5: <i>DEN67</i> . ....	105
FIGURE 3.13: INSTRUMENTATION OF STRUCTURAL COMPONENTS: (A) SCHEMATIC DETAILS OF NORTH FRAME INSTRUMENTATION; (B) LINEAR POTENTIOMETERS INSTALLED AT EAST END OF SECOND FLOOR NORTH BEAM; (C) STRING POTENTIOMETERS INSTALLED AT THE BASE OF THE NORTH EAST COLUMN. ....	107
FIGURE 3.14: COMPARISON OF FE PREDICTED AND MEASURED AVERAGED AXIAL STRAIN TIME HISTORIES FOR FB-5: <i>DEN67</i> AT THE (A) WEST END OF THE SECOND FLOOR NORTH BEAM, (B) EAST END OF THE SECOND FLOOR NORTH BEAM, (C) WEST END OF THE THIRD FLOOR NORTH BEAM, ... ..	108
FIGURE 3.15: COMPARISON OF FE PREDICTED AND MEASURED AVERAGED CURVATURE TIME HISTORIES FOR FB-5: <i>DEN67</i> AT THE (A) WEST END OF THE SECOND FLOOR NORTH BEAM, (B) EAST END OF THE SECOND FLOOR NORTH BEAM, (C) WEST END OF THE THIRD FLOOR NORTH BEAM, ... ..	109
FIGURE 3.16: COMPARISON OF FE PREDICTED AND MEASURED AVERAGED AXIAL STRAIN VS. CURVATURE FOR FB-5: <i>DEN67</i> AT THE (A) WEST END OF THE SECOND FLOOR NORTH BEAM, (B) EAST END OF THE SECOND FLOOR NORTH BEAM, (C) WEST END OF THE THIRD FLOOR NORTH BEAM, ... ..	110

FIGURE 3.17: COMPARISON OF FE PREDICTED AND MEASURED AVERAGED AXIAL STRAIN TIME HISTORIES FOR FB-5: <i>DEN67</i> AT THE (A) BASE OF NORTH MIDDLE COLUMN, (B) BASE OF NORTH EAST COLUMN, (C) BASE OF SOUTH MIDDLE COLUMN, (D) BASE OF SOUTH EAST COLUMN.....	111
FIGURE 3.18: COMPARISON OF FE PREDICTED AND MEASURED AVERAGED CURVATURE TIME HISTORIES FOR FB-5: <i>DEN67</i> AT THE (A) BASE OF NORTH MIDDLE COLUMN, (B) BASE OF NORTH EAST COLUMN, (C) BASE OF SOUTH MIDDLE COLUMN, (D) BASE OF SOUTH EAST COLUMN.....	112
FIGURE 3.19: (A) STRAIN GAUGE INSTALLED ON THE OUTER REBAR AT EAST END OF THE 3 <sup>RD</sup> FLOOR NORTH FRAME BEAM; (B) COMPARISON OF THE FE PREDICTED AND MEASURED LONGITUDINAL REBAR STRAIN FOR FB-5: <i>DEN67</i> . ....	113
FIGURE 3.20: COMPARISON OF FE PREDICTED AND OBSERVED CRACKS ON THE TOP SURFACE OF THE SECOND FLOOR SLAB AFTER FB-5: <i>DEN67</i> : (A) EXPERIMENTAL OBSERVATION; (B) MAXIMUM CRACK OPENING BASED ON FE PREDICTION (UNITS ARE IN MM); ...	114
FIGURE 3.21: (A) POTENTIOMETER (PROTECTED BY PLASTIC COVER) INSTALLED PRIOR TO FB-5: <i>DEN67</i> ACROSS A CRACK ON THE SECOND FLOOR CONCRETE SLAB; (B) COMPARISON OF FE PREDICTED AND MEASURED CRACK OPENING TIME HISTORY FOR FB-5: <i>DEN67</i> . ....	115
FIGURE 3.22: COMPARISON OF THE BUILDING RESPONSE PREDICTION RESULTS OBTAINED USING THE SEQUENTIAL AND INDIVIDUAL ANALYSES; PFAA NORMALIZED BY THE CORRESPONDING MEASURED PFAA FOR: (A) FB-3: <i>ICA50</i> , (B) FB-4: <i>ICA100</i> , AND (C) FB-5: <i>DEN67</i> ; ...	117
FIGURE 3.23: SCHEMATIC PLAN VIEW AND LOCATION OF ACCELEROMETERS. ....	123
FIGURE 4.1: HIERARCHICAL DISCRETIZATION LEVELS IN DISTRIBUTED PLASTICITY STRUCTURAL FE MODELS USING FIBER-SECTION DISPLACEMENT-BASED BEAM-COLUMN ELEMENTS. THE NOTATION IS FURTHER DESCRIBED IN SECTION 3.4.....	147
FIGURE 4.2: (A) CANTILEVER STEEL COLUMN WITH BOX SECTION, (B) DETAILS OF THE DEVELOPED FE MODEL. ....	159
FIGURE 4.3: MODIFIED GIUFFRÉ-MENEGOTTO-PINTO UNIAXIAL MATERIAL CONSTITUTIVE MODEL FOR STEEL. ....	159
FIGURE 4.4: TIME HISTORIES OF THE SELECTED EARTHQUAKE GROUND MOTIONS.....	160
FIGURE 4.5: TIME HISTORIES OF A <i>POSTERIORI</i> MATERIAL PARAMETER ESTIMATES FOR <i>EQI</i> .....	166
FIGURE 4.7: TIME HISTORIES OF THE NORMALIZED FE ACCELERATION RESPONSE SENSITIVITIES TO THE THREE MATERIAL PARAMETERS, OBTAINED USING THE DDM DURING THE ESTIMATION PROCESS FOR <i>EQI</i> (IN THE CASE OF 10% RMS NSR). IN THIS FIGURE, $A = \ddot{u}_{top}$ = ACCELERATION RESPONSE OF THE COLUMN TOP.....	167
FIGURE 4.8: COMPARISON OF SIMULATED (TRUE) RELATIVE ACCELERATION RESPONSE TIME HISTORY OF THE PIER TOP WITH ESTIMATED RESPONSE AFTER FE MODEL UPDATING FOR <i>EQI</i> WITH 10% RMS NSR. ....	168
FIGURE 4.9: COMPARISON OF SIMULATED (TRUE) NORMALIZED BASE SHEAR VS. DRIFT RATIO WITH ESTIMATED RESPONSE AFTER FE MODEL UPDATING FOR <i>EQI</i> WITH 10% RMS NSR. ....	168

FIGURE 4.10: COMPARISON OF SIMULATED (TRUE) MOMENT-CURVATURE RESPONSE OF PIER BASE SECTION WITH ESTIMATED RESPONSE AFTER FE MODEL UPDATING FOR <i>EQ1</i> WITH 10% RMS NSR. ....	169
FIGURE 4.11: COMPARISON OF SIMULATED (TRUE) FIBER STRESS-STRAIN RESPONSE AT MONITORED FIBER IN PIER BASE SECTION WITH ESTIMATED RESPONSE AFTER FE MODEL UPDATING FOR <i>EQ1</i> WITH 10% RMS NSR. ....	169
FIGURE 4.12: TIME HISTORIES OF A <i>POSTERIORI</i> MATERIAL PARAMETER ESTIMATES FOR <i>EQ1</i> AND 10% RMS NSR WHEN FE RESPONSE SENSITIVITIES ARE COMPUTED USING DDM AND FDM (TIME HISTORIES ARE SHOWN FOR A SHORT TIME WINDOW FOR MORE CLARITY). ....	173
FIGURE 4.13: TIME HISTORIES OF A <i>POSTERIORI</i> MATERIAL PARAMETER ESTIMATES FOR <i>EQ1</i> FOR FIVE DIFFERENT INITIAL ESTIMATES OF THE MATERIAL PARAMETERS. ...	174
FIGURE 4.14: TIME HISTORIES OF A <i>POSTERIORI</i> MATERIAL PARAMETER ESTIMATES FOR <i>EQ1</i> FOR FIVE DIFFERENT INITIAL ESTIMATES OF THE MATERIAL PARAMETERS – ZOOM ON THE FIRST 6 SECONDS. ....	175
FIGURE 4.15: TIME HISTORIES OF A <i>POSTERIORI</i> C.O.V.s (%) OF MATERIAL PARAMETERS FOR <i>EQ1</i> FOR FIVE DIFFERENT INITIAL ESTIMATES OF THE MATERIAL PARAMETERS. ....	175
FIGURE 4.16: TIME HISTORIES OF A <i>POSTERIORI</i> C.O.V.s (%) OF MATERIAL PARAMETERS FOR <i>EQ1</i> FOR FIVE DIFFERENT INITIAL ESTIMATES OF THE MATERIAL PARAMETERS – ZOOM ON THE FIRST 6 SECONDS. ....	176
FIGURE 4.17: DETAILS OF 2D FE MODEL OF THREE-STORY THREE-BAY STEEL MOMENT FRAME (DB ELEMENT: DISPLACEMENT-BASED ELEMENT, IP: INTEGRATION POINT, ELE: ELEMENT, CS1: COLUMN SECTION #1, BS1 AND BS2: BEAM SECTIONS #1 AND #2, 1 TON = 1000 KG, LENGTH UNIT: M). ....	178
FIGURE 4.18: TIME HISTORIES OF A <i>POSTERIORI</i> MATERIAL PARAMETER ESTIMATES FOR <i>EQ2</i> . ....	182
FIGURE 4.19: TIME HISTORIES OF A <i>POSTERIORI</i> C.O.V.s (%) OF MATERIAL PARAMETERS FOR <i>EQ2</i> . ....	183
FIGURE 4.20: COMPARISON OF SIMULATED (TRUE) RELATIVE ACCELERATION RESPONSE TIME HISTORIES AT THREE LEVELS – RECORDED AT THE NORTH COLUMN LOCATION – WITH ESTIMATED RESPONSE AFTER FE MODEL UPDATING FOR <i>EQ2</i> WITH 10% RMS NSR AND $r = 0.1$ . ....	186
FIGURE 4.21: COMPARISON OF SIMULATED (TRUE) NORMALIZED BASE SHEAR VS. ROOF DRIFT RATIO WITH ESTIMATED RESPONSE AFTER FE MODEL UPDATING FOR <i>EQ2</i> WITH 10% RMS NSR AND $r = 0.1$ – BASE SHEAR IS NORMALIZED BY $W = 1591G$ kN. ....	186
FIGURE 4.22: COMPARISON OF SIMULATED (TRUE) FIBER STRESS-STRAIN RESPONSE AT MONITORED FIBER IN BEAM CROSS SECTION BS2 WITH ESTIMATED RESPONSE AFTER FE MODEL UPDATING FOR <i>EQ2</i> WITH 10% RMS NSR AND $r = 0.1$ . ....	187
FIGURE 4.23: COMPARISON OF SIMULATED (TRUE) FIBER STRESS-STRAIN RESPONSE AT MONITORED FIBER IN COLUMN SECTION CS1 WITH ESTIMATED RESPONSE AFTER FE MODEL UPDATING FOR <i>EQ2</i> WITH 10% RMS NSR AND $r = 0.1$ . ....	187

FIGURE 5.1: HIERARCHICAL DISCRETIZATION LEVELS IN DISTRIBUTED PLASTICITY STRUCTURAL FE MODELS USING FIBER-SECTION DISPLACEMENT-BASED BEAM-COLUMN ELEMENTS (ADAPTED FROM [2]; NOTATIONS ARE FURTHER DESCRIBED THEREIN). .....	220
FIGURE 5.2: (A) CANTILEVER STEEL COLUMN WITH BUILT-UP BOX SECTION, (B) DETAILS OF THE DEVELOPED FE MODEL (DBE: DISPLACEMENT-BASED FINITE ELEMENT; 1 TON = 1000 KG; LENGTH UNIT: MM). .....	222
FIGURE 5.3: MODIFIED GIUFFRÉ-MENEGOTTO-PINTO UNIAXIAL MATERIAL CONSTITUTIVE MODEL FOR STRUCTURAL STEEL.....	223
FIGURE 5.4: TIME HISTORIES OF THE SELECTED EARTHQUAKE GROUND MOTIONS, TOP: <i>EQ1</i> FROM 1989 LOMA PRIETA EARTHQUAKE, BOTTOM: <i>EQ2</i> FROM 1994 NORTHRIDGE EARTHQUAKE. ....	223
FIGURE 5.5: CONVERGENCE HISTORY OF THE ESTIMATED FE MODEL PARAMETERS AND SIMULATION ERROR VARIANCE FOR THREE MEASUREMENT NOISE LEVELS FOR <i>EQ1</i> (THE LAST GRAPH IS PLOTTED IN SEMI-LOGARITHMIC SCALE). .....	229
FIGURE 5.6: CONVERGENCE HISTORY OF THE ESTIMATED FE MODEL PARAMETERS AND SIMULATION ERROR VARIANCE FOR THREE MEASUREMENT NOISE LEVELS FOR <i>EQ2</i> (THE LAST GRAPH IS PLOTTED IN SEMI-LOGARITHMIC SCALE). .....	230
FIGURE 5.7: COMPARISON OF THE FE PREDICTED STRUCTURAL LEVEL RESPONSE TO <i>EQ1</i> OBTAINED USING THE TRUE VALUES OF THE FE MODEL PARAMETERS, AND THE INITIAL AND FINAL ESTIMATES OF THE FE MODEL PARAMETERS INFERRED FOR THE CASE OF 2% G RMS MEASUREMENT NOISE LEVEL. ....	233
FIGURE 5.8: COMPARISON OF THE FE PREDICTED SECTION LEVEL RESPONSE TO <i>EQ1</i> OBTAINED USING THE TRUE VALUES OF THE FE MODEL PARAMETERS, AND THE INITIAL AND FINAL ESTIMATES OF THE FE MODEL PARAMETERS INFERRED FOR THE CASE OF 2% G RMS MEASUREMENT NOISE LEVEL. ....	234
FIGURE 5.9: HETEROGENEOUS MEASUREMENTS, (A) ACCELERATION RESPONSE TIME HISTORY OF THE COLUMN TOP, (B) CURVATURE RESPONSE TIME HISTORY OF THE COLUMN BASE SECTION.....	239
FIGURE 5.10: CONVERGENCE HISTORY OF THE MODELING PARAMETERS USING LEAST SQUARES ESTIMATION METHOD FOR TWO CASES OF OUTPUT MEASUREMENT FOR <i>EQ2</i> . ....	241
FIGURE 5.11: CONVERGENCE HISTORY OF THE MODELING PARAMETERS USING THE PROPOSED ESTIMATION METHOD FOR TWO CASES OF OUTPUT MEASUREMENT FOR <i>EQ2</i> . ....	241
FIGURE 5.12: CONVERGENCE HISTORY OF THE MODELING PARAMETERS AND THE NOISE VARIANCE FOR FOUR DIFFERENT SETS OF INITIAL ESTIMATES AS CONSIDERED IN CASE STUDY 4 FOR <i>EQ1</i> AND 2% G RMS MEASUREMENT NOISE. ....	243
FIGURE 5.13: COMPARISON OF THE NOISY WITH THE TRUE (NOT NOISY) GROUND ACCELERATION TIME HISTORY OF <i>EQ2</i> . ....	246
FIGURE 5.14: CONVERGENCE HISTORY OF THE MODELING PARAMETERS AND THE NOISE VARIANCE FOR THREE LEVELS OF INPUT NOISE AS CONSIDERED IN CASE STUDY 5 FOR <i>EQ1</i> AND 2% G RMS OUTPUT MEASUREMENT NOISE. ....	246

FIGURE 5.15: CONVERGENCE HISTORY OF THE MODELING PARAMETERS AND THE NOISE VARIANCE FOR THREE LEVELS OF INPUT NOISE AS CONSIDERED IN CASE STUDY 5 FOR <i>EQ2</i> AND 2% G RMS OUTPUT MEASUREMENT NOISE.....	247
FIGURE 5.16: COMPARISON OF THE TRUE RESPONSE WITH THE RESPONSE OBTAINED USING INITIAL AND FINAL ESTIMATES OF THE MODELING PARAMETERS FOR <i>EQ1</i> WITH 2% G RMS MEASUREMENT NOISE AND 2% G RMS INPUT NOISE, (A) RELATIVE ACCELERATION RESPONSE TIME HISTORY OF THE COLUMN TOP... ..	248
FIGURE 5.17: BILINEAR UNIAXIAL MATERIAL CONSTITUTIVE MODEL FOR STRUCTURAL STEEL.....	250
FIGURE 5.18: CONVERGENCE HISTORY OF THE MODELING PARAMETERS AND THE NOISE VARIANCE IN CASE STUDY 5 FOR <i>EQ1</i> AND 0.5% G RMS OUTPUT MEASUREMENT NOISE.....	250
FIGURE 5.19: COMPARISON OF THE TRUE RESPONSE WITH THE RESPONSE OBTAINED USING INITIAL AND FINAL ESTIMATES OF THE MODELING PARAMETERS FOR <i>EQ1</i> WITH 0.5% G RMS MEASUREMENT NOISE, (A) RELATIVE ACCELERATION RESPONSE TIME HISTORY OF THE COLUMN TOP... ..	251
FIGURE 5.20: DETAILS OF THE DEVELOPED 2D FE MODEL OF THE THREE-BAY THREE-STORY MR STEEL FRAME BASED ON THE LA3 MODEL STRUCTURE FROM THE FEMA/SAC PROJECT WITH PRE-NORTHRIDGE DESIGN.....	252
FIGURE 5.21: CONVERGENCE HISTORY OF THE ESTIMATED FE MODEL PARAMETERS AND SIMULATION ERROR VARIANCES FOR THREE MEASUREMENT NOISE LEVELS FOR <i>EQ1</i> . .....	257
FIGURE 5.22: CONVERGENCE HISTORY OF THE ESTIMATED FE MODEL PARAMETERS AND SIMULATION ERROR VARIANCES FOR THREE MEASUREMENT NOISE LEVELS FOR <i>EQ2</i> . .....	258
FIGURE 5.23: COMPARISON OF THE TIME HISTORIES OF THE FE PREDICTED FLOOR RELATIVE (TO BASE) ACCELERATION RESPONSE TO <i>EQ2</i> OBTAINED USING THE TRUE VALUES OF THE FE MODEL PARAMETERS, AND THE INITIAL AND FINAL ESTIMATES OF THE FE MODEL PARAMETERS INFERRED FOR... ..	260
FIGURE 5.24: COMPARISON OF THE FE PREDICTED MOMENT-CURVATURE HYSTERETIC RESPONSES TO <i>EQ2</i> OBTAINED USING THE TRUE VALUES OF THE FE MODEL PARAMETERS, AND THE INITIAL AND FINAL ESTIMATES OF THE FE MODEL PARAMETERS INFERRED FOR.. ..	260
FIGURE 5.25: HETEROGENEOUS STRUCTURAL RESPONSE MEASUREMENTS: ACCELERATION RESPONSE TIME HISTORIES MEASURED AT THE FIRST AND THIRD LEVELS AND CURVATURE RESPONSE TIME HISTORY OF THE COLUMN BASE SECTION (CS1) FOR <i>EQ1</i> ... ..	262
FIGURE 6.1: SCHEMATIC REPRESENTATION OF THE PROPOSED RECURSIVE ESTIMATION APPROACH FOR JOINT ESTIMATION OF THE FE MODEL PARAMETERS, THE SIMULATION ERROR VARIANCES, AND THE BASE ACCELERATION TIME HISTORY. .	298
FIGURE 6.2: RC FRAME BUILDING STRUCTURE: ISOMETRIC VIEW AND CROSS-SECTION OF BEAMS AND COLUMNS. ....	315



FIGURE 6.3: HIERARCHICAL DISCRETIZATION LEVELS IN DISTRIBUTED PLASTICITY STRUCTURAL FE MODELS USING FIBER-SECTION DISPLACEMENT-BASED BEAM-COLUMN ELEMENTS (ADAPTED FROM [8]).	317
FIGURE 6.4: TYPICAL CYCLIC BEHAVIOR OF THE EMPLOYED MATERIAL MODELS: (A) POPOVICS-SAENZ FOR CONCRETE MATERIAL, (B) GIUFFRÉ-MENEGOTTO-PINTO FOR REINFORCING STEEL MATERIAL.	317
FIGURE 6.5: 2004 PARKFIELD EARTHQUAKE GROUND MOTION (CHOLAME 2 WEST STATION, RESAMPLED AT 40 HZ); TOP: 90° COMPONENT APPLIED IN N-S DIRECTION, AND BOTTOM: 360° COMPONENT APPLIED IN E-W DIRECTION.	318
FIGURE 6.6: LEFT: COMPARISON OF THE ESTIMATED AND TRUE BASE ACCELERATION TIME HISTORY IN THE EW DIRECTION; RIGHT: ESTIMATION ERROR OF THE BASE ACCELERATION TIME HISTORY; (A): CASE #1; (B): CASE #2; (C): CASE #3.	322
FIGURE 6.7: STANDARD DEVIATION (S.D.) OF THE ESTIMATED BASE ACCELERATION TIME HISTORY IN THE EAST-WEST DIRECTION; (A): CASE #1; (B): CASE #2; (C): CASE #3.	323
FIGURE 6.8: CONVERGENCE HISTORY OF THE ESTIMATED FE MODEL PARAMETERS FOR CASE #3.	326
FIGURE 6.9: LEFT: COMPARISON OF THE ESTIMATED AND TRUE BASE ACCELERATION TIME HISTORY IN THE EAST-WEST DIRECTION; RIGHT: ESTIMATION ERROR OF THE BASE ACCELERATION TIME HISTORY; (A): CASE #1; (B): CASE #2; (C): CASE #3; (D): CASE #4.	331
FIGURE 6.10: STANDARD DEVIATION (S.D.) OF THE ESTIMATED BASE ACCELERATION TIME HISTORY IN THE EAST-WEST DIRECTION; (A): CASE #1; (B): CASE #2; (C): CASE #3; (D): CASE #4.	333
FIGURE 6.11: TIME HISTORIES OF THE <i>A POSTERIORI</i> MEAN AND C.O.V. OF FE MODEL PARAMETERS FOR CASE #1.	334
FIGURE 6.12: TIME HISTORIES OF THE <i>A POSTERIORI</i> MEAN AND C.O.V. OF FE MODEL PARAMETERS FOR CASE #2.	335
FIGURE 6.13: TIME HISTORIES OF THE <i>A POSTERIORI</i> MEAN AND C.O.V. OF FE MODEL PARAMETERS FOR CASE #3.	336
FIGURE 6.14: TIME HISTORIES OF THE <i>A POSTERIORI</i> MEAN AND C.O.V. OF FE MODEL PARAMETERS FOR CASE #4.	337
FIGURE 7.1: RC FRAME BUILDING STRUCTURE: ISOMETRIC VIEW AND CROSS-SECTION OF BEAMS AND COLUMNS.	374
FIGURE 7.2: HIERARCHICAL DISCRETIZATION LEVELS IN DISTRIBUTED PLASTICITY STRUCTURAL FE MODELS USING FIBER-SECTION DISPLACEMENT-BASED BEAM-COLUMN ELEMENTS (ADAPTED FROM [30]).	376
FIGURE 7.3: TYPICAL CYCLIC BEHAVIOR OF THE EMPLOYED MATERIAL MODELS: (A) GIUFFRÉ-MENEGOTTO-PINTO FOR REINFORCING STEEL MATERIAL, AND (B)POPOVICS-SAENZ FOR CONCRETE MATERIAL.	376
FIGURE 7.4: 1994 NORTHRIDGE EARTHQUAKE GROUND MOTION (SYLMAR COUNTY HOSPITAL STATION); TOP: 90° COMPONENT APPLIED IN N-S DIRECTION, AND BOTTOM: 360° COMPONENT APPLIED IN E-W DIRECTION.	377

FIGURE 7.5: TIME HISTORY OF THE ENTROPY GAIN FOR NINE FE MODEL PARAMETERS FROM DIFFERENT MEASUREMENT DATA SETS. ....	380
FIGURE 7.6: ENTROPY GAIN (IN NATS) TIME HISTORY FOR EACH INDIVIDUAL FE MODEL PARAMETER FROM DIFFERENT MEASUREMENT DATA SETS. ....	381
FIGURE 7.6 (CONTINUED): ENTROPY GAIN (IN NATS) TIME HISTORY FOR EACH INDIVIDUAL FE MODEL PARAMETER FROM DIFFERENT MEASUREMENT DATA SETS. ....	382
FIGURE 7.7: ENTROPY GAIN TIME HISTORY FOR EACH INDIVIDUAL FE MODEL PARAMETER FROM DIFFERENT MEASUREMENT DATA SETS. ....	383
FIGURE 7.7 (CONTINUED): ENTROPY GAIN TIME HISTORY FOR EACH INDIVIDUAL FE MODEL PARAMETER FROM DIFFERENT MEASUREMENT DATA SETS. ....	384
FIGURE 7.8: ENTROPY GAIN (IN NATS) TIME HISTORY FROM DIFFERENT MEASUREMENT DATA SETS. ....	385
FIGURE 7.9: THE CORRELATION OF THE TOTAL ENTROPY GAIN (IN NATS) BETWEEN INDIVIDUAL MODEL PARAMETERS AND MEASUREMENT DATA SETS. ....	386
FIGURE 7.10: COMPARISON OF THE INDIVIDUAL VERSUS CONDITIONAL ENTROPY GAIN FOR S10. ....	388
FIGURE 7.10 (CONTINUED): COMPARISON OF THE INDIVIDUAL VERSUS CONDITIONAL ENTROPY GAIN FOR S10. ....	389
FIGURE 7.11: MUTUAL ENTROPY GAIN (IN NATS) OF THE FE MODEL PARAMETERS. ....	390
FIGURE 7.12: COMPARISON OF THE ENTROPY GAIN COMPUTED USING THE INITIAL AND TRUE VALUES OF FE MODEL PARAMETERS FOR S10. ....	392
FIGURE 7.12 (CONTINUED): COMPARISON OF THE ENTROPY GAIN COMPUTED USING THE INITIAL AND TRUE VALUES OF FE MODEL PARAMETERS FOR S10. ....	393

## LIST OF TABLES

TABLE 2.1: MATERIAL PARAMETERS FOR BEAM 43.....	42
TABLE 2.2: MATERIAL PARAMETERS FOR UNIT 1; (A) CONCRETE MATERIAL PARAMETERS; (B) STEEL MATERIAL PARAMETERS. ....	48
TABLE 2.3: MATERIAL PARAMETERS FOR UNIT 2D-I; (A) CONCRETE MATERIAL PARAMETERS; (B) STEEL MATERIAL PARAMETERS. ....	55
TABLE 3.1: THE SEISMIC TESTS PERFORMED IN THE FIXED BASE CONFIGURATION. ....	80
TABLE 3.2: INTEGRATION SCHEME FOR BEAM-COLUMN ELEMENTS.....	87
TABLE 3.3: LENGTH OF PARTITION WALLS AND BALLOON FRAMING AT DIFFERENT STORIES. ....	99
TABLE 3.4: PARAMETERS SELECTED FOR DIFFERENT CONCRETE MATERIAL MODELS. ..	125
TABLE 3.5: DETAILS OF THE CONCRETE MATERIAL PARAMETERS EVALUATION FOR 1 <sup>ST</sup> FLOOR COLUMNS.....	126
TABLE 3.6: PARAMETERS SELECTED FOR STEEL MATERIAL MODELS. ....	127
TABLE 4.1: DISCRETE-TIME KF ALGORITHM.....	140
TABLE 4.2: PROPOSED ALGORITHM FOR NONLINEAR FE MODEL UPDATING USING THE EKF.....	156
TABLE 4.3: SELECTED EARTHQUAKE GROUND MOTIONS.....	160
TABLE 4.4: MATERIAL PARAMETER ESTIMATION RESULTS FOR ALL EARTHQUAKE INPUT MOTIONS AND NOISE LEVELS IN EXAMPLE 1.....	171
TABLE 4.5: DIFFERENT SETS FOR THE INITIAL ESTIMATES OF THE MATERIAL PARAMETERS .....	174
TABLE 4.6: TRUE MATERIAL PARAMETER VALUES USED FOR EXAMPLE 2. ....	177
TABLE 4.7: INITIAL ESTIMATES OF THE MATERIAL PARAMETERS USED FOR EXAMPLE 2. .....	179
TABLE 4.8: MATERIAL PARAMETER ESTIMATION RESULTS FOR ALL EARTHQUAKE INPUT MOTIONS AND NOISE LEVELS IN EXAMPLE 2.....	184
TABLE 5.1: SELECTED EARTHQUAKE GROUND MOTIONS.....	223
TABLE 5.2: PARAMETER ESTIMATION RESULTS FOR THE THREE MEASUREMENT NOISE LEVELS CONSIDERED IN CASE STUDY #1. ....	231
TABLE 5.3: COMPARISON OF C.O.V.S OF THE ESTIMATED FE MODEL PARAMETERS OBTAINED USING THREE METHODS FOR <i>EQ1</i> .....	237
TABLE 5.4: ESTIMATION RESULTS FOR CASE STUDY 3. ....	242
TABLE 5.5: DIFFERENT SETS OF INITIAL ESTIMATES CONSIDERED IN CASE STUDY 4. ....	242
TABLE 5.6: ESTIMATION RESULTS FOR FOUR SETS OF INITIAL ESTIMATES CONSIDERED IN CASE STUDY 4. ....	244
TABLE 5.7: ESTIMATION RESULTS FOR THREE LEVELS OF INPUT NOISE CONSIDERED IN CASE STUDY 5. ....	247

TABLE 5.8: PARAMETER ESTIMATION RESULTS FOR THE THREE MEASUREMENT NOISE LEVELS CONSIDERED IN CASE STUDY #1. ....	259
TABLE 5.9: PARAMETER ESTIMATION UNCERTAINTY FOR THE THREE MEASUREMENT NOISE LEVELS CONSIDERED IN CASE STUDY #1. ....	259
TABLE 5.10: PARAMETER ESTIMATION RESULTS FOR FOUR DIFFERENT CASES CONSIDERED IN CASE STUDY #2 FOR <i>EQ1</i> . ....	265
TABLE 5.11: PARAMETER ESTIMATION UNCERTAINTY FOR FOUR DIFFERENT CASES CONSIDERED IN CASE STUDY #2 FOR <i>EQ1</i> . ....	265
TABLE 5.12: DIFFERENT SETS OF INITIAL ESTIMATES OF FE MODEL PARAMETERS CONSIDERED IN CASE STUDY #4. ....	266
TABLE 5.13: PARAMETER ESTIMATION RESULTS FOR FOUR SETS OF INITIAL ESTIMATES OF THE FE MODEL PARAMETERS CONSIDERED IN CASE STUDY #3. ....	268
TABLE 5.14: PARAMETER ESTIMATION UNCERTAINTY FOR FOUR SETS OF INITIAL ESTIMATES OF FE MODEL PARAMETERS CONSIDERED IN CASE STUDY #3. ....	268
TABLE 5.15: PARAMETER ESTIMATION RESULTS FOR THREE INPUT MEASUREMENT NOISE LEVELS CONSIDERED IN CASE STUDY #4. ....	272
TABLE 5.16: PARAMETER ESTIMATION UNCERTAINTY FOR THREE INPUT MEASUREMENT NOISE LEVELS CONSIDERED IN CASE STUDY #4. ....	272
TABLE 6.1: RECURSIVE ML ESTIMATION ALGORITHM FOR THE OUTPUT-ONLY PARAMETER ESTIMATION AND NONLINEAR FE MODEL UPDATING PROBLEM. ....	302
TABLE 6.2: STOCHASTIC FILTERING ALGORITHM FOR THE OUTPUT-ONLY PARAMETER ESTIMATION AND NONLINEAR FE MODEL UPDATING PROBLEM. ....	310
TABLE 6.3: VALIDATION CASES STUDIES. ....	321
TABLE 6.4: COMPARISON OF FE MODEL PARAMETER ESTIMATION RESULTS IN THREE CASE STUDIES. ....	324
TABLE 6.5: COMPARISON OF THE ESTIMATED SIMULATION ERROR VARIANCE IN THREE CASE STUDIES. ....	325
TABLE 6.6: COMPARISON OF COMPUTATIONAL TIME IN THREE CASE STUDIES. ....	327
TABLE 6.7: VALIDATION CASES STUDIES. ....	328
TABLE 6.8: COMPARISON OF PARAMETER ESTIMATION RESULTS IN FOURS CASE STUDIES. ....	339
TABLE 6.9: COMPARISON OF COMPUTATIONAL TIME IN FOUR CASE STUDIES. ....	339
TABLE 7.1: MEASUREMENT DATA SETS. ....	378

## ACKNOWLEDGMENTS

Initially and preeminently, I would like to express my humblest gratitude to my advisor, Professor Joel P. Conte, for his intellectual and scientific guidance throughout the course of my Ph.D. studies. Professor Conte, with his deep wellspring of knowledge, passion for teaching, and laser-sharp constructive criticism, contributed greatly by challenging me to improve and reach toward the pinnacle of my abilities. I would also like to extend my appreciation to my doctoral committee members, Professors P. Benson Shing, Gilberto Mosqueda, Robert R. Bitmead, and Raymond A. de Callafon for their time, support, and essential advice and suggestions. Professors Bitmead and de Callafon from the Mechanical and Aerospace Engineering Department have expanded to a great degree my knowledge in the fields of dynamic systems, control, and estimation theory. They both have demonstrated a remarkable dedication to students both in the classroom and through their open door and highly accessible discussion policies. My discussions with them profoundly broadened my vision and provided innovative new concepts to explore as I was undertaking my ongoing Ph.D. research. I feel deeply thankful to Professor Gilberto Mosqueda, for kindly agreeing to be part of my Ph.D. committee and supporting me in this endeavor. I have always looked up to Professor P. Benson Shing. I know him as a brilliant teacher and educator, remarkable scientist, and renowned researcher with a compelling personality. I have been honored to have the opportunity to sit in his class and learn from him.

With the encouragement of my advisor, Professor Conte, and the nonpareil support I received from Professor de Callafon, I was able to complete additional coursework via the pursuit of a concurrent master's degree through the Department of Mechanical and Aerospace Engineering in the field of Dynamic Systems and Control. I am thankful to my master's program committee members, Professors de Callafon, Bitmead, and de Oliveira. I have had many constructive and inspirational scientific discussions with Professor Maurício de Oliveira, who not only was part of my master's program committee, but also kindly helped me with one of the research ideas I explored in the course of my studies.

My gratitude also extends to Professor Jose I. Restrepo, who greatly added to my understanding of the mechanics and behavior of reinforced concrete. His extensive knowledge in the field of earthquake engineering and structural behavior have provided an essential support for the first part of my Ph.D. research as outlined in this dissertation. I would also like to send out my special and warmest gratitude to Professors Bijan and Parvis Banan from the Department of Civil Engineering at Shiraz University; without their help, I would not have had the opportunity to pursue my Ph.D. at UCSD. I have to especially thank Professor Frieder Seible, the former Dean of the Jacobs School of Engineering, who also kindly facilitated my journey toward joining UCSD.

My gratitude also must go out to my fellow students, researchers, co-workers, and friends who loyally stayed by my side during all the vicissitudes of academic life I have experienced in the past five years at UCSD. These include but are not limited to

Sara Salehyar, Professor Andre Barbosa, Dr. Maurizio Gobbato, Dr. Yong Li, Giovanni Montefusco, Yujia Liu, Rodrigo Carreno, Pouria Mirkhosravi, Alireza Sarebanha, Dr. Amedeo Flora, Dr. Giovanni De Francesco, Dr. Armando Lanzi, and Dr. Jakab Gabor. Moreover, I would like to especially acknowledge my close colleague and fellow Ph.D. student, Dr. Rodrigo Astroza for his indispensable contributions and collaboration in our joint research ventures.

Finally, and most significantly, I want to express my sincere and heartfelt gratitude to my fiancée, Ms. Hourieh Fakourfar. With her unconditional love and all-encompassing support, she has provided me with the necessary mental toughness, hope, and inspiration to overcome all the challenges I faced in the last year of my Ph.D. studies.

Partial support for my Ph.D. work was provided by the NSF-NEESR program under grant number CMMI-0936505 with Professor Tara C. Hutchinson as the principal investigator, the Englekirk structural engineering center board of advisors, teaching assistantships from the Department of Structural Engineering at University of California, San Diego and the researcher assistantship received through my advisor, Professor Joel P. Conte.

Chapter 2, in full, is currently being prepared for submission for publication of the material by Hamed Ebrahimian, Rodrigo Astroza, Joel P. Conte, and Jose I. Restrepo. The dissertation author is the primary investigator and author of the work. Chapter 3 is a close reprint of the material as it was prepared for submission for publication in ASCE Journal of Structural Engineering. The dissertation author is the

primary investigator and author of this material. Rodrigo Astroza, Joel P. Conte, Jose I. Restrepo, and Tara C. Hutchinson are co-authors. Chapter 4, in part, is published in the Journal of Earthquake Engineering and Structural Dynamics. It was written by Hamed Ebrahimian, Rodrigo Astroza, and Joel P. Conte, 2015 (DOI: 10.1002/eqe.2532). The dissertation author is the primary investigator and author of this material. Chapter 5, in part, is submitted for publication and may appear in Mechanical Systems and Signal Processing Journal. It was written by Hamed Ebrahimian, Rodrigo Astroza, Joel P. Conte, and Raymond A. de Callafon. The dissertation author is the primary investigator and author of this material. Chapter 6, in part, is currently being prepared for submission for publication. The dissertation author is the primary investigator and author of this material and Rodrigo Astroza, Joel P. Conte, and Costas Papadimitriou are the co-authors. Finally, Chapter 7, in part, is also currently being prepared for submission for publication. The dissertation author is the primary investigator and author of this material and Rodrigo Astroza, Joel P. Conte, and Robert Bitmead are the co-authors.



## VITA

- Sept. 2010 – Dec. 2015      Ph.D., Structural Engineering, Department of Structural Engineering, Jacobs School of Engineering, University of California San Diego, USA. Advisor: Professor Joel P. Conte.
- Jan. 2013 – Dec. 2013      M.Sc., Engineering Sciences (Dynamic Systems and Control), Department of Mechanical and Aerospace Engineering, Jacobs School of Engineering, University of California San Diego, USA. Advisor: Professor Raymond A. de Callafon.
- Sept. 2004 – Sept. 2006      M.Sc., Structural Engineering, Department of Civil Engineering, Shiraz University, Iran. Advisor: Professors Bijan Banan and Parvis Banan.
- Sept. 2000 – Sept. 2004      B.Sc., Civil Engineering, Department of Civil Engineering, Shiraz University, Iran.

## **ABSTRACT OF THE DISSERTATION**

NONLINEAR FINITE ELEMENT MODEL UPDATING FOR NONLINEAR  
SYSTEM AND DAMAGE IDENTIFICATION OF CIVIL STRUCTURES

by

Hamed Ebrahimian

Doctor of Philosophy in Structural Engineering

University of California, San Diego, 2015

Professor Joel P. Conte, Chair

Structural health monitoring (SHM) is defined as the capability to monitor the performance behavior of civil infrastructure systems as well as to detect, localize, and quantify damage in these systems. SHM technologies contribute to enhance the resilience of civil infrastructures, which are vulnerable to structural aging, degradation,

and deterioration, and to extreme events due to natural and man-made hazards. Given the limited financial resources available to renovate or replace civil infrastructures, the implementation of SHM methodologies is crucial to detect safety threats at an early stage, evaluate the operational risk of the infrastructure after a catastrophic event, and prioritize the urgency of the repair/retrofit or replacement of these structures.

This research focuses on the development of a novel framework for nonlinear structural system identification. This framework consists of updating mechanics-based nonlinear finite element (FE) structural models using Bayesian inference methods. Recognizing structural damage as the manifestation of structural material nonlinearity, the developed framework provides a new methodology for post-disaster SHM and DID of real-world civil structures.

This research is subdivided in two parts. The first part investigates the accuracy of state-of-the-art nonlinear FE modeling in predicting the cyclic and dynamic inelastic response behavior of reinforced concrete structural components and systems. Sources of inaccuracy and uncertainty in the FE modeling and simulation approach are investigated by comparing the FE-predicted structural response with high-fidelity experimental results. In the second part of this research, two frameworks for nonlinear FE model updating are proposed, developed, and validated using numerically simulated data. In the proposed frameworks, different Bayesian estimation methods are utilized to update the nonlinear FE model of a civil structure using the recorded input excitation and response of the structure during a damage-inducing earthquake event. The initial frameworks are then extended to output-only nonlinear structural

system and damage identification methods. This extension not only overcomes the shortcomings of the initial frameworks in handling unmeasured or noisy input measurements, but also paves the way to a general approach to account for model uncertainties. Finally, a new information-theoretic approach is developed for the purposes of nonlinear FE model identifiability, experimental design, and optimal sensor placement.

## **CHAPTER 1: INTRODUCTION**

### **1.1. Structural health monitoring**

Critical civil infrastructures are referred to as fundamental facilities and structures that provide commodities and services essential to enable, sustain, and enhance societal living and the economy. Essential building facilities (such as hospitals, emergency management centers, security service centers, airport buildings, shelters, hazardous waste storages, etc.), transportation networks (including tunnels and bridges), utility systems (including dams, water tanks, and power generation plants), and other lifeline structures are categorized as critical civil infrastructures, the incapacitation or destruction of which would have devastating economic and life-safety effects. The U.S. infrastructure recently received an overall D+ grade in the latest report card for America's infrastructure [1] issued by the American Society of Civil Engineers (ASCE). This low grade reflects the poor condition and deficiency of the nation's infrastructure based on several factors, including their physical condition, safety, resilience, and fiscal investments needed for improvement. In the case of

bridges, for example, the ASCE reports that over two hundred million trips are taken daily across deficient bridges in the largest metropolitan areas across the U.S. The average age of bridges is currently 42 years, and over 30% of these bridges have exceeded their 50-year design life limit. While billions of dollars have been spent annually on construction, rehabilitation, and repair of lifeline structures, current funding levels are insufficient to completely repair or replace the nation's critical civil infrastructures and overcome their continual degradation.

In the presence of limited financial resources available to renovate or replace the civil infrastructure, developing and implementing structural health monitoring (SHM) methods is the only practical solution to monitor the risk of operation and the reliability of these critical civil infrastructures and, therefore, assure their sustained usage and public safety. SHM and damage prognosis methods can detect safety threats at an early stage, evaluate the remaining useful life cycle of the infrastructure, and help in prioritizing the urgency of the repair/retrofit or replacement of these structures. SHM is defined as the capabilities for monitoring structural performance behavior and identifying, localizing, and quantifying the existence or occurrence of damage in the structural system, as well as predicting the remaining useful life of the system. Implementing SHM technologies to monitor critical civil infrastructures will not only prevent catastrophic structural failures (such as the I-35W Bridge failure in Minnesota in 2007, see Figure 1.1), but will also provide essential information for emergency management and rehabilitation after damage-inducing events (e.g., earthquakes, blast, fire, etc.).



Figure 1.1: I-35W St. Anthony Bridge Collapse in Minnesota in 2007 (picture is taken from [2]).

Disastrous events such as earthquakes are known to inflict potentially devastating damage to critical civil infrastructures. While the extent of damage is expected to be more significant in deficient structures, new or renovated/retrofitted structures are also vulnerable to experiencing damage during such events. Damage initiation and progression cannot always be detected through visual screening and, sometimes, very deliberate, costly, and invasive post-event inspection and evaluation processes are required to detect them (e.g., the connection failures in steel moment-frame buildings in the Los Angeles area during the 1994 Northridge earthquake [3]). Hidden initiated damage can continue to grow over time, and eventually result in deterioration of structural performance and life-safety threat, which are especially detrimental in the aftermath of a catastrophic event such as an earthquake. Furthermore, the service interruption of critical facilities needed to perform post-event

inspection and evaluation procedure contradicts an efficient emergency response management strategy. Therefore, the potential impact of earthquakes and other natural and man-made hazards on urban societies can be reduced through accurate and time-sensitive risk mitigating decisions, which can be supported and facilitated by the use of advanced SHM methodologies to help assess the safety and remaining strength of critical civil infrastructures.

In conclusion, infrastructure resiliency can be enhanced by implementing advanced SHM and damage identification methodologies for critical civil infrastructures in order to monitor their performance and functionality during normal operation, and after extreme loading and disastrous events. An advanced SHM methodology can diagnose the incidence, location, and extent of damage throughout the structural system and can support decision making related to operation, emergency response management, structural retrofit, and rehabilitation. An advanced SHM methodology can not only assure the continual functionality and sustainability of the civil infrastructure during normal operation, but can also help achieve rapid post-disaster recovery and rehabilitation.

## **1.2. Structural health monitoring based on nonlinear system and damage identification**

Most of the current SHM methods are based on linear system and damage identification (ID). In these methods, the modal parameters of an equivalent linear



elastic, viscously damped model of the civil structure are identified before and after a damage-inducing event using low-amplitude input-output or output-only measured dynamic data. Structural damage is then defined as a statistically significant change in the identified modal parameters (e.g., natural frequencies, mode shapes, curvature mode shapes, modal strain energy, etc.) of the equivalent linear models before and after the damaging events.

Damage ID based on tracking the changes in the modal parameters has been the subject of three important criticisms. First, linearity is an idealization of the response behavior of real structures, which are intrinsically nonlinear from the onset of loading [4]. Therefore, fitting a linear model to data measured from an intrinsically nonlinear structural system results in biased estimation of modal parameters, which in turn may result in erroneous damage ID results. Second, modal parameters and related quantities are global properties of the structure and often are not sensitive enough to local damage at the component or sub-component level [5]. Therefore, it is often difficult or even impossible to correctly identify and quantify localized damage at the component or sub-component levels of a structural system. Third and finally, low-amplitude (e.g., ambient) vibrations used for linear system ID provide information about the loss of effective stiffness in the structural system; however, they do not contain any information about strength and ductility capacity related manifestations of damage in the structural system.

SHM methods for civil infrastructure are required to be capable of identifying different damage manifestations—particularly those that correspond to the hysteretic

nonlinear behavior of the structural system (e.g., dissipated hysteretic energy, strength degradation, loss of ductility capacity). Moreover, the structural response of large and complex real-world civil infrastructures is far from linear elastic, especially during strong damage-inducing events. Therefore, developing reliable, robust, and accurate SHM necessitates methods and techniques that can acknowledge and incorporate the complex nonlinear response behavior of these structures.

### **1.3. Nonlinear system and damage identification based on nonlinear finite element model updating**

State-of-the-art high-fidelity nonlinear finite element (FE) models can be used to reconstruct the nonlinear response process of a structure during a damage-inducing event. This reconstruction can be used to investigate the state of damage in various sub-systems, sub-assemblies, and components of the structure. However, the numerical models are subject to imperfections and inaccuracies caused by modeling and model parameter uncertainties. More specifically, nonlinear structural FE models depend on a set of unknown parameters, the proper selection of which has a dominant influence on the accuracy of the predicted structural response. These parameters can include inertial properties, geometric parameters, restraint and constraint parameters, damping parameters, and parameters characterizing the nonlinear material constitutive laws used in the FE model. Estimating the true values (or the values that best represent the state of nature) for these parameters is often challenging, if not impossible.

Through a nonlinear FE model updating procedure accounting for all significant sources of uncertainty, these parameters can be estimated so that the model predictions closely resemble the true response of the structure.

Nonlinear FE model updating can be viewed as a family of methods used for the purpose of both nonlinear system ID and damage ID of civil structures (e.g., [6]). In this approach, using measured time histories of input-output data, the parameters of a mechanics-based nonlinear FE model of the structure of interest are estimated or updated by minimizing an objective function measuring the discrepancies between the measured and predicted responses in the time domain. Contrary to the modal ID methods, in this approach, the data measured during damage-inducing events (such as earthquakes), which contains valuable information about the nonlinear response behavior of the structure, are used to update the nonlinear FE model. The updated FE model can then be interrogated directly to evaluate the loss of strength and effective stiffness, as well as the history of inelastic deformations and related damages in the structure at different spatial resolution levels, from the global structural level to local component, element, and sub-element levels.

#### **1.4. Research objectives and scopes**

The main objective of the research work presented in this dissertation is to develop a nonlinear system and damage ID methodology for SHM by integrating high-fidelity predictive structural modeling and Bayesian inference methods. The proposed methodology is intended to resolve major hurdles that prevent current SHM techniques

from successful real-world applications. The main objective was sought by pursuing the following five sub-goals.

(1) The first goal of this research work is to systematically assess the fidelity and accuracy of a state-of-the-art FE modeling approach in predicting the behavior of real-world structural components and systems. It was, moreover, intended to quantify the simulation imprecision and point to the likely sources of FE modeling error or uncertainty through comparing experimental results with numerical FE predictions.

(2) The second goal of this research work is to propose, verify, and validate a draft framework for SHM based on nonlinear FE model updating. It was intended to integrate advanced high-fidelity mechanics-based nonlinear FE modeling and analysis techniques, able to capture the damage/failure mechanisms to be identified, with advanced nonlinear estimation techniques, in order to harvest information from the measured structural response data and update the FE model of the structure of interest. Through an advanced and innovative approach, the proposed research aimed at drafting a general framework for the nonlinear system and damage ID of large and complex structures that can be applied to various types of structural systems (e.g., building structures, bridges, dams, and power plants), different types of FE modeling and analysis techniques, and different types of damage-inducing events.

(3) The first version of the framework for SHM to be developed will be based on a set of simplifying and idealizing assumptions and conditions that may prevent it from successful real-world applications. The third goal of this research work

consists of understanding and quantifying the limiting effects of the underlying simplifying assumptions and, moreover, investigating the performance of the initially proposed framework, when these underlying assumptions are violated.

(4) Building on the previous step, the next goal is to overcome problems that can prevent or limit the successful application of the proposed SHM framework to real-world civil structures. The research efforts resulted in developing and initially validating a general approach for addressing model uncertainties, input noise, and unknown/unmeasured input base excitation.

(5) Finally, the last goal of this research work is to develop practical and efficient methods to evaluate model identifiability, which can then be used for optimal sensor placement and experimental design.

## **1.5. Dissertation outline**

The presentation of this research work has been divided into eight chapters, the contents of which are outlined below. Except for the first and last chapters, which are dedicated to the Introduction and Conclusions, respectively, each chapter is an independent and self-contained description of a specific research task performed to pursue the research goals outlined previously. Each chapter, therefore, contains a descriptive introduction that defines the goals and objectives of the performed research task, and includes an in-depth literature review on the specific subject.

The first research goal is treated in Chapters 2 and 3. These two chapters focus on experimental-analytical correlation studies to investigate the sources of discrepancies between experimental results and predictions based on state-of-the-art nonlinear FE modelling and response simulation techniques for RC structures. Chapter 2 uses a number of quasi-static experimental datasets obtained from high-quality tests on reinforced concrete components and subassemblies. By studying the influence of various modeling features, the sources of discrepancies between experimental and numerical simulation results are investigated. The goal of this chapter is first to examine the fidelity of the proposed modeling and simulation approach, and then to address the likely sources of discrepancies. Chapter 3 makes use of the findings and knowledge gained in chapter 2 to develop a predictive FE model of a full-scale building specimen that was tested on the NEES-UCSD large outdoor shake table in 2012. In this landmark test, a full-scale five-story reinforced concrete building specimen, outfitted with a variety of nonstructural components and systems, was tested using a sequence of shake table dynamic tests using scaled and unscaled earthquake motions. A detailed three-dimensional nonlinear finite element (FE) model of the structure was developed and used for pre-test response simulations to predict the seismic response of the test specimen and for decision support in defining the seismic test protocol, as well as in selecting the instrumentation layout. Utilized as blind prediction, the pre-test simulation results at different levels (global structure level, and local member/section/fiber levels) are compared with their experimental counterparts for seismic input (base excitation) of increasing intensity from the serviceability to the

MCE level. The predictive capabilities of the employed FE modeling techniques are evaluated and possible causes of discrepancies between the FE predictions and experimental measurements are investigated and discussed.

Chapter 4 provides the first step toward developing a novel nonlinear FE model updating framework and is aligned with the second research goal. In this chapter, advanced nonlinear structural FE modeling and analysis techniques are used jointly with a stochastic filtering method (the extended Kalman filter, or EKF in brief) to estimate time-invariant parameters associated with the nonlinear material constitutive models of the FE model. To verify the proposed nonlinear FE model updating framework, two proof-of-concept examples based on simulated data are presented in this chapter. The first example consists of a cantilever steel bridge column with three unknown primary material parameters, while a three-story three-bay moment resisting steel frame with six unknown primary material parameters is used as second example. The two examples demonstrate the excellent performance of the proposed parameter estimation framework even in the presence of high measurement noise.

Chapter 5 unveils another approach for nonlinear system and damage identification of civil infrastructures based on nonlinear FE model updating. Focusing on the second and third research goals defined above, the framework proposed in this chapter integrates advanced mechanics-based nonlinear FE modeling and analysis techniques with a batch Bayesian estimation approach to estimate time-invariant model parameters used in the FE model of the structure of interest. The framework

uses measured input excitation and dynamic response of the structure and updates a nonlinear FE model of the structure to minimize the discrepancies between FE predicted and measured response time histories. The updated FE model can then be interrogated to detect, localize, classify, and quantify the state of damage and predict the remaining useful life of the structure. Unlike recursive estimation methods, in the batch Bayesian estimation approach, the entire time histories of the measured input excitation and output response of the structure are used as a single batch of data from which the FE model parameters are estimated through a number of iterations. In the case of a non-informative prior, the batch Bayesian method leads to an extended maximum likelihood (ML) estimation method to estimate jointly time-invariant model parameters and the measurement noise amplitude. The extended ML estimation problem is solved efficiently using a gradient-based interior-point optimization algorithm. The estimation uncertainties are evaluated based on the Cramer-Rao lower bound (CRLB) theorem by computing the exact Fisher information matrix using the FE response sensitivities with respect to the model parameters. The accuracy of the proposed uncertainty quantification approach is verified using a deterministic sampling approach based on the unscented transformation. The same numerical prototype structures as in the previous chapter are used here for validating the proposed framework, namely a bridge pier and a 2D moment-resisting steel frame. To address the third research goal, different case studies are conducted in this chapter to investigate the performance of the proposed parameter estimation and nonlinear FE model updating framework in the presence of high measurement noise, heterogeneous



sensor array, way-out initial estimates, input measurement noise, and modeling uncertainty.

Chapter 6 presents an innovative framework for output-only nonlinear system identification of civil structures based on nonlinear FE model updating, utilizing only the measured structural response to earthquake excitation. The proposed framework provides a computationally feasible approach for health monitoring and damage identification of civil structures when either input seismic excitations are not measured or the measured seismic excitations are incomplete, erroneous, and/or contaminated with measurement noise. Grounded in Bayesian inference, the proposed framework jointly estimates the FE model parameters and the input earthquake ground acceleration time histories using only the measured dynamic response of the structure. Two approaches are investigated herein to solve the augmented input and parameter estimation problem: (i) the recursive maximum likelihood (ML) estimation approach, which reduces to a nonlinear optimization problem, and (ii) a stochastic filtering approach based on the recursive maximum a posteriori (MAP) estimation method, which reduces to an extended Kalman filtering method. Both approaches require the computation of FE response sensitivities with respect to FE model parameters and the input ground acceleration at the discrete times at which the input earthquake records are defined. The FE response sensitivities are computed accurately and efficiently using the direct differentiation method (DDM). The two proposed approaches are validated using the seismic response of a 3D five-story reinforced concrete building structure simulated utilizing an advanced mechanics-based nonlinear FE structural

model. The simulated structural response to a horizontal bidirectional seismic excitation is contaminated with artificial measurement noise and used as measured response data to estimate both the FE model parameters characterizing the nonlinear material constitutive laws of the concrete and reinforcement steel materials of the structure and the full time history of the input ground acceleration in the longitudinal direction.

Chapter 7 aims at providing an innovative tool for sensor placement design for successful application of the proposed nonlinear FE model updating framework. This important goal is achieved by investigating the theoretical identifiability conditions using an information-theoretic approach. The accuracy and robustness of the proposed nonlinear system and damage ID methodologies highly depend on the amount of information contained in the measurements about the model parameters to be identified. It is therefore crucial to systematically identify the model parameters that can be estimated and to optimally select the sensor arrays and output measurements to harvest the maximum information about the model parameters. In this chapter, a statistical metric is developed to quantify the information contained in every individual measurement channel about every individual model parameter. This one-to-one identifiability measure is developed by evaluating the difference between the information entropy of the prior and posterior marginal probability distribution functions (PDF) of the model parameters. This approach provides a measure of identifiability of nonlinear structural FE models, which can have immediate

applications in parameter selection, optimal sensor placement, and design of experiment.

Finally, chapter 8 summarizes the research work performed in this dissertation, emphasizes the main original contributions and findings of the research work, and provides recommendations for future research.

## References

- [1] American Society of Civil Engineers, "2013 Report Card for America's Infrastructure," 2013. [Online]. Available: <http://www.infrastructurereportcard.org/>. [Accessed 8 2015].
- [2] Federal Highway Administration, "Context Sensitive Solutions," [Online]. Available: <http://contextsensitivesolutions.org/>. [Accessed 08 2015].
- [3] D. K. Miller, "Lessons Learned from the Northridge Earthquake," *Engineering Structures*, vol. 20, no. 4-6, p. 249–260, 1998.
- [4] G. Kerschen, K. Worden, A. F. Vakakis and J. C. Golinval, "Past, Present and Future of Nonlinear System Identification in Structural Dynamics," *Mechanical Systems and Signal Processing*, vol. 20, no. 3, p. 505–592, 2006.
- [5] S. Gopalakrishnan, M. Ruzzene and S. Hanagud, *Computational Techniques for Structural Health Monitoring*, London: Springer, 2011.
- [6] F. M. Hemez and S. W. Doebling, "Review and Assessment of Model Updating for Nonlinear Transient Analysis," *Mechanical Systems and Signal Processing*, vol. 15, no. 1, p. 45–74, 2001.

**CHAPTER 2: EXPERIMENTAL-ANALYTICAL CORRELATION  
STUDY OF THE BEHAVIOR OF REINFORCED CONCRETE  
COMPONENTS AND SUB-ASSEMBLIES USING STRUCTURAL  
FINITE ELEMENTS AND SMEARED CRACK APPROACH**

**2.1. Introduction**

Nonlinear structural analysis is an efficient and inexpensive method to predict and understand the complex seismic response of Reinforced Concrete (RC) structures. The nonlinear structural analysis objective is to accurately predict the force deformation response of the components as well as the global and local failure modes of the structure and the sub-structures, at an affordable computational cost.

Two ends of the spectrum can be contrasted for nonlinear structural analysis of RC structures in terms of modeling sophistication and mathematical accuracy. In the lower end of the spectrum, methods such as lumped plasticity are placed. In the lumped plasticity method, the structure is modeled by simplified nonlinear structural

beam-column elements. In the other end of the spectrum, RC structures can be modeled using mechanics-based 3D continuum elements with spatially distributed inelasticity or plasticity of the steel and concrete materials.

In the lumped plasticity approach, an RC structure is modeled as an assembly of interconnected linear elastic elements with zero length (lumped) plastic hinge elements. Each lumped plastic hinge element can represent the nonlinearity of a specific behavioral sub-component such as axial-flexure, beam shear, torsion, beam-column joint, and so on. Several models, such as simplified piece-wise linear models [1], smooth hysteretic models [2], and more advanced stress-resultant models [3] are articulated in the literature and used to define the nonlinear force-deformation relation for plastic hinge elements. Typically, a phenomenological hysteretic model for lumped plastic hinge element is calibrated using quasi-static test results on RC components and sub-assemblies (e.g., [4]). In addition to its simplicity and computational efficiency, the lumped plasticity approach is found efficient in predicting the response of regular RC structures [5]. For more complex structures or under atypical loading conditions, the results obtained by using lumped plasticity approach can be inaccurate.

On the other end of the spectrum, opposite to the simplified lumped plasticity method, an RC structure can be modeled and analyzed using a detailed finite element modeling approach. This approach uses solid elements in conjunction with detailed three-dimensional material constitutive models for concrete and reinforcing steel, and can properly simulate the complicated physics of RC members. Various sources of nonlinearity in concrete material such as cracking, spalling, shear sliding, crushing,

and in steel reinforcements such as interface behavior of concrete and steel, dowel action, yielding, buckling, and rupture can be incorporated in the mathematical constitutive models to enhance the accuracy of the nonlinear structural analysis. Despite its fidelity, this approach is computationally demanding and potentially exposed to a number of numerical problems such as instability and lack of convergence. The associated computational costs and numerical problems render this approach sometimes unsuited for many practical applications especially at the full structural level modeling. Many valuable research efforts in this field are articulated in the literature, among which the works done by Maekawa et al. [6] can be cited as a remarkable contribution.

Classified in between the two end of the spectrum of methods, other methods are reported in the literature to reduce the computational cost and maintain acceptable fidelity. Generally, in these methods, degenerated finite elements (such as structural truss, beam, and shell elements) are used with distributed inelasticity or plasticity. These methods use some underlying kinematic constraints or other simplifying assumptions, enhancing the computational efficiency and reducing the mathematical rigor of the model at the same time. The fidelity of these methods highly depends on the implicit kinematic assumptions and employed material constitutive models.

Using fiber beam-column elements for nonlinear analysis of RC frames [7] is one of the well-established methods in the class of distributed plasticity structural finite element. The initial version of fiber element method uses one-dimensional material constitutive model to capture the nonlinear axial-flexural behavior of RC

sections. To include shear effects, Petrangeli et al. [8] updated the one-dimensional concrete constitutive model by incorporating axial-flexural-shear coupling at the section level. The proposed model by Petrangeli et al., however, is computationally demanding [9]. In another effort, Marini and Spacone [9] successfully aggregated a simple nonlinear hysteretic shear model at the section level of the classical fiber section to incorporate axial-flexural-shear coupling at the element level. The efficiency of the fiber element method is significantly affected by the flexural-shear and flexural-torsional interactions especially during large-amplitude cyclic loadings. This limitation renders the fiber element method unsuitable to model specific RC structures and sub-components such as shear walls, shear-dominated beams under large cyclic loadings, and bridge girders under simultaneous flexural and torsional loadings.

Since the fiber element method has serious limitations in modeling RC shear walls, Panagiotou et al. [10] proposed a nonlinear truss modeling approach to model plane stress RC members, such as concrete walls, subjected to cyclic reversals. In this method, an RC shear wall is modeled by a connected set of longitudinal, transversal and diagonal truss elements representing the concrete and reinforcing steel bars – both longitudinal and transversal –. This model can mimic the modified compression field theory [11] by affecting the stress-strain relationship in compressive trusses – struts – based on tensile strain in the transverse trusses – ties – and includes strength and stiffness degradation. The nonlinear truss model can properly capture the cyclic response of RC walls whose response is dominated by flexural-shear interactions.



Computationally efficient structural elements (such as beam-column elements, plate elements, shell elements, etc.) can be used in conjunction with advanced material constitutive models to develop another method in the class of distributed plasticity finite element. Following the implicit kinematic constraints in the formulation of structural elements, the corresponding multi-axial state of strain is derived from the nodal displacements at the integration point locations. Using the material law for concrete and steel, the multi-axial state of stress is updated at the integration points. The nodal force and stiffness matrix are computed by numerically integrating the stress and stiffness over all the integration points. Even though the designated constitutive models can capture sophisticated behavior of RC material, the structural element restricts the displacement field of the discretized model and consequently reduces the simulation accuracy. To better understand the performance of this compromising approach and to examine its shortcomings and limitations, the correlation between numerical results and the experimental observations must be studied.

In the literature, there is a scarcity of experimental-analytical correlation studies using experimental data together with the state-of-the-art RC material models combined with structural elements. This chapter focuses on a state-of-the-art RC material modeling approach referred to as *total strain rotating smeared crack model*. The results of some selected experimental studies on RC components and sub-assemblies are compared with the numerical simulation results using this modeling approach. By studying the influence of various modeling features, the sources of

discrepancies between experimental results and numerical simulations are explained. The goal of this study is first to examine the fidelity of the proposed modeling approach and to quantify the simulation imprecision, then to address the likely causes of discrepancies. Knowing the vulnerability sources of the proposed modeling approach paves the way for future research to further improve the Finite Element (FE) modeling technique for RC structures and reduce the discrepancies between experimental and analytical results.

## **2.2. Concrete material constitutive model**

### **2.2.1. Background**

Different models are proposed in the literature to formulate the constitutive behavior of plain concrete material in the literature. Linear elastic model [12] combined with a failure criterion is the most basic approach to describe the concrete material law. The material either has a perfectly plastic behavior or possesses a degraded stiffness after failure in compression. In tension, however, the material is assumed to vanish or soften after failure. The complex nonlinear behavior of concrete material can be represented better by nonlinear elastic models such as path-dependent pseudo-elasticity [13] and hypo-elasticity [14] models. Pseudo-elasticity – or secant-elasticity – models define a relationship between the total strain and total stress tensors. In these models the nonlinearity is incorporated into the secant stiffness tensor, which is defined using a path-dependent material law. A class of pseudo-

elasticity models is the elastic-damage model [15], in which a history-dependent internal damage parameter is used to model the stiffness degradation by down-scaling the elastic stiffness matrix. Contrary to the pseudo-elasticity, hypo-elasticity models define a relation between strain and stress rates using a history-dependent tangential stiffness matrix. Classical plasticity models [16] are another popular approach to formulate concrete material law based of flow theory of plasticity. Classical plasticity models are unable to capture the concrete stiffness degradation observed under cyclic loadings. Therefore, to overcome this deficiency, the classical plasticity is combined with damage models to form a new class of material models referred to as plastic-damage models [17]. The Endochronic theory [18], which is based on the thermodynamics theory of internal variables, is also used to formulate concrete material law. This theory, which can be classified as a viscoplasticity model with strain-rate dependent viscosity, assumes that the stress is a function of entire history of deformation, measured using a time scale referred to as endochronic time. Microplane model [19] is another class of methods used to characterize concrete constitutive model by formulating stress and strain vectors relationship acting on a generic plane with arbitrary orientation, named as microplane. The macroscopic stress (or strain) vector is related to the stress (or strain) vector on the microplanes using static (or kinematic) constrains. Different gradually improved models of this class are articulated in the literature (refer to [20] for the most current model).

In the finite element analysis of RC structures, fracturing of concrete material can be modeled following several approaches, two of which have been deliberated

more in the literature, namely the discrete crack approach [12] and the smeared crack approach [21]. In the first approach, cracking is modeled as a geometrical discontinuity and is applied by updating the mesh discretization of the finite element domain upon the formation of a new crack. The onset of cracking is usually defined based on fracture mechanics concepts. In the smeared crack approach, however, the cracked material is considered as a continuum; the effect of cracking is implicitly included in the concrete material law in a spatially averaged way and affects the stress-strain relation at the integration points of the finite element model. The implementation of the smeared crack approach is known to be practically easier than the discrete crack approach. This simplicity makes the smeared crack approach the most widely used one in practice [22]. This approach has been widely referred to in the literature and research studies, and has been implemented in a number of commercial finite element analysis programs, such as DIANA [23].

The smeared crack approach can be further classified into fixed crack model [21] and rotating crack model [24]. In the fixed crack model, the direction of a crack remains fixed once it forms. As the loading increases, the principal stress direction may deviate from the crack direction, and shear stresses appear at the crack surface. Therefore, a shear transfer model along the cracks surface needs to be implemented. To account for multi-directional cracks at a single point, different methods have been suggested in the literature, such as the multi-directional fixed crack model [25] and the quasi-orthogonal 4-way fixed crack model [6]. In the rotating crack model, conversely, the direction of a crack follows the principal tensile strain direction at every iteration

of the finite element analysis, regardless of the previous crack orientation. As a result, the principal stresses and strains are always aligned with the crack direction and no explicit shear transfer model needs to be defined. The rotating crack model has become more popular than the fixed crack model mainly because of its simplicity and computational efficiency [26-27].

Two main approaches exist to incorporate the smeared crack method for tensile behavior into the concrete constitutive model. In the first approach, the total strain of the concrete material is decomposed into two parts: uncracked-concrete strain and smeared-crack strain. Different models can be used to formulate the constitutive behavior of uncracked concrete; for instance, models such as linear elasticity [25] or classical plasticity [28] to name only two. The stress-strain relation of cracked concrete can be formulated by either the fixed crack model [25] or the rotating crack model [29]. In the second approach, the concrete is treated as an orthotropic nonlinear elastic material in which the total stress is defined as a function of the total strain in each principal direction. This *total strain-based* approach can be implemented in either a fixed or rotating crack framework [29]. This approach is conceptually simple to implement in a plane stress state. In a three dimensional state, however, the stress-strain responses of concrete in different directions are strongly coupled because of the cracking and Poisson's effects. Vecchio and Selby [30] proposed an effective and elegant method that uses nonlinear elastic constitute model for concrete in conjunction with the total strain-based rotating crack model in a three dimensional finite element

context. Maekawa et al. [6] also proposed a more sophisticated method that extends the total strain-based fixed crack model into the three dimensional state.

### 2.2.2. Employed constitutive model

This section describes the different ingredients of the concrete constitutive model employed in this study, which is a total strain rotating smeared crack model with an orthotropic pseudo-elastic concrete material law.

### 2.2.3. Uni-axial tensile behavior

The uni-axial tensile behavior of the concrete consists of the initial linear elastic part and successive nonlinear softening part according to Reinhardt exponential softening model [31] (Figure 2.1). The stress and strain – denoted by  $\sigma$  and  $\varepsilon$  – relation in tension is as follows:

$$\sigma = \begin{cases} E_0 \varepsilon, & 0 < |\varepsilon| < |\varepsilon_{tc}| \\ -f'_t \left( 1 - \left( \frac{\varepsilon - \varepsilon_{tc}}{\varepsilon_{tu} - \varepsilon_{tc}} \right)^{0.31} \right), & |\varepsilon_{tc}| < |\varepsilon| < |\varepsilon_{tu}| \end{cases} \quad (2.1)$$

where  $E_0$  = initial linear elastic modulus in tension and compression and is computed

as  $E_0 = \frac{5 f'_{cc}}{3 \varepsilon_{cc}}$ , in which  $f'_{cc}$  = peak confined compressive strength and  $\varepsilon_{cc}$  = peak

confined compressive strain. The tensile strength of concrete  $f'_t = 0.33 \sqrt{f'_c}$  (MPa),

where  $f'_c$  = unconfined compressive strength of concrete, and the peak strain – or

cracking strain  $-\varepsilon_{ic} = -f_t' / E_0$ . The ultimate strain of concrete in tension is  $\varepsilon_{tu}$ . Beyond  $\varepsilon_{tu}$ , the concrete material will vanish in tension, that means both stress and stiffness will be zero.

By incorporating the tensile strain softening behavior in a continuum finite element model, the model becomes spuriously sensitive to the mesh discretization [32]. To resolve this issue in the smeared crack formulation, Bazant [33] and Bazant and Oh [19] proposed the Crack Band Model, based on which the cracking energy dissipated by each element is constant and independent of the element size. This constant cracking energy is referred to as fracture energy, denoted by  $G_f$ , defined as the energy required creating a unit area of a fully developed crack, and considered as a material property. To implement the fracture energy concept in the finite element framework, the ultimate tensile strain for an element of size  $h$  is derived such that the area under the post peak part of the stress-strain curve is equal to  $G_f/h$ . From the second part of Eq. 2.1, it follows that:

$$\frac{G_f}{h} = 0.24 f_t' |\varepsilon_{tu}| - |\varepsilon_{ic}| \quad (2.2)$$

Introduction of the fracture energy removes the unobjective dependency of the FE results to the mesh size; however, the strain softening still concentrates along few elements. Therefore, the localization zones, or zones of strain softening concentration, are still biased by the FE mesh spatial discretization [34]. Other regularization methods to alleviate localization effects are discussed by de Borst [35].

As shown in Figure 2.1, the unloading and reloading in tension is modeled by linear secant paths passing through the origin. This assumption is too simple as, in reality, some residual strains remain after stress removal. Nevertheless, this simplification is made to ensure numerical stability [36].

#### 2.2.4. Uni-axial compressive behavior

The uni-axial compressive constitutive law of concrete consists of an initial linear and two consecutive parabolic parts as shown in Figure 2.1. The unloading and reloading in compression is modeled by linear secant paths passing through the origin. The stress and strain – denoted by  $\sigma$  and  $\varepsilon$  – relation for each part is defined as:

$$\sigma = \begin{cases} E_0 \varepsilon, & 0 < \varepsilon < \frac{1}{5} \varepsilon_{cc} \\ \frac{f'_{cc}}{3} \left[ 5 \frac{\varepsilon}{\varepsilon_{cc}} - 2 \left( \frac{5}{4} \frac{\varepsilon}{\varepsilon_{cc}} - \frac{1}{4} \right)^2 \right], & \frac{1}{5} \varepsilon_{cc} < \varepsilon < \varepsilon_{cc} \\ f'_{cc} \left[ 1 - \left( \frac{\varepsilon - \varepsilon_{cc}}{\varepsilon_{cu} - \varepsilon_{cc}} \right)^2 \right], & \varepsilon_{cc} < \varepsilon < \varepsilon_{cu} \end{cases} \quad (2.3)$$

In which  $E_0$  = initial linear elastic modulus and  $\varepsilon_{cu}$  = ultimate strain of the confined concrete.  $f'_{cc}$ ,  $\varepsilon_{cc}$ , and  $\varepsilon_{cu}$  are computed based on the initial – undamaged – properties of the concrete material and the confinement effect of the transverse reinforcements [37]. In a finite element model using beam-column elements, the confinement effect of transverse reinforcement cannot be included explicitly in the concrete constitutive model. Alternatively, the confinement effect can be incorporated indirectly by



increasing the peak compressive stress and strain and modifying the post-peak behavior of the concrete material. To this end, parameters  $f'_{cc}$  and  $\varepsilon_{cc}$  are determined using the average of various *concrete models* articulated in the literature such as modified Kent and Park's model [38], Mander's model [37], Saatcioglu and Razvi's model [39], and Attard and Setunge's model [40]. The ultimate strain of confined concrete in compression,  $\varepsilon_{cu}$ , is determined following Scott et al. [41].

The strain softening in compression is subjected to the same localization and unphysical mesh-sensitivity problem as in tension. To regularize the localization in compression failure, the softening branch of the compressive stress-strain curve for each finite element is defined as a function of a constant fracture energy in compression [42],  $G_c$ , and the element size,  $h$ , such that the total post peak dissipated energy, dissipated by concrete crushing, is independent of the element size.

As already mentioned, the use of the fracture energy resolves the mesh objectivity of the FE results; however, fracture localization still continues to take place along few elements in a displacement-based finite element model. For example, in modeling a RC frame, the post peak energy dissipation localizes in a few elements referred to as the *plastic hinge elements*. In this study, the size of the plastic hinge elements is selected to represent the physical plastic hinge region of the beam or column of interest, which is taken as one half of the structural member height. The size of slab plastic hinge elements is also selected following the same strategy. For each RC member, by having size of the plastic hinge element,  $h$ , the peak compressive

strain,  $\varepsilon_{cc}$ , and the ultimate compressive strain,  $\varepsilon_{cu}$ , of the confined concrete material,

$G_c$  is computed according to the parabolic relation defined in Eq. 2.3:

$$\frac{G_c}{h} = \frac{2}{3} f'_{cc} (\varepsilon_{cu} - \varepsilon_{cc}) \quad (2.4)$$

The compressive fracture energy,  $G_c$ , is applied as a material constant to all the elements of the proposed RC member and reflects the confinement effects provided by the transverse reinforcement in the plastic hinge region.

Tri-axial state of stress at an integration point produces a *mechanics-based confinement*. In DIANA, this type of confinement is accounted for by gradually increasing the stress and strain at the peak point of the concrete stress-strain curve [23] following the procedure suggested by Selby and Vecchio [43].

Based on the modified compression field theory (MCFT) [11] the compressive behavior of concrete in one principal direction can be substantially reduced by the presence of tensile cracking in the other principal directions. Denoting the strain in the compressive principal direction by  $\varepsilon_0$ , and the average lateral tensile strains by  $\varepsilon_1$ , the stress reduction factor,  $\beta$ , is determined based on *Model B* as proposed by Vecchio and Collins [44]:

$$\beta = \frac{1}{1 + K_c} \quad (2.5)$$

$$K_c = 0.27 \left( \left| \frac{\varepsilon_1}{\varepsilon_0} \right| - 0.37 \right)$$

where  $\varepsilon_1 = \sqrt{\varepsilon_{l,1}^2 + \varepsilon_{l,2}^2}$ , and  $\varepsilon_{l,1}$ ,  $\varepsilon_{l,2}$  denote the maximum observed tensile strain in the lateral principal directions 1 and 2, respectively. This procedure is employed in

DIANA and continually updates the uni-axial stress-strain law for the concrete in compression based on the computed maximum tensile strains in the lateral directions [23].

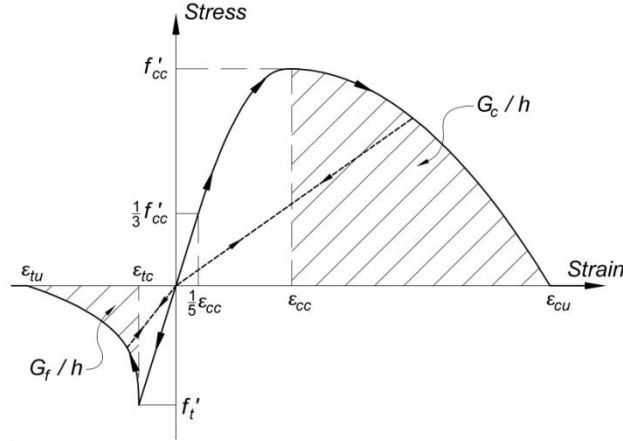


Figure 2.1: Uni-axial stress-strain constitutive law of concrete used in this study.

### 2.2.5. Total strain-based rotating crack formulation

By solving the global equilibrium equations at every iteration of the finite element analysis, the current displacement vector at nodal points and the total strain vector at integration points are computed. Based on the rotating crack approach, at each integration point, the total strain vector in global coordinates ( $\boldsymbol{\varepsilon}_{xyz} = [\varepsilon_{xx}, \varepsilon_{yy}, \varepsilon_{zz}, \varepsilon_{xy}, \varepsilon_{yz}, \varepsilon_{zx}]^T$ ) is transformed into its principal directions ( $\boldsymbol{\varepsilon}_{123} = \varepsilon_{11}, \varepsilon_{22}, \varepsilon_{33}, 0, 0, 0^T$ ) using the strain transformation matrix  $\mathbf{T}$  ( $\boldsymbol{\varepsilon}_{123} = \mathbf{T}\boldsymbol{\varepsilon}_{xyz}$ ). The strain transformation matrix is computed using the principal directions of the strain tensor in global coordinates.

$$\mathbf{T} = \begin{bmatrix} k_1^2 & l_1^2 & m_1^2 & k_1 l_1 & l_1 m_1 & m_1 k_1 \\ k_2^2 & l_2^2 & m_2^2 & k_2 l_2 & l_2 m_2 & m_2 k_2 \\ k_3^2 & l_3^2 & m_3^2 & k_3 l_3 & l_3 m_3 & m_3 k_3 \\ 2k_1 k_2 & 2l_1 l_2 & 2m_1 m_2 & k_1 l_2 + k_2 l_1 & l_1 m_2 + l_2 m_1 & m_1 k_2 + m_2 k_1 \\ 2k_2 k_3 & 2l_2 l_3 & 2m_2 m_3 & k_2 l_3 + k_3 l_2 & l_2 m_3 + l_3 m_2 & m_2 k_3 + m_3 k_2 \\ 2k_3 k_1 & 2l_3 l_1 & 2m_3 m_1 & k_3 l_1 + k_1 l_3 & l_3 m_1 + l_1 m_3 & m_3 k_1 + m_1 k_3 \end{bmatrix} \quad (2.6)$$

in which  $k_i, l_i, m_i^T$  denote the direction cosines of the  $i^{\text{th}}$  principal direction of the strain tensor in global coordinates. Using the orthotropic stress-strain relationship, the principal stress components are computed as

$$\begin{bmatrix} \sigma_{11} \\ \sigma_{22} \\ \sigma_{33} \end{bmatrix} = \begin{bmatrix} E_1 \frac{1-\nu_{23}^2}{\Phi} & E_1 \frac{\nu_{12} + \nu_{31}\nu_{23}}{\Phi} & E_1 \frac{\nu_{31} + \nu_{12}\nu_{23}}{\Phi} \\ E_2 \frac{\nu_{12} + \nu_{31}\nu_{23}}{\Phi} & E_2 \frac{1-\nu_{31}^2}{\Phi} & E_2 \frac{\nu_{23} + \nu_{12}\nu_{31}}{\Phi} \\ E_3 \frac{\nu_{31} + \nu_{12}\nu_{23}}{\Phi} & E_3 \frac{\nu_{23} + \nu_{12}\nu_{31}}{\Phi} & E_3 \frac{1-\nu_{12}^2}{\Phi} \end{bmatrix} \begin{bmatrix} \varepsilon_{11} \\ \varepsilon_{22} \\ \varepsilon_{33} \end{bmatrix} \quad (2.7)$$

By using the orthotropic stress-strain relationship, the associated stiffness matrix will be non-symmetric in general. To resolve the non-symmetry in the stiffness matrix, the stress-strain relation is expressed in terms of equivalent uni-axial strain vector ( $\tilde{\boldsymbol{\varepsilon}}_{123} = \tilde{\varepsilon}_{11}, \tilde{\varepsilon}_{22}, \tilde{\varepsilon}_{33}, 0, 0, 0^T$ ) [23] as

$$\begin{bmatrix} \tilde{\varepsilon}_{11} \\ \tilde{\varepsilon}_{22} \\ \tilde{\varepsilon}_{33} \end{bmatrix} = \mathbf{P} \begin{bmatrix} \varepsilon_{11} \\ \varepsilon_{22} \\ \varepsilon_{33} \end{bmatrix}, \quad \mathbf{P} = \begin{bmatrix} \frac{1-\nu_{23}^2}{\Phi} & \frac{\nu_{12} + \nu_{31}\nu_{23}}{\Phi} & \frac{\nu_{31} + \nu_{12}\nu_{23}}{\Phi} \\ \frac{\nu_{12} + \nu_{31}\nu_{23}}{\Phi} & \frac{1-\nu_{31}^2}{\Phi} & \frac{\nu_{23} + \nu_{12}\nu_{31}}{\Phi} \\ \frac{\nu_{31} + \nu_{12}\nu_{23}}{\Phi} & \frac{\nu_{23} + \nu_{12}\nu_{31}}{\Phi} & \frac{1-\nu_{12}^2}{\Phi} \end{bmatrix} \quad (2.8)$$

in which  $\Phi = 1 - \nu_{23}^2 - \nu_{31}^2 - \nu_{12}^2 - 2\nu_{23}\nu_{31}\nu_{12}$ . Therefore, the relationship between stress vector and equivalent uni-axial strain vector in principal coordinates is simplified as follows.

$$\sigma_{123} = \begin{bmatrix} E_1 & 0 & 0 & 0 & 0 & 0 \\ 0 & E_2 & 0 & 0 & 0 & 0 \\ 0 & 0 & E_3 & 0 & 0 & 0 \\ 0 & 0 & 0 & G_{12} & 0 & 0 \\ 0 & 0 & 0 & 0 & G_{23} & 0 \\ 0 & 0 & 0 & 0 & 0 & G_{31} \end{bmatrix} \tilde{\boldsymbol{\varepsilon}}_{123} \quad (2.9)$$

where  $\sigma_{123} = \sigma_{11}, \sigma_{22}, \sigma_{33}, 0, 0, 0^T$  is the stress vector in principal coordinates,  $E_1$ ,  $E_2$ , and  $E_3$  are the secant modulus in the three principal directions, respectively. The shear modulus term,  $G_{ij}$ , is defined as

$$G_{ij} = \frac{\text{Min } E_{\min,i}, E_{\min,j}}{2(1 + \nu_{ij})} \quad (2.10)$$

in which  $E_{\min,i}$  is the minimum observed secant modulus in the principal direction  $i$ . If  $\sigma_{ii}$  is tensile, then  $E_{\min,i}$  is the minimum observed secant modulus in tensile direction; if  $\sigma_{ii}$  is compressive, then  $E_{\min,i}$  is the minimum observed secant modulus in compressive direction.

The material state determination – i.e. updating the stress vector and the stiffness matrix – at each integration point consists of four steps. In the first step, the  $\mathbf{P}$  matrix is derived. In the second step, the equivalent uniaxial strain vector is computed. Then, the stress and secant modulus are updated in each principal direction separately based on the equivalent uni-axial strains and the uni-axial material constitutive law as introduced earlier. Finally, the shear modulus terms are computed and the secant stiffness matrix, as given in Eq. 2.9, is set up.

The Poisson's ratios, used to derive the  $\mathbf{P}$  matrix, are a function of secant modulus in principal tensile directions. In each principal direction, the Poisson's ratio

is kept constant – in this study  $\nu_0 = 0.2$  – before the concrete cracks in tension. After concrete cracks in a certain direction – for example direction  $i$  –, all the related component of Poisson's ratio – for example  $\nu_{ij}$  and  $\nu_{ik}$  – are reduced as

$$\nu_{reduced,ij} = \nu_{reduced,ik} = \left( \frac{E_{min,i}^{ten}}{E_0} \right) \nu_0 \quad (2.11)$$

where  $E_{min,i}^{ten}$  denotes the minimum observed secant modulus in the tensile direction of the principal direction  $i$ . This relation is based on the fact that in cracked concrete Poisson's effect vanishes – i.e. upon cracking in one direction, contraction in perpendicular directions will be zero. When the concrete cracks in more than one direction, for example directions  $i$  and  $j$ ,  $\nu_{ij}$  is computed based on the minimum observed secant modulus in the tensile direction of the principal directions  $i$  and  $j$ .

$$\nu_{reduced,ij} = Min \left( \frac{E_{min,i}^{ten}}{E_0}, \frac{E_{min,j}^{ten}}{E_0} \right) \nu_0 \quad (2.12)$$

## 2.3. Steel material constitutive model

### 2.3.1. Giuffré-Menegotto-Pinto model

The material law for the longitudinal steel reinforcement bars is based on the modified Giuffré-Menegotto-Pinto model [45]. Using this model, the loading and unloading branches of the uni-axial constitutive law follow a curved transition from two straight line asymptotes as illustrated in Figure 2.2. The stress-strain relationship for this model is summarized as:

$$\sigma^* = b\varepsilon^* + \frac{1-b}{1+|\varepsilon^*|^R} \varepsilon^* \quad (2.13)$$

$$\varepsilon^* = \frac{\varepsilon - \varepsilon_r}{\varepsilon_0 - \varepsilon_r}$$

$$\sigma^* = \frac{\sigma - \sigma_r}{\sigma_0 - \sigma_r}$$

In which  $(\varepsilon_r, \sigma_r)$  = coordinates of the last strain reversal point in the stress-strain plane and  $(\varepsilon_0, \sigma_0)$  = coordinates of the two asymptotes intersection as illustrated in Figure 2.2. These four parameters are updated after each strain reversal. Parameter  $b$ , also a constant material parameter, is the strain hardening ratio. Parameter  $R$  determines the curvature of the transition curve and is updated after each strain reversal by the following relation:

$$R = R_0 - \frac{R_1 \xi}{R_2 + \xi} \quad (2.14)$$

where  $\xi$  referred to as normalized plastic excursion and is updated after each strain reversal. Constant material parameters  $R_0, R_1$ , and  $R_2$  control the curvature of the hysteretic branches. Isotropic hardening can be incorporated into this model by introducing the following stress shift,  $\sigma_{shift}$ , which shifts the position of the yield asymptote and is updated after each strain reversal event.

$$\frac{\sigma_{shift}}{\sigma_y} = \text{Max} \left[ a_1 \left( \frac{\varepsilon_{max}}{\varepsilon_y} - a_2 \right), 0 \right] \quad (2.15)$$

In the above equation,  $\sigma_y$  and  $\varepsilon_y$  denote the initial yield stress and corresponding strain.  $\varepsilon_{max}$  is the absolute maximum strain at the instant of the strain reversal,  $a_1$

determines the magnitude of the stress shift, and  $a_2$  is a threshold for  $\varepsilon_{max} / \varepsilon_y$ , above which the stress shift is activated.

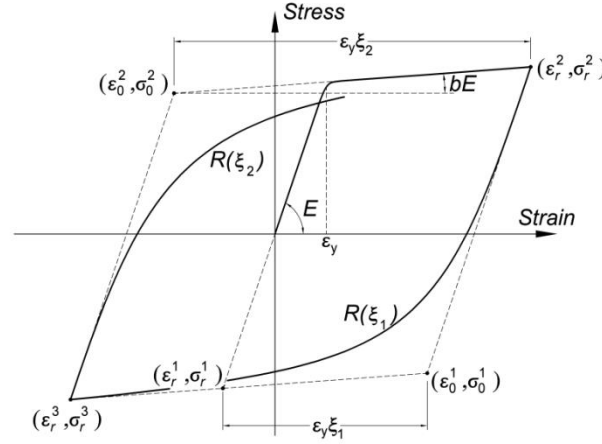


Figure 2.2: Giuffr -Menegotto-Pinto uni-axial constitutive model for steel.

The proposed Giuffr -Menegotto-Pinto steel model has eight free parameters to be set by the user, namely  $\sigma_y$ ,  $\varepsilon_y$ ,  $R_0$ ,  $R_1$ ,  $R_2$ ,  $b$ ,  $a_1$ , and  $a_2$ . The initial yield stress and strain,  $\sigma_y$  and  $\varepsilon_y$ , are obtained from tensile tests performed on rebar samples. In this study, it is further assumed that the kinematic and isotropic hardening parameters,  $b$  and  $a_1$ , respectively, are equal. To estimate  $b$  and  $a_1$  for each rebar sample, a bilinear stress-strain curve fitted to the test results using the equal strain energy concept (Figure 2.3).  $\varepsilon_{max}$ , as shown in this figure, is the maximum expected strain in the rebar.  $\varepsilon_{max}$  is estimated based on the expected ductility demands and updated based on the initial analysis results. The secondary slope of the fitted bilinear stress-strain curve is taken to be  $2b$ . The other parameters for the steel model used in this study are taken as  $R_0 = 21$ ,  $R_1 = 18.96$ ,  $R_2 = 0.024$ , and  $a_2 = 0$ .



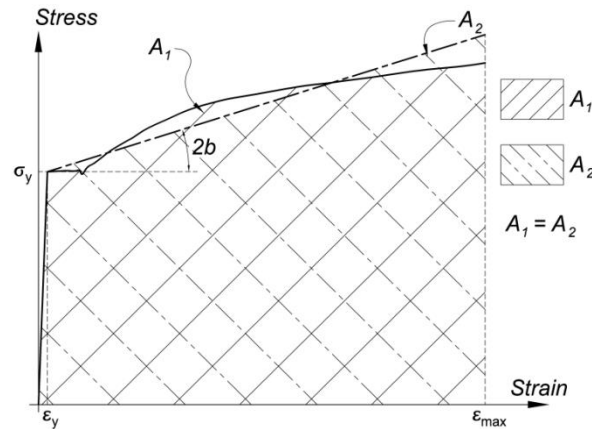
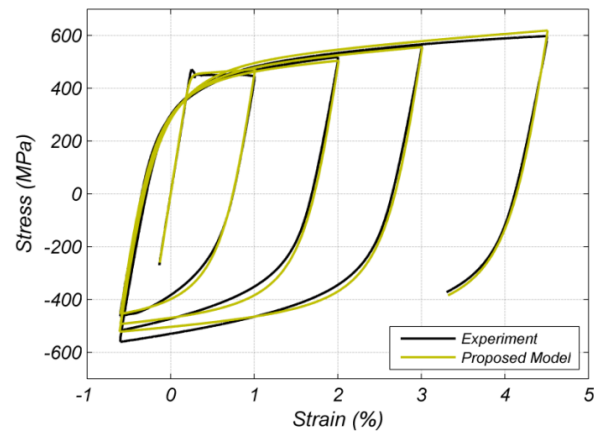


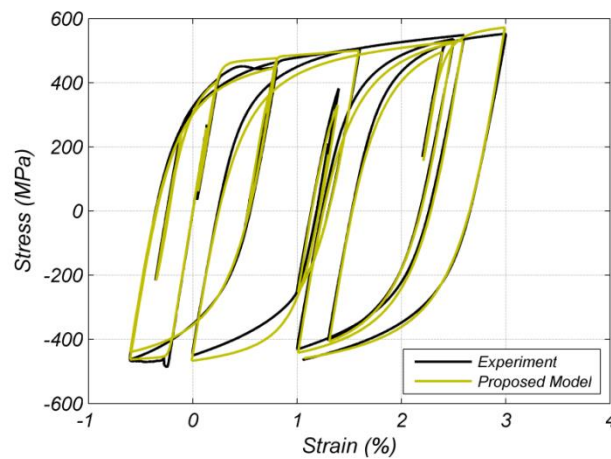
Figure 2.3: Estimation of kinematic hardening parameter,  $b$ , for the steel model based on monotonic tensile test results.

### 2.3.2. Experimental validation of the proposed steel model

The stress-strain curves from some cyclic tests performed on #4 rebar ( $d_b = 12.7mm$ ) samples at the structural engineering laboratory of the University of California at San Diego (UCSD) are used to validate the reinforcement steel model adopted in this study. These tests were performed on samples conforming to the ASTM A706 / A706M - 09b standard for low-alloy steel deformed bars. Only Test results for short rebar specimens ( $l / d_b = 3$ ) are used to avoid the effect of buckling on the experimental stress-strain curve. Figure 2.4(a) and Figure 2.4(b) show very good correlation between the proposed steel model and two sets of experimental results before the onset of rebar buckling.



(a)



(b)

Figure 2.4: Experimental validation of the proposed steel model for #4 rebar (38mm in length), with two different strain loading histories (a, b).

## 2.4. Incremental-iterative nonlinear analysis

In this study, the nonlinear analyses are performed using a displacement-controlled loading. The analysis step size is initially selected as 2-5% of the nominal yield displacement of the test specimen and is adjusted subsequently to improve both the convergence rate and computational time.

The quasi-newton (secant) approach based on the Broyden–Fletcher–Goldfarb–Shanno (BFGS) stiffness update method [46], which is found to be efficient in handling smeared crack problems with softening, is selected to solve nonlinear equilibrium equations. The last obtained stiffness matrix at the end of each time step is used as the initial stiffness for the first iteration of the next time step and is being updated based on the BFGS rule for the subsequent iterations.

The convergence criterion is based on the relative energy norm with a convergence tolerance varying from  $5 \times 10^{-4}$  to  $1 \times 10^{-3}$ . The maximum allowable number of iterations for each time step is limited to be 30. If the convergence criterion is not fulfilled within 30 iterations, the analysis goes on to the next time step and transfers the current unbalance force vector. In such a situation, the iteration history of the unconverged time step, the convergence state of the subsequent time step, and the obtained analysis results are checked manually to ensure the accuracy of the nonlinear analysis results.

## **2.5. Experimental-numerical correlation studies**

### **2.5.1. Cantilever RC beam component tested by Popov et al.**

To study the effects of high shear force on strength, ductility, and energy dissipation characteristics of RC beams, Popov et al. [47] tested three RC cantilever beams. The size and spacing of the web reinforcements were the main difference between the three test specimens. In this study, the experimental response of one of the

three test specimens, referred to as beam 43, is compared with the FE simulation results.

The details of beam 43 and its material properties are shown in Figure 2.5a. The shear reinforcements were designed to carry the maximum possible shear demand without concrete participation. To fabricate the specimen, the fixed end of the cantilever was built into an RC column stub anchored to the reaction frame using a T-beam steel section. The longitudinal beam reinforcements were welded to the T-beam anchorage at the fixed end of the cantilever using connecting plates. Due to bond deterioration, some rebar slippage occurred in the connecting zone and resulted in a fixed end rotation of the specimen during the test. A piece of W24x76 was partially embedded in the free end of the cantilever and connected by a pin to the actuator arm. Loading was controlled by force before yielding of the test specimen and by displacement after yielding. The time history of the tip deflection is shown in Figure 2.5b.

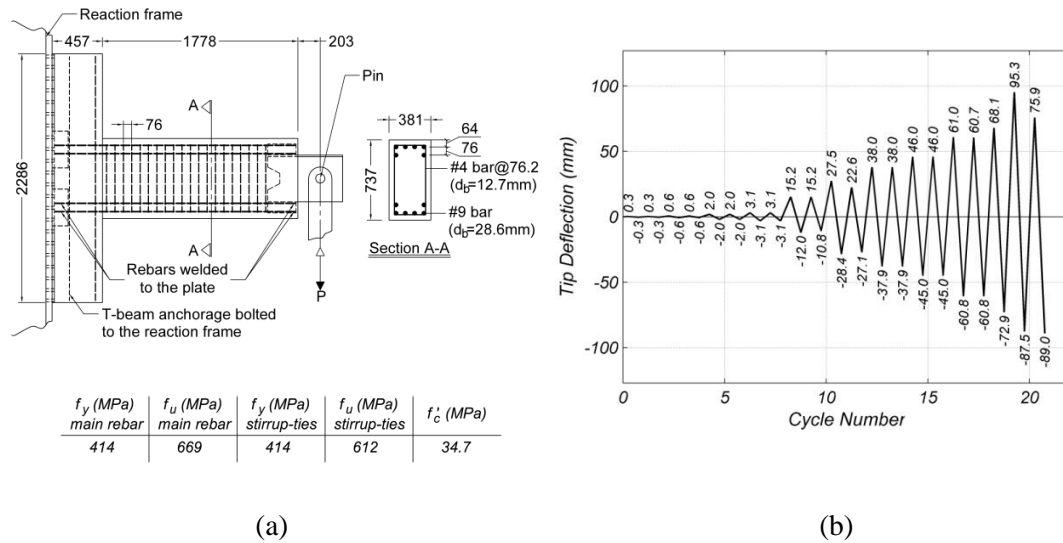


Figure 2.5: Beam 43 as tested by Popov et al. [47];

(a) Specimen configuration and material properties (dimensions are in mm);

(b) Tip deflection loading history.

The specimen is modeled using 3-node Mindlin–Reissner displacement-based beam elements [48]. The element formulation is based on quadratic shape functions that imply a linear variation of the axial strain and constant transverse shear strains over the cross-section. The length of first element adjacent to the fixed support, referred to as *plastic hinge element*, is taken as one half of the specimen’s height. Because the plastic hinge element is expected to experience higher level of nonlinearity compared to the other elements, a higher order integration scheme (*ISI*) is selected for this element as shown in Figure 2.6. Details of the employed concrete material law are described in Section 5.4 of this chapter. Longitudinal rebars are modeled using embedded steel bar elements with a full-bond assumption in conjunction with modified Giuffré–Menegotto–Pinto material law, as introduced in

section 3.1. The concrete and steel material parameters, as used in the FE model, are summarized in Table 2.1. To simulate the rebar slippage at the fixed end of the specimen during the test, two different FE models are developed as shown in Figure 2.6. *Model 1* has a fixed-support at the end of the beam. In *Model 2*, however, a new element with a hinge-roller supports is added at the end of the beam to simulate the rotational flexibility caused by the rebar slippage in the connecting zone during the test. The concrete material for this element has zero tensile strength and the same compressive properties as shown in Table 2.1.

Figure 2.7 compares the experimental results with the force deformation response obtained from *Model 1* (with fixed-end boundary condition) and *Model 2* (with flexible-end boundary condition). This Figure 2.shows that the responses of the specimen in both positive and negative loading branches are better predicted by the *Model 2*. Moreover, the initial elastic stiffness of the experiment matches better with *Model 2*. Therefore, the particular solution adopted to model the flexible support is effective in this case study.

Table 2.1: Material parameters for beam 43.

$f'_{cc} \left( \frac{N}{m^2} \right)$	$57.3 \times 10^6$
$E \left( \frac{N}{m^2} \right)$	$24.5 \times 10^9$
$G_c \left( \frac{N}{m} \right)$	$173.6 \times 10^3$
$f'_r \left( \frac{N}{m^2} \right)$	$1.9 \times 10^6$
$G_f \left( \frac{N}{m} \right)$	125
$\sigma_y \left( \frac{N}{m^2} \right)$	$414 \times 10^6$
$\varepsilon_y$	0.002
$b, a_1$	0.012

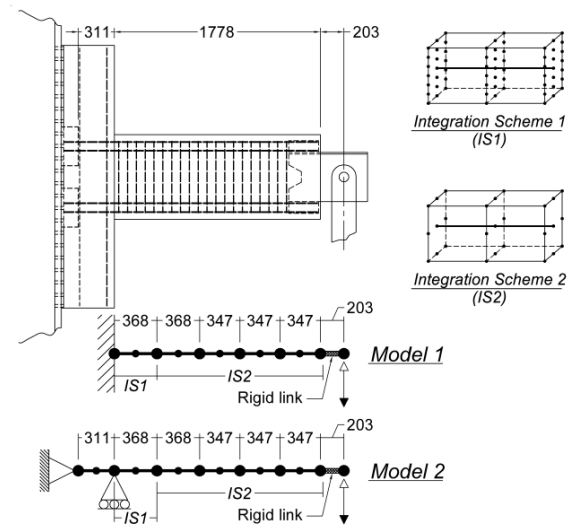


Figure 2.6: Details of finite element model for beam 43 (dimensions are in mm).

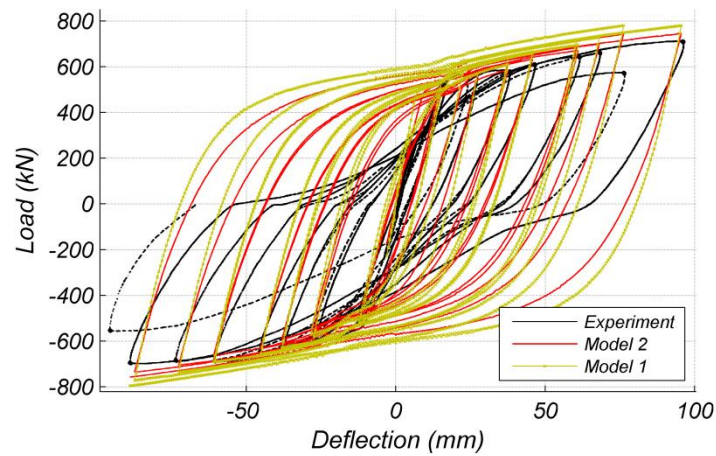


Figure 2.7: Comparison of the FE simulated force-deformation responses of beam 43 with the experimental results.

By studying Figure 2.7, two types of hysteresis loops can be distinguished in force-deformation response obtained from the experiment. The first type is the force-

deformation hysteresis loops with minor shear effects. These hysteresis loops are spindle shaped with minor stiffness degradation in successive cycles. FE simulated results have better agreement with the experimental results both in loading and unloading branches of these loops. The second type of hysteresis loops exhibit major pinching behavior resulting from dominant influence of shear-flexural cracks formed across the web of the specimen during the test. The response of the FE model is different from the experiment during unloading branch of these hysteresis loops and the pinching behavior is not well simulated. The reasons for these differences can be explained by considering the underlying physics that cannot be captured by the FE model, as will be discussed in the following part.

Figure 2.7 shows that upon unloading from an extreme loading point, the FE simulated results does not show any stiffness degradation in excessive loading cycles. The experimental results, however, unloads at a stiffness which deteriorates as the tip deflection increases. Based on observations made by Popov et al. [47] during the test, upon unloading from an extreme loading point, the stirrups became engaged in transferring the lateral force by a small frictional slippage that occurred along the diagonal shear cracks, which were present in the web of the component from the previous load reversals. The large cyclic deformations and the presence of the web diagonal cracks in both directions gradually deteriorate the stirrups bond with concrete, reducing the effectiveness of the stirrups, and degrade the unloading stiffness. At zero load stage, the open diagonal cracks make a physical discontinuity in the web of the specimen and eliminate the continuity of the web concrete and friction



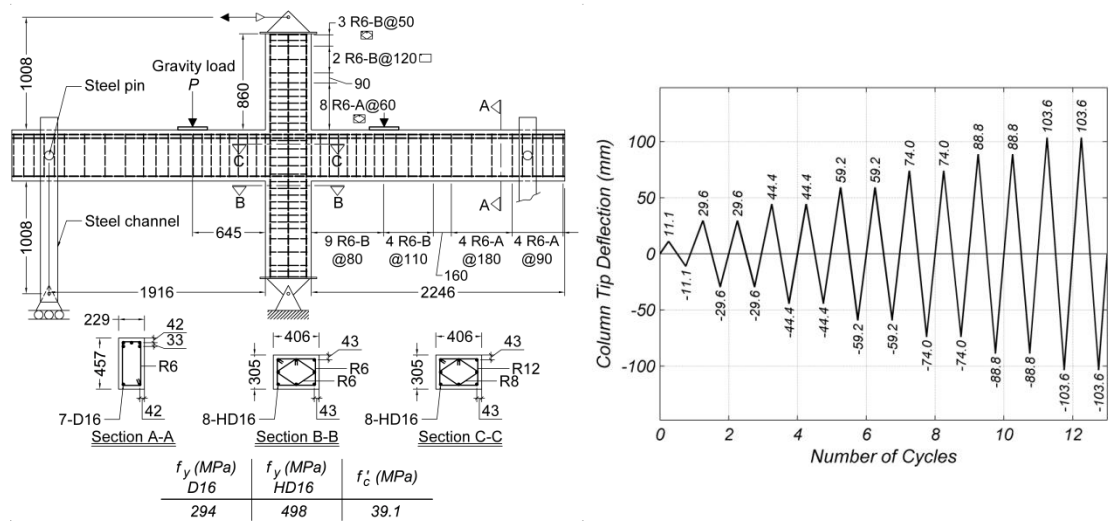
across the crack. Therefore, initial lateral shear resistance and stiffness are mostly developed by dowel action of the longitudinal rebar interfacing the crack opening. The dowel action results in a small stiffness in the force-deformation response of the specimen at zero load stage. As loading increases, the web cracks close, and the *truss mechanism* forms in the web of the specimen. The lateral shear force is resisted collectively by stirrups, dowel action in compression steel, and aggregate interlock and friction in compression zone. The bending resistance is developed by the coupling action of compressive strut of concrete and tensile rebars. At this point the response of the test specimen is dominated by flexural characteristic of the plastic hinge region.

The comparison of the experimental with FE simulated results shows that the described effects of shear mechanism and the resulting pinching behavior in the cyclic force-deformation response of the RC flexural component cannot be properly captured by the current FE model. The shear failure of the RC component, caused by the discontinuity along large diagonal shear cracks or rupture of lateral reinforcements, also cannot be predicted by the FE model. The flexural behavior of the component, however, can be predicted well by the FE model.

### **2.5.2. Beam-column joint tested by Ruitong et al.**

Ruitong and Park [49] tested four different beam-column subassemblies to investigate the effects of bond strength and shear resisting mechanism on the behavior of interior beam-column joints. The selected test specimen for this study is referred to as unit 1, the details of which are shown in Figure 2.8a. This unit was designed

according to the ductile detailing requirements of New Zealand code (NZS 3101-1982). The two ends of the beam constrained against vertical movement using steel channels connected to the beam web by steel pins. This connection allowed free horizontal movement and rotation but restrained vertical movement at the beam end. The tip of the column was connected by a pin to the actuator arm. To test the specimen, first two symmetric gravity loads ( $P = 55\text{ kN}$ ) were applied on the two beams, as shown in Figure 2.8a, and kept constant during the rest of the test. Then, the horizontal loading cycles were applied at the column tip as shown in Figure 2.8b. The loading was force-controlled before yielding of the test specimen and displacement-controlled after yielding.



(a)

(b)

Figure 2.8: Unit 1 as tested by Ruitong et al. [49];

(a) Specimen configuration (dimensions are in mm); (b) Column tip deflection loading history.

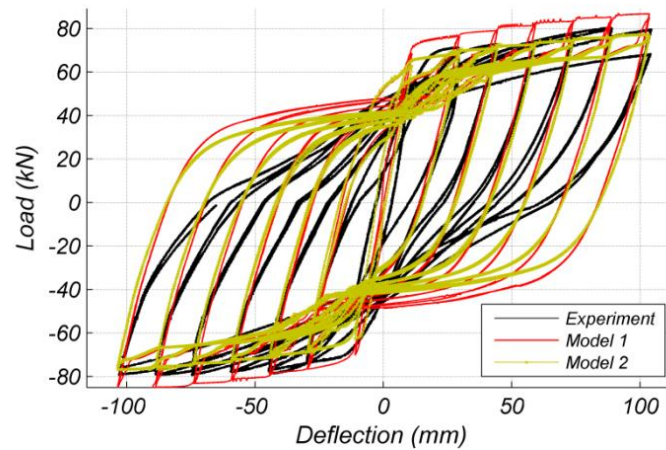
The shear deformation in the beam-column joints has a dominant effect on the overall behavior of RC moment frames. Herein, this effect is simulated by extending the flexibility of beam and column elements into the joint as proposed by Elwood et al. [50]. Four different configurations, referred to as *Model 1* to *Model 4*, are considered in this study as shown in Figure 2.9a. Elwood et al. recommend *Model 1* for joints in which the beams have higher nominal flexural capacity compare to the columns. Conversely, *Model 2* is recommended for joints with columns stronger than the beams and *Model 3* describes an in-between situation. As an extreme for *Model 3*, *Model 4* has zero rigid zone length at the beam and columns joint.

For this specimen, the FE model is developed using 3-node Mindlin–Reissner displacement-based beam elements as used for the previous case study. The length of elements next to the beam-column joint, referred to as *plastic hinge elements*, is taken as one half of the depth of the associated section. The numerical integration schemes for plastic hinge and other elements are the same as previous case study. The longitudinal rebars in both column and beam are modeled using embedded steel bar elements with a full-bond assumption. The employed concrete and steel material laws are introduced in the previous sections of this chapter. The concrete and steel material parameters, as used in the FE model, are summarized in Tables 2a and 2b.

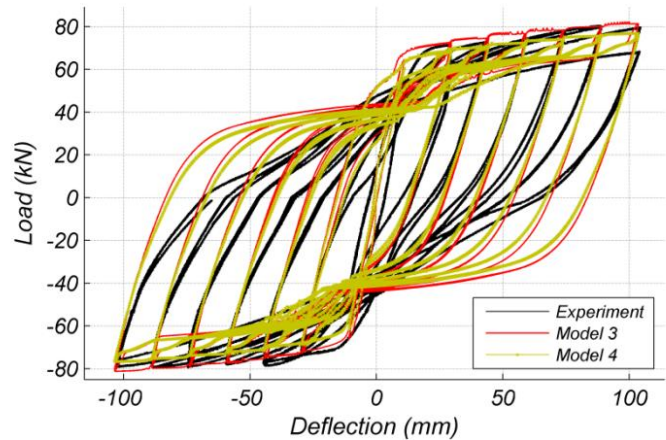


all loading cycles. Based on Figure 2.10b, *Model 4* also underestimates the strength of the specimen in both positive and negative loading cycles. The success of the proposed solution to account for shear deformation in the beam-column joints highly depends on reinforcement detailing and the failure mechanism of the experimental specimen. In unit 1, proper detailing of beams, column, and beam-column joint successfully controlled the shear cracking in joint region. Diagonal cracks formed in the plastic hinge region of the beam with minor extension into the column and joint region. Figures 2.10 (a, b) show that results obtained from *Model 3* have the best agreement with the experiment for this case study. The initial elastic stiffness and the yield strength as estimated by *Model 3* also confirms well with the experiment.

Similar to the previous case study, Figures 2.10 (a, b) also shows that the pinching behavior in the cyclic force-deformation response, caused by shear mechanism in RC beams, cannot be captured by the FE models. The shear mechanism results in poor correlation between the FE simulated and experimental results along the unloading branches, especially at high ductility loading cycles. The reasons of this poor correlation were discussed earlier in the previous section of this chapter and are an inherent part of the used FE modeling technique. The flexural behavior of the component in the positive and negative loading branches, however, can be predicted well by the FE model, the same as the previous case study.



(a)



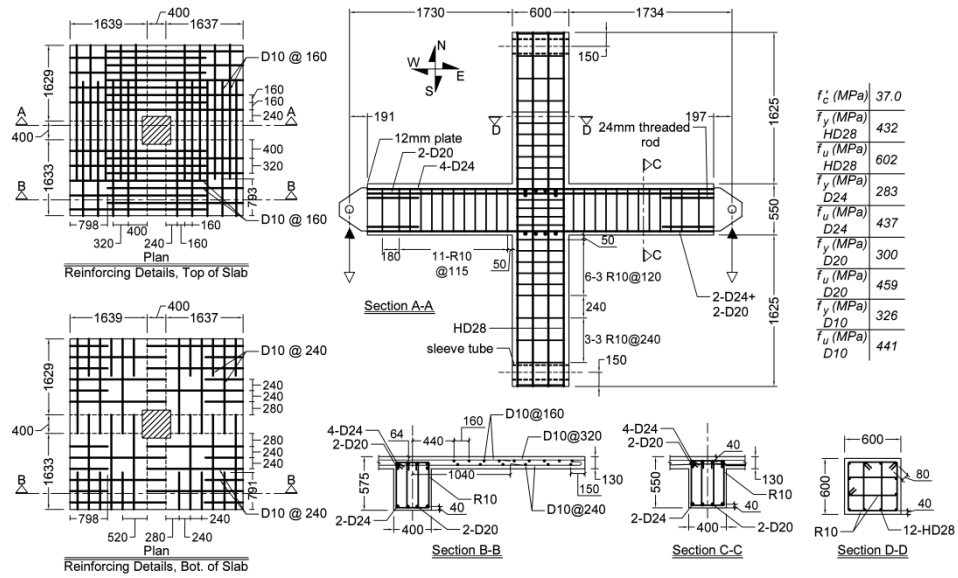
(b)

Figure 2.10: Comparison of the FE simulated force-deformation responses of unit 1 with the experimental results; (a) Models 1 and 2; (b) Models 3 and 4.

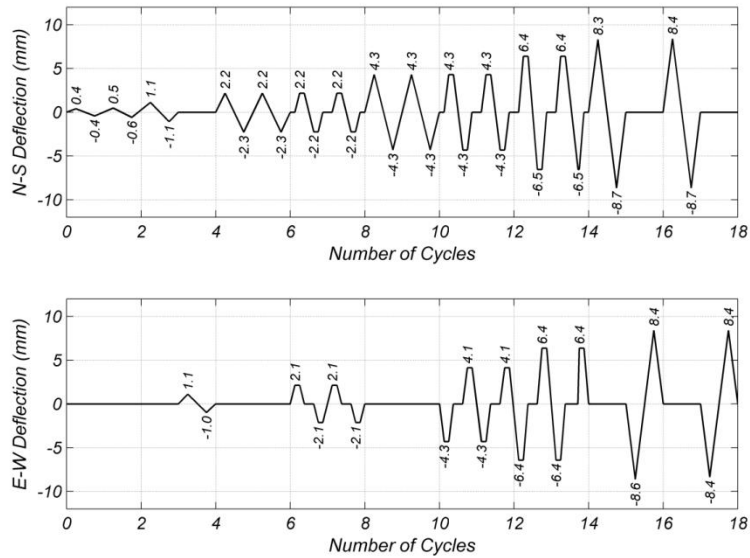
### 2.5.3. Beam-column joint with floor slab tested by Cheung et al.

To study the performance of RC beam-column frames with slab and particularly to investigate the slab contribution in the flexural strength of the beams, Cheung et al. [51] tested a series of two-way and one-way exterior and interior beam-column joints with slab under cyclic loading simulating earthquake actions. The test specimens were designed based on New Zealand code (NZS 3101:1982) to meet

earthquake resistant design requirements, which prevent beam shear failure, joint failure, and column failure under maximum credible loading conditions. A two-way interior frame sub-assembly, named as unit 2D-I, is selected for the current study. The details of unit 2D-I is shown in Figure 2.11a. The top and bottom of the column were pin-connected to allow rotation in two perpendicular directions. Four double-acting jacks were installed at the ends of the north-south and east-west beams to load beams upward or downward. Moreover, the beam ends were free to rotate and move laterally in the plane of the frame while the jacks were kept in a vertical position; so, no axial force was developed in the beams. A sequential cyclic loading was applied on both north-south and east-west beams with increasing deformation level during the test. In the developed FE model, however, the beam ends are restrained by hinge connections and the equivalent column side sways are imposed at the tip of the column. Figure 2.11b shows the equivalent column tip deflection time history in the north-south and east-west directions.



(a)



(b)

Figure 2.11: Unit 2D-I as tested by Cheung et al. [51];

(a) Specimen configuration (dimensions are in mm); (b) Equivalent column tip deflection loading history.



The FE model for this specimen is developed using 3-node Mindlin–Reissner displacement-based beam elements, as used for the previous case studies, to model the beams and column. 8-node Mindlin–Reissner quadrilateral serendipity shell element, which has 6 DOFs per node including drilling degrees of freedom, is used to model the slab. A typical shell element of this type, including the integration points, is shown in Figure 2.12. The in-plane lamina strains ( $\varepsilon_{xx}$ ,  $\varepsilon_{yy}$ , and  $\varepsilon_{xy}$ ) vary linearly along the thickness of the element. The transverse shear strains ( $\varepsilon_{xz}$  and  $\varepsilon_{yz}$ ) are constant along the thickness and a correction factor of  $\frac{5}{6}$  is applied to the section area to obtain the effective shear area. The numerical integration rule is based on Gaussian quadrature over the plane and Simpson along the thickness.

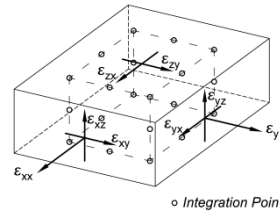


Figure 2.12: Typical shell element with typical integration points.

To investigate the effect of two different modeling approaches for the beam-slab connections, two different finite element models are developed for this case study as shown in Figure 2.13. In *Model 1*, the shell elements are discontinued at the physical boundaries of the beam; therefore, no overlapping exists between beams and slab. *Model 2* is instead the practical solution that is usually employed for simplicity.

In this model the shell elements of the slab are covering the physical width of the beams; therefore, overlapping exists between beams and slab in the model. In both models, the nodes of the beam elements are connected to the corresponding nodes of the slab shell elements using rigid link constraints. Both models are restrained in vertical direction at the end of the beams and hinged at the bottom of the column. The torsional degree of freedom is also restrained at the bottom of the column to provide static stability. To model the beam-column connections, half of the end zone of the beams is modeled as rigid. Same as previous case studies, the length of the elements next to the beam-column joint, referred to as *plastic hinge elements*, is taken as one half of the associated section depth. The numerical integration schemes for plastic hinge and other elements of beams and column are the same as previous case studies. The numerical integration scheme for all slab shell elements is as shown previously in Figure 2.12. Embedded steel bar elements with a full-bond assumption are used to model longitudinal rebars in column and beams. The reinforcement meshes of the slab are modeled using uni-axial membrane elements with equivalent thickness embedded in the slab shell element and fully bonded to the concrete. The employed concrete and steel material laws are introduced in the previous sections of this chapter. The concrete and steel material parameters, as used in the FE model, are summarized in Table 2.3.

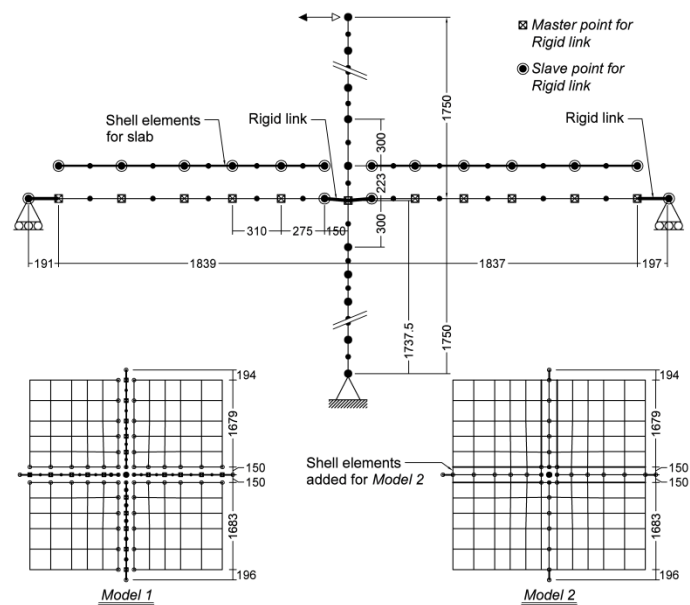


Figure 2.13: Details of finite element models for unit 2D-I (dimensions are in mm).

Table 2.3: Material parameters for unit 2D-I; (a) Concrete material parameters; (b) Steel material parameters.

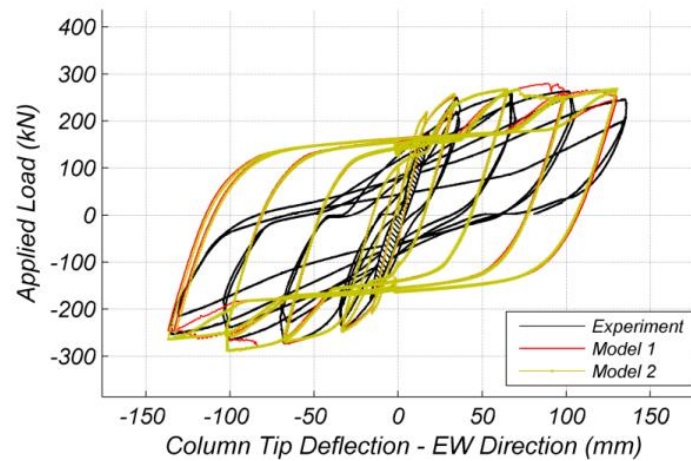
(a)				(b)				
	Beam	Column	Slab		D10	D20	D24	HD28
$f'_{cc} \left( \frac{N}{m^2} \right)$	$45.0 \times 10^6$	$60.8 \times 10^6$	$37.0 \times 10^6$	$\sigma_y \left( \frac{N}{m^2} \right)$	$326.0 \times 10^6$	$300.0 \times 10^6$	$283.0 \times 10^6$	$432.0 \times 10^6$
$E \left( \frac{N}{m^2} \right)$	$25.3 \times 10^9$	$13.9 \times 10^9$	$30.8 \times 10^9$	$\epsilon_y$	$1.8 \times 10^{-3}$	$1.3 \times 10^{-3}$	$1.3 \times 10^{-3}$	$1.8 \times 10^{-3}$
$G_c \left( \frac{N}{m} \right)$	$13.4 \times 10^4$	$13.7 \times 10^4$	$14.2 \times 10^3$	$b, a_1$	0.002	0.0025	0.00375	0.005
$f'_t \left( \frac{N}{m^2} \right)$	$2.0 \times 10^6$	$2.0 \times 10^6$	$2.0 \times 10^6$					
$G_f \left( \frac{N}{m} \right)$	118.0	118.0	118.0					

Following the observations made by Cheung et al. [51] during the test, plastic hinges formed over the whole height of all the four beams while only few minor cracks in the column developed, which indicated that the column remained essentially elastic.

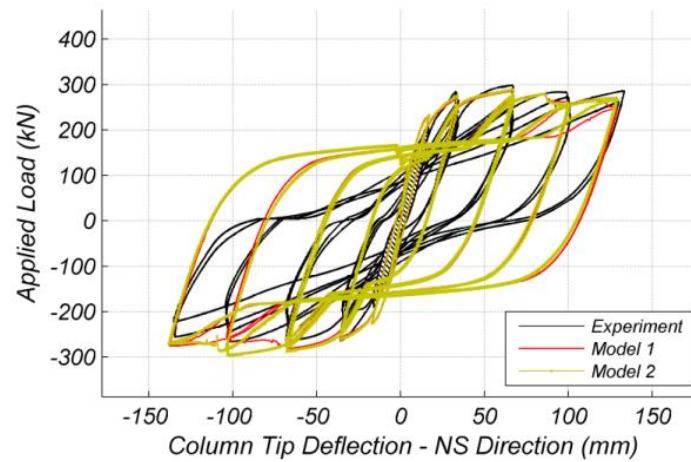
The specimen remained intact until the last cycle of loading in which stretching and buckling of the beam bottom bars became visible after the spalling of concrete cover.

The east-west and north-south force-deformation response of FE models are compared with the experimental results in Figures 2.14a and 2.14b, respectively. Response of *Model 1* and *Model 2* have minor differences. Therefore, the two alternatives in modeling the beams-slab connections result in identical results.

The correlation of the simulated with the experimental results follows the same pattern as observed in the previous case studies. The strength of the sub-assembly at the extreme loading points of both positive and negative loading branches is well predicted by the FE models. The pinching behavior, however, is not captured by the FE models following the same reasoning discussed earlier. The initial elastic stiffness and the yield strength of the test specimen are slightly over predicted by the FE models.



(a)



(b)

Figure 2.14: Comparison of the FE simulated force-deformation responses of unit 1 with the experimental results; (a) East-west direction; (b) North-south direction.

Figure 2.15 compares the measured and the FE-estimated curvature profile in the north and south beams. To obtain the beam curvature during the test, the measurement of linear pots installed on different segments along the beams, as shown in Figure 2.15, were used. Only the measured curvature profiles at the peak positive and negative loading points with the ductility of  $\mu = 2^*$  and  $\mu = 4^*$  are shown in Figure

2.15. The star superscript for the ductility stands for the bi-directional loading condition. In the FE model, the element curvature is the average of three section curvatures, obtained using the axial strain at the integration points of the section.

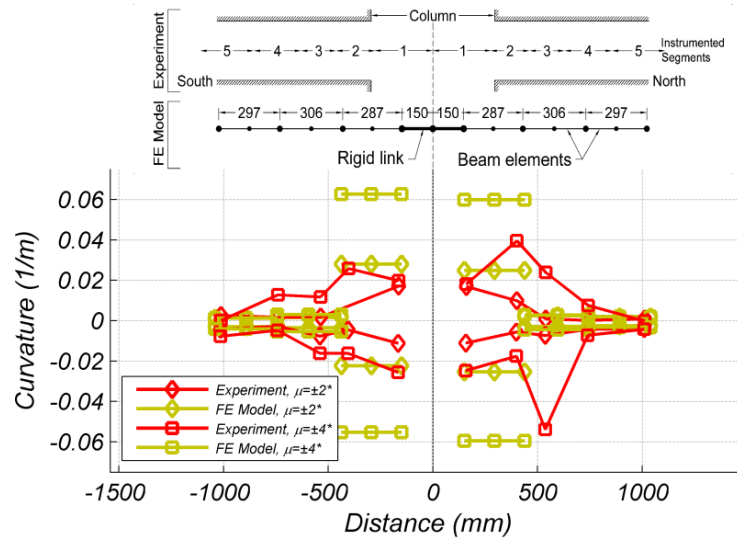
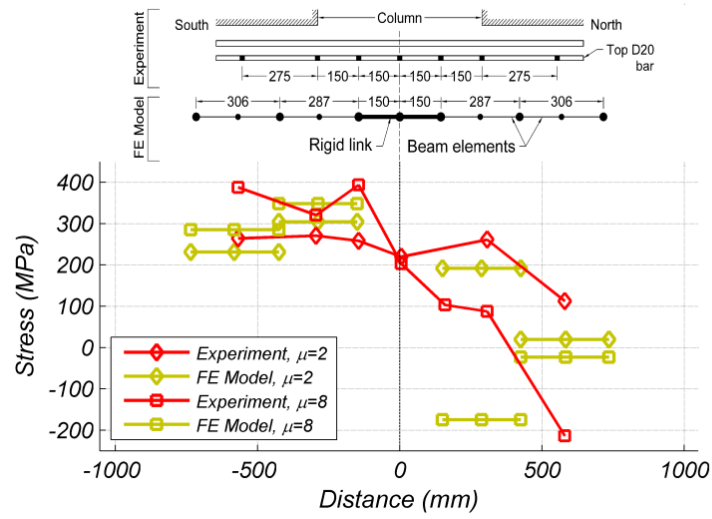


Figure 2.15: Comparison of the measured and FE-estimated curvature profile of the north and south beams at different ductility levels.

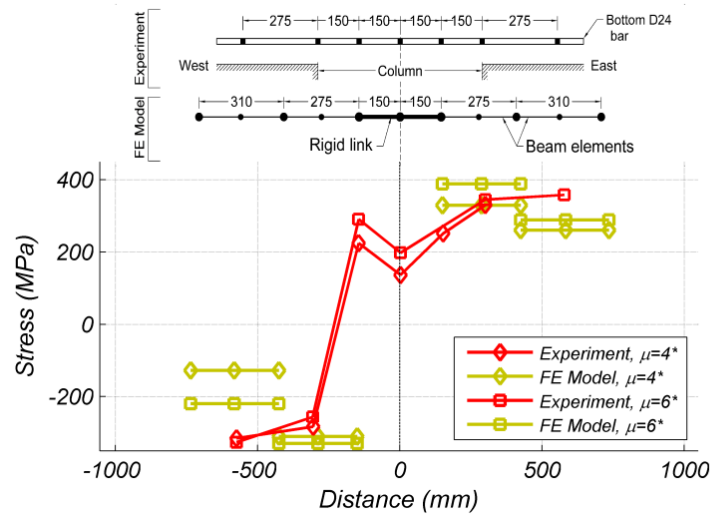
Figure 2.15 shows that the beam elements next to the rigid link, referred to as *plastic hinge elements* earlier, experience accumulated nonlinearity while the other elements along the beam remain elastic. The Figure 2.also shows that the magnitude of FE-estimated curvatures of the plastic hinge elements in the north and south beams are equal at the positive and negative loading points while the experimental measurements are not. The inconsistent experimental measurements were most likely caused by bi-directional loading effects. As can be seen in Figure 2.15, the FE model consistently

overestimates the curvatures; the reason of overestimation is the averaging effects implied in linear pots' measurements.

The longitudinal beam rebars were instrumented by strain gauges to monitor strain variations during the test. The measured strain time history subsequently converted into the equivalent stress time history using a special material law for steel rebar [51]. This material law was a combination of bilinear and Ramberg-Osgood models. The FE-estimated stress in the rebar is the average of uniaxial stress in the three element sections. Figure 2.16a shows the equivalent stress values along the top D20 rebar in the north and south beams at the peak of the first loading cycles with ductility  $\mu = 2$  and  $\mu = 8$  obtained from the experiment, and compares them with the estimated values obtained from the FE model. Figure 2.16b compares the experimentally evaluated and the FE-estimated stress values along the bottom D24 rebar in the east and west beams at the peak of the first loading cycle with ductility  $\mu = 4^*$  and  $\mu = 6^*$ . Once more, the star superscript for the ductility stands for the bi-directional loading condition.



(a)



(b)

Figure 2.16: Comparison of the experimentally measured equivalent stress and the FE-estimated stress in longitudinal beam rebars; (a) strain in top D20 bar of north and south beams; (b) strain in bottom D24 bar of east and west beams.



Figures 2.16a and 2.16b clearly show the accumulation of nonlinearity in the plastic hinge elements in the FE model. Although the material law used to convert the experimentally measured strains into equivalent stresses is different from the one used in the FE modeling, the estimated peak stress values are comparable with the experiment. The mismatch in the peak stress location along the rebars is most likely because of the shift in anchorage point of the rebars during the test. Figure 2.16a also illustrates that the north top D20 bar was in tension at  $\mu=2$ ; while at  $\mu=8$ , compression stress developed in the rebar. The reason of this change in stress is the loss of effectiveness of the top flange concrete due to extensive cyclic damages; as a result, the neutral axis depth migrates toward the center line of the section. This phenomenon is captured by the FE model as can be seen in Figure 2.16a. Figure 2.16b shows some inconsistencies in the measured equivalent stress at the west side of the beam-column joint. These inconsistencies are most likely caused by bi-directional loading effects.

## 2.6. Conclusions

To evaluate the fidelity of the proposed FE modeling approach, to address the simulation inaccuracy, and to explore the likely sources of discrepancies, this chapter compared the experimental results of three RC test specimens, namely a cantilever beam component, a beam-column joint sub-assembly, and a beam-column joint with floor slab sub-assembly, with the numerical simulation results using *total strain rotating smeared crack model* combined with structural elements. Inspecting the

experimental-analytical correlation for these three case studies revealed that the proposed modeling approach cannot properly capture some physical aspects of the cyclic behavior of RC frame components. The main unpronounced aspects can be highlighted as follow:

- Shear mechanism and shear failure in the frame components. Shear mechanism becomes more prominent at higher ductility demands and under poor detailing conditions. The formation of diagonal cracks along the web of the frame components eliminates the continuity of the web concrete and results in deteriorated loading and unloading stiffness and reduced shear resistance of the frame components under cyclic loadings. Dowel action and deterioration of bond resistance in longitudinal rebars are other consequences of shear mechanism in the frame components. In the ultimate condition, the frame component exhibits a large transverse deformation along a main diagonal crack, loses stability, and fails in shear.
- Bond-slip mechanism of the longitudinal and lateral reinforcements. Bond deterioration is more significant under cyclic loading conditions. The bond slippage in longitudinal reinforcements deteriorates the composite action of concrete and rebars resulting in reduced stiffness of the frame component. The deterioration of bond reduces the efficiency of the lateral reinforcements in confining the concrete core and controlling the diagonal crack propagation, and ultimately results in shear failure of the frame components.

- Dowel action of the longitudinal rebars. Dowel action provides the minimum lateral stiffness and shear resistance of the frame component at the neutral loading condition in presence of large open flexural and diagonal cracks. The dowel action also accelerates the bond slippage in the longitudinal bar.
- Pinching behavior of RC frame component under cyclic loading. The pinching behavior is a consequent of shear mechanism, bond-slip mechanism of both longitudinal and lateral reinforcements, and dowel action.

The proposed modeling approach, however, can successfully capture the flexural-dominant behavior of the frame components. The initial elastic stiffness, yield strength, and post-yield flexural strength can be estimated with respectable accuracy.

Moreover, this chapter studied the effects of different finite element modeling techniques. For the cantilever beam component, a simple and effective solution was proposed to account for the fixed-end rotation of the beam caused by support flexibility. For the beam-column joint sub-assembly, four different modeling techniques were proposed to account for the beam-column joint flexibility. The results showed that *Model 3*, in which the end zones of the beams and columns were partially modeled as rigid, had the best correlation with the experimental observation. To model the beam-slab connection in the beam-column joint with floor slab sub-assembly, two different strategies were proposed, the results of which were identical.

## **Acknowledgments**

Partial support for this work was provided by the NSF-NEESR program under grant number CMMI-0936505 with Professor Tara C. Hutchinson as the principal investigator. This Chapter, in full, is currently being prepared for submission for publication of the material by Hamed Ebrahimian, Rodrigo Astroza, Joel P. Conte, and Jose I. Restrepo. The dissertation author is the primary investigator and author of the work.

## References

- [1] T. Takeda, M. A. Sozen, and N. N. Nielsen, "Reinforced Concrete Response to Simulated Earthquakes," *ASCE Journal of the Structural Division*, vol. 96, no. 12, p. 2557-2573, 1970.
- [2] Y. Wen, "Method for Random Vibration of Hysteretic Systems," *ASCE Journal of the Engineering Mechanics Division*, vol. 102, no. 2, p. 249-263, 1976.
- [3] S. El-Tawil and G. G. Deierlein, "Inelastic Dynamic Analysis of Mixed Steel-Concrete Space Frames," Structural Engineering Report No. 96-6, School of Civil and Environmental Engineering, Cornell University, Ithaca, N.Y., 1996.
- [4] L. F. Ibarra, R. A. Medina, and H. Krawinkler, "Hysteretic Models that Incorporate Strength and Stiffness Deterioration," *Earthquake Engineering and Structural Dynamics*, vol. 34, no. 12, p. 1489–1511, 2005.
- [5] F. C. Filippou, A. D'Ambrisi, and A. Issa, "Nonlinear Static and Dynamic Analysis of Reinforced Concrete Subassemblages," Report No. UCB/EERC–92/08, Earthquake Engineering Research Center, College of Engineering, University of California, Berkeley, CA., 1992.
- [6] K. Maekawa, A. Pimanmas, and H. Okamura, *Nonlinear Mechanics of Reinforced Concrete*, London: Spon Press, 2003.
- [7] F. F. Taucer, E. Spacone, and F. C. Filippou, "A Fiber Beam-Column Element for Seismic Response Analysis of Reinforced Concrete Structures," Report No. UBC/EERC-91/17, Earthquake Engineering Research Center, College of Engineering, University of California, Berkeley, CA., 1991.
- [8] M. Petrangeli, P. E. Pinto, and V. Ciampi, "Fiber Element for Cyclic Bending and Shear of RC Structures. I: Theory," *ASCE, Journal of Engineering Mechanics*, vol. 125, no. 9, p. 994-1001, 1999.
- [9] A. Marini and E. Spacone, "Analysis of Reinforced Concrete Elements Including Shear Effects," *ACI Structural Journal*, vol. 103, no. 5, p. 645-655, 2006.
- [10] M. Panagiotou, J. I. Restrepo, M. Schoettler, and G. Kim, "Nonlinear Cyclic Truss Model for Reinforced Concrete Walls," *ACI Structural Journal*, vol. 109, no. 2, p. 205-214, 2012.
- [11] F. J. Vecchio and M. P. Collins, "The Modified Compression Field Theory for Reinforced Concrete Elements Subjected to Shear," *Journal of American Concrete Institute (ACI)*, vol. 83, no. 2, p. 219-231, 1986.
- [12] D. Ngo and A. C. Scordelis, "Finite Element Analysis of Reinforced Concrete

- Beams," *American Concrete Institute (ACI)*, vol. 64, no. 3, p. 152-163, 1967.
- [13] Z. P. Bazant and T. Tsubaki, "Total Strain Theory and Path-Dependence of Concrete," *ASCE Journal of the Engineering Mechanics Division*, vol. 106, no. 6, p. 1151-1173, 1980.
- [14] K. J. Bathe and S. Ramaswamy, "On Three-Dimensional Nonlinear Analysis of Concrete Structures," *Nuclear Engineering and Design*, vol. 52, no. 3, p. 385-409, 1979.
- [15] P. H. Feenstra, "Computational Aspects of Biaxial Stress in Plain and Reinforced Concrete," Ph.D. Dissertation, Delft University of Technology, Delft, The Netherlands, 1993.
- [16] A. C. Chen and W. F. Chen, "Constitutive Relations for Concrete," *ASCE Journal of the Engineering Mechanics Division*, vol. 101, no. 4, p. 465-481, 1975.
- [17] J. C. Simo and J. W. Ju, "Strain and Stress-Based Continuum Damage Models-I. Formulation," *International Journal of Solids and Structures*, vol. 23, no. 7, p. 821-840, 1987.
- [18] Z. P. Bazant and P. D. Bhat, "Endochronic Theory of Inelasticity and Failure of Concrete," *ASCE Journal of the Engineering Mechanics Division*, vol. 102, no. 4, p. 701-722, 1976.
- [19] Z. P. Bazant and B. H. Oh, "Microplane Model for Fracture Analysis of Concrete Structures," in *Symposium on Interaction of Non-Nuclear Munitions with Structures*, U.S. Air Force Academy, Colorado Springs, 1983.
- [20] F. C. Cancer and Z. P. Bazant, "Microplane Model M7 for Plain Concrete: I. Formulation," *ASCE Journal of Engineering Mechanics*, Submitted: January 23, 2012; Accepted: November 16, 2012; Published: November 20, 2012..
- [21] Y. R. Rashid, "Ultimate Strength Analysis of Prestressed Concrete Pressure Vessels," *Nuclear Engineering and Design*, vol. 7, no. 4, p. 334-344, 1968.
- [22] ACI Committee 446, "Finite Element Analysis of Fracture in Concrete Structures," ACI 446.3R-97, American Concrete Institute, 1997.
- [23] T. DIANA, "DIANA User's Manual, Material Library," TNO DIANA bv, Delft, The Netherlands, 2010.
- [24] R. J. Cope, L. A. Rao, L. A. Clark, and R. Norris, "Modeling of Reinforced Concrete Behavior for Finite Element Analysis of Bridge Slabs," in *Numerical Methods for Nonlinear Problems I*, 457-470, Pineridge Press, Swansea, 1980.
- [25] R. de Borst and P. Nauta, "Non-Orthogonal Cracks in a Smearred Finite Element Model," *Engineering Computations*, vol. 2, no. 1, p. 35-46, 1985.

- [26] J. G. Rots, "Computational Modeling of Concrete Fracture," Ph.D. Dissertation, Delft University of Technology, Delft, The Netherlands, 1988.
- [27] M. A. Crisfield and J. Wills, "Analysis of R/C Panels using Different Concrete Models," *ASCE Journal of Engineering Mechanics*, vol. 115, no. 3, p. 578-597, 1989.
- [28] Z. P. Bazant and S. Kim, "Plastic-Fracturing Theory for Concrete," *Journal of the Engineering Mechanics Division*, vol. 105, no. 3, p. 407-428, 1979.
- [29] P. H. Feenstra, R. de Borst, and J. G. Rots, "A Comparison of Different Crack Models Applied to Plain and Reinforced Concrete," in *Fracture Processes in concrete, rock and ceramics, Proceeding of the International RILEM/ESIS conference*, Noordwijk, The Netherlands, 1991.
- [30] F. J. Vecchio, and R. G. Selby, "Toward Compression-Field Analysis of Reinforced Concrete Solids," *Journal of Structural Engineering (ASCE)*, vol. 117, no. 6, p. 1740-1758, 1991.
- [31] H. W. Reinhardt, "Fracture Mechanics of an Elastic Softening Material Like Concrete," *HERON*, vol. 29, no. 2, p. 1-37, 1984.
- [32] Z. P. Bazant, "Instability, Ductility, and Size Effect in Strain-Softening Concrete," *ASCE Journal of the Engineering Mechanics Division*, vol. 102, no. 2, p. 331-344, 1976.
- [33] Z. P. Bazant, "Crack Band Model for Fracture of Geomaterials," in *Proceedings of the 4th International Conference on Numerical Mathematics in Geomechanics*, University of Alberta, Edmonton, 1982.
- [34] L. J. Sluys, "Wave Propagation, Localisation and Dispersion in Softening Solids," Ph.D. Dissertation, Delft University of Technology, Delft, The Netherlands, 1992.
- [35] R. de Borst, "Some Recent Developments in Computational Modelling of Concrete Fracture," *International Journal of Fracture*, vol. 86, no. 1-2, p. 5-36, 1997.
- [36] R. de Borst, *Computational Methods in Non-Linear Solid Mechanics*, Delft, The Netherlands: TNO Building and Construction Research, Department of Civil Engineering, Delft University of Technology, 1993.
- [37] J. B. Mander, M. J. N. Priestley, and R. Park, "Theoretical Stress-Strain Model for Confined Concrete," *Journal of Structural Engineering (ASCE)*, vol. 114, no. 8, p. 1804-1826, 1988.
- [38] R. Park, M. J. N. Priestley, and W. D. Gill, "Ductility of Square-Confined Concrete Columns," *Journal of Structural Division (ASCE)*, vol. 108, no. 4, p. 929-950, 1982.

- [39] M. Saatcioglu and S. R. Razvi, "Strength and Ductility of Confined Concrete," *Journal of Structural Engineering (ASCE)*, vol. 118, no. 6, p. 1590-1607, 1992.
- [40] M. M. Attard and S. Setunge, "Stress-Strain Relationship of Confined and Unconfined concrete," *ACI Materials Journal*, vol. 93, no. 5, p. 432-442, 1996.
- [41] B. D. Scott, R. Park, and M. J. N. Priestley, "Stress-Strain Behavior of Concrete Confined by Overlapping Hoops at Low and High Strain Rates," *American Concrete Institute (ACI)*, vol. 79, no. 1, p. 13-27, 1982.
- [42] K. J. Willam, B. Hurlbut, and S. Sture, "Experimental and Constitutive Aspects of Concrete Failure," in *Finite Element Analysis of Reinforced Concrete Structures (Edited by C. Meyer and H. Okamura)*, New York, ASCE, 1986, p. 226-245.
- [43] R. G. Selby and F. J. Vecchio, "Three-Dimensional Constitutive Relations for Reinforced Concrete," Technical Report 93-02, Department of Civil Engineering, University of Toronto, Toronto, Canada, 1993.
- [44] F. J. Vecchio and M. P. Collins, "Compression Response of Cracked Reinforced Concrete," *Journal of Structural Engineering (ASCE)*, vol. 119, no. 12, p. 3590-3610, 1993.
- [45] F. C. Filippou, E. P. Popov and V. V. Bertero, "Effects of Bond Deterioration on Hysteretic Behavior of Reinforced Concrete Joints," EERC Report 83-19, Earthquake Engineering Research Center, Berkeley, CA, 1983.
- [46] H. Matthies and G. Strang, "The Solution of Nonlinear Finite Element Equations," *International Journal for Numerical Methods in Engineering*, vol. 14, no. 11, p. 1613-1626, 1979.
- [47] E. P. Popov, V. V. Bertero and H. Krawinkler, "Cyclic Behavior of Three R.C. Flexural Members with High Shear," Report No. EERC 72-5, College of Engineering, University of California, Berkeley, Berkeley, CA., 1972.
- [48] T. DIANA, "DIANA User's Manual, Element Library," TNO DIANA bv, Delft, The Netherlands, 2010.
- [49] D. Ruitong and R. Park, "A Comparison of the Behavior of Reinforced Concrete Beam-Column Joints Designed for Ductility and Limited Ductility," Report No. 87-4, Department of Civil Engineering, University of Canterbury, Christchurch, New Zealand, 1987.
- [50] K. J. Elwood, A. B. Matamoros, J. W. Wallace, D. E. Lehman, J. A. Heintz, A. D. Mitchell, M. A. Moore, M. T. Valley, L. N. Lowes, C. D. Comartin, and J. P. Moehle, "Update to ASCE/SEI 41 Concrete Provisions," *Earthquake Spectra*, vol. 23, no. 3, p. 493-523, 2007.
- [51] P. C. Cheung, T. Paulay, and R. Park, "Interior and Exterior Reinforced Concrete



Beam-Column Joints of a Prototype Two-Way Frame with Floor Slab Designed for Earthquake Resistance," Department of Civil Engineering, University of Canterbury, Christchurch, New Zealand, 1989.

## **CHAPTER 3: NONLINEAR FINITE ELEMENT RESPONSE SIMULATION OF THE BNCS BUILDING**

### **3.1. Introduction**

Nowadays, nonlinear Finite Element (FE) modeling and response simulation is an important part of many seismic design procedures. Nonlinear FE simulation techniques are expected not only to predict the global response of the structure, but also to estimate the local response and failure mode at component level of the structure, at an affordable computational cost. Yet, despite remarkable progress made in the field of nonlinear computational structural mechanics, nonlinear FE modeling and response simulation of reinforced concrete (RC) structures remains a challenging task in both research and engineering practice. The challenges are due to the inherent nonlinearity of the RC behavior, which is caused by complex phenomena such as cracking, crushing, biaxial stiffening and strain softening, steel-concrete interaction, etc. As a result of this challenging behavior, many research studies in the literature have been devoted to developing theoretical constitutive models and FE modeling

techniques that can accurately and efficiently capture the complicated mechanics of RC material. Compromising between computational feasibility and fidelity, different techniques are proposed and used for nonlinear FE modeling and response simulation of RC structures (e.g., refer to [1] and references therein for a state-of-the-art review).

Importantly, experimental studies, however time-consuming and costly, are essential to calibrate and validate the accuracy of the nonlinear FE modeling and response simulation techniques, especially for dynamic structural analysis under earthquake loading. Different experimental methods are used to test structural systems at full-scale under seismic loads. The simplest method is perhaps the quasi-static testing method, in which predefined time histories of displacements or forces are directly applied on the structure (e.g., [2]). Since the loading is applied in an extended time-scale, many dynamic features of structural behavior, such as dynamic interaction of structural and/or nonstructural components and systems and various sources of energy dissipation beyond material hysteretic energy dissipation are not properly reflected in the quasi-static testing results. The other testing approaches, such as pseudo-dynamic testing methods, are also subjected to serious shortfalls in simulating the real dynamic behavior of the structural systems at full-scale level under earthquake loading [3].

Large or full-scale shake table testing is definitely the most accurate method to study the behavior of structural systems under seismic loads. Considering various limitations of the shake table tests and testing facilities, such as cost, size and capacity limitation, shake table tests are usually conducted at reduced scales, which will

introduce scaling issues into the testing procedure. Reduced test scales make it difficult to investigate the local failure modes and structural behavior at component and element levels. In a RC test specimen, reducing the testing scale exclusively affects phenomena such as bond-slippage, shear mechanism, anchorage failure, and rebar buckling and fracture. To date only a limited number of large or full-scale shake table tests have been conducted on RC or steel-framed building specimens (e.g., [4-9]).

In 2011-2012, a landmark research project, called BNCS, was completed at the University of California, San Diego (UCSD), which consisted of testing a full-scale five-story RC building specimen on the NEES (Network for Earthquake Engineering Simulation)-UCSD large outdoor shake table ([10-12]). The building was outfitted with a variety of nonstructural components and systems (NCSs), including a fully functional elevator, metal stair subsystem, complete exterior facade, interior partition walls, ceiling sub-system, piping, and various roof mounted equipment, to name a few. Different architectural occupancies including home office, laboratory environment, computer server room, intensive care unit (ICU), and surgery unit were designated at each level of the building. The main objectives of the project were to study the dynamic performance of the full-scale RC building including the NCSs under seismic excitations, to investigate the complex interaction between the structure and NCSs, and to contribute to the development of performance-based design methodologies for NCSs. The building was first tested in base-isolated configuration with the foundation resting on four elastomeric bearings. After completion of base-isolated tests, the

elastomeric bearings removed, the building foundation anchored to the shake table platen and the building tested in fixed base configuration.

Pre-test simulations in the form of advanced nonlinear FE analyses were conducted, using the as-built details of the test specimen. The main goals of the pre-test FE simulations were to predict the response of the test specimen, to estimate the seismic demands for the NCSs, to support the seismic test protocol, and to guide the instrumentation layout for both the structure and NCSs. Maintaining both the computational efficiency and accuracy was essential for the FE simulation framework to meet its objectives. This chapter describes the details of the pre-test simulation efforts for the fixed base building specimen. First, the building specimen and the testing protocol are briefly introduced. Then, the developed FE model is described in details. Finally, the prediction capability of the pre-test FE model is evaluated by comparing the FE predicted response parameters with their experimental counterparts. The experimental-analytical comparisons are performed at different levels varying from global structural level to local member level. The shortcomings of the employed FE modeling techniques are investigated and the possible sources of discrepancies are discussed. Considering the real-life conditions and configurations of the building specimen and the seismic test protocol, the analytical-experimental correlation studies in this chapter will provide realistic metrics to evaluate and validate the accuracy of the employed nonlinear FE simulation techniques for RC building structures. The drawn conclusions in this chapter are critical to pave the way for future research to improve the fidelity of the nonlinear FE simulations for RC structures.

## **3.2. Overview of the shake table test program**

### **3.2.1. Structural system of the building specimen**

The building structural skeleton consisted of a two bays by one bay cast-in-place RC frame with a footprint of 6.6m by 11.0m in plan and uniform floor-to-floor heights of 4.27m resulting in a total height of 21.3 m from the top of the foundation to the top of the roof slab. Figure 3.1(a) shows the structural skeleton and Figure 3.1(b) shows the completed building, including its exterior facade.

The building was designed assuming a high seismic zone in southern California, namely downtown Los Angeles, and considering a stiff soil condition (Class D). A series of seven, spectrally matched, maximum credible earthquake (MCE) ground motions were used to design the fixed base structure. Target performance levels were selected as 2.5% peak inter-story drift ratio and 0.7g-0.8g peak floor acceleration during the conceptual design phase. Moreover, three spectrally matched serviceability level ground motions were selected and used to check the serviceability performance of the building. The building specimen was designed and built based on the current design and construction practice in Southern California.



Figure 3.1: Views of the building specimen; (a) bare structure; (b) completed building.

The building specimen had a 1.5 m thick post-tensioned RC foundation designed to preserve linear elastic behavior during the seismic tests (Figure 3.2). During the first phase of seismic testing, the foundation was elevated from the shake table, resting on four high damping rubber bearings. Subsequently, the bearings were removed; the foundation was anchored to the shake table platen using post-tensioned rods installed at the foundation perimeter rendering a fixed base test configuration. The building specimen had six identical 660mm by 460mm RC columns reinforced with a longitudinal reinforcement ratio of  $\rho_l = 1.42\%$  and #4@102mm prefabricated welded grids as transverse reinforcement. Two identical moment resisting frames, one each on the north and south sides of the building, provided the primary lateral load resistance to the structure in the shaking direction (east-west). Beam-column joints were designed with equivalent beam moment capacities, but with different reinforcement details on each floor. The beams at the first two slabs (floors 2 and 3)

were reinforced with high strength steel with nominal yield strength of 827 MPa. Floor 4 had a special moment frame (SMRF) with post-tensioned hybrid upturned beams. The upturned beams were connected to the columns at both ends using ductile rod connectors (DCs) [13]. The DCs were also used in the fifth floor in combination with conventional moment frame beams. The roof beams were detailed based on prescriptive requirements for SMRF in ACI 318-08 [14]. To provide adequate gravity support for the precast claddings, lateral beams were added in the east bay of the building at floors 4, 5, and roof (axis C as shown in Figure 3.2). The floor system was a 0.2 m thick concrete flat slab doubly reinforced at top and bottom. In addition to a number of smaller openings to allow passage of building services (plumbing, fire sprinklers, and electrical) and sensor/camera cables, two large perforations in the slab at each floor were provided to accommodate a full height elevator and stair shaft. Flat slab-column connections were reinforced using integral beams (embedded in the slab) and spanning all around the free perimeter of the slab. A pair of 0.15 m thick concrete walls, reinforced with a single grid of reinforcement in the middle, was placed in the north-south direction on either side of the elevator shaft to provide gravity support for the elevator system and also to provide additional transverse and torsional stiffness for the building. To partially counterbalance the torsional stiffness of the shear walls, located at the west half of the plan, the east bay of the building (axis C in Figure 3.2) was cross-braced at all floor levels with  $\phi 32$ mm steel rods, the ends of which were anchored in the floor concrete at the corners of the east bay. The estimated total weight of the bare structure was about 3010 kN excluding the foundation, which



approximately weighed 1870 kN. The completed building specimen, including all nonstructural components, approximately weighed 4420 kN, excluding the foundation. Figure 3.3 shows the contribution of different components and sub-systems to the total weight of the completed building. In this figure, the load of the furniture and other fixtures installed on the floor levels are categorized as “contents”. The contents’ weight at the roof level is composed of the penthouse, cooling tower, and air handling unit weight.

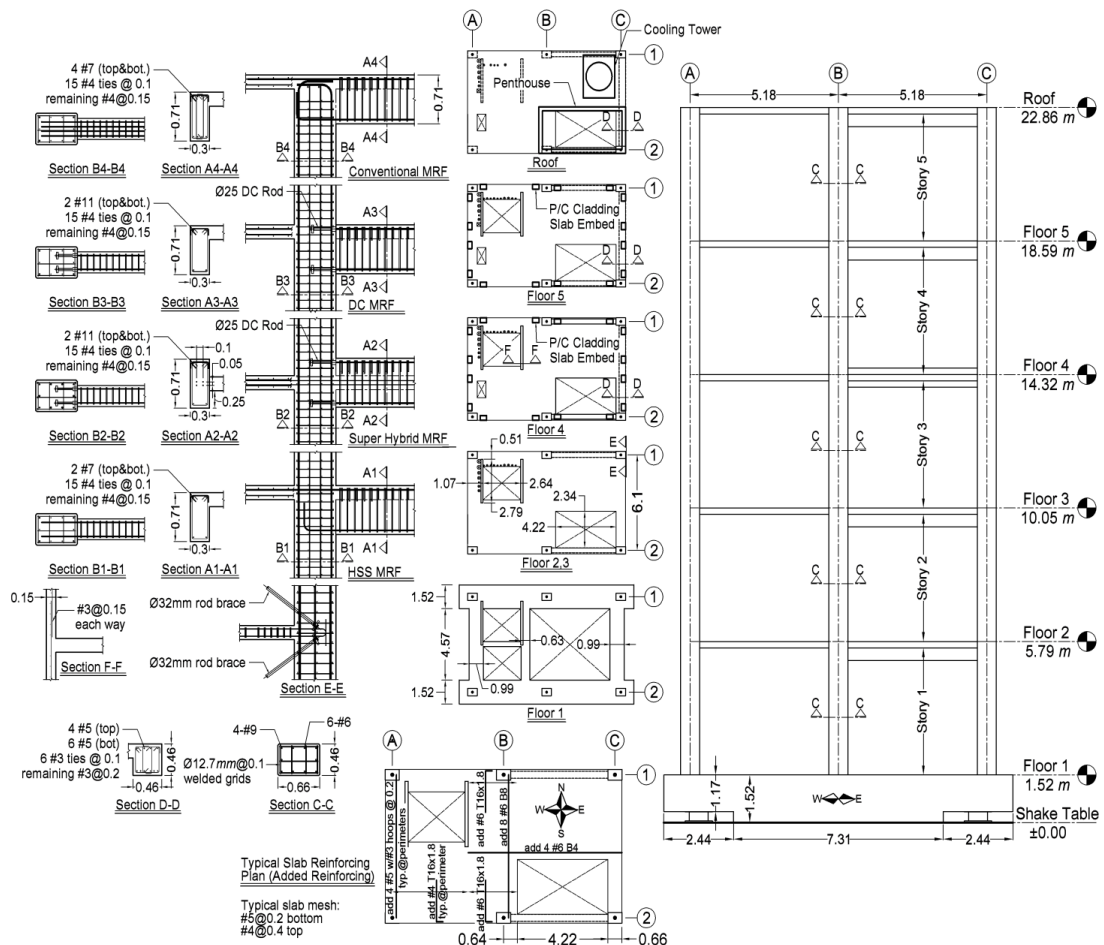


Figure 3.2: Structural details of the building specimen (units are in meters).

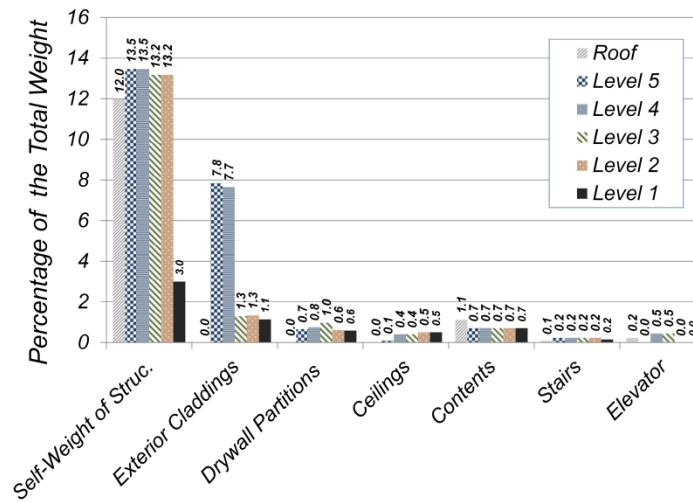


Figure 3.3: Contribution of different components and sub-systems to the total weight of the completed building (excluding foundation).

### 3.2.2. Instrumentation layout

More than 600 sensors including accelerometers, linear potentiometers, string potentiometers, strain gauges, load cells, GPS receivers and digital cameras were deployed in the building specimen to record various responses of structural and NCSs. The main accelerometer array, measuring the response of the structure, consisted of four tri-axial force-balance EpiSensor accelerometers installed at the four corners of each floor's slab and the foundation surface. These accelerometers had an amplitude range of  $\pm 4g$  and a wide frequency range of DC to 200 Hz. A 32-channel Quanterra Q330 data acquisition system from Kinemetric was used in conjunction with this accelerometer array to record data.

Data cleansing of the acceleration records consisted of two steps. In the first step, each acceleration time history was detrended to eliminate linear trends from the

data. In the next step, the detrended data were filtered using two passes (in reverse directions) of a fourth-order Butterworth filter with corner frequencies of 0.07Hz and 25Hz to remove noise effects. Before filtering, each record was zero-padded equally at the beginning and at the end as suggested by Boore [15]. The averaged east-west, north-south, and torsional components of the acceleration time history at the geometric center of each slab were derived using nonlinear least square optimization based on rigid diaphragm assumption. The cleansed acceleration time histories were then integrated to obtain the velocity and displacement time histories. The velocity and displacement time histories were also detrended and filtered following the same procedure used for the acceleration records (see Appendix 3.I).

### **3.2.3. Seismic tests**

The fixed base building specimen subjected to a series of six earthquake motions with increasing intensity (Table 3.1). After completion of shake table tests, the FE model that was developed prior to the shake table tests was rerun with the shake table achieved motions, which differ from the target motions due to the imperfect nature of the shake table controller. Nevertheless, the FE model, as described in the following sections, was not revised to preserve a true comparison between blind predictions and measurement results. The averaged translational acceleration at the foundation level were computed and used as the base input motion in the nonlinear time history analyses. The time histories of the averaged east-west component of the achieved motions at the foundation level and their relative

displacement response spectra for FB-1: *CNP100* to FB-5: *DEN67* are shown in Figure 3.4.

Table 3.1: The seismic tests performed in the fixed base configuration.

Test Name	Seed Motion	Description
FB-1: <i>CNP100</i>	Canoga Park - 1994 Northridge earthquake	Spectrally matched serviceability level
FB-2: <i>LAC100</i>	LA City Terrace - 1994 Northridge earthquake	Spectrally matched serviceability level
FB-3: <i>ICA50</i>	ICA - 2007 Pisco (Peru) earthquake	Original earthquake record, 50% scale
FB-4: <i>ICA100</i>	ICA - 2007 Pisco (Peru) earthquake	Original earthquake record, 100% scale
FB-5: <i>DEN67</i>	TAPS Pump Station 9 - 2002 Denali earthquake	Spectrally matched earthquake, 67% scale (targeted design level)
FB-6: <i>DEN100</i>	TAPS Pump Station 9 - 2002 Denali earthquake	Spectrally matched earthquake, 100% scale

Note: With the exception of FB-3 and FB-4, motions listed are seed motions that were spectrally matched and amplitude scaled as noted in the description of each.

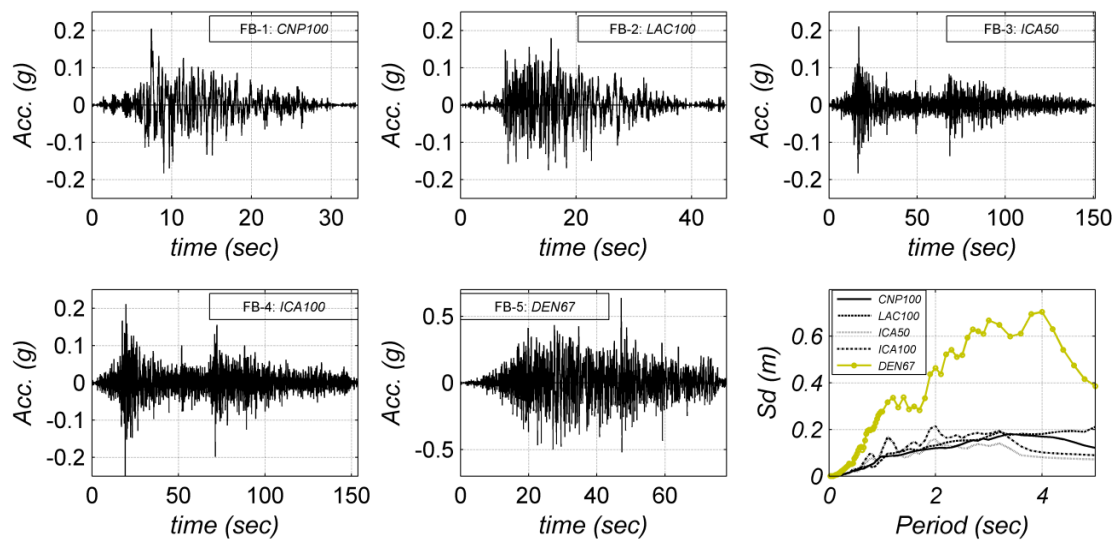


Figure 3.4: Acceleration time histories of the seismic test motions achieved at the foundation level (east-west direction) and their 5% damped relative displacement response spectra.

### **3.3. Nonlinear Finite Element (FE) Modeling and Analysis**

#### **3.3.1. FE Simulation Platform**

The building specimen had a number of unique features that required special attention in the FE modeling. The slabs were expected to influence significantly the earthquake resistance of the structure due to the specific plan configuration of the building specimen. The stairwell opening in the south-east corner of the plans was expected to affect the slab-frame interaction. Accommodating the full-height elevator, the opening in the north-west corner of the plans was likely to disturb the load transfer mechanism in the floor diaphragm. Due to the special configuration of the floor slabs, the “effective width” assumption, which is recommended by design codes to account for the slab-frame interaction, was supposed to be invalid. Furthermore, the flat slab-column connections were expected to effectively contribute in the nonlinear response behavior of the structure. Therefore, it was decided to explicitly include the slabs in the FE modeling of the test specimen. To reach this goal, the DIANA finite element analysis software [16] was selected as the FE simulation platform. This software has dedicated nonlinear constitutive material models for modeling of RC structures. Moreover, it supports a variety of structural type finite elements, such as 3D beam-column and shell elements.

### 3.3.2. Material constitutive models

The employed concrete constitutive model is a total strain rotating smeared crack model with a pseudo-elastic concrete material law. A detailed description of this material model is provided in Chapter 2. The uniaxial tensile behavior of the concrete material model consists of an initial linear elastic part with a successive nonlinear softening behavior according to the Reinhardt exponential softening model [17] as shown in Figure 3.5. In this figure,  $E_c$  denotes the linear elastic modulus defined as

$E_c = \frac{5}{3} \frac{f'_{cc}}{\varepsilon_{cc}}$ , where  $f'_{cc}$  = confined compressive strength and  $\varepsilon_{cc}$  = strain at  $f'_{cc}$ . The

concrete tensile strength  $f'_t = 0.33\sqrt{f'_c}$  (MPa), in which  $f'_c$  = unconfined compressive strength, which is determined based on testing of concrete samples taken during

construction. The cracking strain  $\varepsilon_{ic} = \frac{f'_t}{E_c}$  and the ultimate tensile strain is  $\varepsilon_{tu}$ . The

concrete material fails in tension upon reaching  $\varepsilon_{tu}$ , that means both tensile stress and stiffness will be zero. A fracture energy concept is implemented to handle the spurious mesh sensitivity caused by tensile softening [18]. Denoting the crack band width [19]

of an element by  $h$ , the ultimate tensile strain,  $\varepsilon_{tu}$ , for the element is derived such that the area under the post peak region of the stress-strain curve in tension is equal to

$\frac{G_f}{h}$ , in which  $G_f$  is the tensile fracture energy and is considered as a constant

material property equal to  $125 \text{ N/m}$  (confirmed with various experimental studies such

as [20]). The crack band width is equal to the length of the element for beam-column elements; and for shell elements, it is taken as the square root of the element area [16].

The uniaxial compressive behavior of the concrete material model consists of an initial linear elastic part and two consecutive parabolic parts as shown in Figure 3.5. The values of  $f'_{cc}$ ,  $\varepsilon_{cc}$ , and  $\varepsilon_{cu}$ , the ultimate confined compressive strain, are computed based on the initial – undamaged – properties of the concrete material and the confinement effect of the transverse reinforcements [21]. To account for the confinement effect,  $f'_{cc}$  and  $\varepsilon_{cc}$  are computed using the average results of different concrete models such as modified Kent and Park [22] and Mander model [21].  $\varepsilon_{cu}$  is determined following the suggestion of Scott et al. [23]. As discussed in Chapter 2, in a displacement-based finite element using structural beam-column or shell elements, the fracture localizes in particular elements, referred to as the plastic hinge (PH-) elements in this study. The size of PH-elements is selected to represent the physical plastic hinge region of the beams, columns, or slabs. For slabs, this size is taken equal to the slab thickness, and for beams and columns, it was taken as half of the section depth. Using the PH-element size, and the computed  $f'_{cc}$ ,  $\varepsilon_{cc}$ , and  $\varepsilon_{cu}$  for the PH-element, the fracture energy in compression [24],  $G_c$ , is computed for the beam, column, and slab elements (Figure 3.5). Details of the computed material parameters for various members can be found in Appendix 3.II.

The modified compression field theory (MCFT) [25] is employed as a built-in sub-routine in DIANA to continually update the stress-strain relation for the concrete in compression based on the maximum transverse tensile strain [26]. “Model B” as

proposed by Vecchio and Collins [27] guides the reduction in compressive strength of concrete in one principal direction due to the presence of tensile cracking in other principal directions.

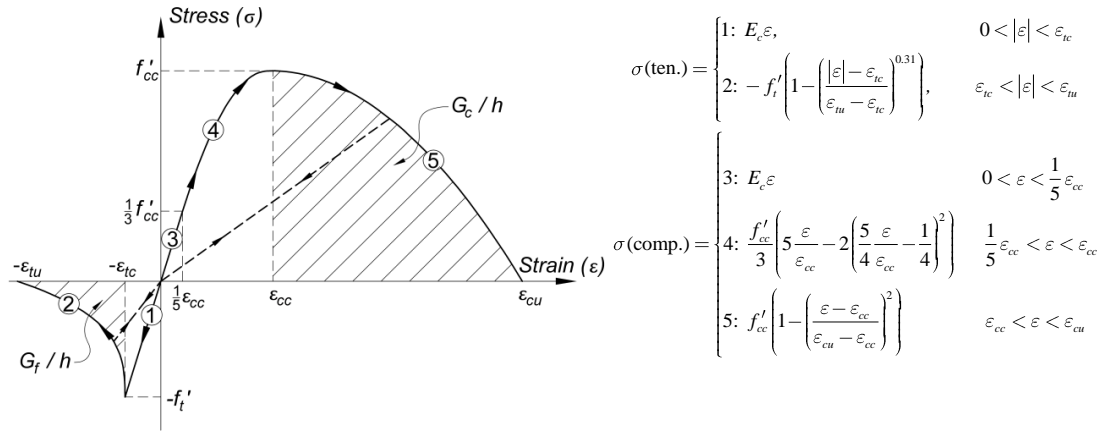


Figure 3.5: Uniaxial stress-strain behavior of concrete model  
(Tensile stresses and strains are negative).

As illustrated in Figure 3.5, the unloading and reloading in tension and compression are modeled via origin-centered linear secant paths. This assumption seems counterintuitive, as in reality the unloading and reloading paths may not pass through the origin due to the residual strains that appear upon crack closure in tension or unloading in compression. Nevertheless, this simplifying assumption provides numerical stability for this material model [28].

The modified Giuffr -Menegotto-Pinto material model as proposed by Filippou et al. [29] is used to model the uniaxial hysteretic stress-strain behavior of the reinforcing steel. It is noted that shear stiffness and dowel action of the rebars are neglected in the model. The parameters of the constitutive model (e.g., modulus of



elasticity, yield strain, and strain hardening ratio) are obtained from tensile tests performed on representative rebar samples. The parameters defining strain hardening are determined based on the approach presented in Appendix 3.II.

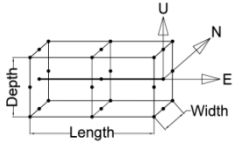
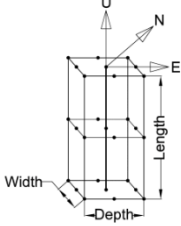
### **3.3.3. Finite elements**

The beam and column members are modeled using three-node Mindlin-Reissner displacement-based 3D beam-column elements with 18 DOFs per element. The element formulation is based on quadratic shape functions that imply a linear variation of the axial and shear strains along the centerline of the element [30]. To maintain computational efficiency, different integration schemes for the beam-column elements – along their length and across their cross-section – are defined based on their expected level of nonlinearity (See Figure 3.6 and Table 3.2). The columns are restrained assuming full fixity at their base due to the large stiffness of the foundation, which was anchored to the shake table during the fixed base tests. The beam and column longitudinal steel reinforcements are defined using fully bonded embedded steel bars. The slabs and shear walls are modeled using eight-node Mindlin-Reissner quadrilateral serendipity shell elements. This element has six DOFs per node including mechanics-based drilling degrees of freedom. A numerical integration rule using two by two Gauss-quadrature integration points over the plane and three Simpson integration points across the thickness is applied to all shell elements. Each of the steel reinforcement meshes at the top and bottom of the slab is modeled as a membrane with an equivalent thickness, embedded in the concrete shell element. Forming RC

strong bands along the free perimeters of the slabs, the integral beams are modeled as regular beam-column elements. The cross section dimensions of these elements are based on the actual dimensions of the integral beam confined core. These elements are reinforced with embedded steel bars, similar to the frame beams. The steel rod braces are modeled using two-node directly integrated – one integration point – 3D truss elements with three DOFs per node.

Some specific elements along each beam and column and across the slabs, which potentially can develop localized nonlinearities, are referred to as PH-elements. As already mentioned, the length of these PH-elements is taken to represent the length of the physical plastic hinge region of the associated member. The slab mesh discretization is designed manually considering five different criteria: (1) retaining proper length for the PH-elements, (2) aligning the nodal points of adjacent beam and shell elements, (3) retaining regularity in the shape and size of shell elements, (4) modeling different beam-column-slab joint details, and (5) accommodating different slab reinforcing details as specified in the design and as-built documents.

Table 3.2: Integration scheme for beam-column elements.

Component	Location	Integration scheme	
Beams	PHs at floors 2, 3, and 4	ISB1: 3 (length), 3 (width), 7(depth)	
	PHs at floor 5 and roof	ISB2: 3 (length), 3 (width), 5(depth)	
	Others	ISB3: 3 (length), 3 (width), 3(depth)	
Columns	PHs at story 1	ISC1: 3 (length), 3 (width), 7(depth)	
	PHs at stories 2 and 3	ISC2: 3 (length), 3 (width), 5(depth)	
	Others	ISC3: 3 (length), 3 (width), 3(depth)	

ISB: Integration scheme for beam, ISC: Integration scheme for column.

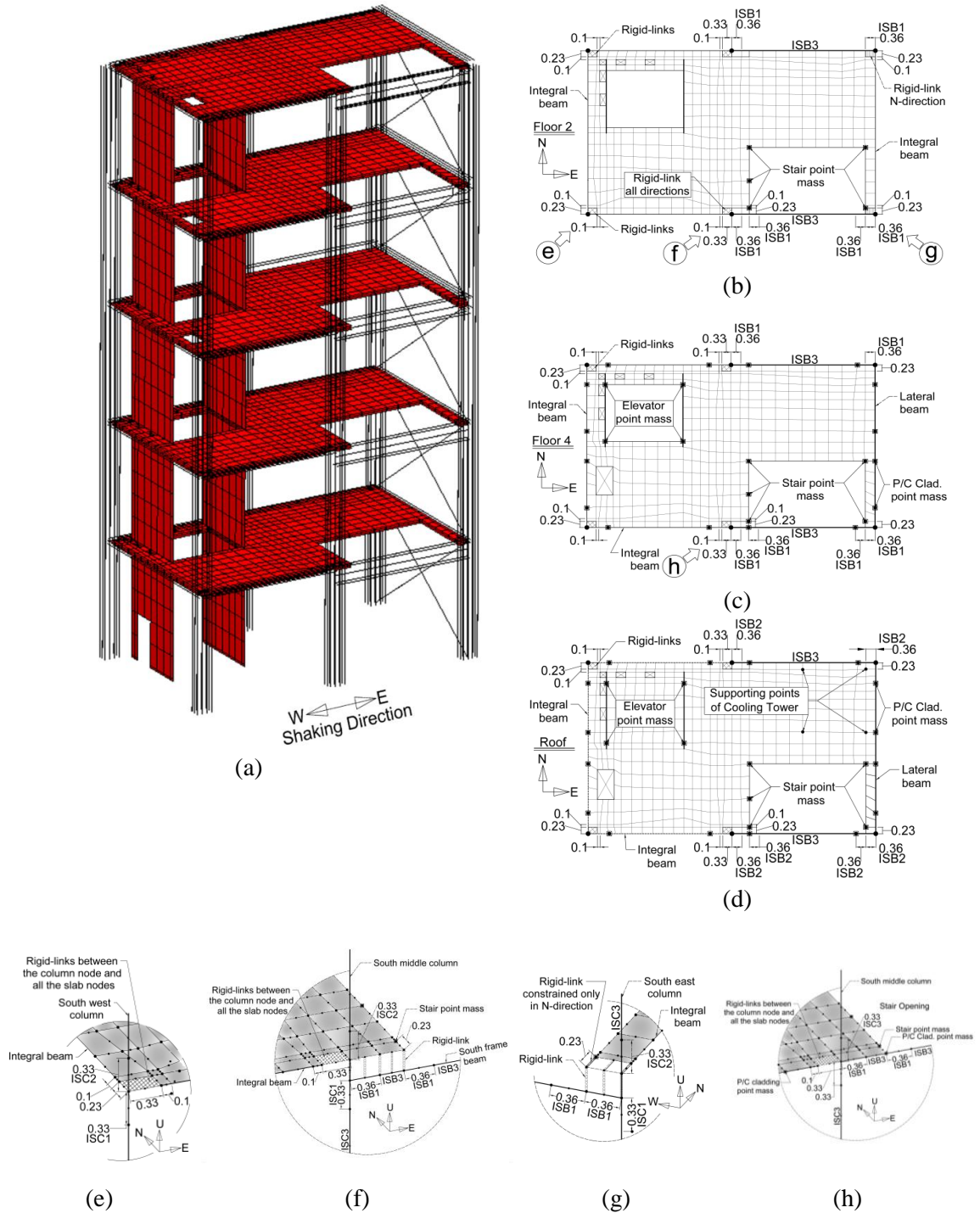


Figure 3.6: (a) Complete FE model of the test specimen structure; FE mesh details at (b) floor 2, (c) floor 4, and (d) roof; joint details at (e) south-west corner of floor 2, (f) south-middle of floor 2, (g) south-east corner of floor 2, and (h) south-middle of floor 4 (N: North, E: East, U: Up, and W: West; units are in meters).

Figure 3.6(a) shows the 3D view of the FE model of the test specimen. Figures 3.6(b), (c), and (d) show the details of the FE mesh at floors 2, 4, and roof, respectively. The FE mesh at floors 3 and 5 are close to floor 2 except for the integration scheme of beam-column elements, which are described in Table 3.2. Figure 3.6(e) shows the column-slab joint detail at the south-west corner of floor 2. Figures 3.6(f), (g), and (h) show the beam-column-slab joint details at the south-middle and south-east corner of floor 2 and south-middle of floor 4, respectively.

#### **3.3.4. Modeling of inertia and damping properties**

The self-mass of the beams, columns, and shear walls is modeled by assigning proper material mass density to the corresponding elements. The overlapping of adjacent components is accounted for by modifying the mass density of the connecting elements. To determine the mass density of the slab shell elements, the mass of all individual non-structural components located in the upper half story below the slab and lower half story above the slab are added to the self-mass of the slab concrete, resulting into an equivalent mass density of the shell elements. Since the individual mass contributions of the interior partition walls, ceilings, balloon frame facade at stories 1 to 3, and the installed contents on each floor are relatively small, their inertial effect is modeled as uniformly distributed mass over the floor slab. On the other hand, the individual mass contributions of the precast concrete claddings at stories 4 and 5, the stairs and elevator – spanning the height of the building – and the penthouse and cooling tower – at the roof level – are significant; therefore, they are each modeled

with lumped masses. Each precast cladding panel is connected at two locations to the lower floor slab at bottom, by means of in situ welded connections, and to the upper floor slab at top, by means of rod connections, restraining the out-of-plane movement of the panel. Lumped masses are assigned based on the connection details and tributary area at the four supporting points of each panel. The translational mass of the panel in its in-plane direction is equally distributed over the two bottom connection points, as the top connections were intended to translate freely during the in-plane motion of the panel. In contrast, the translational mass of the panel in its out-of-plane direction is distributed equally over all four support points. Other items in the building have well-defined lumped masses. For example, since the cabin and counterweight of the elevator system were located at the same level during all fixed base seismic tests, the total mass of the elevator system is equally distributed over four points around the elevator openings at floors 3, 4, and roof as shown in Figures 3.5(c) and (d). The masses of the penthouse and cooling tower are distributed equally over four support points of the penthouse, and support points of the cooling tower at the roof level, respectively (See Figure 3.6(d)). Using the defined mass densities, the consistent mass matrices for all finite elements, including rotational terms, are computed and added to the defined nodal lumped masses to assemble the mass matrix of the whole structure.

The damping characteristics are modeled using proportional Rayleigh damping model [31] by defining a damping ratio of 2% at the first mode – of the undamaged initial linear elastic model of the structure – and at 20Hz. The Rayleigh damping mass and stiffness coefficients are held constant during the time history analyses. The

consistent damping matrix is updated at each time step of the time history analysis, by applying the stiffness coefficient to the current stiffness matrix.

### **3.3.5. Incremental-iterative nonlinear time history analyses**

Each nonlinear analysis starts by applying the gravity loads quasi-statically and incrementally. The regular incremental-iterative Newton method is used to solve the nonlinear static equilibrium equations for gravity loads. The nonlinear time history analysis for an earthquake excitation is then performed from the state of the structure after application of the gravity loads. Newmark averaged acceleration method [31], with a constant time step size of 0.025 sec, is used to integrate the equations of motion in time. The time step size is selected based on a preliminary convergence study of time history analysis results with respect to the time step size to ensure the analysis accuracy. The quasi-Newton (secant) method based on the Broyden–Fletcher–Goldfarb–Shanno (BFGS) stiffness update method [32] is employed as the iterative method to solve the nonlinear dynamic equilibrium equations. At the end of each analysis time step, the last obtained stiffness matrix is stored and used as the initial stiffness matrix for the first iteration of the next time step. The convergence criterion is based on either the relative norm of the last displacement increment vector or the relative norm of the last unbalance force vector with a convergence tolerance of  $10^{-4}$ , whichever occurs first, while the number of iterations per time step is limited to 30. If none of the two convergence criteria are satisfied within 30 iterations, the iterative procedure is terminated, the current unbalance force vector is transferred to the next

time step, and the analysis goes on. The parallel direct sparse solver method [33] is used for solving the systems of linearized incremental equilibrium equations.

To compare the FE predicted and measured building responses, a nonlinear time history analysis is performed by applying the sequence of test ground motions after applying the gravity loads. Thus, the input base motion consists of the sequence of all six ground motions, as reproduced by the shake table, with 5 seconds of zero padding between any two consecutive motions. In this case, the model state is retained from motion to motion and the analysis accounts for cumulative damage in the structural system. In a parallel effort, a nonlinear time history analysis is performed separately for each test ground motion after application of the gravity loads. The former analysis is called “sequential analysis” while the later one is called “individual analysis” hereafter.

### **3.4. Nonlinear time history analyses results**

This section presents the FE predictions – obtained from sequential analysis method – and compares them with the experimental measurements obtained during the shake table tests. Five seismic tests are considered in this section for the analytical-experimental correlation study, namely FB-1: *CNP100*, FB-2: *LAC100*, FB-3: *ICA50*, FB-4: *ICA100*, and FB-5: *DEN67*. The FB-6: *DEN100* is not included in this chapter since during this test, the building specimen experienced modes of structural failure that cannot be simulated by the FE modeling technique described above.



### 3.4.1. Structural level response

Figures 3.7-3.8 compare the FE predictions and experimental measurements from the shake table tests for the peak floor absolute acceleration (PFAA) response, peak interstory drift ratio (PIDR), and peak total (inertial) story shear (PTSS) normalized by the total weight of the building, respectively. The total (inertial) story shear, referred to as story shear hereafter for brevity, is computed as

$$V_i = \sum_{j=i+1}^6 -m_j a_j, i = 1, \dots, 6 \quad (3.1)$$

where  $V_i$  is the story shear evaluated at the section in midway of  $i^{\text{th}}$  and  $(i+1)^{\text{th}}$  floor ( $i^{\text{th}}$  story),  $a_j$  is the averaged absolute acceleration at floor  $j$  in east-west direction, and  $m_j$  is the tributary mass of floor  $j$ .

In Figures 3.7(a)-3.7(c) the coefficient of determination ( $R^2$ ) measures the level of agreement between FE predictions and measurements for the peak values of the considered response parameters at different floor levels or stories for the five different seismic tests. The envelope plots in Figures 3.8(a)-3.8(c) compare the FE predicted and measured PFAA, PIDR, and PTSS along the height of the building – positive and negative peaks are treated separately. To compare the relative difference between the FE predicted and measured responses of the building in a more comprehensive and concise way, a relative error measure ( $E_i$ ) is defined, which shows the relative closeness of the FE predicted and measured peak response value at floor (or story)  $i$  of the building. Denoting a peak response quantity obtained from FE

prediction and experimental measurements at floor (or story)  $i$  by  $R_{i,+}^{FE\ Pred.}$  and  $R_{i,+}^{Meas.}$  in the positive direction, and by  $R_{i,-}^{FE\ Pred.}$  and  $R_{i,-}^{Meas.}$  in the negative direction, respectively, the relative error measure,  $E_i$ , is defined as

$$E_i = \max \left( \left| \frac{R_{i,+}^{FE\ Pred.} - R_{i,+}^{Meas.}}{\max_i R_{i,+}^{Meas.}} \right|, \left| \frac{R_{i,-}^{FE\ Pred.} - R_{i,-}^{Meas.}}{\min_i R_{i,-}^{Meas.}} \right| \right) \geq 0. \quad (3.2)$$

$E_i = 0$  indicates a perfect agreement at floor (or story)  $i$  between the FE prediction and the measurement for the peak response of interest. The more  $E_i$  deviates from zero, the more error exists in the FE prediction. The distribution of this relative prediction error is shown by contour plots for the five seismic tests and the five floor levels in Figures 3.9(a)-3.9(c) for the PFAA, PIDR, and PTSS, respectively.

By comparing parts (a) and (b) of Figures 3.7-3.9, it is concluded that the PFAA results are generally better predicted than PIDRs. The PFAAs are better predicted at upper floors for low intensity seismic tests and at lower floors for high intensity seismic tests (Figure 3.9(a)). Figure 3.8(b) also clearly shows that the FE simulation generally overpredicts the PIDRs in low intensity seismic tests and underpredicts them in high intensity seismic tests. For low intensity tests, the PIDR is typically overestimated at all stories, although more so at the middle stories of the building, while for high intensity tests, the PIDR is underestimated at the lower stories and overestimated at the upper stories of the building. Figure 3.9(b) shows that the PIDR relative prediction error is more significant for the low intensity seismic tests (FB-1: *CNP100* to FB-3: *ICA50*) and at the middle stories of the building (story 3).

Finally, the FE simulation underpredicts the PTSS at all the stories as can be observed in part (c) of Figures 3.7-3.8.

It is hypothesized that the nonstructural components, especially the partition walls, contribute significantly to the discrepancy between the FE predicted and measured PIDR results. The influence of partition walls on the dynamic response of buildings has been the focus of other research studies (e.g., [34]), where it has been noted that their effect is more significant at low IDR, since the walls are intact, well connected to the structure, and contribute their full original stiffness. As the base motion intensifies, the partition walls undergo damage and their connections to the building structure deteriorate at the lower stories of the building, where the IDR demand is usually higher, while at the upper stories, where the IDR demand is lower, they are still influential.

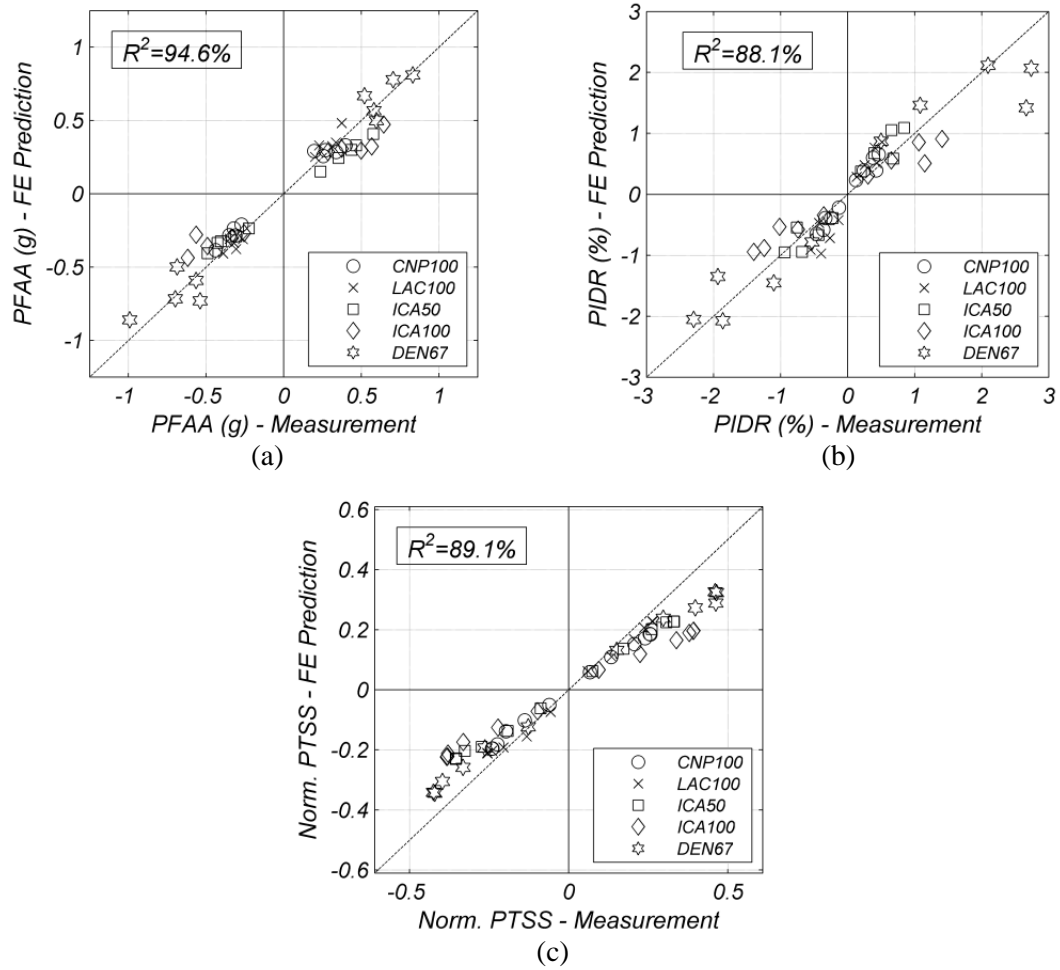


Figure 3.7: Correlation of the FE predicted versus measured  
 (a) peak floor absolute acceleration, (b) peak interstory drift ratio,  
 and (c) peak total story shear normalized by the total weight of the building.

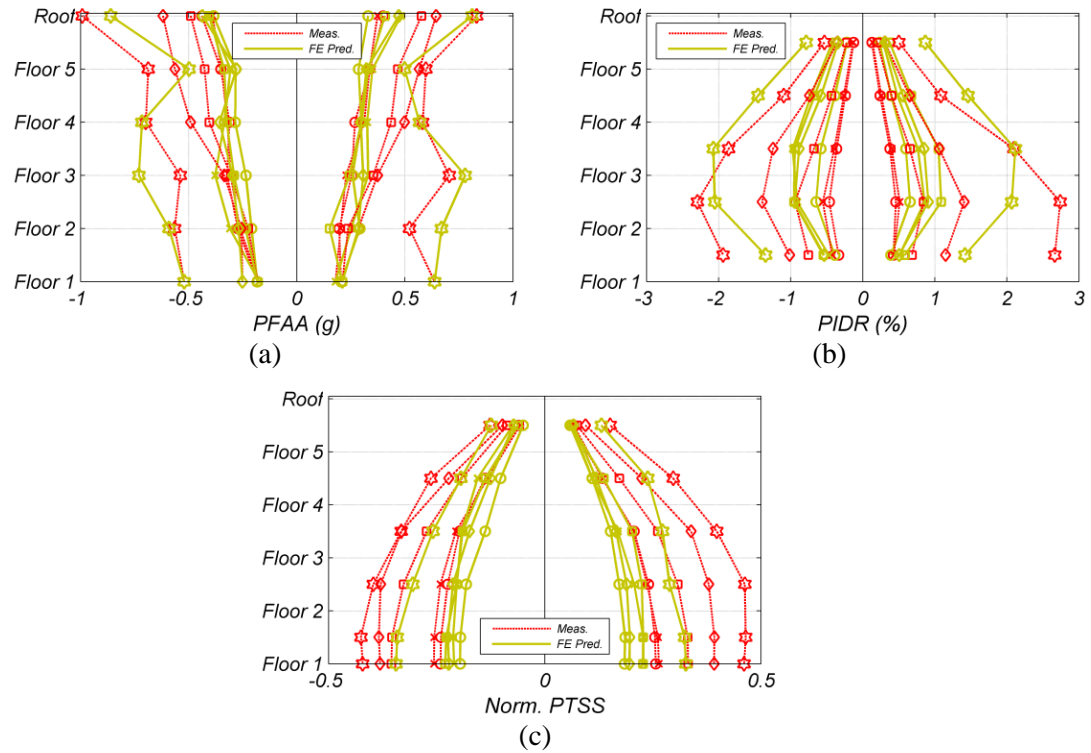


Figure 3.8: Comparison of FE predicted and measured (a) peak floor absolute acceleration envelopes, (b) peak interstory drift ratio envelopes, and (c) peak total story shear envelopes normalized by the total weight of the building.

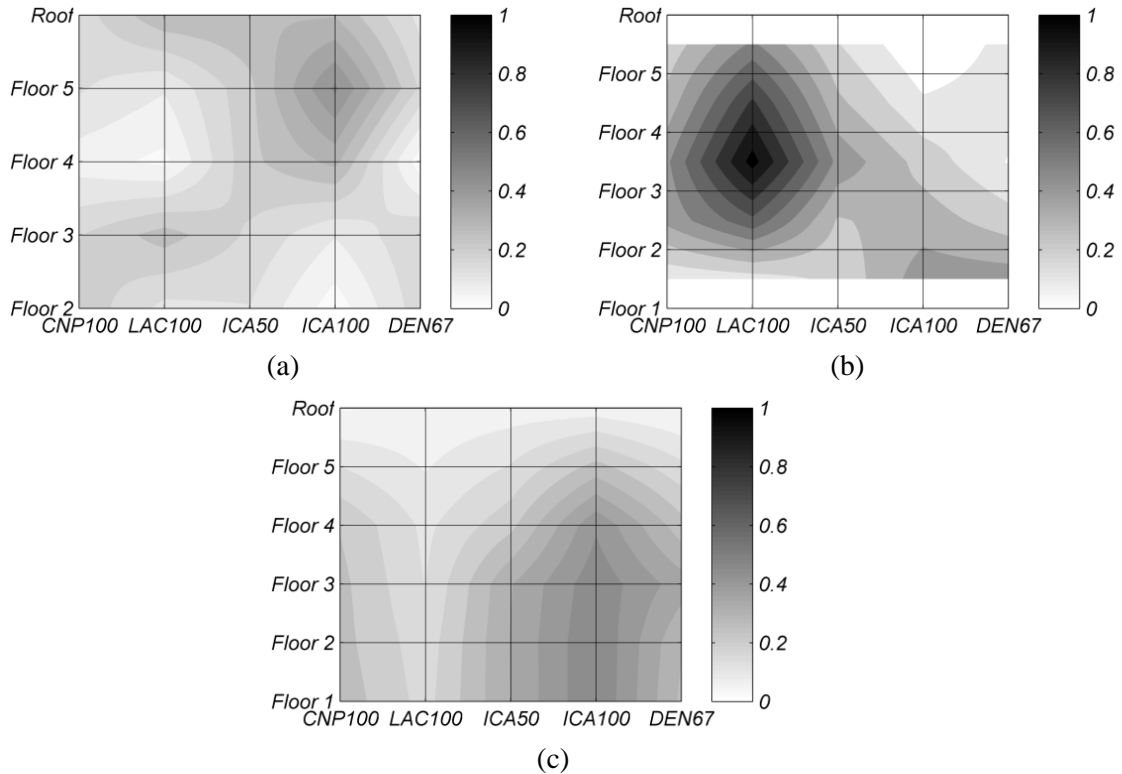


Figure 3.9: Relative prediction error for  
 (a) peak floor absolute acceleration, (b) peak interstory drift ratio, and (c) peak total story shear.

Figure 3.9(b) shows that the PIDR relative prediction error is largest at story 3 for the low intensity seismic tests (FB-1: *CNP100* to FB-3: *ICA50*). This can be explained by comparing the total length of the installed partition walls at each story of the building, as shown in Table 3.3. The exterior balloon framings are excluded in this table, since they have special connection details that reduce their interaction with the structural system. Table 3.3 indicates that at stories 3 and 4 approximately 50% more partition walls are installed compared to other stories. The contribution of the partition walls to the lateral stiffness of the building specimen can also be inferred by

comparing the experimentally identified natural periods for the bare structure and full building as presented in [35].

Table 3.3: Length of partition walls and balloon framing at different stories.

Total length ( $m$ )	Story 1	Story 2	Story 3	Story 4	Story 5
Partition walls in E-W direction	13.5	13.5	22.0	15.0	13.5
Partition walls in N-S direction	3.5	11.0	15.5	7.5	6.0

The underprediction of the PIDR at the lower stories of the building during large intensity tests (See Figure 3.8(b) for FB-4: *ICA100* and FB-5: *DEN67*) can be explained by the difference between the actual and FE predicted hysteretic response of the structural components. The employed FE modeling technique is unable to capture the pinching hysteretic behavior in the beams and columns. As a result, the structural components have larger energy dissipation capacity under cyclic loading in the FE model than in the real structure at the same ductility level. Consequently, the FE predicted floor displacement responses are lower than the test results at the lower stories of the building. Figure 3.8(b) shows that the PIDR is underpredicted at the first story for FB-4: *ICA100* and the first two stories for FB-5: *DEN67*. This explanation is in agreement with the story level response of the building discussed in the next section of this chapter.

To better investigate the effect of nonstructural components on the seismic response of the building, the time histories of selected response parameters are compared in Figures 3.10(a) and 11(b) for FB-1: *CNP100* and FB-5: *DEN67*,

respectively. In these figures, the time histories of (i) roof drift ratio, which is the relative roof displacement normalized by the roof height measured from the top of the foundation, (ii) second story IDR, and (iii) total base overturning moment normalized by the product of the total weight of the building ( $W_t = 4420$  kN) and the roof height ( $h_R = 21.34$  m) are shown. The total (inertial) base overturning moment ( $M_B$ ) is computed as

$$M_B = \sum_{j=2}^6 -m_j a_j h_j \quad (3.3)$$

where  $h_j$  is the height of floor  $j$ , measured from the top of the foundation. Figure 3.10(a) shows a clear difference in the frequency content of all response time histories between the FE predicted and measured results, which is most likely due to the contribution of the nonstructural components – mostly partition walls. This contribution, which is not accounted for in the FE model of the building, results in a shortening of the natural periods of the building. By comparing Figures 3.10(a) and 11(b), it is observed that the discrepancy in the frequency content between FE predicted and measured responses lessens from FB-1: *CNP100* to FB-5: *DEN67* because of extensive physical damage in the nonstructural components developed in the seismic tests prior to FB-5: *DEN67*. As a result, the nonstructural components' contribution is significantly reduced for FB-5: *DEN67*.



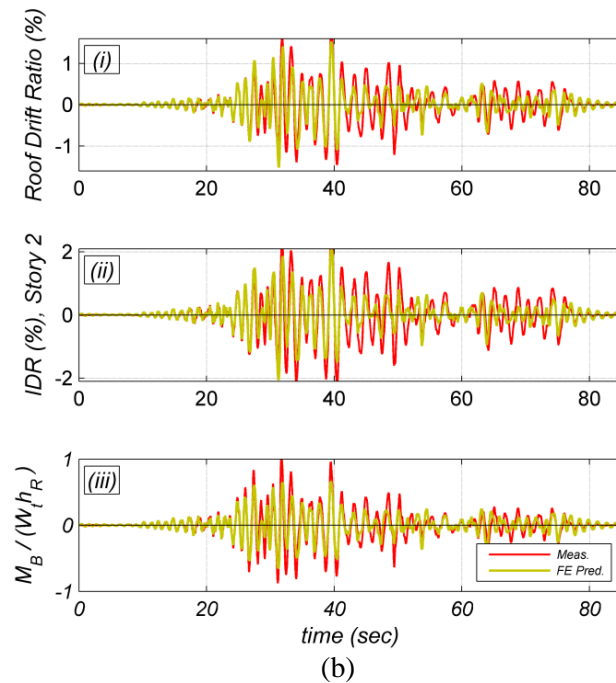
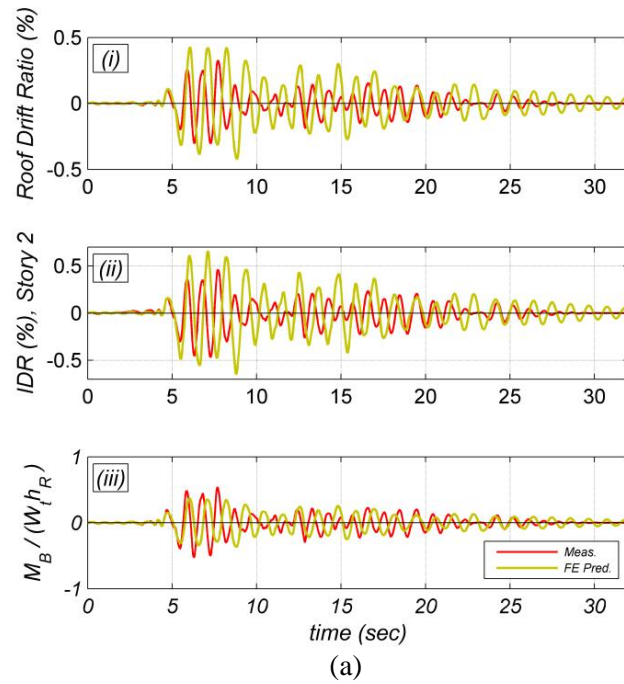


Figure 3.10: Comparison of FE predicted and measured time histories of selected response parameter for (a) FB-1: CNP100 and (b) FB-5: DEN67.

### 3.4.2. Story level response

The plots of TSS versus IDR can show the hysteretic response of the building at the individual story levels. These plots are shown in Figures 3.11(a), (b), and (c) for FB-1: *CNP100*, FB-4: *ICA100*, and FB-5: *DEN67*, respectively. Figure 3.11(a) shows that the FE prediction is in reasonable agreement with the measured response only at the first story for FB-1: *CNP100*, because few partition walls were installed in this story (See Table 3.3). For all other stories, the measured response is significantly stiffer than the predicted one, which can be explained by based on the contribution of the nonstructural components (especially partition walls). As the base excitation intensifies from FB-1: *CNP100* to FB-4: *ICA100* and to FB-5: *DEN67*, the nonstructural components incrementally damage and their contribution to the structural system response decreases, leading to better agreement of the stiffness between the FE predicted and measured response of upper stories. The FE prediction underestimates the IDR demands in the lower stories during FB-4: *ICA100* and FB-5: *DEN67* tests. As discussed earlier, since the employed FE modeling technique has some deficiencies in simulating the hysteretic response of the structural components, the predicted IDR responses are lower than the measured ones. Thus, the measured story responses show higher level of nonlinearity compare to the FE predictions. The difference in the FE predicted and measured response at lower stories during the high intensity seismic test can also be a consequence of improper modeling of damping energy dissipation beyond material hysteretic energy dissipation. As described earlier,

the damping characteristics are modeled using proportional Rayleigh damping by defining a constant damping ratio at two predefined frequencies.

To better study the difference between the FE predicted and measured story-level hysteretic responses, Figures 3.12(a), (b), and (c) show the normalized prediction error of the total absorbed energy ( $E_A$ ) time history at the story level for FB-1: *CNP100*, FB-4: *ICA100*, and FB-5: *DEN67*, respectively.  $E_A$  is computed by integrating the TSS versus IDR responses for each story separately.  $E_A$  consists of both the dissipated hysteretic energy and the recoverable strain energy. The measured absorbed energy is larger than its FE prediction in the first and second stories for FB-1: *CNP100* (Figure 3.12(a)), in the first four stories for FB-4: *ICA100* (Figure 3.12(b)), and in the first three stories for FB-5: *DEN67* (Figure 3.12(c)). As mentioned earlier, a number of factors can explain these discrepancies including imprecision in restrictive kinematic assumptions in the structural FEs adopted, which can result in inaccurate hysteretic response of the structural components, and other energy dissipation mechanisms that are either not represented or not properly modeled in the FE model of test building (such as energy dissipated by nonstructural components or other viscous damping sources).

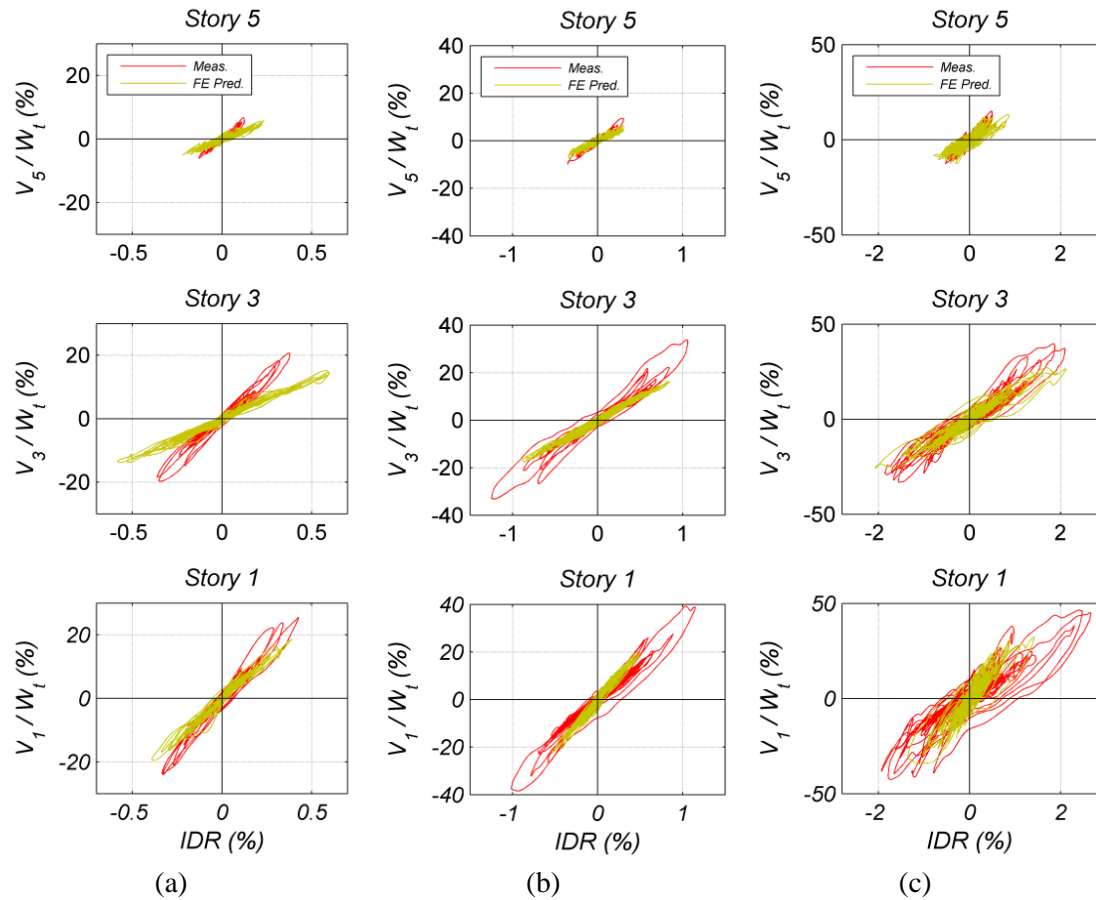


Figure 3.11: Comparison of FE predicted and measured TSS vs. IDR hysteretic response for (a) FB-1: CNP100, (b) FB-4: ICA100, and (c) FB-5: DEN67.

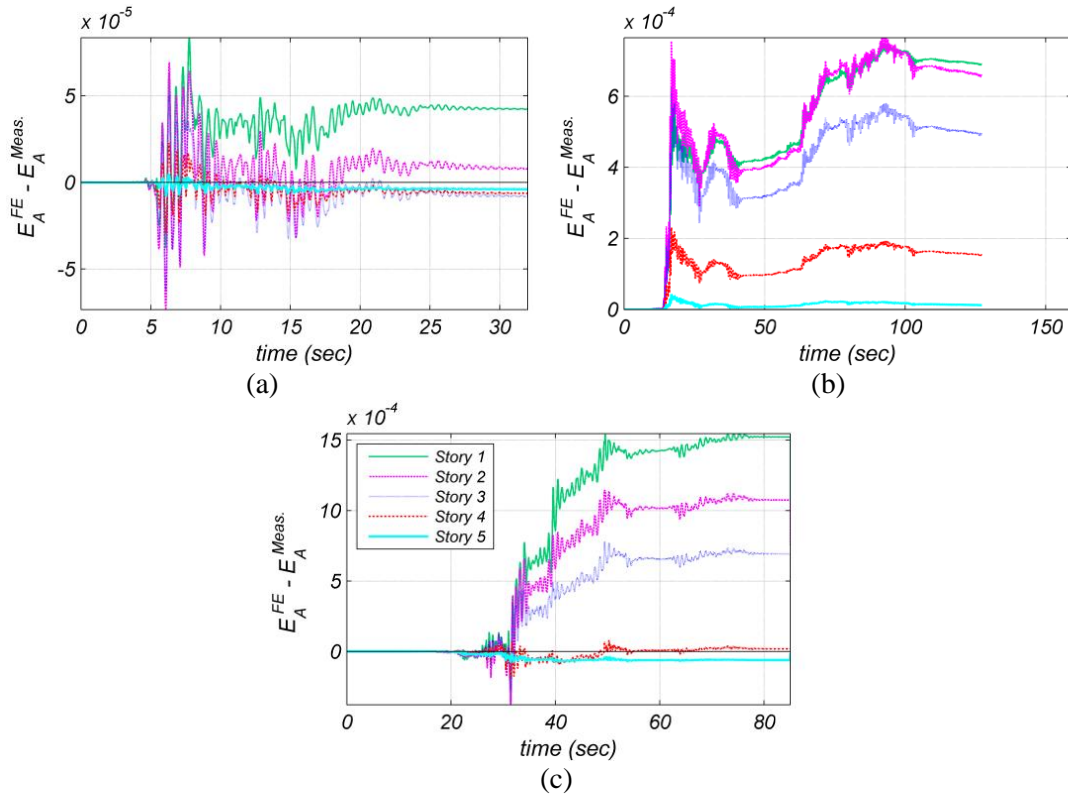


Figure 3.12: Normalized prediction error of the total absorbed energy time history at the story level for (a) FB-1: *CNP100*, (b) FB-4: *ICA100*, and (c) FB-5: *DEN67*.

### 3.4.3. Component level response

To measure the beam-end axial elongation and rotation, the north frame beams of the building were instrumented with a pair of linear potentiometers at each end of the beam. The potentiometers were installed at top and bottom of only the south face of the beams (See Figures 3.13(a) and 3.13(b)). The normalized beam-end axial deformation and average curvature response time histories can be derived using the recorded data of each pair of linear potentiometers. Denoting the length of the sensor by  $l$ , the vertical distance between the two sensors at each beam-end by  $\Delta h$ , and the

potentiometer measurement by  $\delta$ , the measured beam-end axial deformation,  $\varepsilon_{Meas.}$ , and the measured beam-end averaged curvature,  $\phi_{Meas.}$ , are computed as

$$\varepsilon_{Meas.} = \frac{\delta_{bot}/l_{bot} + \delta_{top}/l_{top}}{2}, \quad \phi_{Meas.} = \frac{\left( \delta_{bot}/l_{bot} - \delta_{top}/l_{top} \right)}{\Delta h} \quad (3.4)$$

The FE predictions for the axial deformation and averaged curvature are obtained from the first beam element next to the column element (PH-element) by extracting and processing the axial strain time histories at the proper integration points of the cross section. Figure 3.14 compares the FE predicted and measured beam-end axial deformation time histories at the both ends of the north beam at second and third floor levels (beneath the first and second floor slabs) for FB-5: *DEN67*. Similarly, Figure 3.15 compares the FE predicted and measured beam-end average curvature time histories at the both ends of the north beam at second and third floor levels for FB-5: *DEN67*. Moreover, Figure 3.16 compares the averaged axial strain versus curvature at the similar locations. The comparisons show good correlation between FE prediction and experimental measurement. Although the predicted beam-end axial deformation and averaged curvature time histories have a good agreement with the measured results, the peak values of both the axial deformation and curvature time histories are overpredicted by FE model. This can be due to all the above mentioned modeling uncertainties. Moreover, in this case, the averaging effects implied in the measurement of the sensors can also be a source of discrepancy. The length of the installed linear potentiometers is about 0.5 m, which is clearly larger than the expected length of the physical plastic hinge region at the end of the beam. So, the measured

axial deformation and curvature are averaged along the first 0.5 m portion of the beam, while the FE predicted axial deformation and curvature are averaged over the first beam element next to the column (PH-element), the length of which is about 0.35 m (See Figure 3.6). Therefore, the FE predicted peak values of the beam-end axial deformation and curvature averaged over the expected plastic hinge length are larger than their measured counterparts.

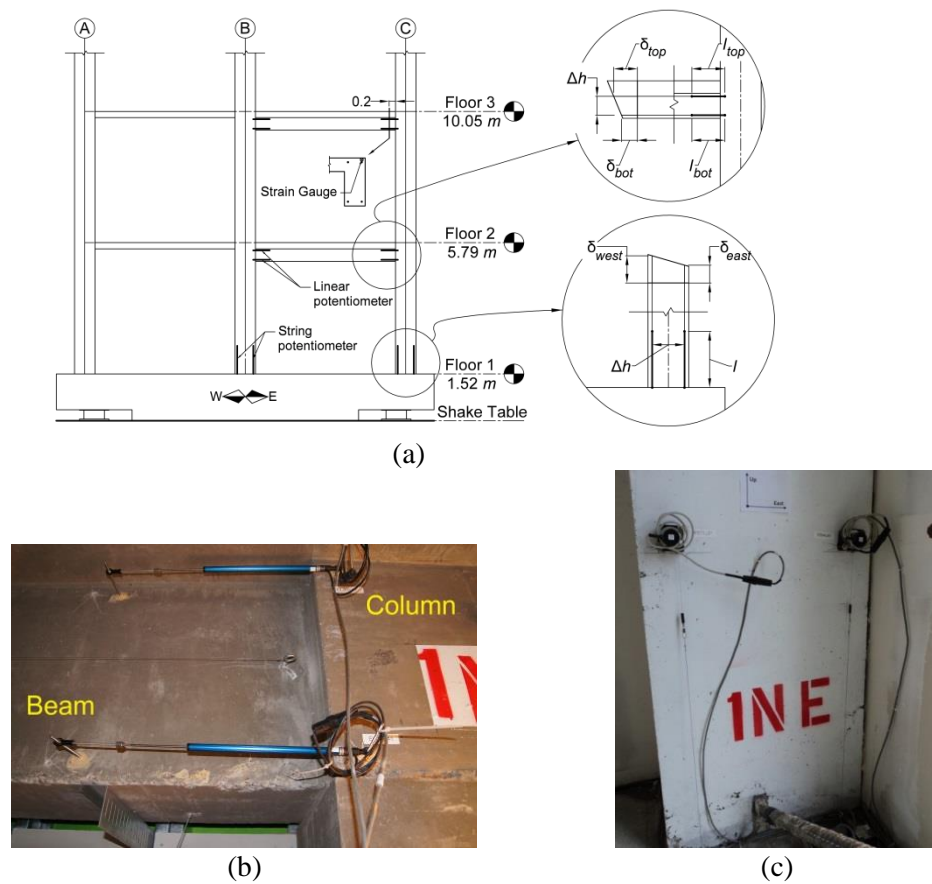


Figure 3.13: Instrumentation of structural components:  
 (a) schematic details of north frame instrumentation;  
 (b) linear potentiometers installed at east end of second floor north beam;  
 (c) string potentiometers installed at the base of the north east column.

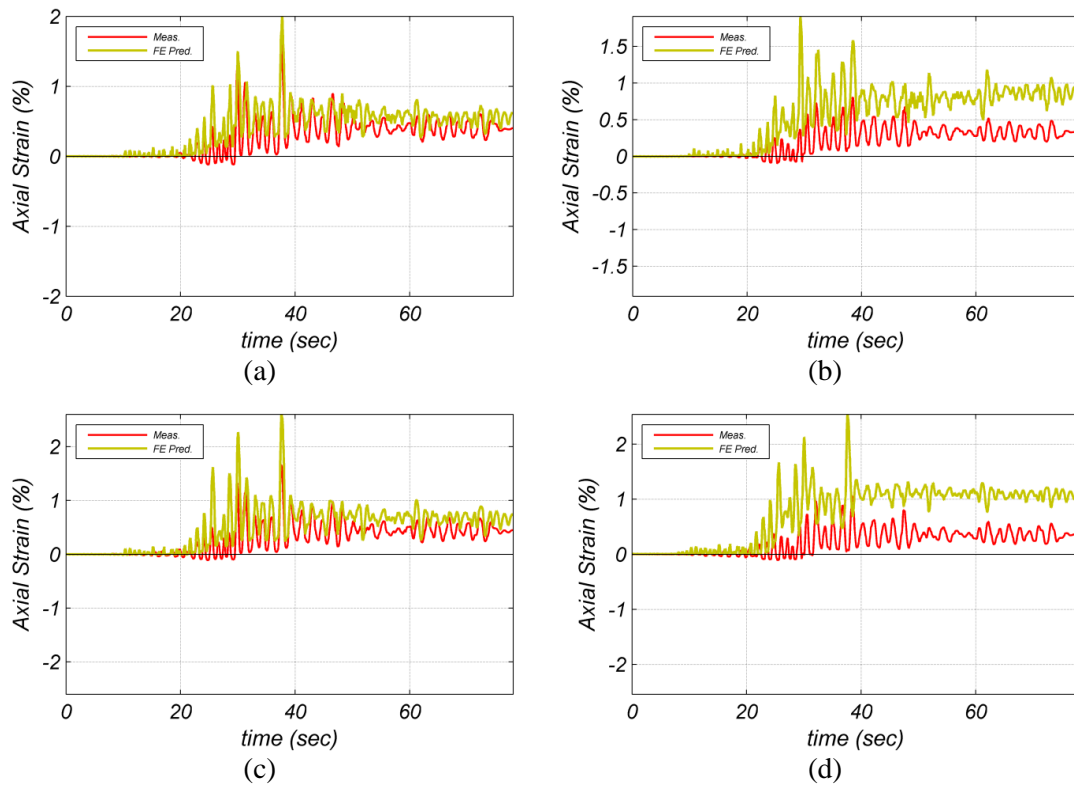


Figure 3.14: Comparison of FE predicted and measured averaged axial strain time histories for FB-5: *DEN67* at the (a) west end of the second floor north beam, (b) east end of the second floor north beam, (c) west end of the third floor north beam, (d) east end of the third floor north beam.



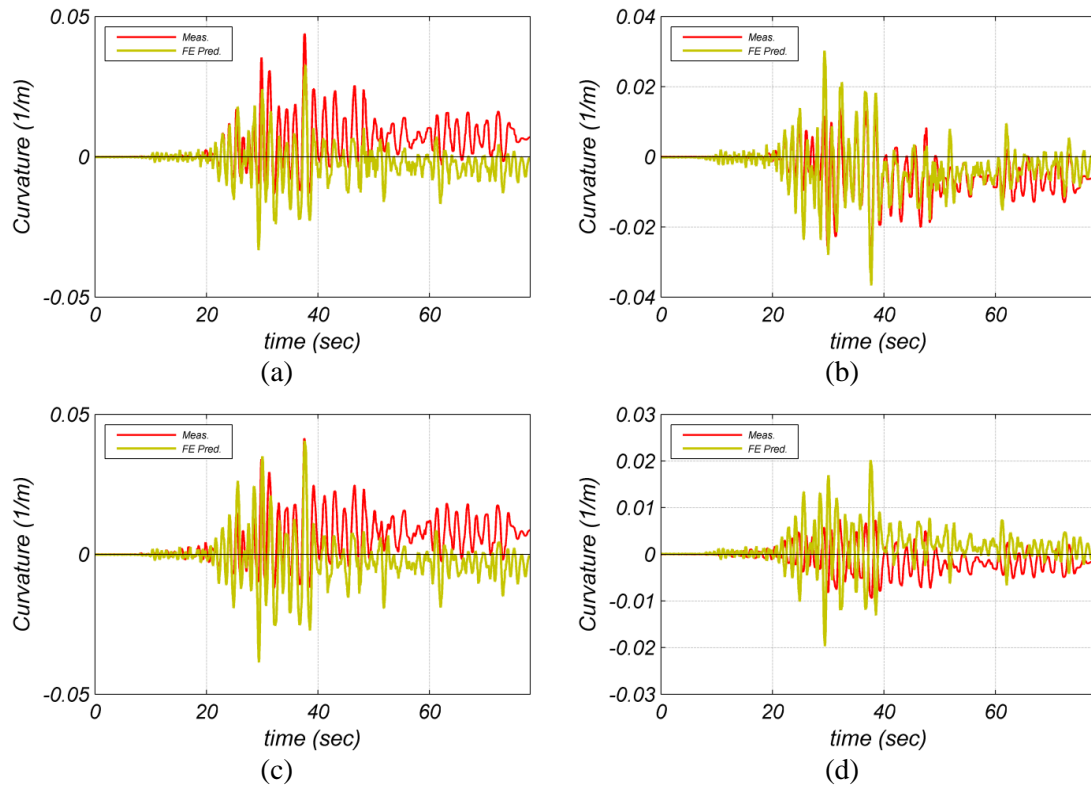


Figure 3.15: Comparison of FE predicted and measured averaged curvature time histories for FB-5: *DEN67* at the (a) west end of the second floor north beam, (b) east end of the second floor north beam, (c) west end of the third floor north beam, (d) east end of the third floor north beam.

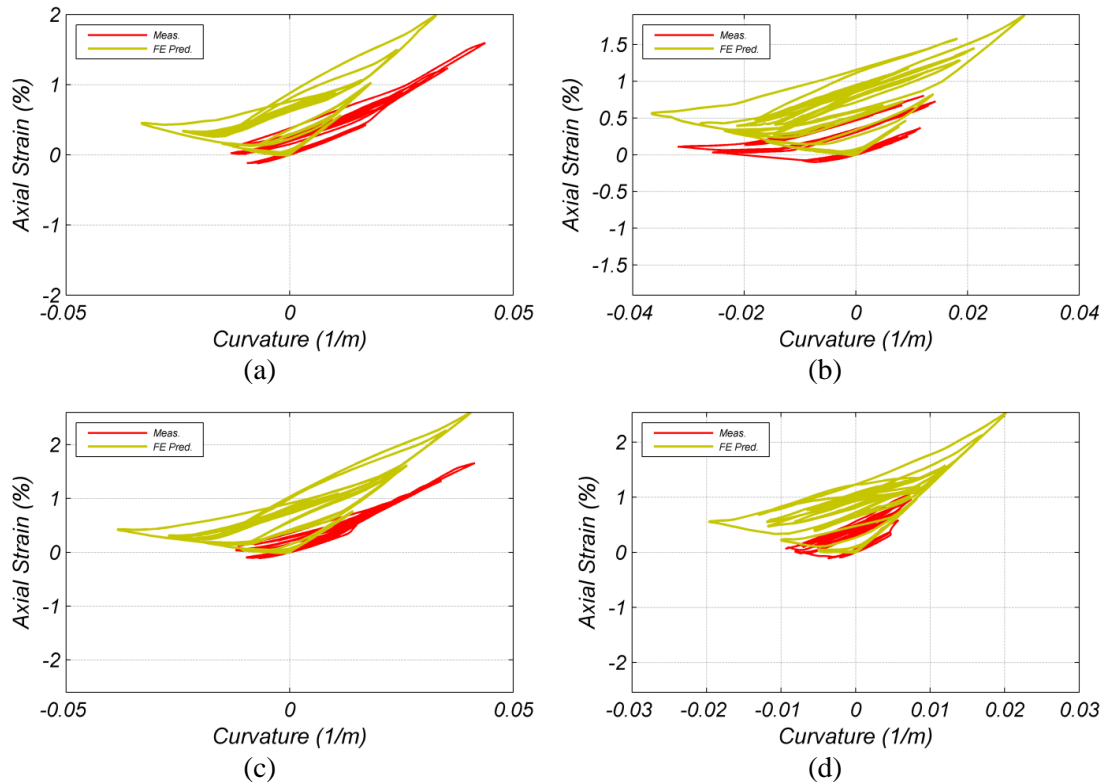


Figure 3.16: Comparison of FE predicted and measured averaged axial strain vs. curvature for FB-5: *DEN67* at the (a) west end of the second floor north beam, (b) east end of the second floor north beam, (c) west end of the third floor north beam, (d) east end of the third floor north beam.

The south, south-east, north, and north-east columns were instrumented at their base with a pair of string potentiometers located on interior faces to measure the axial elongation and averaged curvature of the column bases over the sensor length (See Figures 3.13(a) and 3.13(c)). The procedure used to extract the axial deformation and curvature, from both FE model and experimental measurement, is similar to the one employed for the beams. Figure 3.17 compares the FE predicted and measured averaged axial deformation time history at the base of the four instrumented columns. Likewise, Figure 3.18 compares the FE predicted and measured averaged curvature time histories. The FE predicted and measured responses are in good agreement,

especially given the local nature of these response quantities. As observed for the case of beams, the peak axial strain and curvature responses of column are also overpredicted by the FE model.

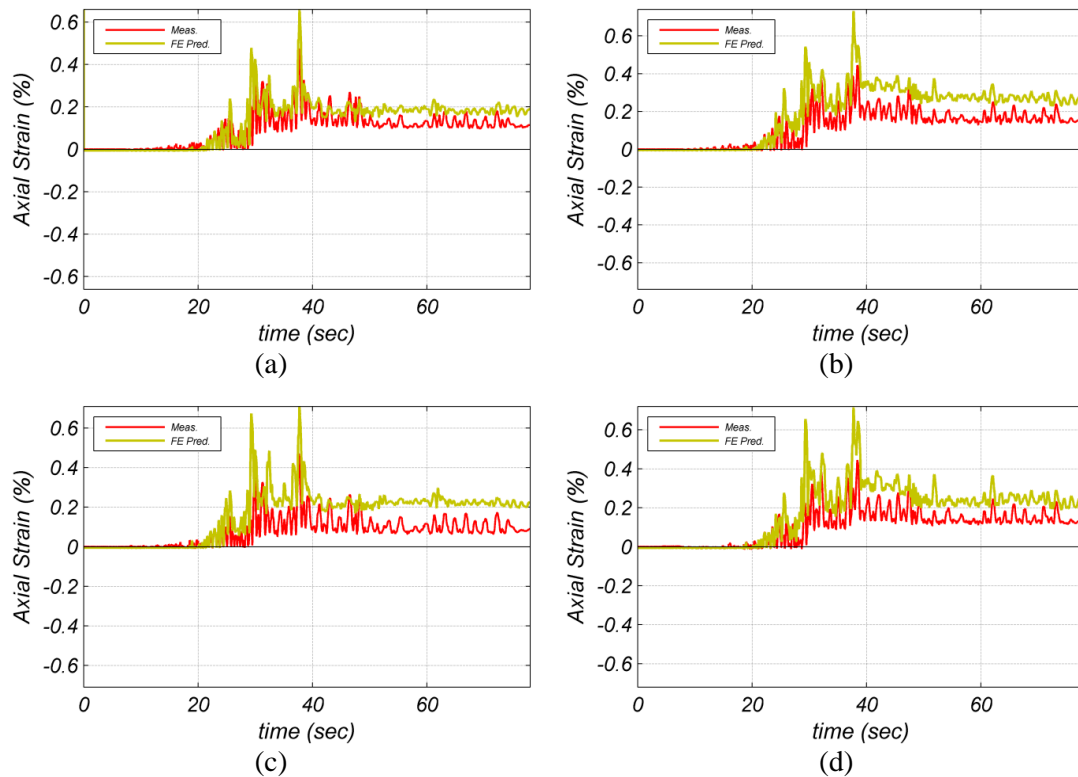


Figure 3.17: Comparison of FE predicted and measured averaged axial strain time histories for FB-5: DEN67 at the (a) base of north middle column, (b) base of north east column, (c) base of south middle column, (d) base of south east column.

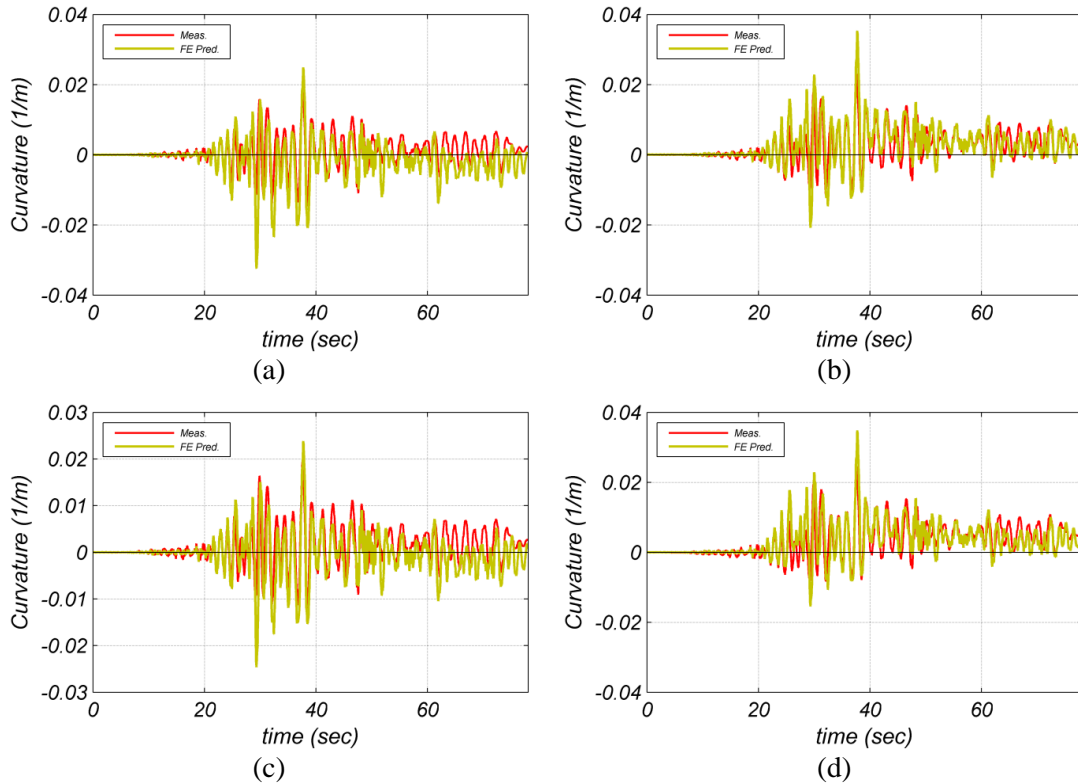


Figure 3.18: Comparison of FE predicted and measured averaged curvature time histories for FB-5: *DEN67* at the (a) base of north middle column, (b) base of north east column, (c) base of south middle column, (d) base of south east column.

#### 3.4.4. Strain gauge and crack level response

Selected longitudinal reinforcing bars placed in the north frame beams were instrumented at different locations with strain gauges. Figure 3.13(a) shows the location of one of the strain gauges installed on the outer longitudinal rebar at the east corner of the third floor beam, which is near the plastic hinge region of that beam. This strain gauge is shown in Figure 3.19(a). The strain time history measured through this strain gauge during the FB-5: *DEN67* test is compared with the corresponding FE prediction in Figure 3.19(b). The FE predicted axial strain at the strain gauge location

is derived by interpolating the axial strain at the integration points of the beam PH-element. Figure 3.19(b) shows that the FE model predicts well both the rebar strain time history and the residual strain at the end of the seismic test.

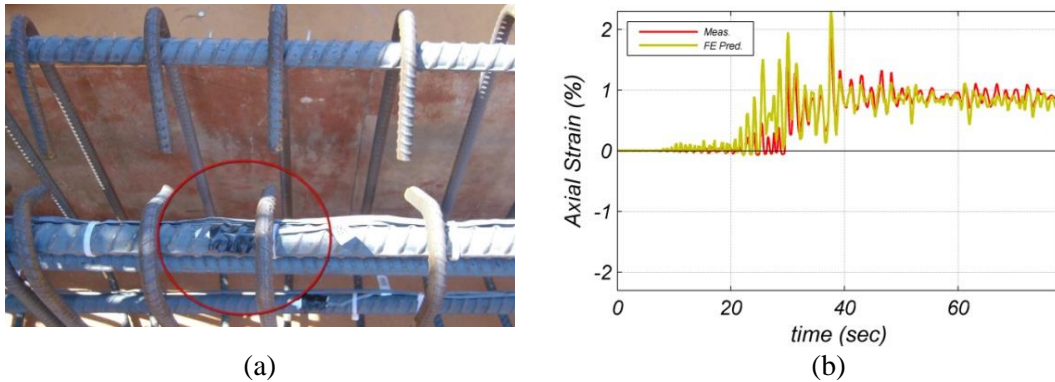


Figure 3.19: (a) Strain gauge installed on the outer rebar at east end of the 3<sup>rd</sup> floor north frame beam; (b) comparison of the FE predicted and measured longitudinal rebar strain for FB-5: *DEN67*.

During the inspection phases, following each seismic test, the propagation of the cracks across each slab was carefully marked and documented. This information was integrated into schematic crack maps such as the one shown in Figure 3.20(a) for the top surface of the second floor slab after the FB-5: *DEN67* test. To obtain the FE predicted crack maps, the computed maximum crack opening at the top surface of the slab shell elements is extracted from the integration points located at the top surface of the slab shell elements, and plotted as a continuous contour map over the slab as shown in Figure 3.20(b). The crack opening is the product of crack strain averaged over the surface integration points and the crack bandwidth of the element. The correlation between the FE predicted and the observed crack maps is excellent, as can

be observed in Figures 3.20(a) and (b). Figures 3.20(c) to 3.20(e) show the actual damage state of second floor slab at different locations after FB-5: *DEN67*.

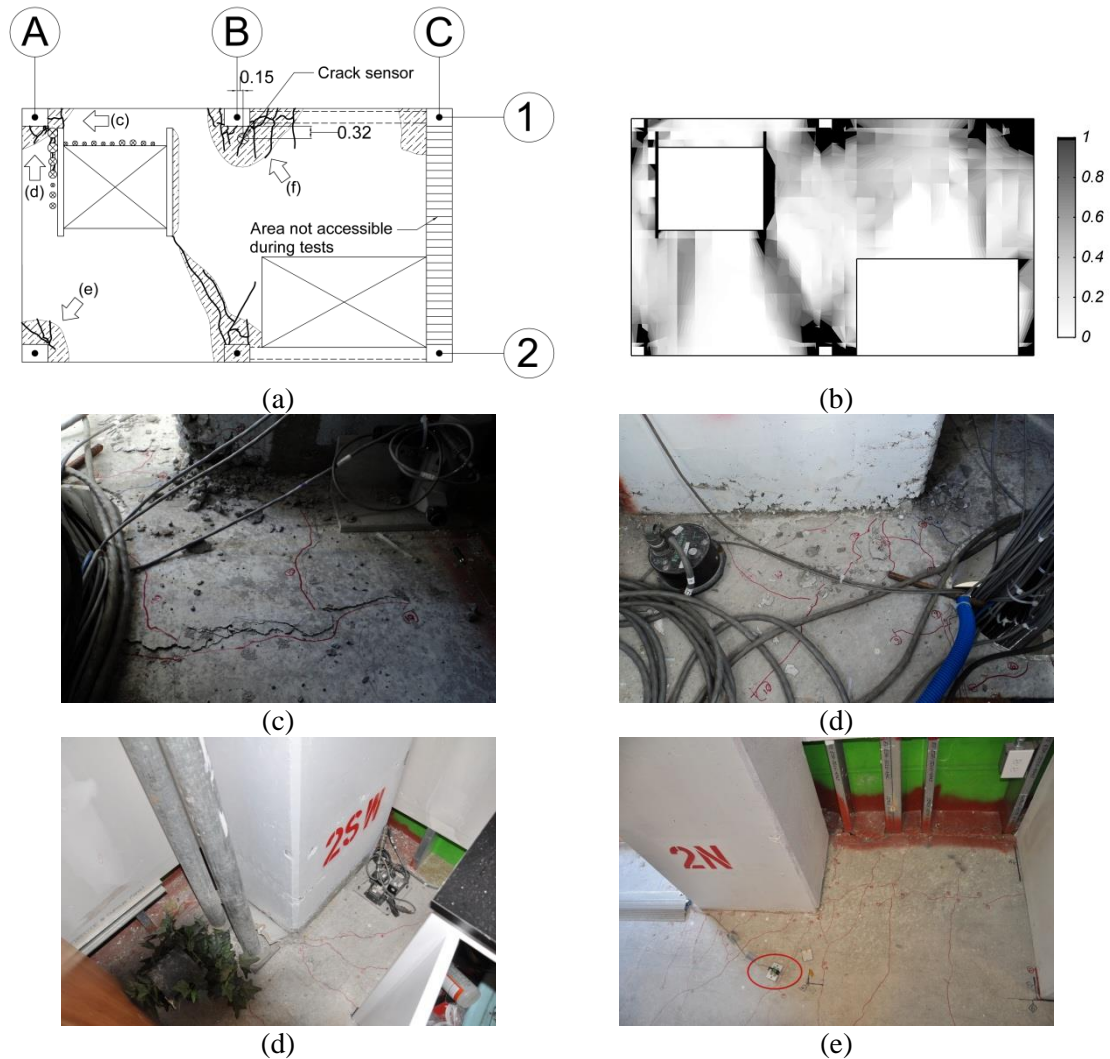


Figure 3.20: Comparison of FE predicted and observed cracks on the top surface of the second floor slab after FB-5: *DEN67*: (a) experimental observation; (b) maximum crack opening based on FE prediction (units are in mm); damaged state of the second floor slab after FB-5: *DEN67* at (c) north-west corner (observed from east side), (d) north-west corner (observed from south side), (e) south-west corner, and (f) around north-middle column.

Before the FB-5: *DEN67* test, a sensitive linear potentiometer was installed on the second floor slab across one of the major cracks near the north-middle column to measure its opening during FB-5: *DEN67*. Figure 3.20(a) shows the crack and the

sensor locations on the crack map, while Figure 3.21(a) shows the sensor, which is also visible in Figure 3.20(e) where it is distinguished by a red circle. The crack opening time history measured through this sensor is compared with its FE predicted counterpart in Figure 3.21(b). The FE predicted crack opening time history is obtained by averaging crack strain over the top surface integration points of the shell element in which the sensor is located. The averaged crack strain is then multiplied by the crack bandwidth of the element to result the crack opening. Considering the various sources of approximation and uncertainties involved in this local scale of comparison, the obtained correlation is remarkable.

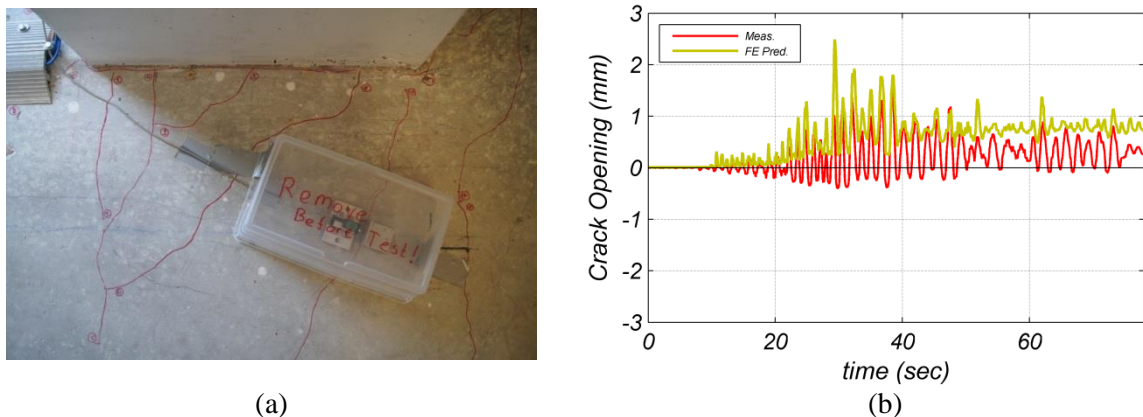


Figure 3.21: (a) Potentiometer (protected by plastic cover) installed prior to FB-5: *DEN67* across a crack on the second floor concrete slab; (b) comparison of FE predicted and measured crack opening time history for FB-5: *DEN67*.

### 3.5. Sequential versus individual nonlinear time history analysis

As mentioned earlier, two types of analysis were performed for pre-test simulation of the building specimen, namely a sequential analysis and a set of

individual analyses. The sequential analysis accounts for damage accumulation in the building structure during the successive earthquake tests and is computationally more demanding than the set of individual analyses starting from an initial undamaged state for each earthquake. To investigate the effect of damage accumulation in the FE model, Figures 3.22(a) to 3.22(c) compare the normalized PFAA predictions obtained from the sequential and individual analyses for FB-3: *ICA50*, FB-4: *ICA100*, and FB-5: *DEN67*. At each floor level of the building, the peak positive and negative values of the predicted FAA are normalized by the peak positive and negative values of the measured FAA, respectively. Similarly, Figures 3.22(d) to 3.22(f) show the normalized PIDRs obtained from the sequential and individual analyses for FB-3: *ICA50*, FB-4: *ICA100*, and FB-5: *DEN67*. The predicted PIDRs are also normalized by the measured PIDRs in the positive and negative directions, separately. It is observed that there are relatively small differences between the two types of the analysis results for the PFAA prediction for all three tests. In the case of PIDR, there are no differences for FB-5: *DEN67*; however, the sequential analysis improves the PIDR predictions for FB-3: *ICA50*.



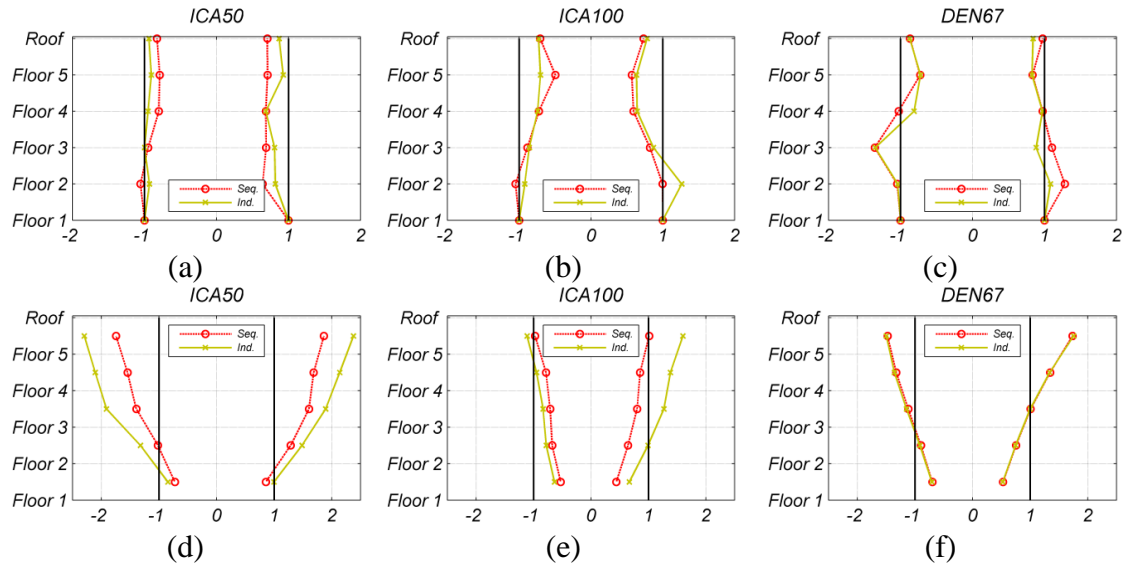


Figure 3.22: Comparison of the building response prediction results obtained using the sequential and individual analyses; PFAA normalized by the corresponding measured PFAA for: (a) FB-3: *ICA50*, (b) FB-4: *ICA100*, and (c) FB-5: *DEN67*; PIDR normalized by the corresponding measured PIDR for: (d) FB-3: *ICA50*, (e) FB-4: *ICA100*, and (f) FB-5: *DEN67*.

### 3.6. Conclusions

Details of the 3D nonlinear FE model utilized for the pre-test numerical simulation of a full scale five-story RC building specimen tested on the NEES-UCSD shake table is described. To investigate the likely shortcomings of the employed FE modeling technique, the selected FE predicted response parameters are compared with the experimental measurements at different response levels varying from global structural level to local sensor and crack levels.

The FE simulation generally better predicts the peak FAAs than the peak IDRs. The peak FAAs are better predicted at upper floor levels for low intensity tests and at lower floor levels for high intensity tests. For low intensity tests, the FE simulation mostly over-predicts the peak IDRs, more in the middle stories of the building, whiles

for high intensity tests it under-predicts the peak IDRs in the lower stories and over-predicts them in the upper stories. The time histories of the measured response time histories have higher frequency content compared to the FE predictions for low intensity tests. The difference in the dominant frequency reduces for FB-5: *DEN67* compared to FB-1: *CNP100*. The measured TSS vs. IDR at story levels show remarkable stiffer response compare to the predicted results at all the stories except the first one, in which the stiffness difference is insignificant. As the test motion intensifies, the stiffness agreement of the story-level responses improves between the FE predictions and experimental measurements. The measured responses at lower stories show higher level of nonlinearity and displacement demand than the FE predicted responses for FB-5: *DEN67*. Moreover, The FE simulation underpredicts the dissipated hysteretic energy at the lower story levels and slightly overpredicts it at upper story levels. The measured beam-ends and column-bases axial deformation and averaged curvature responses show good correlation with the FE predictions. The FE simulation predicts the measured strain of the beam longitudinal reinforcement well. The predicted crack map for floor slab confirms remarkably well with the observed damage state of the slab. The crack opening time history for a specific crack in the second floor level is also predicted reasonably well by the FE simulation. Four different causes can explain the probable sources of discrepancies between the FE prediction and experimental measurement:

- (1) Kinematic interaction between the structural and nonstructural systems, which are not considered in the current FE simulation. This interaction contributes in

the lateral energy dissipation mechanism of the building, increases the measured stiffness of the building, affects the dominant frequency contents of the response time histories, and reduces the measured floor displacement demands compared to the FE predictions. As the intensity of the earthquake increases, the nonstructural components start to get damaged, undergo stiffness and strength degradation, and their kinematic interaction with the structural system diminishes.

(2) The material constitutive laws used in the developed FE model have some imprecisions. Moreover, the adopted FE formulation implies restrictive kinematic assumptions which can result in inaccurate hysteretic response simulation of the structural components. More specifically, the pinching hysteretic behavior of the RC flexural members cannot be captured correctly using the employed FE modeling technique. Therefore, in highly nonlinear regions, the FE model of the test structure has higher energy dissipation capacity for flexural members than the actual specimen. As a consequence, for the high intensity tests, the FE model under-predicts the floor displacement demands of the building at the lower floors.

(3) The damping is modeled using proportional Rayleigh damping model based on constant damping parameters in the employed FE model. The adequacy of the classical Rayleigh damping model for nonlinear time history analysis of structures is questionable. Moreover, the selection of the damping ratios and the implication of the proportional Rayleigh damping model are open problems that require further research.

(4) Uncertainties involved in various stages of parameter selection and modeling are another cause of discrepancies, for example the uncertainties included in

the estimation of the inertia models and uncertainties involved in the selected material parameters such as steel hardening parameters to name only two.

Considering the real-life conditions and configurations of the experimental program, the comparison studies in this chapter provide realistic metrics to evaluate and validate the accuracy of an advanced nonlinear FE simulation technique for RC building structures. The drawn conclusions in this chapter pave the way for future research to improve the fidelity of the nonlinear FE simulations for RC structures. Future research is underway by the Authors to address the various possible sources of discrepancies and modeling uncertainties discussed in this chapter.

## **Acknowledgments**

Partial support for this work was provided by the NSF-NEESR program under grant number CMMI-0936505 with Professor Tara C. Hutchinson as the principal investigator, the Englekirk structural engineering center board of advisors. This Chapter is a close reprint of the material as it was prepared for submission for publication in ASCE Journal of Structural Engineering. The dissertation author is the primary investigator and author of this material. Rodrigo Astroza, Joel P. Conte, Jose I. Restrepo, and Tara C. Hutchinson are co-authors.

## **Appendix 3.I: Data Processing**

### **3.I.1. Data cleansing procedure**

The acceleration time history data obtained from the accelerometer sensors have been processed to remove the artificial noise effects in the recorded signal. The data cleansing procedure involved the following steps:

- a. Obtain the acceleration time history from raw data files and apply the sensor correction factors.
- b. Eliminate linear trends in the acceleration time history by removing the best straight line fit from the data.
- c. Taper the first and last 1 second of the acceleration time history with a half-cosine function.
- d. Zero-pad the acceleration time history at the beginning and the end with 42.8 seconds of zeros (following the procedure suggested by [15]).
- e. Filter the zero-padded acceleration time history with two passes of a 4<sup>th</sup> order Butterworth bandpass filter with corner frequencies of [0.07, 25] Hz.

### **3.I.2. Evaluating the average floor absolute accelerations**

Four tri-axial accelerometers were installed at the four corners of each floor slab. The recorded data from the accelerometers were averaged to obtain the mean translational and rotational accelerations at the center of geometry of the slab. Figure

3.23 shows the schematic plan view and location of the four accelerometers. In this figure,  $A_x$  and  $A_y$  denote the translational acceleration at the geometric center of the slab in  $x$ - and  $y$ -directions, respectively, and  $A_\theta = \ddot{\theta}$  is the rotational acceleration of the slab.  $a_x$  and  $a_y$  denote the two translational components of the acceleration data recorded by a sensor. Assuming a rigid diaphragm condition for the floor slab, the translational accelerations at the sensor location can be related to the translational and rotational accelerations at the geometric center of the slab as follows.

$$a_{x,i} = A_{x,i} - r\dot{\theta}_i^2 \cos \alpha - r\ddot{\theta}_i \sin \alpha \quad (3.5)$$

$$a_{y,i} = A_{y,i} - r\dot{\theta}_i^2 \sin \alpha + r\ddot{\theta}_i \cos \alpha \quad (3.6)$$

where the subscript  $i$  denote the time step. Using a first-order integration rule, the rotational velocity at time step  $i$ ,  $\dot{\theta}_i$ , can be related to the rotational acceleration at time step  $i$ ,  $\ddot{\theta}_i$ , and the rotational velocity and acceleration at previous time step:

$$\begin{aligned} \dot{\theta}_i &= \dot{\theta}_{i-1} + \ddot{\theta}_{i-1} \Delta t + \frac{\ddot{\theta}_i - \ddot{\theta}_{i-1}}{2} \Delta t \\ \Rightarrow \dot{\theta}_i &= \underbrace{\dot{\theta}_{i-1} + \ddot{\theta}_{i-1} \frac{\Delta t}{2}}_{\text{call } \lambda_{i-1}} + \ddot{\theta}_i \frac{\Delta t}{2} \\ \Rightarrow \dot{\theta}_i &= \lambda_{i-1} + \ddot{\theta}_i \frac{\Delta t}{2} \end{aligned}$$

where  $\Delta t$  is the time step size. Therefore,

$$a_{x,i} = A_{x,i} - r \cos \alpha \left( \frac{\Delta t}{2} \right)^2 \ddot{\theta}_i^2 - r \lambda_{i-1} \cos \alpha \Delta t + \sin \alpha \ddot{\theta}_i - r \lambda_{i-1}^2 \cos \alpha \quad (3.7)$$

$$a_{y,i} = A_{y,i} - r \sin \alpha \left( \frac{\Delta t}{2} \right)^2 \ddot{\theta}_i^2 - r \lambda_{i-1} \sin \alpha \Delta t - \cos \alpha \ddot{\theta}_i - r \lambda_{i-1}^2 \sin \alpha \quad (3.8)$$

The same equations can be written for the other three sensors, resulting in 8 equations and 3 unknowns ( $A_x$ ,  $A_y$ , and  $A_\theta = \ddot{\theta}$ ) at each time step. The system of equations is recursively solved in time using a nonlinear least-squares method.

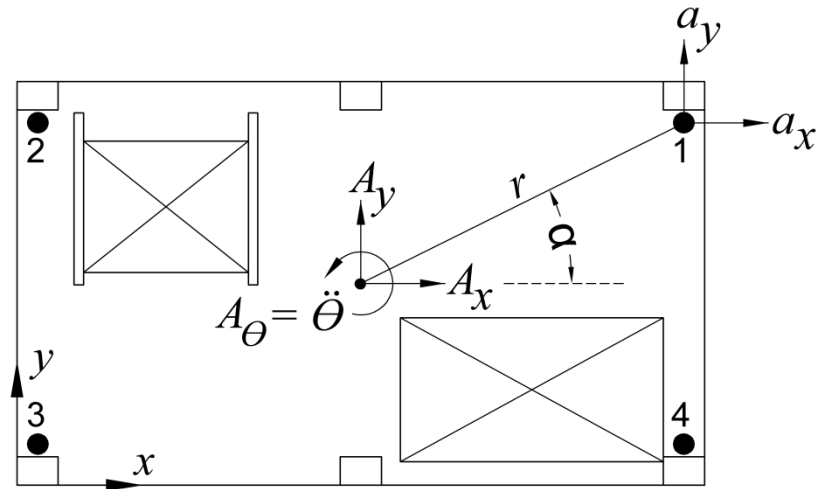


Figure 3.23: Schematic plan view and location of accelerometers.

## **Appendix 3.II: Material Parameters**

### **3.II.1. Concrete material parameters**

37 different sets of concrete material model were defined in this study to specify the variations in the concrete material properties and confinement conditions of different structural components and members. Table 3.4 lists the parameters of these 37 concrete material models. The compressive strength of concrete was obtained from standard compressive tests performed on cylindrical specimens sampled during construction. Most of the compressive tests were performed on 18-days old specimens. Table 3.5 shows a sample spreadsheet used to compute concrete material parameters for 1st floor columns.



Table 3.4: Parameters selected for different concrete material models.

Set #	Member / Component	$f'_c$ (18 days test) (ksi)	$f'_c$ (MPa)	$\epsilon_{cc}$	$f'_{ce}$ (MPa)	$\epsilon_{cu}$	$L_{pm}$ (m)	$E_c$ (MPa)	$G_c$ (N/m)	$f'_t$ (MPa)	$G_f$ (N/m)
1	Columns, First Floor	5.925	40.85	0.0036	56.79	0.0203	0.330	26467.43	209067.46	2.11	124.78
2	Walls, 1st Floor	5.925	40.85	0.0022	40.85	0.0040	0.076	30947.91	3735.44	2.11	117.46
3	Slab, 2nd Floor	5.233	36.08	0.0035	47.78	0.0152	0.102	22949.09	37961.78	1.98	117.46
4	Slab, 2nd Floor	5.233	36.08	0.0035	47.78	0.0152	0.102	22949.09	37961.78	1.98	117.46
5	Slab, 2nd Floor	5.233	36.08	0.0021	36.08	0.0040	0.102	28634.99	4643.27	1.98	117.46
6	Beam, 2nd Floor	5.233	36.08	0.0035	48.66	0.0184	0.356	23507.25	172458.18	1.99	117.46
7	Columns, 2nd Floor	5.7515	39.66	0.0037	55.74	0.0204	0.330	25109.46	204923.90	1.98	117.12
8	Columns, 2nd Floor	5.7515	39.66	0.0037	55.74	0.0204	0.330	25109.46	204923.90	1.98	117.12
9	Walls, 2nd Floor	5.7515	39.66	0.0022	39.66	0.0040	0.076	30041.67	3626.05	2.08	117.12
10	Slab, 3rd Floor	5.34	36.82	0.0035	47.48	0.0152	0.102	22609.52	37626.95	2.00	117.18
11	Slab, 3rd Floor	5.34	36.82	0.0035	47.48	0.0152	0.102	22609.52	37626.95	2.00	117.18
12	Slab, 3rd Floor	5.34	36.82	0.0021	36.82	0.0040	0.102	29220.50	4738.21	2.00	117.18
13	Beam, 3rd Floor	5.34	36.82	0.0035	49.51	0.0183	0.356	23917.87	174296.98	1.98	117.46
14	Columns, 3rd Floor	6.015	41.47	0.0036	57.48	0.0203	0.330	26912.17	211831.85	2.13	125.72
15	Columns, 3rd Floor	6.015	41.47	0.0036	57.48	0.0203	0.330	26912.17	211831.85	2.13	125.72
16	Walls, 3rd Floor	6.015	41.47	0.0022	41.47	0.0040	0.076	31418.00	3792.18	2.13	125.72
17	Slab, 4th Floor	5.41	37.30	0.0034	49.48	0.0150	0.102	24252.45	38872.84	2.02	119.23
18	Slab, 4th Floor	5.41	37.30	0.0034	49.48	0.0150	0.102	24252.45	38872.84	2.02	119.23
19	Slab, 4th Floor	5.41	37.30	0.0022	37.30	0.0040	0.102	28257.92	4547.67	2.02	119.23
20	Lateral Beam, 4th Floor	5.41	37.30	0.0034	49.48	0.0150	0.102	24252.45	38872.84	2.02	119.23
21	Beam, 4th Floor	5.41	37.30	0.0034	50.23	0.0182	0.356	24621.08	176225.78	2.02	119.23
22	Columns, 4th Floor	6.4845	44.71	0.0035	60.67	0.0209	0.330	28892.29	232400.07	2.21	130.54
23	Columns, 4th Floor	6.4845	44.71	0.0035	60.67	0.0209	0.330	28892.29	232400.07	2.21	130.54
24	Walls, 4th Floor	6.4845	44.71	0.0022	44.71	0.0040	0.076	33870.33	4088.18	2.21	130.54
25	Slab, 5th Floor	5.927	40.87	0.0034	53.54	0.0147	0.102	26243.63	40976.51	2.11	124.80
26	Slab, 5th Floor	5.927	40.87	0.0034	53.54	0.0147	0.102	26243.63	40976.51	2.11	124.80
27	Slab, 5th Floor	5.927	40.87	0.0022	40.87	0.0040	0.102	30958.35	4982.26	2.11	124.80
28	Lateral Beam, 5th Floor	5.927	40.87	0.0034	53.54	0.0147	0.102	26243.63	40976.51	2.11	124.80
29	Beam, 5th Floor	5.927	40.87	0.0034	54.35	0.0179	0.356	26643.14	186833.19	2.11	124.80
30	Columns, 5th Floor	7.3265	50.51	0.0034	66.91	0.0217	0.330	32797.55	269530.84	2.35	138.76
31	Columns, 5th Floor	7.3265	50.51	0.0034	66.91	0.0217	0.330	32797.55	269530.84	2.35	138.76
32	Walls, 5th Floor	7.3265	50.51	0.0024	50.51	0.0040	0.076	35079.30	4105.79	2.35	138.76
33	Slab, 6th Floor	6.39	44.06	0.0033	56.71	0.0145	0.102	28640.40	43019.44	2.19	129.59
34	Slab, 6th Floor	6.39	44.06	0.0033	56.71	0.0145	0.102	28640.40	43019.44	2.19	129.59

Table 3.5: Details of the concrete material parameters evaluation for 1<sup>st</sup> floor columns.

Properties of Concrete Material - Columns, 1st Floor

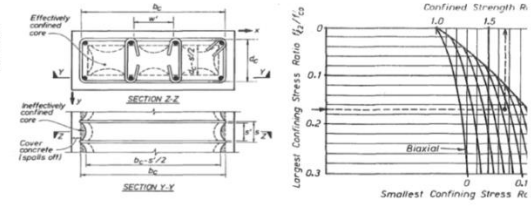
Units m, MN

$f'_{co}$ =	40.85		
$E_c$ =	30039.5822	: traditional formula	=> Use this for subsequent calculations, $E_c$ = 30039.58222
$E_c$ =	32313.3027	ACI 318	$\rho_{con}$ = 2400
$E_s$ =	210000		
$\nu_{con}$ =	0.2		
tesile strength, ACI	$f_t$ = 2.10916216		=> Use this for subsequent calculations, $f_t$ = 2.10916
le strength, from split cylinder test	$f_t$ = 3.45852698		

Estimating Confining Pressure

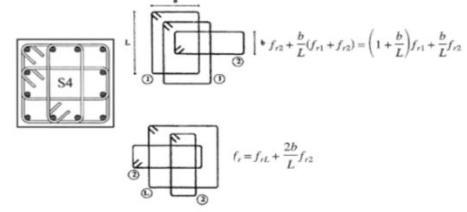
Mander-Priestley-Park

clear spacing between bars	$\lambda w_{cl}^2$ =	0.271	all around
	B =	0.6604	=> $b_c$ = 0.5969
	D =	0.4572	=> $d_c$ = 0.3937
to the outer edge of stirrups	cover =	0.0254	=> $s'$ = 0.0889
stirrup diameter	$d_{stirrup}$ =	0.0127	
longitudinal bar diameter	$d_{long}$ =	0.028575	
stirrup spacing	s =	0.1016	
Long. Reinforcement area	$\lambda A_i$ =	0.00513041	
Stirrup working for x conf.	Asx =	0.00038003	section along y section
Stirrup working for y conf.	Asy =	0.00050671	section along x section
stirrup yield strength	$f_{yh}$ =	414	
	$\rho_{co}$ =	0.02183159	
	ke =	0.67803665	
	$\rho_s$ =	0.00950078	
	$\rho_s'$ =	0.0083553	
confining stress	$f'_{lx}$ =	2.66693829	
confining stress	$f'_{ly}$ =	2.34539254	



Braga-Gigliotti-Laterza (2006)

width of area	b =	0.2032	(d > b)
height of area	d =	0.2032	
Area of single stirrup bar	As =	0.00012668	
Moment of Inertia of stirrup bar	Is =	1.277E-09	
	B <sub>o</sub> =	29524.8009	
	B <sub>d</sub> =	29524.8009	
	k <sub>d</sub> =	0.94742466	
for specified area	$f_{t,rec}$ =	288.748062	
calculate and input manually	$f_{t,total}$ =	288.75	
confining stress	$f'_{lx}$ =	-1.03257745	



=> Use this confining stresses for subsequent calculations  $f'_{lx}$  = -2.667  
 $f'_{ly}$  = -2.345

Mander-Priestley-Park

$f'_{lx}/f'_{co}$ =	-6.53E-02
$f'_{ly}/f'_{co}$ =	-0.05741475
Read factor from curve:	1.4
$f'_{cc}$ =	57.19
$\epsilon_{cc}$ =	0.006

<= if the confining stress in two direction are equal 1.39286

Paulay-Priestley

Steel strain at fu	$\epsilon_{sm}$ =	0.05
	$\epsilon_{cs}$ =	0.01304825

Saatcioglu-Razvi (1992)

k1 =	5.67E+00
$f'_{cc}$ =	55.9739616

Attrd-Setunge (1997)

$\epsilon_0$ =	0.00229145
$\epsilon_{cc}$ =	0.00446797
k =	0.57585619
$f'_{cc}$ =	65.403348

Modified Kent-Park (1971)

k =	1.18096496
$\epsilon_{cc}$ =	0.00236193
$f'_{cc}$ =	48.2424187

Scott-Park-Priestley (1982)

$\epsilon_{cs}$ =	0.02617726
-------------------	------------

Selby-Vecchio (1996)

Hsieh-Ting-chen Model (1979)	$f'_{cc}/f'_e$ =	1.3986
	$f'_{cc}$ =	57.13281
	n =	4.16075353
	k =	1.59149694
	$\epsilon_0$ =	0.00179011
	K <sub>e</sub> =	2.17761858
	$\epsilon_{cc}$ =	0.00389818

Restrepo

$\epsilon_{cs}$ =	0.0218193
-------------------	-----------

Final Results	
$f'_{cc}$ =	56.78850766
$\epsilon_{cc}$ =	0.003576026
$\epsilon_0$ =	0.002040778
$\epsilon_{cs}$ =	2.03E-02

### 3.II.2. Steel material parameters

Different sets of steel material model were defined in this study to specify the variations in the reinforcing steel material properties. Table 3.6 lists the parameters of different steel material models. The yield strength and elastic modulus of steel rebars were obtained using standard tensile (universal) tests performed on rebar coupons.

Table 3.6: Parameters selected for steel material models.

Rebar Size - Location	Test Results		Material Model			
	$\sigma_y$ (ksi)	$E$ (ksi)	$\sigma_y$ (MPa)	$E$ (MPa)	$b$	$\epsilon_y$
#3 - Slab	75.20	30615.67	518.48	211086.57	0.0300	0.0025
#4	68.50	30440.33	472.29	209877.69	0.0129	0.0023
#5 - Slab	73.50	29019.50	506.76	200081.44	0.0246	0.0025
#6 - Column and Slab	71.00	29365.00	489.53	202463.56	0.0267	0.0024
#7 - Beam	71.67	27454.33	494.12	189290.05	0.0147	0.0026
#8	71.67	27454.33	494.12	189290.05	0.0147	0.0026
#9 - Col and Slab	71.67	27454.33	494.12	189290.05	0.0147	0.0026
#7 HSS - Beam	124.67	23606.67	859.54	162761.45	0.0576	0.0053

## References

- [1] Task Group 4.4, "Practitioners' Guide to Finite Element Modelling of Reinforced Concrete Structures," Lausanne, Switzerland, FIB Bulletin 45: State-of-art Report 2008.
- [2] D. A. Foutch, S. C. Goel, and C. W. Roeder, "Seismic Testing of Full-Scale Steel Building-Part I," *ASCE Journal of Structural Engineering*, vol. 113, no. 11, p. 2111-2129, 1987.
- [3] P. B. Shing, M. Nakashima, and O. S. Bursi, "Application of Pseudodynamic Test Method to Structural Research," *Earthquake Spectra*, vol. 12, no. 1, p. 29-56, 1996.
- [4] T. Matsumori, K. Shirai, and T. Kabeyasawa, "Simulated Earthquake Test on a Full-Scale Six-Story Reinforced Concrete Building at E-Defense, Part 1: Outline of Test Program," in *Proceedings of The Second NEES/E-Defense Workshop on Collapse Simulation of Reinforced Concrete building Structures*, Miki, Japan, 2006.
- [5] K. Kasai, Y. Ooki, S. Motoyui, T. Takeuchi, and E. Sato, "E-Defense Tests on Full-Scale Steel Buildings: Part 1 – Experiments Using Dampers or Isolators," in *ASCE Structures Congress*, Long Beach, CA, USA, May 16-19, 2007.
- [6] S. Yamada, K. Suita, M. Tada, K. Kasai, Y. Matsuoka, and Y. Shimada, "Collapse Experiment on 4-Story Steel Moment Frame: Part 1 Outline of Test Results," 14th World Conference on Earthquake Engineering (14WCEE), October 12-17, Beijing, China, 2008.
- [7] M. Panagiotou, J. I. Restrepo, and J. P. Conte, "Shake-Table Test of a Full-Scale 7-Story Building Slice. Phase I: Rectangular Wall," *ASCE Journal of Structural Engineering*, vol. 137, no. 6, p. 691–704, 2011.
- [8] N. D. Dao, K. L. Ryan, E. Sato, T. Okazaki, S. A. Mahin, A. E. Zahgi, K. Kajiwara, and T. Matsumori, "Experimental Evaluation of an Innovative Isolation System for a Lightweight Steel Moment Frame Building at E-Defense," *Proceedings of the ASCE Structures Congress 2011*, March 29-31, Chicago, IL, 2011.
- [9] E. Sato, S. Furukawa, A. Kakehi, and M. Nakashima, "Full-scale Shaking Table Test for Examination of Safety and Functionality of Base-isolated Medical Facilities," *Earthquake Engineering and Structural Dynamics*, vol. 40, p. 1435–1453, 2011.
- [10] M. Chen, E. Pantoli, X. Wang, R. Astroza, H. Ebrahimian, S. Mintz, T. Hutchinson, J. Conte, J. Restrepo, B. Meacham, J. Kim, and H. Park, "BNCS

Report #1: Full-Scale Structural and Nonstructural Building System Performance During Earthquakes and Post-Earthquake Fire - Specimen Design, Construction, and Test Protocol," Structural Systems Research Project, Report No. SSRP-13/09, Department of Structural Engineering, University of California, San Diego, La Jolla, CA, 2013.

- [11] M. C. Chen, E. Pantoli, X. Wang, R. Astroza, H. Ebrahimian, T. C. Hutchinson, J. P. Conte, J. I. Restrepo, C. Marin, K. D. Walsh, R. E. Bachman, M. S. Hoehler, R. Englekirk, and M. Faghihi, "Full-Scale Structural and Nonstructural Building System Performance during Earthquakes: Part I – Specimen Description, Test Protocol and Structural Response," *Earthquake Spectra*, DOI: 10.1193/012414EQS016M, 2014.
- [12] E. Pantoli, M. C. Chen, X. Wang, R. Astroza, H. Ebrahimian, T. C. Hutchinson, J. P. Conte, J. I. Restrepo, C. Marin, K. D. Walsh, R. E. Bachman, M. S. Hoehler, R. Englekirk, and M. Faghihi, "Full-Scale Structural and Nonstructural Building System Performance during Earthquakes: Part II – NCS Damage States," *Earthquake Spectra*, DOI: 10.1193/012414EQS017M, 2014.
- [13] S. D. Nakaki, R. E. Englekirk, and J. L. Plaehn, "Ductile Connectors for a Precast Concrete Frame," *PCI Journal*, vol. 39, no. 5, p. 46-59, September-October 1994.
- [14] American Concrete Institute (ACI) Committee 318, "Building Code Requirements for Structural Concrete and Commentary," Farmington Hills, MI, ACI 318-08 2008.
- [15] David M. Boore, "On Pads and Filters: Processing Strong-Motion Data," *Bulletin of the Seismological Society of America*, vol. 95, no. 2, p. 745-750, 2005.
- [16] TNO DIANA BV, "DIANA Finite Element Analysis User's Manual, Release 9.4.4," Delft, The Netherlands, 2011.
- [17] H. W. Reinhardt, "Fracture Mechanics of an Elastic Softening Material Like Concrete," *HERON*, vol. 29, no. 2, p. 1-37, 1984.
- [18] Z. P. Bazant, "Instability, Ductility, and Size Effect in Strain-Softening Concrete," *ASCE Journal of the Engineering Mechanics Division*, vol. 102, no. 2, p. 331-344, 1976.
- [19] Z. P. Bazant and B.-H. Oh, "Microplane Model for Fracture Analysis of Concrete Structures," in *Symposium on the Interaction of Non-Nuclear Munitions with Structures*, U.S. Air Force Academy, Colorado Springs, 1983.
- [20] R. K. Navalurkar, C. T. Hsu, S. K. Kim, and M. Wecharatana, "True Fracture Energy of Concrete," *ACI Materials Journal*, vol. 96, no. 2, p. 213-225, 1999.
- [21] J. B. Mander, M. J. N. Priestley, and R. Park, "Theoretical Stress-Strain Model for Confined Concrete," *Journal of Structural Engineering (ASCE)*, vol. 114, no. 8, p.

1804-1826, 1988.

- [22] R. Park, M. J. N. Priestley, and W. D. Gill, "Ductility of Square-Confined Concrete Columns," *Journal of Structural Division (ASCE)*, vol. 108, no. 4, p. 929-950, 1982.
- [23] B. D. Scott, R. Park, and M. J. N. Priestley, "Stress-Strain Behavior of Concrete Confined by Overlapping Hoops at Low and High Strain Rates," *American Concrete Institute (ACI)*, vol. 79, no. 1, p. 13-27, 1982.
- [24] K. J. Willam, B. Hurlbut, and S. Sture, "Experimental and Constitutive Aspects of Concrete Failure," in *Finite Element Analysis of Reinforced Concrete Structures (Edited by C. Meyer and H. Okamura)*. New York: ASCE, 1986, p. 226-245.
- [25] F. J. Vecchio and M. P. Collins, "The Modified Compression Field Theory for Reinforced Concrete Elements Subjected to Shear," *ACI Journal*, vol. 83, no. 2, p. 219-231, 1986.
- [26] TNO DIANA, "DIANA User's Manual, Material Library," Delft, The Netherlands, 2010.
- [27] F. J. Vecchio and M. P. Collins, "Compression Response of Cracked Reinforced Concrete," *ASCE Journal of Structural Engineering*, vol. 119, no. 12, p. 3590-3610, 1993.
- [28] R. de Borst, *Computational Methods in Non-Linear Solid Mechanics*. Delft, The Netherlands: TNO Building and Construction Research, Department of Civil Engineering, Delft University of Technology, 1993.
- [29] F. C. Filippou, E. P. Popov, and V. V. Bertero, "Effects of Bond Deterioration on Hysteretic Behavior of Reinforced Concrete Joints," Berkeley, CA, UCB/EERC-83/19 1983.
- [30] T. J. R. Hughes, *The Finite Element Method, Linear Static and Dynamic Finite Element Analysis*. Mineola, NY: Dover Publications, 2000.
- [31] Anil K. Chopra, *Dynamics of Structures*. Upper Saddle River, NJ: Prentice Hall, 4th edition, 2011.
- [32] H. Matthies and G. Strang, "The Solution of Nonlinear Finite Element Equations," *International Journal for Numerical Methods in Engineering*, vol. 14, no. 11, p. 1613-1626, 1979.
- [33] O. Schenk, "Scalable Parallel Sparse LU Factorization Methods on Shared Memory Multiprocessors," Zürich, 2000.
- [34] R. L. Wood, "Partition Wall Subsystem Modeling and Effect on the Coupled Building System Response," La Jolla, CA, 2012.

- [35] R. Astroza, H. Ebrahimian, J. P. Conte, J. Restrepo, and T. C. Hutchinsom, "System Identification of a Full-scale Five-story Reinforced Concrete Building Tested on the NEES-UCSD Shake Table," *Structural Control and Health Monitoring*, p. in review, 2014.

**CHAPTER 4: PARAMETRIC IDENTIFICATION OF  
HYSTERETIC MATERIAL CONSTITUTIVE LAWS IN  
NONLINEAR STRUCTURAL FINITE ELEMENT MODELS  
USING EXTENDED KALMAN FILTER**

**4.1. Introduction**

In the field of structural engineering, system identification (ID) refers to methods and techniques to identify a mathematical model of a structure using input-output (or output only) data. Structural system identification techniques facilitate the detection of damage in structures by tracking the changes in the identified mathematical model or dynamic signatures of the structure. Extensive research efforts have been dedicated to structural health monitoring (SHM), which is the process of implementing damage ID techniques for structures [1]. The reader is referred to [2-4] for an in-depth literature survey on these subjects.



Structural modal ID, or identification of modal properties of a structure using input-output (or output only) data, is one of the most popular structural system ID approaches used for damage ID. The measured response of the structure under low-amplitude forced or ambient vibrations are processed to extract the modal properties of an equivalent linear elastic viscously damped dynamic system [5]. When a structure suffers damage or when its material and/or geometric properties change, the identified modal properties of the structure deviate from its initial undamaged (or baseline) modal properties. These variations in identified modal parameters or features extracted from them can be utilized to identify damage in the structure. Nevertheless, damage ID in structures based on modal ID has been criticized for some technical reasons. Classical modal properties (i.e., natural frequencies, mode shapes, and damping ratios) provide information on the global behavior of the structure and are often not sensitive to local damages in the structural system. Moreover, modal ID and the related damage ID methods are based on the fundamental assumption of linear elastic behavior of the structural system. However, especially in case of civil structures, “nonlinearity is generic in nature, and linear behavior is an exception” [6], even at low-amplitude levels of vibration (e.g., ambient). More importantly, low-amplitude vibrations used for modal ID provide information about loss of effective stiffness, but are unable to disclose any information about loss of strength (i.e., the most important manifestation of damage in the structural systems) and history of the response nonlinearities and related damage experienced by the structure.

Nonlinear FE Model updating in time domain can be considered as a family of methods used for both nonlinear system ID and damage ID of civil structures (e.g., [7-9] to name a few). In this approach, using the measured input-output data, the parameters of a nonlinear FE model of the structure of interest are estimated or updated by minimizing an objective function expressing the discrepancies between the measured and predicted responses in the time domain. Contrary to the modal ID based damage ID methods, in this approach, the data measured during damage-inducing events (such as earthquake), which contains valuable information on the nonlinear behavior of the structure, can be used to update the nonlinear FE model.

Various methods have been proposed and employed for nonlinear FE model updating and parameter estimation of structural models in the literature: methods based on least-square estimation (e.g., [10-12]), methods using the extended Kalman filter (EKF) and its variations (e.g., [13-20]), methods using the unscented Kalman filter (e.g., [8, 21-22]), and methods using particle filters (e.g., [23-25]). Some of these methods (EKF) require linearization of the state space model with respect to the parameters to be identified, which can be performed with (e.g., [19]) or without (e.g., [20]) computation of the relevant derivatives. Other methods avoid linearization using sampling-based methods (e.g., [24]). More recently, combinations of these two types of methods were also proposed (e.g., [25]). However, the studies reported in the literature typically use simplistic structural models such as single-degree-of-freedom or multi-degree-of-freedom mass-spring-dashpot models, and shear-building models, in which the nonlinearities are lumped at the structural or story levels, or one-

dimensional FE models. These basic models are either insufficient to predict the response of a real structure or are based on simplifying assumptions that result in a crude prediction of the real behavior of the structures. Moreover, the force–deformation, behavioral, or material constitutive models assumed in the studies referred to above are typically either linear elastic, nonlinear elastic, bilinear, or based on the empirical Bouc-Wen model. These constitutive models are either inadequate to capture the complex actual nonlinear behavior of real structures or, as in the case of the Bouc-Wen model, are not parameterized with physical material parameters (e.g., Young’s modulus, yield stress) and furthermore require calibration (using experimental data or high-fidelity predictive models) on a case-by-case basis. Consequently, there is a need to introduce state-of-the-art nonlinear structural FE modeling and analysis techniques into the FE model updating and parameter estimation field.

This chapter presents a novel framework that integrates the EKF as a parameter estimation tool with state-of-the-art mechanics-based nonlinear structural finite element modeling and analysis techniques to provide a new nonlinear system and damage identification framework for structural systems. The FE model depends on a set of time-invariant modeling parameters, which are assumed to be unknown and modeled as random variables according to the Bayesian approach of parameter estimation. Estimating the expected values and covariance matrix of these parameters using the input-output measured data is the objective of the parameter estimation and FE model updating framework. The updated FE model can then be interrogated

directly to evaluate the loss of strength and effective stiffness and the history of inelastic deformations and related damages in the structure at different spatial resolution levels, from global structural level to local component and element levels. The proposed framework is general and can be readily applied to different types of nonlinear FE models and to estimate different modeling parameters such as inertia properties, damping parameters, parameters characterizing the nonlinear material constitutive laws, geometric, loading, and constraint parameters. Using the EKF to estimate the modeling parameters and update the FE model requires the computation of structural FE response sensitivities with respect to the modeling parameters. These FE response sensitivities can be computed using the computationally demanding finite difference method (FDM) or the well-established, accurate and computationally more efficient direct differentiation method (DDM) [26]. In this study, DDM is employed as a tool to facilitate the implementation of the EKF in parameter estimation of nonlinear structural FE models.

The chapter is organized in the following way. After the introduction, the second section of the chapter introduces the Kalman filter and its application in parameter estimation. The third section reviews the technical background of the employed FE modeling and analysis techniques and formulates the proposed nonlinear FE model updating framework. Elements of the DDM-based FE response sensitivity analysis method are also provided in the third section. Finally, two proof-of-concept examples including a cantilever steel column and a three-story three-bay moment resisting steel frame are presented in the fourth section to verify the implementation

and the performance of the proposed nonlinear FE model updating framework. Conclusions are provided in the final section.

## 4.2. Kalman Filter (KF)

### 4.2.1. KF for linear systems

In system theory, the mathematical model of a linear dynamic system is often expressed in the state-space representation. The state-space model represents the dynamics of a linear system using two sets of vector equations. The first set is referred to as the state (or process) equation, while the second set is called the measurement equation. In the discrete time domain, the state equation is a set of coupled first-order ordinary difference equations and the measurement equation is a set of algebraic equations combining the states and inputs to yield the outputs (responses) of the system. Eqs. (4.1) and (4.2) provide the general time-variant discrete-time state-space representation of a linear stochastic dynamic system. In the state equation, Eq. (4.1),  $\mathbf{x}_{k+1} \in \mathfrak{R}^{n_x \times 1}$  is the state vector at time step  $(k+1)$ , which is the smallest set of system variables that fully defines the system and its response to given inputs.  $\mathbf{A}_k \in \mathfrak{R}^{n_x \times n_x}$  is the state matrix,  $\mathbf{B}_k \in \mathfrak{R}^{n_x \times n_u}$  is the input matrix,  $\mathbf{u}_k \in \mathfrak{R}^{n_u \times 1}$  is the deterministic input vector, and  $\mathbf{w}_k \in \mathfrak{R}^{n_x \times 1}$  is the stochastic input vector – or process noise vector, accounting for model uncertainties – all at the  $k^{\text{th}}$  time step. The state equation governs the evolution over time of the system state. In the measurement equation, Eq. (4.2),

$\mathbf{y}_k \in \mathfrak{R}^{n_y \times 1}$  is the output (response) of interest of the system,  $\mathbf{C}_{k+1} \in \mathfrak{R}^{n_y \times n_x}$  is the output matrix,  $\mathbf{D}_{k+1} \in \mathfrak{R}^{n_y \times n_u}$  is the feedthrough (or feedforward) matrix, and  $\mathbf{v}_{k+1} \in \mathfrak{R}^{n_y \times 1}$  is the measurement noise vector, all at time step  $(k+1)$ .

$$\mathbf{x}_{k+1} = \mathbf{A}_k \mathbf{x}_k + \mathbf{B}_k \mathbf{u}_k + \mathbf{w}_k \quad (4.1)$$

$$\mathbf{y}_{k+1} = \mathbf{C}_{k+1} \mathbf{x}_{k+1} + \mathbf{D}_{k+1} \mathbf{u}_{k+1} + \mathbf{v}_{k+1} \quad (4.2)$$

Depending on the application, accurate measurement of all the system states is usually impossible in the real world, as it requires numerous numbers of sensors; moreover, the sensor measurement would always be contaminated by measurement noise. Therefore, an interesting question is how to estimate the system states at every time step given the system matrices, the inputs, and the noisy responses of the system. Investigated by Kalman in 1960, this question led to the development of the Kalman Filter (KF) method [27]. Generally speaking, the KF recursively estimates the mean and covariance of the state vector of a linear Gaussian dynamic system, using the input and output vectors of the system. The KF is an unbiased, linear quadratic estimator, which minimizes the variance of the estimated states in time.

The KF algorithm is a recursive prediction-correction process. At the  $k^{\text{th}}$  time step, prior or *a priori* estimates (denoted by the minus sign in the superscript and superimposed hat, respectively) of the state and state covariance matrix are predicted for the next time step (i.e.,  $\hat{\mathbf{x}}_{k+1}^-$  and  $\hat{\mathbf{P}}_{\mathbf{x},k+1}^-$ , respectively). Using the *a priori* state estimate, the predicted system response,  $\hat{\mathbf{y}}_{k+1}^-$ , is evaluated. Then, upon arrival of the

measured response of the system at time step  $(k+1)$ ,  $\mathbf{y}_{k+1}$ ,  $\hat{\mathbf{x}}_{k+1}^-$  and  $\hat{\mathbf{P}}_{\mathbf{x},k+1}^-$  are corrected based on the difference between the observed (measured) and predicted responses, i.e.  $(\mathbf{y}_{k+1} - \hat{\mathbf{y}}_{k+1}^-)$ . The correction procedure results in posterior or *a posteriori* estimates (denoted by the plus sign in the superscript and superimposed hat, respectively) of the state and state covariance matrix (i.e.,  $\hat{\mathbf{x}}_{k+1}^+$  and  $\hat{\mathbf{P}}_{\mathbf{x},k+1}^+$ , respectively). This prediction-correction procedure is then repeated from time step to time step. The discrete-time KF algorithm is provided in Table 4.1 for the case where  $\mathbf{w}$  and  $\mathbf{v}$  are zero-mean independent Gaussian white noise processes, with covariance matrices at the  $k^{\text{th}}$  time step denoted by  $\mathbf{Q}_k$  and  $\mathbf{R}_k$ , respectively. In this table,  $E[.]$  and  $E[.|\cdot]$  denote the expectation and conditional expectation operators, respectively. More details on the mathematical derivation of the KF and its variations can be found in a number of textbooks (e.g., [28]).

Table 4.1: Discrete-time KF algorithm

<u>Initialization:</u>	
Postulate $\hat{\mathbf{x}}_0^+$ and $\hat{\mathbf{P}}_{\mathbf{x},0}^+$ where	Estimates of initial state and state covariance matrix
$\hat{\mathbf{x}}_0^+ = E[\mathbf{x}_0], \hat{\mathbf{P}}_{\mathbf{x},0}^+ = E\left[(\mathbf{x}_0 - \hat{\mathbf{x}}_0^+)(\mathbf{x}_0 - \hat{\mathbf{x}}_0^+)^T\right]$	
For each time step ( $k = 0, 1, \dots$ ):	
<u>Prediction:</u>	
$\hat{\mathbf{x}}_{k+1}^- = E[\mathbf{x}_{k+1}   \mathbf{y}_1, \mathbf{y}_2, \dots, \mathbf{y}_k] = \mathbf{A}_k \hat{\mathbf{x}}_k^+ + \mathbf{B}_k \mathbf{u}_k$	<i>A priori</i> state estimate (4.3)
$\hat{\mathbf{P}}_{\mathbf{x},k+1}^- = E\left[(\mathbf{x}_{k+1} - \hat{\mathbf{x}}_{k+1}^-)(\mathbf{x}_{k+1} - \hat{\mathbf{x}}_{k+1}^-)^T   \mathbf{y}_1, \mathbf{y}_2, \dots, \mathbf{y}_k\right] = \mathbf{A}_k \hat{\mathbf{P}}_{\mathbf{x},k}^+ \mathbf{A}_k^T + \mathbf{Q}_k$	<i>A priori</i> state covariance matrix (4.4)
$\hat{\mathbf{y}}_{k+1}^- = E[\mathbf{y}_{k+1}   \mathbf{y}_1, \mathbf{y}_2, \dots, \mathbf{y}_k] = \mathbf{C}_{k+1} \hat{\mathbf{x}}_{k+1}^- + \mathbf{D}_{k+1} \mathbf{u}_{k+1}$	Predicted response (4.5)
$\hat{\mathbf{P}}_{\mathbf{xy},k+1}^- = E\left[(\mathbf{x}_{k+1} - \hat{\mathbf{x}}_{k+1}^-)(\mathbf{y}_{k+1} - \hat{\mathbf{y}}_{k+1}^-)^T   \mathbf{y}_1, \mathbf{y}_2, \dots, \mathbf{y}_k\right] = \hat{\mathbf{P}}_{\mathbf{x},k+1}^- \mathbf{C}_{k+1}^T$	Estimated state-response cross covariance matrix (4.6)
$\hat{\mathbf{P}}_{\mathbf{y},k+1}^- = E\left[(\mathbf{y}_{k+1} - \hat{\mathbf{y}}_{k+1}^-)(\mathbf{y}_{k+1} - \hat{\mathbf{y}}_{k+1}^-)^T   \mathbf{y}_1, \mathbf{y}_2, \dots, \mathbf{y}_k\right] = \mathbf{C}_{k+1} \hat{\mathbf{P}}_{\mathbf{x},k+1}^- \mathbf{C}_{k+1}^T + \mathbf{R}_{k+1}$	Estimated response covariance matrix (4.7)
<u>Correction:</u> (upon arrival of the measured response at time step ( $k+1$ ))	
$\mathbf{K}_{k+1} = \hat{\mathbf{P}}_{\mathbf{xy},k+1}^- (\hat{\mathbf{P}}_{\mathbf{y},k+1}^-)^{-1}$	Kalman gain matrix (4.8)
$\hat{\mathbf{x}}_{k+1}^+ = E[\mathbf{x}_{k+1}   \mathbf{y}_1, \mathbf{y}_2, \dots, \mathbf{y}_{k+1}] = \hat{\mathbf{x}}_{k+1}^- + \mathbf{K}_{k+1} (\mathbf{y}_{k+1} - \hat{\mathbf{y}}_{k+1}^-)$	<i>A posteriori</i> state estimate (4.9)
$\hat{\mathbf{P}}_{\mathbf{x},k+1}^+ = E\left[(\mathbf{x}_{k+1} - \hat{\mathbf{x}}_{k+1}^+)(\mathbf{x}_{k+1} - \hat{\mathbf{x}}_{k+1}^+)^T   \mathbf{y}_1, \mathbf{y}_2, \dots, \mathbf{y}_{k+1}\right]$	<i>A posteriori</i> state covariance matrix
$= (\mathbf{I} - \mathbf{K}_{k+1} \mathbf{C}_{k+1}) \hat{\mathbf{P}}_{\mathbf{x},k+1}^- (\mathbf{I} - \mathbf{K}_{k+1} \mathbf{C}_{k+1})^T + \mathbf{K}_{k+1} \mathbf{R}_{k+1} \mathbf{K}_{k+1}^T$	(Joseph equation [29]) (4.10)

#### 4.2.2. KF for nonlinear systems

The discrete-time state-space representation of a nonlinear dynamic system is expressed as

$$\mathbf{x}_{k+1} = \mathbf{f}_k(\mathbf{x}_k, \mathbf{u}_k) + \mathbf{w}_k \quad (4.11)$$

$$\mathbf{y}_{k+1} = \mathbf{g}_{k+1}(\mathbf{x}_{k+1}, \mathbf{u}_{k+1}) + \mathbf{v}_{k+1} \quad (4.12)$$

in which  $\mathbf{f}_k(.,.): (\mathfrak{R}^{n_x \times 1}, \mathfrak{R}^{n_u \times 1}) \rightarrow \mathfrak{R}^{n_x \times 1}$  is the nonlinear vector-valued state function

and  $\mathbf{w}_k \in \mathfrak{R}^{n_x \times 1}$  is the process noise vector at the  $k^{\text{th}}$  time step. The term



$\mathbf{g}_{k+1}(\cdot, \cdot): (\mathfrak{R}^{n_x \times 1}, \mathfrak{R}^{n_u \times 1}) \rightarrow \mathfrak{R}^{n_y \times 1}$  is the nonlinear vector-valued measurement function and  $\mathbf{v}_{k+1} \in \mathfrak{R}^{n_y \times 1}$  is the measurement noise vector at time step  $(k+1)$ .

The KF method cannot be directly applied to nonlinear dynamic systems, in which either one or both of the state and measurement equations are nonlinear. The time evolution of the probability distribution of the states in a nonlinear dynamic system can be described by the conditioned Fokker-Planck differential equation [30], the solution of which can be very tedious. To work around the nonlinear filtering problem, a number of methods have been proposed to extend the application of the KF to nonlinear systems using simplifying assumptions. One of these methods is the EKF, in which the nonlinear state space model is linearized around the latest estimated state, using a first-order Taylor series approximation. Then, the KF prediction-correction procedure (for linear systems) is applied to the linearized system and the derived *a posteriori* estimate is used as the center-point for the next time step linearization. The first-order Taylor series expansion of Eq. (4.11) about  $\hat{\mathbf{x}}_k^+$  can be expressed as

$$\begin{aligned} \mathbf{x}_{k+1} &= \left[ \mathbf{f}_k(\hat{\mathbf{x}}_k^+, \mathbf{u}_k) + \frac{\partial \mathbf{f}_k(\mathbf{x}, \mathbf{u}_k)}{\partial \mathbf{x}^T} \Big|_{\mathbf{x}=\hat{\mathbf{x}}_k^+} (\mathbf{x}_k - \hat{\mathbf{x}}_k^+) + H.O.T. \right] + \mathbf{w}_k \\ &\Rightarrow \mathbf{x}_{k+1} \cong \mathbf{A}_k \mathbf{x}_k + \tilde{\mathbf{u}}_k + \mathbf{w}_k \end{aligned} \quad (4.13)$$

where

$$\mathbf{A}_k = \frac{\partial \mathbf{f}_k(\mathbf{x}, \mathbf{u}_k)}{\partial \mathbf{x}^T} \Big|_{\mathbf{x}=\hat{\mathbf{x}}_k^+}, \quad \tilde{\mathbf{u}}_k = \mathbf{f}_k(\hat{\mathbf{x}}_k^+, \mathbf{u}_k) - \mathbf{A}_k \hat{\mathbf{x}}_k^+$$

Using this first-order approximation and assuming that  $\mathbf{w}_k \sim N(\mathbf{0}, \mathbf{Q}_k)$ , in which  $N(\boldsymbol{\mu}, \mathbf{C})$  denotes the normal probability distribution with mean vector  $\boldsymbol{\mu}$  and

covariance matrix  $\mathbf{C}$ , the *a priori* estimates of the state vector and state covariance matrix are obtained as

$$\hat{\mathbf{x}}_{k+1}^- \cong \mathbf{f}_k(\hat{\mathbf{x}}_k^+, \mathbf{u}_k) \quad (4.14)$$

$$\hat{\mathbf{P}}_{\mathbf{x},k+1}^- \cong \mathbf{A}_k \hat{\mathbf{P}}_{\mathbf{x},k}^+ \mathbf{A}_k^T + \mathbf{Q}_k \quad (4.15)$$

To evaluate the *a posteriori* estimates of the state vector and state covariance matrix, the measurement equation must also be linearized with the linearization point taken as the *a priori* state estimate, which at this point is the best available estimate of the state, i.e.,

$$\mathbf{y}_{k+1} = \left[ \mathbf{g}_{k+1}(\hat{\mathbf{x}}_{k+1}^-, \mathbf{u}_{k+1}) + \frac{\partial \mathbf{g}_{k+1}(\mathbf{x}, \mathbf{u}_{k+1})}{\partial \mathbf{x}^T} \Big|_{\mathbf{x}=\hat{\mathbf{x}}_{k+1}^-} (\mathbf{x}_{k+1} - \hat{\mathbf{x}}_{k+1}^-) + H.O.T. \right] + \mathbf{v}_{k+1} \quad (4.16)$$

$$\Rightarrow \mathbf{y}_{k+1} \cong \mathbf{C}_{k+1} \mathbf{x}_{k+1} + \tilde{\mathbf{z}}_{k+1} + \mathbf{v}_{k+1}$$

where

$$\mathbf{C}_{k+1} = \frac{\partial \mathbf{g}_{k+1}(\mathbf{x}, \mathbf{u}_{k+1})}{\partial \mathbf{x}^T} \Big|_{\mathbf{x}=\hat{\mathbf{x}}_{k+1}^-}, \quad \tilde{\mathbf{z}}_{k+1} = \mathbf{g}_{k+1}(\hat{\mathbf{x}}_{k+1}^-, \mathbf{u}_{k+1}) - \mathbf{C}_{k+1} \hat{\mathbf{x}}_{k+1}^-$$

Therefore, assuming that  $\mathbf{v}_k \sim N(0, \mathbf{R}_k)$  and that  $\mathbf{w}$  and  $\mathbf{v}$  are independent white noise processes, the above first-order approximation yields the following results:

$$\hat{\mathbf{y}}_{k+1}^- \cong \mathbf{g}_{k+1}(\hat{\mathbf{x}}_{k+1}^-, \mathbf{u}_{k+1}) \quad (4.17)$$

$$\hat{\mathbf{P}}_{\mathbf{xy},k+1}^- \cong \hat{\mathbf{P}}_{\mathbf{x},k+1}^- \mathbf{C}_{k+1}^T \quad (4.18)$$

$$\hat{\mathbf{P}}_{\mathbf{y},k+1}^- \cong \mathbf{C}_{k+1} \hat{\mathbf{P}}_{\mathbf{x},k+1}^- \mathbf{C}_{k+1}^T + \mathbf{R}_{k+1} \quad (4.19)$$

Eqs. (4.14)-(4.15) and (4.17)-(4.19) can be used to run recursively the Kalman filter prediction-correction procedure summarized in Table 4.1, for the nonlinear dynamic system governed by Eqs. (4.11) and (4.12). It should be mentioned that for the Gaussian process and measurement noises,  $\mathbf{w}$  and  $\mathbf{v}$  respectively, the output of the linearized system is also Gaussian. In other words, the output of the nonlinear system is gaussianized through linearization of the system.

#### 4.2.3. Parameter estimation using EKF

The EKF framework presented in the previous section can also be used for estimating the unknown parameters of a nonlinear model. Suppose that a general nonlinear system is described using a nonlinear model that is parameterized by a set of constant parameters such that the response of the nonlinear model is uniquely defined by the parameters and the input to the model. A set of input-output data, consisting of sample pairs of known input and noisy output (measurement) of the system, is available. The unknown parameters are modeled as random variables according to the Bayesian approach. The objective is to estimate the mean and variance of the parameters using the available set of input-output data. This problem is referred to as nonlinear parameter estimation.

Assume that the output of a nonlinear system is modeled as

$$\mathbf{y}_{k+1} = \mathbf{h}_{k+1}(\boldsymbol{\theta}, \mathbf{u}_{k+1}) + \mathbf{v}_{k+1} \quad (4.20)$$

in which  $\mathbf{y}_{k+1} \in \mathfrak{R}^{n_y \times 1}$  is the noisy output (measurement) vector,  $\boldsymbol{\theta} \in \mathfrak{R}^{n_\theta \times 1}$  is the vector of constant unknown parameters,  $\mathbf{u}_{k+1} \in \mathfrak{R}^{n_u \times 1}$  is the deterministic input vector,  $\mathbf{h}(\cdot, \cdot): (\mathfrak{R}^{n_\theta \times 1}, \mathfrak{R}^{n_u \times 1}) \rightarrow \mathfrak{R}^{n_y \times 1}$  is the nonlinear vector-valued function representing the parameterized model,  $\mathbf{v}_{k+1} \in \mathfrak{R}^{n_y \times 1}$  is the measurement noise vector, and the subscripts indicate the sample number of the input-output data sequence.

To solve the nonlinear parameter estimation problem, the constant unknown parameter vector,  $\boldsymbol{\theta}$ , is modeled as a random vector, the evolution of which is characterized by a Gaussian Markov process – also known as a random walk process. Then, a state space model is set up, in which the state equation governs the evolution of the random parameter vector and the measurement equation corresponds to the output equation of the nonlinear system [31], i.e.,

$$\boldsymbol{\theta}_{k+1} = \boldsymbol{\theta}_k + \boldsymbol{\gamma}_k \quad (4.21)$$

$$\mathbf{y}_{k+1} = \mathbf{h}_{k+1}(\boldsymbol{\theta}_{k+1}, \mathbf{u}_{k+1}) + \mathbf{v}_{k+1} \quad (4.22)$$

in which  $\boldsymbol{\gamma}_k \in \mathfrak{R}^{n_\theta \times 1}$  is a zero-mean Gaussian white noise process. Assuming that the measurement noise vector,  $\mathbf{v}_{k+1}$ , is also a zero-mean Gaussian white noise process, the EKF can be employed to recursively update the mean vector and covariance matrix of the parameter vector,  $\boldsymbol{\theta}$ , using the measured (recorded) input and output (response) of the system. The mean vector is referred to as parameter estimate and the covariance matrix as parameter covariance matrix hereafter. Comparing Eqs. (4.11)-(4.12) with Eqs. (4.21)-(4.22) shows that the process equation is now linear and only the

measurement equation needs to be linearized for the EKF process. This parameter estimation setup is a crucial step that facilitates the implementation of the EKF in the nonlinear FE model updating framework proposed in the next section. Similar parameter estimation setup has been used in [32] to update FE models under quasi-static loading conditions and identify parameters of linear elastic and nonlinear elastic material model using particle filters.

### **4.3. Nonlinear FE model updating using EKF**

#### **4.3.1. Problem statement**

Suppose that the input ground acceleration and the dynamic response of a civil structure (e.g., building, bridge) are recorded during an earthquake event. The dynamic response of civil structures are typically recorded through an array of accelerometers (acceleration sensors), which measure the total acceleration response time histories at various points of the structure. As expected for any physical measurement, the recorded data are polluted by noise, referred to as measurement noise. To simulate the dynamic response of this building structure, a nonlinear FE model is developed. The FE model depends on a set of unknown time-invariant parameters including inertia properties, damping parameters, and parameters characterizing the nonlinear material constitutive laws used in the FE model. These parameters are referred to as material parameters henceforth. Using the recorded input ground acceleration time history and the noisy measured response of the building, the objective is to identify the best set of

unknown material parameters to minimize the discrepancy between FE predicted and measured structural responses for the recorded input ground motion. In this chapter, the estimation problem is tackled by updating recursively (i.e., step by step as we march forward in time during the earthquake) the unknown material parameters of the nonlinear FE model using the EKF parameter estimation framework.

#### **4.3.2. Nonlinear FE modeling and analysis method**

In this study, the proposed nonlinear FE model updating framework is developed by employing a distributed-plasticity, displacement-based, structural finite element modeling and analysis technique [33]. In this technique, which has been widely used in nonlinear analysis and design of frame-type structures, the structural model is spatially discretized using fiber-section displacement-based beam-column elements formulated from Euler-Bernoulli or Timoshenko beam theory. Contrary to lumped plasticity models, in the distributed plasticity models, the element material nonlinearity can spread over several monitored sections along the element, also known as integration points. The sections are further discretized into fibers [34]. A nonlinear uniaxial material constitutive model governs the force-deformation response of each fiber. Figure 4.1 shows the hierarchical discretization levels of the nonlinear FE modeling and analysis method considered here. The reader is referred to [35] for more details about this structural modeling and analysis approach.

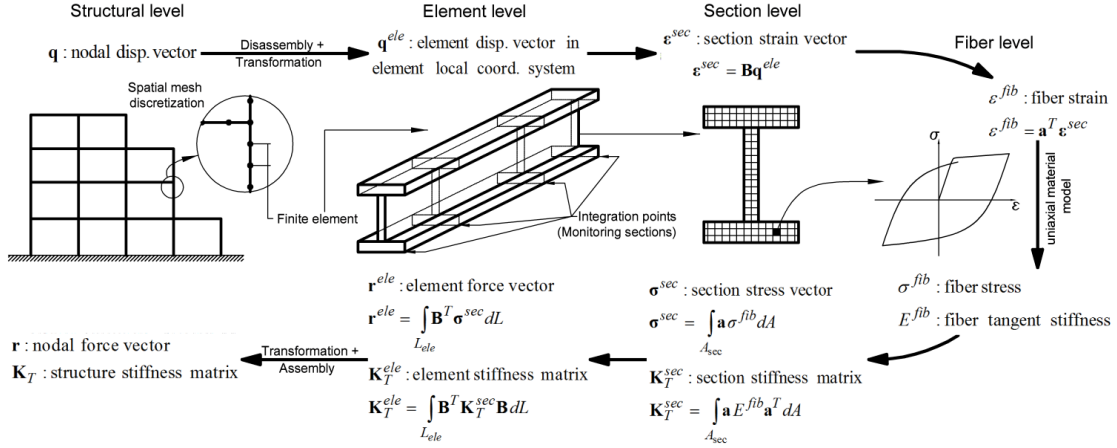


Figure 4.1: Hierarchical discretization levels in distributed plasticity structural FE models using fiber-section displacement-based beam-column elements. The notation is further described in Section 3.4.

### 4.3.3. Parameter estimation – Nonlinear FE model updating framework

The space- and time-discretized (discrete spatio-temporal) equation of motion of a nonlinear FE model at time step  $(k+1)$  is expressed as

$$\mathbf{M}(\boldsymbol{\theta})\ddot{\mathbf{q}}_{k+1}(\boldsymbol{\theta}) + \mathbf{C}(\boldsymbol{\theta})\dot{\mathbf{q}}_{k+1}(\boldsymbol{\theta}) + \mathbf{r}_{k+1}(\mathbf{q}_{k+1}(\boldsymbol{\theta}), \boldsymbol{\theta}) = \mathbf{f}_{k+1} \quad (4.23)$$

in which  $\boldsymbol{\theta}$  = unknown time-invariant material parameter vector;  $\mathbf{q}_{k+1}$ ,  $\dot{\mathbf{q}}_{k+1}$ ,  $\ddot{\mathbf{q}}_{k+1}$  = nodal displacement, velocity, and acceleration vectors;  $\mathbf{M}$  = mass matrix;  $\mathbf{C}$  = damping matrix;  $\mathbf{r}_{k+1}(\mathbf{q}_{k+1}(\boldsymbol{\theta}), \boldsymbol{\theta})$  = history-dependent (or path-dependent) internal resisting force vector;  $\mathbf{f}_{k+1}$  = dynamic load vector; and the subscripts indicate the time step. Note that  $\mathbf{r}(\mathbf{q}, \boldsymbol{\theta})$  depends on  $\boldsymbol{\theta}$  both explicitly and implicitly through  $\mathbf{q}(\boldsymbol{\theta})$ . In the case of earthquake uniform base excitation,  $\mathbf{f}_{k+1} = -\mathbf{M}\mathbf{l}_u \ddot{u}_{g_{k+1}}$ , where  $\mathbf{l}_u$  is the influence coefficient vector and  $\ddot{u}_{g_{k+1}}$  denotes the input ground acceleration. In this chapter, it

is presumed that the level of measurement noise in the input ground acceleration time history is negligible.

Without loss of generality, it is assumed here that the response of the structure is recorded using only accelerometers installed at specific locations within the structure. The absolute acceleration response vector at the instrumented locations is given by

$$\mathbf{y}_{k+1} = \mathbf{L}_y (\mathbf{\dot{q}}_{k+1} + \mathbf{l}_u \ddot{u}_{g_{k+1}}) + \mathbf{v}_{k+1} \quad (4.24)$$

in which  $\mathbf{y}_{k+1}$  = absolute acceleration response vector at time step  $(k+1)$ ,  $\mathbf{L}_y$  = output matrix, and  $\mathbf{v}_k \sim N(\mathbf{0}, \mathbf{R}_k)$  is the measurement noise vector assumed zero-mean and Gaussian (normal) with covariance matrix  $\mathbf{R}_k$ . By combining Eqs. (4.23) and (4.24), the absolute acceleration response vector is expressed as a nonlinear function of the material parameters, input ground acceleration time history, and initial conditions of the FE model, i.e.,

$$\mathbf{y}_{k+1} = \mathbf{h}_{k+1}(\boldsymbol{\theta}, [\ddot{u}_g]_{k+1}, \mathbf{q}_0, \dot{\mathbf{q}}_0) + \mathbf{v}_{k+1} \quad (4.25)$$

In this equation,  $\mathbf{h}_{k+1}(\dots)$  is the  $(k+1)^{\text{th}}$  time step absolute acceleration response function of the nonlinear FE model and  $[\ddot{u}_g]_{k+1} = [\ddot{u}_{g_1}, \ddot{u}_{g_2}, \dots, \ddot{u}_{g_{k+1}}]^T$  denotes the input ground acceleration time history from time  $t_1$  to  $t_{k+1}$ . The terms  $\mathbf{q}_0$  and  $\dot{\mathbf{q}}_0$  are the initial nodal displacement and velocity vectors, respectively. For notational convenience, and without loss of generality, at rest initial conditions, i.e.  $\mathbf{q}_0 = \dot{\mathbf{q}}_0 = \mathbf{0}$ , are assumed hereafter.



Based on the parameter estimation framework presented in Section 2.3,  $\boldsymbol{\theta}$  is modeled as a random vector characterized by a Gaussian Markov process and the nonlinear parameter estimation problem at time step  $(k+1)$  ( $k = 0, 1, 2, \dots$ ) is set up as

$$\boldsymbol{\theta}_{k+1} = \boldsymbol{\theta}_k + \boldsymbol{\gamma}_k \quad (4.26)$$

$$\mathbf{y}_{k+1} = \mathbf{h}_{k+1}(\boldsymbol{\theta}_{k+1}, [\ddot{u}_g]_{k+1}) + \mathbf{v}_{k+1} \quad (4.27)$$

in which  $\boldsymbol{\gamma}_k \sim N(\mathbf{0}, \mathbf{Q}_k)$  and  $\mathbf{v}_{k+1} \sim N(\mathbf{0}, \mathbf{R}_{k+1})$ . Now, the estimation problem posed above can be solved using the EKF recursive prediction-correction procedure described in Section 5.4. The solution starts by defining the mean and covariance of the parameter vector at time step  $k = 0$ . At each time step, the *a priori* parameter estimate and the *a priori* parameter covariance matrix for the next time step are

$$\hat{\boldsymbol{\theta}}_{k+1}^- = \hat{\boldsymbol{\theta}}_k^+ \quad (4.28)$$

$$\hat{\mathbf{P}}_{\boldsymbol{\theta},k+1}^- = \hat{\mathbf{P}}_{\boldsymbol{\theta},k}^+ + \mathbf{Q}_k \quad (4.29)$$

Following the approach used to derive Eq. (4.16), the measurement equation is linearized around the *a priori* estimate,  $\hat{\boldsymbol{\theta}}_{k+1}^-$ , as

$$\mathbf{y}_{k+1} \cong \mathbf{C}_{k+1} \boldsymbol{\theta}_{k+1} + \tilde{\mathbf{z}}_{k+1} + \mathbf{v}_{k+1} \quad (4.30)$$

The predicted response vector is then computed as

$$\hat{\mathbf{y}}_{k+1}^- \cong \mathbf{h}_{k+1}(\hat{\boldsymbol{\theta}}_{k+1}^-, [\ddot{u}_g]_{k+1}) \quad (4.31)$$

Moreover, assuming that  $\gamma$  and  $\mathbf{v}$  are independent white noise processes, the parameter-response cross covariance matrix and the response covariance matrix are estimated as

$$\hat{\mathbf{P}}_{\mathbf{y},k+1}^- \cong \hat{\mathbf{P}}_{\boldsymbol{\theta},k+1}^- \mathbf{C}_{k+1}^T \quad (4.32)$$

$$\hat{\mathbf{P}}_{\mathbf{y},k+1}^- \cong \mathbf{C}_{k+1} \hat{\mathbf{P}}_{\boldsymbol{\theta},k+1}^- \mathbf{C}_{k+1}^T + \mathbf{R}_{k+1} \quad (4.33)$$

in which  $\mathbf{C}_{k+1} = \left. \frac{\partial \mathbf{h}_{k+1}(\boldsymbol{\theta}, [\ddot{u}_g]_{k+1})}{\partial \boldsymbol{\theta}^T} \right|_{\boldsymbol{\theta}=\hat{\boldsymbol{\theta}}_{k+1}^-}$ ,  $\tilde{\mathbf{z}}_{k+1} = [\mathbf{h}_{k+1}(\hat{\boldsymbol{\theta}}_{k+1}^-, [\ddot{u}_g]_{k+1}) - \mathbf{C}_{k+1} \hat{\boldsymbol{\theta}}_{k+1}^-]$ .

The term  $\frac{\partial \mathbf{h}_{k+1}(\boldsymbol{\theta}, [\ddot{u}_g]_{k+1})}{\partial \boldsymbol{\theta}^T}$  is the sensitivity (or rate of variation) of the acceleration response of the structure, obtained from the FE model, with respect to the material parameters,  $\boldsymbol{\theta}$ , and is referred to as the FE acceleration response sensitivity. FE response sensitivity analysis is a well-developed subject with a variety of applications including structural design optimization, probabilistic analysis, and reliability analysis of structural and/or geotechnical systems (e.g., [26, 36-39]). The direct differentiation method (DDM), a well-known FE response sensitivity analysis method, is based on the exact (consistent) differentiation of the finite element numerical scheme with respect to the FE model parameters of interest, here the material parameters,  $\boldsymbol{\theta}$ . The software for finite-element response sensitivity computations using the DDM has been integrated into the OpenSees software architecture using a versatile FE model parameterization framework [40] and extended into nonlinear FE-based optimization problems [39]. DDM is known to be more accurate and/or computationally more

efficient than other methods for FE response sensitivity analysis, such as FDM ([37, 41-42]). The fundamentals of DDM-based FE response sensitivity computation [41] are briefly described in the next section.

#### 4.3.4. FE response sensitivities using DDM

The discrete spatio-temporal equation of motion shown in Eq. (4.23) is solved using recursive numerical integration in time. Using an implicit single-step time integration scheme, such as the Newmark-beta method [43], the acceleration and velocity at time step  $(k+1)$  are interpolated as

$$\ddot{\mathbf{q}}_{k+1} = a_1 \mathbf{q}_{k+1} + a_2 \mathbf{q}_k + a_3 \dot{\mathbf{q}}_k + a_4 \ddot{\mathbf{q}}_k \quad (4.34)$$

$$\dot{\mathbf{q}}_{k+1} = b_1 \mathbf{q}_{k+1} + b_2 \mathbf{q}_k + b_3 \dot{\mathbf{q}}_k + b_4 \ddot{\mathbf{q}}_k \quad (4.35)$$

where  $a_1$  to  $a_4$  and  $b_1$  to  $b_4$  are constant integration coefficients. Substitution of these equations into Eq. (4.23) yields the following nonlinear vector-valued algebraic equation, which can be solved using incremental iterative procedures such as Newton-Raphson method [33].

$$a_1 \mathbf{M}(\boldsymbol{\theta}) \mathbf{q}_{k+1}(\boldsymbol{\theta}) + b_1 \mathbf{C}(\boldsymbol{\theta}) \mathbf{q}_{k+1}(\boldsymbol{\theta}) + \mathbf{r}_{k+1}(\mathbf{q}_{k+1}(\boldsymbol{\theta}), \boldsymbol{\theta}) = \tilde{\mathbf{f}}_{k+1} \quad (4.36)$$

in which

$$\tilde{\mathbf{f}}_{k+1} = \mathbf{f}_{k+1} - \mathbf{M}(\boldsymbol{\theta}) [a_2 \mathbf{q}_k(\boldsymbol{\theta}) + a_3 \dot{\mathbf{q}}_k(\boldsymbol{\theta}) + a_4 \ddot{\mathbf{q}}_k(\boldsymbol{\theta})] - \mathbf{C}(\boldsymbol{\theta}) [b_2 \mathbf{q}_k(\boldsymbol{\theta}) + b_3 \dot{\mathbf{q}}_k(\boldsymbol{\theta}) + b_4 \ddot{\mathbf{q}}_k(\boldsymbol{\theta})] \quad (4.37)$$

and  $\boldsymbol{\theta} = [\theta_1, \theta_2, \dots]^T$  is the vector of time-invariant material parameters. Now, Eq. (4.36) is separately differentiated with respect to each material parameter,  $\theta_i$  ( $i=1, \dots, n_{\boldsymbol{\theta}}$ ), to obtain the response sensitivity with respect to this parameter, i.e.,

$$\underbrace{\left[ a_1 \mathbf{M}(\boldsymbol{\theta}) + b_1 \mathbf{C}(\boldsymbol{\theta}) + \frac{\partial \mathbf{r}_{k+1}(\mathbf{q}_{k+1}, \boldsymbol{\theta})}{\partial \mathbf{q}_{k+1}^T} \right]}_{=\left(\mathbf{K}_T^{dyn}\right)_{k+1}} \frac{\partial \mathbf{q}_{k+1}}{\partial \theta_i} = - \left. \frac{\partial \mathbf{r}_{k+1}(\mathbf{q}, \boldsymbol{\theta})}{\partial \theta_i} \right|_{\mathbf{q}=\mathbf{q}_{k+1}} - \left( a_1 \frac{\partial \mathbf{M}(\boldsymbol{\theta})}{\partial \theta_i} + b_1 \frac{\partial \mathbf{C}(\boldsymbol{\theta})}{\partial \theta_i} \right) \mathbf{q}_{k+1} + \frac{\partial \tilde{\mathbf{f}}_{k+1}}{\partial \theta_i} \quad (4.38)$$

in which  $\frac{\partial \mathbf{r}_{k+1}(\mathbf{q}_{k+1}, \boldsymbol{\theta})}{\partial \mathbf{q}_{k+1}^T} = \left(\mathbf{K}_T^{stat}\right)_{k+1}$  is the static (consistent) tangent stiffness matrix

and is readily available from the FE solution if a Newton-Raphson iterative scheme is used (at least in the last iteration) to solve Eq. (4.36). Moreover, the matrix in the left hand side of Eq. (4.38) is called the dynamic tangent stiffness matrix,  $\left(\mathbf{K}_T^{dyn}\right)_{k+1}$ , which is also available from the FE solution. Using Eq. (37), the last term in the right hand side of Eq. (4.38) is obtained as

$$\begin{aligned} \frac{\partial \tilde{\mathbf{f}}_{k+1}}{\partial \theta_i} = & \frac{\partial \mathbf{f}_{k+1}}{\partial \theta_i} - \frac{\partial \mathbf{M}(\boldsymbol{\theta})}{\partial \theta_i} [a_2 \mathbf{q}_k(\boldsymbol{\theta}) + a_3 \dot{\mathbf{q}}_k(\boldsymbol{\theta}) + a_4 \ddot{\mathbf{q}}_k(\boldsymbol{\theta})] - \mathbf{M}(\boldsymbol{\theta}) \left[ a_2 \frac{\partial \mathbf{q}_k}{\partial \theta_i} + a_3 \frac{\partial \dot{\mathbf{q}}_k}{\partial \theta_i} + a_4 \frac{\partial \ddot{\mathbf{q}}_k}{\partial \theta_i} \right] \\ & - \frac{\partial \mathbf{C}(\boldsymbol{\theta})}{\partial \theta_i} [b_2 \mathbf{q}_k(\boldsymbol{\theta}) + b_3 \dot{\mathbf{q}}_k(\boldsymbol{\theta}) + b_4 \ddot{\mathbf{q}}_k(\boldsymbol{\theta})] - \mathbf{C}(\boldsymbol{\theta}) \left[ b_2 \frac{\partial \mathbf{q}_k}{\partial \theta_i} + b_3 \frac{\partial \dot{\mathbf{q}}_k}{\partial \theta_i} + b_4 \frac{\partial \ddot{\mathbf{q}}_k}{\partial \theta_i} \right] \end{aligned} \quad (4.39)$$

Depending on the type of material parameter,  $\frac{\partial \mathbf{f}_{k+1}}{\partial \theta_i}$ ,  $\frac{\partial \mathbf{M}(\boldsymbol{\theta})}{\partial \theta_i}$ , and  $\frac{\partial \mathbf{C}(\boldsymbol{\theta})}{\partial \theta_i}$  are usually

easy to derive at the element level [37]. Furthermore, the vectors  $\frac{\partial \mathbf{q}_k}{\partial \theta_i}$ ,  $\frac{\partial \dot{\mathbf{q}}_k}{\partial \theta_i}$ , and

$\frac{\partial \ddot{\mathbf{q}}_k}{\partial \theta_i}$  are available from the last time step sensitivity computation. Thus,  $\frac{\partial \tilde{\mathbf{f}}_{k+1}}{\partial \theta_i}$  is obtained from the vectors can be computed without any complication.

The first term in the right-hand-side of Eq. (4.38) represents the partial derivative of the internal resisting force vector with respect to the material parameter,  $\theta_i$ , conditional on the displacement vector,  $\mathbf{u}_{k+1}$ , remaining fixed. To compute this conditional partial derivative, the structure's internal resisting force vector at time step  $(k+1)$  needs to be found explicitly. In a displacement-based FE model of frame-type structures, the structure's internal resisting force vector is derived by assembling the element nodal resisting force vectors as

$$\mathbf{r}_{k+1}(\mathbf{q}_{k+1}(\boldsymbol{\theta}), \boldsymbol{\theta}) = \mathbf{A}_{ele=1}^{\#ele} \left\{ \mathbf{r}_{k+1}^{ele}(\mathbf{q}_{k+1}^{ele}(\boldsymbol{\theta}), \boldsymbol{\theta}) \right\} \quad (4.40)$$

in which  $\mathbf{A}_{ele=1}^{\#ele} \{ \dots \}$  denotes the direct stiffness assembly process including the transformation from the element local coordinate system to the structure global coordinate system,  $\mathbf{r}^{ele}(\mathbf{q}^{ele}, \boldsymbol{\theta})$  = element nodal resisting force vector, and  $\mathbf{q}^{ele}$  = element nodal displacement vector in the element local coordinate system. Following the hierarchical discretization levels shown in Figure 4.1, the element nodal resisting force vector is obtained, through the principle of virtual displacements, as the following weighted integral of the section stress vector,  $\boldsymbol{\sigma}_{k+1}^{sec}$ , [35]

$$\mathbf{r}_{k+1}^{ele}(\mathbf{u}_{k+1}^{ele}(\boldsymbol{\theta}), \boldsymbol{\theta}) = \int_{L_{ele}} \mathbf{B}^T \boldsymbol{\sigma}_{k+1}^{sec}(\boldsymbol{\epsilon}_{k+1}^{sec}(\boldsymbol{\theta}), \boldsymbol{\theta}) dL \quad (4.41)$$

where  $\mathbf{B}$  = strain-displacement transformation matrix,  $\boldsymbol{\sigma}^{sec}(\boldsymbol{\varepsilon}^{sec}, \boldsymbol{\theta})$  = section stress resultant vector, and  $\boldsymbol{\varepsilon}^{sec}$  = section strain (or deformation) vector. Finally, the section stress vector is obtained by integrating the fiber stresses over the cross-section as

$$\boldsymbol{\sigma}_{k+1}^{sec}(\boldsymbol{\varepsilon}_{k+1}^{sec}(\boldsymbol{\theta}), \boldsymbol{\theta}) = \int_{A_{sec}} \mathbf{a} \sigma_{k+1}^{fib}(\boldsymbol{\varepsilon}_{k+1}^{fib}(\boldsymbol{\theta}), \boldsymbol{\theta}) dA \quad (4.42)$$

in which  $\mathbf{a}$  = section kinematic (compatibility) vector,  $\sigma^{fib}(\boldsymbol{\varepsilon}^{fib}, \boldsymbol{\theta})$  = fiber stress (uniaxial), and  $\boldsymbol{\varepsilon}^{fib}$  = fiber strain (uniaxial). The integrals in Eqs. (4.41) and (4.42) are evaluated using numerical quadrature. Now, the conditional partial derivative of the structure's internal resisting force vector with respect to the material parameter,  $\theta_i$ , can be computed as

$$\left. \frac{\partial \mathbf{r}_{k+1}(\mathbf{q}, \boldsymbol{\theta})}{\partial \theta_i} \right|_{\mathbf{q}=\mathbf{q}_{k+1}} = \mathbf{A} \left\{ \int_{L_{ele}} \mathbf{B}^T \int_{A_{sec}} \mathbf{a} \left. \frac{\partial \sigma_{k+1}^{fib}(\boldsymbol{\varepsilon}^{fib}, \boldsymbol{\theta})}{\partial \theta_i} \right|_{\boldsymbol{\varepsilon}^{fib}=\boldsymbol{\varepsilon}_{k+1}^{fib}} dAdL \right\} \quad (4.43)$$

where  $\left. \frac{\partial \sigma_{k+1}^{fib}(\boldsymbol{\varepsilon}^{fib}, \boldsymbol{\theta})}{\partial \theta_i} \right|_{\boldsymbol{\varepsilon}^{fib}=\boldsymbol{\varepsilon}_{k+1}^{fib}}$  is the history-dependent variation of fiber stress with

respect to the material parameter  $\theta_i$  conditional on the fiber strain remaining fixed.

This conditional partial derivative can be computed by analytically differentiating the material constitutive law of the fiber with respect to  $\theta_i$  ([36-37, 41]).

The procedure for DDM-based FE response sensitivity computation at time step  $(k+1)$  can be summarized as follows. First, the nonlinear FE recursive algebraic

equation shown in Eq. (4.36) is solved iteratively using Newton-Raphson method to find  $\mathbf{q}_{k+1}$ . After convergence of the Newton-Raphson iterative process is achieved for the response of the structure at time step  $(k+1)$ , the right-hand-side of Eq. (4.38) is computed for each material parameter  $\theta_i$  ( $i=1, \dots, n_{\theta}$ ). Then, Eq. (4.38), which is a linear algebraic equation, is solved in one-step for  $\frac{\partial \mathbf{q}_{k+1}}{\partial \theta_i}$ . Once Eq. (4.38) is solved for all the material parameters considered, the displacement-response sensitivity matrix,  $\frac{\partial \mathbf{q}_{k+1}}{\partial \boldsymbol{\theta}^T}$ , is available. Sensitivities of nodal velocity or acceleration response parameters can easily be obtained using Eqs. (4.34)-(4.35).

#### **4.3.5. Proposed algorithm for nonlinear FE model updating using EKF**

Table 4.2 summarizes the proposed algorithm for nonlinear FE model updating using the EKF. The notation was previously defined in Section 3.3.

Table 4.2: Proposed algorithm for nonlinear FE model updating using the EKF

<p>Initialization:</p> <p>Postulate <math>\hat{\boldsymbol{\theta}}_0^+</math> and <math>\hat{\mathbf{P}}_{\boldsymbol{\theta},0}^+</math> where <math>\hat{\boldsymbol{\theta}}_0^+ = E[\boldsymbol{\theta}_0]</math>, <math>\hat{\mathbf{P}}_{\boldsymbol{\theta},0}^+ = E\left[\left(\boldsymbol{\theta}_0 - \hat{\boldsymbol{\theta}}_0^+\right)\left(\boldsymbol{\theta}_0 - \hat{\boldsymbol{\theta}}_0^+\right)^T\right]</math></p> <p>For each time step (<math>k = 0, 1, \dots</math>):</p> <p><u>Prediction:</u></p> <p><math>\hat{\boldsymbol{\theta}}_{k+1}^- = E\left[\boldsymbol{\theta}_{k+1} \mid \mathbf{y}_1, \mathbf{y}_2, \dots, \mathbf{y}_k\right] = \hat{\boldsymbol{\theta}}_k^+</math></p> <p><math>\hat{\mathbf{P}}_{\boldsymbol{\theta},k+1}^- = E\left[\left(\boldsymbol{\theta}_{k+1} - \hat{\boldsymbol{\theta}}_{k+1}^-\right)\left(\boldsymbol{\theta}_{k+1} - \hat{\boldsymbol{\theta}}_{k+1}^-\right)^T \mid \mathbf{y}_1, \mathbf{y}_2, \dots, \mathbf{y}_k\right] = \hat{\mathbf{P}}_{\boldsymbol{\theta},k}^+ + \mathbf{Q}_k</math></p> <p>Run the nonlinear FE time history analysis with <math>\hat{\boldsymbol{\theta}}_{k+1}^-</math> from <math>t = \Delta t</math> to <math>t = (k+1)\Delta t</math> and obtain:</p> <p>Predicted acceleration response: <math>\hat{\mathbf{y}}_{k+1}^-</math></p> <p>Predicted acceleration response sensitivities: <math>\mathbf{C}_{k+1} = \frac{\partial \mathbf{h}_{k+1}(\boldsymbol{\theta}, [\ddot{u}_g]_{k+1})}{\partial \boldsymbol{\theta}^T}</math></p> <p><math>\hat{\mathbf{P}}_{\mathbf{y},k+1}^- = E\left[\left(\mathbf{y}_{k+1} - \hat{\mathbf{y}}_{k+1}^-\right)\left(\mathbf{y}_{k+1} - \hat{\mathbf{y}}_{k+1}^-\right)^T \mid \mathbf{y}_1, \mathbf{y}_2, \dots, \mathbf{y}_k\right] = \hat{\mathbf{P}}_{\boldsymbol{\theta},k+1}^- \mathbf{C}_{k+1}^T</math></p> <p><math>\hat{\mathbf{P}}_{\mathbf{y},k+1}^+ = E\left[\left(\mathbf{y}_{k+1} - \hat{\mathbf{y}}_{k+1}^-\right)\left(\mathbf{y}_{k+1} - \hat{\mathbf{y}}_{k+1}^-\right)^T \mid \mathbf{y}_1, \mathbf{y}_2, \dots, \mathbf{y}_k\right] = \mathbf{C}_{k+1} \hat{\mathbf{P}}_{\boldsymbol{\theta},k+1}^- \mathbf{C}_{k+1}^T + \mathbf{R}_{k+1}</math></p> <p><u>Correction:</u></p> <p>Measure/read the acceleration response of the structure at time step (<math>k+1</math>): <math>\mathbf{y}_{k+1}</math></p> <p><math>\mathbf{K}_{k+1} = \hat{\mathbf{P}}_{\boldsymbol{\theta},k+1}^- \left(\hat{\mathbf{P}}_{\mathbf{y},k+1}^-\right)^{-1}</math></p> <p><math>\hat{\boldsymbol{\theta}}_{k+1}^+ = E\left[\boldsymbol{\theta}_{k+1} \mid \mathbf{y}_1, \mathbf{y}_2, \dots, \mathbf{y}_{k+1}\right] = \hat{\boldsymbol{\theta}}_{k+1}^- + \mathbf{K}_{k+1} \left(\mathbf{y}_{k+1} - \hat{\mathbf{y}}_{k+1}^-\right)</math></p> <p><math>\hat{\mathbf{P}}_{\boldsymbol{\theta},k+1}^+ = E\left[\left(\boldsymbol{\theta}_{k+1} - \hat{\boldsymbol{\theta}}_{k+1}^+\right)\left(\boldsymbol{\theta}_{k+1} - \hat{\boldsymbol{\theta}}_{k+1}^+\right)^T \mid \mathbf{y}_1, \mathbf{y}_2, \dots, \mathbf{y}_{k+1}\right]</math></p> <p><math>= (\mathbf{I} - \mathbf{K}_{k+1} \mathbf{C}_{k+1}) \hat{\mathbf{P}}_{\boldsymbol{\theta},k+1}^- (\mathbf{I} - \mathbf{K}_{k+1} \mathbf{C}_{k+1})^T + \mathbf{K}_{k+1} \mathbf{R}_{k+1} \mathbf{K}_{k+1}^T</math></p>	<p>Initial estimates of parameter vector and parameter covariance matrix</p> <p><i>A priori</i> parameter estimate</p> <p><i>A priori</i> parameter covariance matrix</p> <p>Estimated parameter-response cross covariance matrix</p> <p>Estimated response covariance matrix</p> <p>Kalman gain matrix</p> <p><i>A posteriori</i> parameter estimate</p> <p><i>A posteriori</i> parameter covariance matrix</p>
---	--

#### 4.4. Verification case studies

Two numerical examples are provided to verify the proposed nonlinear FE model updating framework. For each example, first the earthquake response of a realistic structure is simulated using the structural FE modeling and analysis method described above. The FE modeling and response simulation are performed using the structural analysis software framework OpenSees [44] assuming a set of predefined



realistic material parameter values considered as the true parameter values. The material parameters are later treated as unknown and are identified in the estimation phase. In these examples, only physical parameters characterizing the nonlinear material constitutive laws defined in the FE model are estimated. The EKF is implemented in MATLAB [45] and interfaced with OpenSees for FE response and response sensitivity computations. A suite of real ground motion records with varying intensity are used for the nonlinear response history simulations. The simulated acceleration response time histories are then artificially contaminated by numerical noise and used as the measured response data in the estimation phase, in which the proposed nonlinear FE model updating framework described above is employed to estimate the material parameters. The performance of the proposed framework is then evaluated and discussed.

#### **4.4.1. Example #1: steel cantilever pier**

The first benchmark structure is a 6.0 m cantilever steel column, with a built-up box section. Representing the pier of a small bridge, the column carries a lumped mass of  $100 \times 10^3$  kg at the top. The structural geometry is presented in Figure 4.2(a). The section design satisfies the compact section requirements [46] and it is therefore assumed that the section retains its full capacity without any strength degradation or softening behavior. Using fiber-section displacement-based beam-column elements, a 2D model of the structure is developed in OpenSees. Figure 4.2(b) shows details of the

FE model including the discretization of the column and the fiber discretization of the cross-section. The FE model has 51 degrees of freedom. The steel fibers are modeled using the modified Giuffr -Menegotto-Pinto material constitutive model [47]. This is a uniaxial material model, in which the stress-strain relation is defined using smooth curved shaped hysteretic loading and unloading branches as illustrated in Figure 4.3. In general, this material model is governed by eight time-invariant parameters, five of which are empirical parameters controlling the curvature of the hysteretic loops (i.e., the Baushinger effect) and the isotropic hardening and are assumed as known constants in this problem. Treated as unknown physical material parameters to be identified, the other three material parameters are  $\sigma_y$  = initial yield strength,  $E$  = elastic modulus, and  $b$  = strain hardening ratio, as shown in Figure 4.3. The true (exact) values of these material parameters are taken as  $\sigma_y^{true} = 250\text{MPa}$ ,  $E^{true} = 200\text{GPa}$ , and  $b^{true} = 0.1$ . Tangent stiffness-proportional Rayleigh damping [43] is used to model the damping characteristics by defining a damping ratio of 2 percent for the first mode.

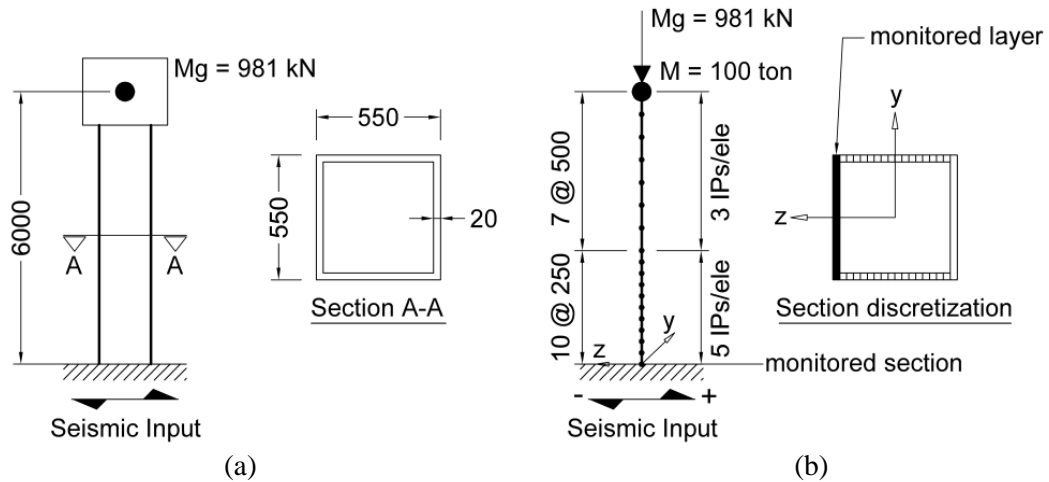


Figure 4.2: (a) Cantilever steel column with box section, (b) details of the developed FE model (IP: integration point, ele: element, 1 ton = 1000 kg, length unit: mm).

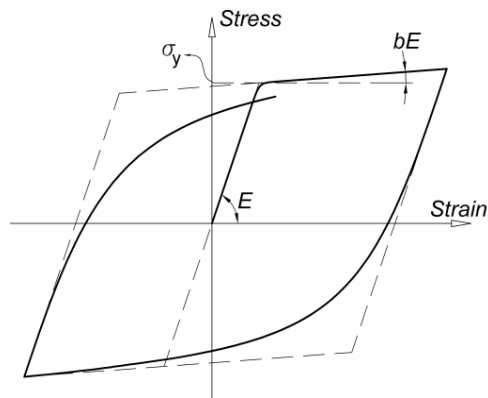


Figure 4.3: Modified Giuffrè-Menegotto-Pinto uniaxial material constitutive model for steel.

Five different earthquake ground motions defined in Table 4.3 and obtained from [48] are selected for the nonlinear time history analyses. Figure 4.4 shows the acceleration time histories of these ground motions. Each nonlinear analysis is started by first applying the gravity loads quasi-statically. Then, the nonlinear time history analysis is performed using the Newmark average acceleration method [43] to integrate the equations of motion using a time step of  $\Delta t = 0.02 \text{ sec}$ . The Newton-

Raphson method is employed to solve iteratively the nonlinear dynamic equilibrium equations at each time step.

Table 4.3: Selected earthquake ground motions.

Motion name	Earthquake (M)	Station / Component	PGA (g)
<i>EQ1</i>	1989 Loma Prieta (M6.9)	Corralitos - Eureka Canyon Road / 90°	0.48
<i>EQ2</i>	1989 Loma Prieta (M6.9)	Los Gatos - Lenihan Dam / 0°	0.45
<i>EQ3</i>	1994 Northridge (M6.7)	14145 Mulholland Dr., Beverly Hills / N09E	0.44
<i>EQ4</i>	1994 Northridge (M6.7)	Castaic - Old Ridge Route / 90°	0.57
<i>EQ5</i>	1994 Northridge (M6.7)	600 E. Grand Ave., San Gabriel / S90W	0.24

Note: all records are sampled at 50 Hz

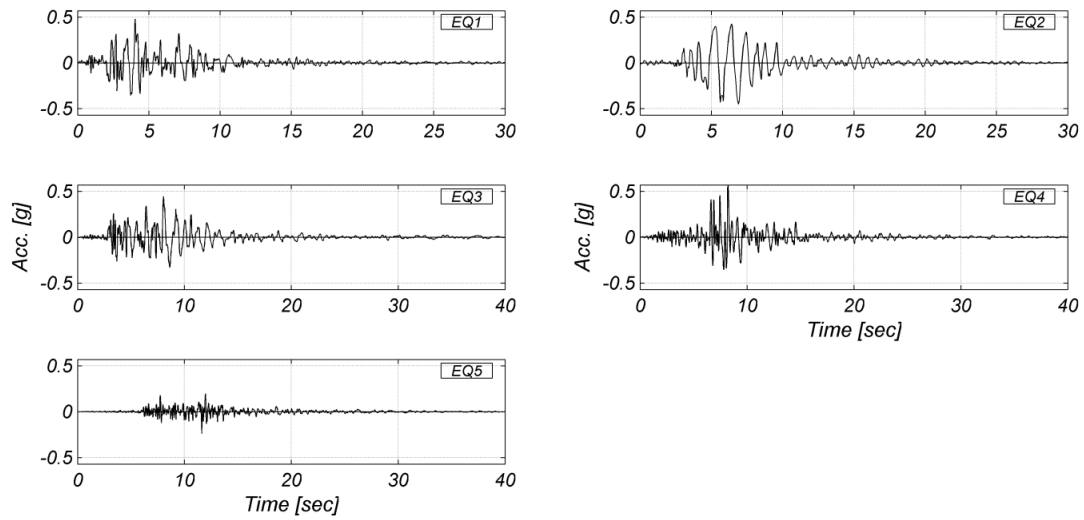


Figure 4.4: Time histories of the selected earthquake ground motions.

### **Structural response simulation**

In simulating the response of the structure, the FE model is analyzed for each earthquake ground motion separately. The acceleration response time history of the column top ( $\ddot{u}_{top}$ ) – in the direction of the seismic input – is obtained, artificially polluted by measurement noise, and used as the measured response in the estimation phase. In the real world, the measurement noise is caused by various sources such as electrical line (sensor cable) noise and sensor and data acquisition system errors. Consequently, the noise level can be approximately assessed by evaluating the noise sources. In this problem, the measurement noise superimposed on the simulated acceleration response time history is modeled as a zero-mean Gaussian white noise with two different amplitude levels: 1% and 10% root mean square (RMS) noise-to-signal ratio (NSR). Therefore, the noise standard deviation (or RMS) for the two cases is  $10^{-2} \times \text{RMS}([\ddot{u}_{top}])$  and  $10^{-1} \times \text{RMS}([\ddot{u}_{top}])$ , respectively. Although the RMS NSR of 10% is unrealistically high, it is applied to investigate the performance and robustness of the proposed estimation framework with respect to the measurement noise level.

### **Estimation of material parameters**

The FE model of the structure employed in the proposed estimation process is the same as the one used for the response simulation – i.e., FE modeling uncertainty is not considered in this basic study. The measurement noise on the seismic input is not considered here as well and the same input ground motion time histories are used in the response simulation and parameter estimation phases. As presented in Table 4.2,

the parameter estimation algorithm requires the setting of a number of variables, i.e.  $\hat{\boldsymbol{\theta}}_0^+$ ,  $\hat{\mathbf{P}}_{\boldsymbol{\theta},0}^+$ ,  $\mathbf{Q}_k$ , and  $\mathbf{R}_{k+1}$ . Below, each of these variables are addressed separately.

Initial estimate of mean vector and covariance matrix of material parameters:  $\hat{\boldsymbol{\theta}}_0^+$  is the vector of initial estimates of the material parameters, which are selected as  $\sigma_{y_0} = 0.80\sigma_y^{true}$ ,  $E_0 = 0.75E^{true}$ , and  $b_0 = 1.50b^{true}$ . The covariance matrix of the initial estimates of the material parameters,  $\hat{\mathbf{P}}_{\boldsymbol{\theta},0}^+$ , quantifies the uncertainty in the initial estimates of the parameters. Here  $\hat{\mathbf{P}}_{\boldsymbol{\theta},0}^+$  is defined as a diagonal matrix, which means that initial estimates of the various material parameters are statistically uncorrelated. The diagonal entries of  $\hat{\mathbf{P}}_{\boldsymbol{\theta},0}^+$  – or the initial estimate variances – are  $(p\sigma_{y_0})^2$ ,  $(pE_0)^2$ , and  $(pb_0)^2$ , where  $p = 0.25$  is the coefficient of variation of the initial parameter estimates. As  $p$  increases, there is more uncertainty (i.e., less confidence) in the initial estimates of the material parameters, and therefore the EKF (at the early time steps) relies more on the information obtained from the response measurements than on the prior information provided by  $\hat{\boldsymbol{\theta}}_0^+$ . Higher variances of the initial parameter estimates may accelerate the convergence rate of the parameter estimation process, but may adversely affect its stability ([13-14, 28]). The effect of  $\hat{\mathbf{P}}_{\boldsymbol{\theta},0}^+$  on the estimated parameters diminishes progressively as the recursive estimation process advances in time and more information is gathered from the response measurements [16].

Process noise covariance matrix: Assuming that the second order statistics of the process noise,  $\boldsymbol{\gamma}$  – see Eq. (4.26) – are time-invariant, the process noise covariance matrix is defined as  $\mathbf{Q}_k = \mathbf{Q} = E(\boldsymbol{\gamma}\boldsymbol{\gamma}^T)$ . The covariance matrix  $\mathbf{Q}$  is a diagonal matrix whose diagonal entries are the process noise variances associated with the parameters to be estimated. Here, these variances are selected as  $(q\sigma_{y_0})^2$ ,  $(qE_0)^2$ , and  $(qb_0)^2$ , where  $q = 10^{-4}$ , i.e., the RMS of each component of the process noise is taken as 0.01 percent of the initial estimate of the corresponding material parameter. Increasing the process noise variance serves to increase the estimation uncertainty and increase the relative importance attributed by the KF to the response measurements,  $\mathbf{y}_{k+1}$ , versus the latest prior estimate of the parameters,  $\hat{\boldsymbol{\theta}}_{k+1}^-$  [28].

Measurement noise covariance matrix: In this first verification example, the measurement vector,  $\mathbf{y}_{k+1}$ , and measurement noise vector,  $\mathbf{v}_{k+1}$ , are scalar quantities (single entry vectors) and therefore the covariance matrix  $\mathbf{R}_{k+1}$  of the measurement noise is a scalar (single entry matrix) corresponding to the variance of the measurement noise associated with the acceleration response of the pier top. The variance of the measurement noise is also assumed to be time-invariant, i.e.,  $R_{k+1} = R$ . In this problem, as mentioned earlier, an artificial measurement noise with two predefined amplitude (1% and 10% RMS NSR) is superimposed on the simulated response. In a real world application, however, the statistics of the measurement noise are unknown; but can be approximately estimated by quantifying the noise sources. Here, the amplitude of the measurement noise is pretended to be unknown and the

measurement noise RMS is estimated as  $RMS(v)=10^{-1.5} \times RMS([y])=0.032 \times RMS([y])$ , where  $[y]$  is the noisy acceleration response time history of the column top; therefore,  $R=10^{-3} \times (RMS([y]))^2$ .

As recognized by many researchers (e.g., [28, 49, 50]), the process and measurement noise covariance matrices ( $\mathbf{Q}$  and  $\mathbf{R}$ , respectively) may have a significant influence on the performance and convergence of the KF estimation process and an appropriate selection of  $\mathbf{Q}$  and  $\mathbf{R}$  is an important issue. Further systematic studies to investigate the effects of  $\mathbf{Q}$  and  $\mathbf{R}$  on the stability and convergence properties of the proposed nonlinear FE model updating framework are needed, but not within the scope of this chapter.

### **Material parameter estimation results**

Figure 4.5 shows the time histories of the *a posteriori* estimates of the material parameters – normalized by the corresponding true parameter values – obtained for *EQI* for the two measurement noise levels considered. Figure 4.6 shows the time histories of the *a posteriori* coefficients of variation (C.O.V.) of these material parameters. These two figures show that all three material parameter are recursively updated from their initial to their final estimates, which are converged to the corresponding true parameter values with very small coefficients of variation, for both measurement noise levels considered. The estimate of the elastic modulus,  $E$ , starts updating from the very beginning of the excitation and converges to the true value ( $E^{true}$ ) much earlier than the other two parameters, since the response of the structure



depends on the stiffness related material parameter,  $E$ , from the start (initial linear elastic response behavior). In contrast, the estimates of the mean and C.O.V. of the yield strength,  $\sigma_y$ , and strain hardening ratio,  $b$ , start with a flat stage followed by a period of rapid change which initiates after the structure has become nonlinear and its measured response sufficiently sensitive to (and informative about) these parameters. Notice that, expectedly, the strength related material parameter  $\sigma_y$  starts updating earlier than the post-yield related material parameter,  $b$ . To support this explanation, Figure 4.7 shows the time histories of the pier top normalized FE acceleration response sensitivities to the three material parameters, obtained using the DDM during the estimation process for *EQ1*. Comparing this figure with Figures 4.5 and 4.6 clearly shows that the estimates of the mean and C.O.V. of  $\sigma_y$  and  $b$  start updating when the pier top acceleration response becomes sensitive to these parameters. Figure 4.7 also shows that the pier top acceleration response is relatively much less sensitive (by a factor of 5) to parameter  $b$  than to parameter  $\sigma_y$ , which explains why updating starts and converges earlier for the strength related parameter  $\sigma_y$  than for the post-yield related parameter  $b$ . Figures 4.5 and 4.6 also display the effect of the measurement noise level. When the noise level is low (i.e., RMS NSR = 1%), the estimation procedure smoothly updates the parameters and reduces the associated C.O.V. as time advances. In the case of high-level noise (i.e., RMS NSR = 10%) the estimates of the parameters fluctuate before convergence. It should be noted that these figures show

only the first 15 seconds of the time histories, since the estimation results do not change after this time.

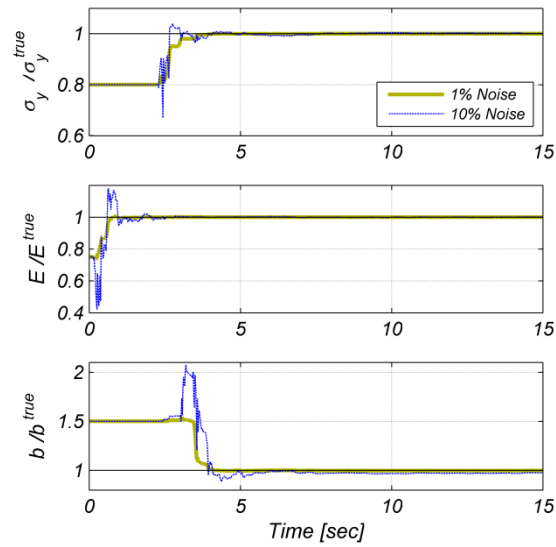


Figure 4.5: Time histories of *a posteriori* material parameter estimates for *EQ1*.

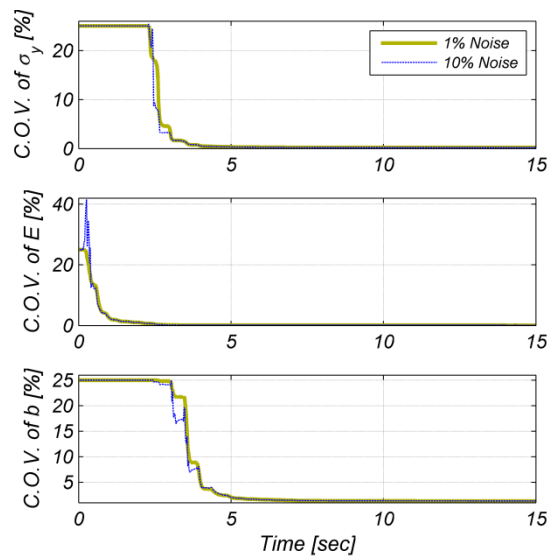


Figure 4.6: Time histories of *a posteriori* C.O.V.s (%) of material parameters for *EQ1*.

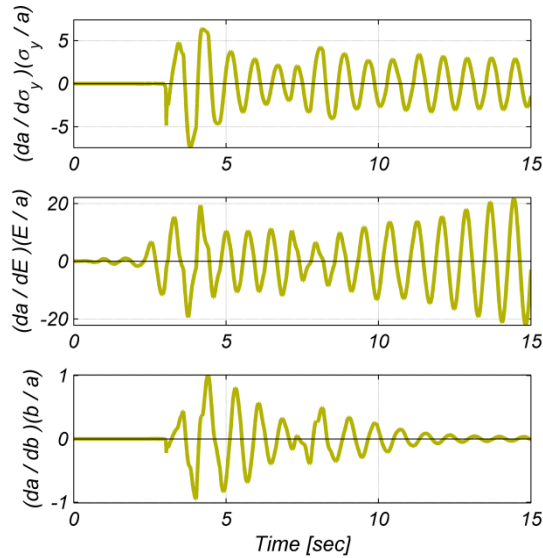


Figure 4.7: Time histories of the normalized FE acceleration response sensitivities to the three material parameters, obtained using the DDM during the estimation process for  $EQI$  (in the case of 10% RMS NSR). In this figure,  $\mathbf{a} = \ddot{u}_{top}$  = acceleration response of the column top.

Figures 4.8 to 4.11 compare structural response obtained at the simulation stage (i.e., true response) with that obtained from the FE model updated using the material parameters estimated based on  $EQI$  for the case of 10% RMS NSR. The comparison is performed at different levels from the global structural level to the local section and fiber levels. To compute the structural response using the updated FE model, the last 100 estimated values for each material parameter, which have minor differences, are averaged to obtain the *final estimation* of each parameter. Then, the FE model is updated using these final material parameter estimates and rerun to obtain the estimated structural response. Figure 4.8 compares the simulated (true) and estimated acceleration response time histories of the pier top. Figure 4.9 compares the simulated (true) and estimated pier base shear ( $V_b$ ) – normalized by the top (i.e., bridge deck) weight ( $W = 981$  kN) supported by the pier – versus pier drift ratio – i.e., displacement

at the pier top normalized by the pier height. The section level simulated (true) and estimated responses are compared in Figure 4.10, which shows the normalized moment-curvature response of the pier base section – see Figure 4.2(b). The section moments ( $M$ ) are normalized by the corresponding section nominal yield moment ( $M_y$ ) and the curvatures ( $\phi$ ) by the section height ( $H = 550\text{mm}$ ).

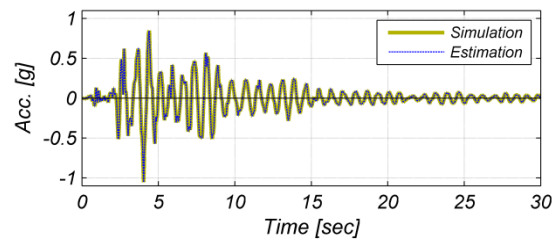


Figure 4.8: Comparison of simulated (true) relative acceleration response time history of the pier top with estimated response after FE model updating for  $EQI$  with 10% RMS NSR.

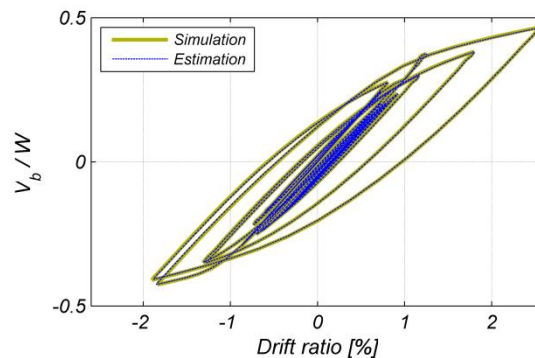


Figure 4.9: Comparison of simulated (true) normalized base shear vs. drift ratio with estimated response after FE model updating for  $EQI$  with 10% RMS NSR.

Finally, Figure 4.11 compares the simulated (true) and estimated normalized stress-strain responses of the monitored extreme fiber (or layer) at the pier base section – see Figure 4.2(b). All these figures show excellent agreement between the simulated (true) and estimated structural responses. The structural response estimated using the

FE model based on the initial material parameter estimates ( $\hat{\theta}_0^+$ ), not shown here, differs significantly from the true structural response. Therefore, it can be concluded that the proposed framework has successfully updated the FE model by steering the crude initial estimates of the material parameters to the true values.

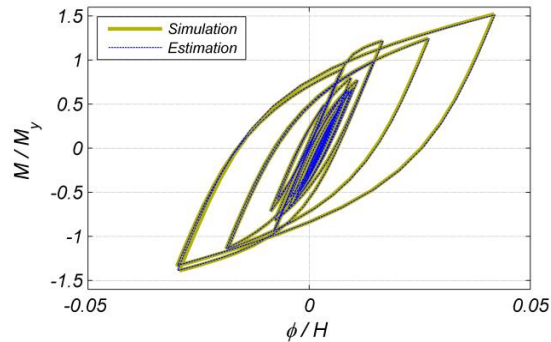


Figure 4.10: Comparison of simulated (true) moment-curvature response of pier base section with estimated response after FE model updating for *EQI* with 10% RMS NSR.

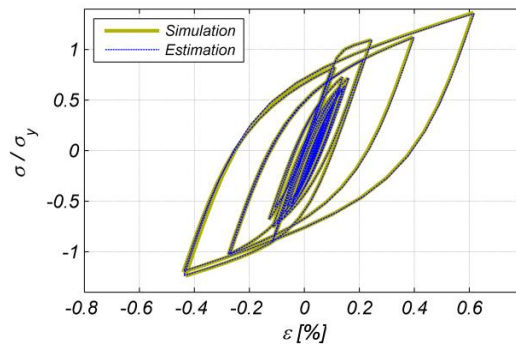


Figure 4.11: Comparison of simulated (true) fiber stress-strain response at monitored fiber in pier base section with estimated response after FE model updating for *EQI* with 10% RMS NSR.

Table 4.4 summarizes the material parameter estimation results normalized with respect to the true parameter values for all five seismic input motions – see Table 4.3 and Figure 4.4 – and the two levels of measurement noise. As mentioned earlier, the *final estimations* are obtained by averaging the last 100 estimated parameters. This table also reports in the last two columns the ductility demands, at the structure and fiber levels, obtained from the simulated (true) and estimated structural responses; the latter is obtained from the FE model updated using the final material parameter estimates. The structure-level displacement ductility demand is defined as the peak relative displacement response of the pier top normalized by yield displacement of the column pier. The fiber-level strain ductility demand is defined as the peak fiber strain response normalized by the yield strain ( $\varepsilon_y = \sigma_y / E$ ). Ductility demands provide a simple way to quantify the peak level of response nonlinearity experienced by a structure. A ductility demand, however, does not provide any information on the number and shapes of the hysteretic cycles of response or the hysteretic energy dissipated in the structure.

Table 4.4: Material parameter estimation results for all earthquake input motions and noise levels in Example 1.

Motion name	Noise level (RMS NSR)	<i>Final estimations</i>			Ductility demand (Simulated) Estimated			
		$\sigma_y / \sigma_y^{true}$	$E / E^{true}$	$b / b^{true}$	Structure level		Fiber level	
<i>EQ1</i>	1%	1.000	1.000	0.998	(2.81)	2.81	(4.93)	4.92
	10%	0.999	0.997	0.980		2.79		4.93
<i>EQ2</i>	1%	1.001	1.000	0.999	(5.42)	5.41	(8.23)	8.23
	10%	1.003	0.998	1.006		5.40		8.20
<i>EQ3</i>	1%	1.000	1.000	1.003	(3.40)	3.40	(5.76)	5.75
	10%	0.997	1.001	1.004		3.40		5.77
<i>EQ4</i>	1%	0.998	1.000	1.011	(2.21)	2.21	(3.82)	3.82
	10%	0.993	0.999	1.005		2.22		3.84
<i>EQ5</i>	1%	0.944	1.000	1.504	(0.71)	0.75	(0.69)	0.73
	10%	1.136	1.000	1.510		0.63		0.61

The material parameter estimation results presented in Table 4.4 reveal that the modulus of elasticity  $E$  is accurately estimated in all cases. In contrast, the strength and post-yield related material parameters,  $\sigma_y$  and  $b$  respectively, are only estimated correctly when the ductility demand is high enough, i.e., when the level of nonlinear behavior experienced by the structure is sufficient. This means that in a real world application, a strong enough earthquake base excitation is required to correctly estimate the parameters governing the strength and post-yield (monotonic and cyclic) behavior of the material model used in the FE model of the structure. When the earthquake excitation is too low, the measured response of the structure contains no information to update these parameters; in other words, these parameters are not identifiable based on the information contained in the measured structural response. Table 4.4 also shows that the estimated model is able to accurately capture the peak values of ductility demand both at structure and fiber levels, except for *EQ5*, for which the response remain linear elastic. It should be noted that in the latter case, the yield

strength ( $\sigma_y$ ) is not estimated correctly; therefore, the estimated yield displacement of column pier and yield strain of fibers are not accurate.

To study the efficiency of the DDM relative to the FDM for computing the FE response sensitivities in the proposed parameter estimation framework, the parameter estimation process is repeated for the case of *EQI* and 10% RMS NSR. The problem setup and initializations are as before. An identical pier top measured acceleration response – with identical measurement noise realization – is used for the comparison. Figure 4.12 compares the time histories of the *a posteriori* material parameter estimates – normalized by the true parameter values – for the DDM and the forward FDM based on two values of the parameter step size. For a specific material parameter ( $\theta_i$ ), the step size is defined as the relative amplitude of the perturbation of the parameter value (i.e.,  $\Delta\theta_i/\theta_i$ ) which is used to estimate the corresponding FE response sensitivity. Running the estimation problem using the DDM for this problem was found to be about four times faster than when using the FDM on a Dell Optiplex 980 desktop workstation with 8GB RAM.



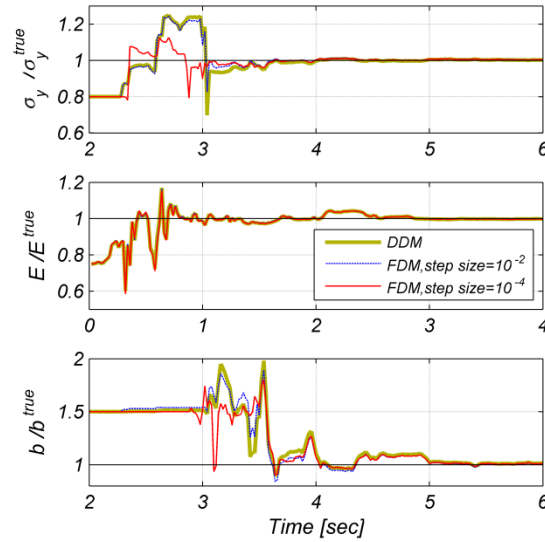


Figure 4.12: Time histories of *a posteriori* material parameter estimates for *EQI* and 10% RMS NSR when FE response sensitivities are computed using DDM and FDM (time histories are shown for a short time window for more clarity).

To study the effect of initial estimates of the material parameters on the performance of the parameter estimation framework, the parameter estimation process is repeated for the case of *EQI* and 1% RMS NSR with five different initial estimates as shown in Table 4.5. All the other filter parameters are the same as before. To better compare the performance of the parameter estimation process in these five cases, the same measured acceleration time history is used for all the cases, i.e., the measurement noise has the same realization in all the cases. Figure 4.13 shows the time histories of the *a posteriori* estimates of the material parameters normalized by the corresponding true parameter values. Similarly, Figure 4.14 shows the first 6 seconds of the time history of the normalized posteriori estimates of the material parameters. Figure 4.15 and Figure 4.16 show the time histories of the *a posteriori* coefficients of variation (C.O.V.) of these material parameters. As can be seen from these figures, for all the

five considered cases, the parameter estimation process successfully estimated the correct values of the material parameters.

Table 4.5: Different sets for the initial estimates of the material parameters

	Initial estimates			Initial estimate RMS Error
	$\sigma_{y0} / \sigma_y^{true}$	$E_0 / E^{true}$	$b_0 / b^{true}$	
Set 1	1.15	1.5	1.2	32.2%
Set 2	0.5	1.2	1.5	42.4%
Set 3	0.7	1.7	0.6	49.7%
Set 4	0.4	0.8	1.6	50.3%
Set 5	1.6	0.4	1.4	54.2%

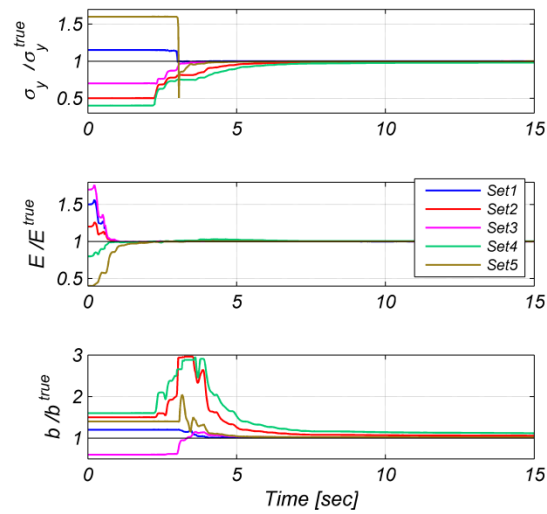


Figure 4.13: Time histories of *a posteriori* material parameter estimates for *EQ1* for five different initial estimates of the material parameters.

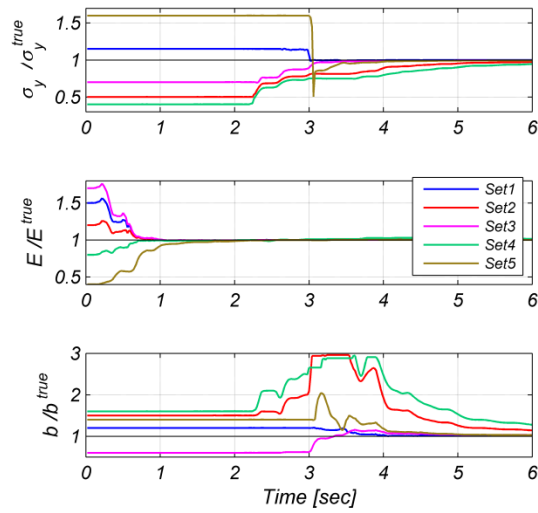


Figure 4.14: Time histories of *a posteriori* material parameter estimates for *EQI* for five different initial estimates of the material parameters – zoom on the first 6 seconds.

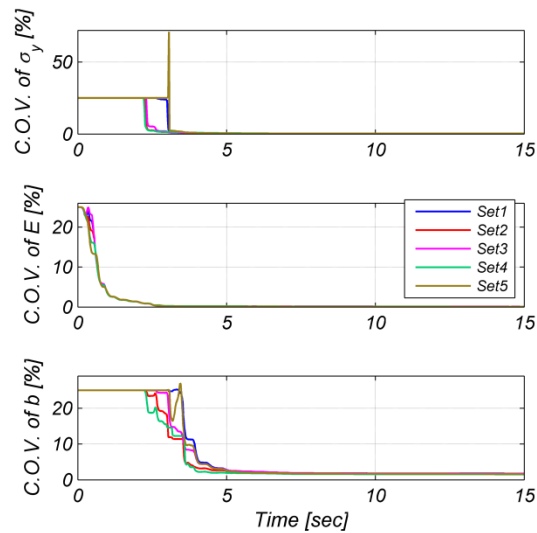


Figure 4.15: Time histories of *a posteriori* C.O.V.s (%) of material parameters for *EQI* for five different initial estimates of the material parameters.

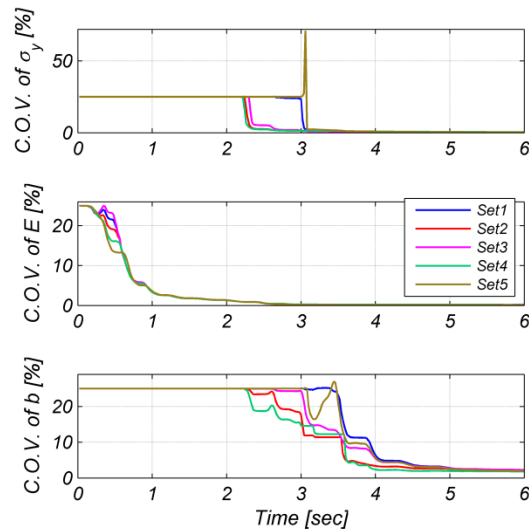


Figure 4.16: Time histories of *a posteriori* C.O.V.s (%) of material parameters for *EQI* for five different initial estimates of the material parameters – zoom on the first 6 seconds.

#### 4.4.2. Example #2: three-story three-bay 2D steel moment frame

The second benchmark structure is the three-story special moment resisting steel frame building designed for the FEMA/SAC project (LA model, pre-Northridge design) [51]. As in the first example, a 2D FE model is developed in OpenSees using fiber-section displacement-based beam-column elements with 348 degrees of freedom. Figure 4.17 shows details of this FE model including the FE mesh discretization, the nodal masses, and the gravity loads. The steel fibers are modeled again using the modified Giuffré-Menegotto-Pinto material constitutive model. Since the steel grades of the beams and columns are different, two steel material models are used in the FE model of the structure for a total of  $2 \times 3 = 6$  unknown time-invariant material parameters to be estimated from input-output data using the proposed FE model parameter estimation framework. The true (exact) values assumed for these six

material parameters are reported in Table 4.6. To model the damping characteristics of the structure (beyond material hysteretic energy dissipation), mass and tangent stiffness proportional Rayleigh damping is used and calibrated for a damping ratio of 2% at the first and second modes of FE structural model ( $T_1 = 1.00\text{sec}$ ,  $T_2 = 0.33\text{sec}$ ). The same five earthquake ground motion records as in the first example are used. The FE model is subjected to the same type of analyses as in the previous example.

Table 4.6: True material parameter values used for Example 2.

Material parameter	Columns	Beams
$\sigma_y^{true}$	350 MPa	250 MPa
$E^{true}$	200 GPa	200 GPa
$b^{true}$	0.04	0.08

### **Structural response simulation**

The nonlinear dynamic response of the building subjected to uniform earthquake base excitation is computed from the FE model developed. The obtained acceleration response time histories at the three floors of the building at the north column location (see Figure 4.17) are artificially polluted by measurement noise to simulate the measured response of the building. As in the previous example, the superimposed measurement noise is modeled as a zero-mean Gaussian white noise of two different levels: 1% and 10% RMS NSR.

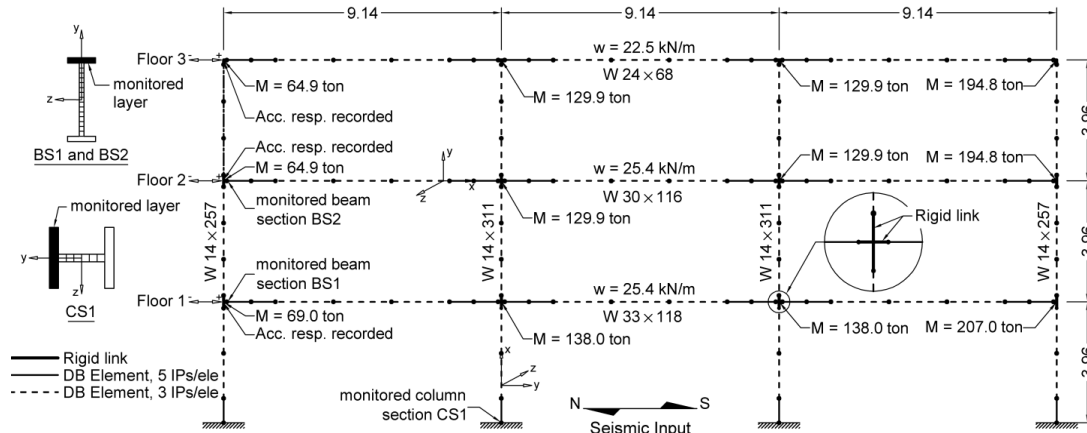


Figure 4.17: Details of 2D FE model of three-story three-bay steel moment frame (DB Element: displacement-based element, IP: Integration point, ele: element, CS1: column section #1, BS1 and BS2: beam sections #1 and #2, 1 ton = 1000 kg, length unit: m).

### Estimation of material parameters

The parameter estimation phase is based on the same FE model of the building structure as the one used to simulate the earthquake response and the noiseless input data and corresponding simulated noisy output data for each of the five ground motion records defined in Table 4.3 and Figure 4.4. The setting of the initial estimates of the material parameters and other variables of the parameter estimation algorithm is addressed below.

Initial estimate of mean vector and covariance matrix of material parameters: Table

4.7 reports the initial estimates of the material parameters, which define the  $\hat{\theta}_0^+$  vector.

The covariance matrix of the initial estimates of the material parameters,  $\hat{\mathbf{P}}_{\theta,0}^+$ , is a diagonal matrix whose diagonal entries are the individual variances of the initial parameter estimates, which are computed assuming a constant coefficient of variation of 0.25 as in Example 1.

Table 4.7: Initial estimates of the material parameters used for Example 2.

Material parameter	Columns	Beams
$\sigma_{y_0} / \sigma_y^{true}$	0.9	0.8
$E_0 / E^{true}$	0.8	0.8
$b_0 / b^{true}$	1.5	0.5

Process noise covariance matrix: Similar to the previous example, the process noise covariance matrix,  $\mathbf{Q}$ , is a diagonal matrix whose diagonal entries are  $(q\sigma_{y_0}^{col})^2$ ,  $(qE_0^{col})^2$ ,  $(qb_0^{col})^2$ ,  $(q\sigma_{y_0}^{beam})^2$ ,  $(qE_0^{beam})^2$ , and  $(qb_0^{beam})^2$ , where  $q = 10^{-4}$ , i.e., the RMS of each component of the process noise is taken as 0.01 percent of the initial estimate of the corresponding material parameter.

Measurement noise covariance matrix: The covariance matrix  $\mathbf{R}$  is taken as a diagonal matrix,  $\mathbf{R} = [R_{ii}]$  ( $i = 1, \dots, n_y$ ), which means that the individual measurement noises are assumed statistically uncorrelated. The  $i^{\text{th}}$  diagonal entry of  $\mathbf{R}$ ,  $R_{ii}$ , represents the variance of the individual measurement noise,  $v_i$ , corresponding to the  $i^{\text{th}}$  measured response. The amplitudes of the measurement noises are pretended to be unknown and taken as  $\text{RMS}(v_i) = r \times \text{RMS}([y_i])$ , where  $[y_i]$  denotes the time history of the  $i^{\text{th}}$  measured response, which is the noisy acceleration response of the  $i^{\text{th}}$  floor of the building at the north column location; thus,  $R_{ii} = r^2 \times (\text{RMS}([y_i]))^2$ . Two values are considered for  $r$ , namely  $r = 10^{-1.5} = 0.032$  and  $r = 10^{-1} = 0.1$ . As will be shown below, the second choice for  $r$  improves the performance of the parameter estimation procedure when the NSR is high.

### **Material parameter estimation results**

The time histories of the *a posteriori* estimates of the six material parameters – normalized by the corresponding true parameter values – obtained for *EQ2* are shown in Figure 4.18. Figure 4.19 presents the time histories of the *a posteriori* C.O.V. of these material parameters. Only the first 20 seconds of the time histories are shown in these figures, since the estimation results do not change after this time. Similar to the previous example, the estimates of the elastic moduli of both the beams and columns start updating from the very beginning of the excitation. However, the other parameters ( $\sigma_y$  and  $b$  for beams and columns), which characterize the nonlinear behavior of the beam and column material models, start updating after the structure starts yielding (during the strong phase of the ground motion excitation), when the parameters become identifiable.

Figure 4.18 also shows that the material parameter estimation accuracy deteriorates in the presence of high NSR. Other researchers (e.g., [16-18, 52]) also report the adverse effect of increasing measurement noise on parameter identification using the EKF. The estimated elastic moduli of beams and columns, however, are less sensitive to the measurement noise than the other material parameters as seen in Figures 4.14 and 4.15. This is due to the fact that the elastic moduli of the beams and columns have a strong influence on the structural response, which therefore is highly sensitive to the variations of these parameters and contains dense information about  $E$ . The relatively high sensitivity of the acceleration response measurements to the



beam and column elastic moduli reduces the sensitivity of the estimated values of elastic moduli of beams and columns to the measurement noise.

Figure 4.18 shows that the choice of  $r = 0.1$  versus  $r = 0.032$  improves overall the parameter estimation performance in the case of high measurement noise intensity (10% RMS NSR). This is due to the fact that when using  $r = 0.032$ , there is a significant difference between the actual measurement noise intensity (i.e., 10% RMS NSR where the signal is defined as the noiseless/true acceleration response) and the noise intensity assumed in the estimation process (3.2% RMS NSR where the signal is defined as the noisy response measurement). Using  $r = 0.032$  underestimates significantly the measurement noise level, while  $r = 0.1$  corresponds to a more accurate estimation (almost exact) of the actual noise level. As mentioned earlier, the appropriate selection of the process and measurement noise covariance matrices,  $\mathbf{Q}$  and  $\mathbf{R}$  respectively, is an important step influencing the performance of the proposed parameter estimation procedure. This step requires more in-depth investigations, which are beyond the scope of this chapter.

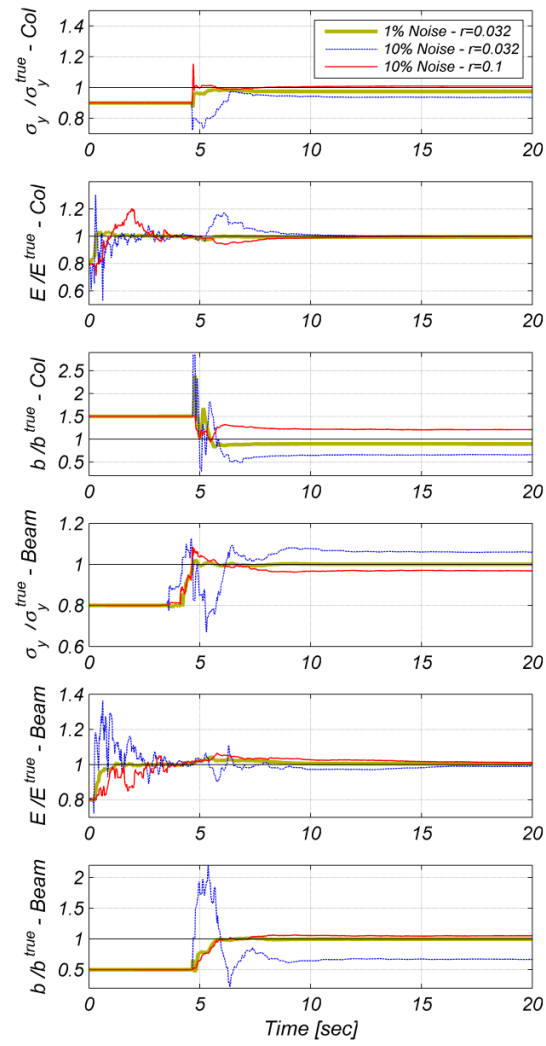


Figure 4.18: Time histories of *a posteriori* material parameter estimates for *EQ2*.

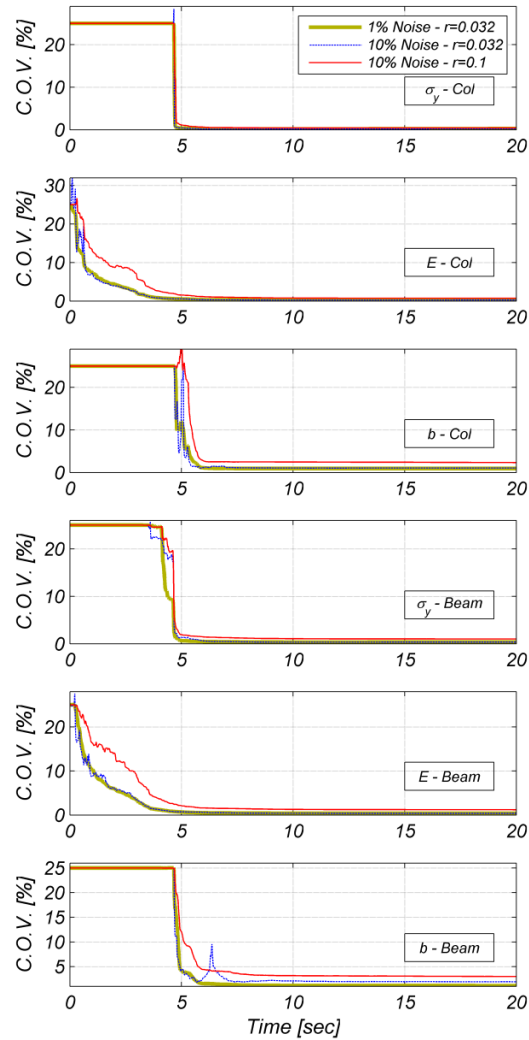


Figure 4.19: Time histories of *a posteriori* C.O.V.s (%) of material parameters for EQ2.

To investigate its performance, the proposed parameter estimation framework was applied for all five seismic input motions (see Table 4.3 and Figure 4.4) and the two levels of measurement noise considered. The estimated material parameters normalized by the corresponding true values are reported in Table 4.8. The ductility demand – obtained from the simulated (true) and estimated structural responses – at the fiber level for one column section and two beam sections – CS1, BS1, and BS2 as shown in Figure 4.17 – are also provided in Table 4.8. The fiber ductility demands in

the column and beam sections considered are larger than in any other column and beam sections in the structure.

Table 4.8: Material parameter estimation results for all earthquake input motions and noise levels in Example 2.

Motion name	Noise level (RMS NSR)	$r$	Final estimations						Fiber level ductility demand (Simulated) Estimated		
			Columns			Beams			CS1	BS1	BS2
			$\sigma_y / \sigma_y^{true}$	$E / E^{true}$	$b / b^{true}$	$\sigma_y / \sigma_y^{true}$	$E / E^{true}$	$b / b^{true}$			
EQ1	1%	0.032	0.996	1.000	1.146	0.998	1.000	1.012	(1.52)	(5.55)	(5.68)
	10%	0.032	1.042	1.001	2.109	1.015	0.997	0.835	1.53	5.56	5.69
	10%	0.1	0.925	1.003	2.962	1.011	0.996	0.810	1.46	5.46	5.58
EQ2	1%	0.032	0.976	0.997	0.890	1.001	1.004	0.995	(8.98)	(12.71)	(12.08)
	10%	0.032	0.931	1.006	0.680	1.062	0.991	0.652	9.18	12.74	12.11
	10%	0.1	1.009	1.002	1.218	0.964	1.005	1.066	9.71	11.86	11.28
EQ3	1%	0.032	0.994	1.099	1.145	0.998	0.928	0.926	(2.79)	(8.83)	(9.64)
	10%	0.032	0.697	1.085	0.593	0.921	0.941	2.449	2.42	8.21	8.96
	10%	0.1	0.970	0.999	1.754	1.002	1.000	1.002	4.34	9.02	9.85
EQ4	1%	0.032	0.983	1.000	1.424	1.020	0.999	0.772	(2.59)	(6.87)	(5.11)
	10%	0.032	0.609	0.999	2.968	1.156	1.014	2.529	2.64	6.73	5.00
	10%	0.1	0.966	1.003	1.670	1.016	0.997	0.682	4.25	6.02	4.48
EQ5	1%	0.032	0.912	0.993	1.503	1.027	1.003	0.436	(0.75)	(1.81)	(1.16)
	10%	0.032	0.966	1.001	1.502	0.986	1.002	1.040	0.81	1.77	1.13
	10%	0.1	1.039	0.998	1.500	1.021	1.001	0.457	0.72	1.84	1.17
									0.77	1.78	1.13

Careful examination of Figure 4.18 and Table 4.8 reveals that a permanent error exists in the estimated strain-hardening ratio ( $b$ ) for columns. Table 4.8 indicates that this estimation error is lowest for EQ2, which produces the highest level of fiber ductility demand in column section CS1 among the seismic inputs considered. Consistent with the conclusions drawn in the first example, successful estimation of the yield strength ( $\sigma_y$ ) and post-yield ( $b$ ) related material parameters requires a

sufficient level of nonlinearity in the response, which is not only measured by the ductility demand, but also the number and extent of hysteretic cycles undergone by the structure. Moreover, if the level of nonlinearity experienced by the structure is not high enough, and the structural response is not very sensitive to some strength or post-yield related material parameter, then the estimation results for such a parameter are sensitive to the measurement noise level. This is illustrated by the estimates of the column strain-hardening ratio obtained for the two measurement noise levels for *EQ1*, *EQ2*, and *EQ3* (see Table 4.8). The results in Table 4.8 also confirm that the choice of  $r = 0.1$  over  $r = 0.032$  for the case of 10% RMS NSR improves the accuracy of the estimated parameters in most cases.

Figure 4.20 compares the simulated (true) acceleration response time histories at all three levels of the frame structure, with their counterparts obtained from the FE model updated using the material parameters estimated for *EQ2* based on 10% RMS NSR and using  $r = 0.1$  (see Table 4.8). Similarly, Figure 4.21 compares the simulated (true) and estimated base shear ( $V_b$ ) versus roof drift ratio hysteretic response for *EQ2*. The match between simulated and estimated global level structural responses in Figure 4.20 and Figure 4.21 is excellent.

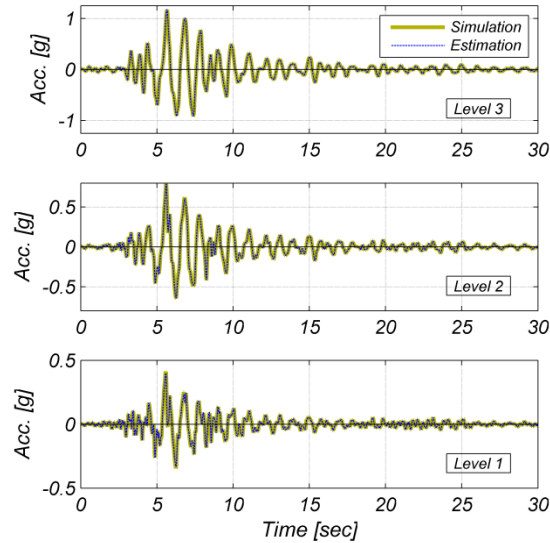


Figure 4.20: Comparison of simulated (true) relative acceleration response time histories at three levels – recorded at the north column location – with estimated response after FE model updating for *EQ2* with 10% RMS NSR and  $r = 0.1$ .

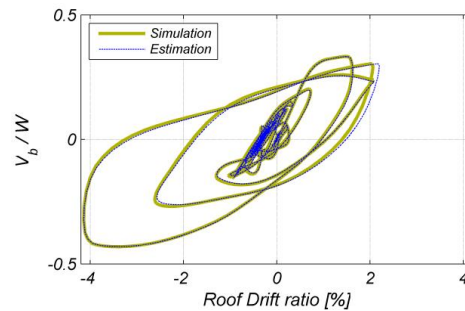


Figure 4.21: Comparison of simulated (true) normalized base shear vs. roof drift ratio with estimated response after FE model updating for *EQ2* with 10% RMS NSR and  $r = 0.1$  – base shear is normalized by  $W = 1591g$  kN.

Finally, simulated (true) and estimated local level responses consisting of the stress-strain responses of the monitored fibers at beam cross-section BS2 and column cross-section CS1 (see Figure 4.17) are compared in Figure 4.22 and Figure 4.23. The match between these simulated and estimated beam local responses (see Figure 4.22) is excellent, while the relatively small differences observed between the simulated and

estimated column local responses (see Figure 4.23) stem from the inaccurate estimation of the strain-hardening ratio for the column material ( $b/b^{true} = 1.218$ ).

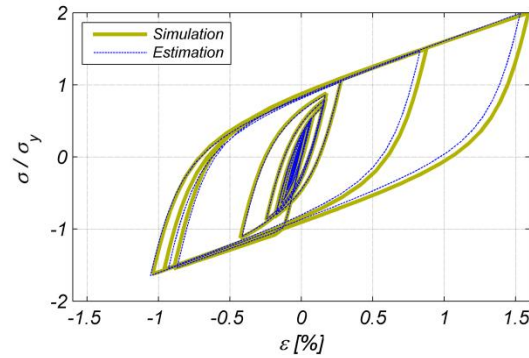


Figure 4.22: Comparison of simulated (true) fiber stress-strain response at monitored fiber in beam cross section BS2 with estimated response after FE model updating for *EQ2* with 10% RMS NSR and  $r = 0.1$ .

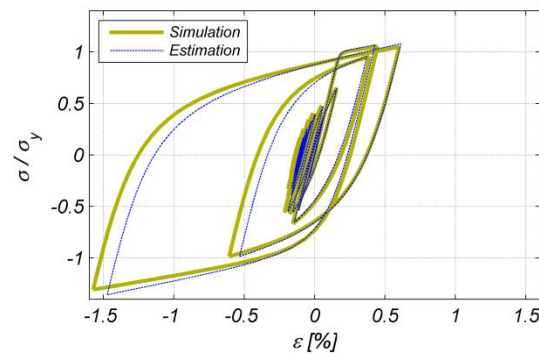


Figure 4.23: Comparison of simulated (true) fiber stress-strain response at monitored fiber in column section CS1 with estimated response after FE model updating for *EQ2* with 10% RMS NSR and  $r = 0.1$ .

## 4.5. Conclusions

This chapter presented a new framework for nonlinear finite element (FE) model updating. In this framework, the extended Kalman filter (EKF) method is used

in combination with state-of-the-art nonlinear structural FE modeling and analysis methods to estimate the time-invariant material parameters used in the FE structural model, including the parameters characterizing the nonlinear material constitutive laws. Using the EKF as a parameter estimation tool requires the computation of the structural response sensitivities to the parameters to be estimated, which is accomplished using the direct differentiation method (DDM). The framework was developed by integrating three advanced analytical tools: nonlinear FE method using fiber-section displacement-based beam-column elements as the modeling and analysis tool, the EKF as the parameter estimation method, and the DDM for FE response sensitivity computation.

The performance of the proposed framework in terms of convergence, accuracy, and robustness was illustrated through two verification examples based on realistic structural designs and numerically simulated response data. For each example, the response of the structure was simulated from the “true” nonlinear FE model and artificially contaminated by measurement noise. The noisy responses were then fed into the proposed nonlinear FE model updating framework and the unknown time-invariant material parameters were estimated. The estimation performance of the proposed framework was found to be very good even in the presence of an unrealistically high level of simulated measurement noise. Careful study of the results obtained for these two examples yields the following important conclusions: (i) For a material parameter to be well identifiable, the measured responses of the structure used in the estimation process must be sensitive enough to that parameter. (ii) A sufficient



level of response nonlinearity is required to identify the material parameters governing the nonlinear aspects of the response. This means that in a real world application, an earthquake excitation strong enough to cause the structure to respond in its nonlinear range of behavior is required to accurately estimate such parameters. Otherwise, if the dynamic excitation is not strong enough, the response of the structure contains no or insufficient information about the material parameters governing its nonlinear behavior. (iii) When the satisfaction of the two aforementioned conditions weakens, the parameter estimation performance becomes increasingly sensitive to the measurement noise.

It is important to mention that the proposed framework can be readily extended to different types of nonlinear finite elements (e.g., force-based beam-column, plate, shell, and solid elements) used to model structural and/or geotechnical systems and to FE model parameters not only limited to material parameters, such as geometric and constraint parameters. Furthermore, it can be applied for FE model updating in the context of quasi-static tests performed on structural components, sub-components, and systems, by simply removing the dynamic (inertia and damping) effects in the formulation presented in this chapter.

Further studies are needed to investigate potentially beneficial or detrimental effects of factors such as filter tuning and modeling uncertainty (error) on the performance of the proposed nonlinear FE model parameter estimation framework. Also, in future work, the proposed framework will be applied to experimental data

from a structural specimen subjected to dynamic (earthquake) loading and undergoing nonlinear response behavior.

## **Acknowledgments**

Partial support for this work was provided by the Englekirk structural engineering center board of advisors, teaching assistantships from the Department of Structural Engineering at University of California, San Diego and the researcher assistantship received through my advisor, Professor Joel P. Conte. Chapter 4, in part, is published in the Journal of Earthquake Engineering and Structural Dynamics. It was written by Hamed Ebrahimian, Rodrigo Astroza, and Joel P. Conte, 2015 (DOI: 10.1002/eqe.2532). The dissertation author is the primary investigator and author of this material.

## References

- [1] K. Worden, C. R. Farrar, G. Manson and G. Park, "The Fundamental Axioms of Structural Health Monitoring," *Proceedings of the Royal Society A*, vol. 463, no. 2082, p. 1639-1664, 2007.
- [2] S. W. Doebling, C. R. Farrar, M. B. Prime and D. W. Shevitz, "Damage Identification and Health Monitoring of Structural and Mechanical Systems from Changes in their Vibration Characteristics: A Literature Review," Report LA-13070-MS, Los Alamos, New Mexico, 1996.
- [3] E. P. Carden and P. Fanning, "Vibration Based Condition Monitoring: A Review," *Structural Health Monitoring*, vol. 3, no. 4, p. 355-377, 2004.
- [4] Y. J. Yan, L. Cheng, Z. Y. Wu and L. H. Yam, "Development in Vibration-based Structural Damage Detection Technique," *Mechanical Systems and Signal Processing*, vol. 21, no. 5, p. 2198–2211, 2007.
- [5] J. Juang, *Applied System Identification*, Upper Saddle River, NJ.: Prentice Hall PTR, 1994.
- [6] G. Kerschen, K. Worden, A. F. Vakakis and J. Golinval, "Past, Present and Future of Nonlinear System Identification in Structural Dynamics," *Mechanical Systems and Signal Processing*, vol. 20, p. 505–592, 2006.
- [7] F. M. Hemez and S. W. Doebling, "Review and Assessment of Model Updating for Nonlinear Transient Analysis," *Mechanical Systems and Signal Processing*, vol. 15, no. 1, p. 45–74, 2001.
- [8] R. Omrani, R. E. Hudson, and E. Taciroglu, "Parametric Identification of Nondegrading Hysteresis in a Laterally and Torsionally Coupled Building Using an Unscented Kalman Filter," *ASCE Journal of Engineering Mechanics*, vol. 139, no. 4, p. 452–468, 2013.
- [9] S. G. Shahidi and S. N. Pakzad, "Generalized Response Surface Model Updating Using Time Domain Data," *ASCE Journal of Structural Engineering*, p. A4014001, 2013.
- [10] R. H. Sues, S. T. Mau, and Y.-K. Wen, "Systems Identification of Degrading Hysteretic Restoring Forces," *ASCE Journal of Engineering Mechanics*, vol. 114, no. 5, p. 833–846, 1988.
- [11] A. W. Smyth, S. F. Masri, A. G. Chassiakos, and T. K. Caughey, "On-line Parametric Identification of MDOF Nonlinear Hysteretic Systems," *ASCE Journal of Engineering Mechanics*, vol. 125, no. 2, p. 133-142, 1999.
- [12] J. Lin, R. Betti, A. W. Smyth, and R. W. Longman, "On-line Identification of Non-linear Hysteretic Structural Systems Using a Variable Trace Approach,"

- Earthquake Engineering and Structural Dynamics*, vol. 30, no. 9, p. 1279–1303, 2001.
- [13] M. Hoshiya and E. Saito, "Structural Identification by Extended Kalman Filter," *ASCE Journal of Engineering Mechanics*, vol. 110, no. 12, p. 1757–1770, 1984.
- [14] C. Loh and Y. Tsaur, "Time Domain Estimation of Structural Parameters," *Engineering Structures*, vol. 10, no. 2, p. 95-105, 1988.
- [15] J. Lin and Y. Zhang, "Nonlinear Structural Identification Using Extended Kalman Filter," *Computers & Structures*, vol. 52, no. 4, p. 757–764, 1994.
- [16] C. G. Koh and L. M. See, "Identification and Uncertainty Estimation of Structural Parameters," *ASCE, Journal of Engineering Mechanics*, vol. 120, no. 6, p. 1219–1236, 1994.
- [17] Y. Yang and F. Ma, "Constrained Kalman Filter for Nonlinear Structural Identification," *Journal of Vibration and Control*, vol. 9, p. 1343–1357, 2003.
- [18] J. N. Yang, S. Lin, H. Huang and L. Zhou, "An Adaptive Extended Kalman Filter for Structural Damage Identification," *Structural Control and Health Monitoring*, vol. 13, no. 4, p. 849-867, 2006.
- [19] A. Corigliano and S. Mariani, "Parameter Identification in Explicit Structural Dynamics: Performance of the Extended Kalman Filter," *Computer Methods in Applied Mechanics and Engineering*, vol. 193, no. 36-38, p. 3807–3835, 2004.
- [20] N. Saha and D. Roy, "Extended Kalman Filters using Explicit and Derivative-free Local Linearizations," *Applied Mathematical Modelling*, vol. 33, no. 6, p. 2545-2563, 2009.
- [21] M. Wu and A. W. Smyth, "Application of the Unscented Kalman Filter for Real-time Nonlinear Structural System Identification," *Structural Control and Health Monitoring*, vol. 14, no. 7, p. 971-990, 2007.
- [22] E. N. Chatzi, A. W. Smyth, and S. F. Masri, "Experimental Application of On-line Parametric Identification for Nonlinear Hysteretic Systems with Model Uncertainty," *Structural Safety*, vol. 32, no. 5, p. 326–337, 2010.
- [23] J. Ching, J. L. Beck, and K. A. Porter, "Bayesian State and Parameter Estimation of Uncertain Dynamical Systems," *Probabilistic Engineering Mechanics*, vol. 21, p. 81-96, 2006.
- [24] E. N. Chatzi and A. W. Smyth, "The Unscented Kalman Filter and Particle Filter Methods for Nonlinear Structural System Identification with Non-collocated Heterogeneous Sensing," *Structural Control and Health Monitoring*, vol. 16, no. 1, p. 99-123, 2009.
- [25] S. Eftekhar Azam and S. Mariani, "Dual Estimation of Partially Observed Nonlinear Structural Systems: A Particle Filter Approach," *Mechanics Research*

*Communications*, vol. 46, p. 54-61, 2012.

- [26] J. J. Tsay and J. S. Arora, "Nonlinear Structural Design Sensitivity Analysis for Path Dependent Problems. Part 1: General Theory," *Computer Methods in Applied Mechanics and Engineering*, vol. 81, no. 2, p. 183–208, 1990.
- [27] R. E. Kalman, "A New Approach to Linear Filtering and Prediction Problems," *ASME Journal of Basic Engineering*, vol. 82, p. 34-45, 1960.
- [28] D. Simon, *Optimal State Estimation: Kalman, H Infinity, and Nonlinear Approaches*, Hoboken, N.J.: John Wiley & Sons, Inc., 2006.
- [29] R. S. Bucy and P. D. Joseph, *Filtering for Stochastic Processes, with Applications to Guidance*, New York: John Wiley & Sons, Inc., 1968.
- [30] H. Risken, *The Fokker-Planck Equation: Methods of Solution and Applications*, Berlin: Springer-Verlag, 1989.
- [31] Edited by: S. Haykin, *Kalman Filtering and Neural Networks*, New York: John Wiley & Sons, Inc., 2001.
- [32] H. A. Nasrellah and C. S. Manohar, "Finite Element Method Based Monte Carlo Filters for Structural System Identification," *Probabilistic Engineering Mechanics*, vol. 26, no. 2, p. 294–307, 2011.
- [33] K. J. Bathe, *Finite Element Procedures*, Upper Saddle River, N.J.: Prentice-Hall, Inc., 1996.
- [34] F. F. Taucer, E. Spacone, and F. C. Filippou, "A Fiber Beam-Column Element for Seismic Response Analysis of Reinforced Concrete Structures," Report No. UBC/EERC-91/17, Earthquake Engineering Research Center, College of Engineering, UC Berkeley, Berkeley, CA., 1991.
- [35] F. C. Filippou and G. L. Fenves, "Methods of Analysis for Earthquake-Resistant Structures," in *Earthquake Engineering: From Engineering Seismology to Performance-Based Engineering*, United Kingdom, CRC Press LLC, 2004, Chapter 6.
- [36] M. Kleiber, H. Antunez, T. D. Hien, and P. Kowalczyk, *Parameter Sensitivity in Nonlinear Mechanics: Theory and Finite Element Computations*, England: John Wiley & Sons Ltd, 1997.
- [37] Y. Zhang and A. Der Kiureghian, "Dynamic Response Sensitivity of Inelastic Structures," *Computer Methods in Applied Mechanics and Engineering*, vol. 108, no. 1-2, p. 23–36, 1993.
- [38] J. P. Conte, "Finite Element Response Sensitivity Analysis in Earthquake Engineering," in *Earthquake Engineering Frontiers in the New Millennium*, Lisse, The Netherlands, 2001.

- [39] Q. Gu, M. Barbato, J. P. Conte, P. E. Gill, and F. McKenna, "OpenSees-SNOPT Framework for Finite-Element-Based Optimization of Structural and Geotechnical Systems," *ASCE Journal of Structural Engineering*, vol. 138, no. 6, p. 822–834, 2012.
- [40] M. H. Scott and T. Haukaas, "Software Framework for Parameter Updating and Finite-Element Response Sensitivity Analysis," *ASCE Journal of Computing in Civil Engineering*, vol. 22, no. 5, p. 281–291, 2008.
- [41] J. P. Conte, P. K. Vijalapura, and M. Meghella, "Consistent Finite-Element Response Sensitivity Analysis," *ASCE Journal of Engineering Mechanics*, vol. 129, no. 12, p. 1380–1393, 2003.
- [42] M. Barbato and J. P. Conte, "Finite Element Response Sensitivity Analysis: A Comparison between Force-based and Displacement-based Frame Element Models," *Computer Methods in Applied Mechanics and Engineering*, vol. 194, no. 12-16, p. 1479–1512, 2005.
- [43] A. K. Chopra, *Dynamics of Structures: Theory and Applications to Earthquake Engineering*, Englewood Cliffs, N.J.: Prentice-Hall, Inc., 4th Ed., 2012.
- [44] OpenSees, "Open System for Earthquake Engineering Simulation," [Online]. Available: <http://opensees.berkeley.edu/>. [Accessed 09 2013].
- [45] "MATLAB (2012)," The MathWorks Inc., Natick, Massachusetts, United States.
- [46] AISC, Steel Construction Manual, 14th edition, 2011.
- [47] F. C. Filippou, E. P. Popov, and V. V. Bertero, "Effects of Bond Deterioration on Hysteretic Behavior of Reinforced Concrete Joints," EERC Report 83-19, Earthquake Engineering Research Center, Berkeley, CA, 1983.
- [48] "Center for Engineering Strong Motion Data, CESMD - A Cooperative Effort," [Online]. Available: <http://strongmotioncenter.org/>. [Accessed September 2013].
- [49] R. K. Mehra, "Approaches to Adaptive Filtering," *IEEE Transactions on Automatic Control*, vol. 17, no. 5, p. 693 - 698, 1972.
- [50] B. F. La Scala, R. R. Bitmead, and M. R. James, "Conditions for Stability of the Extended Kalman Filter and Their Application to the Frequency Tracking Problem," *Mathematics of Control, Signals and Systems*, vol. 8, no. 1, p. 1-26, 1995.
- [51] A. Gupta and H. Krawinkler, "Behavior of Ductile SMRFs at Various Seismic Hazard Levels," *ASCE Journal of Structural Engineering*, vol. 126, no. 1, p. 98–107, 2000.
- [52] C. G. Koh and L. M. See, "Estimation of Structural Parameters in Time Domain: A Substructure Approach," *Earthquake Engineering & Structural Dynamics*, vol. 20, no. 8, p. 787-801, 1991.

## **CHAPTER 5: NONLINEAR STRUCTURAL PARAMETER ESTIMATION AND UNCERTAINTY QUANTIFICATION USING BAYESIAN INFERENCE METHOD**

### **5.1. Introduction**

Existing vibration-based structural health monitoring (SHM) methods use measured input-output or output-only vibration data from a structure before and after a potentially damaging event. These methods typically track the changes in the identified modal properties to detect the occurrence of damage in the structural system. The modal properties are estimated assuming an equivalent linear elastic viscously damped structural model. Damage detection using structural modal identification methods is based on the premise that damage is manifested as a loss of effective stiffness over one or more regions of the structure. While loss of effective stiffness is a correct indication of damage, there are other important manifestations of damage in structural systems that cannot be identified by tracking the loss of effective stiffness. Loss of strength,

loss of ductility capacity, softening, and/or residual deformation in one or more components of a structural system are all important expressions of damage that cannot be directly identified or evaluated by most existing vibration-based SHM methods. Furthermore, accurate SHM after a damage-inducing event requires the correct identification of these important manifestations of damage in the structural system.

This chapter presents a framework for SHM and damage identification (DID) of structural systems by integrating advanced mechanics-based nonlinear FE modeling and analysis techniques, which are able to capture the damage/failure mechanisms to be detected and identified in the structural system of interest, with Bayesian estimation methods. Bayesian methods are employed to update the nonlinear FE model of the structure using the input-output data recorded during dynamic excitations of small, moderate, or large amplitude. The updated FE model can then be interrogated to extract detailed information about various manifestations of damage in the structural components and systems such as stiffness degradation, strength deterioration, loss of ductility capacity, history of inelastic deformations, etc. The proposed methodology can be used not only to detect the occurrence of damage, but also to localize, classify, and quantify the state of damage throughout the structural system at different scales, from the global system level to the local member, section, and fiber levels. This information is essential to accurately predict the remaining useful life of the structure, as well as the reliability and risk of operation. This chapter is part of an extensive research effort that has been pursued in the field of SHM and DID of structural systems using a nonlinear FE model updating approach ([1-5]).



The proposed framework for SHM and DID of structural systems is based on two long-lasting techniques in the field of SHM, namely FE model updating and nonlinear probabilistic (Bayesian) estimation. Defined as the process of calibrating or tuning a FE model to minimize the discrepancies between predicted and measured responses of the structure of interest, FE model updating is a powerful system identification methodology for structural systems ([6-7]). Several FE model updating methods proposed in the literature are based on linear FE structural models (e.g., [6-9]). DID based on linear FE model updating has the ability to capture the loss of effective stiffness in the structural system; but, it can provide little or no information about other important manifestations of damage mentioned above. Moreover, since the behavior of actual civil structures is intrinsically nonlinear from the onset of loading, the assumption of linear elastic structural behavior underlying linear FE model updating is violated even for low amplitude loading. On the other hand, several nonlinear probabilistic estimation methods, including batch estimation methods (e.g., [10-13]) and recursive filtering methods (e.g., [14-22] to name a few) are used in model-based methods for parametric identification of nonlinear structural models. However, applications of these estimation methods have been mostly limited to data simulated from highly idealized nonlinear structural models, such as single degree-of-freedom (DOF) systems, chain-like multi DOF systems, and shear building models, which are very limited or unsuitable for nonlinear response prediction of large and complex real-world civil structures. In other few research studies ([23-24]) nonlinear estimation techniques have been used for nonlinear FE model updating of civil

structures using experimental data. These studies, however, have utilized simplified structural models with lumped nonlinearities modeled using empirical nonlinear material laws, such as the Bouc-Wen model. These simplified and empirical models are incapable of accurately representing the actual nonlinear behavior of civil structures. Other studies such as [25] and [26], have employed more advanced nonlinear FE modeling techniques and material constitutive models, but are using simplistic estimation methods unable to evaluate the parameter estimation uncertainty.

The approach presented in this chapter provides a computationally feasible stochastic framework for nonlinear FE model updating of civil structures. This approach is general and applies to large scale FE models with various levels of complexity. The proposed framework also provides evaluation of the estimation uncertainty and hence, offers the proper tool for remaining useful life prediction (i.e., damage prognosis) and reliability analysis of civil structures following a damage-inducing event.

## **5.2. Nonlinear Finite Element Model Updating**

Given the measured input ground acceleration and dynamic response of a civil structure during an earthquake event, it is intended to accurately identify and quantify the state of damage in the structural system. In this study, this objective is pursued through nonlinear finite element (FE) model updating using the recorded input ground acceleration and dynamic response of the structure, which are contaminated by measurement noise as expected for any physical measurement. The nonlinear FE

model of the structure of interest depends on a set of unknown parameters including but not limited to inertial properties, gravity loading, geometry, restraint and constraint parameters, damping parameters, and parameters characterizing the nonlinear material constitutive laws. These parameters, referred to as model parameters hereafter, are assumed to remain time-invariant during the earthquake event. The main goal of the proposed nonlinear FE model updating is to find the best estimate (i.e., point-estimate) of the model parameters in order to minimize the discrepancy between FE predicted and measured structural response time histories. The parameter estimation procedure is presented in the next section. Another important objective of the proposed nonlinear FE model updating is to provide a quantitative assessment of the parameter estimation uncertainty or, in the Bayesian viewpoint, a measure of plausibility or degree of belief of the parameter estimation results. Evaluation of the parameter estimation uncertainty is referred to as uncertainty quantification and is discussed in Section 5.4 of this chapter.

### 5.3. Parameter Estimation

The time-discretized equation of motion of a nonlinear FE model of the structure can be expressed as, at the  $k^{\text{th}}$  time step,

$$\mathbf{M}(\boldsymbol{\theta})\ddot{\mathbf{q}}_k(\boldsymbol{\theta}) + \mathbf{C}(\boldsymbol{\theta})\dot{\mathbf{q}}_k(\boldsymbol{\theta}) + \mathbf{r}_k(\mathbf{q}_k(\boldsymbol{\theta}), \boldsymbol{\theta}) = \mathbf{f}_k \quad (5.1)$$

where  $\mathbf{M}(\boldsymbol{\theta})$  = mass matrix;  $\mathbf{C}(\boldsymbol{\theta})$  = damping matrix,  $\mathbf{r}_k(\mathbf{q}_k(\boldsymbol{\theta}), \boldsymbol{\theta})$  = history-dependent (or path-dependent) internal resisting force vector;  $\mathbf{q}_k(\boldsymbol{\theta}), \dot{\mathbf{q}}_k(\boldsymbol{\theta}), \ddot{\mathbf{q}}_k(\boldsymbol{\theta}) \in \mathbb{R}^{n_{DOF}} \times 1 =$

nodal displacement, velocity, and acceleration response vectors;  $\boldsymbol{\theta} \in \mathbb{R}^{n_{\theta} \times 1}$  = model parameter vector;  $\mathbf{f}_k \in \mathbb{R}^{n_{DOF} \times 1}$  = dynamic load vector; and the subscripts indicate the time step. In the case of earthquake base excitation,  $\mathbf{f}_k = -\mathbf{M}\mathbf{L}\ddot{\mathbf{u}}_{g_k}$ , where  $\mathbf{L} \in \mathbb{R}^{n_{DOF} \times n_{\ddot{u}_g}}$  is the base acceleration influence matrix and  $\ddot{\mathbf{u}}_{g_k} \in \mathbb{R}^{n_{\ddot{u}_g} \times 1}$  denotes the input ground acceleration vector. Eq. (5.1) can be solved in time through a recursive numerical integration method. Using an implicit single-step time integration scheme, such as the Newmark-beta method [27] the nodal acceleration and velocity response vectors at the  $k^{\text{th}}$  time step can be approximated as

$$\ddot{\mathbf{q}}_k = a_1\mathbf{q}_k + a_2\mathbf{q}_{k-1} + a_3\dot{\mathbf{q}}_{k-1} + a_4\ddot{\mathbf{q}}_{k-1} \quad (5.2)$$

$$\dot{\mathbf{q}}_k = b_1\mathbf{q}_k + b_2\mathbf{q}_{k-1} + b_3\dot{\mathbf{q}}_{k-1} + b_4\ddot{\mathbf{q}}_{k-1} \quad (5.3)$$

in which  $a_1$  to  $a_4$  and  $b_1$  to  $b_4$  are integration coefficients. Substitution of Eqs. (5.2)-(5.3) into Eq. (5.1) results in the following nonlinear algebraic equation in  $\mathbf{q}_k$  that can be solved using incremental iterative solution procedures such as Newton-Raphson method [28].

$$\begin{aligned} a_1\mathbf{M}(\boldsymbol{\theta})\mathbf{q}_k(\boldsymbol{\theta}) + b_1\mathbf{C}(\boldsymbol{\theta})\mathbf{q}_k(\boldsymbol{\theta}) + \mathbf{r}_k(\mathbf{q}_k(\boldsymbol{\theta}), \boldsymbol{\theta}) = \\ -\mathbf{M}(\boldsymbol{\theta})\mathbf{L}\ddot{\mathbf{u}}_{g_k} - \mathbf{M}(\boldsymbol{\theta})[a_2\mathbf{q}_{k-1}(\boldsymbol{\theta}) + a_3\dot{\mathbf{q}}_{k-1}(\boldsymbol{\theta}) + a_4\ddot{\mathbf{q}}_{k-1}(\boldsymbol{\theta})] - \mathbf{C}(\boldsymbol{\theta})[b_2\mathbf{q}_{k-1}(\boldsymbol{\theta}) + b_3\dot{\mathbf{q}}_{k-1}(\boldsymbol{\theta}) + b_4\ddot{\mathbf{q}}_{k-1}(\boldsymbol{\theta})] \end{aligned} \quad (5.4)$$

Upon solution of Eq. (5.4) for  $\mathbf{q}_k$ , the nodal acceleration and velocity response vectors can be obtained using Eqs. (5.2)-(5.3), respectively. The solution for the structural response at the  $k^{\text{th}}$  time step is then complete and the numerical integration algorithm can proceed to the next time step. In essence, by having the initial conditions

$\mathbf{q}_0, \dot{\mathbf{q}}_0$  and the time history of the input ground acceleration, the equation of motion of the structure can be solved recursively in time to find the nodal response of the FE model at each discrete time step. In short-hand notation, the nodal response of the FE model at the  $k^{\text{th}}$  time step can be expressed as a nonlinear function of the model parameter vector ( $\boldsymbol{\theta}$ ), time history of the base acceleration vector, and the initial conditions of the FE model ( $\mathbf{q}_0, \dot{\mathbf{q}}_0$ ), i.e.,

$$[\mathbf{q}_k, \dot{\mathbf{q}}_k, \ddot{\mathbf{q}}_k] = \tilde{\mathbf{h}}_k \left( \boldsymbol{\theta}, \ddot{\mathbf{u}}_{g_1}, \ddot{\mathbf{u}}_{g_2}, \dots, \ddot{\mathbf{u}}_{g_k}, \mathbf{q}_0, \dot{\mathbf{q}}_0 \right) \quad (5.5)$$

where  $\tilde{\mathbf{h}}_k(\dots)$  is referred to herein as the nonlinear nodal response function of the FE model at the  $k^{\text{th}}$  time step for earthquake base excitation.

In general, the response of a FE model at a given time step can be expressed as a (nonlinear) combination of the nodal displacement, velocity, and acceleration responses at the same time step, i.e.,

$$\hat{\mathbf{y}}_k = \mathbf{g}(\mathbf{q}_k, \dot{\mathbf{q}}_k, \ddot{\mathbf{q}}_k) \quad (5.6)$$

where  $\hat{\mathbf{y}}_k \in \mathbb{R}^{n_y \times 1}$  denotes the FE predicted response vector at the  $k^{\text{th}}$  time step, and  $\mathbf{g}(\dots)$  is the (nonlinear) output function. According to Eqs. (5.5) and (5.6), the response of a nonlinear FE model to an earthquake ground motion at each time step can be expressed as a nonlinear function of the model parameters ( $\boldsymbol{\theta}$ ), the input ground acceleration time history from the start of the earthquake until that time step, and the initial conditions ( $\mathbf{q}_0, \dot{\mathbf{q}}_0$ ), i.e.,

$$\hat{\mathbf{y}}_k = \mathbf{h}_k \left( \boldsymbol{\theta}, \ddot{\mathbf{u}}_{g_{1 \rightarrow k}}, \mathbf{q}_0, \dot{\mathbf{q}}_0 \right) \quad (5.7)$$

in which  $\ddot{\mathbf{u}}_{g_{1 \rightarrow k}} = [\ddot{\mathbf{u}}_{g_1}^T, \ddot{\mathbf{u}}_{g_2}^T, \dots, \ddot{\mathbf{u}}_{g_k}^T]^T$ ,  $\mathbf{q}_0 \in \mathbb{R}^{n_{DOF} \times 1}$  = initial nodal displacement vector,  $\dot{\mathbf{q}}_0 \in \mathbb{R}^{n_{DOF} \times 1}$  = initial nodal velocity vector, and  $\mathbf{h}_k(\dots)$  = nonlinear response function of the FE model at the  $k^{\text{th}}$  time step.

The dynamic response of civil structures can be recorded using an array of heterogeneous sensors such as accelerometers, GPS sensors, linear displacement transducers, potentiometers, strain gauges, etc. The measured structural response vector,  $\mathbf{y}_k$ , can be related to the FE predicted response vector,  $\hat{\mathbf{y}}_k$ , as

$$\mathbf{v}_k(\boldsymbol{\theta}) = \mathbf{y}_k - \hat{\mathbf{y}}_k(\boldsymbol{\theta}) \quad (5.8)$$

in which  $\mathbf{v}_k$ , the simulation error, accounts for the misfit between the measured response of the structure and the FE predicted response. This misfit stems from the output measurement noise and the modeling error. Modeling error is classified into two general types [10]:

- (i) Modeling error due to uncertainty in the model parameters. This type of modeling error is minimized during the parameter estimation procedure.
- (ii) Modeling error due to model uncertainties, which means that the selected class of models does not contain the real structure. In other words, the mathematical FE model is an idealized and imperfect representation of the real structure and therefore, the actual structural response is different from the model prediction, no matter how the FE model is tuned.

In nonlinear FE model updating of civil structures, model uncertainties arise from two sources: (1) incorrect or unphysical modeling assumptions, which are not in agreement with the true physical conditions of the structure (e.g., unphysical material

constitutive models, incorrect modeling of damping energy dissipation mechanisms, limiting kinematic assumptions, incorrect model geometry, etc.), and (2) unmodeled physics, which is not included in the FE model (e.g., kinematic interaction between non-structural and structural components and systems in a building structure, foundation flexibility, soil-structure interaction, etc.) [29].

If the effects of model uncertainties are neglected, the simulation error accounts only for the measurement noise and, therefore, a noise model is defined to characterize the simulation error [30] as

$$\mathbf{v}_k = \mathbf{L}(q, \boldsymbol{\eta}) \boldsymbol{\varepsilon}_k \quad (5.9)$$

in which  $\mathbf{L}(q, \boldsymbol{\eta})$  is the noise filter operator, which models the spectrum of the measurement noise polluting  $\mathbf{y}_k$ ,  $\boldsymbol{\eta}$  represents the noise filter parameters, and  $q$  is the unit delay operator (i.e.,  $q^{-i} \boldsymbol{\varepsilon}_k = \boldsymbol{\varepsilon}_{k-i}$ ). Substitution of Eq. (5.9) into Eq. (5.8) results in the prediction error framework for system identification ([30-31]), i.e.,

$$\boldsymbol{\varepsilon}_k(\boldsymbol{\theta}, \boldsymbol{\eta}) = \mathbf{L}^{-1}(q, \boldsymbol{\eta}) (\mathbf{y}_k - \hat{\mathbf{y}}_k(\boldsymbol{\theta})) \quad (5.10)$$

where  $\boldsymbol{\varepsilon}_k(\boldsymbol{\theta}, \boldsymbol{\eta})$  is the prediction error (PE). Once the noise filter model structure is selected, the FE model parameters and noise filter parameters can be estimated as the solution of the following optimization problem:

$$(\hat{\boldsymbol{\theta}}, \hat{\boldsymbol{\eta}}) = \arg \min_{\boldsymbol{\theta}, \boldsymbol{\eta}} \left( \sum_{i=1}^k \text{trace} \left( \boldsymbol{\varepsilon}_i(\boldsymbol{\theta}, \boldsymbol{\eta}) \boldsymbol{\varepsilon}_i(\boldsymbol{\theta}, \boldsymbol{\eta})^T \right) \right) \quad (5.11)$$

It is important to recognize that  $\mathbf{L}(q, \boldsymbol{\eta})$  is used to capture the measurement noise dynamics. The idea of using a filter to capture noise dynamics is sometimes extended to capture possible effects of model uncertainties, although these effects are

in nature completely different from measurement noise. Nevertheless, accounting for model uncertainties in the nonlinear FE model updating is out of the scope of this chapter. Furthermore, it is assumed herein that the measurement noise is a stationary, zero-mean, independent Gaussian white noise (i.e., statistically independent across time and measurement channels) [32]. Therefore, the noise model in Eq. (5.9) is taken as the unit function (i.e.,  $\mathbf{L}(q, \boldsymbol{\eta})=1$ ), and the simulation error is modeled as a stationary, zero-mean, independent Gaussian white noise process. Based on these simplifying assumptions, Eqs. (5.10) and (5.11) lead to the following least squares estimation problem:

$$\hat{\boldsymbol{\theta}} = \arg \min_{\boldsymbol{\theta}} \left( \sum_{i=1}^k \text{trace} \left( \boldsymbol{\varepsilon}_i(\boldsymbol{\theta}) \boldsymbol{\varepsilon}_i(\boldsymbol{\theta})^T \right) \right) = \arg \min_{\boldsymbol{\theta}} \left( \sum_{i=1}^k \left\| \mathbf{y}_i - \mathbf{h}_i \left( \boldsymbol{\theta}, \ddot{\mathbf{u}}_{g_1 \rightarrow i}, \mathbf{q}_0, \dot{\mathbf{q}}_0 \right) \right\|^2 \right) \quad (5.12)$$

The least squares estimation approach for structural model updating can be derived from the Bayesian framework and more specifically the maximum likelihood estimation method under the assumption of a Gaussian white simulation error [10]. It is well known and has been used extensively in the literature (e.g., [11,13,33] to name a few). The least squares method for system identification also has a long history in other engineering fields (e.g., [31-30,34]). The least squares estimation method as presented in Eq. (5.12) is optimal when the measurement noise is characterized as a zero-mean independent and identically distributed white noise vector process (i.e., statistically independent across time and measurement channels). Nevertheless, assuming equal noise characteristics at different measurement channels is a restrictive and often invalid hypothesis. For example, the equal variance assumption is incorrect



in the case of heterogeneous sensor arrays, in which the signals measured from different sensors have different scales, physical units, and noise characteristics. When signals obtained from different sensors have different physical units, the least squares estimation procedure gives relatively higher weight to the measurement data with higher amplitude. This limitation can be lifted by using the weighted least squares method, as suggested and used by many researchers (e.g., [13,30,35]). In the weighted least squares approach, each signal is scaled (or weighted) separately based on its amplitude and/or estimated measurement noise-to-signal ratio. The selection of scaling (or weighting) factors can have significant influence on the estimation results and should be done in a systematic way. Another situation in which least squares estimation may lead to incorrect estimation results is the case of erroneous measurements at one or few measurement channels as a result of sensor or DAQ malfunctioning for example. To remove these limitations of the traditional least squares estimation approach in a systematic way, the Bayesian estimation method in the context of nonlinear FE model updating is revisited in this study. Furthermore, the proposed estimation procedure provides the necessary tools for quantifying the parameter estimation uncertainty using the Fisher information matrix, as will be presented in Section 5.4.

The unknown FE model parameters to be estimated in Eq. (5.8) are modeled as random variables according to the Bayesian approach for parameter estimation. Bayes' rule is employed to infer the *a posteriori* joint probability density function (PDF) of

the model parameters from the time histories of noisy input and output measurements and the *a priori* joint PDF of these parameters as

$$p(\boldsymbol{\theta} | \ddot{\mathbf{u}}_{g_{1 \rightarrow k}}, \mathbf{y}_{1 \rightarrow k}) = \frac{p(\mathbf{y}_{1 \rightarrow k} | \boldsymbol{\theta}, \ddot{\mathbf{u}}_{g_{1 \rightarrow k}}) p(\boldsymbol{\theta}, \ddot{\mathbf{u}}_{g_{1 \rightarrow k}})}{p(\ddot{\mathbf{u}}_{g_{1 \rightarrow k}}, \mathbf{y}_{1 \rightarrow k})} \quad (5.13)$$

where  $\mathbf{y}_{1 \rightarrow k} = [\mathbf{y}_1^T, \mathbf{y}_2^T, \dots, \mathbf{y}_k^T]^T$ . Assuming that the components of measured input ground acceleration are known (deterministic) and noiseless, the effects of input measurement noise are not considered herein. Therefore, Eq. (5.13) simplifies to ([36]):

$$p(\boldsymbol{\theta} | \mathbf{y}_{1 \rightarrow k}) = \frac{1}{c} p(\mathbf{y}_{1 \rightarrow k} | \boldsymbol{\theta}) p(\boldsymbol{\theta}) \quad (5.14)$$

in which  $p(\boldsymbol{\theta} | \mathbf{y}_{1 \rightarrow k})$  is the *a posteriori* joint PDF of the model parameters,  $c = \int p(\mathbf{y}_{1 \rightarrow k} | \boldsymbol{\theta}) p(\boldsymbol{\theta}) d\boldsymbol{\theta}$  is a normalizing constant called evidence, and  $p(\mathbf{y}_{1 \rightarrow k} | \boldsymbol{\theta}) = l(\boldsymbol{\theta}, \mathbf{y}_{1 \rightarrow k})$  is the likelihood function, which represents the contribution of the measured responses in the *a posteriori* joint PDF of the model parameters. The term  $p(\boldsymbol{\theta})$  in Eq. (5.14) is the *a priori* PDF of the model parameters and is assigned based on the prior information and knowledge about the model parameters.

In the Bayesian estimation, the value of  $\boldsymbol{\theta}$  that maximizes the *a posteriori* joint PDF – i.e., the mode of  $p(\boldsymbol{\theta} | \mathbf{y}_{1 \rightarrow k})$  – is called the maximum *a posteriori* (MAP) estimate of  $\boldsymbol{\theta}$ :

$$\hat{\boldsymbol{\theta}}_{MAP} = \arg \max_{\boldsymbol{\theta}} [p(\boldsymbol{\theta} | \mathbf{y}_{1 \rightarrow k})] \quad (5.15)$$

It is usually more convenient to express the estimation problem as a minimization problem. Therefore, the MAP estimate of  $\boldsymbol{\theta}$  can be computed by minimizing the negative natural logarithm of the *a posteriori* joint PDF. Therefore,

$$\begin{aligned}\hat{\boldsymbol{\theta}}_{MAP} &= \arg \min_{\boldsymbol{\theta}} \left[ -\ln \left( p(\boldsymbol{\theta} | \mathbf{y}_{1 \rightarrow k}) \right) \right] \\ &= \arg \min_{\boldsymbol{\theta}} \left[ -\Lambda(\boldsymbol{\theta}, \mathbf{y}_{1 \rightarrow k}) - \ln(p(\boldsymbol{\theta})) \right]\end{aligned}\quad (5.16)$$

where  $\Lambda(\boldsymbol{\theta}, \mathbf{y}_{1 \rightarrow k}) = \ln(l(\boldsymbol{\theta}, \mathbf{y}_{1 \rightarrow k}))$  is the log-likelihood function.

In the case of nonlinear FE model updating for civil structures, prior information or knowledge about FE model parameters is often limited to design and construction documents (e.g., nominal material parameter values), previous destructive or non-destructive material testing results for the structure of interest, the technical literature, engineering experience and expert opinion. It is common to consider minimum prior knowledge about model parameters and assume a uniform *a priori* joint PDF. According to Eq. (5.16), if the *a priori* PDF of  $\boldsymbol{\theta}$ ,  $p(\boldsymbol{\theta})$ , is sufficiently flat and close to uniform, its natural logarithm tends to a constant. This means that when there is little or no information about the model parameters  $\boldsymbol{\theta}$ , the *a posteriori* joint PDF will be maximized, in the limiting case, at the value of  $\boldsymbol{\theta}$  that minimizes the negative log-likelihood function, which is known as the maximum likelihood (ML) estimate of  $\boldsymbol{\theta}$  [34]:

$$\hat{\boldsymbol{\theta}}_{ML} = \arg \min_{\boldsymbol{\theta}} \left[ \Lambda(\boldsymbol{\theta}, \mathbf{y}_{1 \rightarrow k}) \right]\quad (5.17)$$

According to Eq. (5.8),  $l(\boldsymbol{\theta}, \mathbf{y}_{1 \rightarrow k}) = p(\mathbf{y}_{1 \rightarrow k} | \boldsymbol{\theta}) = p(\mathbf{v}_{1 \rightarrow k})$  and since  $\mathbf{v}$  is modeled herein as a stationary, zero-mean, independent Gaussian white noise vector

process ( $\mathbf{v} \sim N(\mathbf{0}, \mathbf{R})$ ), i.e., statistically independent across time and measurement channels; therefore,

$$l(\boldsymbol{\theta}, \mathbf{y}_{1 \rightarrow k}) = \prod_{i=1}^k p(\mathbf{v}_i) \quad (5.18)$$

$$\Rightarrow l(\boldsymbol{\theta}, \mathbf{y}_{1 \rightarrow k}) = \prod_{i=1}^k \frac{1}{(2\pi)^{n_y/2} |\mathbf{R}|^{1/2}} e^{-\frac{1}{2} (\mathbf{y}_i - \mathbf{h}_i(\boldsymbol{\theta}, \ddot{\mathbf{u}}_{g_{1 \rightarrow i}}, \mathbf{q}_0, \dot{\mathbf{q}}_0))^T \mathbf{R}^{-1} (\mathbf{y}_i - \mathbf{h}_i(\boldsymbol{\theta}, \ddot{\mathbf{u}}_{g_{1 \rightarrow i}}, \mathbf{q}_0, \dot{\mathbf{q}}_0))}$$

in which  $|\mathbf{R}|$  denotes the determinant of the diagonal matrix  $\mathbf{R}$ , which is the covariance matrix of the simulation error vector. Eqs. (5.17) and (5.18) result in the following statement of the maximum likelihood (ML) estimation for the model parameters [13]:

$$\hat{\boldsymbol{\theta}}_{ML} = \arg \min_{\boldsymbol{\theta}} \left( \frac{k}{2} \ln(|\mathbf{R}|) + \frac{1}{2} \sum_{i=1}^k (\mathbf{y}_i - \mathbf{h}_i(\boldsymbol{\theta}, \ddot{\mathbf{u}}_{g_{1 \rightarrow i}}, \mathbf{q}_0, \dot{\mathbf{q}}_0))^T \mathbf{R}^{-1} (\mathbf{y}_i - \mathbf{h}_i(\boldsymbol{\theta}, \ddot{\mathbf{u}}_{g_{1 \rightarrow i}}, \mathbf{q}_0, \dot{\mathbf{q}}_0)) \right) \quad (5.19)$$

Assuming equal variances for the simulation error at different measurement channels results in identical diagonal entries for  $\mathbf{R}$  (i.e.,  $\mathbf{R} = r \mathcal{J}_{n_y \times n_y}$ ), where  $r$  is the (assumed to be known) simulation error variance for each measurement channel, which is equivalent to the measurement noise variance based on the assumptions made earlier, and  $\mathcal{J}$  denotes the  $(n_y \times n_y)$  identity matrix. Therefore, the ML estimation problem reduces to a least squares problem as shown in Eq. (5.12).

To allow the use of data obtained from heterogeneous sensor arrays in the nonlinear FE model updating procedure and enhance the robustness of the parameter estimation procedure, an extended ML estimation procedure is used in this study, in which not only the FE model parameters but also the variances of the components of

the simulation error vector are estimated. The idea of estimating jointly the simulation error variances and the model parameters has been proposed and used by other researchers in the field of structural identification (e.g., [36-37]). The variances of the simulation error are the diagonal entries of the covariance matrix ( $\mathbf{R} = [r_j]$ ,  $j = 1, \dots, n_y$ ). The diagonal entries of the covariance matrix are stacked in a row vector called the variance vector  $\mathbf{r} = \{r_j\}$ ,  $j = 1, \dots, n_y$ . Following Eq. (5.19), the extended estimation problem can be formulated as the following optimization problem:

$$\left(\hat{\boldsymbol{\theta}}, \hat{\mathbf{r}}\right)_{ML} = \arg \min_{(\boldsymbol{\theta}, \mathbf{r})} J(\mathbf{r}, \boldsymbol{\theta}, \mathbf{y}_{1 \rightarrow k}, \ddot{\mathbf{u}}_{g_{1 \rightarrow k}}) \quad (5.20)$$

$$J(\mathbf{r}, \boldsymbol{\theta}, \mathbf{y}_{1 \rightarrow k}, \ddot{\mathbf{u}}_{g_{1 \rightarrow k}}) = \frac{k}{2} \sum_{j=1}^{n_y} \ln(r_j) + \frac{1}{2} \sum_{i=1}^k \left( \mathbf{y}_i - \mathbf{h}_i(\boldsymbol{\theta}, \ddot{\mathbf{u}}_{g_{1 \rightarrow i}}) \right)^T \mathbf{R}^{-1} \left( \mathbf{y}_i - \mathbf{h}_i(\boldsymbol{\theta}, \ddot{\mathbf{u}}_{g_{1 \rightarrow i}}) \right) \quad (5.21)$$

in which  $J(\dots)$  is the objective function of the optimization problem and the dependence of  $J$  on the initial conditions of the FE model ( $\mathbf{q}_0$  and  $\dot{\mathbf{q}}_0$ ) is dropped for notational convenience. The objective function in Eq. (5.21) consists of two terms.

The first term,  $\frac{k}{2} \sum_{j=1}^{n_y} \ln(r_j)$ , is a regularization term penalizing the estimation of large

values for the simulation error variance. The second term is the distance between the FE predicted and measured structural responses weighted inversely by the estimated error variances. Therefore, if the error variance is estimated to be high on a certain measurement channel, the contribution of the measured data obtained from that channel in the parameter estimation procedure is downscaled proportionally. This

estimation framework not only resolves the scale problem discussed earlier in the case of a heterogeneous sensor array, but also improves the estimation robustness in the presence of erroneous measurement data due to, for example, malfunctioning sensors and/or DAQ system.

By defining a feasibility range for the model parameters and the simulation error variances (i.e.,  $\boldsymbol{\theta}_{\min} \leq \boldsymbol{\theta} \leq \boldsymbol{\theta}_{\max}$  and  $\mathbf{r}_{\min} \leq \mathbf{r} \leq \mathbf{r}_{\max}$ ), the parameter estimation problem is transformed into a constrained nonlinear optimization problem, which is solved using an interior-point method ([38-39]) in this study. The utilized computational optimization algorithm is available as part of the MATLAB optimization toolbox [40]. It requires the computation of the gradient of the objective function with respect to the model parameters,  $\boldsymbol{\theta}$ , and the simulation error variances,  $\mathbf{r}$ , which can be obtained as

$$\frac{\partial J}{\partial \boldsymbol{\theta}} = -\sum_{i=1}^k (\mathbf{y}_i - \mathbf{h}_i(\boldsymbol{\theta}, \ddot{\mathbf{u}}_{g_{1 \rightarrow i}}))^T \mathbf{R}^{-1} \left( \frac{\partial \mathbf{h}_i(\boldsymbol{\theta}, \ddot{\mathbf{u}}_{g_{1 \rightarrow i}})}{\partial \boldsymbol{\theta}} \right) \quad (5.22)$$

$$\frac{\partial J}{\partial r_j} = \frac{k}{2r_j} - \frac{1}{2} \sum_{i=1}^k \frac{\left( y_{ij} - h_{ij}(\boldsymbol{\theta}, \ddot{\mathbf{u}}_{g_{1 \rightarrow i}}) \right)^2}{r_j^2}, \quad j = 1, \dots, n_y \quad (5.23)$$

in which  $y_{ij}$  is the  $j^{\text{th}}$  component of the response vector at the  $i^{\text{th}}$  time step. The

derivative of vector  $\mathbf{a} \in \mathbb{R}^{m \times 1}$  with respect to vector  $\mathbf{b} \in \mathbb{R}^{n \times 1}$  is denoted as  $\mathbf{C} = \frac{\partial \mathbf{a}}{\partial \mathbf{b}}$ ,

where  $\mathbf{C}$  is a  $m \times n$  matrix defined as  $c_{ij} = \frac{\partial a_i}{\partial b_j}$ .

The term  $\frac{\partial \mathbf{h}_i(\boldsymbol{\theta}, \ddot{\mathbf{u}}_{g1 \rightarrow i})}{\partial \boldsymbol{\theta}}$  in Eq. (5.22) is the sensitivity (or rate of variation) of the FE predicted response at the  $i^{\text{th}}$  time step with respect to the model parameter vector,  $\boldsymbol{\theta}$ , and is referred to herein as the FE response sensitivity matrix. FE response sensitivity analysis has been used for a variety of applications in the literature including structural design optimization, and propagation of uncertainties needed for probabilistic and reliability analysis of structural and geotechnical systems (e.g., [41-45]). FE response sensitivities can be computed approximately using the finite difference method (FDM), which requires at least  $n_{\boldsymbol{\theta}} + 1$  runs of the nonlinear FE model, where  $n_{\boldsymbol{\theta}}$  is the number of parameters with respect to which the sensitivities are computed. The computational cost of the FDM significantly increases as the number of model parameters and the scale of the FE model increase. The direct differentiation method (DDM) is an accurate and computationally efficient alternative method for computing the FE response sensitivities. The DDM is based on the exact differentiation (consistent linearization) of the FE numerical scheme for response computation with respect to the model parameters. The fundamentals of DDM-based FE response sensitivity computation can be found in [43-44,46]. The FE model parameter estimation framework proposed herein uses the DDM to compute FE response sensitivities and therefore, offers a computationally feasible framework for parameter estimation and nonlinear FE model updating especially for large scale nonlinear FE models.

## 5.4. Parameter Estimation Uncertainty Quantification

Due to the presence of output measurement noise, the response of a structure to a deterministic (known) earthquake excitation can be modeled as a random process,  $\mathbf{Y}_{1 \rightarrow k}$ , and the measured response,  $\mathbf{y}_{1 \rightarrow k}$ , can be viewed as a specific realization of  $\mathbf{Y}_{1 \rightarrow k}$ . In the proposed nonlinear FE model updating approach described in the previous section, the ML estimator for the FE model parameters and the simulation error variances is defined as a function of the random variable  $\mathbf{Y}_{1 \rightarrow k}$ ,  $(\Theta, \mathcal{R}) = \mathbf{t}_{ML}(\mathbf{Y}_{1 \rightarrow k})$ , where  $\mathbf{t}_{ML}(\dots)$  denotes the ML estimator. The ML estimate of the model parameters and the simulation error variances,  $(\hat{\theta}, \hat{r}) = \mathbf{t}_{ML}(\mathbf{y}_{1 \rightarrow k})$ , can be computed through the procedure described above. Unlike stochastic estimation approaches such as Kalman filtering methods, the ML estimation process does not directly provide any measure of uncertainty associated with the parameter estimates. The estimation uncertainty (or measure of plausibility or degree of belief) is completely described by the joint PDF of the parameter vector estimator. In other words, if the estimation process is repeated for many realizations of the measured response  $\mathbf{Y}_{1 \rightarrow k}$ , the statistical distribution of the parameter estimates describes the parameter estimation uncertainty.

A ML estimator has some general statistical asymptotic properties that can be used to evaluate the parameter estimation uncertainty. The covariance matrix of a ML estimator can be asymptotically evaluated using the Cramér-Rao lower bound (CRLB) [34]. In general, the CRLB provides a lower bound for the estimation covariance



matrix of any unbiased estimator. It can be shown that a ML estimator is asymptotically unbiased and its estimation covariance asymptotically converges to the CRLB. The asymptotic properties of a ML estimator can be summarized in the following definition and theorems.

**Definition 1 (Unbiased estimator):** An estimator  $\mathbf{t}(\mathbf{Y})$  for  $\boldsymbol{\psi}^{true}$  is said to be unbiased if [31]

$$E_{\mathbf{Y}|\boldsymbol{\Psi}}[\mathbf{t}(\mathbf{Y})] = \int \mathbf{t}(\mathbf{y}) p(\mathbf{y} | \boldsymbol{\Psi} = \boldsymbol{\psi}^{true}) d\mathbf{y} = \boldsymbol{\psi}^{true} \quad (5.24)$$

In other words, an unbiased estimator on the average yields the true value (or the true state of nature) of the unknown parameter vector.

**Theorem 1 (Cramér–Rao):** If  $\hat{\boldsymbol{\psi}} = \mathbf{t}(\mathbf{y})$  is an unbiased estimate of  $\boldsymbol{\psi}^{true}$  based on the measured data  $\mathbf{y}$ , and has a log-likelihood function,  $\Lambda(\boldsymbol{\psi}, \mathbf{y})$ , which is differentiable with respect to  $\boldsymbol{\psi}$ , then the covariance matrix of the estimator satisfies the CRLB, i.e.

$$E_{\mathbf{Y}|\boldsymbol{\Psi}} \left[ (\mathbf{t}(\mathbf{Y}) - \boldsymbol{\psi}^{true})(\mathbf{t}(\mathbf{Y}) - \boldsymbol{\psi}^{true})^T \right] \geq \mathbf{I}^{-1}(\boldsymbol{\psi}^{true}) \quad (5.25)$$

in which the matrix inequality  $\mathbf{A} \geq \mathbf{B}$  means that  $\mathbf{A} - \mathbf{B}$  is a positive semi-definite matrix and  $\mathbf{I}(\boldsymbol{\psi})$  denotes the Fisher information matrix (FIM) defined as

$$\mathbf{I}(\boldsymbol{\psi}) = E_{\mathbf{Y}|\boldsymbol{\Psi}} \left[ \left( \frac{\partial \Lambda(\boldsymbol{\psi}, \mathbf{y})}{\partial \boldsymbol{\psi}} \right)^T \left( \frac{\partial \Lambda(\boldsymbol{\psi}, \mathbf{y})}{\partial \boldsymbol{\psi}} \right) \right] = \int \left( \frac{\partial \Lambda(\boldsymbol{\psi}, \mathbf{y})}{\partial \boldsymbol{\psi}} \right)^T \left( \frac{\partial \Lambda(\boldsymbol{\psi}, \mathbf{y})}{\partial \boldsymbol{\psi}} \right) p(\mathbf{y} | \boldsymbol{\psi}) d\mathbf{y} \quad (5.26)$$

The proof of the Cramér–Rao theorem can be found in [34].

**Theorem 2 (Asymptotic efficiency of the ML estimator):** A ML estimator is asymptotically efficient. In other words, for a large number of informative measured

response data samples (i.e.,  $\mathbf{y}_{1 \rightarrow k}$  with  $k$  large), the ML estimator is unbiased and the parameter estimation covariance matrix achieves the CRLB. The proof of this theorem can be found in [31,47].

The parameter estimation uncertainty is quantified using the estimation covariance matrix which can be approximated by the inverse of the FIM. Two methods to approximate analytically and/or numerically the CRLB are presented below. However, since the CRLB provides only a lower bound for the parameter estimation covariance matrix, a key question that is also investigated herein is how close the actual parameter estimation covariance matrix is to the CRLB approximated by the following two methods. This question will be addressed by using a deterministic sampling method to estimate the parameter estimation covariance matrix, which is further discussed in the context of the application example presented in Section 3.1.

Method 1: CRLB based on the (asymptotically exact) Fisher information matrix

Assuming that  $\boldsymbol{\psi} = \begin{bmatrix} \boldsymbol{\theta}^T & \mathbf{r}^T \end{bmatrix}^T$  in Eq. (5.26), the FIM for the ML estimation problem stated in Eqs. (5.20) and (5.21) can be derived as

$$\mathbf{I}(\boldsymbol{\theta}, \mathbf{r}) = \begin{bmatrix} (\mathbf{I}_{\boldsymbol{\theta}\boldsymbol{\theta}})_{n_{\boldsymbol{\theta}} \times n_{\boldsymbol{\theta}}} & (\mathbf{0})_{n_{\boldsymbol{\theta}} \times n_y} \\ (\mathbf{0})_{n_y \times n_{\boldsymbol{\theta}}} & (\mathbf{I}_{\mathbf{r}\mathbf{r}})_{n_y \times n_y} \end{bmatrix} \quad (5.27)$$

where the sub-matrices  $\mathbf{I}_{\boldsymbol{\theta}\boldsymbol{\theta}}$  and  $\mathbf{I}_{\mathbf{r}\mathbf{r}}$  are derived in Appendix 5.I. Based on the Cramér-Rao theorem, it follows that

$$\begin{bmatrix} E\left[(\boldsymbol{\Theta} - \boldsymbol{\theta})(\boldsymbol{\Theta} - \boldsymbol{\theta})^T\right] & E\left[(\boldsymbol{\Theta} - \boldsymbol{\theta})(\mathcal{R} - \mathbf{r})^T\right] \\ E\left[(\mathcal{R} - \mathbf{r})(\boldsymbol{\Theta} - \boldsymbol{\theta})^T\right] & E\left[(\mathcal{R} - \mathbf{r})(\mathcal{R} - \mathbf{r})^T\right] \end{bmatrix} \geq \begin{bmatrix} \mathbf{I}_{\boldsymbol{\theta}\boldsymbol{\theta}}^{-1} & \mathbf{0} \\ \mathbf{0} & \mathbf{I}_{\mathbf{r}\mathbf{r}}^{-1} \end{bmatrix} \quad (5.28)$$

in which  $E[X] = E_{\mathbf{y}|\boldsymbol{\theta}, \mathbf{r}}[X] = \int X p(\mathbf{y}_{1 \rightarrow k} | \boldsymbol{\theta}, \mathbf{r}) d\mathbf{y}$ . Therefore, the lower bound for the covariance matrix of the estimated FE model parameters is given by

$$\text{Cov}(\boldsymbol{\Theta}) \geq \mathbf{I}_{\boldsymbol{\theta}\boldsymbol{\theta}}^{-1}, \quad \mathbf{I}_{\boldsymbol{\theta}\boldsymbol{\theta}} = \sum_{i=1}^k \left[ \left( \frac{\partial \mathbf{h}_i(\boldsymbol{\theta}, \ddot{\mathbf{u}}_{g_{1 \rightarrow i}})}{\partial \boldsymbol{\theta}} \right)^T \mathbf{R}^{-1} \frac{\partial \mathbf{h}_i(\boldsymbol{\theta}, \ddot{\mathbf{u}}_{g_{1 \rightarrow i}})}{\partial \boldsymbol{\theta}} \right]_{\text{at } \boldsymbol{\theta}, \mathbf{r}} \quad (5.29)$$

where  $\mathbf{I}_{\boldsymbol{\theta}\boldsymbol{\theta}}$  is evaluated for the true values of the FE model parameters and simulation error variances,  $\boldsymbol{\theta}$  and  $\mathbf{r}$ , respectively, which are approximated by the ML estimates  $\hat{\boldsymbol{\theta}}$  and  $\hat{\mathbf{r}}$ . Based on Theorem 2,  $\hat{\boldsymbol{\theta}}$  and  $\hat{\mathbf{r}}$  converge asymptotically to  $\boldsymbol{\theta}$  and  $\mathbf{r}$ , respectively, and therefore, the parameter estimation covariance matrix asymptotically converges to the CRLB computed at  $\hat{\boldsymbol{\theta}}$  and  $\hat{\mathbf{r}}$ . Although the obtained CRLB (i.e., inverse of the FIM) usually has non-zero off-diagonal entries, typically only the diagonal entries are considered in evaluating the variance of the model parameters. Therefore, the lower bound for the variance of parameter  $\theta_i$  ( $\sigma_{\theta_i}^2$ ) is the  $i^{\text{th}}$  diagonal entry of the CRLB matrix. In case the off-diagonal terms of the CRLB are significant compared to the diagonal terms, the CRLB for the variance of each individual parameters can be obtained using the Schur complement method [48]. Assuming that the FE model parameter vector  $\boldsymbol{\theta}$  is partitioned in two parts  $\boldsymbol{\theta} = [\boldsymbol{\theta}_1^T \quad \boldsymbol{\theta}_2^T]^T$ , the FIM is correspondingly partitioned in four blocks as

$$\mathbf{I}_{\boldsymbol{\theta}\boldsymbol{\theta}} = \begin{bmatrix} \mathbf{I}_{11} & \mathbf{I}_{12} \\ \mathbf{I}_{21} & \mathbf{I}_{22} \end{bmatrix} \quad (5.30)$$

It can be shown that the CRLB of the covariance matrix of the estimation of  $\boldsymbol{\theta}_1$  can be found using the generalized Schur complement of  $\mathbf{I}_{11}$  in  $\mathbf{I}_{\boldsymbol{\theta}\boldsymbol{\theta}}$  [49], i.e.,

$$\text{Cov}(\Theta_1) \geq \left( \mathbf{I}_{11} - \mathbf{I}_{12} \mathbf{I}_{22}^{-1} \mathbf{I}_{21} \right)^{-1} \quad (5.31)$$

Since the evaluation of the FIM matrix requires estimates of the simulation error variances,  $\hat{\mathbf{r}}$ , this method of parameter estimation uncertainty quantification is made possible only through the extended estimation problem stated in Eqs. (5.20) and (5.21). It is noteworthy that after estimating the FE model parameters ( $\hat{\boldsymbol{\theta}}$ ) and the simulation error variances ( $\hat{\mathbf{r}}$ ), evaluating their estimation uncertainty using this

method comes at minor additional computational cost. The term  $\left. \frac{\partial \mathbf{h}_r(\boldsymbol{\theta}, \ddot{\mathbf{u}}_{g_i \rightarrow i})}{\partial \boldsymbol{\theta}} \right|_{\text{at } \hat{\boldsymbol{\theta}}, \hat{\mathbf{r}}}$  in

Eq. (5.29) is the FE response sensitivity matrix, which is computed using the DDM during the optimization process for parameter estimation and is therefore already available. The accuracy of the computed FIM in this method depends only on the accuracy of the estimated model parameters and simulation error variances ( $\hat{\boldsymbol{\theta}}$  and  $\hat{\mathbf{r}}$ , respectively). Using a deterministic sampling approach, it will be shown in Section 3.1 in the context of an application example that this method provides a more accurate approximation of the parameter estimation covariance matrix than Method 2 which is described next.

*Method 2: CRLB approximation based on the Hessian of the ML objective function*

It can be shown that the FIM is equal to the negative of the expected value of the Hessian matrix of the log-likelihood function evaluated at the true value of the parameter vector  $\boldsymbol{\theta}$  (refer to [34] for the proof). Therefore, the two sub-matrices  $\mathbf{I}_{\theta\theta}$  and  $\mathbf{I}_{rr}$  in Eq. (5.27) can be written as

$$\mathbf{I}_{\theta\theta} = -E \left[ \frac{\partial}{\partial \boldsymbol{\theta}} \left( \frac{\partial \Lambda(\boldsymbol{\theta}, \mathbf{r}, \mathbf{y}_{1 \rightarrow k})}{\partial \boldsymbol{\theta}} \right) \right]_{\text{at } \boldsymbol{\theta}, \mathbf{r}}, \quad \mathbf{I}_{\mathbf{r}\mathbf{r}} = -E \left[ \frac{\partial}{\partial \mathbf{r}} \left( \frac{\partial \Lambda(\boldsymbol{\theta}, \mathbf{r}, \mathbf{y}_{1 \rightarrow k})}{\partial \mathbf{r}} \right) \right]_{\text{at } \boldsymbol{\theta}, \mathbf{r}} \quad (5.32)$$

Therefore, the CRLB for the FE parameter estimation covariance matrix can be evaluated as

$$\text{Cov}(\boldsymbol{\Theta}) \geq \left( -E \left[ \frac{\partial}{\partial \boldsymbol{\theta}} \left( \frac{\partial \Lambda(\boldsymbol{\theta}, \mathbf{r}, \mathbf{y}_{1 \rightarrow k})}{\partial \boldsymbol{\theta}} \right) \right]_{\text{at } \boldsymbol{\theta}, \mathbf{r}} \right)^{-1} \quad (5.33)$$

where, as in Eq. (5.32), the expectation is taken with respect to  $p(\mathbf{y}_{1 \rightarrow k} | \boldsymbol{\theta}, \mathbf{r})$ . In the presence of a single realization of the measured structural response data (which is often the case in real-world applications), the expectation operation can be dropped and the FIM can be approximated by the negative of the Hessian of the log-likelihood function  $\Lambda(\boldsymbol{\theta}, \mathbf{y}_{1 \rightarrow k})$  evaluated at the ML estimates  $\hat{\boldsymbol{\theta}}$  and  $\hat{\mathbf{r}}$ . Since the objective function of the ML optimization problem is the negative log-likelihood function, see Eq. (5.21), the CRLB of the parameter estimation covariance matrix can be approximated as the inverse of the Hessian of the ML objective function. Some gradient-based optimization algorithms (e.g., interior-point method) also make use of an approximation of the Hessian matrix (e.g., using Broyden-Fletcher-Goldfarb-Shanno (BFGS) method [50]) to solve the optimization problem. For such ML optimization algorithms, approximating the FIM using the estimated Hessian matrix at the converged optimal point would be at no additional computational cost.

This method for approximating the CRLB of the parameter estimation covariance matrix has been extensively used in the structural model updating literature (e.g., [10,13,33]) to evaluate parameter estimation uncertainty. Nevertheless, this

approximation of the CRLB is expected to be less accurate than the first method because of the following two approximations used in the second method:

- (1) Eq. (5.33) is strictly valid when the expected value is taken over an infinite number of realizations of the measured structural response data. However, as mentioned earlier, the expectation operation in Eq. (5.33) is dropped in the presence of a single realization of the measured structural response data and the FIM is approximated by the negative Hessian matrix of the log-likelihood function.
- (2) An approximation of the Hessian matrix is used.

## **5.5. Validation Studies using Simulated Data**

Two numerical validation studies are provided to validate and further investigate the performance of the proposed parameter estimation and nonlinear FE model updating framework. For each validation study, first the earthquake response of a proposed full-scale structure, designed according to previous or current seismic design provisions, is simulated using a structural FE modeling and analysis technique [28] to be described later. A set of predefined realistic FE model parameter values, referred to herein as the true parameter values, are used in the simulation phase. The simulated structural response time histories are then contaminated with numerical noise and used as measured structural response data for the following parameter estimation phase. In the latter, the FE model parameters are treated as unknown and modeled as random variables. The FE model parameters are estimated following the

procedure described in Section 2.1, and their estimation uncertainty is evaluated using the methods described in Section 5.4.

The FE modeling and analysis technique used in this study is based on distributed-plasticity, displacement-based, structural FE models. In this approach, which has been widely used in nonlinear analysis and design of frame-type structures, the structure is spatially discretized using fiber-section, displacement-based, beam-column elements formulated using Bernoulli-Euler beam theory. The material nonlinearity can spread over several sections monitored along the element, which are called integration points. The sections are further discretized into layers or fibers [51], the stress-strain behavior of which is governed by associated (nonlinear) uniaxial material constitutive laws. Material constitutive models depend on a set of material model parameters (e.g., elastic modulus, yield stress, post-yield strain hardening ratio, etc.), the estimation of which is the objective of the proposed nonlinear FE model updating framework. A structural system is typically composed of a relatively small number of materials (e.g., two types of steel and three types of concrete) with different sets of nominal material parameters, each of which is represented by a single nonlinear uniaxial material model. Adapted from [2], Figure 5.1 shows the hierarchical discretization levels of the nonlinear FE modeling and analysis method considered in this study.

The ML estimation procedure is implemented in MATLAB [52] and interfaced with OpenSees [53] for FE response and response sensitivity computations. Although a specific nonlinear FE modeling and analysis technique is employed in the validation





based (DB) elements of length 250 mm and 5 Gauss-Lobatto (GL) integration points each, while the top part is discretized into 7 DB elements of length 500 mm and 3 GL integration points each. The steel fibers are modeled using the modified Giuffr -Menegotto-Pinto material constitutive model [54] with smooth curved shaped loading and unloading branches as illustrated in Figure 5.3. This material model is characterized by eight (time-invariant) parameters subdivided into three primary parameters and five secondary parameters. The three primary parameters are:  $E$  = elastic modulus,  $\sigma_y$  = initial yield strength, and  $b$  = strain hardening ratio (see Figure 5.3), while the five secondary parameters control the curvature of the hysteresis loops and the isotropic hardening. In this study, the three primary material parameters are treated as unknown FE model parameters to be identified, while the five secondary parameters are assumed known (deterministic) constants. For the simulation phase, the true (exact) values of the primary parameters are taken as  $E^{true} = 200\text{GPa}$ ,  $\sigma_y^{true} = 250\text{MPa}$ , and  $b^{true} = 0.1$ , while the true values of the secondary parameters are set to the values recommended in [54].

Two ground acceleration records from the 1989 Loma Prieta and 1994 Northridge earthquakes are selected [55] for the nonlinear time history analyses (see Table 5.1). Figure 5.4 shows the acceleration time histories for these two earthquake ground motions. Each nonlinear analysis is performed by first applying the gravity load quasi-statically and then the base excitation dynamically. The nonlinear time history analyses are performed using the Newmark average acceleration method [27] to recursively integrate the equations of motion in time using a constant time step size

of  $\Delta t = 0.02 \text{ sec}$ , and the Newton-Raphson method to solve iteratively the nonlinear incremental dynamic equations of equilibrium at each time step. Tangent stiffness-proportional damping [27] is used to model the damping energy dissipation characteristics (beyond material hysteretic energy dissipation) of the column by assuming a damping ratio of 2 percent for the first elastic mode ( $T_1 = 0.76 \text{ sec}$ ).

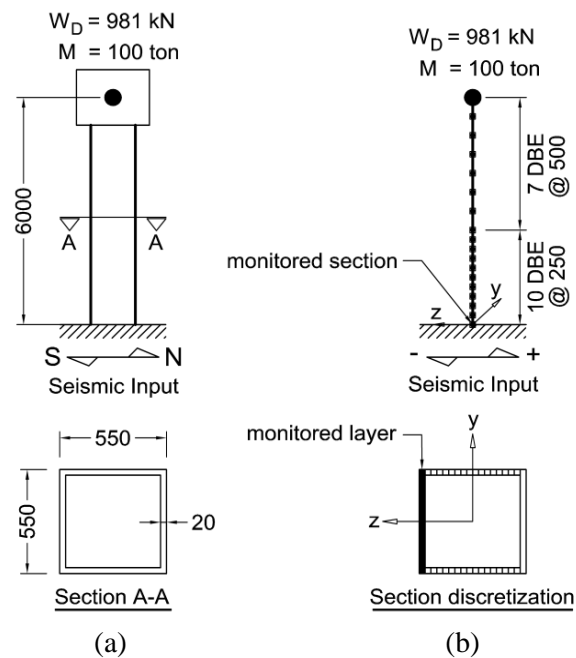


Figure 5.2: (a) Cantilever steel column with built-up box section, (b) details of the developed FE model (DBE: displacement-based finite element; 1 ton = 1000 kg; length unit: mm).

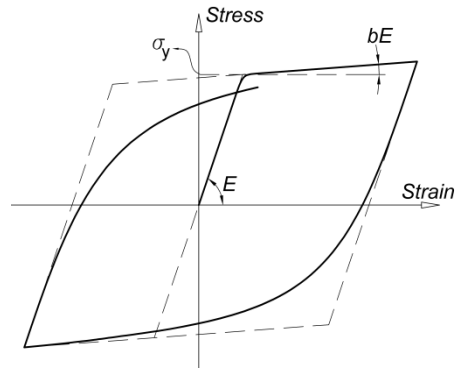


Figure 5.3: Modified Giuffré-Menegotto-Pinto uniaxial material constitutive model for structural steel.

Table 5.1: Selected earthquake ground motions.

Motion name	Earthquake	Station / Component	PGA (g)
<i>EQ1</i>	1989 Loma Prieta (M 6.9)	Corralitos - Eureka Canyon Road / 90°	0.48
<i>EQ2</i>	1994 Northridge (M 6.7)	Castaic - Old Ridge Route / 90°	0.57

Note: both records are sampled at 50 Hz.

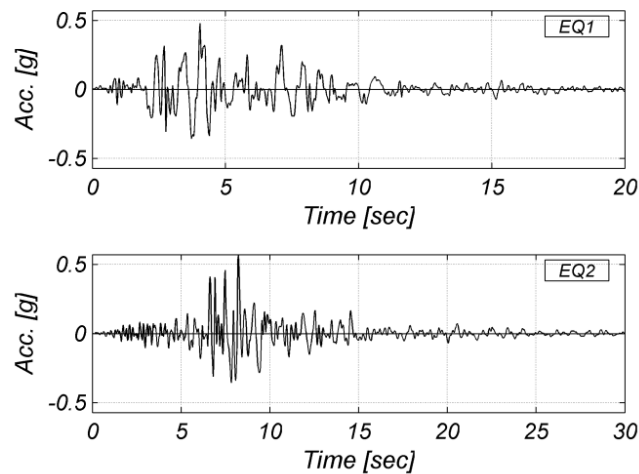


Figure 5.4: Time histories of the selected earthquake ground motions, top: *EQ1* from 1989 Loma Prieta earthquake, bottom: *EQ2* from 1994 Northridge earthquake.

The acceleration response time history of the column top in the direction of the seismic input is simulated and artificially polluted with measurement noise to represent the measured structural response. The measurement noise is modeled as a zero-mean Gaussian white noise. In the real world, the amplitude of the measurement noise for acceleration response time histories depends on the type of sensor and DAQ system (including sensor cables) and the environmental conditions. Using current sensor technology for structural response monitoring, the measurement noise is expected to be lower than 0.5% g root-mean-square (RMS).

The proposed parameter estimation and nonlinear FE model updating framework is utilized to evaluate point estimates of the FE model parameters ( $\hat{\boldsymbol{\theta}} = [\hat{E}, \hat{\sigma}_y, \hat{b}]^T$ ) and the measurement noise variance  $\hat{r}$  (which in this case is a single component vector). The FE model parameter estimation uncertainty is evaluated by computing the CRLB using the two methods presented in Section 5.4. To increase the computational efficiency, only the response of the structure to the first 16 and 20 seconds of *EQ1* and *EQ2*, respectively, are used in the parameter estimation process. In this validation study, the same FE model is used for the response simulation and parameter estimation phases; therefore, the effects of model uncertainties are not considered in this study. Moreover, the same input ground motion time history is used in the response simulation and parameter estimation phases; therefore, the effects of measurement noise on the seismic input are not considered, i.e., the seismic input is assumed noiseless. The detrimental effects of measurement noise on the input ground

acceleration on the performance of the proposed framework are investigated in the second validation example.

Two different cases are considered in this validation study. In the first case study, the performance of the parameter estimation procedure is investigated for different levels of output measurement noise. In the second case study, a deterministic sampling method is employed to obtain the statistical distribution of the estimated FE model parameters, which is then used to assess the accuracy of the FE model parameter estimation uncertainty evaluated from the two methods presented in Section 5.4.

**Case study 1: Effects of output measurement noise amplitude**

To investigate the robustness and sensitivity of the proposed parameter estimation and nonlinear FE model updating framework to the output measurement noise level, the estimation process is performed for different amplitudes of the contaminating measurement noise. The simulated absolute acceleration response of the cantilever column is contaminated with zero-mean Gaussian white noise of three different amplitudes, namely 0.5% g, 2% g, and 5% g RMS. The 2% g and 5% g RMS noise levels are unrealistically high and are unlikely to be seen in the real world; nevertheless, they are considered here to exercise the estimation framework under extreme noisy conditions. As mentioned earlier, by neglecting the effects of the input noise and model uncertainties in the parameter estimation process, the simulation error accounts for the measurement noise only. Therefore, the simulation error variance is expected to be equal to the measurement noise variance. The measurement noise

variance corresponding to a zero-mean Gaussian white noise signal with  $x\%$  g RMS amplitude is equal to  $\left(\frac{x}{100} \times 9.81\right)^2 \left[m/s^2\right]^2$ . Therefore, the true values of the simulation error variance for the three considered noise levels (0.5% g, 2% g, and 5% g RMS) are  $r^{true} = 0.24 \times 10^{-2}$ ,  $3.85 \times 10^{-2}$ , and  $24.06 \times 10^{-2} \left[m/s^2\right]^2$ , respectively. These true values are used later to assess the accuracy of the estimated simulation error variance. The initial estimates of the FE model parameters are selected as  $E_0 = 1.30E^{true}$ ,  $\sigma_{y_0} = 0.75\sigma_y^{true}$ , and  $b_0 = 1.35b^{true}$ , which represents a significant departure from their true values given the physical nature of these parameters and the fact that their true values are expected to not be far from their nominal values. For all three cases, the initial estimate of the simulation error variance is selected as  $r_0 = 0.62 \times 10^{-2} \left[m/s^2\right]^2$ , which corresponds to a 0.8% g RMS measurement noise signal. The feasible search domain for the model parameters is selected as  $0.4\theta_0 \leq \theta \leq 2.5\theta_0$  where  $\theta_0 =$  vector of initial estimates of the FE model parameters, and the feasible search domain for the simulation error variance is set as  $0.01r_0 \leq r \leq 100r_0$ . Since there is minor prior knowledge about the true value of the simulation error variance, its feasible search domain is selected to be much wider than for the FE model parameters. To improve the performance of the optimization process, the FE model parameters and the simulation error variances are normalized by their corresponding initial estimates. Through this normalization, the derivatives of the ML objective function with respect to the estimation parameters have the same order of magnitude.

Figure 5.5 shows the convergence history of the three FE model parameters and the simulation error variance for the three considered levels of measurement noise amplitude for *EQ1*. In this figure, the number of iterations is equal to the number of evaluation of the ML objective function, which in turn is equal to the number of FE model runs. The converged point estimates are depicted with filled circular dots to facilitate comparison of the number of iterations to achieve convergence in the three cases. Figure 5.6 shows similar results for *EQ2*. Spike-like behavior is observed in the convergence histories in Figures 5.5 and 5.6. This spike-like behavior is the result of perturbation in the estimation parameters to escape local minima. The optimization algorithm detects when iterations appear to be converging to a local minimum, and then perturbs the parameters to escape the domain of attraction of that local minimum. The convergence criterion consists of two conditions; if any of the two conditions is satisfied, the optimization process is considered converged. The first condition is based on the absolute variation in the estimation parameters and the second condition is based on the first-order optimality measure of the ML objective function as

$$\text{Condition 1: } \left\| \begin{bmatrix} \hat{\boldsymbol{\theta}}_m \\ \hat{\mathbf{r}}_m \end{bmatrix} - \begin{bmatrix} \hat{\boldsymbol{\theta}}_{m-1} \\ \hat{\mathbf{r}}_{m-1} \end{bmatrix} \right\|_2 \leq 10^{-7} \quad (5.34)$$

$$\text{Condition 2: } \|\nabla J(\boldsymbol{\theta}, \mathbf{r})\|_\infty \leq 10^{-7} \quad (5.35)$$

where  $\hat{\boldsymbol{\theta}}_m$  is the estimated normalized FE model parameter vector at the  $m^{\text{th}}$  optimization iteration,  $\|\dots\|_2$  denotes the second order (or Euclidean) norm, and

$\|\dots\|_{\infty}$  denotes the infinity norm (= the maximum absolute value of vector components).

Table 5.2 reports the converged estimated FE model parameters and simulation error variance, normalized by the corresponding true parameter values, for all cases considered. This table also reports the estimation standard deviation of each model parameter (evaluated using the two methods presented in Section 5.4) normalized by the corresponding point estimate of the parameter; the  $\hat{\sigma}_{\theta_i}/\hat{\theta}_i$  can be loosely interpreted as the coefficient of variation (C.O.V.) of the FE model parameter.

Figures 5.5 and 5.6, and Table 5.2 indicate the successful performance of the proposed parameter estimation method in correctly estimating the model parameters and measurement noise variance. The estimated values of the FE model parameters for the case of 5% g RMS measurement noise level (see Table 5.2) show that this excessively high level of measurement noise results in erroneous (biased) estimation of the strain hardening ratio parameter  $b$ . Furthermore, these detrimental effects of high measurement noise are more significant for *EQ2* than *EQ1*. To correctly estimate post-yield material parameters such as  $b$ , the earthquake base excitation should be strong enough to exercise the post-yield branches of the material model at the fiber level and moreover, the measured response of the structure should be sensitive enough to the variation of these parameters. The FE predicted curvature ductility demand (defined as the ratio of the peak curvature response to the yield curvature) at the base section (marked as monitored section in Figure 5.2b) of the structure are listed in the last column of Table 5.2 for both the estimated and true FE model parameter values.



The curvature ductility demands reported in Table 5.2 show that the structure exhibits higher level of nonlinear behavior during *EQ1* than during *EQ2*; consequently, the response of the structure to *EQ1* contains more information about the yield and post-yield material parameters than for *EQ2* and therefore, the parameter estimation results are less sensitive to the measurement noise level for *EQ1* than for *EQ2*. These observations are in agreement with previous studies [2-3].

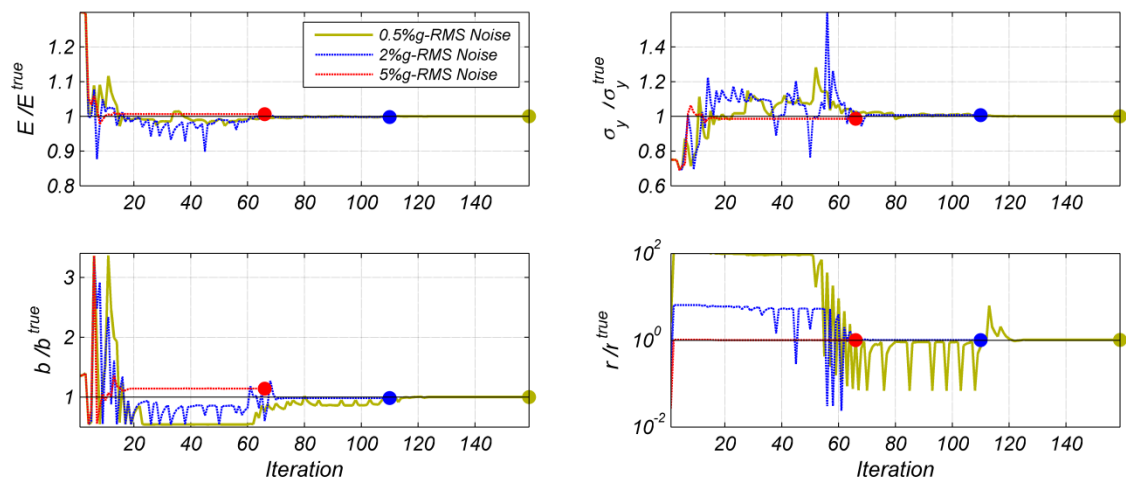


Figure 5.5: Convergence history of the estimated FE model parameters and simulation error variance for three measurement noise levels for *EQ1* (The last graph is plotted in semi-logarithmic scale).

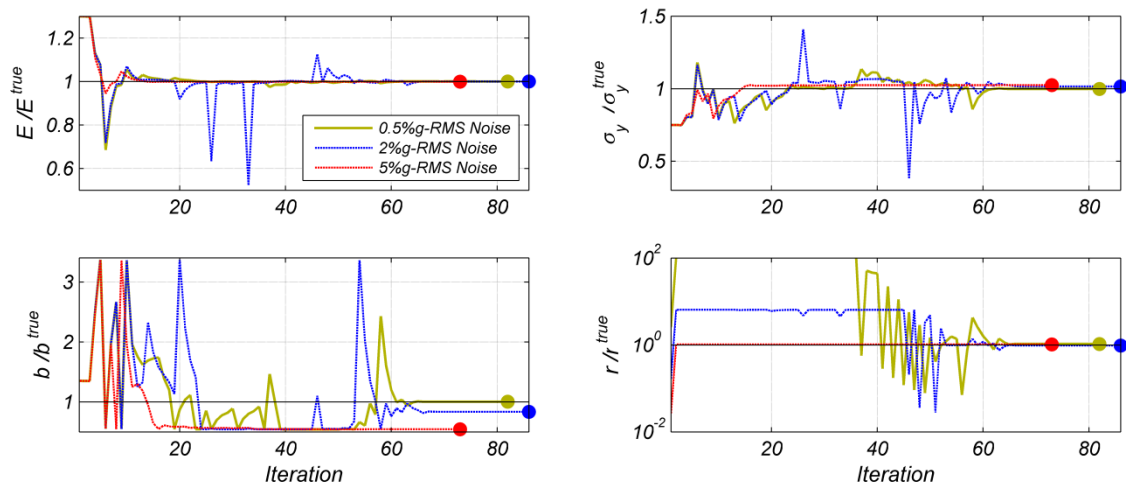


Figure 5.6: Convergence history of the estimated FE model parameters and simulation error variance for three measurement noise levels for *EQ2* (The last graph is plotted in semi-logarithmic scale).

The estimated C.O.V.s of the estimation parameters are in good agreement with the parameter estimation accuracy, i.e., the C.O.V.s are larger when the estimated FE model parameters are less accurate. For all cases considered here, the modulus of elasticity  $E$  has the lowest C.O.V., followed by the yield strength  $\sigma_y$ , and the strain hardening ratio  $b$  which has the largest C.O.V. Moreover, the C.O.V.s of the estimated parameters consistently increase as the level of measurement noise increases. For FE model parameters that are not estimated accurately, the corresponding C.O.V.s estimated from the two methods used for computing the CRLB are more distant, as in the case of the strain hardening ratio,  $b$ , for *EQ2* with 5% g RMS measurement noise level.

Table 5.2: Parameter estimation results for the three measurement noise levels considered in Case study #1.

Ground motion name	Noise level (%g RMS)	Model parameters			Simulation error variance $r/r^{true}$	C.O.V. (%) Method 1			C.O.V. (%) Method 2			Section curvature ductility demand (True value)
		$E/E^{true}$	$\sigma_y/\sigma_y^{true}$	$b/b^{true}$		$E$	$\sigma_y$	$b$	$E$	$\sigma_y$	$b$	
EQ1	0.5	1.00	1.00	1.00	1.02	0.03	0.14	1.05	0.03	0.13	0.86	5.06
	2	1.00	1.01	0.98	1.01	0.12	0.55	4.26	0.12	0.56	4.43	5.06
	5	1.01	0.99	1.14	1.00	0.32	1.45	9.49	0.34	1.50	13.36	4.95
EQ2	0.5	1.00	1.00	1.00	1.05	0.02	0.20	2.27	0.02	0.19	1.97	3.93
	2	1.00	1.02	0.83	0.97	0.09	0.75	10.08	0.09	0.79	10.72	4.07
	5	1.00	1.02	0.54	1.03	0.23	1.72	33.49	0.25	10.05	247.9	4.55

Figures 5.7 and 5.8 compare the FE predicted structural response to *EQI* obtained using the true values of the FE model parameters, and the initial and final estimates of the FE model parameters inferred for the case of 2% g RMS measurement noise level. Figure 5.7 compares the structural level response, with the column top relative (to the base) acceleration response time history in Figure 5.7(a), and the base shear ( $V_b$ ) normalized by the total dead load supported by the column versus the column drift ratio (ratio of column top horizontal relative displacement to column height) in Figure 5.7(b). The local section and fiber level FE predicted responses are compared in Figure 5.8. Figure 5.8(a) shows the normalized moment-curvature response of the pier base section, in which the section moment ( $M$ ) is normalized by the corresponding section nominal yield moment ( $M_y = S \sigma_y$ , where  $S$  denotes the section modulus) and the curvature ( $\phi$ ) is multiplied by the section height ( $H = 550\text{mm}$ ). Figure 5.8(b) compares the FE predicted stress-strain responses of the monitored layer (or fiber) at the column base section (see Figure 5.2(b)). It is observed that at both the global structural and local section and fiber levels, (a) the FE predicted response based on the initial estimates of the model parameters differs significantly from the true response, and (b) the FE predicted response based on the final estimates of the model parameters practically coincides with the true response.

This validation study illustrates the application of the proposed parameter estimation and nonlinear FE model updating framework for structural damage identification. Using the measured input excitation and the structural response time histories recorded during a damage-inducing earthquake, an initial FE model of the

structure is successfully updated in the time domain by correctly estimating the unknown FE model parameters. The updated FE model successfully estimates the structural response at both the global structural and local section and fiber levels, which can be used to investigate and identify (detect, localize, classify and quantify) structural damage in the structure. The parameter estimation process for each of the cases considered in this example required less than one hour on a Dell Precision T7610 desktop workstation with two Intel Xeon E5-2630 (2.6 GHz) processors with 6 cores each.

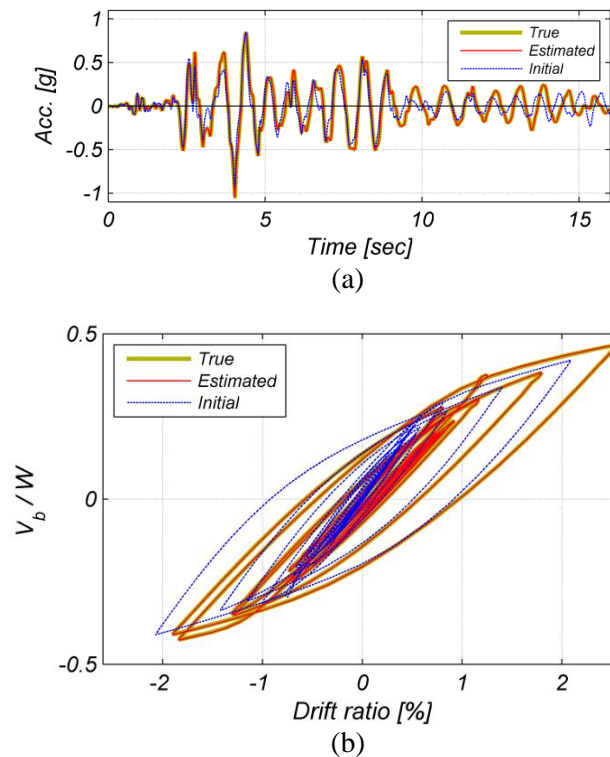


Figure 5.7: Comparison of the FE predicted structural level response to *EQI* obtained using the true values of the FE model parameters, and the initial and final estimates of the FE model parameters inferred for the case of 2% g RMS measurement noise level: (a) relative acceleration response time history of the column top, and (b) normalized base shear versus column drift ratio.

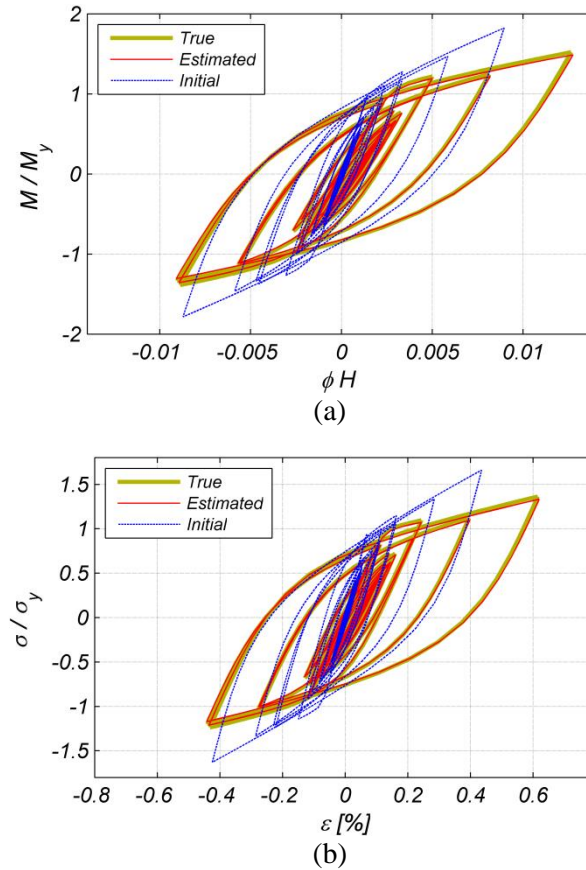


Figure 5.8: Comparison of the FE predicted section level response to  $EQI$  obtained using the true values of the FE model parameters, and the initial and final estimates of the FE model parameters inferred for the case of 2% g RMS measurement noise level: (a) normalized moment-curvature response of the column base section, and (b) normalized fiber stress-strain response of the monitored layer at the column base section.

**Case study 2: Deterministic sampling method for evaluating the estimation uncertainty**

Two methods are described in Section 5.4 to approximate the CRLB, which provides an asymptotic limit for the parameter estimation covariance matrix. The question that is investigated in this case study is how close the actual parameter estimation covariance matrix can get to the approximated CRLB for a nonlinear FE

model updating problem using dynamic input-output data recorded during an earthquake event. For this purpose, a deterministic sampling method is employed to obtain a statistical distribution of the ML estimator for the FE model parameter vector. The estimator  $\Theta = \mathbf{t}(\mathbf{Y}_{1 \rightarrow k})$  can be viewed as a nonlinear function (mapping) of the random variables  $\mathbf{Y}_{1 \rightarrow k}$ . The conditional joint PDF of the measured response  $\mathbf{Y}_{1 \rightarrow k}$ , denoted as  $p(\mathbf{y}_{1 \rightarrow k} | \boldsymbol{\theta}^{true}, \mathbf{r}^{true})$  and assumed to be Gaussian, is propagated through the nonlinear estimator function  $\mathbf{t}(\dots)$  to find the joint PDF of the FE model parameters  $\Theta$ . Here, the nonlinear transformation of the Gaussian joint PDF  $p(\mathbf{y}_{1 \rightarrow k} | \boldsymbol{\theta}^{true}, \mathbf{r}^{true})$  is performed using the unscented transformation method [56], which is a deterministic sampling approach. The unscented transformation is an approximate method to propagate the mean vector and covariance matrix of a Gaussian random vector through a nonlinear function. It can be shown that the unscented transformation can provide a third order approximation of the true mean vector and covariance matrix of the estimator [57].

In the unscented transformation method, a set of deterministic samples called sigma points are selected so that the ensemble mean and covariance of these samples match the first and second moment of  $p(\mathbf{y}_{1 \rightarrow k} | \boldsymbol{\theta}^{true}, \mathbf{r}^{true})$ . Each sigma point herein is a realization of the stochastic response of the structure  $\mathbf{Y}_{1 \rightarrow k}$  for the true FE model parameters. In this case study,  $2n$  sigma points are selected and denoted as  $\mathbf{y}_{1 \rightarrow k}^{(i)}$ ,  $i = 1 \rightarrow 2n$ , where  $n = k \times n_y$  [57]. Each sigma point is used as the measured response

of the structure to estimate a sample of the FE model parameter vector through the ML estimation procedure, i.e.,  $\hat{\boldsymbol{\theta}}^{(i)} = \mathbf{t}_{ML}(\mathbf{y}_{1 \rightarrow k}^{(i)})$ . The ensemble covariance of the resulting  $2n$  estimated FE model parameter vectors approximates the parameter estimation covariance matrix. The sigma points  $\mathbf{y}_{1 \rightarrow k}^{(i)}$  are computed as ([57-58]).

$$\begin{aligned}\mathbf{y}_{1 \rightarrow k}^{(i)} &= \mathbf{y}_{1 \rightarrow k}^{true} + \tilde{\mathbf{y}}_{1 \rightarrow k}^{(i)}, \quad i = 1 \rightarrow 2n \\ \tilde{\mathbf{y}}_{1 \rightarrow k}^{(i)} &= (\sqrt{n\mathbf{P}})_i^T, \quad i = 1 \rightarrow n \\ \tilde{\mathbf{y}}_{1 \rightarrow k}^{(n+i)} &= -(\sqrt{n\mathbf{P}})_i^T, \quad i = 1 \rightarrow n\end{aligned}\tag{5.36}$$

where  $\mathbf{y}_{1 \rightarrow k}^{true} = E[\mathbf{Y}_{1 \rightarrow k} \mid \boldsymbol{\Theta} = \boldsymbol{\theta}^{true}, \mathcal{R} = \mathbf{r}^{true}]$  = response time histories of the structure simulated using the true FE model parameters. Matrix  $\sqrt{n\mathbf{P}}$  is the matrix square root of matrix  $n\mathbf{P}$  such that  $(\sqrt{n\mathbf{P}})^T(\sqrt{n\mathbf{P}}) = n\mathbf{P}$ , and  $(\sqrt{n\mathbf{P}})_i$  in Eq. (5.36) denotes the  $i^{\text{th}}$  row of matrix  $\sqrt{n\mathbf{P}}$ . Matrix  $\mathbf{P}$  is the covariance matrix of  $(\mathbf{Y}_{1 \rightarrow k} \mid \boldsymbol{\Theta} = \boldsymbol{\theta}^{true}, \mathcal{R} = \mathbf{r}^{true})$  and is defined as

$$\mathbf{P} = \begin{bmatrix} \mathbf{R}_{n_y \times n_y} & & & \mathbf{0} \\ & \mathbf{R}_{n_y \times n_y} & & \\ & & \ddots & \\ \mathbf{0} & & & \mathbf{R}_{n_y \times n_y} \end{bmatrix}_{(k.n_y) \times (k.n_y)}\tag{5.37}$$

where  $\mathbf{R}$  is the diagonal covariance matrix of the simulation error vector as introduced earlier following Eq. (5.18); in the present case, it is equal to the covariance matrix of the artificially imposed (true) measurement noise.

While the deterministic sampling approach is still an approximate method to evaluate the parameter estimation uncertainty based on a limited number of samples, it



can provide some insight on the accuracy of the two methods for evaluating the parameter estimation covariance matrix presented in Section 5.4. Table 5.3 compares for *EQ1* the C.O.V.s of the estimated model parameters obtained using *Method 1* and *Method 2* in Case study # 1 (see Table 5.2) with the C.O.V. estimated here using the deterministic sampling approach. It is observed that the C.O.V.s obtained using *Method 1* are closer to the corresponding C.O.V.s estimated using the deterministic sampling method for all three measurement noise levels. Therefore, in this validation study, *Method 1* provides a more accurate estimation of the C.O.V. of the estimated model parameters than *Method 2*, which is a widely used approach for computing parameter estimation uncertainty. The C.O.V.s obtained using the sampling method are lower than the CRLB estimated using *Method 1* due to the estimation error in the sampling method and the source of error in *Method 1* discussed in Section 5.4.

Table 5.3: Comparison of C.O.V.s of the estimated FE model parameters obtained using three methods for *EQ1*.

Ground motion name	Noise level (%g RMS)	C.O.V. (%) Sampling Method			C.O.V. (%) Method 1			C.O.V. (%) Method 2		
		$E$	$\sigma_y$	$b$	$E$	$\sigma_y$	$b$	$E$	$\sigma_y$	$b$
<i>EQ1</i>	0.5	0.0	0.1	1.0	0.0	0.1	1.0	0.0	0.1	0.86
	2	0.1	0.5	4.1	0.1	0.5	4.2	0.1	0.5	4.43
	5	0.3	1.3	8.8	0.3	1.4	9.4	0.3	1.5	13.3

Although the deterministic sampling method requires a limited number of sigma points, the process of evaluating the ML estimates of the FE model parameters for every sigma point is computationally demanding. Running the deterministic sampling procedure for each of the three levels of measurement noise in this problem

required about 26 hours of parallel processing on a Dell Precision T7610 desktop workstation with two Intel Xeon E5-2630 (2.6 GHz) CPUs (with 12 cores).

### **Case study 3: Heterogeneous sensor array**

To highlight the dominance of the proposed nonlinear FE model updating and parameter estimation framework compared to the current least squares estimation method in the literature, this case study investigates the case of having measurement data obtained from heterogeneous sensor array with one or more data channels having erroneous data. As stated before, the least squares estimation method gives equal weights to the different measurement data channels. As will be shown in this case study, when the measured signals have different unit scale and amplitude, the least squares method is unable to completely extract information from the measured data.

In this case study, the simulated acceleration response of the cantilever steel column (as considered in Case study 1) is polluted by colored measurement noise. The noise is considered to be Gaussian colored with 5% g RMS amplitude and [0.5,4] Hz frequency bandwidth. The colored noise can be a result of sensor malfunctioning and/or improper sensor installation. Since the noise is non-white, it is expected to have biased estimation of modeling parameters. To enhance the estimation accuracy, a second channel of data is added by measuring the curvature of the column base section. The curvature of steel sections can be measured by a pair of strain gauges installed on the outer faces of the section. Figure 5.9 shows the time histories of the measured data for *EQ2* including both the acceleration of the column top and the

curvature of the column base section. The curvature data is assumed to have  $2 \times 10^{-4}$  RMS measurement noise.

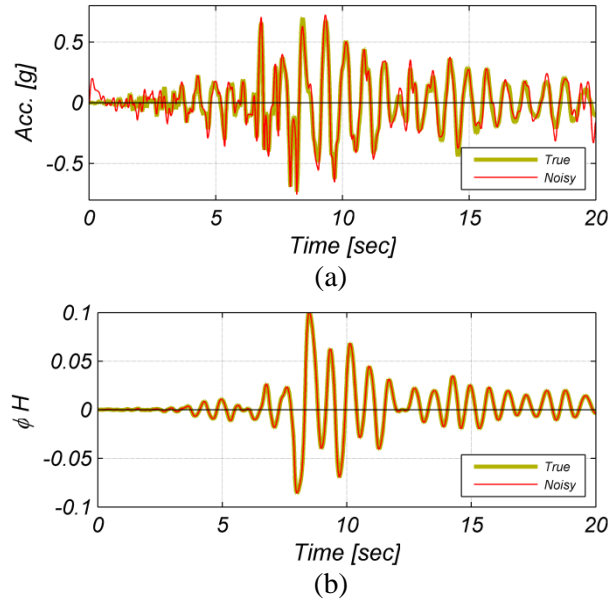


Figure 5.9: Heterogeneous measurements, (a) acceleration response time history of the column top, (b) curvature response time history of the column base section.

In this case study, both the least squares estimation method and the parameter estimation method proposed in this study are used. The estimations are performed by considering only the measured acceleration time history as output measurement (1-Output), and both the measured acceleration and curvature time histories as output measurement (2-Outputs). The same as Case study 1, initial estimates of the modeling parameters are selected as  $\sigma_{y_0} = 0.75\sigma_y^{true}$ ,  $E_0 = 1.30E^{true}$ ,  $b_0 = 1.35b^{true}$ . The initial estimate of noise variance is selected as  $r_0^{acc} = 0.62 \times 10^{-2} \left[ \frac{m}{s^2} \right]^2$  for acceleration response and  $r_0^{cur} = 1.00 \times 10^{-6}$  for curvature response. The feasible search domain for the modeling parameters is set as  $0.4\theta_0 \leq \theta \leq 2.5\theta_0$ , where  $\theta_0 =$  vector of initial

estimates of the modeling parameters, and the feasible search domain for noise variance is set as  $0.025r_0 \leq r \leq 40r_0$ .

Figures 5.10 and 5.11 show the convergence history for the two cases of output measurement using the least squares estimation and the proposed estimation method, respectively. Figure 5.10 clearly shows that the inclusion of the second measurement data set does not affect the least squares estimation results, and in both cases the material parameter estimations are inaccurate. The scale difference of the two measurement signals makes the least squares method to automatically ignore the curvature data in the presence of the higher amplitude acceleration signal and the least squares estimation cannot extract any information from the cleaner (less noisy) curvature data. The proposed estimation procedure, however, can correctly use the measured curvature data to enhance the estimation accuracy.

Table 5.4 lists the estimation results including the estimation COVs. Although the acceleration data is contaminated by a colored noise, the estimation COVs in this table shows that the proposed estimation algorithm successfully extracts all the useful information contained in the curvature data and the estimation uncertainties associated with the 1-Output case are significantly reduced by adding the extra measurement data.

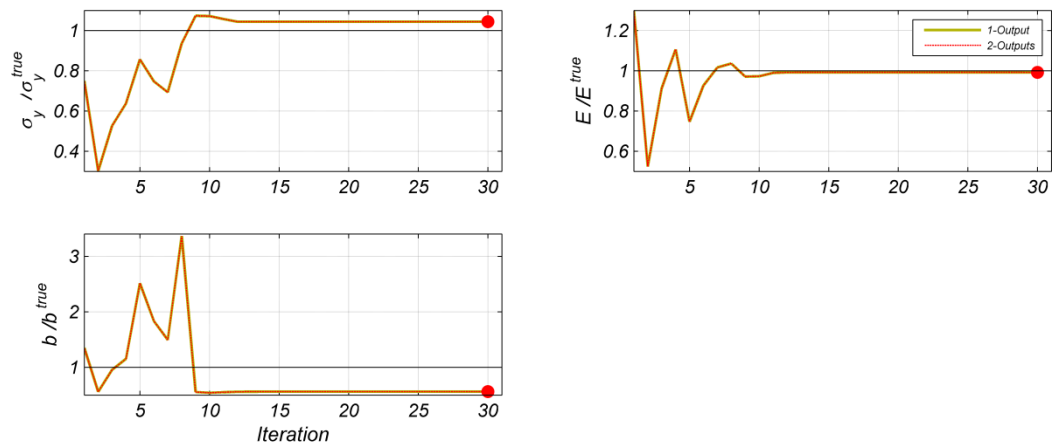


Figure 5.10: Convergence history of the modeling parameters using least squares estimation method for two cases of output measurement for *EQ2*.

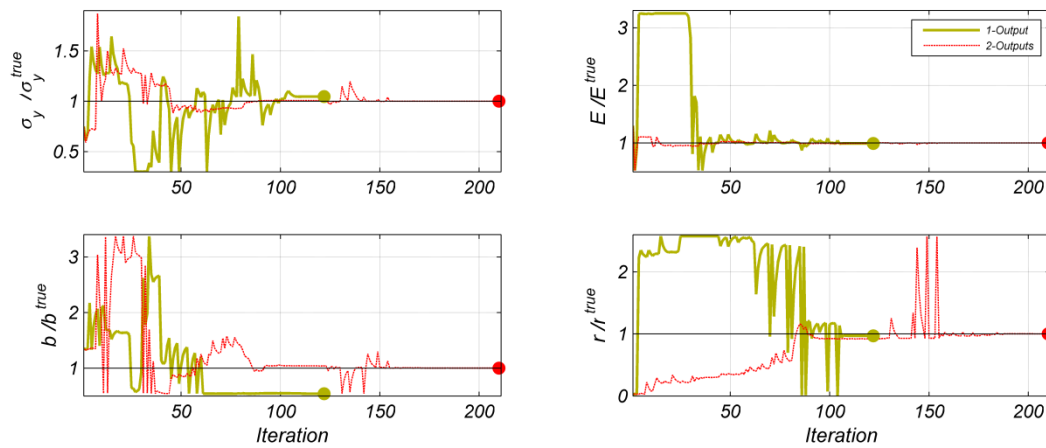


Figure 5.11: Convergence history of the modeling parameters using the proposed estimation method for two cases of output measurement for *EQ2*.

Table 5.4: Estimation results for Case study 3.

Estimation method	Modeling parameters			Accelerat ion Noise variance	Curvature Noise variance	COV (%) Method 1			COV (%) Method 2		
	$\sigma_y / \sigma_y^{true}$	$E / E^{true}$	$b / b^{true}$	$r / r^{true}$	$r / r^{true}$	$\sigma_y$	$E$	$b$	$\sigma_y$	$E$	$b$
LS Method-1 Output	1.04	0.99	0.56	-	-	-	-	-	0.17	0.01	2.05
LS Method-2 Outputs	1.04	0.99	0.56	-	-	-	-	-	0.17	0.01	2.04
Prop. Method- 1 Output	1.05	0.99	0.54	0.97	-	0.01	0.0	0.17	0.05	0.00	0.69
Prop. Method- 2 Outputs	1.00	1.00	1.00	1.00	1.02	0.00	0.0	0.00	0.00	0.00	0.00

#### Case study 4: Effects of initial estimation error

To investigate the sensitivity of the proposed parameter estimation framework to initial estimates of the modeling parameters, the FE model updating procedure for cantilever steel column is repeated for  $EQI$  with 2% g RMS measurement noise level with four different sets of initial estimates as shown in Table 5.5. The initial estimation error in this table is defined as the relative distance between the initial estimates and the true values of modeling parameters:

$$Error(\%) = \sqrt{\frac{\left(\frac{\sigma_{y_0} - \sigma_y^{true}}{\sigma_y^{true}}\right)^2 + \left(\frac{E_0 - E^{true}}{E^{true}}\right)^2 + \left(\frac{b_0 - b^{true}}{b^{true}}\right)^2}{3}} \times 100 \quad (5.38)$$

Table 5.5: Different sets of initial estimates considered in Case study 4.

Set #	$\sigma_{y_0} / \sigma_y^{true}$	$E_0 / E^{true}$	$b_0 / b^{true}$	Error (%)
Set 1	1.33	0.78	1.34	~30%
Set 2	0.50	0.60	1.27	~40%
Set 3	0.50	1.55	1.45	~50%
Set 4	1.55	1.81	0.65	~60%

The same as Case study 1, the initial estimate of noise variance is  $r_0 = 0.62 \times 10^{-2}$

$\left[ \frac{m}{s^2} \right]^2$ , and the feasible search domain for the modeling parameters is set as

$0.4\theta_0 \leq \theta \leq 2.5\theta_0$  and for noise variance is set as  $0.025r_0 \leq r \leq 40r_0$ .

Figure 5.12 illustrates the convergence history of the three modeling parameters and the noise variance for the four different sets of initial modeling parameter estimates. Table 5.6 lists the estimated modeling parameters and noise variance in addition to the coefficient of variation (COV) of the modeling parameters. More combinations of randomly generated initial parameter estimates are also studied, but are not presented here due to space limitations. It is concluded that for initial estimation error less than 60% (as defined by Eq. (5.38)), the proposed nonlinear FE model updating and parameter estimation framework is almost insensitive to the initial parameter estimates.

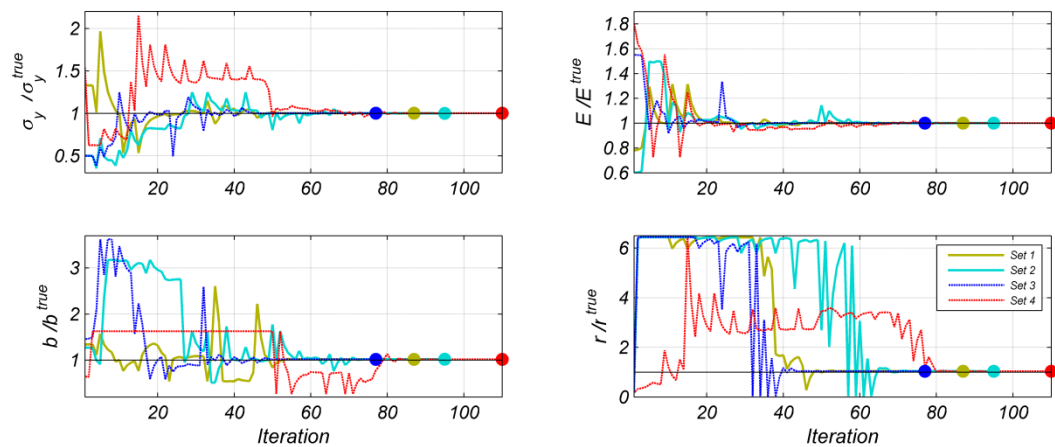


Figure 5.12: Convergence history of the modeling parameters and the noise variance for four different sets of initial estimates as considered in Case study 4 for  $EQI$  and 2% g RMS measurement noise.

Table 5.6: Estimation results for four sets of initial estimates considered in Case study 4.

Motion name	Set #	Modeling parameters			Noise variance	COV (%) Method 1			COV (%) Method 2		
		$\sigma_y / \sigma_y^{true}$	$E / E^{true}$	$b / b^{true}$	$r / r^{true}$	$\sigma_y$	$E$	$b$	$\sigma_y$	$E$	$b$
EQ1	1	1.00	1.00	1.02	1.04	0.57	0.12	4.22	0.58	0.12	4.08
	2	1.00	1.00	1.02	1.04	0.57	0.12	4.21	0.62	0.13	4.41
	3	1.00	1.00	1.02	1.04	0.57	0.12	4.22	0.58	0.13	4.30
	4	1.00	1.00	1.02	1.04	0.57	0.12	4.22	0.59	0.14	4.30

### **Case study 5: Effects of input measurement noise**

The effects of input measurement noise on the proposed parameter estimation framework are examined by considering slightly different input motions in the simulation and estimation phases. In the simulation phase, the ground acceleration time histories of *EQ1* and *EQ2* as shown in Figure 5.4 are used to simulate the acceleration response of the structure. The acceleration response is then polluted by 2% g RMS measurement noise to obtain measured response of the structure. In the estimation phase, the acceleration time history of the two earthquake motions is contaminated by zero-mean Gaussian white noise to mimic the presence of noise in the measured ground acceleration. To investigate the sensitivity of the parameter estimation framework to the input measurement noise, three levels of input noise are considered here: 0.5% g, 2% g, and 5% g RMS. As stated before, the last two noise levels are unphysical and large; they are included to examine the robustness of the estimation framework under extreme input noise levels. Figure 5.13 compares the true ground acceleration time history, which used in the simulation phase, with the noisy ground acceleration time histories used in the estimation phase for *EQ2*.



Figures 5.14 and 5.15 illustrate the convergence history of the three modeling parameters and noise variance for three levels of input noise for *EQ1* and *EQ2*, respectively. Because the current parameter estimation framework does not account for the effects of input noise, the presence of input noise biases the estimation results and the estimation errors increase as the level of input noise increases. Table 5.7 lists the estimation results including the estimation uncertainties for the three input noise level for *EQ1* and *EQ2*. Table 5.7 shows that as the input noise level increases, the estimated prediction error variance also increases. In other words, the estimation framework tries to indirectly account for the effects of input noise by estimating higher level of output noise. However, the input white noise signal, which is filtered through the nonlinear structural system, is transformed into a colored noise signal at the output channel and therefore, approximating the resulting colored output noise with a white noise model leads to biased estimation results. As can be inferred from Figures 5.14 and 5.15 and Table 5.7, the estimation errors are more significant for the strength-related material parameters (i.e.,  $\sigma_y, b_0$ ) as compared to the modulus of elasticity  $E$ . Moreover, the estimation errors increase as the level of input motion and the seismic demands decrease from *EQ1* to *EQ2*.

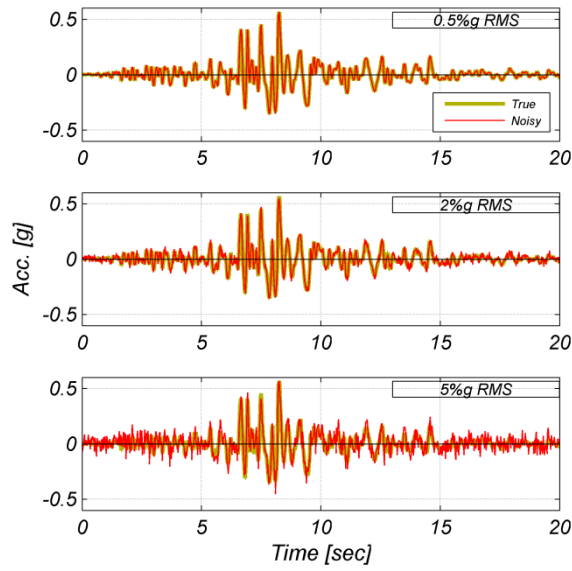


Figure 5.13: Comparison of the noisy with the true (not noisy) ground acceleration time history of EQ2.

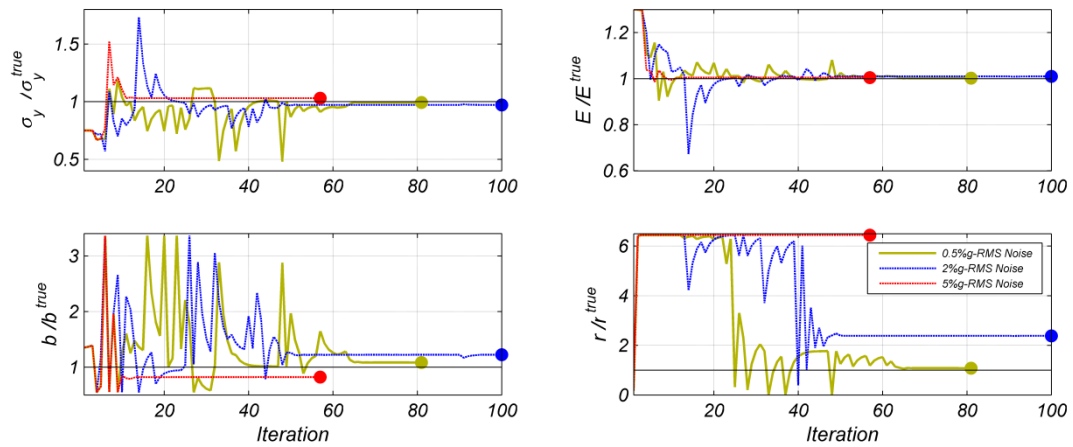


Figure 5.14: Convergence history of the modeling parameters and the noise variance for three levels of input noise as considered in Case study 5 for EQ1 and 2% g RMS output measurement noise.

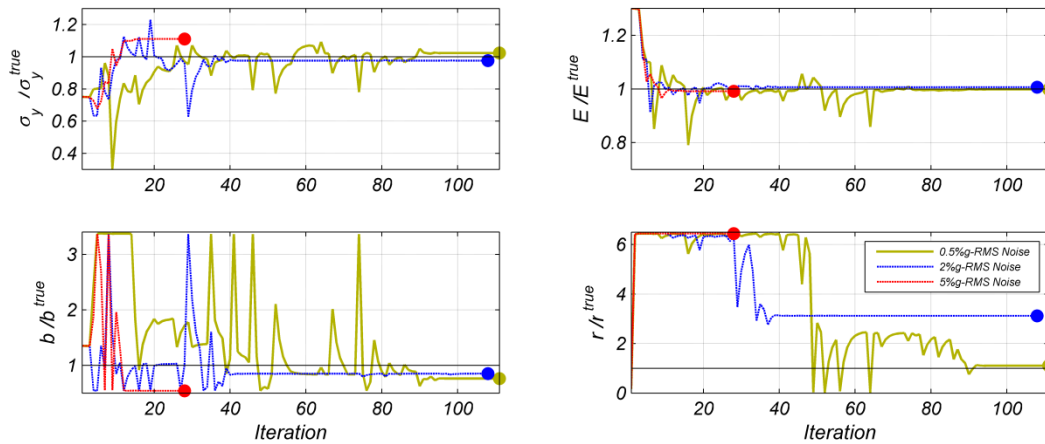


Figure 5.15: Convergence history of the modeling parameters and the noise variance for three levels of input noise as considered in Case study 5 for EQ2 and 2%g RMS output measurement noise.

Table 5.7: Estimation results for three levels of input noise considered in Case study 5.

Motion name	Input noise level (%g RMS)	Modeling parameters			Noise variance	COV (%) Method 1			COV (%) Method 2		
		$\sigma_y / \sigma_y^{true}$	$E / E^{true}$	$b / b^{true}$		$r / r^{true}$	$\sigma_y$	$E$	$b$	$\sigma_y$	$E$
EQ1	0.5	0.99	1.00	1.08	1.08	0.59	0.13	4.10	0.57	0.13	4.05
	2	0.97	1.01	1.22	2.38	0.90	0.20	5.55	3.68	0.71	30.67
	5	1.03	1.00	0.82	6.44	1.34	0.32	12.46	14.10	5.59	161.37
EQ2	0.5	1.02	1.00	0.76	1.10	0.78	0.09	11.52	0.82	0.11	11.03
	2	0.98	1.01	0.85	3.12	1.30	0.15	17.13	2.50	0.21	37.68
	5	1.11	0.99	0.54	6.44	1.61	0.20	34.70	253.6	10.6	5886.6
									9	6	8

Similar to Case study 1, Figure 5.16 compares the true structural response with the response obtained using initial and final estimated modeling parameters responses. The comparisons are made only for EQ1 for the case of 2% g RMS output measurement noise and 2% g RMS input noise. The relative acceleration response time history of the column top is shown Figure 5.16a and the stress-strain response of

the monitored fiber (or layer) at the column base section is shown Figure 5.16b. In spite of the simultaneous presence of relatively high levels of input and output measurement noises, Figure 5.16 shows that the proposed nonlinear FE model updating and parameter estimation framework is able to estimate the dynamic responses of the structure at both global and local level with acceptable level of accuracy.

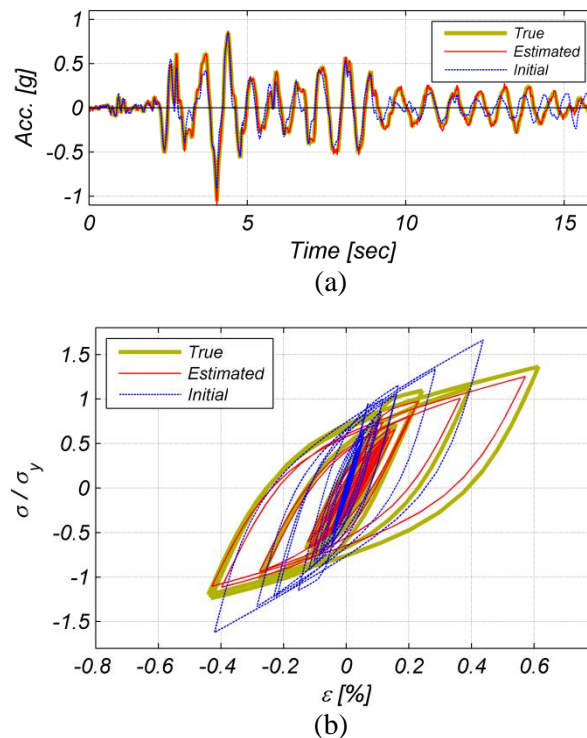


Figure 5.16: Comparison of the true response with the response obtained using initial and final estimates of the modeling parameters for *EQI* with 2% g RMS measurement noise and 2% g RMS input noise, (a) relative acceleration response time history of the column top, and (b) fiber stress-strain response of monitored fiber at the column base section.

**Case study 6: Effects of model uncertainties**

To study the detrimental effects of neglecting model uncertainties on the performance of the proposed parameter estimation framework, the nonlinear FE model updating of the cantilever steel column is repeated considering different material models for the steel fibers in the simulation and estimation phases. In this case study, the response of the structure is simulated using the modified Giuffré-Menegotto-Pinto material model for the steel fibers. The same as Case study 1, the true (exact) material parameters are selected as  $\sigma_y^{true} = 250\text{MPa}$ ,  $E^{true} = 200\text{GPa}$ , and  $b^{true} = 0.1$ . The simulated acceleration response time history of the column top is computed for *EQI* and polluted by 0.5% g RMS measurement noise to obtain the measured response. In the estimation phase, the employed FE model has identical geometry as the one used in the simulation phase, but uses bilinear material model to define the stress-strain relation of the steel fibers (Figure 5.17). The initial estimates of the modeling parameters are taken the same as Case study 1.

The estimation convergence time history for the three modeling parameters and the noise variance are shown in Figure 5.18. As can be seen, the mismatch between the models used in the simulation and estimation phases results in remarkable bias in the estimated material parameters. Figure 5.19a compares the time histories of the acceleration response and Figure 5.19b compares the monitored fiber stress-strain responses between the true, initial, and final updated models. In spite of the acceptable match between the simulated and estimated acceleration response time histories in

Figures 5.19a and 5.19b shows a notable difference in the fiber level response, which is an inherent outcome of the material model mismatch.

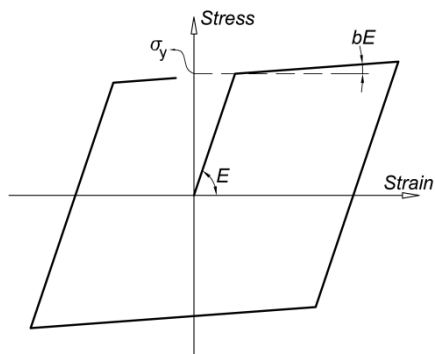


Figure 5.17: Bilinear uniaxial material constitutive model for structural steel.

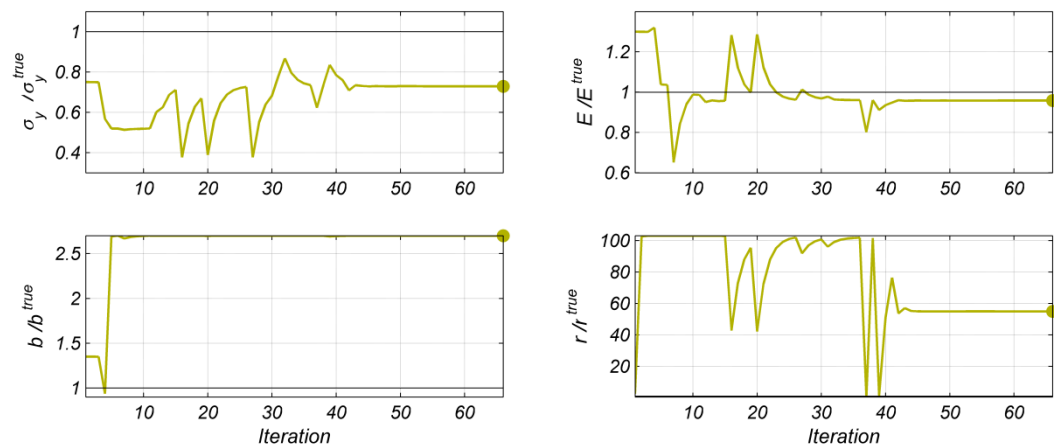


Figure 5.18: Convergence history of the modeling parameters and the noise variance in Case study 5 for *EQ1* and 0.5% g RMS output measurement noise.

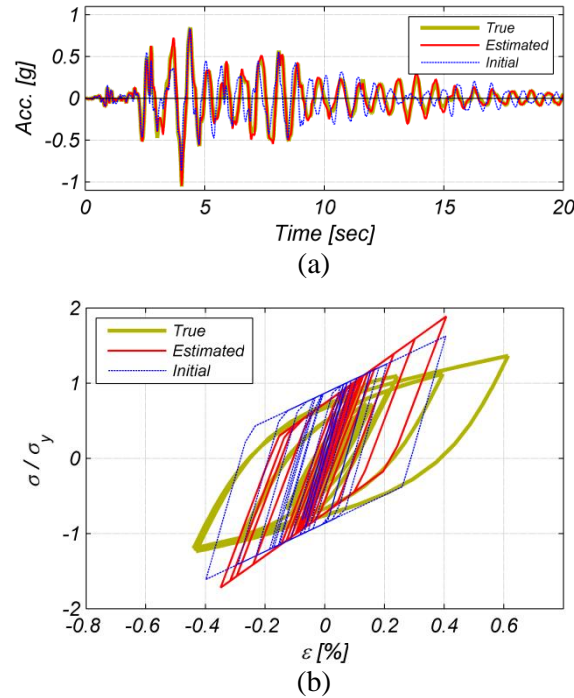


Figure 5.19: Comparison of the true response with the response obtained using initial and final estimates of the modeling parameters for *EQI* with 0.5% g RMS measurement noise, (a) relative acceleration response time history of the column top, and (b) fiber stress-strain response of monitored fiber at column base section.

### 5.5.2. Validation Study 2: 2D Moment Resisting Steel Frame

The benchmark structure used for the second validation study is the three-story moment resisting (MR) steel frame designed for the FEMA/SAC project (LA3 model structure, pre-Northridge design) [59]. The FE model of this frame structure (see Figure 5.20) is also developed in OpenSees using fiber-section displacement-based beam-column elements and the modified Giuffr -Menegotto-Pinto material constitutive model (see Figure 5.3) for the structural steel. According to the design details, the beams and columns are made of two different steel grades and therefore, two sets of the Giuffr -Menegotto-Pinto material model are used in the FE model. For

each set, three material parameters ( $E$ ,  $\sigma_y$  and  $b$ ) are treated as unknown FE model parameters and are estimated using the proposed parameter estimation and nonlinear FE model updating framework. The true (exact) values of these six FE model parameters are selected as:  $E_{col}^{true} = 200\text{GPa}$ ,  $\sigma_{y,col}^{true} = 350\text{MPa}$ ,  $b_{col}^{true} = 4\%$ ,  $E_{beam}^{true} = 200\text{GPa}$ ,  $\sigma_{y,beam}^{true} = 250\text{MPa}$ , and  $b_{beam}^{true} = 8\%$ .

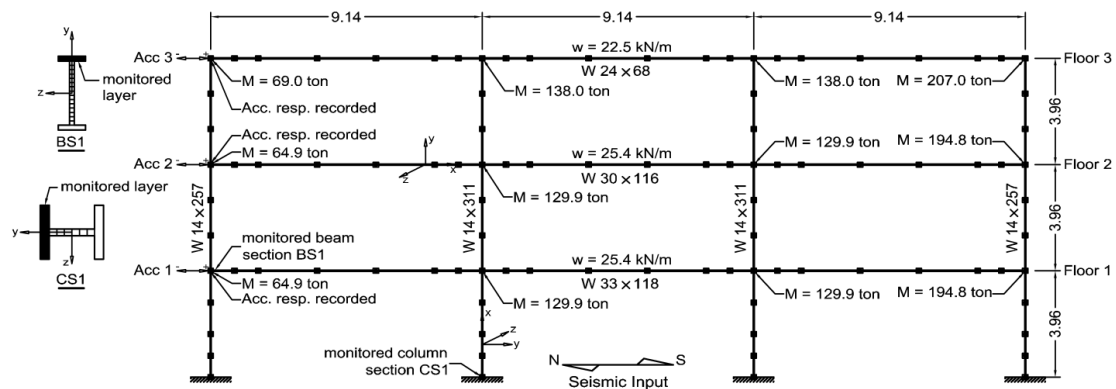


Figure 5.20: Details of the developed 2D FE model of the three-bay three-story MR steel frame based on the LA3 model structure from the FEMA/SAC project with pre-Northridge design [59]. (1 ton = 1000 kg, length unit: m).

The two ground acceleration records from the 1989 Loma Prieta and 1994 Northridge earthquakes defined in Table 5.1 and shown in Figure 5.4 are also used in this validation study. Each nonlinear analysis is performed by first applying the gravity loads quasi-statically and then the base excitation dynamically, as in the first validation study. Rayleigh damping is used to model the damping characteristics (beyond the hysteretic energy dissipated through inelastic action of the structural material) by defining a damping ratio of 2 percent for the first two elastic modes of the structure ( $T_1 = 1.06$  sec and  $T_2 = 0.35$  sec) and using the tangent stiffness matrix.



The floor acceleration response time histories of the structure are simulated, using the true values of the FE model parameters, and artificially polluted with measurement noise to represent the measured structural response. The measured response is then used in the proposed parameter estimation and nonlinear FE model updating framework to compute the point estimates of the FE model parameters,  $\hat{\theta} = [\hat{E}_{col}, \hat{\sigma}_{y,col}, \hat{b}_{col}, \hat{E}_{beam}, \hat{\sigma}_{y,beam}, \hat{b}_{beam}]^T$ , and the simulation error variances,  $\hat{r}$ . The parameter estimation uncertainty is evaluated by computing the CRLB using the two methods presented in Section 5.4. This validation study is subdivided into four case studies to better investigate the performance of the proposed parameter estimation and nonlinear FE model updating framework. In the first case study, the performance of the proposed parameter estimation framework is investigated for increasing levels of output measurement noise. Heterogeneous measurement data are used in the second case study to compare the performance of the proposed parameter estimation framework with the traditional least squares approach. The sensitivity of the proposed parameter estimation procedure to the initial estimates of the FE model parameters is investigated in the third case study. Finally, the last case study examines the detrimental effects of the input measurement noise on the performance of the proposed parameter estimation framework.

### **Case study 1: Effects of output measurement noise amplitude**

The simulated floor acceleration response of the structure recorded at the north column location (see Figure 5.20) is polluted with independent and identically

distributed zero mean Gaussian white noises to obtain the measured response of the structure. Similar to the first validation study, three different levels of measurement noise (i.e., 0.5% g, 2% g, and 5% g RMS) are considered. The initial estimate of the FE model parameter vector is selected as:

$$\boldsymbol{\theta}_0 = [0.80 \times E_{col}^{true}, 1.30 \times \sigma_{y,col}^{true}, 0.70 \times b_{col}^{true}, 0.75 \times E_{beam}^{true}, 1.25 \times \sigma_{y,beam}^{true}, 0.80 \times b_{beam}^{true}]^T.$$

The initial estimates of the simulation error variances at the three measurement channels are selected as:  $\mathbf{r}_0 = [0.62 \times 10^{-2}, 0.62 \times 10^{-2}, 0.62 \times 10^{-2}]^T$   $[m/s^2]^2$ , which corresponds to a 0.8% g RMS noise signal at each measurement channel. Similar to the first validation study, the feasible search domain for the FE model parameters is taken as  $0.4\boldsymbol{\theta}_0 \leq \boldsymbol{\theta} \leq 2.5\boldsymbol{\theta}_0$ , where  $\boldsymbol{\theta}_0$  = vector of initial estimates of the FE model parameters, while the feasible search domain for the simulation error variance vector is set as  $0.01\mathbf{r}_0 \leq \mathbf{r} \leq 100\mathbf{r}_0$ . The optimization convergence criterion is the same as in the first validation study (see Eqs. (5.34)-(5.35)).

Figures 5.21 and 5.22 show the convergence history of the six FE model parameters and three simulation error variances (corresponding to the three measurement channels) for the three considered levels of measurement noise amplitude for *EQ1* and *EQ2*, respectively. Table 5.8 reports the converged estimated FE model parameters and simulation error variances, normalized by their corresponding true values, for all cases considered. Curvature ductility demand of the column section CS1 and beam section BS1 (see Figure 5.20) are given in the last two columns of Table 5.8 for both the estimated and true FE model parameter values. The

low curvature ductility demand for the column section, especially for *EQ1*, indicates that the response of the column experiences a low level of nonlinearity and therefore, the response of the structure contains little information about the post yield characteristics of the column material. Consequently, the strain hardening ratio for the column material is not correctly estimated. Moreover, since the structural response has limited information about the post yield behavior of the column material, the estimation of the strain hardening ratio is more sensitive to the measurement noise level. Table 5.9 reports the estimated coefficient of variation (C.O.V.) of the estimated parameters for all cases considered. As in the first validation study, it is observed that the C.O.V.s are larger (i.e., higher estimation uncertainty) when the estimated FE model parameters are less accurate, with the strain hardening parameter of the column material for *EQ1* as the most extreme case. It should also be noted that in this validation study, *EQ2* imposes higher seismic demand on the structure than *EQ1* (as shown by the column and beam section curvature ductility demands in Table 5.8) and therefore, the estimated FE model parameters are more accurate and the estimated C.O.V.s lower for *EQ2* than for *EQ1*. Figure 5.23 compares the time histories of the FE predicted floor relative (to base) acceleration response to *EQ2* obtained using the true values of the FE model parameters, and the initial and final estimates of the FE model parameters inferred for the case of 2% g RMS measurement noise level. Figure 5.24 shows a similar comparison for the normalized moment-curvature hysteretic responses of column section CS1 and beam section BS1 (see Figure 5.20). The results presented in Figures 21- 24 and Tables 8-9 show the successful performance of the

proposed parameter estimation and nonlinear FE model updating framework. This framework is able to successfully estimate the identifiable (i.e., with structural response containing enough information about these parameters) material parameters of the nonlinear FE model. By correctly estimating the FE model parameters, the initially inaccurate FE model is updated and the structural response is estimated correctly at both the global structural and local section levels. The estimation process for each level of measurement noise in this example required about one and a half hour on a Dell Precision T7610 desktop workstation with two Intel Xeon E5-2630 (2.6 GHz) processors with 6 cores each.

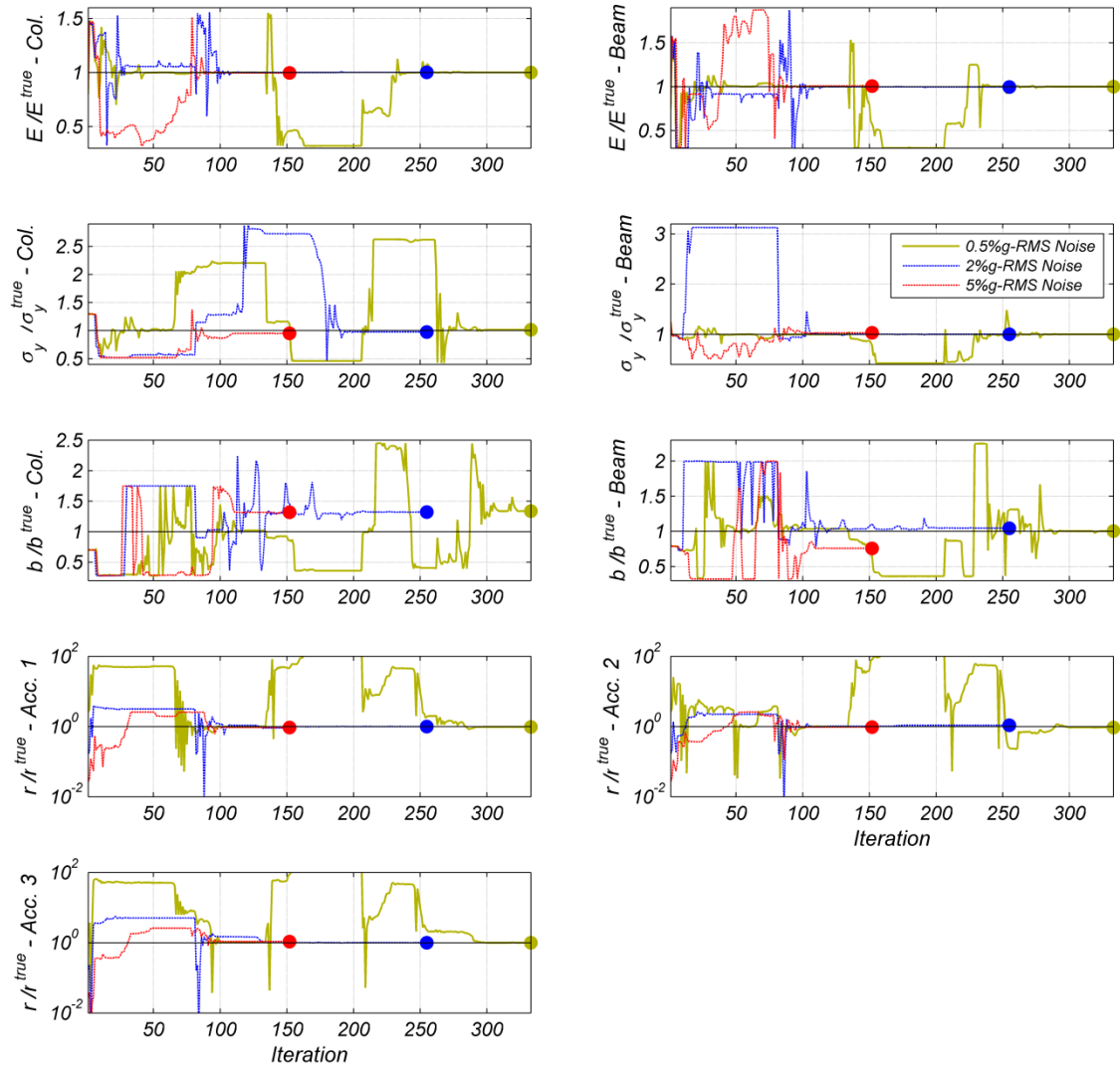


Figure 5.21: Convergence history of the estimated FE model parameters and simulation error variances for three measurement noise levels for *EQI* (the convergence histories of the simulation error variances are plotted in semi-logarithmic scale).

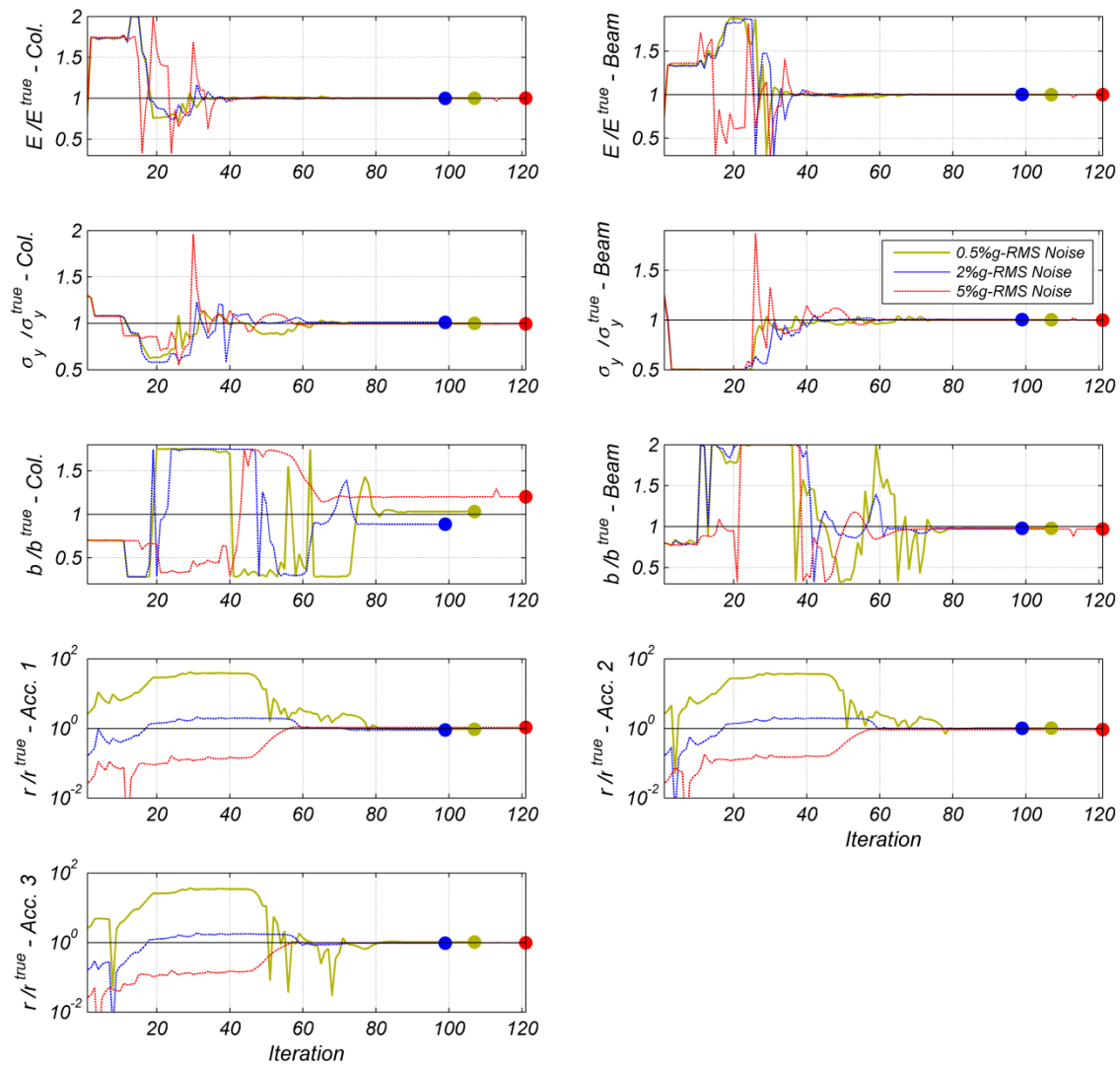


Figure 5.22: Convergence history of the estimated FE model parameters and simulation error variances for three measurement noise levels for  $EQ2$  (the convergence histories of the simulation error variances are plotted in semi-logarithmic scale).

Table 5.8: Parameter estimation results for the three measurement noise levels considered in Case study #1.

Ground motion name	Noise level (%g RMS)	Model parameters						Simulation error variances						Section curvature ductility demand (True value)	
		Column material parameters			Beam material parameters			Ch. 1 (Acc.1)	Ch. 2 (Acc.2)	Ch. 3 (Acc.3)	Column		Beam		
		$E/E^{true}$	$\sigma_y/\sigma_y^{true}$	$b/b^{true}$	$E/E^{true}$	$\sigma_y/\sigma_y^{true}$	$b/b^{true}$	$r/r^{true}$	$r/r^{true}$	$r/r^{true}$	$r/r^{true}$	$r/r^{true}$			
EQ1	0.5	1.00	1.01	1.34	1.00	1.00	1.00	0.97	0.93	0.99	1.25	5.13			
	2	1.00	0.98	1.32	1.00	1.00	1.00	0.99	1.09	0.99	1.30	(1.27) 5.11			
	5	1.00	0.95	1.32	1.01	1.03	0.76	0.94	0.95	1.07	1.33	5.03			
EQ2	0.5	1.00	1.00	1.03	1.00	1.00	0.98	0.95	1.02	1.03	2.44	6.01			
	2	1.00	1.01	0.89	1.00	1.00	0.98	0.90	1.00	0.96	2.41	(2.44) 6.01			
	5	1.00	0.99	1.20	1.00	1.00	0.97	1.07	0.92	0.98	2.46	6.03			

Table 5.9: Parameter estimation uncertainty for the three measurement noise levels considered in Case study #1.

Ground motion name	Noise level (%g RMS)	C.O.V. (%) – Method 1						C.O.V. (%) – Method 2					
		Column material parameters			Beam material parameters			Column material parameters			Beam material parameters		
		$E$	$\sigma_y$	$b$	$E$	$\sigma_y$	$b$	$E$	$\sigma_y$	$b$	$E$	$\sigma_y$	$b$
EQ1	0.5	0.04	2.54	65.80	0.06	0.16	1.55	2.38	2.47	48.23	0.34	1.13	4.45
	2	0.15	7.34	131.14	0.23	0.68	6.33	0.17	4.79	27.77	0.47	0.72	6.13
	5	0.36	12.01	161.32	0.59	1.47	17.10	5.44	106.02	496.47	6.66	5.45	36.38
EQ2	0.5	0.03	0.20	9.29	0.05	0.15	1.88	0.03	0.20	9.03	0.06	0.16	1.95
	2	0.13	0.81	44.93	0.20	0.57	7.31	0.13	0.84	46.88	0.21	0.59	7.45
	5	0.32	2.03	80.95	0.51	1.44	18.62	5.24	1.89	68.19	4.39	2.76	15.34

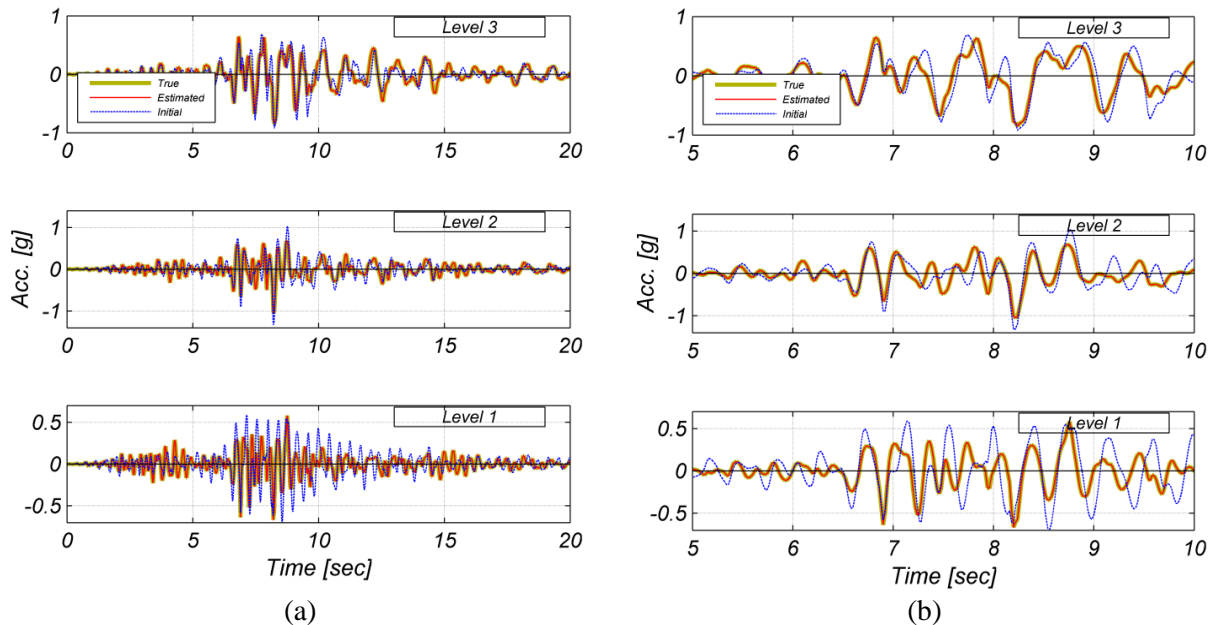


Figure 5.23: Comparison of the time histories of the FE predicted floor relative (to base) acceleration response to *EQ2* obtained using the true values of the FE model parameters, and the initial and final estimates of the FE model parameters inferred for the case of 2% g RMS measurement noise level; (a) complete response time histories between 0-20 seconds; (b) response time histories zoomed between 5-10 seconds.

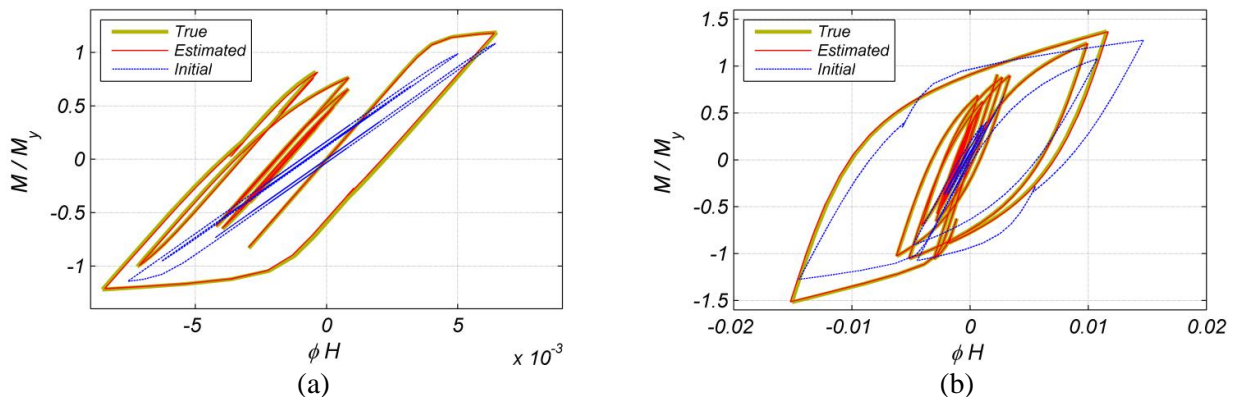


Figure 5.24: Comparison of the FE predicted moment-curvature hysteretic responses to *EQ2* obtained using the true values of the FE model parameters, and the initial and final estimates of the FE model parameters inferred for the case of 2% g RMS measurement noise level: (a) moment-curvature response of the column base section CS1, and (b) moment-curvature response of the beam section BS1 ( $H_{col} = 416\text{mm}$ ,  $H_{beam} = 762\text{mm}$ ).



**Case study 2: Heterogeneous sensor array**

The advantage of the proposed parameter estimation and nonlinear FE model updating framework over the traditional least squares approach is better highlighted by considering heterogeneous measurement data. In this case study, the acceleration response time histories at the first and third floors of the structure and the curvature time history of the column base section CS1 (see Figure 5.20) are selected as output measurements. The section curvature can be measured using a pair of strain gauges (or displacement transducers) mounted on opposite sides of the column at its base. The FE predicted acceleration time histories are polluted with zero-mean, 2% g RMS Gaussian white noise, while the curvature time history is polluted with zero-mean,  $2 \times 10^{-4} [m^{-1}]$  RMS measurement noise. Figure 5.25 shows the measured structural response time histories for *EQ1*. The scale difference between the acceleration and curvature response time histories is evident in this figure. The initial estimates of the FE model parameters are the same as for Case study #1. The initial estimates of the simulation error variances are selected as:  $r_0^{acc} = 6.2 \times 10^{-3} [m/s^2]^2$  for acceleration responses and  $r_0^{cur} = 1.00 \times 10^{-6} [m^{-1}]^2$  for curvature response, which respectively correspond to 0.8% g RMS and  $1.00 \times 10^{-3} [m^{-1}]$  RMS measurement noise. The feasible search domain and other conditions for the parameter estimation procedure are the same as for Case study #1. Due to space limitation, the estimation results for this case study are presented only for *EQ1*.

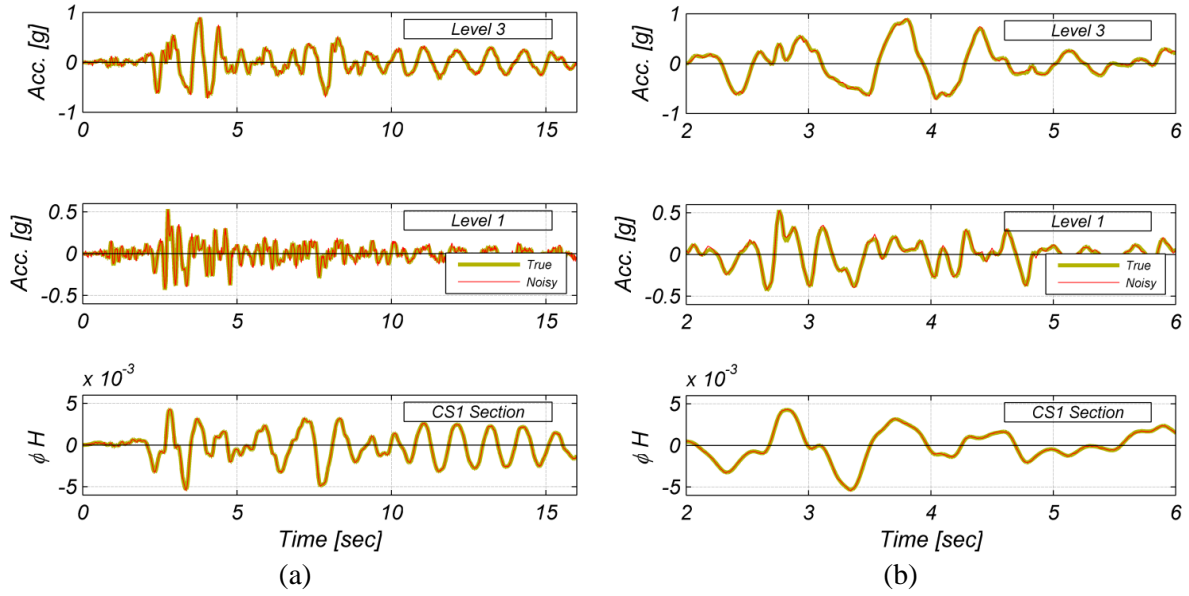


Figure 5.25: Heterogeneous structural response measurements: acceleration response time histories measured at the first and third levels and curvature response time history of the column base section (CS1) for *EQ1*; (a): complete response time histories between 0-16 seconds; (b) response time histories zoomed between 5-10 seconds.

To investigate the influence of local response measurements (such as curvature) on the parameter estimation process, first the nonlinear FE model updating is performed utilizing only structural level measured response quantities (i.e., acceleration response at first and third levels) using two estimation methods: the traditional least squares method, see Eq. (5.12), and the proposed parameter estimation method, see Eqs. (5.20) and (5.21). The first row of results in Table 5.10 show the estimated values of the six FE model parameters based on the least squares method; the second row shows the estimated values of the FE model parameters and the simulation error variances based on the proposed parameter estimation and nonlinear FE model updating method. It is observed that some of the FE model parameters (i.e.,  $\sigma_{y,col}$ ,  $b_{col}$ ,  $b_{beam}$ ) are not identified correctly due to the fact that the two acceleration

response time histories contain limited information about these parameters. The first two rows of Table 5.11 report the C.O.V.s of the estimated parameters. The parameter estimation C.O.V.s for the least squares method can be obtained only through *Method 2* described in Section 5.4; however, for the proposed nonlinear FE model updating method, both *Method 1* and *Method 2* have been used. Although the point estimates of the strain hardening ratio for the column steel material are close to the true value of this parameter, their extremely large estimated C.O.V.s indicate the high uncertainty (and therefore likely inaccuracy) associated with the estimation of this parameter, i.e., its estimations are accurate here by coincidence.

Now, the curvature response time history at column section CS1 is added as third measurement channel and the nonlinear FE model updating procedure is repeated using both the traditional least squares and the proposed parameter estimation approaches. The estimation results are summarized in the last two rows of Tables 10-11. It can be seen that the inclusion of the curvature measurement improves significantly the estimation accuracy (for parameters  $\sigma_{y,col}$ ,  $b_{col}$ ,  $b_{beam}$ ) of the proposed parameter estimation and nonlinear FE model updating framework. The last row in Table 5.11 shows that the parameter estimation uncertainties are remarkably reduced as the third measurement (curvature) data channel is included in the estimation process. However, the conventional least squares approach is unable to properly extract information from the third measurement channel. Comparing the first and third rows of Table 5.10 clearly shows that the inclusion of the curvature measurement data has minor influence on the FE model parameter estimation results

obtained using the least squares method. The least-squares method automatically overlooks the curvature data in the presence of the acceleration signals which are of much larger magnitude numerically. The least squares method can be replaced by the weighted least squares method, which improves the performance of the traditional least squares method in the case of heterogeneous measurement data. However, selection of the weighting factors for each measurement channel is user-dependent. Nevertheless, the proposed nonlinear FE model updating procedure provides a systematic solution (without the need for user-dependent scaling) to correctly infer information from heterogeneous measurements.

Table 5.10: Parameter estimation results for four different cases considered in Case study #2 for *EQ1*.

Estimation method	Model parameters				Noise variance					
	Column material parameters		Beam material parameters		Ch. 1 (Acc.1)		Ch. 2 (Acc.3)		Ch. 3 (Cur.)	
	$E/E^{true}$	$\sigma_y/\sigma_y^{true}$	$b/b^{true}$	$E/E^{true}$	$\sigma_y/\sigma_y^{true}$	$b/b^{true}$	$r/r^{true}$	$r/r^{true}$	$r/r^{true}$	$r/r^{true}$
Method - 2 Outputs	1.00	1.89	1.02	1.00	1.00	0.89	-	-	-	-
Prop. Method - 2 Outputs	1.00	1.42	1.01	1.00	1.01	0.92	1.00	0.92	-	-
Method - 3 Outputs	1.00	1.88	1.02	1.00	1.02	0.80	-	-	-	-
Prop. Method - 3 outputs	1.00	1.00	1.00	1.00	1.00	1.01	1.00	0.98	0.96	0.96

Table 5.11: Parameter estimation uncertainty for four different cases considered in Case study #2 for *EQ1*.

Estimation method	C.O.V.(%) – Method 1				C.O.V.(%) – Method 2										
	Column material parameters		Beam material parameters		Column material parameters				Beam material parameters						
	$E$	$\sigma_y$	$b$	$\sigma_y$	$E$	$\sigma_y$	$b$	$\sigma_y$	$E$	$\sigma_y$	$b$	$\sigma_y$	$E$	$\sigma_y$	$b$
LS Method - 2 Outputs	-	-	-	-	32.38	400.82	445.79	28.05	49.38	114.53	-	-	-	-	-
Prop. Method - 2 Outputs	0.18	8.46	563.88	0.27	0.29	10.97	483.30	0.49	0.40	4.56	7.42	483.30	0.49	0.40	4.56
LS Method - 3 Outputs	-	-	-	-	24.22	274.83	260.23	2.24	20.11	36.08	-	-	-	-	-
Prop. Method - 3 outputs	0.10	0.44	48.13	0.12	0.21	0.61	80.44	0.23	0.15	2.11	2.24	260.23	2.24	0.15	2.11

**Case study 3: Effects of initial estimates of FE model parameters**

The sensitivity of the proposed parameter estimation and nonlinear FE model updating framework to initial estimates of the FE model parameters is investigated for the 2D steel MR frame structure. The FE model updating procedure is repeated for both *EQ1* and *EQ2* (with 2% g RMS measurement noise on each of the three acceleration measurement channels) using four different sets of initial estimates of the FE model parameters as shown in Table 5.12. The norm of the initial estimation error, reported in the last column of Table 5.12, is defined as the relative root mean square of the difference between the initial estimates and the true values of the FE model parameters, i.e.,

$$Error(\%) = \sqrt{\frac{\sum_{i=1}^6 \left( \frac{\theta_{0,i} - \theta_i^{true}}{\theta_i^{true}} \right)^2}{6}} \times 100 \quad (5.39)$$

Table 5.12: Different sets of initial estimates of FE model parameters considered in Case study #4.

Set #	Column material parameters			Beam material parameters			Error (%)
	$E_0 / E^{true}$	$\sigma_{y0} / \sigma_y^{true}$	$b_0 / b^{true}$	$E_0 / E^{true}$	$\sigma_{y0} / \sigma_y^{true}$	$b_0 / b^{true}$	
Set 1	0.41	0.62	1.18	0.88	0.97	1.05	~ 30%
Set 2	1.54	1.44	0.49	0.64	1.08	1.28	~ 40%
Set 3	1.95	1.47	0.53	0.97	1.38	1.02	~ 50%
Set 4	1.87	1.68	1.20	0.47	0.51	1.62	~ 60%

The initial estimates of the simulation error variances are selected as  $\mathbf{r}_0 = [0.62 \times 10^{-2}, 0.62 \times 10^{-2}, 0.62 \times 10^{-2}]^T$   $[m/s^2]^2$ . Other conditions for the ML estimation procedure are the same as in Case study #1.

The estimated FE model parameters and simulation error variances for the four different cases considered here are reported in Table 5.13 and the corresponding estimation C.O.V.s are reported in Table 5.14. It is observed that when FE model parameters are estimated accurately (i.e., ratio of estimated-to-true parameter value close to 1.0 and estimation C.O.V. below 1.0 percent), their converged estimated values are independent of their initial estimates. However, in the case when FE model parameters are not estimated accurately, their converged estimated values vary from set to set of initial parameter estimates, but this variation may only be due to the stochastic nature of the estimation problem (i.e., estimation uncertainty) and unrelated to the specific initial estimates of the FE model parameters. From the results in Tables 5.13 and 5.14, it appears that the accuracy of the estimated FE model parameters does not depend on the norm of the initial estimation error defined in Eq. (5.39).

Table 5.13: Parameter estimation results for four sets of initial estimates of the FE model parameters considered in Case study #3.

Ground motion name	Set #	Model parameters						Noise variance					
		Column material parameters			Beam material parameters			Ch. 1 (Acc.1)		Ch. 2 (Acc.2)		Ch. 3 (Acc.3)	
		$E/E^{true}$	$\sigma_y/\sigma_y^{true}$	$b/b^{true}$	$E/E^{true}$	$\sigma_y/\sigma_y^{true}$	$b/b^{true}$	$r/r^{true}$	$r/r^{true}$	$r/r^{true}$	$r/r^{true}$	$r/r^{true}$	$r/r^{true}$
EQ1	1	1.00	1.00	1.55	1.00	1.00	1.00	0.97	0.96	1.04	0.96	1.04	
	2	1.00	0.94	0.71	1.00	1.00	1.00	0.97	0.96	1.04	0.96	1.04	
	3	1.00	1.02	0.77	1.00	1.00	1.00	0.98	0.96	1.02	0.96	1.02	
	4	1.00	0.92	1.50	1.00	1.00	1.00	0.97	0.96	1.04	0.96	1.04	
EQ2	1	1.00	0.99	1.10	1.00	1.00	1.00	1.06	0.94	1.05	0.94	1.05	
	2	1.00	1.00	0.99	1.00	1.00	1.00	0.98	1.01	0.98	1.01	0.98	
	3	1.00	0.99	1.05	1.00	1.00	1.00	1.07	0.94	1.04	0.94	1.04	
	4	1.00	0.99	1.11	1.00	1.00	1.00	1.07	0.94	1.04	0.94	1.04	

Table 5.14: Parameter estimation uncertainty for four sets of initial estimates of FE model parameters considered in Case study #3.

Ground motion name	Set #	C.O.V.(%) – Method 1						C.O.V.(%) – Method 2					
		Column material parameters			Beam material parameters			Column material parameters			Beam material parameters		
		$E$	$\sigma_y$	$b$	$E$	$\sigma_y$	$b$	$E$	$\sigma_y$	$b$	$E$	$\sigma_y$	$b$
EQ1	1	0.15	9.53	161.96	0.24	0.66	6.25	1.36	7.71	47.17	0.22	2.23	42.06
	2	0.15	8.16	124.53	0.25	0.66	6.20	5.57	3.09	46.76	20.49	1.32	25.82
	3	0.16	9.24	156.11	0.25	0.65	6.17	0.13	6.79	17.50	0.24	0.23	3.77
	4	0.15	9.68	132.73	0.24	0.66	6.19	0.14	3.61	29.48	0.18	0.31	3.87
EQ2	1	0.13	0.81	34.54	0.21	0.58	7.92	0.12	0.75	33.65	0.18	0.52	7.16
	2	0.13	0.79	37.73	0.21	0.59	7.16	0.13	0.83	40.44	0.21	0.65	7.68
	3	0.13	0.81	36.17	0.21	0.58	7.91	0.13	0.79	37.48	0.18	0.59	7.75
	4	0.13	0.81	34.50	0.21	0.58	7.91	0.13	0.84	35.39	0.20	0.56	7.80



#### **Case study 4: Effects of input measurement noise**

The effects of input measurement noise on the parameter estimation results obtained from the proposed parameter estimation framework are examined by polluting the input ground acceleration time history with artificial measurement noise prior to the estimation phase. The noiseless time history of the earthquake ground acceleration shown in Figure 5.4 is used to simulate the acceleration response of the structure in the simulation phase. The simulated floor acceleration response time histories are then polluted with 2% g RMS measurement noise to simulate the noisy measured response of the structure. In the estimation phase, the time history of the input ground acceleration is contaminated with a zero-mean Gaussian white noise of three different amplitudes, namely 0.5% g, 2% g, and 5% g RMS. The second and third noise levels are unrealistically high; however, they are included to examine the detrimental effects of extreme input noise amplitude on the parameter estimation results. As mentioned earlier, the proposed parameter estimation and nonlinear FE model updating framework is based on deterministic (noiseless) input ground acceleration(s); therefore, the presence of input noise is expected to adversely affect the performance of the parameter estimation procedure.

Table 5.15 reports the estimated FE model parameters and simulation error variances, normalized by the corresponding true parameter values, for all cases considered herein. The detrimental effects of the input measurement noise on the estimated FE model parameters and simulation error variances are evident. The presence of input noise biases the FE model parameter estimation results and the

estimation error increases with increasing amplitude of the input noise. Moreover, as the amplitude of the input noise increases, the estimated simulation error variances increase. This means that the estimation framework indirectly accounts for the effects of input noise by estimating large amplitude measurement noise at the output channels. However, the input Gaussian white noise signal is filtered through the nonlinear structural FE model and transformed into non-white and non-Gaussian signals at the output channels. The estimation framework approximates these non-white, non-Gaussian signals as equivalent Gaussian white measurement noise. This approximation results in erroneous estimation results. It is worth mentioning that state-of-the-art accelerometers (e.g., force-balance EpiSensor from Kinemetrics, Inc.) have a residual electrical noise of 0.15% g RMS, which is significantly lower than the lowest RMS value (i.e., 0.5% g) considered here for the input measurement noise.

Table 5.16 reports the estimated C.O.V.s of the estimation parameters obtained using the two methods presented in Section 5.4. Unlike in the previous case studies, the estimated C.O.V.s in this case do not correlate with the accuracy of the estimated FE model parameters, i.e., although some FE model parameters have significant estimation errors, the corresponding C.O.V.s are relatively small (especially in the case of 5 % g RMS input noise). In the case of 5% g RMS input noise for *EQI*, the computed Hessian matrix was badly conditioned and therefore, the C.O.V.s of the estimated FE model parameters could not be computed using *Method 2*.

From this case study, it is concluded that, in order to increase the accuracy and robustness, the proposed parameter estimation framework should be further extended

to account for input measurement noise as well as non-white and/or non-Gaussian and/or correlated (across channels) output measurement noise.

Table 5.15: Parameter estimation results for three input measurement noise levels considered in Case study #4.

Ground motion name	Input noise level (%g RMS)	Model parameters						Noise variance					
		Column material parameters			Beam material parameters			Ch. 1 (Acc.1)		Ch. 2 (Acc.2)		Ch. 3 (Acc.3)	
		$E/E^{tme}$	$\sigma_y/\sigma_y^{tme}$	$b/b^{tme}$	$E/E^{tme}$	$\sigma_y/\sigma_y^{tme}$	$b/b^{tme}$	$r/r^{tme}$	$r/r^{tme}$	$r/r^{tme}$	$r/r^{tme}$	$r/r^{tme}$	$r/r^{tme}$
EQ1	0.5	1.00	0.95	1.02	1.00	1.00	1.01	1.08	1.12	1.05			
	2	0.99	0.83	1.62	1.02	0.97	1.54	2.75	2.94	3.07			
	5	0.32	0.52	0.28	0.30	0.50	0.32	16.11	16.11	16.11			
EQ2	0.5	1.00	0.99	1.39	1.01	1.01	0.82	1.09	1.13	1.11			
	2	0.99	0.99	1.27	1.04	1.02	0.69	2.64	2.72	2.86			
	5	1.00	0.59	1.75	1.06	2.35	0.57	14.69	12.94	16.10			

Table 5.16: Parameter estimation uncertainty for three input measurement noise levels considered in Case study #4.

Ground motion name	Input noise level (%g RMS)	C.O.V. (%) – Method 1						C.O.V. (%) – Method 2							
		Column material parameters			Beam material parameters			Column material parameters		Beam material parameters		Column material parameters		Beam material parameters	
		$E$	$\sigma_y$	$b$	$E$	$\sigma_y$	$b$	$E$	$\sigma_y$	$b$	$E$	$\sigma_y$	$b$	$E$	$\sigma_y$
EQ1	0.5	0.15	6.10	12.13	0.24	0.70	6.76	2.16	2.37	288.04	2.01	0.77	7.03		
	2	0.23	2.10	89.45	0.43	1.34	9.24	0.25	2.42	87.76	0.41	1.21	8.41		
	5	0.49	10.32	63.44	0.81	2.45	55.30	-	-	-	-	-	-		
EQ2	0.5	0.14	0.87	30.67	0.22	0.56	8.48	0.15	0.91	31.22	0.23	0.45	7.88		
	2	0.22	1.46	58.48	0.35	0.76	13.33	0.76	1.41	50.25	0.38	2.17	47.43		
	5	0.39	1.50	13.04	0.59	280.65	16.88	0.61	3.73	13.52	1.03	1.45	49.92		

## 5.6. Conclusions

This study presented a framework for nonlinear system identification, structural health monitoring (SHM), and damage identification (DID) of civil structures. The proposed framework uses an extended maximum likelihood (ML) estimation method to estimate finite element (FE) model parameters as well as simulation error variances and update the nonlinear FE model of the structure based on input-output data measured during a damage-inducing event such as an earthquake. The computational efficiency of the parameter estimation and nonlinear FE model updating procedure was improved using the direct differentiation method (DDM) to compute FE response sensitivities with respect to FE model parameters. The FE model parameter estimation uncertainties were quantified using the estimation covariance matrix which was approximated by the Cramer-Rao lower bound (CRLB). Two methods to approximate analytically and/or numerically the CRLB were presented. The first method, referred to as *Method 1*, estimated the CRLB based on the (asymptotically exact) Fisher information matrix (FIM). Evaluation of the FIM required the computation of the FE response sensitivities with respect to the FE model parameters, which were estimated through the extended ML estimation framework. The second method, referred to as *Method 2*, approximated the FIM through the Hessian of the extended ML objective function. The accuracy of these two approaches for parameter estimation uncertainty quantification was investigated using a deterministic sampling approach in the context of an application example.

The proposed framework is general and applies to different types of structural and/or geotechnical systems, different types of FE modeling and analysis techniques, and different types of loads (e.g., static, quasi-static, time-dependent, dynamic). Although the proposed framework is general, the validation studies presented in this study were based on simple but realistic nonlinear frame-type structural models and earthquakes as potentially damaging events. Two proof-of-concept studies using numerically simulated structural response data were conducted to investigate the performance and evaluate the accuracy of the proposed framework. In both validation studies, the proposed framework successfully estimated the identifiable model parameters as well as the simulation error variances and updated the FE model of interest, even in the presence of high output measurement noise levels and/or way-out initial estimates of the FE model parameters. The superiority of the proposed nonlinear FE model parameter estimation framework over the traditional least squares method was highlighted by considering heterogeneous output measurements (i.e., structural response measured from different types of sensors). The proposed estimation procedure was able to systematically infer information from the heterogeneous measured data and estimate the FE model parameters, while the traditional least squares method fell short in extracting information consistently from all measured data. Furthermore, the detrimental effects of input measurement noise on the performance of the proposed framework were investigated and quantified.

The presented parameter estimation and nonlinear model updating framework does not account for the effects of model uncertainties, input measurement noise,

unmeasured (unknown) excitations, and non-white, non-Gaussian, and/or correlated output measurement noise. Research is underway to remove these current limitations, and to validate the framework using experimental data obtained from large-scale shake table tests.

## **Acknowledgments**

Partial support for this work was provided by the Englekirk structural engineering center board of advisors, teaching assistantships from the Department of Structural Engineering at University of California, San Diego and the researcher assistantship received through my advisor, Professor Joel P. Conte. This Chapter, in part, is submitted for publication and may appear in Mechanical Systems and Signal Processing Journal. It was written by Hamed Ebrahimian, Rodrigo Astroza, Joel P. Conte, and Raymond A. de Callafon. The dissertation author is the primary investigator and author of this material.

## Appendix 5.I: Derivation of the Exact Fisher Information Matrix

The FIM is defined as  $\mathbf{I} = E[\mathbf{ss}^T]$  where  $\mathbf{s}(\dots)$  denotes the score function and the expectation is taken with respect to  $p(\mathbf{y}_{1 \rightarrow k} | \boldsymbol{\theta}, \mathbf{r})$  (see Eq. (5.26)). The score function is defined as the gradient of the log-likelihood function with respect to the parameters to be estimated [34]. For the ML estimation problem stated in Eqs. (5.20) and (5.21), the score function can be derived as

$$\mathbf{s}(\boldsymbol{\theta}, \mathbf{r}, \mathbf{y}_{1 \rightarrow k}) = \begin{bmatrix} \left( \frac{\partial \Lambda(\boldsymbol{\theta}, \mathbf{r}, \mathbf{y}_{1 \rightarrow k})}{\partial \boldsymbol{\theta}} \right)^T \\ \left( \frac{\partial \Lambda(\boldsymbol{\theta}, \mathbf{r}, \mathbf{y}_{1 \rightarrow k})}{\partial \mathbf{r}} \right)^T \end{bmatrix} \quad (5.40)$$

in which  $\mathbf{r} = \text{diag}(\mathbf{R}) = [r_1 \ r_2 \ \dots \ r_{n_y}]^T$  where  $r_i$  is the  $i^{\text{th}}$  diagonal entry of matrix  $\mathbf{R}$ , and  $\Lambda$  is the log-likelihood function defined as the natural logarithm of the likelihood function given in Eq. (5.18), i.e.,

$$\Lambda(\boldsymbol{\theta}, \mathbf{r}, \mathbf{y}_{1 \rightarrow k}) = \left( -\frac{kn_y}{2} \ln(2\pi) - \frac{k}{2} \sum_{j=1}^{n_y} \ln(r_j) - \frac{1}{2} \sum_{i=1}^k (\mathbf{y}_i - \hat{\mathbf{y}}_i(\boldsymbol{\theta}))^T \mathbf{R}^{-1} (\mathbf{y}_i - \hat{\mathbf{y}}_i(\boldsymbol{\theta})) \right) \quad (5.41)$$

where  $\hat{\mathbf{y}}_i(\boldsymbol{\theta}) = \mathbf{h}_i(\boldsymbol{\theta}, \ddot{\mathbf{u}}_{g_{1 \rightarrow i}}, \mathbf{q}_0, \dot{\mathbf{q}}_0)$  is the FE predicted response at the  $i^{\text{th}}$  time step and the dependence of  $\hat{\mathbf{y}}_i(\boldsymbol{\theta})$  on  $\ddot{\mathbf{u}}_{g_{1 \rightarrow i}}$ ,  $\mathbf{q}_0$ , and  $\dot{\mathbf{q}}_0$  is dropped for notational convenience.

As mentioned before, the simulation error (defined in Eq. (5.8)) is characterized as a zero-mean independent Gaussian white noise vector process, i.e., statistically independent across time and measurement channels. Substituting Eq. (5.41) into Eq. (5.40) yields



$$\mathbf{s}(\boldsymbol{\theta}, \mathbf{r}, \mathbf{y}_{1 \rightarrow k}) = \begin{bmatrix} \sum_{i=1}^k \left( \frac{\partial \hat{\mathbf{y}}_i(\boldsymbol{\theta})}{\partial \boldsymbol{\theta}} \right)^T \mathbf{R}^{-1} (\mathbf{y}_i - \hat{\mathbf{y}}_i(\boldsymbol{\theta})) \\ -\frac{k}{2} \mathbf{r}^{-1} + \frac{1}{2} \sum_{i=1}^k \mathbf{w}_i \end{bmatrix} \quad (5.42)$$

in which  $\mathbf{r}^{-1} = \begin{bmatrix} 1 & & & \\ & 1 & & \\ & & \dots & \\ & & & 1 \end{bmatrix}^T$  and  $\mathbf{w}_i = \begin{bmatrix} v_{i1}(\boldsymbol{\theta})^2 & v_{i2}(\boldsymbol{\theta})^2 & \dots & v_{in_y}(\boldsymbol{\theta})^2 \end{bmatrix}^T$  where

$v_{ij}(\boldsymbol{\theta}) = y_{ij} - \hat{y}_{ij}(\boldsymbol{\theta})$  is the  $j^{\text{th}}$  component of the simulation error vector at the  $i^{\text{th}}$  time step. The FIM can be obtained as

$$\mathbf{I}(\boldsymbol{\theta}, \mathbf{r}) = \begin{bmatrix} \mathbf{I}_{\boldsymbol{\theta}\boldsymbol{\theta}} & \mathbf{I}_{\boldsymbol{\theta}\mathbf{r}} \\ \mathbf{I}_{\boldsymbol{\theta}\mathbf{r}}^T & \mathbf{I}_{\mathbf{r}\mathbf{r}} \end{bmatrix} \quad (5.43)$$

The first submatrix  $\mathbf{I}_{\boldsymbol{\theta}\boldsymbol{\theta}}$  can be derived as

$$\begin{aligned} \mathbf{I}_{\boldsymbol{\theta}\boldsymbol{\theta}} &= E \left[ \left( \frac{\partial \Lambda(\boldsymbol{\theta}, \mathbf{r}, \mathbf{Y}_{1 \rightarrow k})}{\partial \boldsymbol{\theta}} \right)^T \left( \frac{\partial \Lambda(\boldsymbol{\theta}, \mathbf{r}, \mathbf{Y}_{1 \rightarrow k})}{\partial \boldsymbol{\theta}} \right) \right] \\ &= E \left[ \sum_{i=1}^k \left[ \left( \frac{\partial \hat{\mathbf{y}}_i(\boldsymbol{\theta})}{\partial \boldsymbol{\theta}} \right)^T \mathbf{R}^{-1} (\mathbf{Y}_i - \hat{\mathbf{y}}_i(\boldsymbol{\theta})) \right] \sum_{j=1}^k \left[ (\mathbf{Y}_j - \hat{\mathbf{y}}_j(\boldsymbol{\theta}))^T \mathbf{R}^{-1} \left( \frac{\partial \hat{\mathbf{y}}_j(\boldsymbol{\theta})}{\partial \boldsymbol{\theta}} \right) \right] \right] \\ &= \sum_{i=1}^k \sum_{j=1}^k \left( \frac{\partial \hat{\mathbf{y}}_i(\boldsymbol{\theta})}{\partial \boldsymbol{\theta}} \right)^T \mathbf{R}^{-1} \underbrace{E \left[ (\mathbf{Y}_i - \hat{\mathbf{y}}_i(\boldsymbol{\theta})) (\mathbf{Y}_j - \hat{\mathbf{y}}_j(\boldsymbol{\theta}))^T \right]}_{=\mathbf{R}\delta_{ij}} \mathbf{R}^{-1} \left( \frac{\partial \hat{\mathbf{y}}_j(\boldsymbol{\theta})}{\partial \boldsymbol{\theta}} \right) = \sum_{i=1}^k \left( \frac{\partial \hat{\mathbf{y}}_i(\boldsymbol{\theta})}{\partial \boldsymbol{\theta}} \right)^T \mathbf{R}^{-1} \left( \frac{\partial \hat{\mathbf{y}}_i(\boldsymbol{\theta})}{\partial \boldsymbol{\theta}} \right) \end{aligned} \quad (5.44)$$

The second submatrix  $\mathbf{I}_{\boldsymbol{\theta}\mathbf{r}}$  can be obtained as

$$\begin{aligned} \mathbf{I}_{\boldsymbol{\theta}\mathbf{r}} &= E \left[ \left( \frac{\partial \Lambda(\boldsymbol{\theta}, \mathbf{r}, \mathbf{Y}_{1 \rightarrow k})}{\partial \boldsymbol{\theta}} \right)^T \left( \frac{\partial \Lambda(\boldsymbol{\theta}, \mathbf{r}, \mathbf{Y}_{1 \rightarrow k})}{\partial \mathbf{r}} \right) \right] \\ &= E \left[ -\frac{k}{2} \sum_{i=1}^k \left[ \left( \frac{\partial \hat{\mathbf{y}}_i(\boldsymbol{\theta})}{\partial \boldsymbol{\theta}} \right)^T \mathbf{R}^{-1} (\mathbf{Y}_i - \hat{\mathbf{y}}_i(\boldsymbol{\theta})) \right] (\mathbf{r}^{-1})^T + \frac{1}{2} \sum_{i=1}^k \left[ \left( \frac{\partial \hat{\mathbf{y}}_i(\boldsymbol{\theta})}{\partial \boldsymbol{\theta}} \right)^T \mathbf{R}^{-1} (\mathbf{Y}_i - \hat{\mathbf{y}}_i(\boldsymbol{\theta})) \right] \left[ \sum_{j=1}^k \mathbf{W}_j^T \right] \right] \\ &= -\frac{k}{2} \sum_{i=1}^k \left[ \left( \frac{\partial \hat{\mathbf{y}}_i(\boldsymbol{\theta})}{\partial \boldsymbol{\theta}} \right)^T \mathbf{R}^{-1} \underbrace{E \left[ \mathbf{Y}_i - \hat{\mathbf{y}}_i(\boldsymbol{\theta}) \right]}_{=0} \right] (\mathbf{r}^{-1})^T + \frac{1}{2} \sum_{i=1}^k \sum_{j=1}^k \left[ \left( \frac{\partial \hat{\mathbf{y}}_i(\boldsymbol{\theta})}{\partial \boldsymbol{\theta}} \right)^T \mathbf{R}^{-1} E \left[ (\mathbf{Y}_i - \hat{\mathbf{y}}_i(\boldsymbol{\theta})) \mathbf{W}_j^T \right] \right] \end{aligned} \quad (5.45)$$

in which the term  $E \left[ (\mathbf{Y}_i - \hat{\mathbf{y}}_i(\boldsymbol{\theta})) \mathbf{W}_j^T \right]$  can be derived as

$$E[(\mathbf{Y}_i - \hat{\mathbf{y}}_i(\boldsymbol{\theta})) \mathbf{W}_j^T] = \begin{bmatrix} \frac{E[(Y_{i1} - \hat{y}_{i1}(\boldsymbol{\theta}))(Y_{j1} - \hat{y}_{j1}(\boldsymbol{\theta}))^2]}{r_1^2} & \frac{E[(Y_{i1} - \hat{y}_{i1}(\boldsymbol{\theta}))(Y_{j2} - \hat{y}_{j2}(\boldsymbol{\theta}))^2]}{r_2^2} & \dots & \frac{E[(Y_{i1} - \hat{y}_{i1}(\boldsymbol{\theta}))(Y_{jn_y} - \hat{y}_{jn_y}(\boldsymbol{\theta}))^2]}{r_{n_y}^2} \\ \frac{E[(Y_{i2} - \hat{y}_{i2}(\boldsymbol{\theta}))(Y_{j1} - \hat{y}_{j1}(\boldsymbol{\theta}))^2]}{r_1^2} & \frac{E[(Y_{i2} - \hat{y}_{i2}(\boldsymbol{\theta}))(Y_{j2} - \hat{y}_{j2}(\boldsymbol{\theta}))^2]}{r_2^2} & \dots & \frac{E[(Y_{i2} - \hat{y}_{i2}(\boldsymbol{\theta}))(Y_{jn_y} - \hat{y}_{jn_y}(\boldsymbol{\theta}))^2]}{r_{n_y}^2} \\ \vdots & \vdots & \ddots & \vdots \\ \frac{E[(Y_{in_y} - \hat{y}_{in_y}(\boldsymbol{\theta}))(Y_{j1} - \hat{y}_{j1}(\boldsymbol{\theta}))^2]}{r_1^2} & \frac{E[(Y_{in_y} - \hat{y}_{in_y}(\boldsymbol{\theta}))(Y_{j2} - \hat{y}_{j2}(\boldsymbol{\theta}))^2]}{r_2^2} & \dots & \frac{E[(Y_{in_y} - \hat{y}_{in_y}(\boldsymbol{\theta}))(Y_{jn_y} - \hat{y}_{jn_y}(\boldsymbol{\theta}))^2]}{r_{n_y}^2} \end{bmatrix}$$

The simulation error is modeled as a zero-mean Gaussian white noise (across time) vector with statistically independent components. Therefore, when  $t_1 \neq t_2$  or  $m \neq n$ , it follows that

$$E[(Y_{t_1 m} - \hat{y}_{t_1 m}(\boldsymbol{\theta})) (Y_{t_2 n} - \hat{y}_{t_2 n}(\boldsymbol{\theta}))^2] = \underbrace{E[(Y_{t_1 m} - \hat{y}_{t_1 m}(\boldsymbol{\theta}))]}_{=0} \times E[(Y_{t_2 n} - \hat{y}_{t_2 n}(\boldsymbol{\theta}))^2] = 0$$

On the other hand, when  $t_1 = t_2$  and  $m = n$ , it follows that

$$E[(Y_{t_1 m} - \hat{y}_{t_1 m}(\boldsymbol{\theta})) (Y_{t_2 n} - \hat{y}_{t_2 n}(\boldsymbol{\theta}))^2] = E[(Y_{t_1 m} - \hat{y}_{t_1 m}(\boldsymbol{\theta}))^3] = 0$$

Since  $(Y_{t_1 m} - \hat{y}_{t_1 m}(\boldsymbol{\theta}))$  is Gaussian. Therefore,  $E[(\mathbf{Y}_i - \hat{\mathbf{y}}_i(\boldsymbol{\theta})) \mathbf{W}_j^T] = \mathbf{0}$  and Eq. (5.45)

reduces to

$$\mathbf{I}_{\mathbf{0r}} = \mathbf{I}_{\mathbf{r0}}^T = \mathbf{0} \quad (5.46)$$

Finally, the last submatrix in Eq. (5.43),  $\mathbf{I}_{\mathbf{rr}}$ , can be obtained as

$$\begin{aligned} \mathbf{I}_{\mathbf{rr}} &= E \left[ \left( \frac{\partial \Lambda(\boldsymbol{\theta}, \mathbf{r}, \mathbf{Y}_{1 \rightarrow k})}{\partial \mathbf{r}} \right)^T \left( \frac{\partial \Lambda(\boldsymbol{\theta}, \mathbf{r}, \mathbf{Y}_{1 \rightarrow k})}{\partial \mathbf{r}} \right) \right] \\ &= \frac{k^2}{4} \mathbf{r}^{-1} (\mathbf{r}^{-1})^T - \frac{k}{4} \mathbf{r}^{-1} \sum_{i=1}^k E[\mathbf{W}_i^T] - \frac{k}{4} \sum_{i=1}^k E[\mathbf{W}_i] (\mathbf{r}^{-1})^T + \frac{1}{4} \sum_{i=1}^k \sum_{j=1}^k E[\mathbf{W}_i \mathbf{W}_j^T] \end{aligned} \quad (5.47)$$

The term  $E[\mathbf{W}_i]$  can be derived as

$$E[\mathbf{W}_i] = \left[ \frac{E[(Y_{i1} - \hat{y}_{i1}(\boldsymbol{\theta}))^2]}{r_1^2} \quad \frac{E[(Y_{i2} - \hat{y}_{i2}(\boldsymbol{\theta}))^2]}{r_2^2} \quad \dots \quad \frac{E[(Y_{in_y} - \hat{y}_{in_y}(\boldsymbol{\theta}))^2]}{r_{n_y}^2} \right]^T = \left[ \frac{1}{r_1} \quad \frac{1}{r_2} \quad \dots \quad \frac{1}{r_{n_y}} \right]^T = \mathbf{r}^{-1}$$

Also, the term  $E[\mathbf{W}_i \mathbf{W}_j^T]$  can be expressed as

$$E[\mathbf{W}_i \mathbf{W}_j^T] = \begin{bmatrix} \frac{E[(Y_{i1} - \hat{y}_{i1}(\boldsymbol{\theta}))^2 (Y_{j1} - \hat{y}_{j1}(\boldsymbol{\theta}))^2]}{r_1^4} & \frac{E[(Y_{i1} - \hat{y}_{i1}(\boldsymbol{\theta}))^2 (Y_{j2} - \hat{y}_{j2}(\boldsymbol{\theta}))^2]}{r_1^2 r_2^2} & \dots & \frac{E[(Y_{i1} - \hat{y}_{i1}(\boldsymbol{\theta}))^2 (Y_{jn_y} - \hat{y}_{jn_y}(\boldsymbol{\theta}))^2]}{r_1^2 r_{n_y}^2} \\ \frac{E[(Y_{i2} - \hat{y}_{i2}(\boldsymbol{\theta}))^2 (Y_{j1} - \hat{y}_{j1}(\boldsymbol{\theta}))^2]}{r_2^2 r_1^2} & \frac{E[(Y_{i2} - \hat{y}_{i2}(\boldsymbol{\theta}))^2 (Y_{j2} - \hat{y}_{j2}(\boldsymbol{\theta}))^2]}{r_2^4} & \dots & \frac{E[(Y_{i2} - \hat{y}_{i2}(\boldsymbol{\theta}))^2 (Y_{jn_y} - \hat{y}_{jn_y}(\boldsymbol{\theta}))^2]}{r_2^2 r_{n_y}^2} \\ \vdots & \vdots & \ddots & \vdots \\ \frac{E[(Y_{in_y} - \hat{y}_{in_y}(\boldsymbol{\theta}))^2 (Y_{j1} - \hat{y}_{j1}(\boldsymbol{\theta}))^2]}{r_{n_y}^2 r_1^2} & \frac{E[(Y_{in_y} - \hat{y}_{in_y}(\boldsymbol{\theta}))^2 (Y_{j2} - \hat{y}_{j2}(\boldsymbol{\theta}))^2]}{r_{n_y}^2 r_2^2} & \dots & \frac{E[(Y_{in_y} - \hat{y}_{in_y}(\boldsymbol{\theta}))^2 (Y_{jn_y} - \hat{y}_{jn_y}(\boldsymbol{\theta}))^2]}{r_{n_y}^4} \end{bmatrix}$$

When  $t_1 \neq t_2$  or  $m \neq n$ , it follows that

$$E[(Y_{t_1 m} - \hat{y}_{t_1 m}(\boldsymbol{\theta}))^2 (Y_{t_2 n} - \hat{y}_{t_2 n}(\boldsymbol{\theta}))^2] = E[(Y_{t_1 m} - \hat{y}_{t_1 m}(\boldsymbol{\theta}))^2] \times E[(Y_{t_2 n} - \hat{y}_{t_2 n}(\boldsymbol{\theta}))^2] = r_m r_n$$

However, when  $t_1 = t_2$  and  $m = n$ , it follows that

$$E[(Y_{t_1 m} - \hat{y}_{t_1 m}(\boldsymbol{\theta}))^2 (Y_{t_2 n} - \hat{y}_{t_2 n}(\boldsymbol{\theta}))^2] = E[(Y_{t_1 m} - \hat{y}_{t_1 m}(\boldsymbol{\theta}))^4] = 3r_m^2$$

Therefore, the term  $\sum_{i=1}^k \sum_{j=1}^k E[\mathbf{W}_i \mathbf{W}_j^T]$  in Eq. (5.47) can be expressed as

$$\sum_{i=1}^k \sum_{j=1}^k E[\mathbf{W}_i \mathbf{W}_j^T] = (k^2 - k) \begin{bmatrix} \frac{1}{r_1^2} & \frac{1}{r_1 r_2} & \dots & \frac{1}{r_1 r_{n_y}} \\ \frac{1}{r_2 r_1} & \frac{1}{r_2^2} & \dots & \frac{1}{r_2 r_{n_y}} \\ \vdots & \vdots & \ddots & \vdots \\ \frac{1}{r_{n_y} r_1} & \frac{1}{r_{n_y} r_2} & \dots & \frac{1}{r_{n_y}^2} \end{bmatrix} + k \begin{bmatrix} \frac{3}{r_1^2} & \frac{1}{r_1 r_2} & \dots & \frac{1}{r_1 r_{n_y}} \\ \frac{1}{r_2 r_1} & \frac{3}{r_2^2} & \dots & \frac{1}{r_2 r_{n_y}} \\ \vdots & \vdots & \ddots & \vdots \\ \frac{1}{r_{n_y} r_1} & \frac{1}{r_{n_y} r_2} & \dots & \frac{3}{r_{n_y}^2} \end{bmatrix}$$

$$\Rightarrow \sum_{i=1}^k \sum_{j=1}^k E[\mathbf{W}_i \mathbf{W}_j^T] = k^2 \mathbf{r}^{-1} (\mathbf{r}^{-1})^T + 2k \begin{bmatrix} \frac{1}{r_1^2} & 0 & \cdots & 0 \\ 0 & \frac{1}{r_2^2} & \cdots & 0 \\ \vdots & \vdots & \ddots & \vdots \\ 0 & 0 & \cdots & \frac{1}{r_{n_y}^2} \end{bmatrix}$$

Therefore, according to Eq. (5.47), the submatrix  $\mathbf{I}_{\mathbf{r}\mathbf{r}}$  reduces to

$$\mathbf{I}_{\mathbf{r}\mathbf{r}} = \frac{k^2}{4} \mathbf{r}^{-1} (\mathbf{r}^{-1})^T - \frac{k^2}{4} \mathbf{r}^{-1} (\mathbf{r}^{-1})^T - \frac{k^2}{4} \mathbf{r}^{-1} (\mathbf{r}^{-1})^T + \frac{k^2}{4} \mathbf{r}^{-1} (\mathbf{r}^{-1})^T + \frac{k}{2} \begin{bmatrix} \frac{1}{r_1^2} & 0 & \cdots & 0 \\ 0 & \frac{1}{r_2^2} & \cdots & 0 \\ \vdots & \vdots & \ddots & \vdots \\ 0 & 0 & \cdots & \frac{1}{r_{n_y}^2} \end{bmatrix}$$

$$\Rightarrow \mathbf{I}_{\mathbf{r}\mathbf{r}} = \frac{k}{2} \begin{bmatrix} \frac{1}{r_1^2} & 0 & \cdots & 0 \\ 0 & \frac{1}{r_2^2} & \cdots & 0 \\ \vdots & \vdots & \ddots & \vdots \\ 0 & 0 & \cdots & \frac{1}{r_{n_y}^2} \end{bmatrix} \quad (5.48)$$

## References

- [1] H. Ebrahimian, R. Astroza, and J. P. Conte, "Parametric Identification of Hysteretic Material Constitutive Laws in Nonlinear Finite Element Models using Extended Kalman Filter," SSRP 14/06, Department of Structural Engineering, University of California, San Diego, La Jolla, CA, 2014.
- [2] H. Ebrahimian, R. Astroza, and J. P. Conte, "Extended Kalman Filter for Material Parameter Estimation in Nonlinear Structural Finite Element Models using Direct Differentiation Method," *Earthquake Engineering and Structural Dynamics*, DOI: 10.1002/eqe.2532, 2015.
- [3] R. Astroza, H. Ebrahimian, and J. P. Conte, "Material Parameter Identification in Distributed Plasticity FE Models of Frame-Type Structures Using Nonlinear Stochastic Filtering," *ASCE Journal of Engineering Mechanics*, DOI: 10.1061/(ASCE)EM.1943-7889.0000851, p. 04014149: 1-14, 2014.
- [4] H. Ebrahimian, R. Astroza, and J. P. Conte, "Nonlinear Structural Finite Element Model Updating using Batch Bayesian Estimation," in *Model Validation and Uncertainty Quantification, Proceedings of 33rd IMAC*, Orlando, FL, 2015.
- [5] R. Astroza, H. Ebrahimian, and J. P. Conte, "Nonlinear Structural Finite Element Model Updating using Stochastic Filtering," in *Model Validation and Uncertainty Quantification, Proceedings of 33rd IMAC*, Orlando, FL, 2015.
- [6] M. I. Friswell, and J. E. Mottershead, *Finite Element Model Updating in Structural Dynamics*, Dordrecht, The Netherlands: Kluwer Academic Publishers, 1995.
- [7] T. Marwala, *Finite Element Model Updating Using Computational Intelligence Techniques: Applications to Structural Dynamics*, Heidelberg, Germany: Springer, 2010.
- [8] E. Simoen, B. Moaveni, J. P. Conte, and G. Lombaert, "Uncertainty Quantification in the Assessment of Progressive Damage in a Seven-Story Full-Scale Building Slice," *ASCE Journal of Engineering Mechanics*, vol. 139, no. 12, p. 1818-1830, 2013.
- [9] B. Moaveni, X. He, J. P. Conte, and J. I. Restrepo, "Damage Identification Study of a Seven-Story Full-Scale Building Slice Tested on the UCSD-NEES Shake Table," *Structural Safety*, vol. 32, no. 5, p. 347-356, 2010.
- [10] J. L. Beck and L. S. Katafygiotis, "Updating Models and their Uncertainties. Part I: Bayesian Statistical Framework," *ASCE Journal of Engineering Mechanics*, vol. 124, no. 4, p. 455-461, 1998.

- [11] K.-V. Yuen, J. L. Beck, and L. S. Katafygiotis, "Unified Probabilistic Approach for Model Updating and Damage Detection," *ASME Journal of Applied Mechanics*, vol. 73, no. 4, p. 555-564, 2006.
- [12] M. Muto and J. L. Beck, "Bayesian Updating and Model Class Selection for Hysteretic Structural Models using Stochastic Simulation," *Journal of Vibration and Control*, vol. 14, no. 1-2, p. 7-34, 2008.
- [13] K.-V. Yuen and S.-C. Kuok, "Bayesian Methods for Updating Dynamic Models," *ASME Applied Mechanics Reviews*, vol. 64, no. 1, 2011.
- [14] M. Hoshiya and E. Saito, "Structural Identification by Extended Kalman Filter," *ASCE Journal of Engineering Mechanics*, vol. 110, no. 12, p. 1757–1770, 1984.
- [15] C. Loh and Y. Tsaur, "Time Domain Estimation of Structural Parameters," *Engineering Structures*, vol. 10, no. 2, p. 95-105, 1988.
- [16] J. Lin and Y. Zhang, "Nonlinear Structural Identification using Extended Kalman Filter," *Computers & Structures*, vol. 52, no. 4, p. 757–764, 1994.
- [17] N. Saha and D. Roy, "Extended Kalman Filters using Explicit and Derivative-free Local Linearizations," *Applied Mathematical Modelling*, vol. 33, no. 6, p. 2545-2563, 2009.
- [18] M. Wu and A. W. Smyth, "Application of the Unscented Kalman Filter for Real-time Nonlinear Structural System Identification," *Structural Control and Health Monitoring*, vol. 14, no. 7, p. 971-990, 2007.
- [19] E. N. Chatzi, A. W. Smyth, and S. F. Masri, "Experimental Application of On-line Parametric Identification for Nonlinear Hysteretic Systems with Model Uncertainty," *Structural Safety*, vol. 32, no. 5, p. 326–337, 2010.
- [20] R. Omrani, R. E. Hudson, and E. Taciroglu, "Parametric Identification of Nondegrading Hysteresis in a Laterally and Torsionally Coupled Building Using an Unscented Kalman Filter," *ASCE Journal of Engineering Mechanics*, vol. 139, no. 4, p. 452–468, 2013.
- [21] J. Ching, J. L. Beck, and K. A. Porter, "Bayesian State and Parameter Estimation of Uncertain Dynamical Systems," *Probabilistic Engineering Mechanics*, vol. 21, p. 81-96, 2006.
- [22] E. N. Chatzi and A. W. Smyth, "The Unscented Kalman Filter and Particle Filter Methods for Nonlinear Structural System Identification with Non-collocated Heterogeneous Sensing," *Structural Control and Health Monitoring*, vol. 16, no. 1, p. 99-123, 2009.
- [23] W. Song and S. Dyke, "Real-time Dynamic Model Updating of a Hysteretic Structural System," *ASCE Journal of Structural Engineering*, Vols.

- 10.1061/(ASCE)ST.1943-541X.0000857, p. 04013082(14), 2013.
- [24] J. N. Yang, Y. Xia, and C.-H. Loh, "Damage Detection of Hysteretic Structures with a Pinching Effect," *ASCE Journal of Engineering Mechanics*, vol. 140, no. 3, p. 462-472, 2014.
- [25] W. Song, S. Dyke, and T. Harmon, "Application of Nonlinear Model Updating for a Reinforced Concrete Shear Wall," *ASCE Journal of Engineering Mechanics*, vol. 139, no. 5, p. 635-649, 2013.
- [26] S. G. Shahidi and S. N. Pakzad, "Generalized Response Surface Model Updating using Time Domain Data," *ASCE Journal of Structural Engineering*, Vols. 10.1061/(ASCE)ST.1943-541X.0000915, p. A4014001(13), 2014.
- [27] A. K. Chopra, *Dynamics of Structures: Theory and Applications to Earthquake Engineering*, Englewood Cliffs, NJ: Prentice-Hall, 4th Ed., 2012.
- [28] K. J. Bathe, *Finite Element Procedures*, Upper Saddle River, NJ: Prentice-Hall, 1996.
- [29] J. L. Beck and S. Au, "Bayesian Updating of Structural Models and Reliability using Markov Chain Monte Carlo Simulation," *ASCE Journal of Engineering Mechanics*, vol. 128, no. 4, p. 380-391, 2002.
- [30] L. Ljung, *System Identification: Theory for the User*, Upper Saddle River, N.J.: PTR Prentice Hall, 2nd Edition, 1999.
- [31] G. C. Goodwin and R. L. Payne, *Dynamic System Identification: Experiment Design and Data Analysis*, New York: Academic Press, 1977.
- [32] J. L. Beck, "Bayesian System Identification based on Probability Logic," *Structural Control and Health Monitoring*, vol. 17, no. 7, p. 825-847, 2010.
- [33] P. Liu and S.-K. Au, "Bayesian Parameter Identification of Hysteretic Behavior of Composite Walls," *Probabilistic Engineering Mechanics*, vol. 34, p. 101-109, 2013.
- [34] T. K. Moon and W. C. Stirling, *Mathematical Methods and Algorithms for Signal Processing*, Upper Saddle River, N.J.: Prentice-Hall, 2000.
- [35] J. V. Beck and K. J. Arnold, *Parameter Estimation in Engineering and Science*, New York: John Wiley and Sons, 1977.
- [36] K.-V. Yuen, *Bayesian Methods for Structural Dynamics and Civil Engineering*, Clementi Loop, Singapore: John Wiley & Sons, 2010.
- [37] K.-V. Yuen, J. L. Beck, and L. S. Katafygiotis, "Efficient Model Updating and Health Monitoring Methodology using Incomplete Modal Data without Mode Matching," *Structural Control and Health Monitoring*, vol. 13, no. 1, p. 91-107,

2006.

- [38] R. H. Byrd, M. E. Hribar, and J. Nocedal, "An Interior Point Algorithm for Large-scale Nonlinear Programming," *SIAM Journal on Optimization*, vol. 9, no. 4, p. 877–900, 1999.
- [39] R. H. Byrd, J. C. Gilbert, and J. Nocedal, "A Trust Region Method Based on Interior Point Techniques for Nonlinear Programming," *Mathematical Programming*, vol. 89, no. 1, p. 149–185, 2000.
- [40] The MathWorks, "MATLAB Optimization Toolbox, User's Guide, R2014a," The MathWorks Inc., Natick, MA, 2014.
- [41] C. A. Vidal, H.-S. Lee, and R. B. Haber, "The Consistent Tangent Operator for Design Sensitivity Analysis of History-Dependent Response," *Computing Systems in Engineering*, vol. 2, no. 5-6, p. 509–523, 1991.
- [42] J. J. Tsay and J. S. Arora, "Nonlinear Structural Design Sensitivity Analysis for Path Dependent Problems. Part 1: General Theory," *Computer Methods in Applied Mechanics and Engineering*, vol. 81, no. 2, p. 183–208, 1990.
- [43] M. Kleiber, H. Antunez, T. D. Hien, and P. Kowalczyk, *Parameter Sensitivity in Nonlinear Mechanics: Theory and Finite Element Computations*, England: John Wiley & Sons Ltd, 1997.
- [44] Y. Zhang and A. Der Kiureghian, "Dynamic Response Sensitivity of Inelastic Structures," *Computer Methods in Applied Mechanics and Engineering*, vol. 108, no. 1-2, p. 23–36, 1993.
- [45] J. P. Conte, "Finite Element Response Sensitivity Analysis in Earthquake Engineering," in *Earthquake Engineering Frontiers in the New Millennium*, Lisse, The Netherlands, 2001.
- [46] J. P. Conte, P. K. Vijalapura, and M. Meghella, "Consistent Finite-Element Response Sensitivity Analysis," *ASCE Journal of Engineering Mechanics*, vol. 129, no. 12, p. 1380–1393, 2003.
- [47] S. M. Kay, *Fundamentals of Statistical Signal Processing. Volume 1: Estimation Theory*, Upper Saddle River, NJ: Prentice Hall, 1993.
- [48] Edited by: F. Zhang, *The Schur Complement and its Applications*, New York, NY: Springer, 2005.
- [49] P. Tichavsky, C. H. Muravchik and A. Nehorai, "Posterior Cramer–Rao Bounds for Discrete-Time Nonlinear Filtering," *IEEE Transactions on Signal Processing*, vol. 46, no. 5, p. 1386–1396, 1998.
- [50] P. E. Gill, W. Murray, and M. H. Wright, *Practical Optimization*, London:



Academic Press, 1981.

- [51] F. F. Taucer, E. Spacone, and F. C. Filippou, "A Fiber Beam-Column Element for Seismic Response Analysis of Reinforced Concrete Structures," UBC/EERC-91/17, Earthquake Engineering Research Center, College of Engineering, UC Berkeley, Berkeley, CA., 1991.
- [52] "MATLAB (2012)," The MathWorks Inc., Natick, Massachusetts, United States.
- [53] OpenSees, "Open System for Earthquake Engineering Simulation," [Online]. Available: <http://opensees.berkeley.edu/>. [Accessed September 2014].
- [54] F. C. Filippou, E. P. Popov, and V. V. Bertero, "Effects of Bond Deterioration on Hysteretic Behavior of Reinforced Concrete Joints," EERC Report 83-19, Earthquake Engineering Research Center, College of Engineering, UC Berkeley, Berkeley, CA, 1983.
- [55] "Center for Engineering Strong Motion Data, CESMD - A Cooperative Effort," [Online]. Available: <http://strongmotioncenter.org/>. [Accessed September 2014].
- [56] S. J. Julier and J. K. Uhlmann, "New Extension of the Kalman Filter to Nonlinear Systems," in *The Proceedings of SPIE 3068, Signal Processing, Sensor Fusion, and Target Recognition VI*, 182, Orlando, FL, 1997.
- [57] S. Julier, J. Uhlmann, and H. F. Durrant-Whyte, "A New Method for the Nonlinear Transformation of Means and Covariances in Filters and Estimators," *IEEE Transactions on Automatic Control*, vol. 45, no. 3, p. 477-482, 2000.
- [58] D. Simon, *Optimal State Estimation: Kalman, H-Infinity, and Nonlinear Approaches*, Hoboken, New Jersey: John Wiley & Sons, Inc., 2006.
- [59] A. Gupta and H. Krawinkler, "Behavior of Ductile SMRFs at Various Seismic Hazard Levels," *ASCE Journal of Structural Engineering*, vol. 126, no. 1, p. 98-107, 2000.

## **CHAPTER 6: OUTPUT-ONLY STRUCTURAL SYSTEM AND DAMAGE IDENTIFICATION USING STOCHASTIC NONLINEAR FINITE ELEMENT MODEL UPDATING**

### **6.1. Introduction**

Disastrous events such as earthquakes are known to inflict potentially devastating damage to critical civil infrastructures. Potential impacts of earthquakes and other natural and man-made hazards on urban societies can be reduced through accurate and timely risk mitigation decisions after the catastrophic event, which can be supported and facilitated by the use of advanced structural health monitoring (SHM) methods to help identify damage in critical civil infrastructures. Damage identification (ID) in civil infrastructures based on changes in the identified modal properties of an equivalent linear elastic model is perhaps the most popular SHM approach ([1-3] to name only a few). Nevertheless, damage ID based on linear modal ID is subjected to three key shortcomings: (i) the underlying linearity assumption is an idealization of the

real structure behavior, which is intrinsically nonlinear from the onset of loading [4]; (ii) modal parameters are global properties of the structure and often insensitive to local damages; and (iii) low-amplitude vibrations used for modal identification contain information about loss of effective stiffness, but cannot provide any information about other important manifestations of damage (such as loss of strength, ductility capacity, etc.).

Nonlinear finite element (FE) model updating in time domain is an advanced system and damage ID approach for civil structures that can overcome the shortcomings of the damage ID based on linear modal ID methods (e.g., [5-10]). The measured input excitation and output response of the structure are utilized in this method to update the nonlinear FE model of the structure of interest. The updated FE model can then be interrogated to extract detailed information about various manifestations of damage in the structural components and systems. Nonetheless, measuring the exact input excitation for real world civil structures is often unattainable. For example, besides the possibility of measuring incomplete, erroneous, and/or noisy input data for typical civil structures, measuring the input earthquake excitations for underground structures, multi-span bridges spanning over deep water, and buildings with deep underground basement can be impractical or impossible. It is therefore rational to extend state-of-the-art input-output nonlinear FE model updating methods to account for the effects of unknown, erroneous, and/or noisy input excitations. This objective is pursued in this study through a joint structural system and input excitation estimation approach.

Estimating the unknown exciting forces in structural systems has been the subject of past studies in the literature. In [11,12], the conjugate gradient estimation method has been used to estimate the external forces and time-dependent system parameters of simple structural models including a linear elastic MDOF mass-spring model and a cantilever beam. An extended inverse estimation algorithm based on the extended Kalman filter and intelligent recursive least squares method is developed in [13] to estimate the unknown input load in a SDOF nonlinear mass-spring model representing a tower structure. An inverse method to identify input forces of non-linear structural systems based on the extended Kalman filter method is developed and applied to a MDOF mass-spring [14] and a linear elastic cantilever beam model [15]. A method based on sensitivity of structural responses is presented in [16] for identifying both the system parameters and the input excitation force for a simply supported steel beam. Based on linear minimum-variance unbiased estimation method, an algorithm is proposed in [17] for estimating jointly the input and state of a structure from a limited number of acceleration measurements. The algorithm is validated using the experimental data obtained from an instrumented steel beam and vibration data recorded from a full-scale bridge in Wetteren (Belgium). Recently, a procedure for joint system and input identification based on the unscented Kalman filtering method is proposed in [18] and validated using 2D linear elastic structural frame models. The structural applications in all the above-mentioned studies consist of either linear elastic structural models, or SDOF or MDOF nonlinear mass-spring models. These models are either insufficient to predict the response of a real civil structure or are based on

simplifying assumptions that result in a crude prediction of the real behavior of the structural systems. Consequently, there is a need to develop output-only nonlinear structural system and input estimation methodologies that are applicable to large and complex real world civil structure.

This chapter proposes a novel framework for blind nonlinear system and damage ID of civil structures based on output-only advanced mechanics-based nonlinear finite element (FE) model updating using seismic excitations. This framework offers a computationally feasible tool for SHM and damage ID of civil structures when input seismic excitations are not measured or the measured seismic excitations are incomplete, erroneous, and/or contaminated with measurement noise. Two data fusion approaches based on Bayesian inference methodology are proposed in this study to estimate jointly the nonlinear structural model parameters and input earthquake excitations. Furthermore, the estimation uncertainties are quantified by providing a measure of plausibility or degree of belief of the estimation results. The proposed framework in this study is rooted in the Authors' previous studies on nonlinear FE model updating of civil structures using the input-output measurement data ([8-10]).

## **6.2. Output-only nonlinear system and input identification**

The time-discretized equation of motion of a nonlinear FE model at time step  $k$  is expressed as

$$\mathbf{M}(\boldsymbol{\theta}) \ddot{\mathbf{q}}_k(\boldsymbol{\theta}) + \mathbf{C}(\boldsymbol{\theta}) \dot{\mathbf{q}}_k(\boldsymbol{\theta}) + \mathbf{r}_k(\mathbf{q}_k(\boldsymbol{\theta}), \boldsymbol{\theta}) = \mathbf{f}_k(\boldsymbol{\theta}) \quad (6.1)$$

where  $\mathbf{M}(\boldsymbol{\theta}) \in \mathbb{R}^{n_{DOF} \times n_{DOF}}$  = mass matrix;  $\mathbf{C}(\boldsymbol{\theta}) \in \mathbb{R}^{n_{DOF} \times n_{DOF}}$  = damping matrix;  $\mathbf{r}_k(\mathbf{q}_k(\boldsymbol{\theta}), \boldsymbol{\theta}) \in \mathbb{R}^{n_{DOF} \times 1}$  = history-dependent (or path-dependent) internal resisting force vector;  $\mathbf{q}_k(\boldsymbol{\theta}), \dot{\mathbf{q}}_k(\boldsymbol{\theta}), \ddot{\mathbf{q}}_k(\boldsymbol{\theta}) \in \mathbb{R}^{n_{DOF} \times 1}$  = nodal displacement, velocity, and acceleration vectors, respectively;  $\boldsymbol{\theta} \in \mathbb{R}^{n_{\theta} \times 1}$  = the FE model parameter vector;  $\mathbf{f}_k(\boldsymbol{\theta}) \in \mathbb{R}^{n_{DOF} \times 1}$  = dynamic load vector. The FE model parameters include parameters characterizing the nonlinear material constitutive laws, inertial properties, loading, damping, geometry, restraint and constraint parameters [10]. In the case of uniform base excitation,  $\mathbf{f}_k(\boldsymbol{\theta}) = -\mathbf{M}(\boldsymbol{\theta})\mathbf{L}\ddot{\mathbf{u}}_k^g$  where  $\mathbf{L} \in \mathbb{R}^{n_{DOF} \times n_{u^g}}$  is the base acceleration influence matrix, and  $\ddot{\mathbf{u}}_k^g \in \mathbb{R}^{n_{u^g} \times 1}$  denotes the input ground acceleration vector. Using a recursive numerical integration rule, such as Newmark-beta method [19], Eq. (6.1) is reduced to a nonlinear vector-valued algebraic equation that can be recursively solved in time to find the nodal displacement vector. Therefore, by having the initial conditions of the FE model (i.e.,  $\mathbf{q}_0, \dot{\mathbf{q}}_0$ ) and the time history of the input ground acceleration, the equation of motion of the structure can be solved recursively in time to find the nodal response of the FE model at each discrete time step. In short, the nodal response of the FE model at time step  $k$  can be expressed as a nonlinear function of the model parameter vector  $(\boldsymbol{\theta})$ , time history of the base acceleration vector  $(\ddot{\mathbf{u}}_{1:k}^g = [\ddot{\mathbf{u}}_1^{gT}, \ddot{\mathbf{u}}_2^{gT}, \dots, \ddot{\mathbf{u}}_k^{gT}]^T)$ , and the initial conditions of the FE model  $(\mathbf{q}_0, \dot{\mathbf{q}}_0)$ , i.e. [10],

$$[\mathbf{q}_k, \dot{\mathbf{q}}_k, \ddot{\mathbf{q}}_k] = \tilde{\mathbf{h}}_k(\boldsymbol{\theta}, \ddot{\mathbf{u}}_{1:k}^g, \mathbf{q}_0, \dot{\mathbf{q}}_0) \quad (6.2)$$

where  $\tilde{\mathbf{h}}_k(\dots)$  is referred to as the nonlinear nodal response function of the FE model at time step  $k$ . In general, the response of a FE model at each time step is expressed as a linear or nonlinear function of the nodal displacement, velocity, and acceleration vectors. Denoting the response quantity estimated from the FE model at time step  $k$  by  $\hat{\mathbf{y}}_k \in \mathbb{R}^{n_y \times 1}$ , it follows that

$$\hat{\mathbf{y}}_k = \mathbf{h}_k(\boldsymbol{\theta}, \ddot{\mathbf{u}}_{1:k}^g, \mathbf{q}_0, \dot{\mathbf{q}}_0) \quad (6.3)$$

where  $\mathbf{h}_k(\dots)$  is the nonlinear response function of the FE model at time step  $k$ .

The actual dynamic response of a civil structure can be measured using sensors deployed in the structure or installed on its components. The measured response vector of the structure,  $\mathbf{y}_k$ , is related to the FE predicted response,  $\hat{\mathbf{y}}_k$ , as

$$\mathbf{v}_k(\boldsymbol{\theta}, \ddot{\mathbf{u}}_{1:k}^g) = \mathbf{y}_k - \hat{\mathbf{y}}_k(\boldsymbol{\theta}, \ddot{\mathbf{u}}_{1:k}^g) \quad (6.4)$$

in which  $\mathbf{v}_k \in \mathbb{R}^{n_y \times 1}$  is the simulation error vector and accounts for the misfit between the measured response of the structure and the FE predicted response. This misfit stems from the output measurement noise, parameter uncertainty, and model uncertainties. The latter stands for the mathematical idealizations and imperfections underlying the FE model, which result in an inherent misfit between the model prediction and the actual structural response ([10,20]). By neglecting the effects of model uncertainties, the simulation error due to model parameter uncertainty is minimized in the parameter estimation procedure and therefore,  $\mathbf{v}_k$  in Eq. (6.4) accounts for only the measurement noise. Furthermore, it is assumed herein that the

measurement noise is stationary, zero-mean, and independent Gaussian white noise (i.e., statistically independent across time and measurement channels) [21] Therefore, the probability distribution function (PDF) of the simulation error in Eq. (6.4) is expressed as

$$p(\mathbf{v}_i) = \frac{1}{(2\pi)^{n_y/2} |\mathbf{R}|^{1/2}} e^{-\frac{1}{2} \mathbf{v}_i^T \mathbf{R}^{-1} \mathbf{v}_i} \quad (6.5)$$

in which  $|\mathbf{R}|$  denotes the determinant of the diagonal matrix  $\mathbf{R} \in \mathbb{R}^{n_y \times n_y}$ , which is the (time-invariant) covariance matrix of the simulation error vector (i.e.,  $\mathbf{R} = E(\mathbf{v}_i \mathbf{v}_i^T), \forall i$ ).

In the output-only structural system and input identification problem of interest, the FE model parameter vector ( $\boldsymbol{\theta}$ ) and the components of the input ground acceleration time history ( $\ddot{\mathbf{u}}_{1:k}^g$ ) are time-invariant unknown parameters, which are modeled as random variables according to Bayesian inference method (the corresponding random variables are shown by  $\boldsymbol{\Theta}$  and  $\ddot{\mathbf{U}}_{1:k}^g$ , respectively). The objective of the output-only system and input identification problem is to jointly estimate the unknown parameters such that their joint *a posteriori* PDF given the measured response of the structure is maximized, i.e.,

$$\left( \hat{\boldsymbol{\theta}}, \hat{\ddot{\mathbf{u}}}_{1:k}^g \right)_{\text{MAP}} = \underset{\left( \boldsymbol{\theta}, \ddot{\mathbf{u}}_{1:k}^g \right)}{\text{argmax}} p\left( \boldsymbol{\theta}, \ddot{\mathbf{u}}_{1:k}^g \mid \mathbf{y}_{1:k} \right) \quad (6.6)$$

in which  $\mathbf{y}_{1:k} = [\mathbf{y}_1^T, \mathbf{y}_2^T, \dots, \mathbf{y}_k^T]^T$  = time history of the measured response of the structure, and MAP stands for maximum *a posteriori* estimate. Two approaches are



proposed in this study to solve the estimation problem shown by Eq. (6.6): (i) recursive maximum likelihood (ML) estimation method, and (ii) stochastic filtering method based on recursive maximum *a posteriori* estimation.

### 6.3. Recursive ML estimation method

Using Bayes' rule, the *a posteriori* probability distribution in Eq. (6.6) can be expressed as

$$p(\boldsymbol{\theta}, \ddot{\mathbf{u}}_{1:k}^g \mid \mathbf{y}_{1:k}) = \frac{p(\mathbf{y}_{1:k} \mid \boldsymbol{\theta}, \ddot{\mathbf{u}}_{1:k}^g) p(\boldsymbol{\theta}, \ddot{\mathbf{u}}_{1:k}^g)}{p(\mathbf{y}_{1:k})} \quad (6.7)$$

where  $p(\mathbf{y}_{1:k} \mid \boldsymbol{\theta}, \ddot{\mathbf{u}}_{1:k}^g)$  = the likelihood function,  $p(\boldsymbol{\theta}, \ddot{\mathbf{u}}_{1:k}^g)$  = the joint *a priori* distribution of the random variables  $\boldsymbol{\Theta}$  and  $\ddot{\mathbf{U}}_{1:k}^g$ , and  $p(\mathbf{y}_{1:k})$  = constant independent of the random variables  $\boldsymbol{\Theta}$  and  $\ddot{\mathbf{U}}_{1:k}^g$ , and. It is assumed herein that the *a priori* distribution of  $\boldsymbol{\Theta}$  is independent of the *a priori* distribution of  $\ddot{\mathbf{U}}_{1:k}^g$ ; therefore,  $p(\boldsymbol{\theta}, \ddot{\mathbf{u}}_{1:k}^g) = p(\boldsymbol{\theta}) \times p(\ddot{\mathbf{u}}_{1:k}^g)$ . Moreover, the *a priori* distributions are assumed uniform.

Thus, Eq. (6.7) is reduced to:

$$p(\boldsymbol{\theta}, \ddot{\mathbf{u}}_{1:k}^g \mid \mathbf{y}_{1:k}) = c \times p(\mathbf{y}_{1:k} \mid \boldsymbol{\theta}, \ddot{\mathbf{u}}_{1:k}^g) \quad (6.8)$$

in which  $c = \frac{p(\boldsymbol{\theta}) p(\ddot{\mathbf{u}}_{1:k}^g)}{p(\mathbf{y}_{1:k})}$  is a constant. As a result, the MAP estimation problem shown

in Eq. (6.6) is reduced to a ML estimation problem [22] as

$$\left( \hat{\boldsymbol{\theta}}, \hat{\mathbf{u}}_{1:k}^g \right)_{\text{ML}} = \underset{(\boldsymbol{\theta}, \mathbf{u}_{1:k}^g)}{\text{argmax}} p(\mathbf{y}_{1:k} | \boldsymbol{\theta}, \mathbf{u}_{1:k}^g) \quad (6.9)$$

According to Eq. (6.4), the likelihood function is equal to the PDF of the simulation error time history, i.e.,  $p(\mathbf{y}_{1:k} | \boldsymbol{\theta}, \mathbf{u}_{1:k}^g) = p(\mathbf{v}_{1:k})$ . Since the simulation error is modeled as an independent Gaussian white noise process, the likelihood function is derived as

$$\begin{aligned} p(\mathbf{y}_{1:k} | \boldsymbol{\theta}, \mathbf{u}_{1:k}^g) &= \prod_{i=1}^k p(\mathbf{v}_i) \\ \Rightarrow p(\mathbf{y}_{1:k} | \boldsymbol{\theta}, \mathbf{u}_{1:k}^g) &= \prod_{i=1}^k \frac{1}{(2\pi)^{n_y/2} |\mathbf{R}|^{1/2}} e^{-\frac{1}{2}(\mathbf{y}_i - \mathbf{h}_i(\boldsymbol{\theta}, \mathbf{u}_{1:k}^g, \mathbf{q}_0, \dot{\mathbf{q}}_0))^T \mathbf{R}^{-1} (\mathbf{y}_i - \mathbf{h}_i(\boldsymbol{\theta}, \mathbf{u}_{1:k}^g, \mathbf{q}_0, \dot{\mathbf{q}}_0))} \end{aligned} \quad (6.10)$$

As proposed in [10], to enhance the robustness of the parameter estimation procedure, variance of the components of the simulation error vector (i.e., the diagonal entries of  $\mathbf{R}$  matrix) are also treated as unknowns and estimated jointly with the other unknown parameters (i.e.,  $\boldsymbol{\theta}$  and  $\mathbf{u}_{1:k}^g$ ) through an extended ML estimation framework. The diagonal entries of the covariance matrix  $\mathbf{R}$  are stacked in a row vector called the variance vector  $\mathbf{r} = \{r_j\}$ ,  $1 \leq j \leq n_y$ , where  $r_j$  is the  $j^{\text{th}}$  diagonal entry of  $\mathbf{R}$ .

To solve the ML estimation problem, it is more convenient to minimize the negative natural logarithm of the likelihood function, which results in the following nonlinear optimization problem to jointly estimate the FE model parameters, the ground acceleration time history, and the variance vector:

$$\left( \hat{\boldsymbol{\theta}}, \hat{\mathbf{u}}_{1:k}^g, \hat{\mathbf{r}} \right) = \underset{(\boldsymbol{\theta}, \mathbf{u}_{1:k}^g, \mathbf{r})}{\text{argmin}} J(\mathbf{y}_{1:k}, \boldsymbol{\theta}, \mathbf{u}_{1:k}^g, \mathbf{r}) \quad (6.11)$$

$$J(\mathbf{y}_{1:k}, \boldsymbol{\theta}, \ddot{\mathbf{u}}_{1:k}^g, \mathbf{r}) = \left( \frac{k}{2} \sum_{j=1}^{n_y} \ln(r_j) + \frac{1}{2} \sum_{i=1}^k \sum_{j=1}^{n_y} \frac{(y_{ij} - h_{ij}(\boldsymbol{\theta}, \ddot{\mathbf{u}}_{1:i}^g))^2}{r_j} \right) \quad (6.12)$$

in which  $J(\dots)$  = the objective function of the resulting optimization problem,  $y_{ij}$  = the  $j^{\text{th}}$  component of the structural response vector at  $i^{\text{th}}$  time step, and similarly  $h_{ij}$  = the  $j^{\text{th}}$  component of the predicted FE response vector at  $i^{\text{th}}$  time step, and the dependence of  $J(\dots)$  on the initial conditions of the FE model ( $\mathbf{q}_0$  and  $\dot{\mathbf{q}}_0$ ) is dropped for notational convenience. The nonlinear optimization problem in Eqs. (11)-(12) can be solved using gradient-based optimization procedures, which require the computation of the gradient of the objective function with respect to the estimation parameters. The gradient can be exactly derived as

$$\nabla J = \left[ \frac{\partial J}{\partial \boldsymbol{\theta}} \quad \frac{\partial J}{\partial \ddot{\mathbf{u}}_{1:k}^g} \quad \frac{\partial J}{\partial \mathbf{r}} \right]^T \quad (6.13)$$

where

$$\frac{\partial J}{\partial \boldsymbol{\theta}} = - \sum_{i=1}^k \sum_{j=1}^{n_y} \frac{(y_{ij} - h_{ij}(\boldsymbol{\theta}, \ddot{\mathbf{u}}_{1:i}^g))}{r_j} \left( \frac{\partial h_{ij}(\boldsymbol{\theta}, \ddot{\mathbf{u}}_{1:i}^g)}{\partial \boldsymbol{\theta}} \right), \quad 1 \leq j \leq n_y \quad (6.14)$$

$$\frac{\partial J}{\partial \ddot{\mathbf{u}}_l^g} = - \sum_{i=1}^k \sum_{j=1}^{n_y} \frac{(y_{ij} - h_{ij}(\boldsymbol{\theta}, \ddot{\mathbf{u}}_{1:i}^g))}{r_j} \left( \frac{\partial h_{ij}(\boldsymbol{\theta}, \ddot{\mathbf{u}}_{1:i}^g)}{\partial \ddot{\mathbf{u}}_l^g} \right), \quad 1 \leq l \leq k \quad (6.15)$$

$$\frac{\partial J}{\partial r_j} = \frac{k}{2r_j} - \frac{1}{2} \sum_{i=1}^k \frac{(y_{ij} - h_{ij}(\boldsymbol{\theta}, \ddot{\mathbf{u}}_{1:i}^g))^2}{r_j^2}, \quad 1 \leq j \leq n_y \quad (6.16)$$

The term  $\left( \frac{\partial h_{ij}(\boldsymbol{\theta}, \ddot{\mathbf{u}}_{1:i}^g)}{\partial \boldsymbol{\theta}} \right)$  in Eq. (6.14) is the rate of variation (or sensitivity) of

the  $j^{\text{th}}$  component of the FE response vector at  $i^{\text{th}}$  time step with respect to the FE model parameter vector  $\boldsymbol{\theta}$ , and is referred to as the FE response sensitivity with

respect to FE model parameters. Likewise, the vector  $\left( \frac{\partial h_{ij}(\boldsymbol{\theta}, \ddot{\mathbf{u}}_{1:i}^g)}{\partial \ddot{\mathbf{u}}_l^g} \right)$  in Eq. (6.15) is the

rate of variation (or sensitivity) of the  $j^{\text{th}}$  component of the FE response vector at  $i^{\text{th}}$  time step with respect to the input base acceleration vector at the  $l^{\text{th}}$  time step  $\ddot{\mathbf{u}}_l^g$ , and

is referred to as the FE response sensitivity with respect to base accelerations. It should

be noted that since the structural system is a causal system, its response depends on the past and current input, but not on the future inputs. Therefore, in Eq. (6.15),

$\frac{\partial h_{ij}(\boldsymbol{\theta}, \ddot{\mathbf{u}}_{1:i}^g)}{\partial \ddot{\mathbf{u}}_l^g} = 0$  if  $l > i$ . FE response sensitivities can be computed approximately using

the finite difference method (FDM), which requires multiple runs of the FE model.

The computational cost of the FDM significantly increases as the number of sensitivity parameters and the scale of the FE model increase. As a more resourceful alternative

method, FE response sensitivities can be computed using the direct differentiation method (DDM), which is based on the exact (consistent) differentiation of the FE

numerical scheme for response sensitivity computation with respect to the sensitivity parameters ([23-26]). The proposed framework in this study uses the DDM to

compute FE response sensitivities with respect to the FE model parameters and the components of the input base acceleration time history and therefore, offers a

computationally feasible framework for output-only nonlinear FE model updating especially for large scale nonlinear FE models.

A recursive estimation approach is proposed herein to solve the extended ML estimation problem. In this approach, the estimation time domain is split into successive overlapping windows, referred to as estimation windows. The ML estimation is solved recursively across each window to find the unknown parameter estimates, which are then transferred to the next window and utilized as initial estimates. The unknown parameters consist of the FE model parameters, the base accelerations time history across the window, and the simulation error variances. The estimated FE model parameters and simulation error variances are directly transferred from one window to the next and used as initial estimates. The first part of the estimated base acceleration time history that is not overlapped with the next window, is taken as final estimate; while, the overlapped part is transferred and re-estimated over the next window.

Figure 6.1 schematically illustrates the recursive estimation approach. The estimation windows have an identical length ( $t_l$  = window length in number of time steps) and overlap with the following windows ( $t_o$  = overlap length in number of time steps). The sliding (or moving) rate is defined as time step difference between the starting points of two successive windows, i.e.,  $t_s = t_l - t_o$ . As shows in this figure, the  $m^{\text{th}}$  estimation window spans from time step  $t_1^m$  to time step  $t_2^m$ , where  $t_1^m = t_1^{m-1} + t_s$ , and  $t_2^m = t_1^m + t_l$ . The first part of the estimated base acceleration time history at the  $m^{\text{th}}$  estimation window that is not overlapped with the  $(m+1)^{\text{th}}$  window is denoted by

$\hat{\mathbf{u}}_{t_1^m:t_1^m+t_s-1}^{g,m,1}$  herein. Likewise,  $\hat{\mathbf{u}}_{t_1^m+t_s:t_2^m}^{g,m,2}$  denotes the second part of the estimated base

acceleration time history that is transferred to the next window as initial estimates.

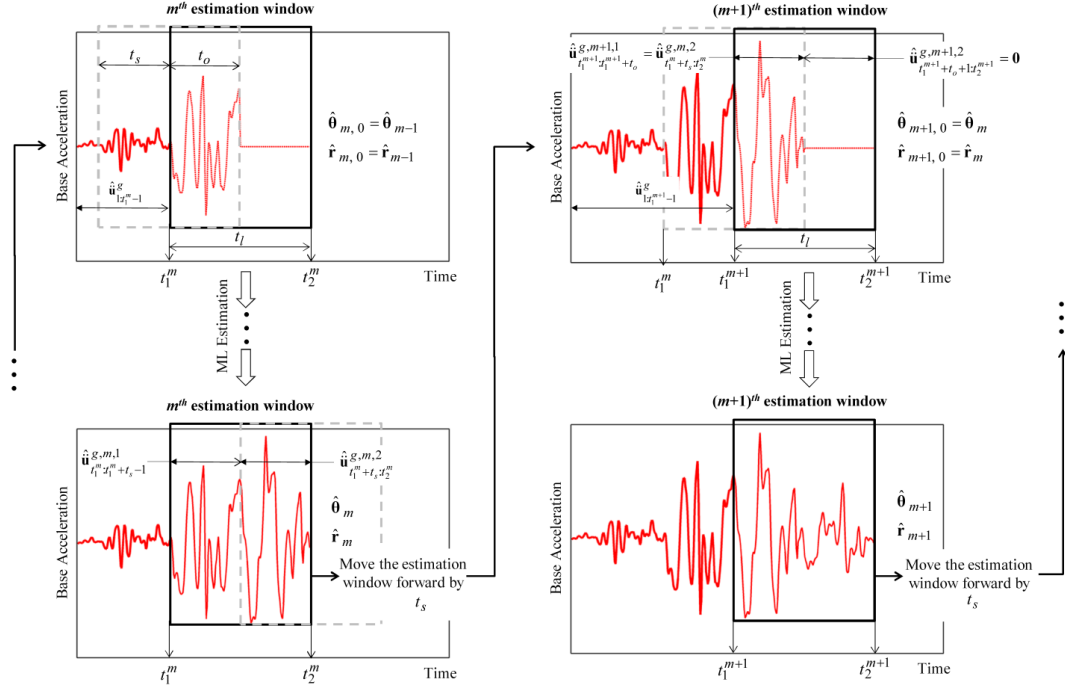


Figure 6.1: Schematic representation of the proposed recursive estimation approach for joint estimation of the FE model parameters, the simulation error variances, and the base acceleration time history.

The proposed recursive ML estimation method for the  $m^{\text{th}}$  estimation window can be summarized as

$$\left( \hat{\boldsymbol{\theta}}, \hat{\mathbf{u}}_{t_1^m:t_2^m}^g, \hat{\mathbf{r}} \right)_m = \underset{\left( \boldsymbol{\theta}, \mathbf{u}_{t_1^m:t_2^m}^g, \mathbf{r} \right)}{\operatorname{argmin}} J \left( \mathbf{y}_{t_1^m:t_2^m}, \boldsymbol{\theta}, \hat{\mathbf{u}}_{1:t_1^m-1}^g, \hat{\mathbf{u}}_{t_1^m:t_2^m}^g, \mathbf{r} \right) \quad (6.17)$$

$$J \left( \mathbf{y}_{t_1^m:t_2^m}, \boldsymbol{\theta}, \hat{\mathbf{u}}_{1:t_1^m-1}^g, \hat{\mathbf{u}}_{t_1^m:t_2^m}^g, \mathbf{r} \right) = \left( \frac{k}{2} \sum_{j=1}^{n_y} \ln(r_j) + \frac{1}{2} \sum_{i=t_1^m}^{t_2^m} \sum_{j=1}^{n_y} \frac{\left( y_{ij} - h_{ij} \left( \boldsymbol{\theta}, \hat{\mathbf{u}}_{1:t_1^m-1}^g, \hat{\mathbf{u}}_{t_1^m:i}^g \right) \right)^2}{r_j} \right) \quad (6.18)$$

in which,  $\hat{\mathbf{u}}_{1:t_1^m-1}^g$  is the base acceleration time history from time step 1 to time step  $t_1^m - 1$  estimated from past estimation windows and is used as known quantity at the  $m^{\text{th}}$  estimation window.

The estimation uncertainty is quantified using the estimation joint covariance matrix which can be approximated by the Cramér–Rao lower bound (CRLB) [27]. As presented in [10], the estimation covariance matrix for the ML estimation can be asymptotically approximated by the inverse of the Fisher information matrix (FIM). Similar to the process shown in [10], the FIM for the recursive estimation problem shown by Eqs. (17)-(18) can be derived as (see Appendix 6.I)

$$\mathbf{I}\left(\boldsymbol{\theta}, \hat{\mathbf{u}}_{t_1^m:t_2^m}^g, \mathbf{r}\right) = \begin{bmatrix} (\mathbf{I}_{\boldsymbol{\theta}\boldsymbol{\theta}})_{n_{\boldsymbol{\theta}} \times n_{\boldsymbol{\theta}}} & (\mathbf{I}_{\boldsymbol{\theta}\ddot{\mathbf{u}}^g})_{n_{\boldsymbol{\theta}} \times t_l n_{\ddot{\mathbf{u}}^g}} & (\mathbf{0})_{n_{\boldsymbol{\theta}} \times n_y} \\ (\mathbf{I}_{\ddot{\mathbf{u}}^g\boldsymbol{\theta}})_{t_l n_{\ddot{\mathbf{u}}^g} \times n_{\boldsymbol{\theta}}} & (\mathbf{I}_{\ddot{\mathbf{u}}^g\ddot{\mathbf{u}}^g})_{t_l n_{\ddot{\mathbf{u}}^g} \times t_l n_{\ddot{\mathbf{u}}^g}} & (\mathbf{0})_{t_l n_{\ddot{\mathbf{u}}^g} \times n_y} \\ (\mathbf{0})_{n_y \times n_{\boldsymbol{\theta}}} & (\mathbf{0})_{n_y \times t_l n_{\ddot{\mathbf{u}}^g}} & (\mathbf{I}_{\mathbf{r}\mathbf{r}})_{n_y \times n_y} \end{bmatrix} \quad (6.19)$$

where  $t_l n_{\ddot{\mathbf{u}}^g}$  is the size of  $\hat{\mathbf{u}}_{t_1^m:t_2^m}^g$ , which is the base acceleration time history to be estimated at the  $m^{\text{th}}$  estimation window. The sub-matrices  $\mathbf{I}_{\boldsymbol{\theta}\boldsymbol{\theta}}$ ,  $\mathbf{I}_{\boldsymbol{\theta}\ddot{\mathbf{u}}^g}$ , and  $\mathbf{I}_{\ddot{\mathbf{u}}^g\ddot{\mathbf{u}}^g}$  is derived as

$$\mathbf{I}_{\boldsymbol{\theta}\boldsymbol{\theta}} = \sum_{i=t_1^m}^{t_2^m} \sum_{j=1}^{n_y} \frac{1}{r_j} \left( \frac{\partial h_{ij}\left(\boldsymbol{\theta}, \hat{\mathbf{u}}_{1:t_1^m-1}^g, \hat{\mathbf{u}}_{t_1^m:i}^g\right)}{\partial \boldsymbol{\theta}} \right)^T \left( \frac{\partial h_{ij}\left(\boldsymbol{\theta}, \hat{\mathbf{u}}_{1:t_1^m-1}^g, \hat{\mathbf{u}}_{t_1^m:i}^g\right)}{\partial \boldsymbol{\theta}} \right) \quad (6.20)$$

$$\mathbf{I}_{\ddot{\mathbf{u}}^g\ddot{\mathbf{u}}^g} = \sum_{i=t_1^m}^{t_2^m} \sum_{j=1}^{n_y} \frac{1}{r_j} \left( \frac{\partial h_{ij}\left(\boldsymbol{\theta}, \hat{\mathbf{u}}_{1:t_1^m-1}^g, \hat{\mathbf{u}}_{t_1^m:i}^g\right)}{\partial \boldsymbol{\theta}} \right)^T \left( \frac{\partial h_{ij}\left(\boldsymbol{\theta}, \hat{\mathbf{u}}_{1:t_1^m-1}^g, \hat{\mathbf{u}}_{t_1^m:i}^g\right)}{\partial \hat{\mathbf{u}}_{t_1^m:t_2^m}^g} \right) \quad (6.21)$$

$$\mathbf{I}_{\mathbf{u}^g \ddot{\mathbf{u}}^g} = \sum_{i=t_1^m}^{t_2^m} \sum_{j=1}^{n_y} \frac{1}{r_j} \left( \frac{\partial h_{ij}(\boldsymbol{\theta}, \ddot{\mathbf{u}}_{1:t_1^m-1}^g, \ddot{\mathbf{u}}_{t_1^m:i}^g)}{\partial \ddot{\mathbf{u}}_{t_1^m:t_2^m}^g} \right)^T \left( \frac{\partial h_{ij}(\boldsymbol{\theta}, \ddot{\mathbf{u}}_{1:t_1^m-1}^g, \ddot{\mathbf{u}}_{t_1^m:i}^g)}{\partial \ddot{\mathbf{u}}_{t_1^m:t_2^m}^g} \right) \quad (6.22)$$

Furthermore,  $\mathbf{I}_{\mathbf{u}^g \boldsymbol{\theta}} = \mathbf{I}_{\boldsymbol{\theta} \mathbf{u}^g}^T$ . Considering that the FIM as shown in Eq. (6.19) is a block matrix, the lower bound for the FE model parameters and the base acceleration time history estimation covariance matrix is derived as

$$\text{Cov} \left( \begin{bmatrix} \boldsymbol{\theta}^T & \ddot{\mathbf{u}}_{t_1^m:t_2^m}^g \end{bmatrix}^T \right) \geq \left[ \begin{array}{cc} \mathbf{I}_{\boldsymbol{\theta}\boldsymbol{\theta}} & \mathbf{I}_{\boldsymbol{\theta}\mathbf{u}^g} \\ \mathbf{I}_{\mathbf{u}^g\boldsymbol{\theta}} & \mathbf{I}_{\mathbf{u}^g\mathbf{u}^g} \end{array} \right]^{-1} \Bigg|_{\text{at } \boldsymbol{\theta}, \mathbf{u}^g, \mathbf{r}} \quad (6.23)$$

where

$$\text{Cov} \left( \begin{bmatrix} \boldsymbol{\theta}^T & \ddot{\mathbf{u}}_{t_1^m:t_2^m}^g \end{bmatrix}^T \right) = \left[ \begin{array}{cc} E[(\boldsymbol{\theta} - E[\boldsymbol{\theta}])(\boldsymbol{\theta} - E[\boldsymbol{\theta}])^T] & E[(\boldsymbol{\theta} - E[\boldsymbol{\theta}]) \left( \ddot{\mathbf{u}}_{t_1^m:t_2^m}^g - E[\ddot{\mathbf{u}}_{t_1^m:t_2^m}^g] \right)^T] \\ E \left[ \left( \ddot{\mathbf{u}}_{t_1^m:t_2^m}^g - E[\ddot{\mathbf{u}}_{t_1^m:t_2^m}^g] \right) (\boldsymbol{\theta} - E[\boldsymbol{\theta}])^T \right] & E \left[ \left( \ddot{\mathbf{u}}_{t_1^m:t_2^m}^g - E[\ddot{\mathbf{u}}_{t_1^m:t_2^m}^g] \right) \left( \ddot{\mathbf{u}}_{t_1^m:t_2^m}^g - E[\ddot{\mathbf{u}}_{t_1^m:t_2^m}^g] \right)^T \right] \end{array} \right] \quad (6.24)$$

in which  $E[\mathbf{X}] = E_{\mathbf{Y}_{t_1^m:t_2^m}^m} \mathbf{X} | \boldsymbol{\theta}, \ddot{\mathbf{u}}_{t_1^m:t_2^m}^g$ ,  $\mathcal{R}[\mathbf{X}] = \int \mathbf{X} p(\mathbf{y}_{t_1^m:t_2^m}^m | \boldsymbol{\theta}, \ddot{\mathbf{u}}_{t_1^m:t_2^m}^g, \mathbf{r}) d\mathbf{y}$  and the matrix

inequality  $\mathbf{A} \geq \mathbf{B}$  means that  $\mathbf{A} - \mathbf{B}$  is a positive semidefinite matrix. The right hand side of Eq. (6.19) is evaluated for the true values of the FE model parameters, the base

acceleration time history, and simulation error variances ( $\boldsymbol{\theta}$ ,  $\ddot{\mathbf{u}}_{t_1^m:t_2^m}^g$ , and  $\mathbf{r}$ ,

respectively). Based on the asymptotic efficiency of the ML estimation ([28-29]), for

an identifiable problem,  $\hat{\boldsymbol{\theta}}$ ,  $\hat{\ddot{\mathbf{u}}}_{t_1^m:t_2^m}^g$ , and  $\hat{\mathbf{r}}$  converge asymptotically to their true values

respectively and therefore, the parameter estimation covariance matrix asymptotically

converges to the CRLB computed at the estimated parameter values.



A lower bound for the covariance matrix of the FE model parameters and base acceleration time history can be derived as ([30-31])

$$\text{Cov}(\Theta) \geq \left( \mathbf{I}_{\theta\theta} - \mathbf{I}_{\theta\ddot{u}^g} \left( \mathbf{I}_{\ddot{u}^g\ddot{u}^g} \right)^{-1} \mathbf{I}_{\ddot{u}^g\theta} \right)^{-1} \quad (6.25)$$

$$\text{Cov} \left( \ddot{\mathbf{U}}_{t_1^m:t_2^m}^g \right) \geq \left( \mathbf{I}_{\ddot{u}^g\ddot{u}^g} - \mathbf{I}_{\ddot{u}^g\theta} \left( \mathbf{I}_{\theta\theta} \right)^{-1} \mathbf{I}_{\theta\ddot{u}^g} \right)^{-1} \quad (6.26)$$

Table 6.1 summarizes the proposed recursive ML estimation algorithm.

Table 6.1: Recursive ML estimation algorithm for the output-only parameter estimation and nonlinear FE model updating problem.

<p>1. Set the estimation window length <math>t_l</math>, and the sliding rate <math>t_s</math>. Find the overlap length <math>t_o = t_l - t_s</math>. Set <math>t_1^0 = 1</math>.</p> <p>2. Initialize <math>\hat{\boldsymbol{\theta}}_0, \hat{\mathbf{r}}_0</math>. Set <math>\hat{\mathbf{u}}_{t_1^0:t_2^0}^{g,0} = \mathbf{0}</math>.</p> <p>3. For the <math>m^{\text{th}}</math> estimation window (<math>m = 1, 2, \dots</math>):</p> <p>3.1. Set <math>t_1^m = t_1^{m-1} + t_s</math>, and <math>t_2^m = t_1^m + t_l</math>.</p> <p>3.2. Retrieve the estimated FE model parameters, simulation error variances, and base acceleration time history from the last estimation window (i.e., <math>\hat{\boldsymbol{\theta}}_{m-1}, \hat{\mathbf{r}}_{m-1}</math>, and <math>\hat{\mathbf{u}}_{t_1^{m-1}:t_2^{m-1}}^{g,m-1}</math>).</p> <p>3.3. Set <math>\hat{\boldsymbol{\theta}}_{m,0} = \hat{\boldsymbol{\theta}}_{m-1}</math>, and <math>\hat{\mathbf{r}}_{m,0} = \hat{\mathbf{r}}_{m-1}</math>.</p> <p>3.4. Set <math>\hat{\mathbf{u}}_{t_1^m:t_1^m+t_o}^{g,m,1} = \hat{\mathbf{u}}_{t_1^{m-1}+t_s:t_2^{m-1}}^{g,m-1,2}</math>, and <math>\hat{\mathbf{u}}_{t_1^m+t_o+1:t_2^m}^{g,m,2} = \mathbf{0}</math>.</p> <p>3.5. Solve the optimization problem shown in Eqs. (17)-(18).</p> <p>3.6. Find <math>\mathbf{I}_{\boldsymbol{\theta}\boldsymbol{\theta}}, \mathbf{I}_{\boldsymbol{\theta}\ddot{\mathbf{u}}^g}</math>, and <math>\mathbf{I}_{\ddot{\mathbf{u}}^g\ddot{\mathbf{u}}^g}</math> using Eqs. (20)-(22).</p> <p>3.7. Compute the CRLB for the estimation covariance matrix for the FE model parameters and the base acceleration time history using Eqs. (25) and (26), respectively.</p> <p>3.8. Move on to the next estimation window (<math>m = m + 1</math>, go to step 3).</p>
---

In spite of its simplicity, the proposed recursive ML estimation method has two important shortcomings that may adversely affect its estimation accuracy and/or computational efficiency:

- (i) The ML estimation is asymptotically efficient [27]. In other words, for a large number of informative data samples (e.g.,  $\mathbf{y}_{t_1^m:t_2^m}$  with large estimation window length  $t_l = t_2^m - t_1^m$ ), the ML estimator is unbiased and the parameter estimation covariance matrix achieves the CRLB. Thus, to achieve the estimator efficiency, the estimation windows should be long enough. Nevertheless, by lengthening the estimation window, the number of estimation parameters and therefore, the dimension of the optimization problem increase, which in turn requires more iteration for the optimization algorithm to converge. In short, enhancing the estimation accuracy is at the cost of increasing computational demands.
- (ii) Although the parameter estimates are transferred from one estimation window to the other, no information about the plausibility or degree of belief of the parameter estimates is transferred between the windows. The *a priori* distribution of the estimation parameters at each estimation window is always assumed to be uniform, regardless of the estimation accuracy achieved at the last window. This loss of information results in more iteration for the optimization algorithm to converge at each estimation window and thus, results in remarkable computational demands.

## 6.4. Stochastic filtering method

To overcome the abovementioned shortcomings of the proposed recursive ML estimation method, an improved alternative approach is proposed in this section. This approach is based on a recursive maximum *a posteriori* (MAP) estimation, in which the *a posteriori* joint PDF of the FE model parameters and base acceleration time history are maximized at each estimation window using an iterative first order approximation method. The *a posteriori* point estimates and covariance matrix of the parameters are then transferred to the next estimation window and used as *a priori* information to solve the MAP estimation problem at the next estimation window. As will be shown later, this method reduces to an extended Kalman filtering (EKF) approach ([32]).

Utilizing the recursive estimation approach introduced earlier, the natural logarithm of the *a posteriori* joint PDF of the FE model parameters and base acceleration time history at the  $m^{\text{th}}$  estimation window is derived as

$$\log \left( p \left( \boldsymbol{\theta}, \ddot{\mathbf{u}}_{t_1^m:t_2^m}^{g,m} \mid \mathbf{y}_{t_1^m:t_2^m}^m \right) \right) = c + \log p \left( \left( \mathbf{y}_{t_1^m:t_2^m}^m \mid \boldsymbol{\theta}, \ddot{\mathbf{u}}_{t_1^m:t_2^m}^{g,m} \right) \right) + \log \left( p \left( \boldsymbol{\theta}, \ddot{\mathbf{u}}_{t_1^m:t_2^m}^{g,m} \right) \right) \quad (6.27)$$

in which  $c = -\log \left( p \left( \mathbf{y}_{t_1^m:t_2^m}^m \right) \right)$  and is constant. It is assumed that  $\ddot{\mathbf{u}}_{1:t_1^m-1}^g$  is estimated

from previous estimation windows and is known. For notational convenience, an extended parameter vector at the  $m^{\text{th}}$  estimation window is defined as

$\boldsymbol{\Psi}_m = \left[ \boldsymbol{\theta}^T, \ddot{\mathbf{u}}_{t_1^m:t_2^m}^{g,m} \right]^T$ , where  $\boldsymbol{\Psi}_m \in \mathbb{R}^{(n_\theta + t_l n_{\ddot{u}^g}) \times 1}$ . By substituting Eq. (6.10) for the

likelihood function into Eq. (6.27) and assuming a Gaussian distribution for the *a priori* joint PDF, it follows that

$$\log(p(\boldsymbol{\psi}_m | \mathbf{y}_{t_1^m:t_2^m})) = k_0 - \frac{1}{2} \left( \mathbf{y}_{t_1^m:t_2^m} - \mathbf{h}_{t_1^m:t_2^m}(\boldsymbol{\psi}_m, \ddot{\mathbf{u}}_{1:t_1^m-1}^g) \right)^T \tilde{\mathbf{R}}^{-1} \left( \mathbf{y}_{t_1^m:t_2^m} - \mathbf{h}_{t_1^m:t_2^m}(\boldsymbol{\psi}_m, \ddot{\mathbf{u}}_{1:t_1^m-1}^g) \right) - \frac{1}{2} (\boldsymbol{\psi}_m - \hat{\boldsymbol{\psi}}_m^-)^T (\hat{\mathbf{P}}_{\boldsymbol{\psi}}^-)^{-1} (\boldsymbol{\psi}_m - \hat{\boldsymbol{\psi}}_m^-) \quad (6.28)$$

where  $k_0$  is a constant;  $\hat{\boldsymbol{\psi}}_m^-$  and  $\hat{\mathbf{P}}_{\boldsymbol{\psi}}^-$  are the *a priori* mean vector and covariance matrix of the extended parameter vector at the  $m^{\text{th}}$  estimation window.  $\tilde{\mathbf{R}} \in \mathbb{R}^{t_1 n_y \times t_1 n_y}$  is a block diagonal matrix whose diagonals are the simulation error covariance matrix  $\mathbf{R}$ , i.e.,

$$\tilde{\mathbf{R}} = \begin{bmatrix} (\mathbf{R})_{n_y \times n_y} & & & \\ & (\mathbf{R})_{n_y \times n_y} & & \\ & & \ddots & \\ & & & (\mathbf{R})_{n_y \times n_y} \end{bmatrix}_{t_1 n_y \times t_1 n_y} \quad (6.29)$$

in which  $t_l = t_2^m - t_1^m$  is the estimation window length. To find the MAP estimate of  $\boldsymbol{\psi}_m$ ,

the *a posteriori* PDF in Eq. (6.28) is maximized, i.e.,  $\frac{\partial \log(p(\boldsymbol{\psi}_m | \mathbf{y}_{t_1^m:t_2^m}))}{\partial \boldsymbol{\psi}_m} = \mathbf{0}$ .

Therefore,

$$\left( \frac{\partial \mathbf{h}_{t_1^m:t_2^m}(\boldsymbol{\psi}_m, \ddot{\mathbf{u}}_{1:t_1^m-1}^g)}{\partial \boldsymbol{\psi}_m} \right)^T \tilde{\mathbf{R}}^{-1} \left( \mathbf{y}_{t_1^m:t_2^m} - \mathbf{h}_{t_1^m:t_2^m}(\boldsymbol{\psi}_m, \ddot{\mathbf{u}}_{1:t_1^m-1}^g) \right) - (\hat{\mathbf{P}}_{\boldsymbol{\psi}}^-)^{-1} (\boldsymbol{\psi}_m - \hat{\boldsymbol{\psi}}_m^-) = 0 \quad (6.30)$$

Eq. (6.30), which is a nonlinear algebraic equation in  $\boldsymbol{\psi}_m$  can be solved using an iterative first order approximations method such as Newton-Raphson. The first-order Taylor series expansion of  $\mathbf{h}_{t_1^m:t_2^m}(\boldsymbol{\psi}_m, \ddot{\mathbf{u}}_{1:t_1^m-1}^g)$  about  $\hat{\boldsymbol{\psi}}_m^-$  is expressed as

$$\mathbf{h}_{t_1^m:t_2^m}(\boldsymbol{\psi}_m, \ddot{\mathbf{u}}_{1:t_1^m-1}^g) = \mathbf{h}_{t_1^m:t_2^m}(\hat{\boldsymbol{\psi}}_m^-, \ddot{\mathbf{u}}_{1:t_1^m-1}^g) + \left. \frac{\partial \mathbf{h}_{t_1^m:t_2^m}(\boldsymbol{\psi}_m, \ddot{\mathbf{u}}_{1:t_1^m-1}^g)}{\partial \boldsymbol{\psi}_m} \right|_{\boldsymbol{\psi}_m = \hat{\boldsymbol{\psi}}_m^-} (\boldsymbol{\psi}_m - \hat{\boldsymbol{\psi}}_m^-) + H.O.T. \quad (6.31)$$

The matrix  $\left. \frac{\partial \mathbf{h}_{t_1^m:t_2^m}(\boldsymbol{\psi}_m, \ddot{\mathbf{u}}_{1:t_1^m-1}^g)}{\partial \boldsymbol{\psi}_m} \right|_{\boldsymbol{\psi}_m = \hat{\boldsymbol{\psi}}_m^-}$  is the FE response sensitivities with

respect to the extended parameter vector, evaluated at the *a priori* mean values of the extended parameter vector,  $\hat{\boldsymbol{\psi}}_m^-$ . This matrix is denoted by  $\mathbf{C}$  hereafter for notational convenience. Substituting Eq. (6.31) into Eq. (6.30) and neglecting the higher order terms results in the following (first order approximate) equation for the MAP estimate of  $\boldsymbol{\psi}_m$ :

$$\hat{\boldsymbol{\psi}}_m^+ = \hat{\boldsymbol{\psi}}_m^- + \left( \mathbf{C}^T \tilde{\mathbf{R}}^{-1} \mathbf{C} + (\hat{\mathbf{P}}_{\boldsymbol{\psi}}^-)^{-1} \right)^{-1} \mathbf{C}^T \tilde{\mathbf{R}}^{-1} \left( \mathbf{y}_{t_1^m:t_2^m} - \mathbf{h}_{t_1^m:t_2^m}(\hat{\boldsymbol{\psi}}_m^-, \ddot{\mathbf{u}}_{1:t_1^m-1}^g) \right) \quad (6.32)$$

in which  $\hat{\boldsymbol{\psi}}_m^+$  is the updated (or the *a posteriori*) estimate of  $\boldsymbol{\psi}_m$ . It can be shown that the term  $\left( \mathbf{C}^T \tilde{\mathbf{R}}^{-1} \mathbf{C} + (\hat{\mathbf{P}}_{\boldsymbol{\psi}}^-)^{-1} \right)^{-1} \mathbf{C}^T \tilde{\mathbf{R}}^{-1}$  is equivalent to the Kalman gain matrix [32] (see Appendix 6.II). According to the Newton-Raphson approach, the estimated (predicted)  $\hat{\boldsymbol{\psi}}_m^+$  from Eq. (6.32) is iteratively used as the new center-point for the linearization of Eq. (6.30) to find an improved (corrected) estimation. Therefore, the prediction-

correction procedure at each estimation window reduces to an iterative EKF method ([32]).

Following the EKF procedure, the *a priori* covariance matrix of the extended parameter vector  $\hat{\mathbf{P}}_{\Psi,m}^-$  is updated to the *a posteriori* covariance matrix  $\hat{\mathbf{P}}_{\Psi,m}^+$  after each prediction-correction iteration. It is moreover assumed that both the *a priori* and *a posteriori* joint PDF of the extended parameter vector are Gaussian. The updated estimation covariance matrix, is derived as (refer to [32,33] for proof)

$$\hat{\mathbf{P}}_{\Psi,m}^+ = E\left[\left(\Psi_m - \hat{\Psi}_m^+\right)\left(\Psi_m - \hat{\Psi}_m^+\right)^T\right] = (\mathbf{I} - \mathbf{K}\mathbf{C})\hat{\mathbf{P}}_{\Psi,m}^-(\mathbf{I} - \mathbf{K}\mathbf{C})^T + \mathbf{K}\tilde{\mathbf{R}}\mathbf{K} \quad (6.33)$$

Furthermore, to improve the convergence of the iterative prediction-correction procedure, a definite disturbance is added to the *a posteriori* covariance matrix at each iteration to provide the *a priori* covariance matrix for the next iteration, i.e.,

$$\hat{\mathbf{P}}_{\Psi,i+1}^- = \hat{\mathbf{P}}_{\Psi,i}^+ + \mathbf{Q} \quad (6.34)$$

where  $\mathbf{Q}$  is a constant diagonal matrix with small (relative to the diagonal entries of matrix  $\hat{\mathbf{P}}_{\Psi,i}^+$ ) positive diagonal entries. The matrix  $\mathbf{Q}$  is referred to as process noise covariance matrix in Kalman filtering approach. The subscript  $i$  in Eq. (6.34) denotes the iteration number.

The recursive MAP estimation procedure can be summarized as follows. At each estimation window, *a priori* estimate of the extended parameter vector and its covariance matrix is being updated iteratively following an iterative EKF approach, until some convergence criteria are met. The resulting *a posteriori* mean and

covariance matrix of the extended parameter vector are then transferred to the next estimation window and utilized as the *a priori* information. As described earlier, the estimated FE model parameters and simulation error variances are directly transferred from one window to the next and used as initial estimates. The first part of the estimated base acceleration time history that is not overlapped with the next window, is taken as final estimate; while, the overlapped part is transferred and re-estimated over the next window. Suppose that the final *a posteriori* estimates of the mean of the extended parameter vector for the  $(m-1)^{\text{th}}$  estimation window is derived as

$$\hat{\Psi}_{m-1}^+ = \left[ \hat{\theta}_{m-1}^T, \hat{\mathbf{u}}_{t_1^{m-1}:t_1^{m-1}+t_o}^{g,m-1,1}{}^T, \hat{\mathbf{u}}_{t_1^{m-1}+t_o+1:t_2^{m-1}}^{g,m-1,2}{}^T \right]^T \quad (6.35)$$

Likewise, that the final *a posteriori* estimates of the covariance matrix of the extended parameter vector for the  $(m-1)^{\text{th}}$  estimation window is correspondingly partitioned as

$$\hat{\mathbf{P}}_{\Psi,m-1}^+ = \begin{bmatrix} \hat{\mathbf{P}}_{\theta\theta} & \hat{\mathbf{P}}_{\theta\mathbf{u}^{g,1}} & \hat{\mathbf{P}}_{\theta\mathbf{u}^{g,2}} \\ \hat{\mathbf{P}}_{\mathbf{u}^{g,1}\theta} & \hat{\mathbf{P}}_{\mathbf{u}^{g,1}\mathbf{u}^{g,1}} & \hat{\mathbf{P}}_{\mathbf{u}^{g,1}\mathbf{u}^{g,2}} \\ \hat{\mathbf{P}}_{\mathbf{u}^{g,2}\theta} & \hat{\mathbf{P}}_{\mathbf{u}^{g,2}\mathbf{u}^{g,1}} & \hat{\mathbf{P}}_{\mathbf{u}^{g,2}\mathbf{u}^{g,2}} \end{bmatrix} \quad (6.36)$$

Therefore, the *a priori* estimates of mean of the extended parameter vector for the  $m^{\text{th}}$  estimation window is defined as

$$\hat{\Psi}_m^- = \left[ \hat{\theta}_{m-1}^T, \hat{\mathbf{u}}_{t_1^m:t_1^m+t_o}^{g,m,1}{}^T, \hat{\mathbf{u}}_{t_1^m+t_o+1:t_2^m}^{g,m,2}{}^T \right]^T \quad (6.37)$$

where  $\hat{\mathbf{u}}_{t_1^m:t_1^m+t_o}^{g,m,1} = \hat{\mathbf{u}}_{t_1^{m-1}+t_o+1:t_2^{m-1}}^{g,m-1,2}$  is transferred from the previous window, and

$\hat{\mathbf{u}}_{t_1^m+t_o+1:t_2^m}^{g,m,2}$  is initialized as zero vector, i.e.  $\hat{\mathbf{u}}_{t_1^m+t_o+1:t_2^m}^{g,m,2} = \mathbf{0}$ . The conditional *a*



*posteriori* covariance matrix of the parameters that are transferred from the  $(m-1)^{\text{th}}$  window to the  $m^{\text{th}}$  window can be derived as

$$\begin{aligned} \hat{\mathbf{P}}_{\boldsymbol{\theta}, \ddot{\mathbf{u}}^{g,2} | \ddot{\mathbf{u}}^{g,1}, m-1} &= E \left[ \left( \begin{bmatrix} \boldsymbol{\Theta} \\ \ddot{\mathbf{U}}^{g,2} \end{bmatrix} - \begin{bmatrix} \hat{\boldsymbol{\theta}}_{m-1} \\ \ddot{\mathbf{u}}^{g,m-1,2} \end{bmatrix} \right) \left( \begin{bmatrix} \boldsymbol{\Theta} \\ \ddot{\mathbf{U}}^{g,2} \end{bmatrix} - \begin{bmatrix} \hat{\boldsymbol{\theta}}_{m-1} \\ \ddot{\mathbf{u}}^{g,m-1,2} \end{bmatrix} \right)^T \middle| \ddot{\mathbf{u}}^{g,m-1,1} \right] \\ &= \begin{bmatrix} \hat{\mathbf{P}}_{\boldsymbol{\theta}\boldsymbol{\theta}} & \hat{\mathbf{P}}_{\boldsymbol{\theta}\ddot{\mathbf{u}}^{g,2}} \\ \hat{\mathbf{P}}_{\ddot{\mathbf{u}}^{g,2}\boldsymbol{\theta}} & \hat{\mathbf{P}}_{\ddot{\mathbf{u}}^{g,2}\ddot{\mathbf{u}}^{g,2}} \end{bmatrix} - \begin{bmatrix} \hat{\mathbf{P}}_{\boldsymbol{\theta}\ddot{\mathbf{u}}^{g,1}} \\ \hat{\mathbf{P}}_{\ddot{\mathbf{u}}^{g,2}\ddot{\mathbf{u}}^{g,1}} \end{bmatrix} \left( \hat{\mathbf{P}}_{\ddot{\mathbf{u}}^{g,1}\ddot{\mathbf{u}}^{g,1}} \right)^{-1} \begin{bmatrix} \hat{\mathbf{P}}_{\boldsymbol{\theta}\ddot{\mathbf{u}}^{g,1}} \\ \hat{\mathbf{P}}_{\ddot{\mathbf{u}}^{g,2}\ddot{\mathbf{u}}^{g,1}} \end{bmatrix}^T \end{aligned} \quad (6.38)$$

in which  $\hat{\mathbf{u}}_{t_1^{m-1}, t_1^{m-1}+t_o}^{g,m-1,1}$  is replaced by  $\ddot{\mathbf{u}}^{g,m-1,1}$  and  $\hat{\mathbf{u}}_{t_1^{m-1}+t_o+1:t_2^{m-1}}^{g,m-1,2}$  is replaced by  $\ddot{\mathbf{u}}^{g,m-1,2}$  for notational convenience. Finally, the *a priori* covariance matrix of the extended parameter vector for the  $(m)^{\text{th}}$  estimation window is defined as

$$\hat{\mathbf{P}}_{\Psi}^- = \begin{bmatrix} \hat{\mathbf{P}}_{\boldsymbol{\theta}, \ddot{\mathbf{u}}^{g,2} | \ddot{\mathbf{u}}^{g,1}, m-1} & \mathbf{0} \\ \mathbf{0} & \hat{\mathbf{P}}_{\ddot{\mathbf{u}}^{g,2}, \ddot{\mathbf{u}}^{g,2}, 0} \end{bmatrix} \quad (6.39)$$

where  $\hat{\mathbf{P}}_{\ddot{\mathbf{u}}^{g,2}, \ddot{\mathbf{u}}^{g,2}, 0} = E \left[ \left( \hat{\mathbf{u}}_{t_1^m+t_o+1:t_2^m}^{g,m,2} \right) \left( \hat{\mathbf{u}}_{t_1^m+t_o+1:t_2^m}^{g,m,2} \right)^T \right]$  is the initial estimate of the

covariance matrix of  $\hat{\mathbf{u}}_{t_1^m+t_o+1:t_2^m}^{g,m,2}$  and is selected as a constant diagonal matrix. Table

6.2 summarizes the proposed stochastic filtering algorithm for output-only parameter estimation and nonlinear FE model updating problem.

Table 6.2: Stochastic filtering algorithm for the output-only parameter estimation and nonlinear FE model updating problem.

<p>1. Set the estimation window length <math>t_l</math>, and the sliding rate <math>t_s</math>. Find the overlap length <math>t_o = t_l - t_s</math>. Set <math>t_1^0 = 1</math>.</p> <p>2. Initialize: <math>\hat{\boldsymbol{\theta}}_0</math>, <math>\hat{\mathbf{P}}_{\boldsymbol{\theta}\boldsymbol{\theta},0}</math>, <math>\hat{\mathbf{P}}_{\hat{\mathbf{u}}^g \hat{\mathbf{u}}^g,0}</math>. Set <math>\hat{\mathbf{u}}_{t_1^1:t_2^1}^{g,0} = \mathbf{0}</math>.</p> <p>3. Set <math>\hat{\boldsymbol{\psi}}_0^+ = \begin{bmatrix} \hat{\boldsymbol{\theta}}_0^T &amp; \hat{\mathbf{u}}_{t_1^1:t_2^1}^{g,0T} \end{bmatrix}^T</math>, and <math>\hat{\mathbf{P}}_{\boldsymbol{\psi},0}^+ = \begin{bmatrix} \hat{\mathbf{P}}_{\boldsymbol{\theta}\boldsymbol{\theta},0} &amp; \mathbf{0} \\ \mathbf{0} &amp; \hat{\mathbf{P}}_{\hat{\mathbf{u}}^g \hat{\mathbf{u}}^g,0} \end{bmatrix}</math>.</p> <p>4. Postulate the process noise covariance matrix <math>\mathbf{Q}</math>. Postulate the simulation error covariance matrix <math>\mathbf{R}</math>. Set up <math>\tilde{\mathbf{R}}</math> using Eq. (6.29).</p> <p>5. For <math>m^{\text{th}}</math> estimation window (<math>m = 1, 2, \dots</math>):</p> <p>5.1. Set <math>t_1^m = t_1^{m-1} + t_s</math>, and <math>t_2^m = t_1^m + t_l</math>.</p> <p>5.2. Retrieve the <i>a posteriori</i> estimates of mean and covariance matrix of the extended parameter vector from the last estimation window (i.e., <math>\hat{\boldsymbol{\psi}}_{m-1}^+</math>, and <math>\hat{\mathbf{P}}_{\boldsymbol{\psi},m-1}^+</math>).</p> <p>5.3. Set <math>\hat{\boldsymbol{\psi}}_{m,0}^+ = \hat{\boldsymbol{\psi}}_m^-</math>, where <math>\hat{\boldsymbol{\psi}}_m^-</math> is defined in Eq. (6.37).</p> <p>5.4. Set <math>\hat{\mathbf{P}}_{\boldsymbol{\psi},m,0}^+ = \hat{\mathbf{P}}_{\boldsymbol{\psi},m}^-</math>, where <math>\hat{\mathbf{P}}_{\boldsymbol{\psi},m}^-</math> is defined in Eq. (6.39).</p> <p>5.5. Iterate (<math>i = 1, 2, \dots</math>):</p> <p>a. Set <math>\hat{\boldsymbol{\psi}}_{m,i}^- = \hat{\boldsymbol{\psi}}_{m,i-1}^+</math>, <math>\hat{\mathbf{P}}_{\boldsymbol{\psi},m,i}^- = \hat{\mathbf{P}}_{\boldsymbol{\psi},m,i-1}^+ + \mathbf{Q}</math>.</p> <p>b. Evaluate the FE model using <math>\hat{\boldsymbol{\psi}}_{m,i}^-</math>; obtain response and response sensitivities:</p> $\hat{\mathbf{y}}_{t_1^m:t_2^m} = \mathbf{h}_{t_1^m:t_2^m} \left( \hat{\boldsymbol{\psi}}_{m,i}^-, \hat{\mathbf{u}}_{1:t_1^{m-1}-1}^g \right), \quad \mathbf{C} = \left. \frac{\partial \mathbf{h}_{t_1^m:t_2^m} \left( \boldsymbol{\psi}_m, \hat{\mathbf{u}}_{1:t_1^{m-1}-1}^g \right)}{\partial \boldsymbol{\psi}_m} \right _{\boldsymbol{\psi}_m = \hat{\boldsymbol{\psi}}_{m,i}^-}.$ <p>c. Find Kalman gain matrix: <math>\mathbf{K} = \left( \mathbf{C}^T \tilde{\mathbf{R}}^{-1} \mathbf{C} + \left( \hat{\mathbf{P}}_{\boldsymbol{\psi},m,i}^- \right)^{-1} \right)^{-1} \mathbf{C}^T \tilde{\mathbf{R}}^{-1}</math>.</p> <p>d. Find the corrected estimates of mean and covariance matrix of the extended parameter vector:</p> $\hat{\boldsymbol{\psi}}_{m,i}^+ = \hat{\boldsymbol{\psi}}_{m,i}^- + \mathbf{K} \left( \mathbf{y}_{t_1^m:t_2^m} - \hat{\mathbf{y}}_{t_1^m:t_2^m} \right),$ $\hat{\mathbf{P}}_{\boldsymbol{\psi},m,i}^+ = (\mathbf{I} - \mathbf{K}\mathbf{C}) \left( \hat{\mathbf{P}}_{\boldsymbol{\psi},m,i}^- \right) (\mathbf{I} - \mathbf{K}\mathbf{C})^T + \mathbf{K}\tilde{\mathbf{R}}\mathbf{K}.$ <p>e. Check for convergence:</p> <p>if <math>\left  \hat{\boldsymbol{\psi}}_{m,i}^+ - \hat{\boldsymbol{\psi}}_{m,i-1}^+ \right  &lt; \text{tol1} \times \left  \hat{\boldsymbol{\psi}}_{m,i-1}^+ \right </math> or <math>i \geq \text{tol2}</math> (where <i>tol1</i> = tolerance limit for relative change in the estimated parameter vector, and <i>tol2</i> = iteration limit): iteration is converged; move onto the next estimation window (<math>m = m + 1</math>, go to step 5); otherwise iterate again at the current estimation window (<math>i = i + 1</math>, go to step 5.5).</p>
--

## 6.5. Direct differentiation method (DDM) for finite element response sensitivity analysis with respect to uniform base excitation

DDM is based on the exact (consistent) differentiation of the finite element numerical scheme with respect to the sensitivity parameters. As mentioned earlier, the equation of motion (shown in Eq. (6.1)) can be transferred into a nonlinear algebraic equation using a single-step time integration scheme, e.g., the Newmark-beta method. Based on the Newmark-beta method, the acceleration and velocity vectors at time step  $k$  are approximated as

$$\ddot{\mathbf{q}}_k = a_1 \mathbf{q}_k + a_2 \mathbf{q}_{k-1} + a_3 \dot{\mathbf{q}}_{k-1} + a_4 \ddot{\mathbf{q}}_{k-1}, \quad \dot{\mathbf{q}}_k = b_1 \mathbf{q}_k + b_2 \mathbf{q}_{k-1} + b_3 \dot{\mathbf{q}}_{k-1} + b_4 \ddot{\mathbf{q}}_{k-1} \quad (6.40)$$

where  $a_1$  to  $a_4$  and  $b_1$  to  $b_4$  are integration coefficients. Substitution of these equations into Eq. (6.1) results in the following nonlinear vector-valued algebraic equation in  $\mathbf{q}_k$ :

$$a_1 \mathbf{M}(\boldsymbol{\psi}) \mathbf{q}_k(\boldsymbol{\psi}) + b_1 \mathbf{C}(\boldsymbol{\psi}) \mathbf{q}_k(\boldsymbol{\psi}) + \mathbf{r}_k(\mathbf{q}_k(\boldsymbol{\psi}), \boldsymbol{\psi}) = \tilde{\mathbf{f}}_k(\boldsymbol{\psi}) \quad (6.41)$$

in which

$$\tilde{\mathbf{f}}_k(\boldsymbol{\psi}) = \mathbf{f}_k(\boldsymbol{\psi}) - \mathbf{M}(\boldsymbol{\psi}) [a_2 \mathbf{q}_{k-1}(\boldsymbol{\psi}) + a_3 \dot{\mathbf{q}}_{k-1}(\boldsymbol{\psi}) + a_4 \ddot{\mathbf{q}}_{k-1}(\boldsymbol{\psi})] - \mathbf{C}(\boldsymbol{\psi}) [b_2 \mathbf{q}_{k-1}(\boldsymbol{\psi}) + b_3 \dot{\mathbf{q}}_{k-1}(\boldsymbol{\psi}) + b_4 \ddot{\mathbf{q}}_{k-1}(\boldsymbol{\psi})] \quad (6.42)$$

and  $\boldsymbol{\psi}$  is the sensitivity parameter vector, i.e., parameters with respect to which the FE response sensitivity is computed. Sensitivity parameters are the FE model parameters and/or the components of the uniform base acceleration time history. FE response sensitivity computation for FE model parameters using DDM is discussed in the

literature (e.g., [23-26]). This section emphasizes on the FE response sensitivity computation with respect to the input base acceleration.

For the sake of derivation simplicity, it is assumed herein that  $\boldsymbol{\psi} = \ddot{\mathbf{u}}_i^g$ , which is the uniform base acceleration vector at  $i^{\text{th}}$  time step. As mentioned earlier, in the case of earthquake base excitation, the external force vector in Eqs. (41) and (42) is written as  $\mathbf{f}_k = -\mathbf{M}\mathbf{L}\ddot{\mathbf{u}}_k^g$ . Eq. (6.41) is differentiated with respect to  $\boldsymbol{\psi} = \ddot{\mathbf{u}}_i^g$  to derive the response sensitivity with respect to the uniform base acceleration vector at  $i^{\text{th}}$  time step, i.e.,

$$\underbrace{\left[ a_1\mathbf{M} + b_1\mathbf{C} + \frac{\partial \mathbf{r}_k(\mathbf{q}_k)}{\partial \mathbf{q}_k^T} \right]}_{=(\mathbf{K}_T^{dyn})_{k+1}} \frac{\partial \mathbf{q}_{k+1}}{\partial \ddot{\mathbf{u}}_i^g} = \frac{\partial \tilde{\mathbf{f}}_k}{\partial \ddot{\mathbf{u}}_i^g} \quad (6.43)$$

in which the matrix in the left hand side of Eq. (6.43) is called the dynamic tangent stiffness matrix,  $(\mathbf{K}_T^{dyn})_{k+1}$  and is available from the FE solution if a Newton-Raphson iterative scheme is used to solve Eq. (6.41). Following Eq. (6.42), the right hand side of Eq. (6.43) is derived as

$$\begin{aligned} \frac{\partial \tilde{\mathbf{f}}_{k+1}}{\partial \ddot{\mathbf{u}}_i^g} = & -\mathbf{M}\mathbf{L} \frac{\partial \ddot{\mathbf{u}}_k^g}{\partial \ddot{\mathbf{u}}_i^g} - \mathbf{M} \left[ a_2 \frac{\partial \mathbf{q}_k}{\partial \ddot{\mathbf{u}}_i^g} + a_3 \frac{\partial \dot{\mathbf{q}}_k}{\partial \ddot{\mathbf{u}}_i^g} + a_4 \frac{\partial \ddot{\mathbf{q}}_k}{\partial \ddot{\mathbf{u}}_i^g} \right] \\ & - \mathbf{C} \left[ b_2 \frac{\partial \mathbf{q}_k}{\partial \ddot{\mathbf{u}}_i^g} + b_3 \frac{\partial \dot{\mathbf{q}}_k}{\partial \ddot{\mathbf{u}}_i^g} + b_4 \frac{\partial \ddot{\mathbf{q}}_k}{\partial \ddot{\mathbf{u}}_i^g} \right] \end{aligned} \quad (6.44)$$

in which the vectors  $\frac{\partial \mathbf{q}_k}{\partial \ddot{\mathbf{u}}_i^g}$ ,  $\frac{\partial \dot{\mathbf{q}}_k}{\partial \ddot{\mathbf{u}}_i^g}$ , and  $\frac{\partial \ddot{\mathbf{q}}_k}{\partial \ddot{\mathbf{u}}_i^g}$  are available from the last time step

sensitivity computation. Moreover, it is clear that  $\frac{\partial \ddot{\mathbf{u}}_k^g}{\partial \ddot{\mathbf{u}}_i^g} = \delta_{ki} \mathbf{I}_{n_{\ddot{\mathbf{u}}^g} \times n_{\ddot{\mathbf{u}}^g}}$ , where  $\delta$  is the

Kronecker delta. Therefore, Eq. (6.43), which is a linear algebraic equation, can be solved in one-step to compute the FE response sensitivity with respect to the uniform base acceleration vector at  $i^{\text{th}}$  time step,  $\ddot{\mathbf{u}}_i^g$ . Once Eq. (6.43) is solved, sensitivities of nodal velocity or acceleration with respect to  $\ddot{\mathbf{u}}_i^g$  can be easily obtained using Eq. (6.40). The sensitivity computation is repeated for each time step in the same way. To provide the required computational tool in this study, the DDM method to compute the FE response sensitivities with respect to the uniform base excitation is implemented in the open source structural analysis software framework OpenSees [35].

## 6.6. Validation study

Numerically simulated data from a three-dimensional (3D) 5-story 2-by-1 bay reinforced concrete (RC) frame building subjected to bidirectional seismic excitation is used to verify the performance of the proposed framework (Figure 6.2). The north-south component of the base excitation is assumed to be measured and known, while the east-west component is assumed to be unmeasured and unknown. Moreover a set of five unknown material parameters characterizing the nonlinear material constitutive model of reinforced concrete are treated as unknowns and are identified in the estimation phase. A mechanics-based nonlinear finite element (FE) model of the building, developed in the OpenSees, is used to simulate the response of the building to the earthquake event. In this simulation phase, the FE model of the building and the seismic input excitation are assumed to be completely known. The simulated

responses of the structure are then extracted and contaminated by artificial measurement noise to obtain the measured response of the structure. In the estimation phase, the measured response of the structure is utilized to estimate the five FE model parameters and the time history of the base acceleration in the EW direction. The output-only parameter estimation and nonlinear FE model updating frameworks presented in this study are implemented in MATLAB [36] and interfaced with OpenSees [35] for FE response and response sensitivity computations.

### **6.6.1. 3D RC frame building structure**

The building has two and one bays in the longitudinal and transverse directions, respectively, with plan dimensions of 10.0×6.0 m. The building has a total height of 20.0 m with constant story height of 4.0 m. The structure is designed as an intermediate moment-resisting RC frame for a moderate seismic risk zone (downtown Seattle, WA) with Site Class D and short-period and one-second spectral accelerations of  $S_{MS} = 1.37g$  and  $S_{M1} = 0.53g$ , respectively. Dead and live loads and corresponding seismic masses are calculated according to the 2012 International Building Code [37]. Longitudinal beams have a square cross-section of 0.40×0.40 m and are reinforced with 3 #8 longitudinal reinforcement bars at top and bottom, and #3 @ 100 mm transverse reinforcement. Transverse beams have a rectangular cross-section of 0.40×0.45 m and are reinforced with 4 #8 longitudinal reinforcement bars at top and bottom, and #3 @ 100 mm transverse reinforcement. The building has six identical 0.45×0.45 m RC columns reinforced with 8 #8 longitudinal reinforcement

bars and #3 @ 150 mm transverse reinforcement. Grade 60 reinforcing steel is considered for the columns and beams. Figure 6.2 shows the building view, and details of the RC beam and column sections.

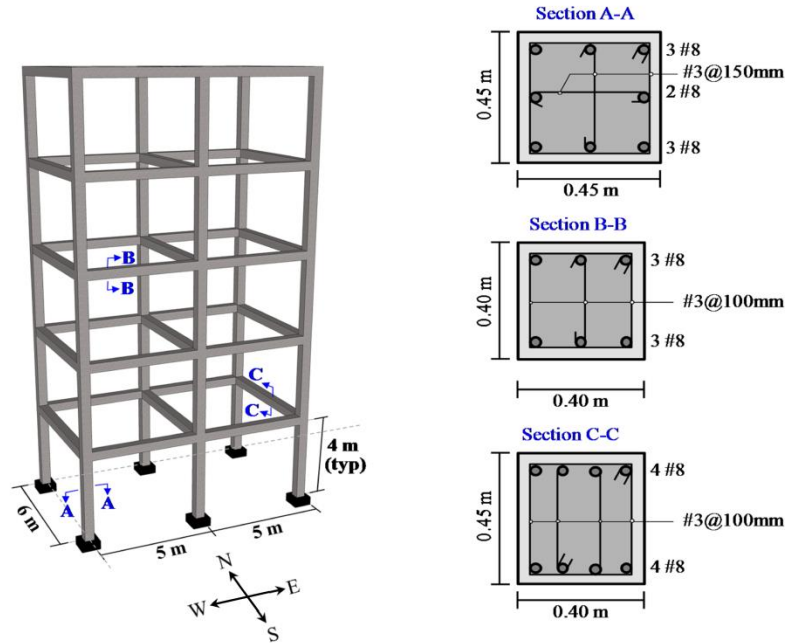


Figure 6.2: RC frame building structure: isometric view and cross-section of beams and columns.

The FE model of the structure is developed using distributed-plasticity, displacement-based, structural FE models. In this approach, the structure is spatially discretized using fiber-section, displacement-based, beam-column elements formulated using Bernoulli-Euler beam theory. The material nonlinearity can spread over several sections monitored along the element, which are called integration points. The sections are further discretized into layers or fibers [38], the stress-strain behavior of which is governed by associated (nonlinear) uniaxial material constitutive laws (see Figure 6.3). In this study, the selected constitutive law for the concrete material is

based on the Popovics-Saenz concrete model ([39,40]), a typical cyclic response of which is shown in Figure 6.4(a). In general, this material model is governed by six parameters, which are subdivided into two primary parameters and four secondary parameters. The two primary parameters ( $E_c$  = initial tangent stiffness, and  $f'_c$  = concrete compressive strength) are treated as unknown FE model parameters to be identified while the other four parameters are assumed known and constant. The steel reinforcements are modeled using the modified Giuffr -Menegotto-Pinto material constitutive model [41] with smooth curved shaped loading and unloading branches as illustrated in Figure 6.4(b). This material model is characterized by eight parameters, which are subdivided into three primary parameters and five secondary parameters. Treated as unknown FE model parameters, the three primary parameters are  $E$  = elastic modulus,  $\sigma_y$  = initial yield strength, and  $b$  = strain hardening ratio. The other five secondary parameters are assumed known and constant and are selected based on the suggested values in [41]. The FE model parameter vector is defined as  $\hat{\theta} = [E \ \sigma_y \ b \ E_c \ f'_c]$ . The true (exact) values of the FE model parameters are taken as  $E^{true} = 200\text{GPa}$ ,  $\sigma_y^{true} = 400\text{MPa}$ , and  $b^{true} = 0.05$ ,  $E_c^{true} = 30\text{GPa}$ , and  $f'_c{}^{true} = 40\text{MPa}$ .



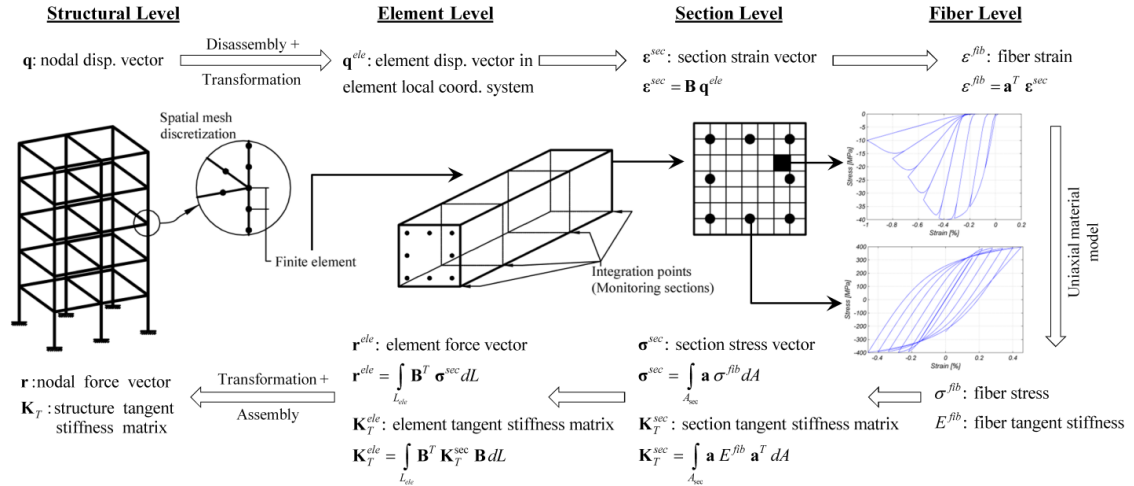


Figure 6.3: Hierarchical discretization levels in distributed plasticity structural FE models using fiber-section displacement-based beam-column elements (adapted from [8]).

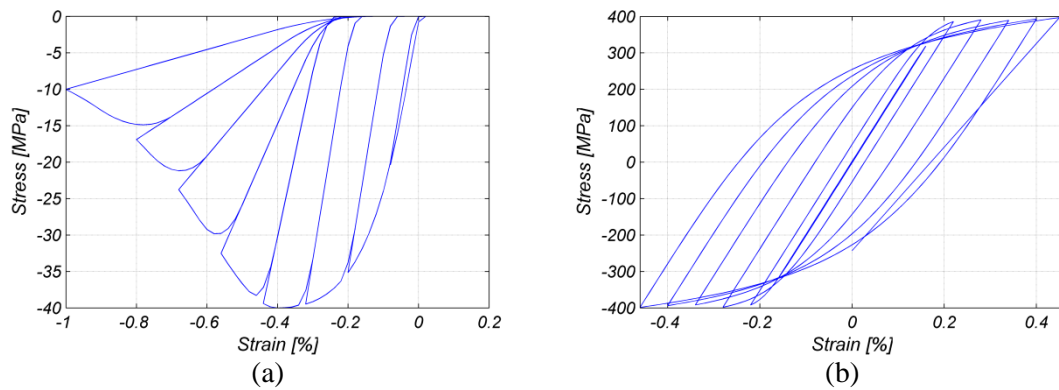


Figure 6.4: Typical cyclic behavior of the employed material models: (a) Popovics-Saenz for concrete material, (b) Giuffrè-Menegotto-Pinto for reinforcing steel material.

A ground acceleration record from the 2004 Parkfield earthquakes (Cholame 2 west station) [42] is selected for this study (see Figure 6.5). Nonlinear analysis is performed by first applying the gravity load quasi-statically and then the base excitation dynamically. The nonlinear dynamic time history analysis is performed using the Newmark average acceleration method [19] to recursively integrate the equations of motion in time using a constant time step size of  $\Delta t = 0.025 \text{sec}$ , and the

Newton-Raphson method to solve iteratively the nonlinear incremental dynamic equations of equilibrium at each time step. Rayleigh damping [19] is used to model the damping energy dissipation characteristics (beyond material hysteretic energy dissipation) of the structure by assuming a damping ratio of 2 percent for the first and third modes after applying gravity loads ( $T_1 = 1.43$  sec,  $T_2 = 1.37$  sec, and  $T_3 = 1.30$  sec).

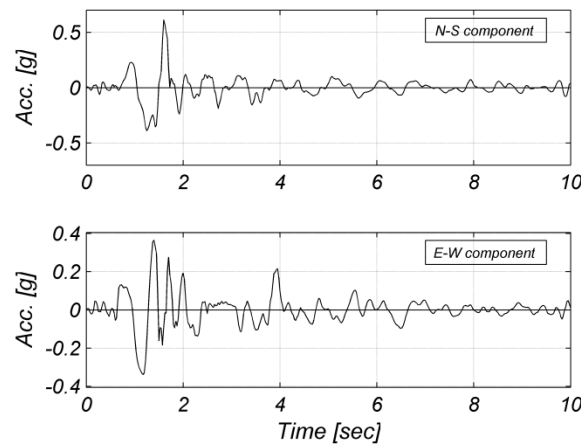


Figure 6.5: 2004 Parkfield earthquake ground motion (Cholame 2 west station, resampled at 40 Hz); top: 90° component applied in N-S direction, and bottom: 360° component applied in E-W direction.

### 6.6.2. Recursive ML estimation method

In the simulation phase, eight FE simulated response time histories are obtained and polluted by artificial measurement noise to provide measured response of the structure. The measured response time histories consist of first, fourth, and fifth (or roof) level absolute acceleration response and roof relative (to base) displacement response. All the responses are measured in both north-south and east-west directions at the north-east corner of each level (see Figure 6.2). The acceleration response time histories are polluted by a 1% g RMS zero-mean Gaussian white noise, and the

displacement response time histories are polluted by a 0.5% [m] RMS zero-mean Gaussian white noise. Although the earthquake base excitation as shown in Figure 6.5 is longer than 5 seconds, only the first 5 seconds of the base acceleration time history are estimated herein. Three case as listed in Table 6.3 are studied to investigate the performance of the proposed ML recursive estimation method for the purpose of output-only parameter estimation and nonlinear FE model updating framework. The specifications of these case studies are further described in the following part.

Estimation window: Three types of estimation window are considered herein: EW1, EW2, and EW3. EW1 has a length of 100 time steps (i.e.,  $t_l = 100 \times 0.025 = 2.5$  sec), with a moving rate of 50 time steps ( $t_s = 50 \times 0.025 = 1.25$ sec). EW2 has a length of 140 time steps and moving rate of 70 time steps (i.e.,  $t_l = 140 \times 0.025 = 3.5$  sec, and  $t_s = 70 \times 0.025 = 1.75$ sec). The overlap ratio (i.e.,  $t_o / t_l$ , where  $t_o = t_l - t_s$ ) for both EW1 and EW2 is 50%. EW3 expands over the whole 5 seconds of the estimation time domain; in other words, EW3 is a batch estimation case in which the whole time history of the base acceleration is estimated jointly with the FE model parameters, and the estimation noise variances. By using EW1, EW2, the estimation time domain is divided into three and two estimation windows, respectively.

Initial estimate of the FE model parameters and base accelerations: The initial estimates of FE model parameters ( $\hat{\theta}_0$ ) are selected as  $\hat{\theta}_{0,1} = 0.80E^{true}$ ,  $\hat{\theta}_{0,2} = 1.40\sigma_y^{true}$ ,  $\hat{\theta}_{0,3} = 1.20b^{true}$ ,  $\hat{\theta}_{0,4} = 0.80E_c^{true}$ , and  $\hat{\theta}_{0,5} = 0.70f_c^{true}$ . The initial

estimates of the base accelerations are selected as zero. The feasible search domain for the FE model parameters and base accelerations are selected as  $0.5\mathbf{\theta}_0 \leq \mathbf{\theta} \leq 2.0\mathbf{\theta}_0$ ,  $-1g \leq \ddot{u}^g \leq 1g$ , respectively.

Initial estimate of the simulation error variances: The simulation error variance is expected to be equal to the measurement noise variance. The true value of the measurement noise variance for the acceleration and time histories, which are respectively polluted by 1% g and 0.5% [m] RMS Gaussian white noise, are  $r_{Acc}^{true} = 9.6 \times 10^{-3} [m/s^2]^2$ , and  $r_{Disp}^{true} = 2.5 \times 10^{-5} [m^2]$ . The initial estimate of the simulation error variance for acceleration response data is selected as  $r_{Acc,0} = 2.2 \times 10^{-2} [m/s^2]^2$ , and for displacement response data is selected as  $r_{Disp,0} = 9 \times 10^{-6} [m^2]$ , which correspond to 1.5% g RMS and 0.3% [m] RMS measurement noise, respectively. The feasible search domain for the simulation error variance is set as  $0.1\mathbf{r}_0 \leq \mathbf{r} \leq 10\mathbf{r}_0$ .

Optimization algorithm and convergence criteria: The nonlinear optimization problem shown in Eqs. (17)-(18) is solved using an interior-point method ([43,44]) herein, which is available as part of the MATLAB optimization toolbox [45]. The convergence criterion for the optimization algorithm consists of the two following conditions; the optimization process is considered converged if any of the two conditions is met:

$$\text{Condition 1: } \left\| \begin{bmatrix} \hat{\Psi}_m \\ \hat{\mathbf{r}}_m \end{bmatrix} - \begin{bmatrix} \hat{\Psi}_{m-1} \\ \hat{\mathbf{r}}_{m-1} \end{bmatrix} \right\|_2 \leq 10^{-4} \quad (6.45)$$

$$\text{Condition 2: } \|\nabla J(\boldsymbol{\psi}, \mathbf{r})\|_\infty \leq 10^{-4} \quad (6.46)$$

where  $\hat{\boldsymbol{\psi}}_m$  is the vector of estimated parameters at the  $m^{\text{th}}$  optimization iteration normalized by the corresponding initial estimates,  $\|\dots\|_2$  denotes the second order (or Euclidean) norm, and  $\|\dots\|_\infty$  denotes the infinity norm (= the maximum absolute value of vector components).

Table 6.3: Validation cases studies.

Case #	Estimation window	Window length	Overlap length
1	EW1	100	50
2	EW2	140	70
3	EW3	200	-

Figure 6.6 compares the true and estimated EW component of the base acceleration time history for three cases considered. Defined as the difference between true and estimated acceleration time history, the estimation error time history is also shown in Figure 6.9 for each case. It can be observed that the base acceleration time history is very well estimated in all three cases.

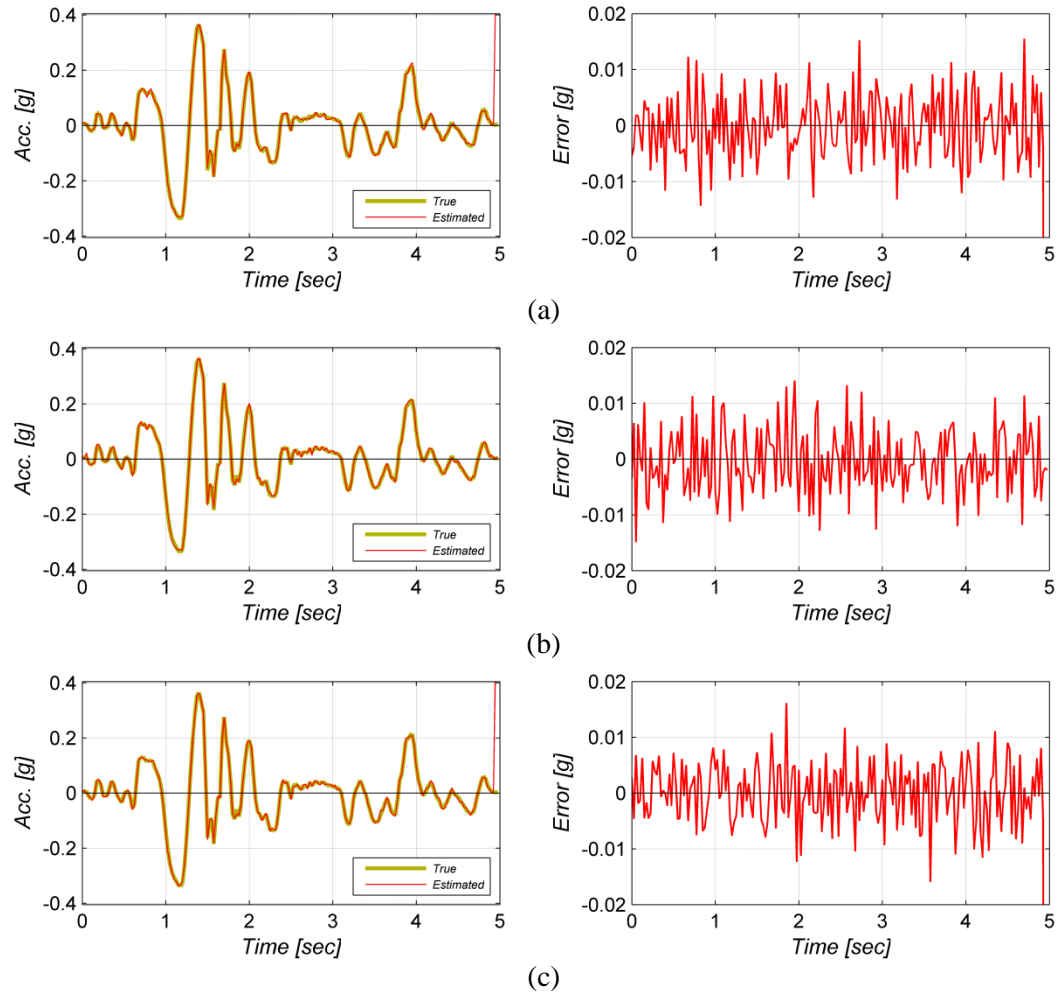


Figure 6.6: Left: Comparison of the estimated and true base acceleration time history in the EW direction; Right: estimation error of the base acceleration time history; (a): Case #1; (b): Case #2; (c): Case #3.

Figure 6.7 shows the standard deviation (S.D.) of the estimated base acceleration time history. The S.D.s are obtained from the marginal *a posteriori* covariance matrix as introduced in Eq. (6.26). As can be observed, the estimated S.D.s are the largest and smallest in Case #1 and Case #3, respectively. In other words, by increasing the estimation window length, the uncertainties associated with the estimated base acceleration time history is decreased. It should be noted that the

sudden drops (notch point) in Figures 6.7(a), and 6.7(b) coincide with the starting point of each estimation window.

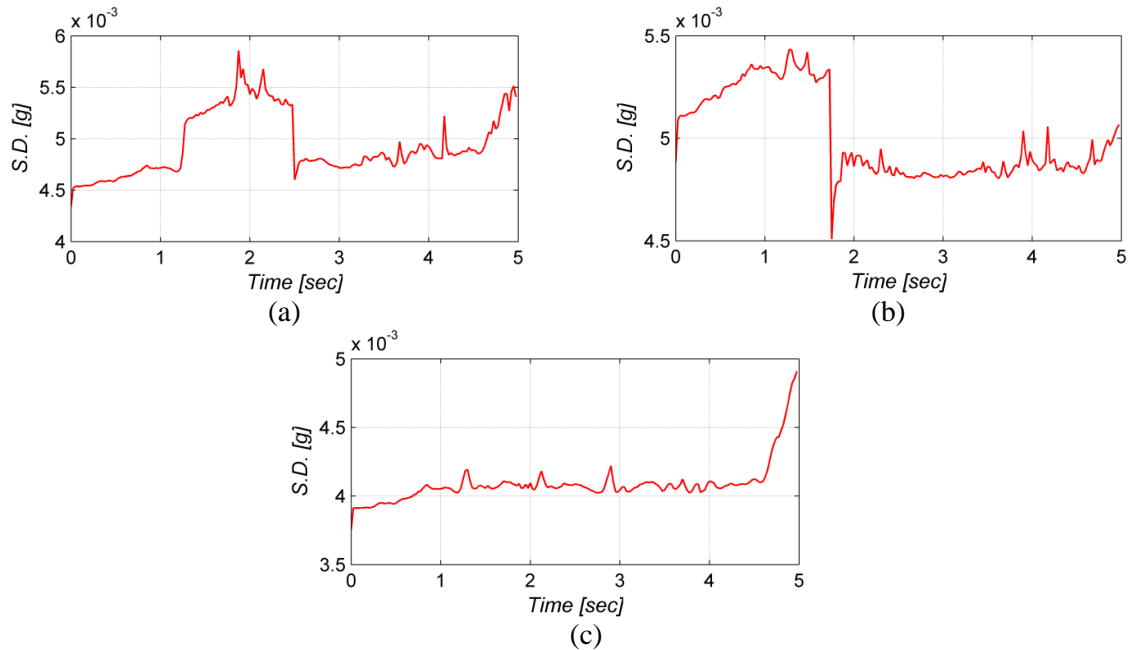


Figure 6.7: Standard deviation (S.D.) of the estimated base acceleration time history in the east-west direction; (a): Case #1; (b): Case #2; (c): Case #3.

Table 6.4 compares the converged estimates of the five FE model parameters normalized by their corresponding true parameter values and the estimation standard deviation of each model parameter (evaluated using the CRLB) normalized by the corresponding point estimate of the parameter; the  $\hat{\sigma}_{\theta_i} / \hat{\theta}_i$  can be loosely interpreted as the coefficient of variation (C.O.V.) of the estimated material parameter. This table also reports the relative root mean square error (RRMSE) of the predicted base acceleration time history in EW direction. The RRMSE is defined as

$$\text{RRMSE}(\hat{\mathbf{u}}_{1:N}^g)(\%) = \sqrt{\frac{\sum_{i=1}^N (\hat{\mathbf{u}}_i^g - \ddot{\mathbf{u}}_i^{g,true})^2}{\sum_{i=1}^N (\ddot{\mathbf{u}}_i^{g,true})^2}} \times 100 \quad (6.47)$$

As can be observed, the FE model parameters are estimated with comparable accuracy in all the three cases; however, the RRMSE of the estimated base acceleration time history is slightly smaller for Case #3 than the two other cases.

Table 6.4: Comparison of FE model parameter estimation results in three case studies.

Case study #	Final estimates of material parameters					Final estimates of C.O.V. (%)					RRMSE( $\hat{\mathbf{u}}^g$ ) (%)
	$\hat{E}/E^{true}$	$\hat{\sigma}_y/\sigma_y^{true}$	$\hat{b}/b^{true}$	$\hat{E}_c/E_c^{true}$	$\hat{f}_c'/f_c'^{true}$	C.O.V.( $\hat{E}$ )	C.O.V.( $\hat{\sigma}_y$ )	C.O.V.( $\hat{b}$ )	C.O.V.( $\hat{E}_c$ )	C.O.V.( $\hat{f}_c'$ )	
1	1.000	0.993	1.019	1.004	1.001	0.372	0.317	1.784	0.931	1.281	5.236
2	1.001	0.999	1.022	1.001	0.992	0.295	0.279	1.475	0.741	1.078	5.251
3	1.000	0.997	1.024	0.999	1.009	0.444	0.345	1.463	1.261	1.482	4.812

Furthermore, Table 6.5 reports the converged estimated simulation error variances for the eight measurement channels, normalized by their corresponding measurement noise variance. The simulation error variance estimation is inaccurate and no difference can be observed between the three case studies. As illustrated in Appendix 6.I, the CRLB for the  $i^{\text{th}}$  component of simulation error variance vector is approximated as  $\frac{2}{k} \hat{r}_i^2$ , in which  $k$  is the total number of data samples used in the estimation process (i.e.,  $k = 200$  herein). Therefore, the approximate C.O.V. of the simulation error variance is 14.1%, 12.0%, and 10% respectively for Cases #1, #2 and #3, which represent relatively large uncertainty in the estimated simulation error variances due to the limited time samples of the measured data used in the estimation.



It should be recognized that incorrect estimation of the simulation error variances adversely affects the estimation of the CRLB for the estimated FE model parameters and base acceleration time history, since the FIM as shown in Eqs. (20)-(22) depends on the estimated simulation error variances.

Table 6.5: Comparison of the estimated simulation error variance in three case studies.

Case study #	Final estimates of simulation error variance, $r/r^{true}$							
	Acc1-EW	Acc1-NS	Acc4-EW	Acc4-NS	Acc5-EW	Acc5-NS	Disp5-EW	Disp5-NS
1	2.078	1.170	0.625	0.896	0.631	0.960	0.796	0.794
2	0.758	0.885	0.580	0.895	1.970	0.856	0.789	0.797
3	0.522	0.877	0.673	1.007	0.632	1.129	0.712	0.778

Figure 6.8 shows the convergence history of the five FE model parameters for Case #3. In this figure, the number of iterations is equal to the number of evaluation of the ML objective function, which in turn is equal to the number of FE model runs. Spike-like behavior is observed in the convergence histories in this figure. This spike-like behavior is the result of perturbation in the estimation parameters to escape local minima. The optimization algorithm detects when iterations appear to be converging to a local minimum, and then perturbs the parameters to escape the domain of attraction of that local minimum.

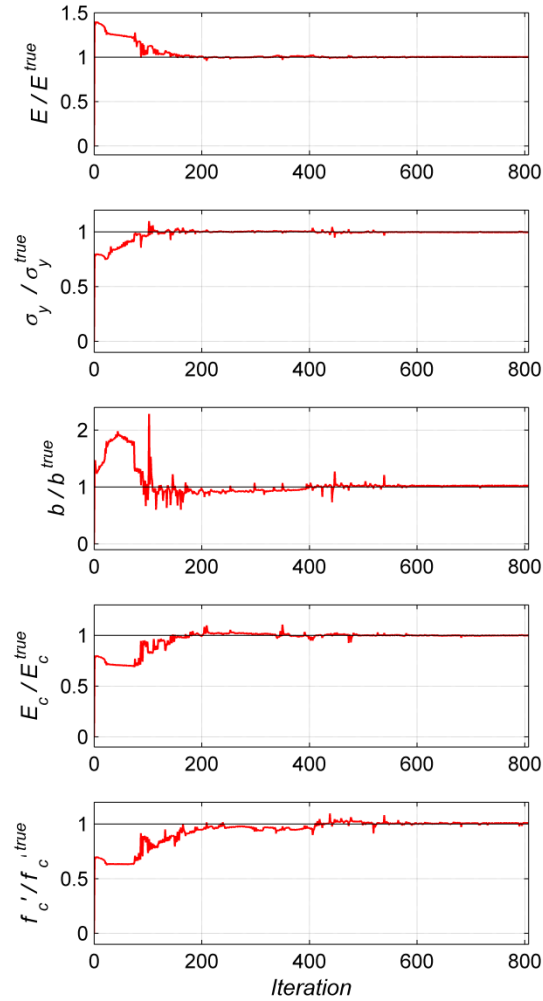


Figure 6.8: Convergence history of the estimated FE model parameters for Case #3.

Finally, Table 6.6 reports the total number of estimation iterations (which is equal to the total number of runs of the FE model) and total computation time (in hour) required for each case study. Each case study was run in parallel on a Dell Precision T7610 desktop workstation using only one Intel Xeon E5-2630 (2.6 GHz) processor with 6 cores. As can be seen, the output-only parameter estimation and nonlinear FE model updating using the recursive (or batch) ML estimation method requires significant number of iterations and is computationally demanding.

Consequently, the method may perceive to be unsuitable for applications including large scale structural FE models.

Table 6.6: Comparison of computational time in three case studies.

Case study #	Total number of iterations	Total computation time (hr)
1	806	61
2	712	78
3	808	168

### 6.6.3. Stochastic filtering method

Similar to the first validation study, the simulated time histories of absolute acceleration response of first, fourth, and fifth (or roof) level and relative (to base) displacement response of roof level in both north-south and east-west directions, measured at north-east corner of the building, are used as the measured structural responses. The acceleration and displacement response time histories are respectively polluted by 1%  $g$  and 0.5%  $[m]$  RMS zero-mean Gaussian white noise. Different case studies, as listed in Table 6.7 are considered herein to investigate the performance of the proposed output-only parameter estimation and nonlinear FE model updating framework using stochastic filtering method. Case studies #1 and #2 examines the effects of estimation window length on the performance of the proposed framework. Case #3 studies the effect of convergence criteria (as introduced in Table 6.2) on the accuracy of the parameter estimation results. Finally, in Case study #4, only six

measured response time histories (i.e., absolute acceleration response time histories of third, and fifth levels, and displacement response time histories of roof level, measured at north-east corner of the building, in both north-south and east-west directions) are used to study the performance of the framework with sparse measured structural response data.

Table 6.7: Validation cases studies.

Case #	Estimation window	Convergence criteria		Measured data set
		$tol1$	$tol2$	
1	EW1	0.01	40	8 channels (6 accelerations, 2 displacements)
2	EW2	0.01	40	8 channels (6 accelerations, 2 displacements)
3	EW2	0.0075	60	8 channels (6 accelerations, 2 displacements)
4	EW2	0.0075	60	6 channels (4 accelerations, 2 displacements)

Estimation window: Two types of estimation window are considered herein: EW1, and EW2. The length of both estimation windows is equal to 50 time steps (i.e.,  $t_l = 50 \times 0.025 = 1.25$  sec). For EW1,  $t_s = 25 \times 0.025 = 0.625$  sec, and for EW2  $t_s = 15 \times 0.025 = 0.375$  sec, where  $t_s$  denotes the moving (or sliding) rate of the estimation window. Therefore, the overlap ratio (i.e.,  $t_o / t_l$ , where  $t_o = t_l - t_s$ ) is 50% and 70%, respectively for EW1 and EW2. By using EW1, the estimation time domain (i.e., the first five seconds of the earthquake excitation) is divided into seven estimation windows; while, it is divided into eleven estimation windows by using EW2. EW2 has a wider overlap length; therefore, the parameter estimation results using EW2 are expected to be more accurate than those using EW1. However, the accurate estimation

results of EW2 are expected to be at the cost of higher computational demands than those of EW1.

Initial estimate of mean vector and covariance matrix of FE model

parameters: The initial estimates of FE model parameters ( $\hat{\boldsymbol{\theta}}_0$ ) are selected as

$$\hat{\theta}_{0,1} = 0.80E^{true}, \quad \hat{\theta}_{0,2} = 1.40\sigma_y^{true}, \quad \hat{\theta}_{0,3} = 1.20b^{true}, \quad \hat{\theta}_{0,4} = 0.80E_c^{true}, \quad \text{and}$$

$$\hat{\theta}_{0,5} = 0.70f_c^{true}. \text{ The covariance matrix of the initial estimates of the FE model}$$

parameter vector, which quantifies the uncertainty in the initial estimates of the FE

model parameters, is selected as a diagonal matrix  $\hat{\mathbf{P}}_{\boldsymbol{\theta}\boldsymbol{\theta},0} = [p_i]$ . The term  $p_i$ , or the  $i^{\text{th}}$

diagonal entry of  $\hat{\mathbf{P}}_{\boldsymbol{\theta}\boldsymbol{\theta},0}$ , is the variance of the initial estimate of the  $i^{\text{th}}$  FE model

parameter and is selected as  $p_i = (0.10\hat{\theta}_{0,i})^2$ .

Initial estimate of mean vector and covariance matrix of base accelerations:

As mentioned earlier, the initial estimates of the base acceleration is zero. The

covariance matrix of the initial estimates of the base acceleration vector  $\hat{\mathbf{P}}_{\mathbf{u}^g\mathbf{u}^g,0}$  is

selected as a diagonal matrix with constant diagonal entries of  $0.0625 \left[ m/s^2 \right]^2$ , which

is the variance of the initial estimate of the base accelerations.

Process noise covariance matrix: The process noise covariance matrix,  $\mathbf{Q}$  as

introduced in Eq. (6.34), serves to increase the *a priori* estimation uncertainties and

therefore, increases the relative importance attributed by the filtering method to the

response measurements versus the *a priori* information transferred from the last

estimation iteration. The matrix  $\mathbf{Q}$  is a time-invariant (constant) diagonal matrix

herein. The first  $n_{\theta}$  diagonal entries, which correspond to the FE model parameters, are selected as  $10^{-8}$ , and the other diagonal entries, which correspond to the estimated base accelerations, are selected as  $10^{-4}$ . It should be recognized that the selection of the diagonal entries of  $\mathbf{Q}$  matrix has a dominant influence on the performance and convergence rate of the proposed estimation method.

Simulation error covariance matrix: The diagonal entries of the simulation error covariance matrix,  $\mathbf{R}$  as introduced following Eq. (6.5), represent the measurement noise variances herein. In a real world application, the statistics of the measurement noise are unknown, but can be approximately estimated by quantifying the noise sources. Here, the amplitude of the measurement noise for acceleration response time histories is estimated as 1.5% g RMS, and for displacement response time histories is estimated as 0.3% [m] RMS.

Figure 6.9 compares the true and estimated EW component of the base acceleration time history for four cases considered in Table 6.7. Defined as the difference between the true and estimated acceleration time history, the estimation error time histories are also shown in Figure 6.9. It can be observed that the base acceleration time history is very well estimated in all four cases.

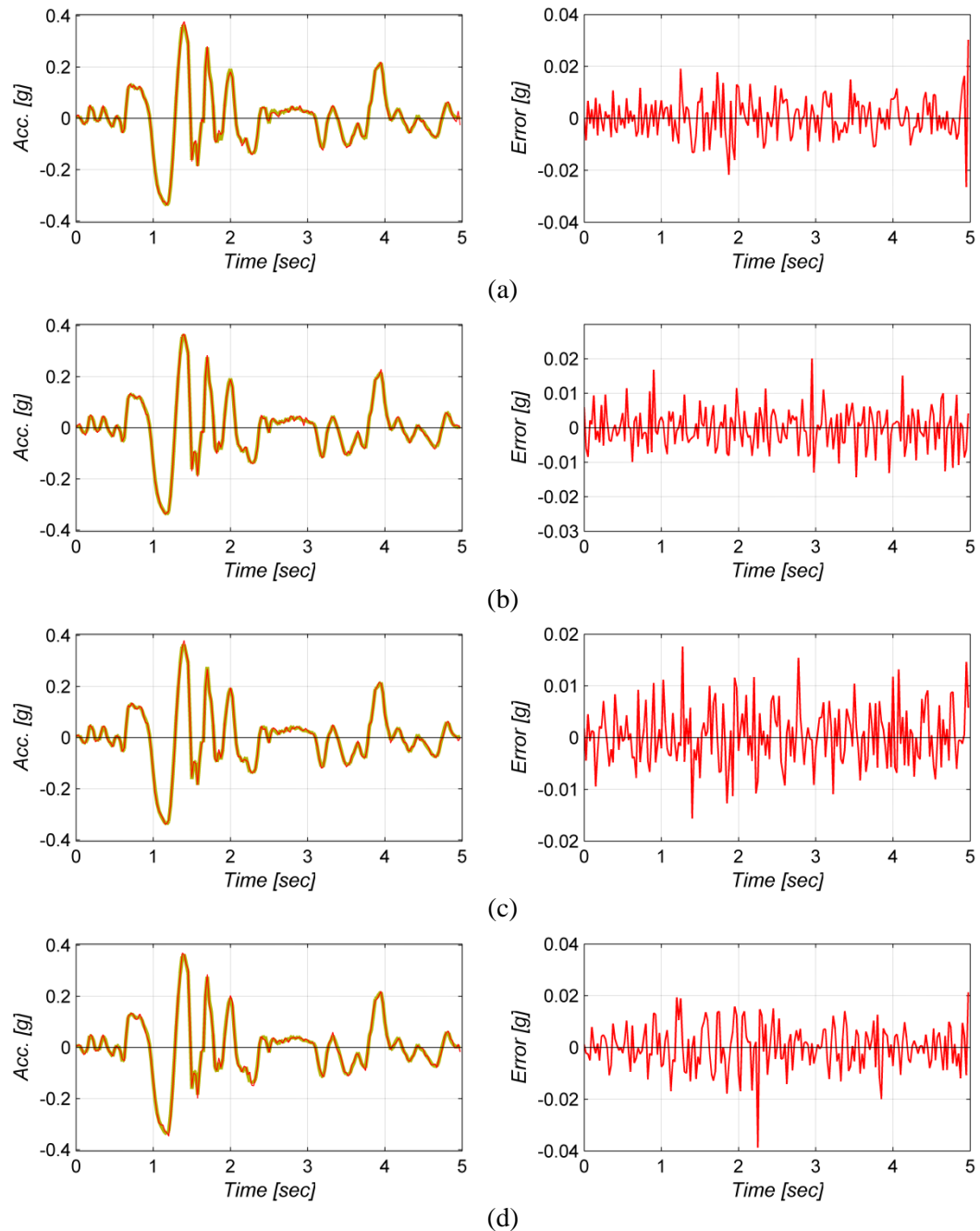


Figure 6.9: Left: Comparison of the estimated and true base acceleration time history in the east-west direction; Right: estimation error of the base acceleration time history; (a): Case #1; (b): Case #2; (c): Case #3; (d): Case #4.

Likewise, Figure 6.10 shows the standard deviation (S.D.) of the estimated base acceleration time history. The S.D.s are obtained from the marginal *a posteriori*

covariance matrix of the first part of the estimated acceleration time history in each estimation windows (i.e.,  $\hat{\mathbf{u}}^{g,1}$ ), which is equal to the submatrix  $\hat{\mathbf{P}}_{\hat{\mathbf{u}}^{g,1}\hat{\mathbf{u}}^{g,1}}$  as shown in Eq. (6.36). Figure 6.10 shows notch points in the estimated S.D. time histories, which are the result of a sudden drop in the estimated S.D.s. The notch points coincide with the starting point of each estimation window (i.e.,  $t_1^m$ , where  $m$  denotes the  $m^{\text{th}}$  estimation window). Since the structural system is causal, all the structural response data samples measured across the  $m^{\text{th}}$  estimation window are sensitive to  $\hat{\mathbf{u}}_{t_1^m}^g$  and therefore, they have more information about  $\hat{\mathbf{u}}_{t_1^m}^g$  than other time samples of the base acceleration vector. Consequently,  $\hat{\mathbf{u}}_{t_1^m}^g$  has a relatively smaller estimation uncertainty than the other samples of the base acceleration time history. Moreover, comparing Figure 6.10(a) with the other parts of Figure 6.10 demonstrates that the EW2, which has larger overlap ratio than EW1, results in less uncertainty in the estimated base acceleration time history. Finally, for all four cases, the estimated S.D. time history has a tail with significantly large estimated S.D. values, which are associated with the last estimation window. The measured response across the last estimation window has limited information about the base acceleration time history and therefore, the estimated base accelerations have larger uncertainties.



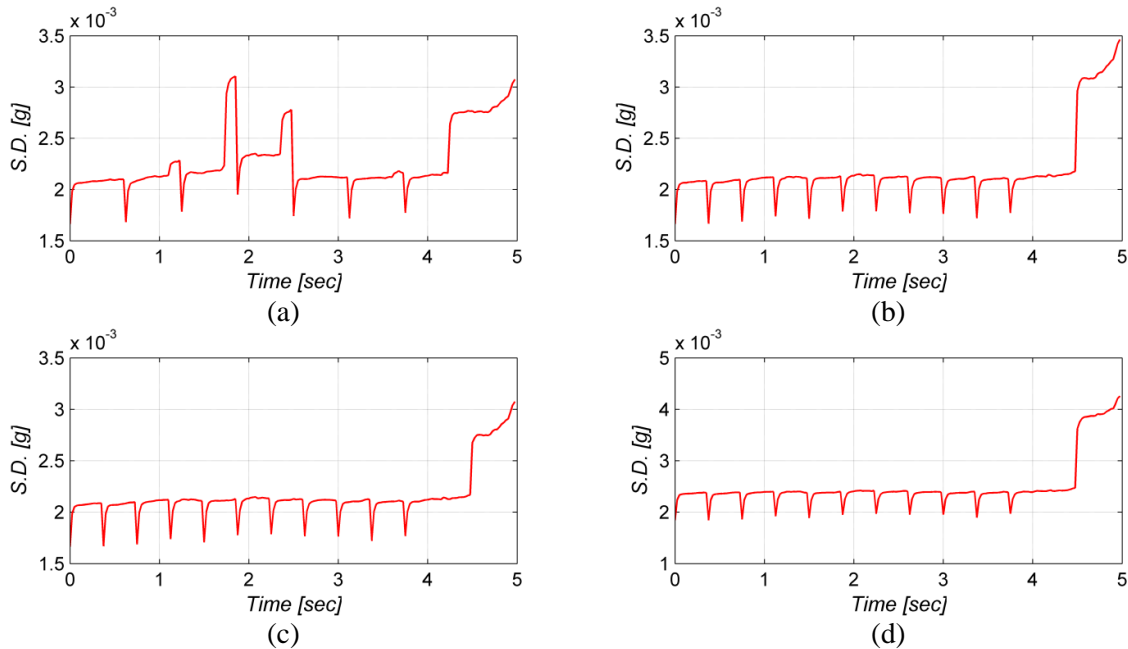


Figure 6.10: Standard deviation (S.D.) of the estimated base acceleration time history in the east-west direction; (a): Case #1; (b): Case #2; (c): Case #3; (d): Case #4.

Figures 6.11-6.14 show the time histories of the *a posteriori* mean (normalized by their corresponding true parameter values) and coefficient of variation (C.O.V.) of the FE model parameters for all four cases studies. The vertical black lines in these figures indicate the iteration limits for each estimation window. As can be seen, all the material parameter are recursively updated from their initial to their final estimates, which are (closely) converged to the corresponding true parameter values with very small C.O.V. in all four cases considered. The elastic response related material parameters (such as elastic modulus of steel and concrete) start updating from the beginning of the excitation and eventually converge to the true parameter values; while, the estimation time history of other material parameters start with a flat-like stage followed by a period of rapid change, which expectedly indicates that the

structural response becomes nonlinear and sensitive to strength and post-yield related material parameters. Comparing Figures 6.11-6.13 reveals the dominant estimation accuracy in Case #3 as compared to Cases #1 and #2. Moreover, Figure 6.14 demonstrates the excellent performance of the proposed estimation procedure in correctly estimating the material parameters in case of reduced output response measurement channels (i.e., Case #4).

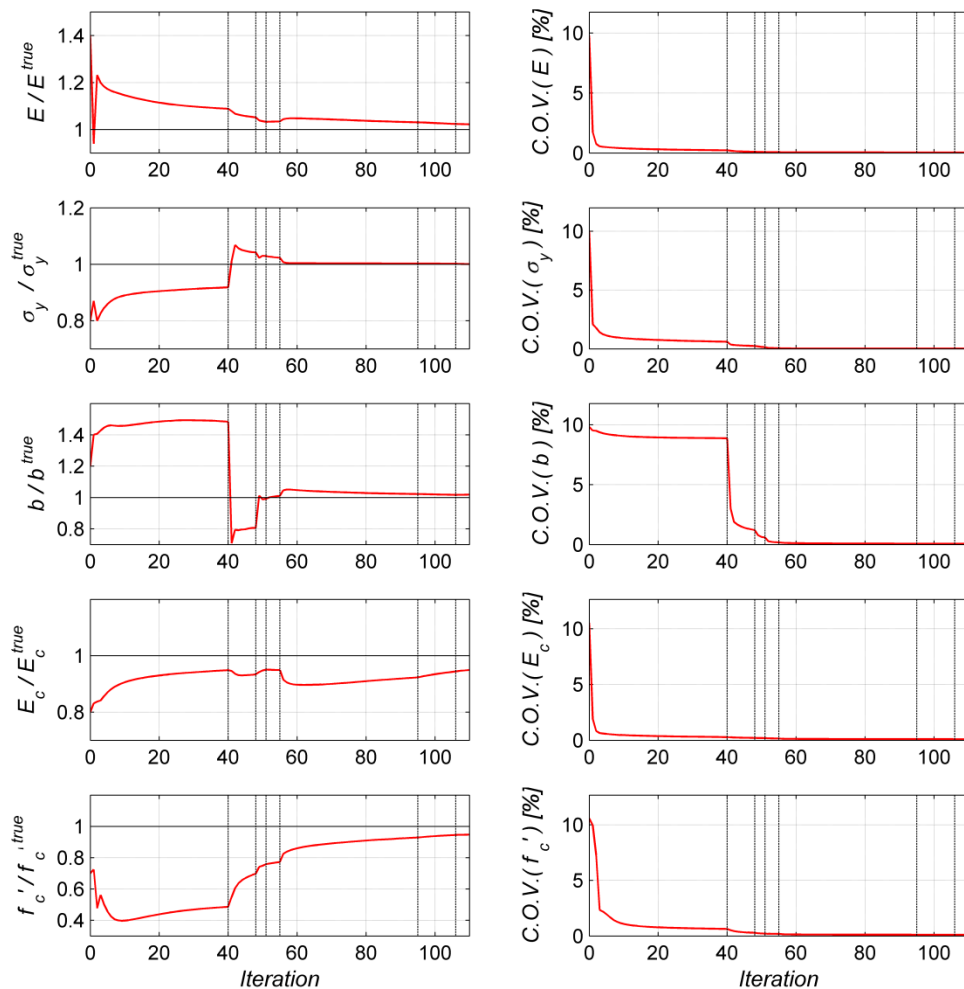


Figure 6.11: Time histories of the *a posteriori* mean and C.O.V. of FE model parameters for Case #1.

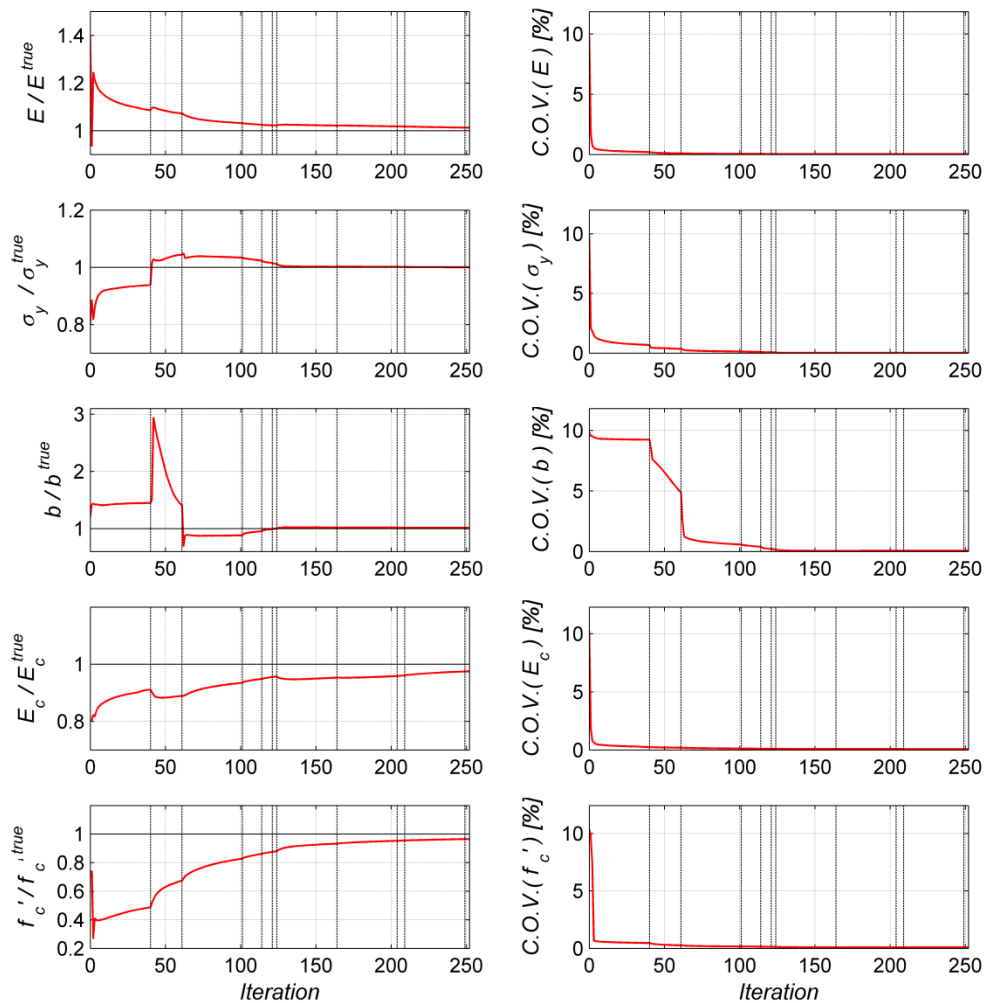


Figure 6.12: Time histories of the *a posteriori* mean and C.O.V. of FE model parameters for Case #2.

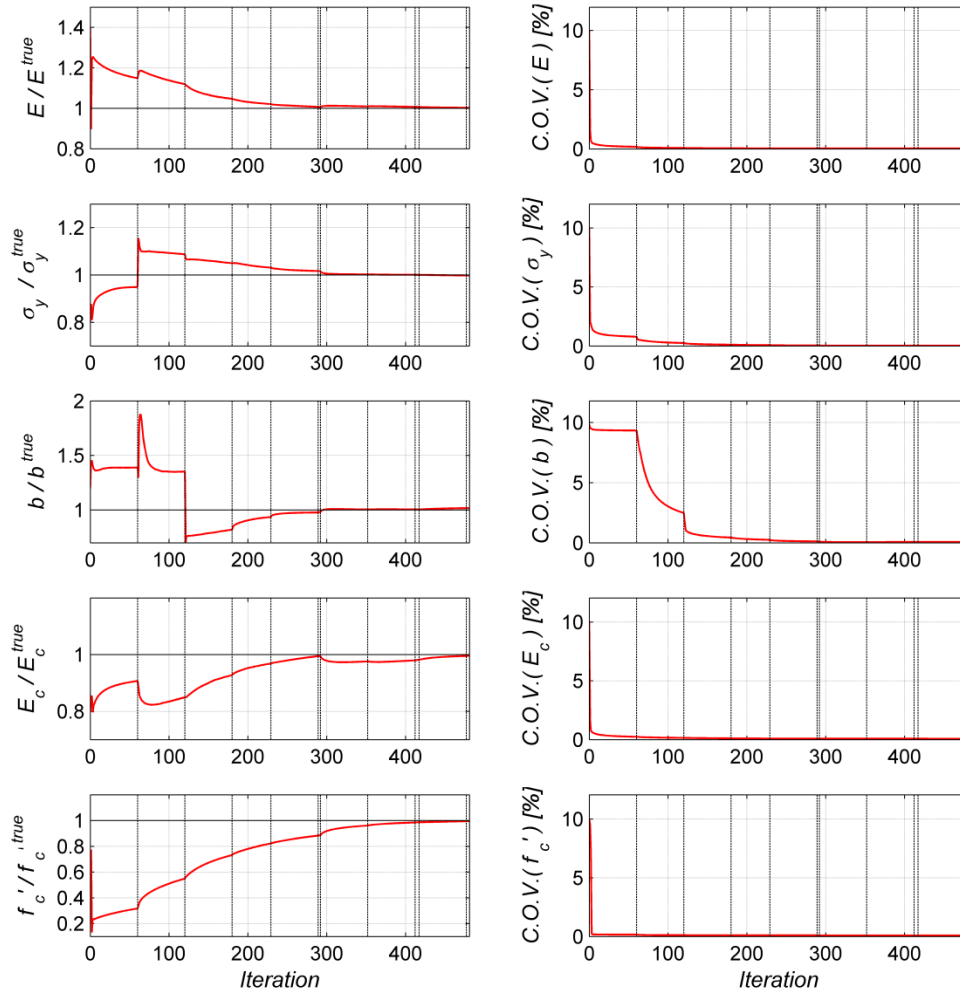


Figure 6.13: Time histories of the *a posteriori* mean and C.O.V. of FE model parameters for Case #3.

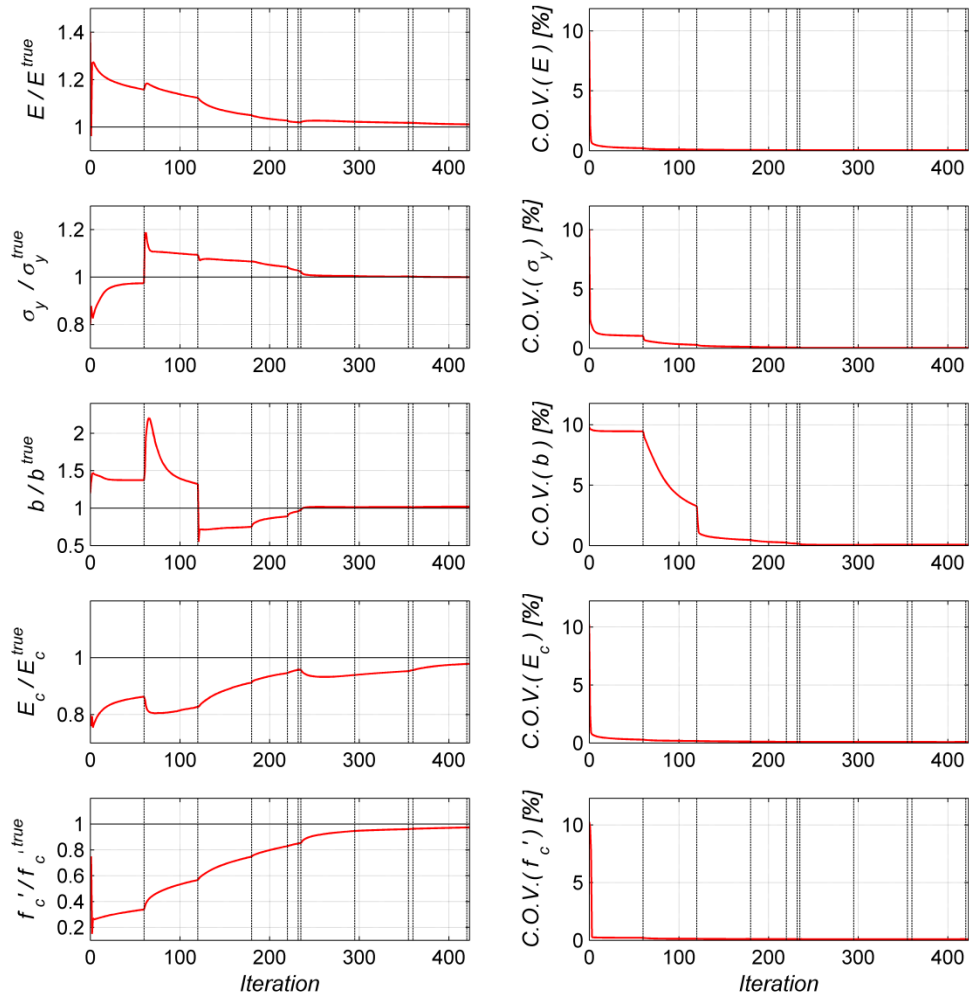


Figure 6.14: Time histories of the *a posteriori* mean and C.O.V. of FE model parameters for Case #4.

Table 6.8 compares the final estimates of the material parameters (i.e., the *a posteriori* estimate of mean FE model parameter vector obtained at the last estimation iteration), the final estimates of the C.O.V. of material parameters and the relative root mean square error (RRMSE) of the estimated base acceleration time history in EW direction. The RRMSE is defined as

$$\text{RRMSE}(\hat{\mathbf{u}}_{1:N}^g)(\%) = \sqrt{\frac{\sum_{i=1}^N (\hat{u}_i^g - \ddot{u}_i^{g,true})^2}{\sum_{i=1}^N (\ddot{u}_i^{g,true})^2}} \times 100 \quad (6.48)$$

Moreover, Table 6.9 shows the total number of estimation iterations (which is equal to the total number of runs of the FE model) and total computation time (in hour) required for each case study. Each case study was run in parallel on a Dell Precision T7610 desktop workstation using only one Intel Xeon E5-2630 (2.6 GHz) processor with 6 cores.

The presented results clearly demonstrate the successful performance of the proposed stochastic filtering method for output-only model parameter estimation and nonlinear FE model updating. The estimation results for Case studies #1 to #3 show progressively improved accuracy in the parameter estimation results by using larger overlap length for the estimation windows and tighter convergence criteria. The improved accuracy, however, attains at the cost of significantly higher computational demands as can be inferred from Table 6.9. Furthermore, the estimation framework successfully performed with exceptional accuracy in Case study #4, where limited measurement data channels were used. However, it should be noted that in general, reducing the number of measurement data channels may compromise the identifiability of the estimation problem.

Table 6.8: Comparison of parameter estimation results in four case studies.

Case study #	Final estimates of material parameters					Final estimates of C.O.V. (%)					RMSE (%)
	$\hat{E}/E^{true}$	$\hat{\sigma}_y/\sigma_y^{true}$	$\hat{b}/b^{true}$	$\hat{E}_c/E_c^{true}$	$\hat{f}_c'/f_c'^{true}$	C.O.V. ( $\hat{E}$ )	C.O.V. ( $\hat{\sigma}_y$ )	C.O.V. ( $\hat{b}$ )	C.O.V. ( $\hat{E}_c$ )	C.O.V. ( $\hat{f}_c'$ )	
1	1.022	1.000	1.018	0.949	0.947	0.037	0.018	0.064	0.090	0.099	6.689
2	1.013	1.000	1.015	0.975	0.965	0.031	0.019	0.064	0.075	0.090	5.102
3	1.003	0.998	1.017	0.996	0.995	0.031	0.019	0.064	0.074	0.090	5.023
4	1.011	1.000	1.019	0.978	0.974	0.031	0.019	0.064	0.074	0.090	7.388

Table 6.9: Comparison of computational time in four case studies.

Case study #	Total number of iterations	Total computation time (hr)
1	111	7.1
2	253	13.8
3	482	23.6
4	424	21.1

## 6.7. Conclusions

This chapter presented a novel framework for nonlinear system identification of civil structures based on nonlinear finite element (FE) model updating utilizing the measured structural response to earthquake excitations. Grounded in Bayesian inference methodology, the proposed framework estimates simultaneously the FE model parameters and the input ground acceleration time history using only the measured dynamic response of the structure. Two data fusion approaches were presented in this study to solve the augmented input and parameter estimation problem: (i) recursive maximum likelihood (ML) estimation approach, which reduces

to a nonlinear optimization method, and (ii) stochastic filtering approach based on recursive maximum *a posteriori* (MAP) estimation method, which reduces to an iterative extended Kalman filtering method. Both approaches require the computation of FE response sensitivities with respect to FE model parameters and components of the input ground acceleration time history. The FE response sensitivities are computed accurately and efficiently using the direct differentiation method (DDM). For this purpose, the DDM to compute the FE response sensitivities with respect to the uniform base acceleration is implemented in the open source structural analysis software framework OpenSees.

Numerically simulated data from a three-dimensional 5-story 2-by-1 bay realistic reinforced concrete (RC) frame building subjected to bidirectional seismic excitation is used to verify the performance of the two proposed approaches. While the recursive ML estimation method accurately estimated the unknown FE model parameters and the input ground acceleration time history, it realized to be computationally demanding. Nevertheless, the stochastic filtering approach based on recursive maximum *a posteriori* (MAP) estimation method offered a computationally feasible framework with outstanding estimation accuracy, which can pave the way for future applications to real world civil structures.

## **Acknowledgments**

Partial support for this work was provided by teaching assistantships from the Department of Structural Engineering at University of California, San Diego and the



researcher assistantship received through my advisor, Professor Joel P. Conte. Chapter 6, in part, is currently being prepared for submission for publication. The dissertation author is the primary investigator and author of this material and Rodrigo Astroza, Joel P. Conte, and Costas Papadimitriou are the co-authors.

## Appendix 6.I: Derivation of the Exact Fisher Information Matrix for the Joint Input-model Parameter Estimation Problem

The FIM is defined as  $\mathbf{I} = E[\mathbf{ss}^T]$  where  $\mathbf{s}(\dots)$  denotes the score function and the expectation is taken with respect to  $p\left(\mathbf{y}_{t_1^m:t_2^m} \mid \boldsymbol{\theta}, \hat{\mathbf{u}}_{t_1^m:t_2^m}^g, \mathbf{r}\right)$ . The score function is defined as the gradient of the log-likelihood function with respect to the parameters to be estimate [27] For the ML estimation problem stated in Eqs. (17)-(18), the score function can be derived as

$$\mathbf{s}\left(\boldsymbol{\theta}, \mathbf{r}, \hat{\mathbf{u}}_{1:t_1^m-1}^g, \hat{\mathbf{u}}_{t_1^m:t_2^m}^g, \mathbf{y}_{t_1^m:t_2^m}\right) = \begin{bmatrix} \left( \frac{\partial \Lambda\left(\boldsymbol{\theta}, \mathbf{r}, \hat{\mathbf{u}}_{1:t_1^m-1}^g, \hat{\mathbf{u}}_{t_1^m:t_2^m}^g, \mathbf{y}_{t_1^m:t_2^m}\right)}{\partial \boldsymbol{\theta}} \right)^T \\ \left( \frac{\partial \Lambda\left(\boldsymbol{\theta}, \mathbf{r}, \hat{\mathbf{u}}_{1:t_1^m-1}^g, \hat{\mathbf{u}}_{t_1^m:t_2^m}^g, \mathbf{y}_{t_1^m:t_2^m}\right)}{\partial \hat{\mathbf{u}}_{t_1^m:t_2^m}^g} \right)^T \\ \left( \frac{\partial \Lambda\left(\boldsymbol{\theta}, \mathbf{r}, \hat{\mathbf{u}}_{1:t_1^m-1}^g, \hat{\mathbf{u}}_{t_1^m:t_2^m}^g, \mathbf{y}_{t_1^m:t_2^m}\right)}{\partial \mathbf{r}} \right)^T \end{bmatrix} \quad (6.49)$$

in which  $\Lambda$  is the log-likelihood function defined as the natural logarithm of the likelihood function, i.e.,

$$\Lambda\left(\boldsymbol{\theta}, \mathbf{r}, \hat{\mathbf{u}}_{t_1^m:t_2^m}^g, \mathbf{y}_{t_1^m:t_2^m}\right) = \left( -\frac{kn_{\mathbf{y}}}{2} \ln(2\pi) - \frac{k}{2} \sum_{j=1}^{n_{\mathbf{y}}} \ln(r_j) - \frac{1}{2} \sum_{i=t_1^m}^{t_2^m} \left( \mathbf{y}_i - \hat{\mathbf{y}}_i\left(\boldsymbol{\theta}, \hat{\mathbf{u}}_{t_1^m:i}^g\right) \right)^T \mathbf{R}^{-1} \left( \mathbf{y}_i - \hat{\mathbf{y}}_i\left(\boldsymbol{\theta}, \hat{\mathbf{u}}_{t_1^m:i}^g\right) \right) \right) \quad (6.50)$$

where  $\hat{\mathbf{y}}_i(\boldsymbol{\theta}, \ddot{\mathbf{u}}_{t_1^m:i}^g) = \mathbf{h}_i(\boldsymbol{\theta}, \hat{\mathbf{u}}_{1:t_1^m-1}^g, \ddot{\mathbf{u}}_{t_1^m:i}^g)$  is the FE predicted response vector at the  $i^{\text{th}}$  time step and the dependence of  $\hat{\mathbf{y}}_i(\dots)$  on  $\hat{\mathbf{u}}_{1:t_1^m-1}^g$  is dropped for notational convenience. Substituting Eq. (6.50) into Eq. (6.49) yields

$$\mathbf{s}(\boldsymbol{\theta}, \mathbf{r}, \hat{\mathbf{u}}_{1:t_1^m-1}^g, \ddot{\mathbf{u}}_{t_1^m:t_2^m}^g, \mathbf{y}_{t_1^m:t_2^m}) = \begin{bmatrix} \sum_{i=1}^k \left( \frac{\partial \hat{\mathbf{y}}_i(\boldsymbol{\theta}, \ddot{\mathbf{u}}_{t_1^m:i}^g)}{\partial \boldsymbol{\theta}} \right)^T \mathbf{R}^{-1} \left( \mathbf{y}_i - \hat{\mathbf{y}}_i(\boldsymbol{\theta}, \ddot{\mathbf{u}}_{t_1^m:i}^g) \right) \\ \sum_{i=1}^k \left( \frac{\partial \hat{\mathbf{y}}_i(\boldsymbol{\theta}, \ddot{\mathbf{u}}_{t_1^m:i}^g)}{\partial \ddot{\mathbf{u}}_{t_1^m:t_2^m}^g} \right)^T \mathbf{R}^{-1} \left( \mathbf{y}_i - \hat{\mathbf{y}}_i(\boldsymbol{\theta}, \ddot{\mathbf{u}}_{t_1^m:i}^g) \right) \\ -\frac{k}{2} \mathbf{r}^{-1} + \frac{1}{2} \sum_{i=1}^k \mathbf{w}_i \end{bmatrix} \quad (6.51)$$

in which  $\mathbf{r}^{-1} = \begin{bmatrix} \frac{1}{r_1} & \frac{1}{r_2} & \dots & \frac{1}{r_{n_y}} \end{bmatrix}^T$  and the vector  $\mathbf{w}_i$  is defined as

$$\mathbf{w}_i = \begin{bmatrix} \frac{\left( y_{i1} - \hat{y}_{i1}(\boldsymbol{\theta}, \ddot{\mathbf{u}}_{t_1^m:i}^g) \right)^2}{r_1^2} & \frac{\left( y_{i2} - \hat{y}_{i2}(\boldsymbol{\theta}, \ddot{\mathbf{u}}_{t_1^m:i}^g) \right)^2}{r_2^2} & \dots & \frac{\left( y_{in_y} - \hat{y}_{in_y}(\boldsymbol{\theta}, \ddot{\mathbf{u}}_{t_1^m:i}^g) \right)^2}{r_{n_y}^2} \end{bmatrix}^T \quad (6.52)$$

where  $\mathbf{v}_i(\boldsymbol{\theta}) = \mathbf{y}_i - \hat{\mathbf{y}}_i(\boldsymbol{\theta}, \ddot{\mathbf{u}}_{t_1^m:i}^g)$  is the simulation error vector at the  $i^{\text{th}}$  time step, which is characterized as a zero-mean independent Gaussian white noise vector process, i.e., statistically independent across time and measurement channels. The FIM, which is a symmetric matrix, can be obtained as

$$\mathbf{I}\left(\boldsymbol{\theta}, \ddot{\mathbf{u}}_{t_1^m:t_2^m}^g, \mathbf{r}\right) = \begin{bmatrix} (\mathbf{I}_{\boldsymbol{\theta}\boldsymbol{\theta}})_{n_{\boldsymbol{\theta}} \times n_{\boldsymbol{\theta}}} & (\mathbf{I}_{\boldsymbol{\theta}\ddot{\mathbf{u}}^g})_{n_{\boldsymbol{\theta}} \times t_1 n_{\ddot{\mathbf{u}}^g}} & (\mathbf{I}_{\boldsymbol{\theta}\mathbf{r}})_{n_{\boldsymbol{\theta}} \times n_y} \\ (\mathbf{I}_{\ddot{\mathbf{u}}^g\boldsymbol{\theta}})_{t_1 n_{\ddot{\mathbf{u}}^g} \times n_{\boldsymbol{\theta}}} & (\mathbf{I}_{\ddot{\mathbf{u}}^g\ddot{\mathbf{u}}^g})_{t_1 n_{\ddot{\mathbf{u}}^g} \times t_1 n_{\ddot{\mathbf{u}}^g}} & (\mathbf{I}_{\ddot{\mathbf{u}}^g\mathbf{r}})_{t_1 n_{\ddot{\mathbf{u}}^g} \times n_y} \\ (\mathbf{I}_{\mathbf{r}\boldsymbol{\theta}})_{n_y \times n_{\boldsymbol{\theta}}} & (\mathbf{I}_{\mathbf{r}\ddot{\mathbf{u}}^g})_{n_y \times t_1 n_{\ddot{\mathbf{u}}^g}} & (\mathbf{I}_{\mathbf{r}\mathbf{r}})_{n_y \times n_y} \end{bmatrix} \quad (6.53)$$

The first submatrix  $\mathbf{I}_{\boldsymbol{\theta}\boldsymbol{\theta}}$  can be derived as

$$\begin{aligned} \mathbf{I}_{\boldsymbol{\theta}\boldsymbol{\theta}} &= E \left( \left( \frac{\partial \Lambda(\boldsymbol{\theta}, \mathbf{r}, \hat{\mathbf{u}}_{1:t_1^m-1}^g, \ddot{\mathbf{u}}_{t_1^m:t_2^m}^g, \mathbf{Y}_{t_1^m:t_2^m})}{\partial \boldsymbol{\theta}} \right)^T \left( \frac{\partial \Lambda(\boldsymbol{\theta}, \mathbf{r}, \hat{\mathbf{u}}_{1:t_1^m-1}^g, \ddot{\mathbf{u}}_{t_1^m:t_2^m}^g, \mathbf{Y}_{t_1^m:t_2^m})}{\partial \boldsymbol{\theta}} \right) \right) \\ &= E \left( \sum_{i=t_1^m}^{t_2^m} \left( \frac{\partial \hat{\mathbf{y}}_i(\boldsymbol{\theta}, \ddot{\mathbf{u}}_{t_1^m:i}^g)}{\partial \boldsymbol{\theta}} \right)^T \mathbf{R}^{-1} \left( \mathbf{Y}_i - \hat{\mathbf{y}}_i(\boldsymbol{\theta}, \ddot{\mathbf{u}}_{t_1^m:i}^g) \right) \sum_{j=t_2^m}^{t_1^m} \left( \mathbf{Y}_j - \hat{\mathbf{y}}_j(\boldsymbol{\theta}, \ddot{\mathbf{u}}_{t_1^m:i}^g) \right)^T \mathbf{R}^{-1} \left( \frac{\partial \hat{\mathbf{y}}_j(\boldsymbol{\theta}, \ddot{\mathbf{u}}_{t_1^m:i}^g)}{\partial \boldsymbol{\theta}} \right) \right) \\ &= \sum_{i=t_1^m}^{t_2^m} \sum_{j=t_1^m}^{t_2^m} \left( \frac{\partial \hat{\mathbf{y}}_i(\boldsymbol{\theta}, \ddot{\mathbf{u}}_{t_1^m:i}^g)}{\partial \boldsymbol{\theta}} \right)^T \mathbf{R}^{-1} \underbrace{E \left( \left( \mathbf{Y}_i - \hat{\mathbf{y}}_i(\boldsymbol{\theta}, \ddot{\mathbf{u}}_{t_1^m:i}^g) \right) \left( \mathbf{Y}_j - \hat{\mathbf{y}}_j(\boldsymbol{\theta}, \ddot{\mathbf{u}}_{t_1^m:i}^g) \right)^T \right)}_{=\mathbf{R}\delta_{ij}} \mathbf{R}^{-1} \left( \frac{\partial \hat{\mathbf{y}}_j(\boldsymbol{\theta}, \ddot{\mathbf{u}}_{t_1^m:i}^g)}{\partial \boldsymbol{\theta}} \right) \\ &= \sum_{i=t_1^m}^{t_2^m} \left( \frac{\partial \hat{\mathbf{y}}_i(\boldsymbol{\theta}, \ddot{\mathbf{u}}_{t_1^m:i}^g)}{\partial \boldsymbol{\theta}} \right)^T \mathbf{R}^{-1} \left( \frac{\partial \hat{\mathbf{y}}_i(\boldsymbol{\theta}, \ddot{\mathbf{u}}_{t_1^m:i}^g)}{\partial \boldsymbol{\theta}} \right) \end{aligned} \quad (6.54)$$

Therefore,

$$\mathbf{I}_{\boldsymbol{\theta}\boldsymbol{\theta}} = \sum_{i=t_1^m}^{t_2^m} \sum_{j=1}^{n_y} \frac{1}{r_j} \left( \frac{\partial h_{ij}(\boldsymbol{\theta}, \ddot{\mathbf{u}}_{g_{1:t_1^m-1}}, \ddot{\mathbf{u}}_{g_{t_1^m:i}})}{\partial \boldsymbol{\theta}} \right)^T \left( \frac{\partial h_{ij}(\boldsymbol{\theta}, \ddot{\mathbf{u}}_{g_{1:t_1^m-1}}, \ddot{\mathbf{u}}_{g_{t_1^m:i}})}{\partial \boldsymbol{\theta}} \right) \quad (6.55)$$

The second submatrix  $\mathbf{I}_{\boldsymbol{\theta}\ddot{\mathbf{u}}^g}$  can be obtained as

$$\begin{aligned}
\mathbf{I}_{\mathbf{0}\ddot{\mathbf{u}}^g} &= E \left[ \left( \frac{\partial \Lambda(\mathbf{0}, \mathbf{r}, \hat{\mathbf{u}}_{1:t_1^m-1}^g, \ddot{\mathbf{u}}_{t_1^m:t_2^m}^g, \mathbf{Y}_{t_1^m:t_2^m}^m)}{\partial \boldsymbol{\theta}} \right)^T \left( \frac{\partial \Lambda(\mathbf{0}, \mathbf{r}, \hat{\mathbf{u}}_{1:t_1^m-1}^g, \ddot{\mathbf{u}}_{t_1^m:t_2^m}^g, \mathbf{Y}_{t_1^m:t_2^m}^m)}{\partial \ddot{\mathbf{u}}_{t_1^m:t_2^m}^g} \right) \right] \\
&= E \left[ \sum_{i=t_1^m}^{t_2^m} \left( \frac{\partial \hat{\mathbf{y}}_i(\mathbf{0}, \ddot{\mathbf{u}}_{t_1^m:i}^g)}{\partial \boldsymbol{\theta}} \right)^T \mathbf{R}^{-1} (\mathbf{Y}_i - \hat{\mathbf{y}}_i(\mathbf{0})) \sum_{j=t_2^m}^{t_2^m} (\mathbf{Y}_j - \hat{\mathbf{y}}_j(\mathbf{0}))^T \mathbf{R}^{-1} \left( \frac{\partial \hat{\mathbf{y}}_j(\mathbf{0}, \ddot{\mathbf{u}}_{t_1^m:j}^g)}{\partial \ddot{\mathbf{u}}_{t_1^m:t_2^m}^g} \right) \right] \\
&= \sum_{i=t_1^m}^{t_2^m} \sum_{j=t_1^m}^{t_2^m} \left( \frac{\partial \hat{\mathbf{y}}_i(\mathbf{0}, \ddot{\mathbf{u}}_{t_1^m:i}^g)}{\partial \boldsymbol{\theta}} \right)^T \mathbf{R}^{-1} \underbrace{E[(\mathbf{Y}_i - \hat{\mathbf{y}}_i(\mathbf{0}))(\mathbf{Y}_j - \hat{\mathbf{y}}_j(\mathbf{0}))^T]}_{=\mathbf{R}\delta_{ij}} \mathbf{R}^{-1} \left( \frac{\partial \hat{\mathbf{y}}_j(\mathbf{0}, \ddot{\mathbf{u}}_{t_1^m:j}^g)}{\partial \ddot{\mathbf{u}}_{t_1^m:t_2^m}^g} \right) \\
&= \sum_{i=t_1^m}^{t_2^m} \left( \frac{\partial \hat{\mathbf{y}}_i(\mathbf{0}, \ddot{\mathbf{u}}_{t_1^m:i}^g)}{\partial \boldsymbol{\theta}} \right)^T \mathbf{R}^{-1} \left( \frac{\partial \hat{\mathbf{y}}_i(\mathbf{0}, \ddot{\mathbf{u}}_{t_1^m:i}^g)}{\partial \ddot{\mathbf{u}}_{t_1^m:t_2^m}^g} \right)
\end{aligned} \tag{6.56}$$

Therefore,

$$\mathbf{I}_{\mathbf{0}\ddot{\mathbf{u}}^g} = \sum_{i=t_1^m}^{t_2^m} \sum_{j=1}^{n_y} \frac{1}{r_j} \left( \frac{\partial h_{ij}(\mathbf{0}, \ddot{\mathbf{u}}_{g_{1:t_1^m-1}}, \ddot{\mathbf{u}}_{g_{t_1^m:i}})}{\partial \boldsymbol{\theta}} \right)^T \left( \frac{\partial h_{ij}(\mathbf{0}, \ddot{\mathbf{u}}_{g_{1:t_1^m-1}}, \ddot{\mathbf{u}}_{g_{t_1^m:i}})}{\partial \ddot{\mathbf{u}}_{g_{t_1^m:t_2^m}}} \right) \tag{6.57}$$

The third submatrix  $\mathbf{I}_{\mathbf{0}\mathbf{r}}$  can be derived as

$$\begin{aligned}
\mathbf{I}_{\mathbf{0}\mathbf{r}} &= E \left[ \left( \frac{\partial \Lambda(\mathbf{0}, \mathbf{r}, \hat{\mathbf{u}}_{1:t_1^m-1}^g, \ddot{\mathbf{u}}_{t_1^m:t_2^m}^g, \mathbf{Y}_{t_1^m:t_2^m}^m)}{\partial \boldsymbol{\theta}} \right)^T \left( \frac{\partial \Lambda(\mathbf{0}, \mathbf{r}, \hat{\mathbf{u}}_{1:t_1^m-1}^g, \ddot{\mathbf{u}}_{t_1^m:t_2^m}^g, \mathbf{Y}_{t_1^m:t_2^m}^m)}{\partial \mathbf{r}} \right) \right] \\
&= E \left[ -\frac{k}{2} \sum_{i=1}^k \left( \frac{\partial \hat{\mathbf{y}}_i(\mathbf{0}, \ddot{\mathbf{u}}_{t_1^m:i}^g)}{\partial \boldsymbol{\theta}} \right)^T \mathbf{R}^{-1} (\mathbf{Y}_i - \hat{\mathbf{y}}_i(\mathbf{0}, \ddot{\mathbf{u}}_{t_1^m:i}^g)) (\mathbf{r}^{-1})^T + \frac{1}{2} \sum_{i=1}^k \left( \frac{\partial \hat{\mathbf{y}}_i(\mathbf{0}, \ddot{\mathbf{u}}_{t_1^m:i}^g)}{\partial \boldsymbol{\theta}} \right)^T \mathbf{R}^{-1} (\mathbf{Y}_i - \hat{\mathbf{y}}_i(\mathbf{0}, \ddot{\mathbf{u}}_{t_1^m:i}^g)) \sum_{j=1}^k \mathbf{W}_j^T \right] \\
&= -\frac{k}{2} \sum_{i=1}^k \left( \frac{\partial \hat{\mathbf{y}}_i(\mathbf{0}, \ddot{\mathbf{u}}_{t_1^m:i}^g)}{\partial \boldsymbol{\theta}} \right)^T \mathbf{R}^{-1} \underbrace{E[\mathbf{Y}_i - \hat{\mathbf{y}}_i(\mathbf{0}, \ddot{\mathbf{u}}_{t_1^m:i}^g)]}_{=\mathbf{0}} (\mathbf{r}^{-1})^T + \frac{1}{2} \sum_{i=1}^k \sum_{j=1}^k \left( \frac{\partial \hat{\mathbf{y}}_i(\mathbf{0})}{\partial \boldsymbol{\theta}} \right)^T \mathbf{R}^{-1} E[(\mathbf{Y}_i - \hat{\mathbf{y}}_i(\mathbf{0}, \ddot{\mathbf{u}}_{t_1^m:i}^g)) \mathbf{W}_j^T]
\end{aligned} \tag{6.58}$$

in which the term  $E[(\mathbf{Y}_i - \hat{\mathbf{y}}_i(\mathbf{0}, \ddot{\mathbf{u}}_{t_1^m:i}^g)) \mathbf{W}_j^T]$  can be derived as

$$E[(\mathbf{Y}_i - \hat{\mathbf{y}}_i(\boldsymbol{\theta})) \mathbf{W}_j^T] = \begin{bmatrix} \frac{E[(Y_{i1} - \hat{y}_{i1})(Y_{j1} - \hat{y}_{j1})^2]}{r_1^2} & \frac{E[(Y_{i1} - \hat{y}_{i1})(Y_{j2} - \hat{y}_{j2})^2]}{r_2^2} & \dots & \frac{E[(Y_{i1} - \hat{y}_{i1})(Y_{jn_y} - \hat{y}_{jn_y})^2]}{r_{n_y}^2} \\ \frac{E[(Y_{i2} - \hat{y}_{i2})(Y_{j1} - \hat{y}_{j1})^2]}{r_1^2} & \frac{E[(Y_{i2} - \hat{y}_{i2})(Y_{j2} - \hat{y}_{j2})^2]}{r_2^2} & \dots & \frac{E[(Y_{i2} - \hat{y}_{i2})(Y_{jn_y} - \hat{y}_{jn_y})^2]}{r_{n_y}^2} \\ \vdots & \vdots & \ddots & \vdots \\ \frac{E[(Y_{in_y} - \hat{y}_{in_y})(Y_{j1} - \hat{y}_{j1})^2]}{r_1^2} & \frac{E[(Y_{in_y} - \hat{y}_{in_y})(Y_{j2} - \hat{y}_{j2})^2]}{r_2^2} & \dots & \frac{E[(Y_{in_y} - \hat{y}_{in_y})(Y_{jn_y} - \hat{y}_{jn_y})^2]}{r_{n_y}^2} \end{bmatrix}$$

When  $t_1 \neq t_2$  or  $m \neq n$ , it is clear that

$$E[(Y_{t_1 m} - \hat{y}_{t_1 m})(Y_{t_2 n} - \hat{y}_{t_2 n})^2] = \underbrace{E[(Y_{t_1 m} - \hat{y}_{t_1 m})]}_{=0} \times E[(Y_{t_2 n} - \hat{y}_{t_2 n})^2] = 0$$

On the other hand, when  $t_1 = t_2$  and  $m = n$ , it follows that

$$E[(Y_{t_1 m} - \hat{y}_{t_1 m})(Y_{t_2 n} - \hat{y}_{t_2 n})^2] = E[(Y_{t_1 m} - \hat{y}_{t_1 m})^3] = 0$$

Therefore,  $E[(\mathbf{Y}_i - \hat{\mathbf{y}}_i(\boldsymbol{\theta})) \mathbf{W}_j^T] = \mathbf{0}$ , and based on Eq. (6.58), it follows that

$$\mathbf{I}_{\mathbf{0r}} = \mathbf{I}_{\mathbf{r0}}^T = \mathbf{0}. \text{ Similarly, it can be shown that } \mathbf{I}_{\ddot{\mathbf{u}}^g \mathbf{r}} = \mathbf{I}_{\mathbf{r} \ddot{\mathbf{u}}^g}^T = \mathbf{0}.$$

The term  $\mathbf{I}_{\ddot{\mathbf{u}}^g \ddot{\mathbf{u}}^g}$  in Eq. (6.53) can be derived as

$$\begin{aligned}
\mathbf{I}_{\ddot{\mathbf{u}}^g \ddot{\mathbf{u}}^g} &= E \left[ \left( \frac{\partial \Lambda(\boldsymbol{\theta}, \mathbf{r}, \hat{\mathbf{u}}_{1:t_1^m-1}^g, \ddot{\mathbf{u}}_{t_1^m:t_2^m}^g, \mathbf{Y}_{t_1^m:t_2^m}^m)}{\partial \ddot{\mathbf{u}}_{t_1^m:t_2^m}^g} \right)^T \left( \frac{\partial \Lambda(\boldsymbol{\theta}, \mathbf{r}, \hat{\mathbf{u}}_{1:t_1^m-1}^g, \ddot{\mathbf{u}}_{t_1^m:t_2^m}^g, \mathbf{Y}_{t_1^m:t_2^m}^m)}{\partial \ddot{\mathbf{u}}_{t_1^m:t_2^m}^g} \right) \right] \quad (6.59) \\
&= E \left[ \sum_{i=t_1^m}^{t_2^m} \left( \frac{\partial \hat{y}_i(\boldsymbol{\theta}, \ddot{\mathbf{u}}_{t_1^m:i}^g)}{\partial \ddot{\mathbf{u}}_{t_1^m:t_2^m}^g} \right)^T \mathbf{R}^{-1} \left( \mathbf{Y}_i - \hat{y}_i(\boldsymbol{\theta}, \ddot{\mathbf{u}}_{t_1^m:i}^g) \right) \sum_{j=t_2^m}^{t_2^m} \left( \mathbf{Y}_j - \hat{y}_j(\boldsymbol{\theta}, \ddot{\mathbf{u}}_{t_1^m:i}^g) \right)^T \mathbf{R}^{-1} \left( \frac{\partial \hat{y}_j(\boldsymbol{\theta}, \ddot{\mathbf{u}}_{t_1^m:i}^g)}{\partial \ddot{\mathbf{u}}_{t_1^m:t_2^m}^g} \right) \right] \\
&= \sum_{i=t_1^m}^{t_2^m} \sum_{j=t_1^m}^{t_2^m} \left( \frac{\partial \hat{y}_i(\boldsymbol{\theta}, \ddot{\mathbf{u}}_{t_1^m:i}^g)}{\partial \ddot{\mathbf{u}}_{t_1^m:t_2^m}^g} \right)^T \mathbf{R}^{-1} \underbrace{E \left[ \left( \mathbf{Y}_i - \hat{y}_i(\boldsymbol{\theta}, \ddot{\mathbf{u}}_{t_1^m:i}^g) \right) \left( \mathbf{Y}_j - \hat{y}_j(\boldsymbol{\theta}, \ddot{\mathbf{u}}_{t_1^m:i}^g) \right)^T \right]}_{=\mathbf{R}\delta_{ij}} \mathbf{R}^{-1} \left( \frac{\partial \hat{y}_j(\boldsymbol{\theta}, \ddot{\mathbf{u}}_{t_1^m:i}^g)}{\partial \ddot{\mathbf{u}}_{t_1^m:t_2^m}^g} \right) \\
&= \sum_{i=t_1^m}^{t_2^m} \left( \frac{\partial \hat{y}_i(\boldsymbol{\theta}, \ddot{\mathbf{u}}_{t_1^m:i}^g)}{\partial \ddot{\mathbf{u}}_{t_1^m:t_2^m}^g} \right)^T \mathbf{R}^{-1} \left( \frac{\partial \hat{y}_i(\boldsymbol{\theta}, \ddot{\mathbf{u}}_{t_1^m:i}^g)}{\partial \ddot{\mathbf{u}}_{t_1^m:t_2^m}^g} \right)
\end{aligned}$$

Therefore,

$$\mathbf{I}_{\ddot{\mathbf{u}}^g \ddot{\mathbf{u}}^g} = \sum_{i=t_1^m}^{t_2^m} \sum_{j=1}^{n_y} \frac{1}{r_j} \left( \frac{\partial h_{ij}(\boldsymbol{\theta}, \ddot{\mathbf{u}}_{g_{1:t_1^m-1}}, \ddot{\mathbf{u}}_{g_{t_1^m:i}})}{\partial \ddot{\mathbf{u}}_{g_{t_1^m:t_2^m}}} \right)^T \left( \frac{\partial h_{ij}(\boldsymbol{\theta}, \ddot{\mathbf{u}}_{g_{1:t_1^m-1}}, \ddot{\mathbf{u}}_{g_{t_1^m:i}})}{\partial \ddot{\mathbf{u}}_{g_{t_1^m:t_2^m}}} \right) \quad (6.60)$$

Finally, the last submatrix in Eq. (6.53),  $\mathbf{I}_{\mathbf{r}\mathbf{r}}$ , can be obtained as

$$\begin{aligned}
\mathbf{I}_{\mathbf{r}\mathbf{r}} &= E \left[ \left( \frac{\partial \Lambda(\boldsymbol{\theta}, \mathbf{r}, \hat{\mathbf{u}}_{1:t_1^m-1}^g, \ddot{\mathbf{u}}_{t_1^m:t_2^m}^g, \mathbf{Y}_{t_1^m:t_2^m}^m)}{\partial \mathbf{r}} \right)^T \left( \frac{\partial \Lambda(\boldsymbol{\theta}, \mathbf{r}, \hat{\mathbf{u}}_{1:t_1^m-1}^g, \ddot{\mathbf{u}}_{t_1^m:t_2^m}^g, \mathbf{Y}_{t_1^m:t_2^m}^m)}{\partial \mathbf{r}} \right) \right] \quad (6.61) \\
&= \frac{k^2}{4} \mathbf{r}^{-1} (\mathbf{r}^{-1})^T - \frac{k}{4} \mathbf{r}^{-1} \sum_{i=1}^k E[\mathbf{W}_i^T] - \frac{k}{4} \sum_{i=1}^k E[\mathbf{W}_i] (\mathbf{r}^{-1})^T + \frac{1}{4} \sum_{i=1}^k \sum_{j=1}^k E[\mathbf{W}_i \mathbf{W}_j^T]
\end{aligned}$$

It is clear that

$$\begin{aligned}
E[\mathbf{W}_i] &= \left[ \frac{E \left[ \left( Y_{i1} - \hat{y}_{i1}(\boldsymbol{\theta}, \ddot{\mathbf{u}}_{t_1^m:i}^g) \right)^2 \right]}{r_1^2} \quad \frac{E \left[ \left( Y_{i2} - \hat{y}_{i2}(\boldsymbol{\theta}, \ddot{\mathbf{u}}_{t_1^m:i}^g) \right)^2 \right]}{r_2^2} \quad \dots \quad \frac{E \left[ \left( Y_{in_y} - \hat{y}_{in_y}(\boldsymbol{\theta}, \ddot{\mathbf{u}}_{t_1^m:i}^g) \right)^2 \right]}{r_{n_y}^2} \right]^T \\
&= \left[ \frac{1}{r_1} \quad \frac{1}{r_2} \quad \dots \quad \frac{1}{r_{n_y}} \right]^T = \mathbf{r}^{-1}
\end{aligned}$$

Also, it can be observed that

$$E[\mathbf{w}_i \mathbf{w}_j^T] = \begin{bmatrix} \frac{E[(Y_{i1} - \hat{y}_{i1})^2 (Y_{j1} - \hat{y}_{j1})^2]}{r_1^4} & \frac{E[(Y_{i1} - \hat{y}_{i1})^2 (Y_{j2} - \hat{y}_{j2})^2]}{r_1^2 r_2^2} & \dots & \frac{E[(Y_{i1} - \hat{y}_{i1})^2 (Y_{jn_y} - \hat{y}_{jn_y})^2]}{r_1^2 r_{n_y}^2} \\ \frac{E[(Y_{i2} - \hat{y}_{i2})^2 (Y_{j1} - \hat{y}_{j1})^2]}{r_2^2 r_1^2} & \frac{E[(Y_{i2} - \hat{y}_{i2})^2 (Y_{j2} - \hat{y}_{j2})^2]}{r_2^4} & \dots & \frac{E[(Y_{i2} - \hat{y}_{i2})^2 (Y_{jn_y} - \hat{y}_{jn_y})^2]}{r_2^2 r_{n_y}^2} \\ \vdots & \vdots & \ddots & \vdots \\ \frac{E[(Y_{in_y} - \hat{y}_{in_y})^2 (Y_{j1} - \hat{y}_{j1})^2]}{r_{n_y}^2 r_1^2} & \frac{E[(Y_{in_y} - \hat{y}_{in_y})^2 (Y_{j2} - \hat{y}_{j2})^2]}{r_{n_y}^2 r_2^2} & \dots & \frac{E[(Y_{in_y} - \hat{y}_{in_y})^2 (Y_{jn_y} - \hat{y}_{jn_y})^2]}{r_{n_y}^4} \end{bmatrix}$$

When  $t_1 \neq t_2$  or  $m \neq n$ , it follows that

$$E[(Y_{t_1 m} - \hat{y}_{t_1 m})^2 (Y_{t_2 n} - \hat{y}_{t_2 n})^2] = E[(Y_{t_1 m} - \hat{y}_{t_1 m})^2] \times E[(Y_{t_2 n} - \hat{y}_{t_2 n})^2] = r_m r_n$$

However, when  $t_1 = t_2$  and  $m = n$ , it follows that

$$E[(Y_{t_1 m} - \hat{y}_{t_1 m})^2 (Y_{t_2 n} - \hat{y}_{t_2 n})^2] = E[(Y_{t_1 m} - \hat{y}_{t_1 m})^4] = 3r_m^2$$

Therefore,

$$\begin{aligned} \sum_{i=1}^k \sum_{j=1}^k E[\mathbf{w}_i \mathbf{w}_j^T] &= (k^2 - k) \begin{bmatrix} \frac{1}{r_1^2} & \frac{1}{r_1 r_2} & \dots & \frac{1}{r_1 r_{n_y}} \\ \frac{1}{r_2 r_1} & \frac{1}{r_2^2} & \dots & \frac{1}{r_2 r_{n_y}} \\ \vdots & \vdots & \ddots & \vdots \\ \frac{1}{r_{n_y} r_1} & \frac{1}{r_{n_y} r_2} & \dots & \frac{1}{r_{n_y}^2} \end{bmatrix} + k \begin{bmatrix} \frac{3}{r_1^2} & \frac{1}{r_1 r_2} & \dots & \frac{1}{r_1 r_{n_y}} \\ \frac{1}{r_2 r_1} & \frac{3}{r_2^2} & \dots & \frac{1}{r_2 r_{n_y}} \\ \vdots & \vdots & \ddots & \vdots \\ \frac{1}{r_{n_y} r_1} & \frac{1}{r_{n_y} r_2} & \dots & \frac{3}{r_{n_y}^2} \end{bmatrix} \\ \Rightarrow \sum_{i=1}^k \sum_{j=1}^k E[\mathbf{w}_i \mathbf{w}_j^T] &= k^2 \mathbf{r}^{-1} (\mathbf{r}^{-1})^T + 2k \begin{bmatrix} \frac{1}{r_1^2} & 0 & \dots & 0 \\ 0 & \frac{1}{r_2^2} & \dots & 0 \\ \vdots & \vdots & \ddots & \vdots \\ 0 & 0 & \dots & \frac{1}{r_{n_y}^2} \end{bmatrix} \end{aligned}$$

Therefore, following Eq. (6.61) it can be concluded that:



$$\begin{aligned}
 \mathbf{I}_{\mathbf{r}\mathbf{r}} &= \frac{k^2}{4} \mathbf{r}^{-1} (\mathbf{r}^{-1})^T - \frac{k^2}{4} \mathbf{r}^{-1} (\mathbf{r}^{-1})^T - \frac{k^2}{4} \mathbf{r}^{-1} (\mathbf{r}^{-1})^T + \frac{k^2}{4} \mathbf{r}^{-1} (\mathbf{r}^{-1})^T + \frac{k}{2} \begin{bmatrix} \frac{1}{r_1^2} & 0 & \cdots & 0 \\ 0 & \frac{1}{r_2^2} & \cdots & 0 \\ \vdots & \vdots & \ddots & \vdots \\ 0 & 0 & \cdots & \frac{1}{r_{n_y}^2} \end{bmatrix} \\
 \Rightarrow \mathbf{I}_{\mathbf{r}\mathbf{r}} &= \frac{k}{2} \begin{bmatrix} \frac{1}{r_1^2} & 0 & \cdots & 0 \\ 0 & \frac{1}{r_2^2} & \cdots & 0 \\ \vdots & \vdots & \ddots & \vdots \\ 0 & 0 & \cdots & \frac{1}{r_{n_y}^2} \end{bmatrix}
 \end{aligned} \tag{6.62}$$

## Appendix 6.II: Derivation of the traditional Kalman gain matrix

It can be proved that the term  $\tilde{\mathbf{K}} = \left( \mathbf{C}^T \tilde{\mathbf{R}}^{-1} \mathbf{C} + \left( \hat{\mathbf{P}}_{\psi}^{-} \right)^{-1} \right)^{-1} \mathbf{C}^T \tilde{\mathbf{R}}^{-1}$  in Eq. (6.32) is

equivalent to the Kalman gain matrix. The Kalman gain matrix is traditionally defined

as  $\mathbf{K} = \hat{\mathbf{P}}_{\psi y} \left( \hat{\mathbf{P}}_{yy} \right)^{-1}$ . Call  $\mathbf{X} = \left( \mathbf{C}^T \tilde{\mathbf{R}}^{-1} \mathbf{C} + \left( \hat{\mathbf{P}}_{\psi}^{-} \right)^{-1} \right)^{-1}$ . It can be followed that:

$$\tilde{\mathbf{K}} = \mathbf{X} \mathbf{C}^T \tilde{\mathbf{R}}^{-1} = \mathbf{X} \mathbf{C}^T \tilde{\mathbf{R}}^{-1} \left( \mathbf{C} \hat{\mathbf{P}}_{\psi}^{-} \mathbf{C}^T + \tilde{\mathbf{R}} \right) \left( \mathbf{C} \hat{\mathbf{P}}_{\psi}^{-} \mathbf{C}^T + \tilde{\mathbf{R}} \right)^{-1}$$

$$\tilde{\mathbf{K}} = \left( \mathbf{X} \mathbf{C}^T \tilde{\mathbf{R}}^{-1} \mathbf{C} \hat{\mathbf{P}}_{\psi}^{-} \mathbf{C}^T + \mathbf{X} \mathbf{C}^T \right) \left( \mathbf{C} \hat{\mathbf{P}}_{\psi}^{-} \mathbf{C}^T + \tilde{\mathbf{R}} \right)^{-1}$$

$$\tilde{\mathbf{K}} = \mathbf{X} \underbrace{\left( \mathbf{C}^T \tilde{\mathbf{R}}^{-1} \mathbf{C} + \left( \hat{\mathbf{P}}_{\psi}^{-} \right)^{-1} \right)^{-1}}_{\mathbf{X}^{-1}} \hat{\mathbf{P}}_{\psi}^{-} \mathbf{C}^T \left( \mathbf{C} \hat{\mathbf{P}}_{\psi}^{-} \mathbf{C}^T + \tilde{\mathbf{R}} \right)^{-1}$$

$$\tilde{\mathbf{K}} = \underbrace{\hat{\mathbf{P}}_{\psi}^{-} \mathbf{C}^T}_{\hat{\mathbf{P}}_{\psi y}} \left( \underbrace{\mathbf{C} \hat{\mathbf{P}}_{\psi}^{-} \mathbf{C}^T + \tilde{\mathbf{R}}}_{\hat{\mathbf{P}}_{yy}} \right)^{-1} \Rightarrow \tilde{\mathbf{K}} = \hat{\mathbf{P}}_{\psi y} \left( \hat{\mathbf{P}}_{yy} \right)^{-1}$$

## References

- [1] R. Astroza, H. Ebrahimian, J. P. Conte, J. I. Restrepo, and T. C. Hutchinson, "System Identification of a Full-scale Five-story Reinforced Concrete Building Tested on the NEES-UCSD Shake Table," *Structural Control and Health Monitoring*, vol. in review, 2015.
- [2] E. Ntotsios, C. Karakostas, V. Lekidis, P. Panetsos, I. Nikolaou, C. Papadimitriou, and T. Salonikos, "Structural Identification of Egnatia Odos Bridges based on Ambient and Earthquake Induced Vibrations," *Bulletin of Earthquake Engineering*, vol. 7, p. 485-501, 2009.
- [3] B. Moaveni, X. He, J. P. Conte, J. I. Restrepo, and M. Panagiotou, "Damage Identification Study of a Seven-Story Full-Scale Building Slice Tested on the UCSD-NEES Shake Table," *ASCE Journal of Structural Engineering*, vol. 137, no. 6, p. 705-717, 2011.
- [4] G. Kerschen, K. Worden, A. F. Vakakis, and J. Golinval, "Past, Present and Future of Nonlinear System Identification in Structural Dynamics," *Mechanical Systems and Signal Processing*, vol. 20, p. 505–592, 2006.
- [5] R. Omrani, R. E. Hudson, and E. Taciroglu, "Parametric Identification of Nondegrading Hysteresis in a Laterally and Torsionally Coupled Building Using an Unscented Kalman Filter," *ASCE Journal of Engineering Mechanics*, vol. 139, no. 4, p. 452–468, 2013.
- [6] S. G. Shahidi and S. N. Pakzad, "Generalized Response Surface Model Updating using Time Domain Data," *ASCE Journal of Structural Engineering*, Vols. 10.1061/(ASCE)ST.1943-541X.0000915, p. A4014001(13), 2014.
- [7] H. A. Nasrellah and C. S. Manohar, "Finite Element Method Based Monte Carlo Filters for Structural System Identification," *Probabilistic Engineering Mechanics*, vol. 26, no. 2, p. 294–307, 2011.
- [8] H. Ebrahimian, R. Astroza, and J. P. Conte, "Extended Kalman Filter for Material Parameter Estimation in Nonlinear Structural Finite Element Models using Direct Differentiation Method," *Earthquake Engineering and Structural Dynamics*, vol. 44, no. 10, p. 1495-1522, 2015.
- [9] R. Astroza, H. Ebrahimian, and J. P. Conte, "Material Parameter Identification in Distributed Plasticity FE Models of Frame-Type Structures Using Nonlinear Stochastic Filtering," *ASCE Journal of Engineering Mechanics*, vol. 141, no. 5, p. 04014149 1-17, 2015.
- [10] H. Ebrahimian, R. Astroza, J. P. Conte, and R. A. de Callafon, "Nonlinear Finite Element Model Updating for Damage Identification of Civil Structures using

- Batch Bayesian Estimation," *Mechanical Systems and Signal Processing*, in review, 2015.
- [11] C.-H. Huang, "An Inverse Nonlinear Force Vibration Problem of Estimating the External Forces in a Damped System with Time-dependent System Parameters," *Journal of Sound and Vibration*, vol. 242, p. 749-756, 2001.
- [12] C.-H. Huang, C.-C. Shih, and S. Kim, "An Inverse Vibration Problem in Estimating the Spatial and Temporal-dependent External Forces for Cutting Tools," *Applied Mathematical Modelling*, vol. 33, p. 2683-2698, 2009.
- [13] M.-H. Lee and Y.-W. Liu, "Input Load Identification of Nonlinear Tower Structural System using Intelligent Inverse Estimation Algorithm," *Procedia Engineering*, vol. 79, p. 540- 549 , 2014.
- [14] C.-K. Ma and C.-C. Ho, "An Inverse Method for the Estimation of Input Forces Acting on Non-linear Structural Systems," *Journal of Sound and Vibration*, vol. 2004, no. 275, p. 953-971, 2004.
- [15] C.-K. Ma, J.-M. Chang, and D.-C. Lin, "Input Forces Estimation of Beam Structures by an Inverse Method," *Journal of Sound and Vibration*, vol. 259, no. 2, p. 387-407, 2003.
- [16] Z. R. Lu and S. S. Law, "Identification of System Parameters and Input Force from Output Only," *Mechanical Systems and Signal Processing*, vol. 21, p. 2099-2111, 2007.
- [17] E. Lourens, C. Papadimitriou, S. Gillijns, E. Reynders, G. De Roeck, and G. Lombaert, "Joint Input-Response Estimation for Structural Systems based on Reduced-order Models and Vibration Data from a Limited Number of Sensors," *Mechanical Systems and Signal Processing*, vol. 29, p. 310-327, 2012.
- [18] A. Al-Hussein and A. Haldar, "Novel Unscented Kalman Filter for Health Assessment of Structural Systems with Unknown Input," *ASCE Journal of Engineering Mechanics*, p. 10.1061/(ASCE)EM.1943-7889.0000926, 2015.
- [19] A. K. Chopra, *Dynamics of Structures: Theory and Applications to Earthquake Engineering*, Englewood Cliffs, N.J.: Prentice-Hall, Inc., 4th Ed., 2012.
- [20] J. L. Beck and L. S. Katafygiotis, "Updating Models and their Uncertainties. Part I: Bayesian Statistical Framework," *ASCE Journal of Engineering Mechanics*, vol. 124, no. 4, p. 455-461, 1998.
- [21] J. L. Beck, "Bayesian System Identification based on Probability Logic," *Structural Control and Health Monitoring*, vol. 17, no. 7, p. 825-847, 2010.
- [22] H. Ebrahimian, R. Astroza, and J. P. Conte, "Output-only Identification of Civil Structures using Nonlinear Finite Element Model Updating," in *SPIE 9438*,

*Health Monitoring of Structural and Biological Systems*, San Diego, CA, 2015.

- [23] C. A. Vidal, H.-S. Lee, and R. B. Haber, "The Consistent Tangent Operator for Design Sensitivity Analysis of History-Dependent Response," *Computing Systems in Engineering*, vol. 2, no. 5-6, p. 509-523, 1991.
- [24] M. Kleiber, H. Antunez, T. D. Hien, and P. Kowalczyk, *Parameter Sensitivity in Nonlinear Mechanics: Theory and Finite Element Computations*, England: John Wiley & Sons Ltd, 1997.
- [25] Y. Zhang and A. Der Kiureghian, "Dynamic Response Sensitivity of Inelastic Structures," *Computer Methods in Applied Mechanics and Engineering*, vol. 108, no. 1-2, p. 23–36, 1993.
- [26] J. P. Conte, P. K. Vijalapura and M. Meghella, "Consistent Finite-Element Response Sensitivity Analysis," *ASCE Journal of Engineering Mechanics*, vol. 129, no. 12, p. 1380–1393, 2003.
- [27] T. K. Moon and W. C. Stirling, *Mathematical Methods and Algorithms for Signal Processing*, Upper Saddle River, N.J.: Prentice-Hall, 2000.
- [28] G. C. Goodwin and R. L. Payne, *Dynamic System Identification: Experiment Design and Data Analysis*, New York: Academic Press, 1977.
- [29] S. M. Kay, *Fundamentals of Statistical Signal Processing. Volume 1: Estimation Theory*, Upper Saddle River, N.J.: Prentice Hall, 1993.
- [30] P. Tichavsky, C. H. Muravchik and A. Nehorai, "Posterior Cramer–Rao Bounds for Discrete-Time Nonlinear Filtering," *IEEE Transactions on Signal Processing*, vol. 46, no. 5, p. 1386-1396, 1998.
- [31] H. L. Van Trees, *Optimum Array Processing, Part IV of Detection, Estimation, and Modulation Theory*, New York, NY: John Wiley & Sons, 2002.
- [32] D. Simon, *Optimal State Estimation: Kalman, H Infinity, and Nonlinear Approaches*, Hoboken, New Jersey: John Wiley & Sons, Inc., 2006.
- [33] R. S. Bucy and P. D. Joseph, *Filtering for Stochastic Processes with Applications to Guidance*, New York: John Wiley & Sons Inc., 1968.
- [34] J. P. Conte, "Finite Element Response Sensitivity Analysis in Earthquake Engineering," in *Earthquake Engineering Frontiers in the New Millennium*, Lisse, The Netherlands, 2001.
- [35] OpenSees, "Open System for Earthquake Engineering Simulation," [Online]. Available: <http://opensees.berkeley.edu/>. [Accessed September 2014].
- [36] "MATLAB (2012)," The MathWorks Inc., Natick, Massachusetts, United States.

- [37] International Code Council, 2012 international building code, Country Club Hills, 2011.
- [38] F. F. Taucer, E. Spacone, and F. C. Filippou, "A Fiber Beam-Column Element for Seismic Response Analysis of Reinforced Concrete Structures," UBC/EERC-91/17, Earthquake Engineering Research Center, College of Engineering, UC Berkeley, Berkeley, CA., 1991.
- [39] T. A. Balan, F. C. Filippou, and E. P. Popov, "Constitutive Model for 3D Cyclic Analysis of Concrete Structures," *ASCE Journal of Engineering Mechanics*, vol. 123, no. 2, p. 143–153, 1997.
- [40] A. Zona, M. Barbato, and J. P. Conte, "Finite Element Response Sensitivity Analysis of Continuous Steel-Concrete Composite Girders," *Steel and Composite Structures*, vol. 6, no. 3, p. 183-202, 2006.
- [41] F. C. Filippou, E. P. Popov, and V. V. Bertero, "Effects of Bond Deterioration on Hysteretic Behavior of Reinforced Concrete Joints," EERC Report 83-19, Earthquake Engineering Research Center, College of Engineering, UC Berkeley, Berkeley, CA, 1983.
- [42] "Center for Engineering Strong Motion Data, CESMD - A Cooperative Effort," [Online]. Available: <http://strongmotioncenter.org/>. [Accessed September 2014].
- [43] R. H. Byrd, M. E. Hribar, and J. Nocedal, "An Interior Point Algorithm for Large-scale Nonlinear Programming," *SIAM Journal on Optimization*, vol. 9, no. 4, p. 877–900, 1999.
- [44] R. H. Byrd, J. C. Gilbert, and J. Nocedal, "A Trust Region Method Based on Interior Point Techniques for Nonlinear Programming," *Mathematical Programming*, vol. 89, no. 1, p. 149-185, 2000.
- [45] The MathWorks, "MATLAB Optimization Toolbox, User's Guide, R2014a," The MathWorks Inc., Natick, MA, 2014.

# CHAPTER 7: IDENTIFIABILITY ASSESSMENT FOR NONLINEAR STRUCTURAL SYSTEM IDENTIFICATION PROBLEMS

## 7.1. Introduction

Identifiability of parametric models investigates the question of existence and uniqueness of solution of the associated parameter estimation problem. The identifiability problem is closely related to experimental design and optimal sensor placement problems, which respectively aims at designing the input excitation and sensor locations to measure the most informative data about the estimation parameters. Identifiability of dynamic models can be expressed at two different levels: (i) *a priori* identifiability, which is a function of the parametric model structure of the dynamic system, and the strength and richness of the input excitation. *a priori* identifiability pertains to whether the model parameters can be uniquely identified using ideal (noiseless) measurements (e.g., [1-3]); (ii) *a posteriori* identifiability, which addresses

the effects of measurement noise and model uncertainties and examines quality of the actual measured data to identify the model parameters [4]. Indeed, *a posteriori* identifiability implies *a priori* identifiability.

An extensive amount of attention has been given to the concept of identifiability (or observability) of nonlinear models from various scientific disciplines. In spite of their apparent differences, many of the definitions and statements can be proved to be interchangeable or mathematically equivalent under certain conditions ([5-6]). Following the inverse function theorem, Tunali and Tarn [7] showed that model identifiability can be investigated based on the rank of the Jacobian matrix ( = partial derivative of the model outputs with respect to the model parameters). Tunali and Tarn showed that if the Jacobian matrix is full rank, the model parameters are locally identifiable. Likewise, Reid [8] proposed the notion of sensitivity identifiability based on the rank of the sensitivity matrix. Suppose  $\hat{\mathbf{y}} = \mathbf{h}(\boldsymbol{\theta})$  denotes a nonlinear model parametrized by  $\boldsymbol{\theta}$ . Based on Reid, the model parameters are sensitivity identifiable if  $\det(\mathbf{C}^T \mathbf{C}) \neq 0$ , where  $\mathbf{C} = \frac{\partial \mathbf{h}}{\partial \boldsymbol{\theta}}$  is the sensitivity (or Jacobian) matrix. Other investigators have followed similar approaches (e.g., [9-10] to name only two). Bellman and Astrom [11] proposed the positive definiteness of the Hessian matrix of the least squares parameter estimation objective function ( = second order partial derivative of the sum of squared residuals with respect to the model parameters) as a sufficient condition for identifiability. Staley and Yue [12] showed that the positive definiteness of the Fisher information matrix (FIM) can provide the necessary and sufficient condition for identifiability of a parametric model. Similarly,



Rothenberg [13] showed that the model parameters are locally identifiable if the FIM evaluated at the parameter values is non-singular. Bowden [14] made the same conclusion based on an information-theoretic approach. It can be shown that under certain conditions, the abovementioned criteria are mathematically equivalent. In the context of optimal input design, Mehra [3] has proposed various scalar measures of identifiability based on the FIM. As suggested in [3], the identifiability can be quantitatively evaluated and compared using the trace, maximum eigenvalue, or determinant of the inverse of the FIM, which are respectively referred to as A-measure, E-measure, and D-measure for identifiability. The smaller these measures are, the more identifiable the parametric model is.

Identifiability of structural models has been fairly studied in the structural engineering field in the context of linear system identification and especially, optimal sensor placement (e.g., [15-16]). Most of the proposed approaches utilize the determinant ([17-20]) or trace ([21]) of the FIM to evaluate model identifiability. As a departure from state-of-the-art identifiability assessment approaches in structural engineering, Papadimitriou et al. ([22-24]) used the concept of information entropy to provide systematic measure of information contained in the model outputs about the estimation parameters. Other researchers also pursued similar approaches (e.g., [25-26]). Chatzis et al. followed a different path in [27], where they used three methods based on geometric and algebraic observability from the control literature and studied their application for observability and identifiability of nonlinear structural models. Danai et al. [28] proposed the use of wavelet method to transform the sensitivities of

the model outputs with respect to the model parameters into the time-scale domain. This method provides an efficient tool to evaluate the contribution of each measurement channel in the individual parameter identifiability. Nevertheless, the structural applications in all the above-mentioned studies consist of either linear elastic structural models or nonlinear mass-spring models. These basic models are based on simplifying assumptions that result in a crude prediction of the real behavior of the civil structures and therefore, are futile for real world applications.

This chapter investigates the model identifiability in structural system identification based on mechanics-based nonlinear finite element (FE) model updating approach. Recently, the authors have developed a novel framework for health monitoring and damage identification of civil structures capable of real-world applications ([29-33]). In this approach, the measured input excitation and output response of a civil structure are utilized to update state-of-the-art nonlinear mechanics-based FE model of the structure in time domain using Bayesian inference methods. Closely resembling the actual state of the structure, the updated FE model can then be interrogated to extract detailed information about various manifestations of damage in the structural systems. The nonlinear FE model of the structure depends on a set of unknown parameters including but not limited to inertial properties, gravity loading, geometry, restraint and constraint parameters, damping parameters, and parameters characterizing the nonlinear material constitutive laws. These parameters, referred to as model parameters hereafter, are estimated by minimizing the discrepancy between the time histories of the FE predicted and actual structural responses, measured during

a damage-inducing event. As for any parametric system identification problem, the accuracy and robustness of the underlying parameter estimation procedure depends on the information contained in the measurements about model parameters. It is therefore crucial to systematically select the model parameters, and optimally select the sensors arrangements and output measurements to harvest maximum information about the model parameters. In this study, a statistical metrics is developed to quantify the information contained in every individual measurement channel about every individual model parameter. This one-to-one identifiability measure is developed by evaluating the difference between the entropy [34] of the *a priori* and *a posteriori* probability distribution function (PDF) of the model parameters. Being similar to the method proposed in [23] for optimal sensor placement, this approach provides a measure of identifiability of nonlinear structural FE models, which can have immediate applications in parameter selection, optimal sensor placement, and design of experiment. The framework presented in this study offers a generic one-to-one identifiability measure that can find useful applications in nonlinear system identification problems from various engineering disciplines.

## **7.2. Structural system identification through nonlinear FE model updating – Problem Statement**

The time-discretized equation of motion of a nonlinear FE model at time step  $k$  is expressed as

$$\mathbf{M}(\boldsymbol{\theta}) \ddot{\mathbf{q}}_k(\boldsymbol{\theta}) + \mathbf{C}(\boldsymbol{\theta}) \dot{\mathbf{q}}_k(\boldsymbol{\theta}) + \mathbf{r}_k(\mathbf{q}_k(\boldsymbol{\theta}), \boldsymbol{\theta}) = \mathbf{f}_k(\boldsymbol{\theta}) \quad (7.1)$$

where  $\mathbf{M}(\boldsymbol{\theta}) \in \mathbb{R}^{n_{DOF} \times n_{DOF}}$  = mass matrix;  $\mathbf{C}(\boldsymbol{\theta}) \in \mathbb{R}^{n_{DOF} \times n_{DOF}}$  = damping matrix;  $\mathbf{r}_k(\mathbf{q}_k(\boldsymbol{\theta}), \boldsymbol{\theta}) \in \mathbb{R}^{n_{DOF} \times 1}$  = history-dependent (or path-dependent) internal resisting force vector;  $\mathbf{q}_k(\boldsymbol{\theta}), \dot{\mathbf{q}}_k(\boldsymbol{\theta}), \ddot{\mathbf{q}}_k(\boldsymbol{\theta}) \in \mathbb{R}^{n_{DOF} \times 1}$  = nodal displacement, velocity, and acceleration vectors, respectively;  $\boldsymbol{\theta} \in \mathbb{R}^{n_{\theta} \times 1}$  = the FE model parameter vector;  $\mathbf{f}_k(\boldsymbol{\theta}) \in \mathbb{R}^{n_{DOF} \times 1}$  = dynamic load vector, and  $n_{DOF}$  is the number of degrees of freedom of the FE model. Using a recursive numerical integration rule, such as Newmark-beta method [35], Eq. (7.1) is reduced to a nonlinear vector-valued algebraic equation that can be recursively solved in time for the nodal displacement vector. Considering the recursive nature of the solution approach, by having the initial conditions of the FE model (i.e.,  $\mathbf{q}_0, \dot{\mathbf{q}}_0$ ) and the time history of the dynamic load, the equation of motion of the structure can be solved to find the nodal response of the FE model at a specific discrete time step, say time step  $k$ . In short, the nodal response of the FE model at time step  $k$  can be expressed as a nonlinear function of the model parameter vector ( $\boldsymbol{\theta}$ ), and the initial conditions of the FE model ( $\mathbf{q}_0, \dot{\mathbf{q}}_0$ ), i.e. [31],

$$[\mathbf{q}_k, \dot{\mathbf{q}}_k, \ddot{\mathbf{q}}_k] = \tilde{\mathbf{h}}_k(\boldsymbol{\theta}, \mathbf{q}_0, \dot{\mathbf{q}}_0) \quad (7.2)$$

where  $\tilde{\mathbf{h}}_k(\dots)$  is referred to as the nonlinear nodal response function of the FE model at time step  $k$ . In general, the response of a FE model at each time step is expressed as a linear or nonlinear combination of the nodal displacement, velocity, and acceleration vectors. Denoting the response quantity estimated from the FE model at time step  $k$  by  $\hat{\mathbf{y}}_k \in \mathbb{R}^{n_y \times 1}$ , it follows that

$$\hat{\mathbf{y}}_k = \mathbf{h}_k(\boldsymbol{\theta}, \mathbf{q}_0, \dot{\mathbf{q}}_0) \quad (7.3)$$

where  $\mathbf{h}_k(\dots)$  is the nonlinear response function of the FE model at time step  $k$ . Assuming that the initial conditions of the FE model are deterministic and known, the dependence of the nonlinear response function of the FE model on  $\mathbf{q}_0, \dot{\mathbf{q}}_0$  are dropped henceforward for notational convenience.

The actual dynamic response of civil structures can be recorded using an array of heterogeneous sensors such as accelerometers, GPS sensors, LDTVs, potentiometers, strain gauges, etc. The measured response vector of the structure,  $\mathbf{y}_k$ , is related to the FE predicted response,  $\hat{\mathbf{y}}_k$ , as

$$\mathbf{v}_k(\boldsymbol{\theta}) = \mathbf{y}_k - \hat{\mathbf{y}}_k(\boldsymbol{\theta}) \quad (7.4)$$

in which  $\mathbf{v}_k \in \mathbb{R}^{n_y \times 1}$  is the simulation error vector and accounts for the misfit between the measured response of the structure and the FE predicted response. This misfit arises from various sources, namely output measurement noise, parameter uncertainties, and model uncertainties. The latter stems from the mathematical idealizations and imperfections of the FE model technique, and results in an inevitable misfit between the model prediction and the actual structural response [36]. By neglecting the effects of model uncertainties herein, the simulation error due to model parameter uncertainty is minimized in the parameter estimation procedure and therefore, the simulation error accounts for only the measurement noise. Furthermore, it is assumed herein that the measurement noise is stationary, zero-mean, and independent Gaussian white noise (i.e., statistically independent across time and

measurement channels). Therefore, the probability distribution function (PDF) of the simulation error in Eq. (7.4) is expressed as

$$p(\mathbf{v}_i) = \frac{1}{(2\pi)^{n_y/2} |\mathbf{R}|^{1/2}} e^{-\frac{1}{2} \mathbf{v}_i^T \mathbf{R}^{-1} \mathbf{v}_i} \quad (7.5)$$

in which  $|\mathbf{R}|$  denotes the determinant of the diagonal matrix  $\mathbf{R} \in \mathbb{R}^{n_y \times n_y}$ , which is the (time-invariant) covariance matrix of the simulation error vector (i.e.,  $\mathbf{R} = E(\mathbf{v}_i \mathbf{v}_i^T), \forall i$ ).

To estimate the unknown FE model parameter vector ( $\boldsymbol{\theta}$ ) in Eq. (7.4), it is modeled as random vector (shown by  $\Theta$ ) according to the Bayesian estimation approach. The objective of the parameter estimation is to find the maximum *a posteriori* (MAP) estimates of the FE parameters, which maximize the *a posteriori* joint PDF, i.e.,

$$\hat{\boldsymbol{\theta}}_{\text{MAP}} = \underset{\boldsymbol{\theta}}{\text{argmax}} p^{\text{pos}}(\boldsymbol{\theta}) \quad (7.6)$$

in which  $p^{\text{pos}}(\boldsymbol{\theta}) = p(\boldsymbol{\theta} | \mathbf{y}_{1:k})$ , where  $\mathbf{y}_{1:k} = [\mathbf{y}_1^T, \mathbf{y}_2^T, \dots, \mathbf{y}_k^T]^T$  = time history of the measured response of the structure. According to Bayes' rule, the *a posteriori* joint PDF of the model parameters is expressed as

$$p^{\text{pos}}(\boldsymbol{\theta}) = \frac{p(\mathbf{y}_{1:k} | \boldsymbol{\theta}) p^{\text{pri}}(\boldsymbol{\theta})}{p(\mathbf{y}_{1:k})} \quad (7.7)$$

where  $p(\mathbf{y}_{1:k} | \boldsymbol{\theta}) = l(\boldsymbol{\theta}, \mathbf{y}_{1:k})$  = the likelihood function,  $p^{\text{pri}}(\boldsymbol{\theta})$  = the joint *a priori* distribution of the FE model parameters, and  $p(\mathbf{y}_{1:k})$  = normalizing constant independent of the random variables  $\Theta$ . Eq. (7.7) is simplified to ([31]):

$$p^{pos}(\boldsymbol{\theta}) = c \times l(\boldsymbol{\theta}, \mathbf{y}_{1:k}) \times p^{pri}(\boldsymbol{\theta}) \quad (7.8)$$

in which  $c = 1/p(\mathbf{Y} = \mathbf{y}_{1:k})$ , and random variable  $\mathbf{Y}$  denotes the random measured response of the structure. Two different approaches have been proposed by the authors to solve the estimation problem expressed in Eq. (7.6) for nonlinear structural system identification and nonlinear FE model updating. The first approach is based on stochastic filtering methods, in which the model parameters are recursively estimated in time using an extended ([30]) or unscented Kalman filtering method ([29]). The second approach is based on a batch estimation method, in which the model parameters are estimated through a nonlinear optimization process to maximize the log-likelihood function ([33]). It has been recognized in these studies that the successful estimation of the FE model parameters depends not only on the FE model, but also on the characteristics and intensity of the input dynamic load (earthquake excitation therein), the measured data set, and the level of measurement noise. Except for the latter one, the other factors are important components influencing the *a priori* identifiability of the FE model parameters, which is addressed in the next section.

### 7.3. Identifiability assessment based on the Cramér–Rao lower bound

The identifiability of the model parameter vector  $\boldsymbol{\theta} \in \boldsymbol{\Omega}$  in the nonlinear FE model  $\hat{\mathbf{y}}_k = \mathbf{h}_k(\boldsymbol{\theta})$  (see Eq. (7.3)) can be defined as follows ([6, 13]):

**Definition 1 (local identifiability):** A parameter vector  $\boldsymbol{\theta}$  is said to be locally identifiable if there exist no other  $\boldsymbol{\theta}' \in \boldsymbol{\Omega}$  in an open neighborhood of  $\boldsymbol{\theta}$  such that  $p(\mathbf{Y} = \mathbf{y}_{1:k} | \boldsymbol{\theta}) = p(\mathbf{Y} = \mathbf{y}_{1:k} | \boldsymbol{\theta}')$  for any realization of the measured response,  $\mathbf{y}_{1:k}$ .

The mathematical condition for local identifiability has been partially developed by Cramér [37] and is expressed by Rothenberg [13] through the following theorem.

**Theorem 1 (Rothenberg condition for local identifiability):** Assume:

- (i) The log-likelihood function, i.e.,  $\Lambda(\boldsymbol{\theta}, \mathbf{y}_{1:k}) = \log(l(\boldsymbol{\theta}, \mathbf{y}_{1:k}))$ , is continuously differentiable with respect to  $\boldsymbol{\theta}$ ;
- (ii) the elements of the Fisher Information matrix (FIM) exist and are continuous functions of  $\boldsymbol{\theta}$  everywhere in  $\boldsymbol{\Omega}$ , where the FIM is defined as [38]

$$\mathbf{I}(\boldsymbol{\theta}) = E_{\mathbf{Y}|\boldsymbol{\theta}} \left[ \left( \frac{\partial \Lambda(\boldsymbol{\theta}, \mathbf{y}_{1:k})}{\partial \boldsymbol{\theta}} \right)^T \left( \frac{\partial \Lambda(\boldsymbol{\theta}, \mathbf{y}_{1:k})}{\partial \boldsymbol{\theta}} \right) \right] = -E_{\mathbf{Y}|\boldsymbol{\theta}} \left[ \frac{\partial}{\partial \boldsymbol{\theta}} \left( \frac{\partial \Lambda(\boldsymbol{\theta}, \mathbf{y}_{1:k})}{\partial \boldsymbol{\theta}} \right)^T \right] \quad (7.9)$$

- (iii) there exists an open neighborhood of  $\boldsymbol{\theta}_0$  where  $\mathbf{I}(\boldsymbol{\theta})$  has constant rank.

Then,  $\boldsymbol{\theta}_0$  is locally (*a priori*) identifiable if and only if  $\mathbf{I}(\boldsymbol{\theta}_0)$  is nonsingular.

Theorem 1 provides a strict binary measure of identifiability. Nevertheless, in many practical situations, the information matrix is nonsingular but poorly conditioned. This may occur when the measurement data contain relatively little information about a certain subset of the model parameters, which consequently may not be estimated correctly. In such a case, although the FIM is nonsingular, the model parameters are not practically identifiable.



The identifiability condition can alternatively be expressed as a scalar measure of the parameter estimation performance, which is most conveniently expressed in terms of the estimation covariance. Under some regularity conditions, the estimation covariance can be asymptotically approximated with the Cramér-Rao lower bound (CRLB) [39].

**Theorem 2 (Cramér–Rao lower bound):** If  $\hat{\boldsymbol{\theta}} = \mathbf{t}(\mathbf{y})$  is an unbiased estimate of  $\boldsymbol{\theta}$  based on the measured data  $\mathbf{y}$  with a non-informative (uniform) prior, a differentiable log-likelihood function with respect to  $\boldsymbol{\theta}$ , and an invertible FIM, the covariance matrix of the estimator satisfies the CRLB [38]:

$$E_{\mathbf{Y}|\boldsymbol{\theta}}[(\mathbf{t}(\mathbf{Y}) - \boldsymbol{\theta})(\mathbf{t}(\mathbf{Y}) - \boldsymbol{\theta})^T] \geq \mathbf{I}^{-1}(\boldsymbol{\theta}) \quad (7.10)$$

where  $\boldsymbol{\theta} = E_{\mathbf{Y}|\boldsymbol{\theta}}[\mathbf{t}(\mathbf{Y})]$  is the true value (or the true state of nature) of the parameter vector, assuming that the estimator  $\boldsymbol{\Theta} = \mathbf{t}(\mathbf{Y})$  is an unbiased estimator.

Identifiable parameters are those who can be estimated with little uncertainty or with small estimation variances, which can be approximated asymptotically with the CRLB. Therefore, the (*a priori*) identifiability can be assessed quantitatively using some scalar measures of the CRLB, for example, D-measure, which is the determinant of the CRLB (i.e.,  $|\mathbf{I}^{-1}(\boldsymbol{\theta})|$ ) as proposed by Mehra [3]. This scalar measure of identifiability offers a useful tool for the experimental design and/or sensor placement, where different candidates for input excitation and/or sensor configuration are to be compared in order to maximize the identifiability of the estimation parameters. Nevertheless, the D-measure of the FIM provides an overall assessment of the

estimation problem identifiability and offers no details on the contribution of different measurement data channels and/or the identifiability of individual parameters. These shortcomings are lifted in the next section by introducing a new measure of identifiability based on information entropy, which can offer a one-to-one identifiability measure between each output measurement channel and each individual model parameter. This proposed approach is inspired by the method presented in [23].

#### **7.4. Identifiability assessment based on Information-entropy approach**

In an identifiable parametric model, the measurements contain rich information about the model parameters and therefore, the parameter uncertainties are reduced significantly through the estimation process. Hence, the difference between the *a priori* and the *a posteriori* uncertainties of a model parameter can be used as a quantitative measure of information gained about the model parameter, or its identifiability. The Shannon Information entropy is a scalar measure of the uncertainty associated with a random variable. The gain in the information about the model parameters, which is expressed as the difference between the *a priori* and the *a posteriori* information entropy, can be used as a quantitative measure of identifiability of the model parameters. The information entropy gain (or entropy gain for brevity) is defined as

$$\Delta H(\boldsymbol{\theta}) = H(\boldsymbol{\theta}^{pri}) - H(\boldsymbol{\theta}^{pos}) \quad (7.11)$$

where  $H(\boldsymbol{\theta})$  denotes the Shannon Information entropy and is defined as [34]

$$H(\boldsymbol{\theta}) = -E_{\boldsymbol{\theta}} [\ln(p(\boldsymbol{\theta}))] \quad (7.12)$$

Assuming a Gaussian *a priori* distribution, i.e.,  $\boldsymbol{\theta}^{pri} \sim N(\boldsymbol{\theta}_0, \mathbf{P}_0)$ , the *a priori* entropy can be expressed as (see [40] for proof)

$$H(\boldsymbol{\theta}^{pri}) = \frac{n}{2} \ln(2\pi) + \frac{1}{2} \ln(|\mathbf{P}_0|) \quad (7.13)$$

where  $n = n_{\boldsymbol{\theta}}$ , and  $|\mathbf{X}| = \det(\mathbf{X})$  herein. Using Eqs. (8) and (12), the *a posteriori* entropy can be expressed as

$$\begin{aligned} H(\boldsymbol{\theta}^{pos}) &= -E_{\boldsymbol{\theta}^{pos}} [\ln(p^{pos}(\boldsymbol{\theta}))] \\ &= -E_{\boldsymbol{\theta}^{pos}} [\ln(l(\boldsymbol{\theta}, \mathbf{y}_{1:k}))] - E_{\boldsymbol{\theta}^{pos}} [\ln(p^{pri}(\boldsymbol{\theta}))] - \ln(c) \end{aligned} \quad (7.14)$$

The first term in the right-hand side of Eq. (7.14) is expressed as

$$E_{\boldsymbol{\theta}^{pos}} [\ln(l(\boldsymbol{\theta}, \mathbf{y}_{1:k}))] = \int_{\Omega} \Lambda(\boldsymbol{\theta}, \mathbf{y}_{1:k}) p^{pos}(\boldsymbol{\theta}) d\boldsymbol{\theta} \quad (7.15)$$

Assuming that the *a posteriori* PDF is densely distributed around the MAP estimates ( $\hat{\boldsymbol{\theta}}$ ), the integral in Eq. (7.15) can be simplified as (see Appendix 7.I)

$$E_{\boldsymbol{\theta}^{pos}} [\ln(l(\boldsymbol{\theta}, \mathbf{y}_{1:k}))] \approx \Lambda(\hat{\boldsymbol{\theta}}, \mathbf{y}_{1:k}) \quad (7.16)$$

It should be recognized that the underlying conditions stated in Appendix 7.I requires the successful solution of the MAP estimation problem with ideally small estimation uncertainties. These conditions may often be violated, especially when some of the considered model parameters are not identifiable.

Likewise, the second term in the right-hand side of Eq. (7.14) can be derived as

$$E_{\boldsymbol{\theta}^{pos}} [\ln(p^{pri}(\boldsymbol{\theta}))] \approx \ln(p^{pri}(\hat{\boldsymbol{\theta}})) \quad (7.17)$$

The last term in the right-hand side of Eq. (7.14) can be asymptotically (using large number of data samples) derived as (see Appendix 7.II for proof)

$$\ln(c) \approx \frac{1}{2} \ln \left( \left| \mathbf{I}(\hat{\boldsymbol{\theta}}) + \mathbf{P}_0^{-1} - \mathbf{J}(\hat{\boldsymbol{\theta}}) \right| \right) - \frac{n}{2} \ln(2\pi) - \Lambda(\hat{\boldsymbol{\theta}}, \mathbf{y}_{1:k}) - \ln(p^{pri}(\hat{\boldsymbol{\theta}})) \quad (7.18)$$

Substitution of Eqs. (12) and (16)-(18) back into Eq.(11) results in an approximate expression for the information gain as

$$\Delta H(\boldsymbol{\theta}) = \frac{1}{2} \ln \left( \left| \mathbf{I}(\hat{\boldsymbol{\theta}}) + \mathbf{P}_0^{-1} - \mathbf{J}(\hat{\boldsymbol{\theta}}) \right| \right) - \frac{1}{2} \ln \left( \left| \mathbf{P}_0^{-1} \right| \right) \quad (7.19)$$

The term  $\mathbf{I}(\hat{\boldsymbol{\theta}})$  in Eq. (7.19) is the FIM evaluated at the MAP estimates, which can be asymptotically expressed as (see Appendix 7.III)

$$\mathbf{I}(\hat{\boldsymbol{\theta}}) = \sum_{i=1}^k \left( \frac{\partial \hat{\mathbf{y}}_i(\boldsymbol{\theta})}{\partial \boldsymbol{\theta}} \right)_{\boldsymbol{\theta}=\hat{\boldsymbol{\theta}}}^T \mathbf{R}^{-1} \left( \frac{\partial \hat{\mathbf{y}}_i(\boldsymbol{\theta})}{\partial \boldsymbol{\theta}} \right)_{\boldsymbol{\theta}=\hat{\boldsymbol{\theta}}} \quad (7.20)$$

in which  $\mathbf{R}$  is the covariance matrix of the simulation error vector (see Eq. (7.5)). As mentioned earlier, by neglecting the model uncertainty, the simulation error accounts only for the measurement noise and therefore, the diagonal entries of  $\mathbf{R}$  are equal to the measurement noise variance at measurement channels. The diagonal entries of matrix  $\mathbf{R}$  work as weighting factors in Eq. (7.20); the more the measurement noise variance, the less the contribution of the corresponding measurement channel in the FIM. The measurement noise variances can be estimated through the estimation method (e.g., [31]), or they can be estimated in prior by quantifying different sources of measurement noise (e.g., sensor noise, DAQ noise, etc.).

The term  $\mathbf{P}_0^{-1}$  in Eq. (7.19) accounts for the *a priori* uncertainties in the model parameters. Moreover, the term  $\mathbf{J}(\hat{\boldsymbol{\theta}})$  in Eq. (7.19) is a function of the second order

sensitivities of the FE predicted response with respect to the material parameters, and the simulation error, which is the misfit between the FE predicted and measured response. The term  $\mathbf{J}(\hat{\boldsymbol{\theta}})$  accounts partially for the *a posteriori* identifiability and merges zero asymptotically (i.e., using large number of data samples,  $k$ ) under some idealizing conditions. The effects of this term are neglected herein assuming ideal asymptotic behavior; therefore, Eq. (7.19) reduces to:

$$\Delta H(\boldsymbol{\theta}) = \frac{1}{2} \ln\left(\left|\mathbf{I}(\hat{\boldsymbol{\theta}}) + \mathbf{P}_0^{-1}\right|\right) - \frac{1}{2} \ln\left(\left|\mathbf{P}_0^{-1}\right|\right) \quad (7.21)$$

Assuming non-informative prior (i.e., if the *a priori* PDF is sufficiently flat and close to uniform), the entropy gain in Eq. (7.19) is reduced to the following equation:

$$\Delta H(\boldsymbol{\theta}) = \frac{1}{2} \ln\left(\left|\mathbf{I}(\hat{\boldsymbol{\theta}})\right|\right) \quad (7.22)$$

Therefore, in the limiting case of non-informative prior, the information gain is a function of the determinant of the FIM. This is in agreement with D-measure for identifiability as proposed by Mehra [3]. It should be recognized that Eqs. (7.21) and (7.22) are derived based on the following conditions/assumptions:

- (i) The effects of model uncertainties are neglected. In other words, the real structure is assumed to be in the class of FE models.
- (ii) The measurement noise is assumed to be stationary, zero-mean, and independent Gaussian white noise.
- (iii) The MAP estimates of FE model parameters (i.e.,  $\hat{\boldsymbol{\theta}}$ ) exists and can be determined (or, equivalently, the estimator is unbiased).

(iv)  $\mathbf{I}(\hat{\boldsymbol{\theta}})$  is non-singular for any subset of data samples (i.e., Rothenberg condition for local identifiability is satisfied).

(v) The number of data samples is large enough (i.e., asymptotic behavior).

(vi) The *a posteriori* is unimodal and densely distributed around  $\hat{\boldsymbol{\theta}}$ . In other

words,  $\left| \frac{\partial^2 (\ln p^{pos}(\boldsymbol{\theta}))}{\partial \boldsymbol{\theta}^2} \right|_{\boldsymbol{\theta}=\hat{\boldsymbol{\theta}}} \ll 1$ . It should be noted that using the efficiency

properties of the estimator, this condition can be resulted from (iii), (iv), and (v).

Any violation of the abovementioned conditions adversely affects the validity of Eqs. (7.21) and (7.22). Although some of these conditions are partially violated in practical applications of identifiability assessment, Eqs. (7.21) and (7.22) still can be used as an approximate measure of identifiability for nonlinear models.

Eq. (7.21) can furthermore be related to the resolution analysis (i.e., the analysis of uncertainty) as proposed by Duijndam [41] and used by Tarantola [42]. Eq. (7.21) can be re-written as

$$\Delta H(\boldsymbol{\theta}) = -\frac{1}{2} \ln \left( \left( \mathbf{P}_0 \right)^{-1} \left( \mathbf{I}(\hat{\boldsymbol{\theta}}) + \mathbf{P}_0^{-1} \right)^{-1} \right) \quad (7.23)$$

where  $\left( \mathbf{I}(\hat{\boldsymbol{\theta}}) + \mathbf{P}_0^{-1} \right)^{-1}$  is the *a posteriori* CRLB (PCRLB) [43] and is the lower bound for the *a posteriori* covariance matrix of the parameter estimation, denoted by  $\mathbf{P}_{pos}$ . It

follows that  $\mathbf{P}_{pos} \geq \left( \mathbf{I}(\hat{\boldsymbol{\theta}}) + \mathbf{P}_0^{-1} \right)^{-1}$  and  $\mathbf{P}_{pos}$  asymptotically merges to the PCRLB.

Therefore, under the aforementioned conditions, Eq. (7.23) reduces to

$$\Delta H(\boldsymbol{\theta}) = -\frac{1}{2} \ln \left( \left| (\mathbf{P}_0)^{-1} \mathbf{P}_{pos} \right| \right) = -\frac{1}{2} \sum_{i=1}^n \ln(\lambda_i) \quad (7.24)$$

in which  $\lambda_i$  is the  $i^{\text{th}}$  eigenvalue of the generalized eigen problem  $\mathbf{P}_{pos} \mathbf{X} = \mathbf{P}_0 \mathbf{X} \lambda$ . Each eigenvalue gives a measure of the ratio of the *a posteriori* to the *a priori* variance in the direction expressed by the eigenvector  $\mathbf{x}_i$  in the parameter space. For example, the eigenvector  $\mathbf{x}_i$  corresponding to the smallest eigenvalue  $\lambda_i = \lambda_{\min}$  expresses the direction in the parameter space that has the most reduction in the uncertainties from *a priori* to *a posteriori*. In other words, the values of the eigenvalues express the relative degree of the reduction from *a priori* to *a posteriori* uncertainties in the principal directions in the parameter space.

In summary, the entropy gain as shown in Eq. (7.21) can be used as a measure of identifiability, i.e., the information contained in every measurement channel (or set of measurement channels) for every single (or a group of) material parameter. Following Eq. (7.21), the entropy gain is derived using the FIM and the *a priori* covariance matrix of the model parameters. The FIM (Eq. (7.20)) is derived using the  $\mathbf{R}$  matrix, and the FE response sensitivities with respect to the model parameters, which are evaluated at the MAP estimates of model parameters. However, in practical situations, the identifiability is often addressed before estimating the model parameters; therefore, the MAP estimates of model parameters are not available at the identifiability assessment stage. Hence, it is suggested herein to use the initial estimates of the model parameters to derive the FIM. Given the physical nature of a mechanics-based FE model parameters, the true values of the parameters are not

expected to be significantly far from their initial estimates, which are usually based on nominal engineering values. The error in the entropy gain resulted by approximating the MAP estimates of the model parameters with their initial estimates are quantified in the case study presented in the next section. Finally, as mentioned earlier, the diagonal entries of  $\mathbf{R}$  matrix in Eq. (7.21), or the measurement noise variances, are approximately estimated in prior by quantifying the sources of measurement noise.

### **7.5. Numerical case study**

A three-dimensional (3D) 5-story 2-by-1 bay reinforced concrete (RC) frame building model subjected to bidirectional seismic excitation is used to demonstrate the proposed framework for identifiability assessment (Figure 7.2). A set of nine parameters characterizing the nonlinear material constitutive model of the reinforced concrete are treated as unknown model parameters. The mechanics-based nonlinear finite element (FE) model of the building is developed in the open source software framework for earthquake simulation, OpenSees [44], and used to compute the response and response sensitivities of the building. Various response sets are extracted from the FE model and used to assess the identifiability of the individual model parameters based on the Information-theoretic approach presented in the previous section.



### 7.5.1. Description of the RC building structure and developed FE model

The building has two and one bays in the longitudinal and transverse directions, respectively, with plan dimensions of 10.0×6.0 m. The building has a total height of 20.0 m with constant story height of 4.0 m. The structure is designed as an intermediate moment-resisting RC frame for a moderate seismic risk zone (downtown Seattle, WA) with Site Class D and short-period and one-second spectral accelerations of  $S_{MS} = 1.37g$  and  $S_{M1} = 0.53g$ , respectively. Dead and live loads and corresponding seismic masses are calculated according to the 2012 International Building Code [45]. Longitudinal beams have a square cross-section of 0.40×0.40 m and are reinforced with 3 #8 longitudinal reinforcement bars at top and bottom, and #3 @ 100 mm transverse reinforcement. Transverse beams have a rectangular cross-section of 0.40×0.45 m and are reinforced with 4 #8 longitudinal reinforcement bars at top and bottom, and #3 @ 100 mm transverse reinforcement. The building has six identical 0.45×0.45 m RC columns reinforced with 8 #8 longitudinal reinforcement bars and #3 @ 150 mm transverse reinforcement. Grade 60 reinforcing steel is considered for the columns and beams. Figure 7.1 shows the building view, and details of the RC beam and column sections.

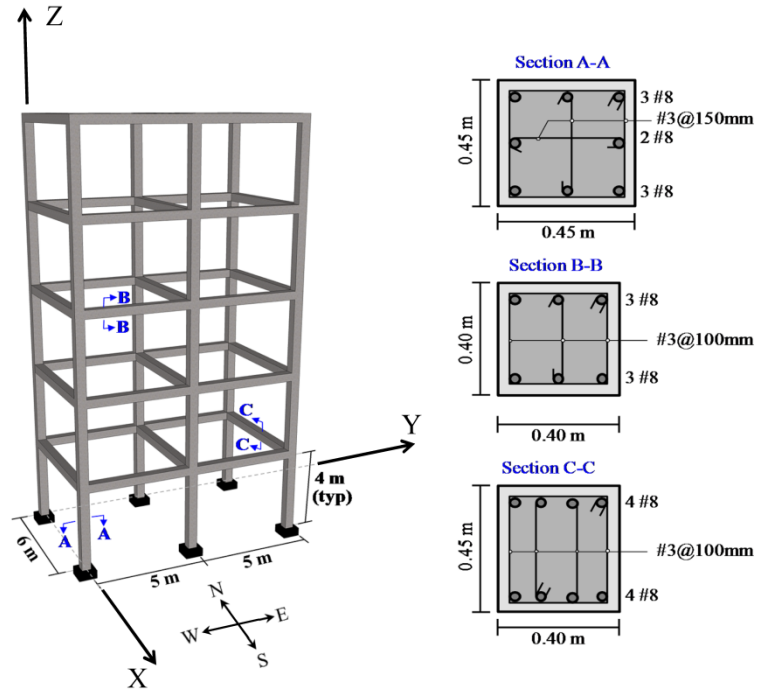


Figure 7.1: RC frame building structure: isometric view and cross-section of beams and columns.

The FE model of the structure is developed using distributed-plasticity, displacement-based, structural FE models. In this approach, the structure is spatially discretized using fiber-section, displacement-based, beam-column elements formulated using Bernoulli-Euler beam theory. The material nonlinearity can spread over several sections monitored along the element, which are called integration points. The sections are further discretized into layers or fibers [46], the stress-strain behavior of which is governed by associated (nonlinear) uniaxial material constitutive laws (see Figure 7.2). The steel reinforcements are modeled using the modified Giuffrè-Menegotto-Pinto material constitutive model [47] with smooth curved shaped loading and unloading branches as illustrated in Figure 7.3(a). This material model is characterized by eight parameters, which are subdivided into three primary parameters

and five secondary parameters. Treated as unknown FE model parameters, the three primary parameters are  $f_y$  = initial yield strength,  $E$  = elastic modulus, and  $b$  = strain hardening ratio. The other five secondary parameters are assumed known and constant and are selected based on the suggested values in [47]. The longitudinal steel reinforcements in beams are grade 60 and in columns, grade 75 steel reinforcements are used for longitudinal rebars. The selected constitutive law for the concrete material is based on the Popovics-Saenz concrete model ([48-49]), a typical cyclic response of which is shown in Figure 7.3(b). In general, this material model is governed by six parameters, which are subdivided into three primary parameters and three secondary parameters. The three primary parameters ( $f'_c$  = concrete compressive strength,  $E_c$  = initial tangent stiffness, and  $\varepsilon_c$  = concrete strain at maximum strength point) are treated as unknown FE model parameters while the other three parameters are assumed known and constant. The FE model parameter vector is defined as  $\hat{\theta} = [f_y^{col} \ E^{col} \ b^{col} \ f_y^{beam} \ E^{beam} \ b^{beam} \ f'_c \ E_c \ \varepsilon_c]$ . The true (exact) values of the FE model parameters are taken as  $f_{y,true}^{col} = 520$  MPa,  $E_{true}^{col} = 200$  GPa,  $b_{true}^{col} = 0.01$ ,  $f_{y,true}^{beam} = 410$  MPa,  $E_{true}^{beam} = 200$  GPa,  $b_{true}^{beam} = 0.02$ ,  $f'_{c,true} = 40$  MPa,  $E_{c,true} = 28$  GPa,  $\varepsilon_{c,true} = 0.004$ .

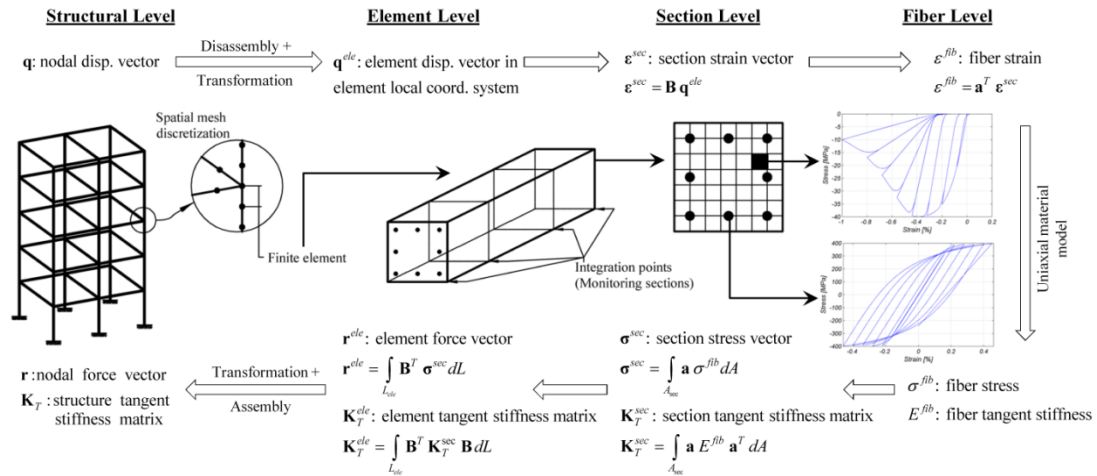


Figure 7.2: Hierarchical discretization levels in distributed plasticity structural FE models using fiber-section displacement-based beam-column elements (adapted from [30]).

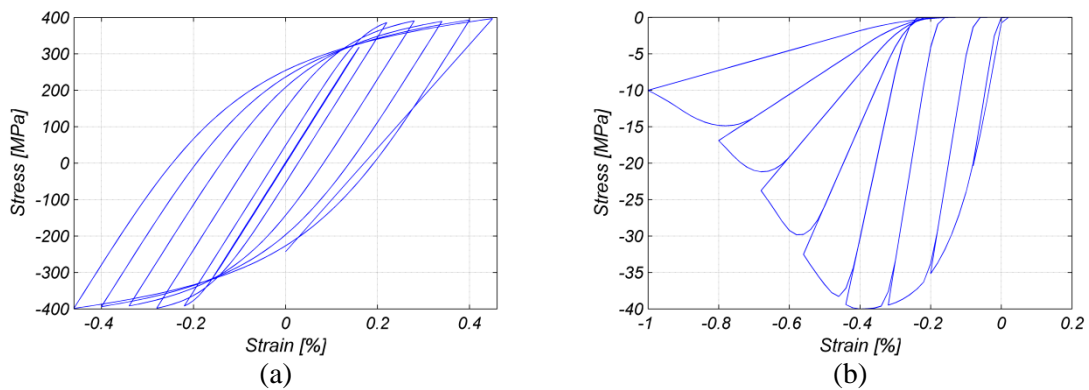


Figure 7.3: Typical cyclic behavior of the employed material models: (a) Giuffrè-Menegotto-Pinto for reinforcing steel material, and (b) Popovics-Saenz for concrete material.

A ground acceleration record from the 1994 Northridge earthquake (Sylmar County hospital station) [50] is selected for this study (see Figure 7.4). Both the north-south and east-west components of the base excitation are assumed to be deterministic (noiseless) and known. Nonlinear analysis is performed by first applying the gravity load quasi-statically and then the base excitation dynamically. The nonlinear dynamic time history analysis is performed using the Newmark average acceleration method

[35] to recursively integrate the equations of motion in time using a constant time step size of  $\Delta t = 0.02 \text{ sec}$ , and the Newton-Raphson method to solve iteratively the nonlinear incremental dynamic equations of equilibrium at each time step. Rayleigh damping [35] is used to model the damping energy dissipation characteristics (beyond material hysteretic energy dissipation) of the structure by assuming a damping ratio of 2 percent for the first and third modes after applying gravity loads ( $T_1 = 1.43 \text{ sec}$ ,  $T_2 = 1.37 \text{ sec}$ , and  $T_3 = 1.30 \text{ sec}$ ).

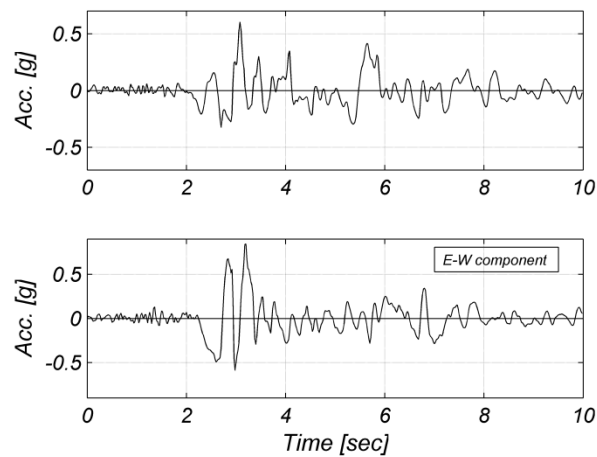


Figure 7.4: 1994 Northridge earthquake ground motion (Sylmar County hospital station); top:  $90^\circ$  component applied in N-S direction, and bottom:  $360^\circ$  component applied in E-W direction.

### 7.5.2. Identifiability assessment of the FE model parameters

The identifiability of the nine FE model parameters are evaluated in this case study by computing the gain in entropy of model parameters from various combinations of measurement data. To highlight the excellency of the proposed methodology in providing a one-to-one identifiability measure between different

measurement data sets and estimation parameters, ten different measurement data sets are considered herein and summarized in Table 7.1 (see Figure 7.1 for reference).

Table 7.1: Measurement data sets.

Set #	Description
S1	Absolute acceleration response in NS and EW directions measured at the north west corner of the first slab.
S2	Absolute acceleration response in NS and EW directions measured at the north west corner of the third slab.
S3	Absolute acceleration response in NS and EW directions measured at the north west corner of the fifth slab.
S4	Displacement response (relative to base) in NS and EW directions measured at the north west corner of the fifth slab.
S5	Base rotation in XX and YY directions of north middle column.
S6	Beam end rotation of the first floor west beam at the north end + beam end rotation of the first floor north-west beam at the west end.
S7	S5 + S6 (beam and column end rotation responses).
S8	S1 + S2 + S3 (absolute acceleration responses of three slabs).
S9	S1 + S2 + S3 + S4 (absolute acceleration responses of three slabs + roof drift response).
S10	S1 + S2 + S3 + S4 + S5 + S6 (absolute acceleration responses of three slabs + roof drift response + beam and column end rotation responses).

As mentioned before, the information gain is evaluated using the FIM, and the *a priori* covariance matrix of the model parameters. The FIM is approximated using the initial estimates of the FE model parameters and the  $\mathbf{R}$  matrix. The initial estimates of FE model parameters ( $\hat{\boldsymbol{\theta}}_0$ ) are selected as  $\hat{\theta}_{0,1} = 1.30 f_{y,true}^{col}$ ,  $\hat{\theta}_{0,2} = 1.20 E_{true}^{col}$ ,  $\hat{\theta}_{0,3} = 1.25 b_{true}^{col}$ ,  $\hat{\theta}_{0,4} = 0.80 f_{y,true}^{beam}$ ,  $\hat{\theta}_{0,5} = 0.70 E_{true}^{beam}$ ,  $\hat{\theta}_{0,6} = 0.75 b_{true}^{beam}$ ,  $\hat{\theta}_{0,7} = 0.85 f'_{c,true}$ ,  $\hat{\theta}_{0,8} = 1.20 E_{c,true}$ ,  $\hat{\theta}_{0,9} = 0.70 \varepsilon_{c,true}$ . The diagonal entries of  $\mathbf{R}$  matrix, which are used in computing the FIM, are the measurement variance corresponding to different measurement channels. The amplitude of the measurement noise for the acceleration measurements is estimated as 1% g RMS, for the

displacement measurements is estimated as 0.5 % [*m*] RMS, and for beam and column rotation measurements is estimated as 0.05% [*Rad*] RMS. The covariance matrix of the initial estimates of the FE model parameter vector, which quantifies the uncertainty in the initial estimates of the FE model parameters, is selected as a diagonal matrix  $\mathbf{P}_0 = [p_i]$ . The term  $p_i$ , which is the  $i^{\text{th}}$  diagonal entry of  $\mathbf{P}_0$ , is the variance of the initial estimate of the  $i^{\text{th}}$  FE model parameter and is selected as  $p_i = (0.10 \hat{\theta}_{0,i})^2$ . Finally, it should be mentioned that the FE model parameters are normalized by their corresponding initial estimates as recommended in [30-31]. As a result of the normalization, the sensitivities of the FE response with respect to the model parameters will have the same order of magnitude. This recommendation is followed herein and the presented results are based on FE model parameters normalized by their corresponding initial estimates.

Figure 7.5 shows the time history of the entropy gain (measured in nats) for all the nine FE model parameters from the ten different measurement data sets as listed in Table 7.1. As is expected, S10 has the highest information content about the model parameters, while the local responses (S5 and S6) have the lowest. The initial flat stage in this figure corresponds to the first 2.5 seconds of the earthquake, where the level of base excitation is small and the dynamic response of the structure contains information only about the elastic-related model parameters. As the input motion intensifies, the response becomes more sensitive to the yield and post-yield related material parameters and therefore, the information gain jumps up remarkably.

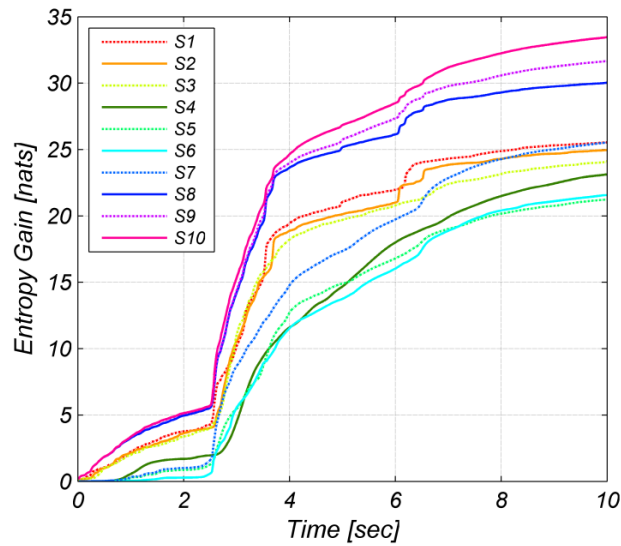


Figure 7.5: Time history of the entropy gain for nine FE model parameters from different measurement data sets.

Although Figure 7.5 can provide quantitative measure of information contained in various measurement data sets (and therefore can be used for optimal sensor design and placement purposes), it does not provide any insight about the information gain of individual parameters. The information gain of parameter  $\theta_i$ , or  $\Delta H(\theta_i)$  (see Eq. (7.21)), provides the information contained in the corresponding measurement data set about  $\theta_i$ . Figure 7.6 shows the information gain for each one of the nine FE model parameters from different measurement data sets. The one-to-one measure of identifiability in this figure clearly represents the amount of information each measurement channel carries about each individual parameter. This representation provides an excellent tool for estimation problem design, i.e., choosing the identifiable parameter sets, and deciding on the most informative sensor configuration. Figure 7.7 shows the same results in a graph format.



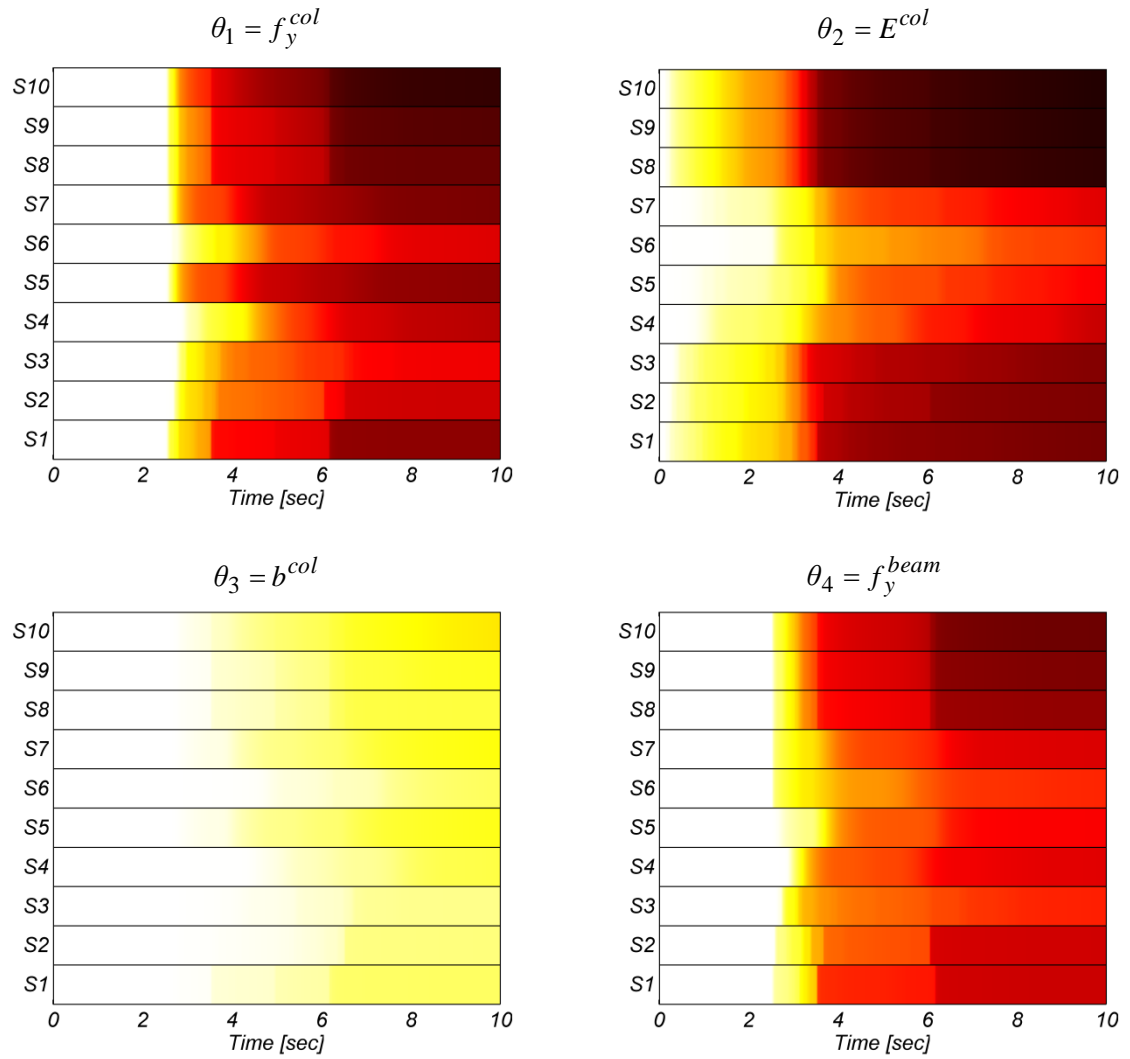


Figure 7.6: Entropy gain (in nats) time history for each individual FE model parameter from different measurement data sets.

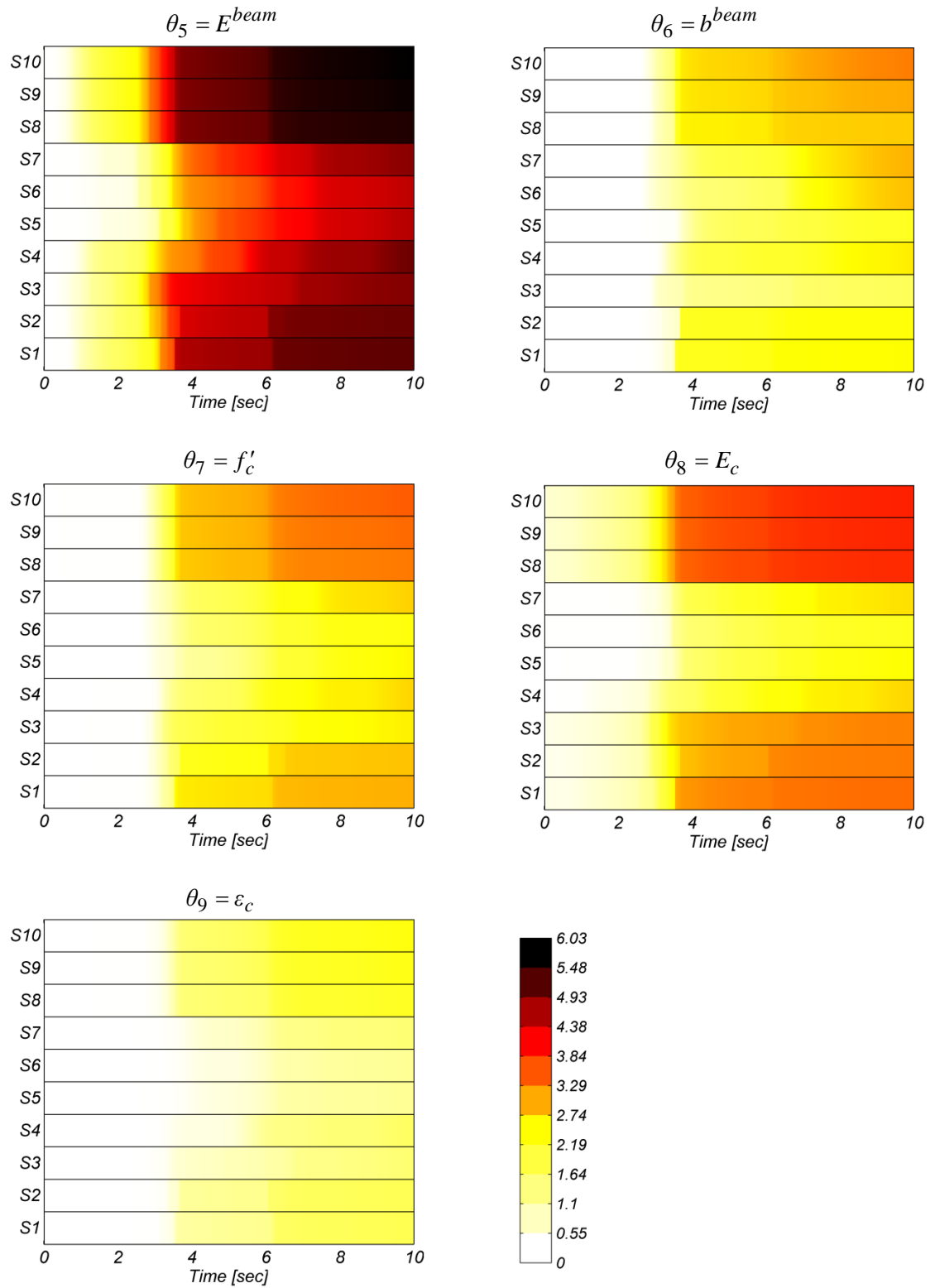


Figure 7.6 (continued): Entropy gain (in nats) time history for each individual FE model parameter from different measurement data sets.

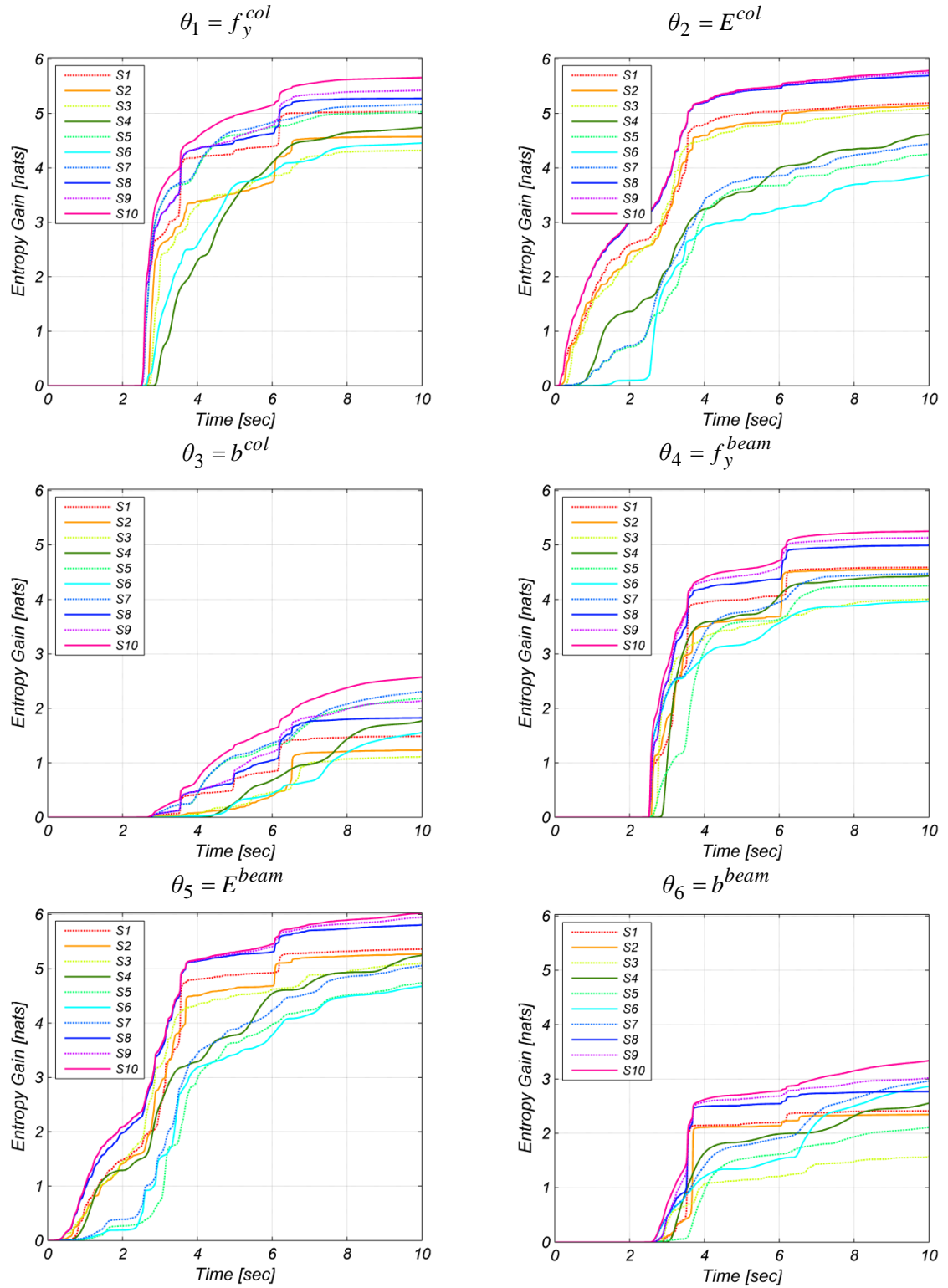


Figure 7.7: Entropy gain time history for each individual FE model parameter from different measurement data sets.

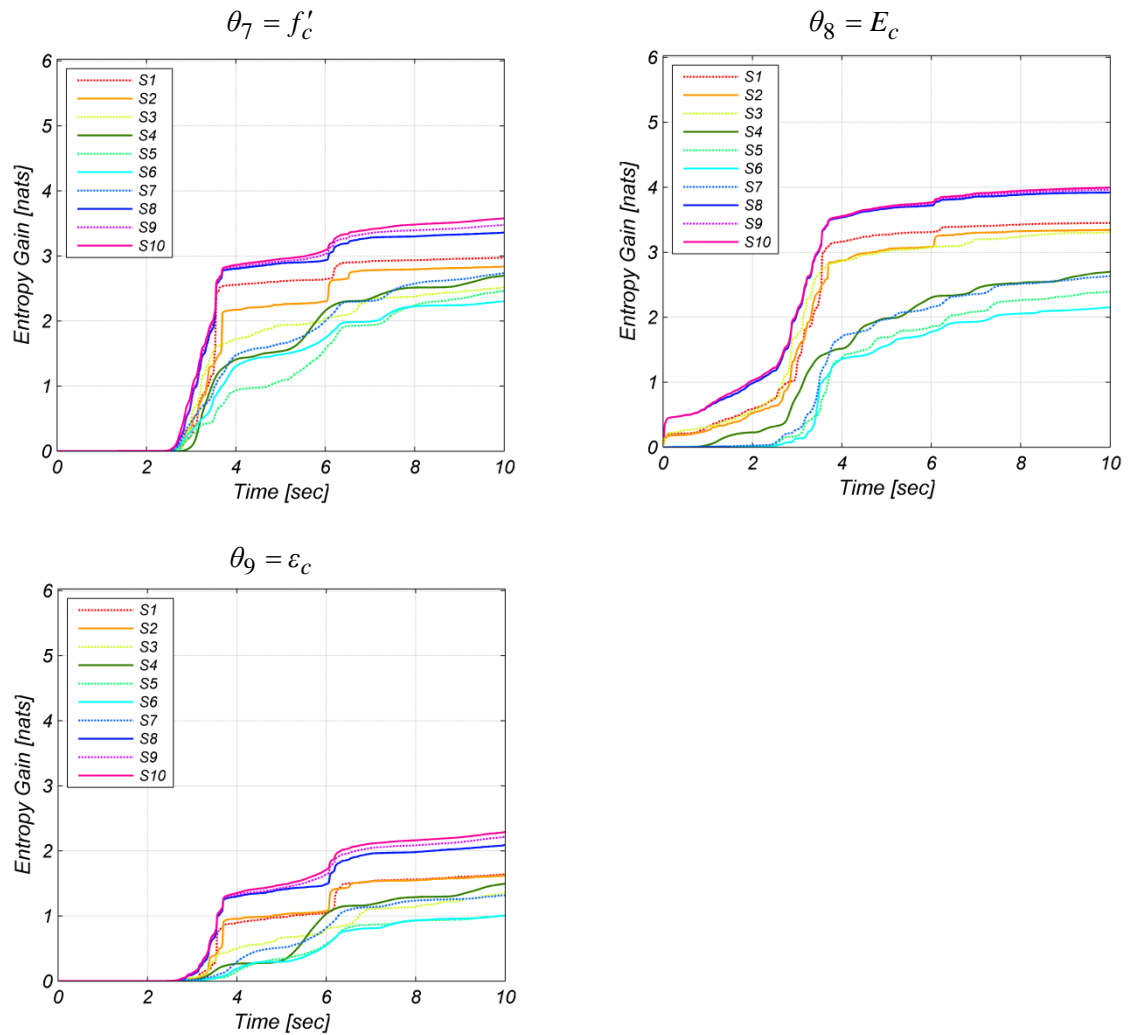


Figure 7.7 (continued): Entropy gain time history for each individual FE model parameter from different measurement data sets.

Likewise, Figure 7.8 shows the breakdown of information contained in each measurement data set about the nine FE model parameters. The results are only shown for some selected data sets for brevity. Finally, Figure 7.9 correlates the information contained in each measurement data set with each FE model parameter. This one-to-one identifiability measure is an elegant way to evaluate the identifiability of individual model parameters versus the candidate measurement data set.

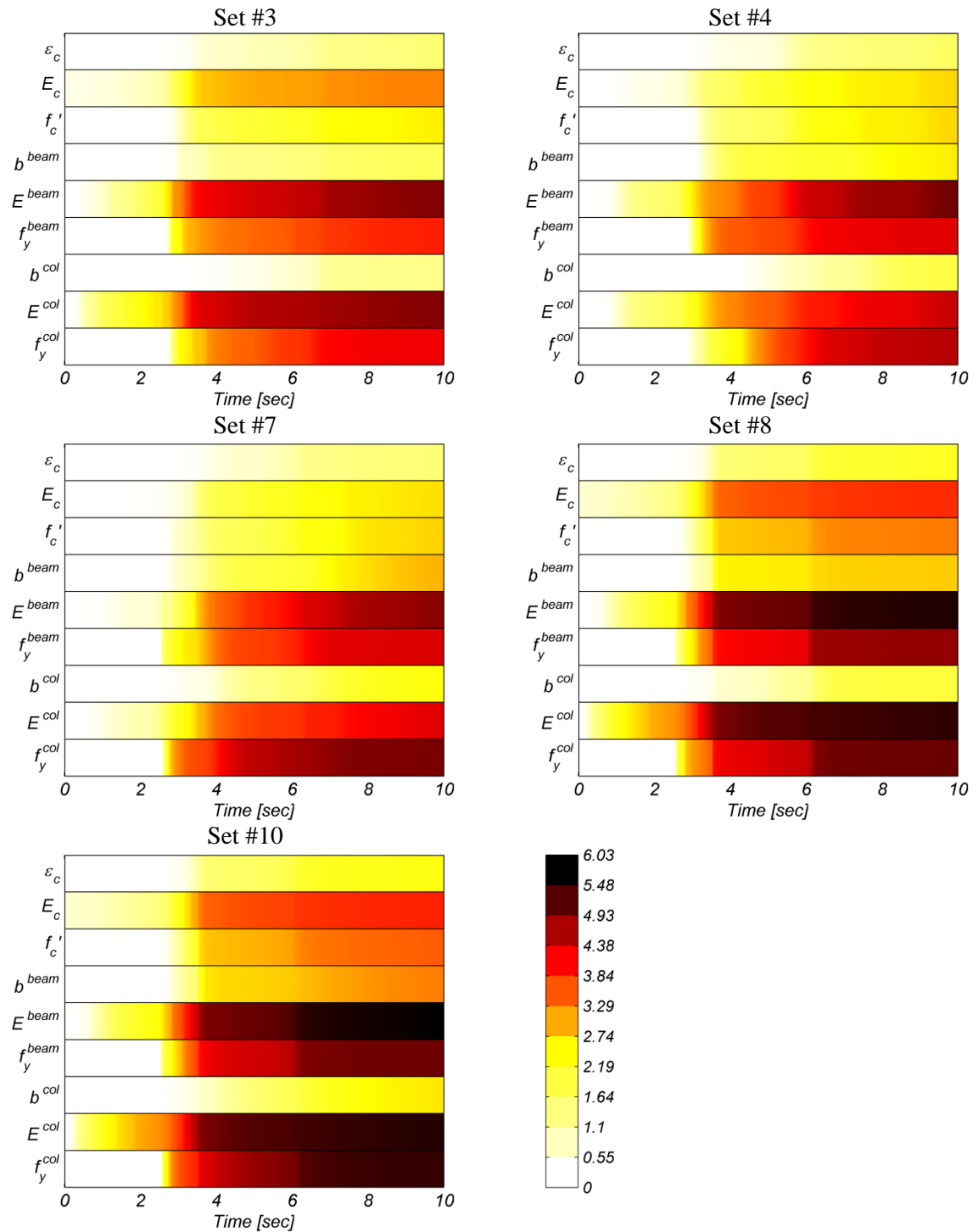


Figure 7.8: Entropy gain (in nats) time history from different measurement data sets.

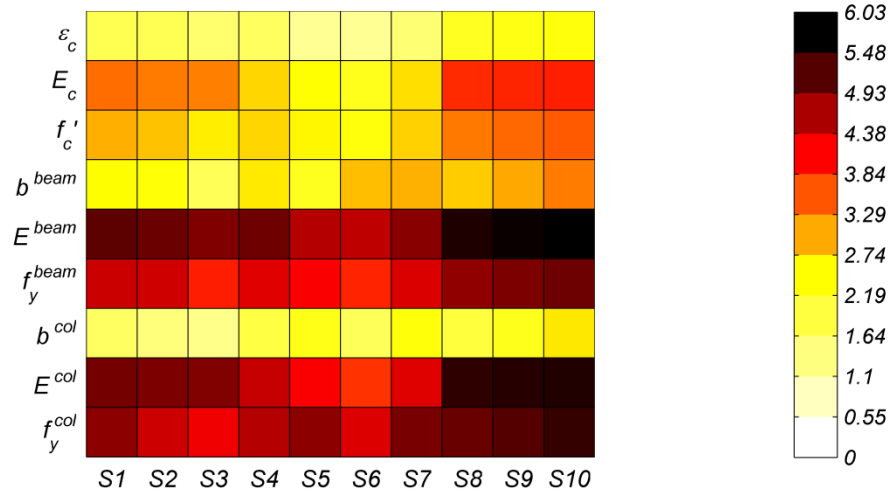


Figure 7.9: The correlation of the total entropy gain (in nats) between individual model parameters and measurement data sets.

### 7.5.3. Miscellaneous discussions

The results presented in the previous section are based on the information gain of each parameter, as if it is estimated individually. However, in a practical estimation problem, a group of parameters are estimated together and therefore, it can be realized intuitively that the amount of information each parameter receives among a group is less than the information the parameter receives when it is alone. This concept can be expressed mathematically by introducing conditional information entropy [34] as

$$H(\boldsymbol{\theta}_i|\boldsymbol{\theta}_j) = -E_{\boldsymbol{\theta}_i, \boldsymbol{\theta}_j} [\ln(p(\boldsymbol{\theta}_i|\boldsymbol{\theta}_j))] = H(\boldsymbol{\theta}_i, \boldsymbol{\theta}_j) - H(\boldsymbol{\theta}_j) \quad (7.25)$$

in which  $H(\boldsymbol{\theta}_i|\boldsymbol{\theta}_j)$  expresses the amount of information  $\boldsymbol{\theta}_i$  receives when it is jointly estimated with  $\boldsymbol{\theta}_j$ . Following Eq. (7.25), the conditional information gain can be derived as

$$\Delta H(\boldsymbol{\theta}_i | \boldsymbol{\theta}_j) = \frac{1}{2} \ln \left( \left| \mathbf{I}(\hat{\boldsymbol{\theta}}) + \mathbf{P}_0^{-1} \right| \right) - \frac{1}{2} \ln \left( \left| \mathbf{P}_0^{-1} \right| \right) - \frac{1}{2} \ln \left( \left| \mathbf{I}(\hat{\boldsymbol{\theta}}_j) + \mathbf{P}_{0, \boldsymbol{\theta}_j}^{-1} \right| \right) + \frac{1}{2} \ln \left( \left| \mathbf{P}_{0, \boldsymbol{\theta}_j}^{-1} \right| \right) \quad (26)$$

where  $\mathbf{P}_{0, \boldsymbol{\theta}_j}$  is the initial covariance matrix of  $\boldsymbol{\theta}_j$ , and it is assumed that

$$\boldsymbol{\theta} = \begin{bmatrix} \boldsymbol{\theta}_i^T & \boldsymbol{\theta}_j^T \end{bmatrix}^T. \text{ It can be proved that } \Delta H(\boldsymbol{\theta}_i | \boldsymbol{\theta}_j) \leq \Delta H(\boldsymbol{\theta}_i).$$

Figure 7.10 compares the individual entropy gain for each of the nine FE model parameters with the conditional information gain of each parameter given the other eight parameters for data set S10. This figure clearly shows the reduction in entropy gain of a parameter as it is estimated among a group of parameters.

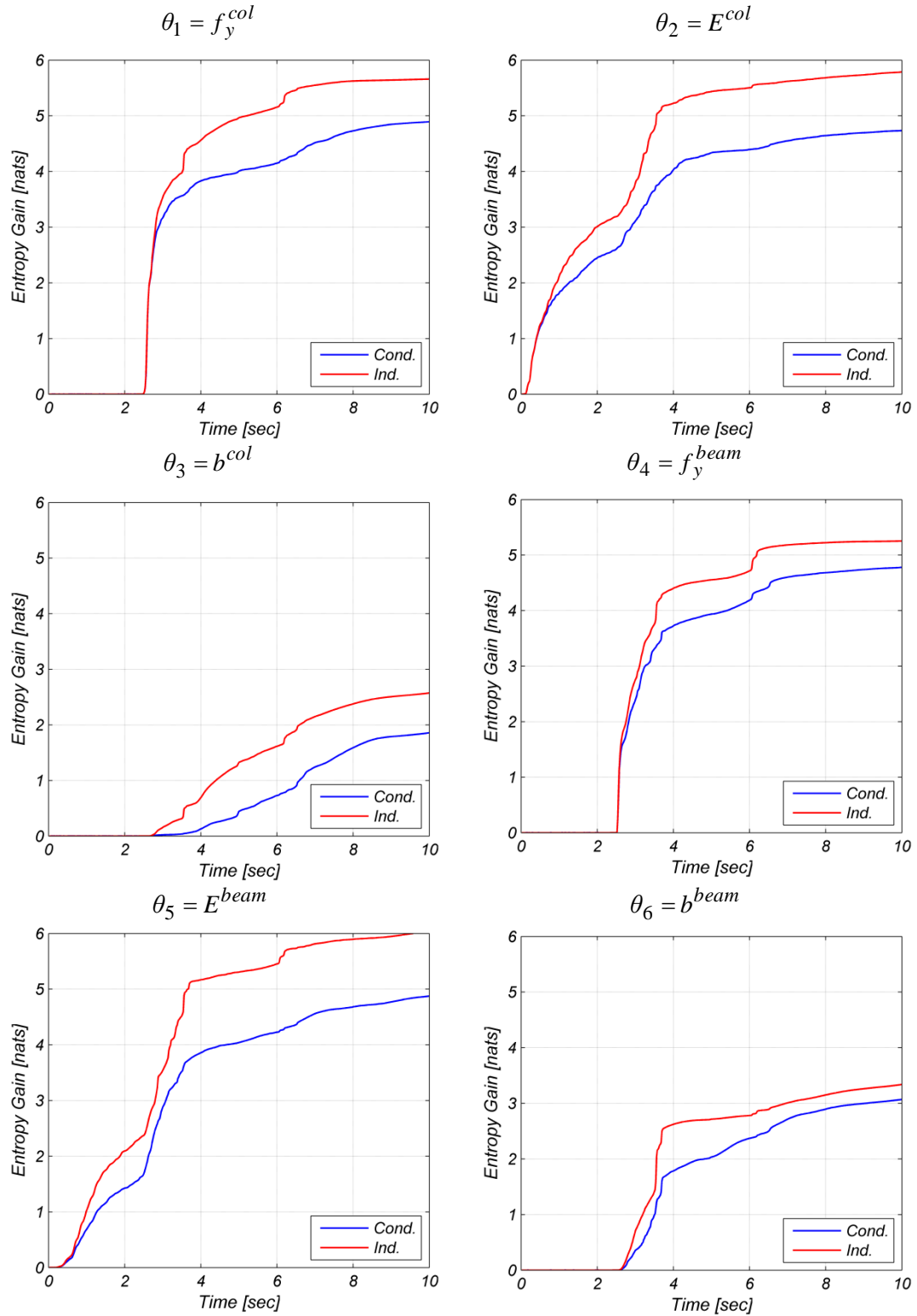


Figure 7.10: Comparison of the individual versus conditional entropy gain for S10.



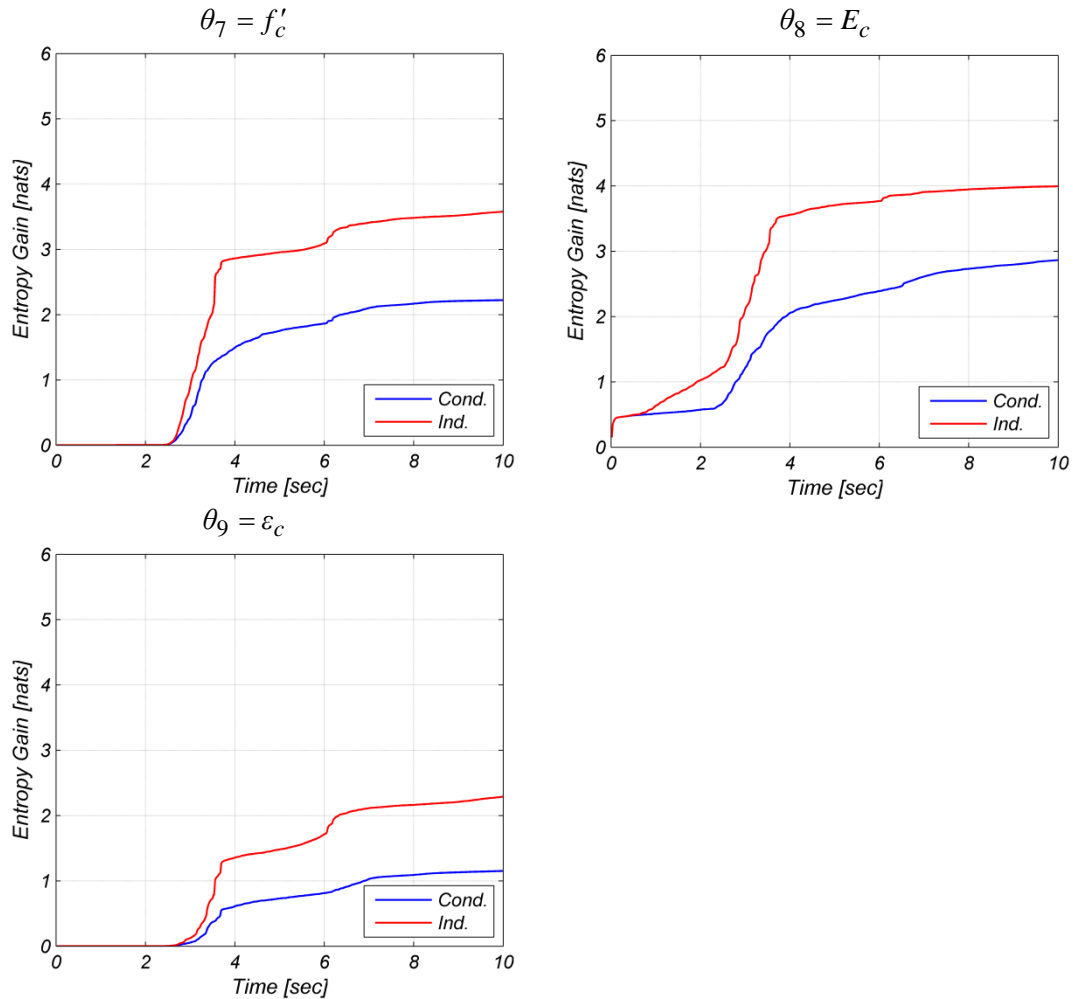


Figure 7.10 (continued): Comparison of the individual versus conditional entropy gain for S10.

The difference between the individual versus conditional information gain for a model parameter (as shown in Figure 7.10) expresses the amount of mutual information between the parameters. The mutual information between  $\theta_i$  and  $\theta_j$  is defined as [34]

$$I(\theta_i, \theta_j) = E_{\theta_i, \theta_j} \left[ \ln \left( \frac{p(\theta_i, \theta_j)}{p(\theta_i)p(\theta_j)} \right) \right] = H(\theta_i) - H(\theta_i | \theta_j) = H(\theta_i) + H(\theta_j) - H(\theta_i, \theta_j) \quad (7.27)$$

Mutual information  $I(\theta_i, \theta_j)$  measures the amount of information  $\theta_i$  carries about  $\theta_j$  and can be interpreted loosely as the measure of statistical dependence between  $\theta_i$  and  $\theta_j$ . Figure 7.11 shows the mutual entropy gain between each pair of the model parameters. The diagonals in this figure are the entropy gain of the corresponding parameter, and the off diagonals are the mutual entropy gain between the two corresponding parameters. This figure clearly illustrates the dependence between model parameters. For example, it can be observed that  $f'_c$  has noticeable dependence on  $\varepsilon_c$  and  $E^{beam}$ , and some dependence on  $E_c$ . This figure can facilitate the choice of model parameter set to be estimated. As a rule of thumb, if the measurement data set contains significant information about a pair of strongly dependent parameters, they (most likely) can be estimated jointly; however, if the information is limited, the strong dependence between the two parameters may adversely affect their successful identification.

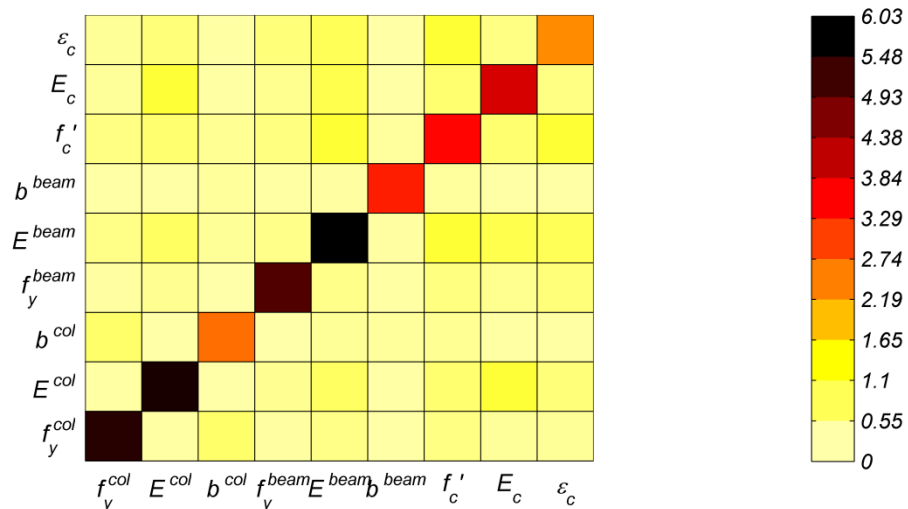


Figure 7.11: Mutual entropy gain (in nats) of the FE model parameters.

As mentioned earlier, since the MAP estimates of the model parameters may not be available at the stage of identifiability assessment, the FIM and therefore, the entropy gain are computed based on the initial estimates of model parameters. It is, however, hypothesized that this approximation for the case of FE model parameters does not introduce any significant error in the computed entropy gains. Figure 7.12 compares the entropy gain of individual FE model parameters computed using the initial and true values of the model parameters. As was hypothesized, the differences between the entropy gains are minor.

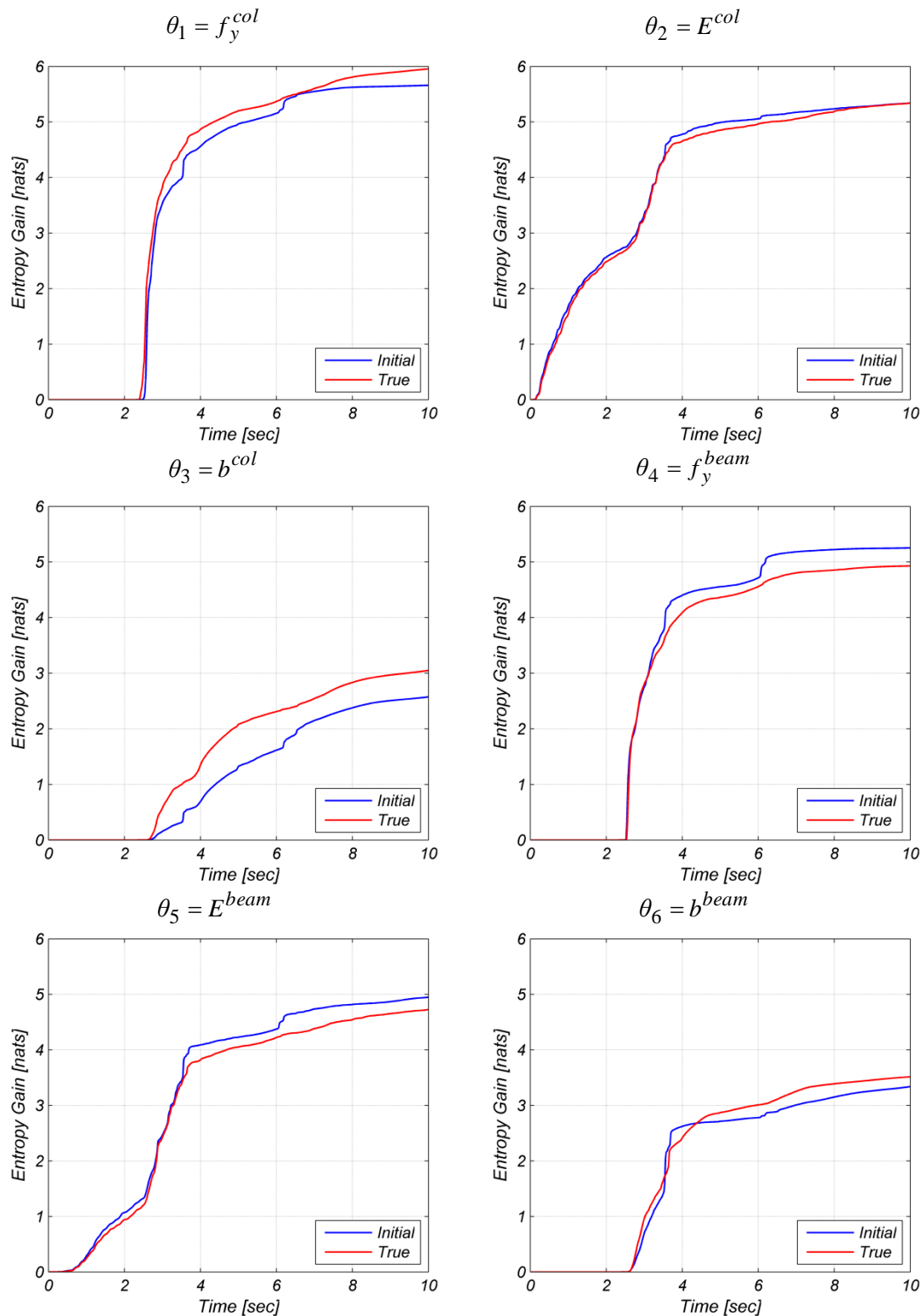


Figure 7.12: Comparison of the entropy gain computed using the initial and true values of FE model parameters for S10.

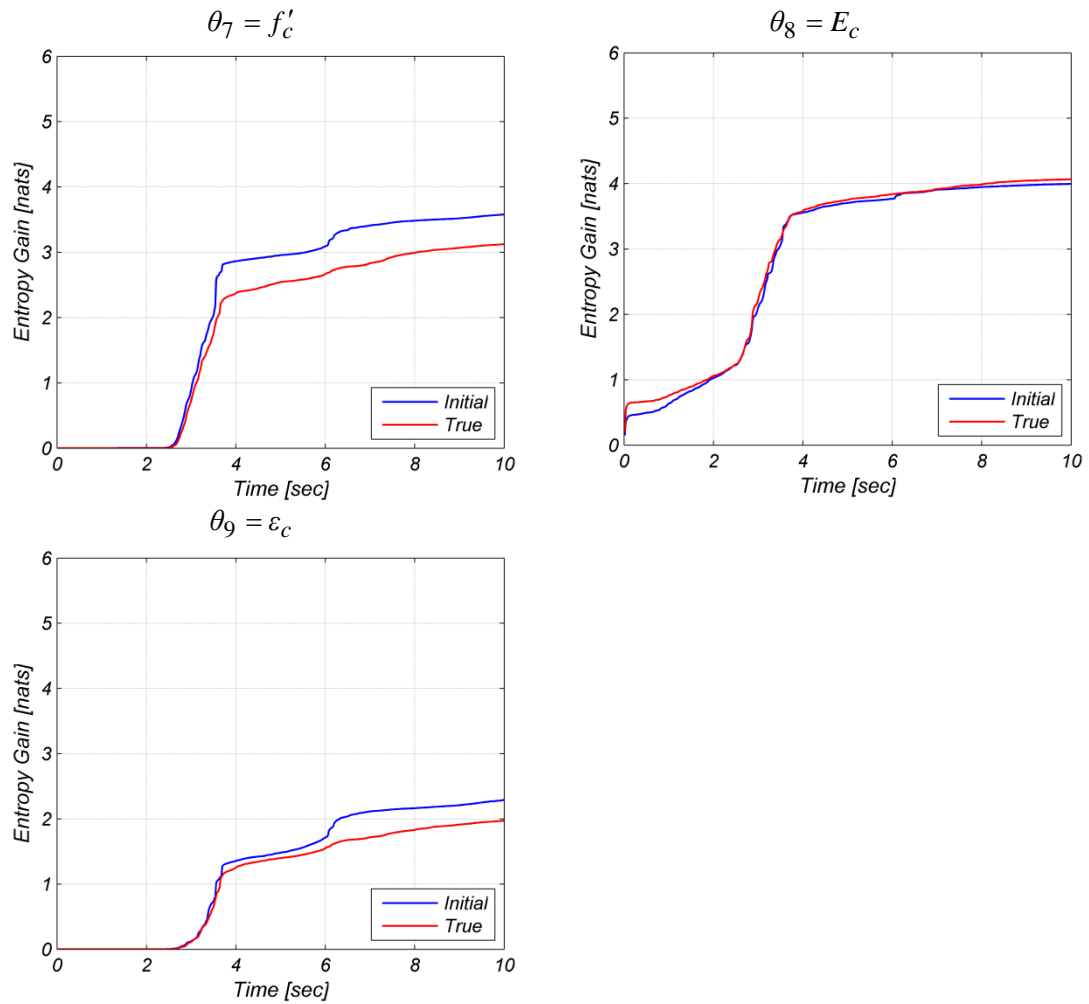


Figure 7.12 (continued): Comparison of the entropy gain computed using the initial and true values of FE model parameters for S10.

## 7.6. Conclusions

This study proposed a novel approach based on information theory for identifiability assessment of finite element (FE) model parameters in nonlinear FE model updating, which is used for nonlinear system and damage identification of civil structures. The proposed approach is rooted in the Bayesian inference method and

utilizes the Shannon entropy as a measure of inherent uncertainty in the model parameters. The difference in the entropy of *a priori* and *a posteriori* model parameters, which is referred to as entropy gain, is interpreted as the reduction in uncertainties of model parameter and used as a measure of identifiability. The entropy gain approach offers a one-to-one measure of identifiability to evaluate the amount of information contained in each measurement data set about each model parameter. The proposed approach provides an excellent tool for systematic parameter selection, optimal sensor design, selection of measurement data sets, and experiment design.

An approximate expression for entropy gain was derived under some regularizing assumptions (i.e., estimator unbiasedness and efficiency, asymptotic conditions, etc.). The entropy gain, in its most general case, was found to be a approximate function of the Fisher Information matrix (FIM), the second order sensitivities of the FE predicted response with respect to the material parameters, the simulation error (= the difference between the FE predicted and measured structural responses), and the *a priori* covariance matrix of the model parameters. Assuming a large number of measurement data (i.e., asymptotic conditions), the entropy gain was reduced to a function of the FIM and the *a priori* covariance matrix. The FIM depends on the FE response sensitivities, and the covariance matrix of the measurement noise, which is estimated in prior by approximately quantifying the noise sources affecting each measurement channel.

The application of the proposed approach in this study is not limited to the structural system identification problems; yet, it offers a general framework for

evaluating the identifiability of model parameters in any nonlinear system identification problem. The one-to-one measure of identifiability between model parameters and measurement data sets and the time resolution (i.e., the entropy gain time history for each individual parameter) are unique features of the proposed method that can be used in various applications from other engineering fields. A 3D five story reinforced concrete frame building model was used as a case study to illustrate the proposed identifiability assessment method. The FE model of the structure was developed using state-of-the-art mechanics-based nonlinear structural FE modeling technique, and subjected to a bi-directional earthquake base excitation. The FE model depended on nine model parameters, characterizing the nonlinear material law of reinforced concrete. The identifiability of the FE model parameters were evaluated by computing the gain in entropy of model parameters from various combinations of measurement data sets. The application example illustrated the perfection of the proposed method in evaluating the information content of each measurement channel about each estimation parameter.

## **Acknowledgments**

Partial support for this work was provided by the teaching assistantships from the Department of Structural Engineering at University of California, San Diego and the researcher assistantship received through my advisor, Professor Joel P. Conte. Chapter 7, in part, is currently being prepared for submission for publication. The

dissertation author is the primary investigator and author of this material and Rodrigo Astroza, Joel P. Conte, and Robert Bitmead are the co-authors.



## Appendix 7.I: Approximating the a posteriori Expectation

Suppose the *a posteriori* expectation of a general scalar function  $h(\boldsymbol{\theta})$  as:

$$I = E_{\boldsymbol{\theta}^{pos}} [h(\boldsymbol{\theta})] = \int_{\Omega} h(\boldsymbol{\theta}) p^{pos}(\boldsymbol{\theta}) d\boldsymbol{\theta} \quad (7.28)$$

where  $p^{pos}(\boldsymbol{\theta}) = c \times l(\boldsymbol{\theta}, \mathbf{y}_{1:k}) \times p^{pri}(\boldsymbol{\theta})$  (see Eq. (7.8)). Suppose  $\hat{\boldsymbol{\theta}}$  to be the MAP

estimate, which means that  $p^{pos}(\boldsymbol{\theta})$  has a (local) maximum at  $\boldsymbol{\theta} = \hat{\boldsymbol{\theta}}$ , i.e.,  $\frac{\partial p^{pos}(\boldsymbol{\theta})}{\partial \boldsymbol{\theta}} = \mathbf{0}$ .

Define minus log *a posteriori* PDF as

$$\Delta(\boldsymbol{\theta}) = -\ln(p^{pos}(\boldsymbol{\theta})) \quad (7.29)$$

The Taylor series expansion of  $\Delta(\boldsymbol{\theta})$  around  $\hat{\boldsymbol{\theta}}$  yields:

$$\Delta(\boldsymbol{\theta}) \approx \Delta(\hat{\boldsymbol{\theta}}) + \frac{\partial \Delta(\boldsymbol{\theta})}{\partial \boldsymbol{\theta}} \Big|_{\boldsymbol{\theta}=\hat{\boldsymbol{\theta}}} (\boldsymbol{\theta} - \hat{\boldsymbol{\theta}}) + \frac{1}{2} (\boldsymbol{\theta} - \hat{\boldsymbol{\theta}})^T \frac{\partial^2 \Delta(\boldsymbol{\theta})}{\partial \boldsymbol{\theta}^2} \Big|_{\boldsymbol{\theta}=\hat{\boldsymbol{\theta}}} (\boldsymbol{\theta} - \hat{\boldsymbol{\theta}}) \quad (7.30)$$

in which  $\frac{\partial \Delta(\boldsymbol{\theta})}{\partial \boldsymbol{\theta}} \Big|_{\boldsymbol{\theta}=\hat{\boldsymbol{\theta}}} = \mathbf{0}$ , and  $\frac{\partial^2 \Delta(\boldsymbol{\theta})}{\partial \boldsymbol{\theta}^2} = \frac{\partial}{\partial \boldsymbol{\theta}} \left( \frac{\partial \Delta(\boldsymbol{\theta})}{\partial \boldsymbol{\theta}} \right)^T$ . The function  $\Delta(\boldsymbol{\theta})$  has a local

minimum at  $\boldsymbol{\theta} = \hat{\boldsymbol{\theta}}$ ; therefore,  $\frac{\partial^2 \Delta(\boldsymbol{\theta})}{\partial \boldsymbol{\theta}^2}$  is positive definite at  $\boldsymbol{\theta} = \hat{\boldsymbol{\theta}}$ . Substitution of Eq.

(7.30) into Eq. (7.28) results in:

$$I = \int_{\Omega} h(\boldsymbol{\theta}) e^{-\Delta(\boldsymbol{\theta})} d\boldsymbol{\theta} \approx \int_{\Omega} h(\boldsymbol{\theta}) e^{-\Delta(\hat{\boldsymbol{\theta}})} e^{-\frac{1}{2} (\boldsymbol{\theta} - \hat{\boldsymbol{\theta}})^T \frac{\partial^2 \Delta(\boldsymbol{\theta})}{\partial \boldsymbol{\theta}^2} \Big|_{\boldsymbol{\theta}=\hat{\boldsymbol{\theta}}} (\boldsymbol{\theta} - \hat{\boldsymbol{\theta}})} d\boldsymbol{\theta} \quad (7.31)$$

This integral can be solved using the Laplace method for Gaussian Integrals [51].

Assuming that  $\left| \frac{\partial^2 \Delta(\boldsymbol{\theta})}{\partial \boldsymbol{\theta}^2} \Big|_{\boldsymbol{\theta}=\hat{\boldsymbol{\theta}}} \gg 1$ , the main contribution of the integral comes from

small neighborhood of  $\hat{\boldsymbol{\theta}}$ . Moreover, it is assumed that  $h(\boldsymbol{\theta})$  is sufficiently flat around  $\hat{\boldsymbol{\theta}}$ , and  $h(\hat{\boldsymbol{\theta}}) \neq 0$ ; therefore, it follows that:

$$I \approx \int_{\hat{\boldsymbol{\theta}}-\boldsymbol{\varepsilon}}^{\hat{\boldsymbol{\theta}}+\boldsymbol{\varepsilon}} h(\boldsymbol{\theta}) e^{-\Delta(\boldsymbol{\theta})} d\boldsymbol{\theta} \approx h(\hat{\boldsymbol{\theta}}) e^{-\Delta(\hat{\boldsymbol{\theta}})} \int_{\hat{\boldsymbol{\theta}}-\boldsymbol{\varepsilon}}^{\hat{\boldsymbol{\theta}}+\boldsymbol{\varepsilon}} e^{-\frac{1}{2}(\boldsymbol{\theta}-\hat{\boldsymbol{\theta}})^T \frac{\partial^2 \Delta(\boldsymbol{\theta})}{\partial \boldsymbol{\theta}^2} \Big|_{\boldsymbol{\theta}=\hat{\boldsymbol{\theta}}} (\boldsymbol{\theta}-\hat{\boldsymbol{\theta}})} d\boldsymbol{\theta} \quad (7.32)$$

The multi-dimensional Gaussian integral can be found as

$$\int_{\hat{\boldsymbol{\theta}}-\boldsymbol{\varepsilon}}^{\hat{\boldsymbol{\theta}}+\boldsymbol{\varepsilon}} e^{-\frac{1}{2}(\boldsymbol{\theta}-\hat{\boldsymbol{\theta}})^T \frac{\partial^2 \Delta(\boldsymbol{\theta})}{\partial \boldsymbol{\theta}^2} \Big|_{\boldsymbol{\theta}=\hat{\boldsymbol{\theta}}} (\boldsymbol{\theta}-\hat{\boldsymbol{\theta}})} d\boldsymbol{\theta} \approx \int_{\boldsymbol{\Omega}} e^{-\frac{1}{2}(\boldsymbol{\theta}-\hat{\boldsymbol{\theta}})^T \frac{\partial^2 \Delta(\boldsymbol{\theta})}{\partial \boldsymbol{\theta}^2} \Big|_{\boldsymbol{\theta}=\hat{\boldsymbol{\theta}}} (\boldsymbol{\theta}-\hat{\boldsymbol{\theta}})} d\boldsymbol{\theta} = \frac{(2\pi)^{n/2}}{\left| \frac{\partial^2 \Delta(\boldsymbol{\theta})}{\partial \boldsymbol{\theta}^2} \Big|_{\boldsymbol{\theta}=\hat{\boldsymbol{\theta}}} \right|^{1/2}} \quad (7.33)$$

where  $n = n_{\boldsymbol{\theta}} = \dim(\boldsymbol{\theta})$ . Therefore,

$$I \approx h(\hat{\boldsymbol{\theta}}) e^{-\Delta(\hat{\boldsymbol{\theta}})} \frac{(2\pi)^{n/2}}{\left| \frac{\partial^2 \Delta(\boldsymbol{\theta})}{\partial \boldsymbol{\theta}^2} \Big|_{\boldsymbol{\theta}=\hat{\boldsymbol{\theta}}} \right|^{1/2}} = h(\hat{\boldsymbol{\theta}}) p^{pos}(\hat{\boldsymbol{\theta}}) \frac{(2\pi)^{n/2}}{\left| \frac{\partial^2 \Delta(\boldsymbol{\theta})}{\partial \boldsymbol{\theta}^2} \Big|_{\boldsymbol{\theta}=\hat{\boldsymbol{\theta}}} \right|^{1/2}} \quad (7.34)$$

For a unimodal *a posteriori* PDF that is densely distributed around  $\hat{\boldsymbol{\theta}}$ , it is followed that

$$\int_{\boldsymbol{\Omega}} p^{pos}(\boldsymbol{\theta}) d\boldsymbol{\theta} = 1 \Rightarrow p^{pos}(\hat{\boldsymbol{\theta}}) \frac{(2\pi)^{n/2}}{\left| \frac{\partial^2 \Delta(\boldsymbol{\theta})}{\partial \boldsymbol{\theta}^2} \Big|_{\boldsymbol{\theta}=\hat{\boldsymbol{\theta}}} \right|^{1/2}} = 1 \quad (7.35)$$

Therefore,

$$I \approx h(\hat{\boldsymbol{\theta}}) \quad (7.36)$$

In other words, when  $p^{pos}(\boldsymbol{\theta})$  is densely distributed around  $\hat{\boldsymbol{\theta}}$  (or in loose terms the distribution has small uncertainties),  $p^{pos}(\boldsymbol{\theta})$  behaves similar to a Dirac delta function.

## Appendix 7.II: Finding the evidence

It is known that  $p(\mathbf{Y} = \mathbf{y}_{1:k}) = \int_{\Omega} l(\boldsymbol{\theta}, \mathbf{y}_{1:k}) p^{pri}(\boldsymbol{\theta}) d\boldsymbol{\theta}$ . Define

$\Sigma(\boldsymbol{\theta}) = -\Lambda(\boldsymbol{\theta}, \mathbf{y}_{1:k}) - \ln(p^{pri}(\boldsymbol{\theta}))$ ; it follows that

$$p(\mathbf{y}_{1:k}) = \int_{\Omega} e^{-\Sigma(\boldsymbol{\theta})} d\boldsymbol{\theta} \quad (7.37)$$

The Taylor series expansion of  $\Sigma(\boldsymbol{\theta})$  around  $\hat{\boldsymbol{\theta}}$  yields:

$$\Sigma(\boldsymbol{\theta}) \approx \Sigma(\hat{\boldsymbol{\theta}}) + \left. \frac{\partial \Sigma(\boldsymbol{\theta})}{\partial \boldsymbol{\theta}} \right|_{\boldsymbol{\theta}=\hat{\boldsymbol{\theta}}} (\boldsymbol{\theta} - \hat{\boldsymbol{\theta}}) + \frac{1}{2} (\boldsymbol{\theta} - \hat{\boldsymbol{\theta}})^T \left. \frac{\partial^2 \Sigma(\boldsymbol{\theta})}{\partial \boldsymbol{\theta}^2} \right|_{\boldsymbol{\theta}=\hat{\boldsymbol{\theta}}} (\boldsymbol{\theta} - \hat{\boldsymbol{\theta}}) \quad (7.38)$$

It can be followed from Eq. (7.8) that  $\Delta(\boldsymbol{\theta}) = -\ln(p^{pos}(\boldsymbol{\theta})) = -\ln(c) + \Sigma(\boldsymbol{\theta})$ , in which

$\Delta(\boldsymbol{\theta})$  is the minus log *a posteriori* PDF defined in Eq. (7.29). Suppose  $\hat{\boldsymbol{\theta}}$  is the MAP

estimate; therefore,  $\left. \frac{\partial \Sigma(\boldsymbol{\theta})}{\partial \boldsymbol{\theta}} \right|_{\boldsymbol{\theta}=\hat{\boldsymbol{\theta}}} = \left. \frac{\partial \Delta(\boldsymbol{\theta})}{\partial \boldsymbol{\theta}} \right|_{\boldsymbol{\theta}=\hat{\boldsymbol{\theta}}} = \mathbf{0}$ , and  $\left. \frac{\partial^2 \Sigma(\boldsymbol{\theta})}{\partial \boldsymbol{\theta}^2} \right|_{\boldsymbol{\theta}=\hat{\boldsymbol{\theta}}} = \left. \frac{\partial^2 \Delta(\boldsymbol{\theta})}{\partial \boldsymbol{\theta}^2} \right|_{\boldsymbol{\theta}=\hat{\boldsymbol{\theta}}} > \mathbf{0}$ .

Substitution of Eq. (7.38) into Eq. (7.37) results in:

$$p(\mathbf{y}_{1:k}) \approx e^{-\Sigma(\hat{\boldsymbol{\theta}})} \int_{\Omega} e^{-\frac{1}{2} (\boldsymbol{\theta} - \hat{\boldsymbol{\theta}})^T \left. \frac{\partial^2 \Sigma(\boldsymbol{\theta})}{\partial \boldsymbol{\theta}^2} \right|_{\boldsymbol{\theta}=\hat{\boldsymbol{\theta}}} (\boldsymbol{\theta} - \hat{\boldsymbol{\theta}})} d\boldsymbol{\theta} = \frac{(2\pi)^{n/2}}{\left| \left. \frac{\partial^2 \Sigma(\boldsymbol{\theta})}{\partial \boldsymbol{\theta}^2} \right|_{\boldsymbol{\theta}=\hat{\boldsymbol{\theta}}} \right|^{1/2}} l(\hat{\boldsymbol{\theta}}, \mathbf{y}_{1:k}) p^{pri}(\hat{\boldsymbol{\theta}}) \quad (7.39)$$

Assuming a normal distribution for the *a priori* PDF, the term  $\left. \frac{\partial^2 \Sigma(\boldsymbol{\theta})}{\partial \boldsymbol{\theta}^2} \right|_{\boldsymbol{\theta}=\hat{\boldsymbol{\theta}}}$  can be

expressed as

$$\left. \frac{\partial^2 \Sigma(\boldsymbol{\theta})}{\partial \boldsymbol{\theta}^2} \right|_{\boldsymbol{\theta}=\hat{\boldsymbol{\theta}}} = - \left. \frac{\partial^2 \Lambda(\boldsymbol{\theta}, \mathbf{y}_{1:k})}{\partial \boldsymbol{\theta}^2} \right|_{\boldsymbol{\theta}=\hat{\boldsymbol{\theta}}} + \mathbf{P}_0^{-1} \quad (7.40)$$

where  $\mathbf{P}_0$  is the *a priori* covariance matrix of  $\boldsymbol{\theta}$ . According to Eqs. (7.4) and (7.5), the likelihood function is Gaussian, i.e.,

$$\Lambda(\boldsymbol{\theta}, \mathbf{y}_{1:k}) = \ln(l(\boldsymbol{\theta}, \mathbf{y}_{1:k})) = \ln\left(\frac{1}{(2\pi)^{kn_y/2} |\mathbf{R}|^{k/2}}\right) - \frac{1}{2} \sum_{i=1}^k (\mathbf{y}_i - \hat{\mathbf{y}}_i(\boldsymbol{\theta}))^T \mathbf{R}^{-1} (\mathbf{y}_i - \hat{\mathbf{y}}_i(\boldsymbol{\theta})) \quad (7.41)$$

Therefore, the term  $\frac{\partial^2 \Lambda(\boldsymbol{\theta}, \mathbf{y}_{1:k})}{\partial \boldsymbol{\theta}^2}$  in Eq. (7.40) can be further expressed as

$$\begin{aligned} \frac{\partial^2 \Lambda(\boldsymbol{\theta}, \mathbf{y}_{1:k})}{\partial \boldsymbol{\theta}^2} &= \frac{\partial}{\partial \boldsymbol{\theta}} \left( \frac{\partial \Lambda(\boldsymbol{\theta}, \mathbf{y}_{1:k})}{\partial \boldsymbol{\theta}} \right)^T \\ &= - \sum_{i=1}^k \left( \frac{\partial \hat{\mathbf{y}}_i(\boldsymbol{\theta})}{\partial \boldsymbol{\theta}} \right)^T \mathbf{R}^{-1} \left( \frac{\partial \hat{\mathbf{y}}_i(\boldsymbol{\theta})}{\partial \boldsymbol{\theta}} \right) + \sum_{i=1}^k \frac{\partial}{\partial \boldsymbol{\theta}} \left( \frac{\partial \hat{\mathbf{y}}_i(\boldsymbol{\theta})}{\partial \boldsymbol{\theta}} \right)^T \mathbf{R}^{-1} (\mathbf{y}_i - \hat{\mathbf{y}}_i(\boldsymbol{\theta})) \end{aligned} \quad (7.42)$$

The first term in the right-hand side of Eq. (7.42) is the Fisher Information matrix (see Appendix 7.III for proof). The term  $\frac{\partial}{\partial \boldsymbol{\theta}} \left( \frac{\partial \hat{\mathbf{y}}_i(\boldsymbol{\theta})}{\partial \boldsymbol{\theta}} \right)^T = \frac{\partial^2 \hat{\mathbf{y}}_i(\boldsymbol{\theta})}{\partial \boldsymbol{\theta}^2}$  is the second order sensitivities of the FE predicted response with respect to the material parameters, and is a 3<sup>rd</sup> order  $n_{\boldsymbol{\theta}} \times n_{\boldsymbol{\theta}} \times n_y$  tensor and is shown by  $\mathbf{J}(\boldsymbol{\theta}, \mathbf{y}_{1:k})$  hereafter. Therefore,

$$\frac{\partial^2 \Lambda(\boldsymbol{\theta}, \mathbf{y}_{1:k})}{\partial \boldsymbol{\theta}^2} = -\mathbf{I}(\boldsymbol{\theta}) + \mathbf{J}(\boldsymbol{\theta}, \mathbf{y}_{1:k}) \quad (7.43)$$

where  $\mathbf{J}(\boldsymbol{\theta}, \mathbf{y}_{1:k}) = \sum_{i=1}^k \frac{\partial^2 \hat{\mathbf{y}}_i(\boldsymbol{\theta})}{\partial \boldsymbol{\theta}^2} \mathbf{R}^{-1} (\mathbf{y}_i - \hat{\mathbf{y}}_i(\boldsymbol{\theta}))$ . Substitution of Eq. (7.43) into Eq. (7.40)

results:

$$\frac{\partial^2 \Sigma(\boldsymbol{\theta})}{\partial \boldsymbol{\theta}^2} = \mathbf{I}(\boldsymbol{\theta}) + \mathbf{P}_0^{-1} - \mathbf{J}(\boldsymbol{\theta}) \quad (7.44)$$

It should be noted that for large number of data samples (i.e., large  $k$ ), the term

$$E_{\mathbf{Y}|\Theta}[\mathbf{J}(\boldsymbol{\theta}, \mathbf{y}_{1:k})] = \sum_{i=1}^k \frac{\partial^2 \hat{\mathbf{y}}_i(\boldsymbol{\theta})}{\partial \boldsymbol{\theta}^2} \mathbf{R}^{-1} E_{\mathbf{Y}|\Theta}[(\mathbf{y}_i - \hat{\mathbf{y}}_i(\boldsymbol{\theta}))] = \mathbf{0}, \text{ and therefore, } \frac{\partial^2 \Lambda(\boldsymbol{\theta}, \mathbf{y}_{1:k})}{\partial \boldsymbol{\theta}^2}$$

merges asymptotically to  $-\mathbf{I}(\boldsymbol{\theta})$ . This conclusion is consistent with the definition of the FIM as stated in Eq. (7.9), i.e.,

$$-E_{\mathbf{Y}|\Theta} \left[ \frac{\partial^2 \Lambda(\boldsymbol{\theta}, \mathbf{y}_{1:k})}{\partial \boldsymbol{\theta}^2} \right] = \mathbf{I}(\boldsymbol{\theta}) \quad (7.45)$$

In conclusion, the term  $\mathbf{J}(\boldsymbol{\theta})$  reflects the misfit effects between the FE model predictions and measurements, which merges zero under ideal estimation conditions (i.e., large number of informative data sets, no model uncertainties, independent Gaussian measurement noise, etc.). Considering asymptotic behavior, Eq. (7.44) results in the inverse of *a posteriori* Cramér–Rao lower bound [43] for  $k$  large enough:

$$\frac{\partial^2 \Sigma(\boldsymbol{\theta})}{\partial \boldsymbol{\theta}^2} \sim \mathbf{I}(\boldsymbol{\theta}) + \mathbf{P}_0^{-1} \quad (7.46)$$

The *a posteriori* Cramér–Rao lower bound can be interpreted as the lower bound for covariance matrix of a MAP estimation problem. The term  $\mathbf{P}_0^{-1}$  indicates the contribution of the *a priori* information; if the *a priori* PDF of  $\boldsymbol{\theta}$  is sufficiently flat and close to uniform (non-informative prior), then  $\mathbf{P}_0^{-1} \rightarrow \mathbf{0}$ , and consequently the *a posteriori* CRLB merges to the regular CRLB.

Substitution of Eq. (7.44) back into Eq. (7.39) results in:

$$p(\mathbf{Y} = \mathbf{y}_{1:k}) \approx \frac{(2\pi)^{n/2} l(\hat{\boldsymbol{\theta}}, \mathbf{y}_{1:k}) p^{pri}(\hat{\boldsymbol{\theta}})}{|\mathbf{I}(\hat{\boldsymbol{\theta}}) + \mathbf{P}_0^{-1} - \mathbf{J}(\hat{\boldsymbol{\theta}})|^{1/2}} \quad (7.47)$$

### Appendix 7.III: Derivation of the Fisher Information Matrix

The FIM is defined in Eq. (7.9) as  $\mathbf{I}(\boldsymbol{\theta}) = E_{\mathbf{Y}|\boldsymbol{\theta}} \left[ \left( \frac{\partial \Lambda(\boldsymbol{\theta}, \mathbf{y}_{1:k})}{\partial \boldsymbol{\theta}} \right)^T \left( \frac{\partial \Lambda(\boldsymbol{\theta}, \mathbf{y}_{1:k})}{\partial \boldsymbol{\theta}} \right) \right]$ ,

where the log-likelihood function is shown in Eq. (7.41). Therefore, The FIM can be asymptotically derived as

$$\begin{aligned}
 \mathbf{I}(\boldsymbol{\theta}) &= E \left( \left( \frac{\partial \Lambda(\boldsymbol{\theta}, \mathbf{y}_{1:k})}{\partial \boldsymbol{\theta}} \right)^T \left( \frac{\partial \Lambda(\boldsymbol{\theta}, \mathbf{y}_{1:k})}{\partial \boldsymbol{\theta}} \right) \right) \\
 &= E \left( \sum_{i=1}^k \left( \frac{\partial \hat{\mathbf{y}}_i(\boldsymbol{\theta})}{\partial \boldsymbol{\theta}} \right)^T \mathbf{R}^{-1} (\mathbf{y}_i - \hat{\mathbf{y}}_i(\boldsymbol{\theta})) \sum_{j=1}^k (\mathbf{y}_j - \hat{\mathbf{y}}_j(\boldsymbol{\theta}))^T \mathbf{R}^{-1} \left( \frac{\partial \hat{\mathbf{y}}_j(\boldsymbol{\theta})}{\partial \boldsymbol{\theta}} \right) \right) \quad (7.48) \\
 &= \sum_{i=1}^k \sum_{j=1}^k \left( \frac{\partial \hat{\mathbf{y}}_i(\boldsymbol{\theta})}{\partial \boldsymbol{\theta}} \right)^T \mathbf{R}^{-1} \underbrace{E \left( (\mathbf{y}_i - \hat{\mathbf{y}}_i(\boldsymbol{\theta})) (\mathbf{y}_j - \hat{\mathbf{y}}_j(\boldsymbol{\theta}))^T \right)}_{=\mathbf{R}\delta_{ij}} \mathbf{R}^{-1} \left( \frac{\partial \hat{\mathbf{y}}_j(\boldsymbol{\theta})}{\partial \boldsymbol{\theta}} \right) \sim \sum_{i=1}^k \left( \frac{\partial \hat{\mathbf{y}}_i(\boldsymbol{\theta})}{\partial \boldsymbol{\theta}} \right)^T \mathbf{R}^{-1} \left( \frac{\partial \hat{\mathbf{y}}_i(\boldsymbol{\theta})}{\partial \boldsymbol{\theta}} \right)
 \end{aligned}$$

## References

- [1] J. Teergele and K. Danai, "Selection of Outputs for Distributed Parameter Systems by Identifiability Analysis in the Time-scale Domain," *International Journal of Systems Science*, vol. 46, no. 16, p. 2939-2954, 2015.
- [2] L. Ljung and T. Glad, "On Global Identifiability for Arbitrary Model Parametrizations," *Automatica*, vol. 30, no. 2, p. 265-276, 1994.
- [3] R. K. Mehra, "Optimal Input Signals for Parameter Estimation in Dynamic Systems - Survey and New Results," *IEEE Transactions on Automatic Control*, vol. 19, no. 6, p. 753-768, 1974.
- [4] A. Raue, V. Becker, U. Klingmüller, and J. Timmer, "Identifiability and Observability Analysis for Experimental Design," *Chaos*, vol. 20, no. 4, p. 045105-1-8, 2010.
- [5] J. J. DiStefano and C. Cobelli, "On Parameter and structural identifiability: Nonunique observability/reconstructibility for identifiable systems, other ambiguities, and new definitions," *IEEE Transactions on Automatic Control*, vol. 25, no. 4, p. 830-833, 1980.
- [6] V. V. Nguyen and E. F. Wood, "Review and Unification of Linear Identifiability Concepts," *SIAM Review*, vol. 24, no. 1, p. 34-51, 1982.
- [7] E. T. Tunali and T.-J. Tarn, "New Results for Identifiability of Nonlinear Systems," *IEEE Transactions on Automatic Control*, vol. 32, no. 2, p. 146-154, 1987.
- [8] J. G. Reid, "Structural Identifiability in Linear Time-invariant Systems," *IEEE Transactions on Automatic Control*, vol. 22, no. 2, p. 242-246, 1977.
- [9] J. A. Jacquez and P. Greif, "Numerical Parameter Identifiability and Estimability: Integrating Identifiability, Estimability, and Optimal Sampling Design," *Mathematical Biosciences*, vol. 77, p. 201-227, 1985.
- [10] X. Xia and C. H. Moog, "Identifiability of Nonlinear Systems With Application to HIV/AIDS Models," *IEEE Transaction on Automatic Control*, vol. 48, no. 2, p. 330-336, 2003.
- [11] R. Bellman and K. J. Astrom, "On Structural Identifiability," *Mathematical Biosciences*, vol. 7, p. 329-339, 1970.
- [12] R. M. Staley and P. C. Yue, "On System Parameter Identifiability," *Information Science*, vol. 2, p. 127-138, 1970.

- [13] T. J. Rothenberg, "Identification in Parametric Models," *Econometrica*, vol. 39, no. 3, p. 577-591, 1971.
- [14] R. Bowden, "The Theory of Parametric Identification," *Econometrica*, vol. 41, no. 6, p. 1069-1074, 1973.
- [15] L. S. Katafygiotis and J. L. Beck, "Updating Models and Their Uncertainties. Part II: Model Identifiability," *ASCE Journal of Engineering Mechanics*, vol. 124, no. 4, p. 463-467, 1998.
- [16] L. S. Katafygiotis, C. Papadimitriou, and H.-F. Lam, "A Probabilistic Approach to Structural Model Updating," *Soil Dynamics and Earthquake Engineering*, vol. 17, no. 7-8, p. 495-507, 1998.
- [17] D. S. Bayard, F. Y. Hadaegh, and D. R. Meldrum, "Optimal Experiment Design for Identification of Large Space Structures," *Automatica*, vol. 24, no. 3, p. 357-364, 1988.
- [18] D. C. Kammer, "Sensor Placement for On-Orbit Modal Identification and Correlation of Large Space Structures," *Journal of Guidance, Control, and Dynamics*, vol. 14, no. 2, p. 251-259, 1991.
- [19] P. H. Kirkegaard and R. Brincker, "On the Optimal Location of Sensors for Parametric Identification of Linear Structural Systems," *Mechanical Systems and Signal Processing*, vol. 8, no. 6, p. 639-647, 1994.
- [20] F. E. Udawadia, "Methodology for Optimum Sensor Locations for Parameter Identification in Dynamic Systems," *ASCE Journal of Engineering Mechanics*, vol. 120, no. 2, p. 368-390, 1994.
- [21] E. Heredia-Zavoni and L. Esteva, "Optimal Instrumentation of Uncertain Structural systems Subject to Earthquake Ground Motions," *Earthquake Engineering and Structural Dynamics*, vol. 27, no. 4, p. 343-362, 1998.
- [22] C. Papadimitriou, J. L. Beck, and S.-K. Au, "Entropy-Based Optimal Sensor Location for Structural Model Updating," *Journal of Vibration and Control*, vol. 6, no. 5, p. 781-800, 2000.
- [23] C. Papadimitriou, "Optimal Sensor Placement Methodology for Parametric Identification of Structural Systems," *Journal of Sound and Vibration*, vol. 278, no. 4-5, p. 923-947, 2004.
- [24] C. Papadimitriou and G. Lombaert, "The Effect of Prediction Error Correlation on Optimal Sensor Placement in Structural Dynamics," *Mechanical Systems and Signal Processing*, vol. 28, p. 105-127, 2012.
- [25] K.-V. Yuen and S.-C. Kuok, "Efficient Bayesian Sensor Placement Algorithm for Structural Identification: a General Approach for Multi-Type Sensory Systems,"



- Earthquake Engineering and Structural Dynamics*, vol. 44, no. 5, p. 757-774, 2015.
- [26] H. M. Chow, H. F. Lam, T. Yin, and S. K. Au, "Optimal Sensor Configuration of a Typical Transmission Tower for the Purpose of Structural Model Updating," *Structural Control and Health Monitoring*, vol. 18, no. 3, p. 305-320, 2011.
- [27] M. N. Chatzis, E. N. Chatzi, and A. W. Smyth, "On the Observability and Identifiability of Nonlinear Structural and Mechanical Systems," *Structural Control and Health Monitoring*, vol. 22, no. 3, p. 574-593, 2015.
- [28] K. Danai, S. A. Civjan, and M. M. Styckiewicz, "Sensor Location Selection for Structures via Identifiability Analysis in the Time-scale Domain," *Journal of Sound and Vibration*, vol. 332, no. 24, p. 6296-6311, 2013.
- [29] R. Astroza, H. Ebrahimian, and J. P. Conte, "Material Parameter Identification in Distributed Plasticity FE Models of Frame-Type Structures Using Nonlinear Stochastic Filtering," *ASCE Journal of Engineering Mechanics*, Vols. 10.1061/(ASCE)EM.1943-7889.0000851, p. 04014149: 1-14, 2014.
- [30] H. Ebrahimian, R. Astroza and J. P. Conte, "Extended Kalman Filter for Material Parameter Estimation in Nonlinear Structural Finite Element Models using Direct Differentiation Method," *Earthquake Engineering and Structural Dynamics*, vol. 44, no. 10, p. 1495-1522, 2015.
- [31] H. Ebrahimian, R. Astroza, J. P. Conte and R. A. de Callafon, "Nonlinear Finite Element Model Updating for Damage Identification of Civil Structures using Batch Bayesian Estimation," *Mechanical Systems and Signal Processing*, vol. in review, 2015.
- [32] R. Astroza, H. Ebrahimian, and J. P. Conte, "Nonlinear Structural Finite Element Model Updating Using Stochastic Filtering," in *Model Validation and Uncertainty Quantification, Proceedings of 33rd IMAC*, Orlando, FL, 2015.
- [33] H. Ebrahimian, R. Astroza, and J. P. Conte, "Nonlinear Structural Finite Element Model Updating using Batch Bayesian Estimation," in *Model Validation and Uncertainty Quantification, Proceedings of 33rd IMAC*, Orlando, FL, 2015.
- [34] T. M. Cover and J. A. Thomas, *Elements of Information Theory*, Hoboken, N.J.: John Wiley & Sons, 2006.
- [35] A. K. Chopra, *Dynamics of Structures: Theory and Applications to Earthquake Engineering*, Englewood Cliffs, New Jersey: Prentice-Hall, Inc., 4th Ed., 2012.
- [36] J. L. Beck and L. S. Katafygiotis, "Updating Models and their Uncertainties. Part I: Bayesian Statistical Framework," *ASCE Journal of Engineering Mechanics*, vol. 124, no. 4, p. 455-461, 1998.

- [37] H. Cramer, *Mathematical Methods of Statistics*, Princeton, N.J.: Princeton University Press, 1946.
- [38] T. K. Moon and W. C. Stirling, *Mathematical Methods and Algorithms for Signal Processing*, Upper Saddle River, N.J.: Prentice-Hall, 2000.
- [39] G. C. Goodwin and R. L. Payne, *Dynamic System Identification: Experiment Design and Data Analysis*, New York: Academic Press, 1977.
- [40] N. A. Ahmed and D. V. Gokhale, "Entropy Expressions and their Estimators for Multivariate Distributions," *IEEE Transactions on Information Theory*, vol. 35, no. 3, p. 688-692, 1989.
- [41] A. J. W. Duijndam, "Bayesian Estimation in Seismic Inversion. Part II: Uncertainty Analysis," *Geophysical Prospecting*, vol. 36, no. 8, p. 899-918, 1988.
- [42] A. Tarantola, *Inverse Problem Theory and Methods for Model Parameter Estimation*, Philadelphia, PA: Society for Industrial and Applied Mathematics, 2005.
- [43] H. L. Van Trees, *Optimum Array Processing, Part IV of Detection, Estimation, and Modulation Theory*, New York, NY: John Wiley & Sons, 2002.
- [44] OpenSees, "Open System for Earthquake Engineering Simulation," [Online]. Available: <http://opensees.berkeley.edu/>. [Accessed 10 2014].
- [45] International Code Council, 2012 international building code, Country Club Hills, 2011.
- [46] F. F. Taucer, E. Spacone, and F. C. Filippou, "A Fiber Beam-Column Element for Seismic Response Analysis of Reinforced Concrete Structures," UBC/EERC-91/17, Earthquake Engineering Research Center, College of Engineering, UC Berkeley, Berkeley, CA., 1991.
- [47] F. C. Filippou, E. P. Popov, and V. V. Bertero, "Effects of Bond Deterioration on Hysteretic Behavior of Reinforced Concrete Joints," EERC Report 83-19, Earthquake Engineering Research Center, College of Engineering, UC Berkeley, Berkeley, CA, 1983.
- [48] T. A. Balan, F. C. Filippou, and E. P. Popov, "Constitutive Model for 3D Cyclic Analysis of Concrete Structures," *ASCE Journal of Engineering Mechanics*, vol. 123, no. 2, p. 143-153, 1997.
- [49] A. Zona, M. Barbato, and J. P. Conte, "Finite Element Response Sensitivity Analysis of Continuous Steel-Concrete Composite Girders," *Steel and Composite Structures*, vol. 6, no. 3, p. 183-202, 2006.
- [50] "Center for Engineering Strong Motion Data, CESMD - A Cooperative Effort,"

[Online]. Available: <http://strongmotioncenter.org/>. [Accessed September 2014].

- [51] K. Breitung, "Asymptotic Approximations for Probability Integrals," *Probabilistic Engineering Mechanics*, vol. 4, no. 4, p. 187-190, 1989.

## **CHAPTER 8: CONCLUSIONS**

### **8.1. Summary of research work performed and novel contributions**

The research work presented in this dissertation was focused on development of an advanced nonlinear system and damage identification (ID) framework for structural health monitoring (SHM). This framework is based on high-fidelity mechanics-based nonlinear finite element (FE) model updating. The proposed framework in this research provides a transformative methodology that will eventually be capable of real-world application on large and complex civil infrastructures.

The research work was mainly divided into two parts. The first part is the object of Chapters 2 and 3. It systematically studies the fidelity and accuracy of state-of-the-art FE modeling approaches in predicting the actual behavior of reinforced concrete structural components and systems. In chapter 2, the experimental results of three reinforced concrete (RC) test sub-assemblies were compared with numerical simulation results obtained using an advanced nonlinear FE modeling approach. Chapter 3 presented the pre-test FE modeling and response simulation of a full-scale

five-story RC building specimen tested on the NEES-UCSD shake table. The likely shortcomings of the employed FE modeling technique were investigated. Comparisons were made between the FE prediction and experimental measurement of selected structural response parameters from the global structural level to the local member, sub-member, and concrete crack levels for base excitations of increasing intensity. Considering the near real-world conditions of the test specimen, this study provided a unique opportunity to identify the main sources of inaccuracy and uncertainty of state-of-the-art nonlinear FE modeling of RC building structures.

The second part of the research, which is covered in Chapters 4 through 7, was focused on developing, evaluating, and further extending the proposed SHM and damage ID framework. Chapter 4 drafted a novel framework for nonlinear finite element (FE) model updating. In this framework, the extended Kalman filter (EKF) method is utilized jointly with advanced nonlinear structural FE modeling and analysis methods to estimate the time-invariant parameters of the material constitutive laws used in the FE structural model. The parameter estimation procedure required the computation of the structural response sensitivities with respect to the material parameters. This was achieved using the direct differentiation method (DDM). Therefore, the proposed framework took advantage of three existing analytical tools: nonlinear FE methodology using fiber-section displacement-based beam-column elements as the structural modeling and analysis tool, the EKF as the parameter estimation method, and the DDM for FE response sensitivity computation. Furthermore, the performance of the proposed framework in terms of convergence,

accuracy, and robustness was investigated through two validation case studies based on numerically simulated structural response data.

A different framework for nonlinear system identification, SHM, and damage ID of civil structures was presented in Chapter 5. This framework utilized an extended maximum likelihood (ML) estimation method to estimate FE model parameters. Additionally, this framework facilitated the estimation of simulation error variances and enabled the updating of the nonlinear FE model of the structure based on input-output data measured during a damage-inducing earthquake. The parameter estimation uncertainties were quantified using the Cramer-Rao lower bound (CRLB) theorem. Two methods to approximate the CRLB analytically and/or numerically were presented in this chapter. The first method estimated the CRLB based on the analytically exact Fisher information matrix (FIM). The second method approximated the FIM through the Hessian computation of the extended ML objective function. The accuracy of these two approaches for parameter uncertainty quantification was investigated using a deterministic sampling approach in the context of an application example. In addition, the advantage of the proposed nonlinear FE model parameter estimation framework over the traditional least squares method was highlighted by considering heterogeneous output measurements. The proposed estimation procedure was able to systematically extract information from the heterogeneous measured data and estimate the FE model parameters, while the traditional least squares method fell short of extracting information consistently from all measurement data. Moreover, different cases were studied in this chapter to investigate the performance limits of the

proposed framework under extreme measurement noise conditions and exaggerated (way-out) initial estimates of the model parameters to be estimated. Furthermore, the detrimental effects of input measurement noise and modeling uncertainty on the performance of the proposed nonlinear FE model updating were investigated and quantified.

Chapter 6 extended, in an innovative way, the proposed framework for nonlinear FE model updating using input-output data to a framework using output data only. This extension not only overcomes the shortcomings of the initially proposed framework in handling unmeasured, erroneous, or noisy input measurements, but also paves the way to a more general approach for addressing FE modeling uncertainty. Grounded in Bayesian inference, the proposed output-only nonlinear FE model updating approach estimates jointly the FE model parameters and the input earthquake ground acceleration time histories using only the measured dynamic response of the structure. Two data fusion approaches were presented in Chapter 6 to solve the augmented input and parameter estimation problem: (a) the recursive maximum likelihood (ML) estimation approach, which reduces to solving a nonlinear optimization problem, and (b) the stochastic filtering approach based on a recursive maximum *a posteriori* (MAP) estimation method, which reduces to an iterative extended Kalman filtering method. Both approaches required the computation of FE response sensitivities with respect to FE model parameters and the discrete input ground accelerations. For this purpose, the DDM was implemented in the open source structural analysis software framework, OpenSees, which was used for nonlinear FE

modeling and analysis and to compute the FE response sensitivities with respect to the input ground acceleration for the uniform base acceleration case. To validate the performance and evaluate the efficiency of the two proposed methods, numerically simulated structural response data were used for a three-dimensional five-story two-by-one bay RC frame building subjected to horizontal bidirectional seismic excitation. Although both methods were accurate in jointly estimating the model parameters and input ground acceleration, the recursive ML estimation method was found to be computationally more demanding than the recursive MAP method. Therefore, the stochastic filtering approach based on a recursive MAP estimation method was concluded to offer a computationally feasible framework with excellent estimation accuracy.

Finally, a new approach based on information theory for assessing the identifiability of FE model parameters in nonlinear FE model updating was proposed in Chapter 7. This approach is based on Bayesian inference and utilizes the Shannon Information entropy as a measure of inherent uncertainty in the model parameters. The difference in entropy between the prior and posterior probability distributions of the model parameters, which is referred to as entropy gain, is interpreted as the reduction in uncertainty of the model parameters and used as a measure of identifiability. The approach presented in this chapter offers a one-to-one measure of identifiability to evaluate the amount of information contained in each measurement dataset about each model parameter. Moreover, the proposed approach provides an excellent decision-support tool for selecting the model parameters to be identified, optimal sensor array



and location design, selection of measurement datasets, and experiment design. In this chapter, an approximate expression for the entropy gain was derived under some regularizing assumptions (i.e., estimator unbiasedness and efficiency, asymptotic conditions, etc.). The entropy gain was found to be an approximate function of: (a) the FIM, (b) the second order sensitivities of the FE predicted response with respect to the model parameters, (c) the simulation error (= the difference between the FE predicted and measured structural responses), and (d) the prior covariance matrix of the model parameters. Assuming a large number of measurement data (i.e., to satisfy the asymptotic conditions), the entropy gain was reduced to a function of the FIM and the prior covariance matrix. The FIM depends on the FE response sensitivities and the covariance matrix of the measurement noise, which can be estimated upfront through approximate quantification of the various noise sources affecting each measurement channel. A 3D five story reinforced concrete frame building model was used as a case study to illustrate the proposed identifiability assessment method. The FE model was dependent on nine model parameters characterizing the nonlinear material laws of reinforced concrete. The identifiability of the FE model parameters was evaluated by computing the gain in entropy of the model parameters for various measurement datasets. The approach presented in this chapter is not limited to structural system identification problems, but can be used for evaluating the identifiability of model parameters for any system. The one-to-one measure of identifiability between model parameters and measurement datasets and the time resolution (i.e., the entropy gain

time history for each individual parameter) were unique features of the proposed method that can be used in various applications from other engineering fields.

## **8.2. Summary of major findings and limitations of the research work**

The first part of this research work, which focused on nonlinear FE modeling and response simulation of RC structural subassemblies and systems, reveals important lessons about the shortcomings of state-of-the-art FE modeling techniques for RC structures. The response behavior of RC components, sub-assemblies, and structures is governed by complex physical phenomena. In order for a FE response simulation technique to be successful in predicting the actual response behavior of RC components and sub-assemblies, the following important physical phenomena, which are an inherent part of RC behavior, should be properly captured by the numerical modeling technique:

### **(1) Shear mechanism and shear failure in beam-column frame members.**

Shear mechanisms become more prominent at higher ductility demands and under poor detailing conditions. The formation of diagonal cracks over the web of frame components eliminates the continuity of the web concrete and results in deteriorated loading and unloading stiffness and reduced shear resistance of frame components under cyclic loading. Dowel action and deterioration of bond resistance in the longitudinal reinforcement are other consequences of

shear mechanisms in frame components. In the ultimate condition, the frame component exhibits a large transverse deformation along a main diagonal crack, loses stability, and fails in shear.

**(2) Bond-slip mechanism along the longitudinal and lateral reinforcements.**

Bond deterioration is more significant under cyclic loading conditions. The bond slippage along the longitudinal reinforcement deteriorates the composite action of the concrete and reinforcing steel resulting in reduced stiffness of the frame component. The deterioration of bond reduces the efficiency of the lateral reinforcement in confining the concrete core and controlling the diagonal crack propagation and ultimately results in shear failure of the frame components.

**(3) Dowel action of the longitudinal reinforcement.**

Dowel action provides the minimum lateral stiffness and shear resistance of the frame component at the neutral loading condition in the presence of large open flexural and diagonal (shear) cracks. Dowel action also accelerates bond slippage along the longitudinal reinforcing bars.

**(4) Pinching behavior of RC frame components under cyclic loading.**

The pinching behavior is a consequence of shear mechanisms, bond-slip mechanisms along both the longitudinal and lateral reinforcement, and dowel action.

Moreover, when the aim of FE modeling is to predict and simulate the response of a building structure to dynamic excitations (especially earthquakes), other system-level

sources of modeling uncertainty and inaccuracy come into play. If not addressed correctly, the following important aspects can cause significant bias in the FE predicted versus actual building response:

**(1) Kinematic interaction between structural and nonstructural components and systems (NCSs).**

This interaction is usually not considered in the FE simulation. It influences the lateral energy dissipation mechanism of the building, increases the measured stiffness of the building, affects the predominant period of the response time histories at the global structural level, and reduces the measured floor displacement demands compared to the FE predictions. As the intensity of the dynamic excitations increases, the NCSs suffer progressive damage, undergo stiffness and strength degradation, and therefore, their influence on the stiffness and strength of the structural system diminishes.

**(2) Energy dissipation mechanisms.**

These are usually modeled using the proportional Rayleigh damping model and are found to be a major source of uncertainty. The adequacy of the classical Rayleigh damping model for nonlinear time history analysis of structures is questionable. Moreover, the selection of the damping ratios and the implication of the proportional Rayleigh damping model are open problems that require further investigations.

**(3) Uncertainty related to the FE model parameters.**

The uncertainty of the FE model parameters is another source of discrepancy between FE predicted and measured responses. Such parameters include the inertia properties, gravity loading, damping properties, material constitutive model parameters, and boundary conditions.

The findings and conclusions that resulted from the first part of this research work led to development of nonlinear FE model updating procedures. These were the focal point of the second part of the research work. The research performed on the subject of nonlinear system and damage ID using nonlinear FE model updating resulted in the following major outcomes and findings:

- (1) Two novel frameworks for nonlinear FE model updating are proposed, developed, and validated using numerically simulated structural response data. The first framework is based on a recursive parameter estimation approach and uses the EKF to estimate FE model parameters. The second framework is based on batch Bayesian estimation and results in an extended maximum likelihood estimation to jointly estimate FE model parameters and measurement noise variances.
- (2) The two above-mentioned frameworks are developed under the following simplifying and idealizing assumptions and conditions, which may often be violated in real-world applications: (a) the dynamic input excitations are assumed to be known and noiseless (deterministic); (b) the effects of FE modeling uncertainties are neglected. In other words, the actual structure is assumed to belong to the FE model class used to estimate the parameters. In all

the validation studies performed in this research, the same FE model was used for the simulation and estimation. Therefore, no model uncertainty was considered; (c) the measurement noise processes at the various measurement channels are assumed to be independent Gaussian white noises. Moreover, it has been found that the input measurement noise and the model uncertainty can have strong detrimental effects on the performance and accuracy of the proposed FE model parameter estimation frameworks.

- (3) Through an innovative approach, the initially proposed framework is extended to account for the effects of unmeasured, erroneous, or noisy input excitations. The same approach can also be used to address the effects of modeling uncertainty. The proposed output-only framework is found to be accurate and efficient in jointly estimating FE model parameters and input excitations.
- (4) Validation of the developed input-output and output-only nonlinear FE model updating approaches was performed using realistic and progressively complicated structures: from a 2D cantilever steel bridge column to a 3D RC building structure designed according to current design procedures. However, the validation process in this research work was limited to numerically simulated structural response data and no real-world data were used to evaluate the performance of the proposed frameworks.
- (5) The correct estimation of the model parameters characterizing the nonlinear features of the structural response requires a strong enough dynamic excitation to exercise sufficiently the nonlinear branches of structural behavior. The

successful estimation of these material parameters can be evaluated through the identifiability assessment process.

- (6) An identifiability assessment method to evaluate the amount of information contained in a measurement dataset about each FE model parameter is obtained based on an information theoretic approach. This method has developed based on a set of restrictive theoretical assumptions (as stated in Chapter 7); however, it still provides a useful quantitative tool for model parameter selection, and optimal sensor types and sensor placement.

### **8.3. Recommendations for future research work**

- (1) Successful performance of the proposed SHM frameworks for real-world applications requires advancement of both FE modeling of civil structures and nonlinear parameter estimation approaches. To reduce the modeling uncertainty, FE modeling techniques need to be improved to closely capture the important mechanics and physical phenomena governing the actual behavior of civil structures, such as nonlinear shear-flexure interaction in beam-column elements, bond-slip mechanism, dowel action, and pinching behavior in RC structural components, and kinematic interaction between structural and NCSs. Therefore, the first recommendation for future work is to develop and validate more advanced modeling and simulation techniques for nonlinear FE response simulation of building and other civil structures.

- (2) The proposed nonlinear FE model updating frameworks should be further extended to incorporate the effects of modeling uncertainty. Modeling uncertainties arise from two sources: (a) incorrect or nonphysical modeling assumptions, which are not in agreement with the true physical conditions of the structure (e.g., nonphysical material constitutive models, incorrect modeling of energy dissipation mechanisms, restrictive kinematic assumptions, incorrect model geometry, incorrect boundary conditions, etc.), and (b) unmodeled physics, which are not included in the FE model (e.g., foundation flexibility, soil-structure interaction, non-structural components and systems, etc.).
- (3) The proposed nonlinear FE model updating frameworks should be further modified to account for the effects of non-white, non-Gaussian, and/or correlated measurement noise.
- (4) The proposed frameworks for nonlinear FE model updating should be validated using real-world data. For this purpose, the frameworks should be validated using large-scale shake table test data at the first stage. At the following stage, the validation should be performed with data recorded from real-world building structures during damaging earthquakes.
- (5) The application of the proposed frameworks should be extended from building structures to other civil infrastructures, such as bridges, dams, power plants, etc. The validation process is recommended to be performed in a two-stage



approach for these new applications, starting from simulated structural response data and then using data measured from real-world structures.

- (6) The proposed frameworks for SHM should be further advanced to include other damaging events besides earthquakes. Depending on the type of civil infrastructure, damaging events may include explosions, fires, impacts, terrorist attacks, hurricanes, tsunamis, etc.